AD-A056 811 HONEYWELL INC MINNEAPOLIS MINN SYSTEMS AND RESEARCH --ETC F/G 17/7
INDEPENDENT STABILITY AND CONTROL ANALYSIS OF NAVIGATION DEVELO--ETC(U).
JAN 78 R E POPE, M D WARD, M F BARRETT F04701-75-C-0135
UNCLASSIFIED 78SRC10-VOL-1 SAMSO-TR-78-74-VOL-1 NL

1 OF 4
ADA
056811

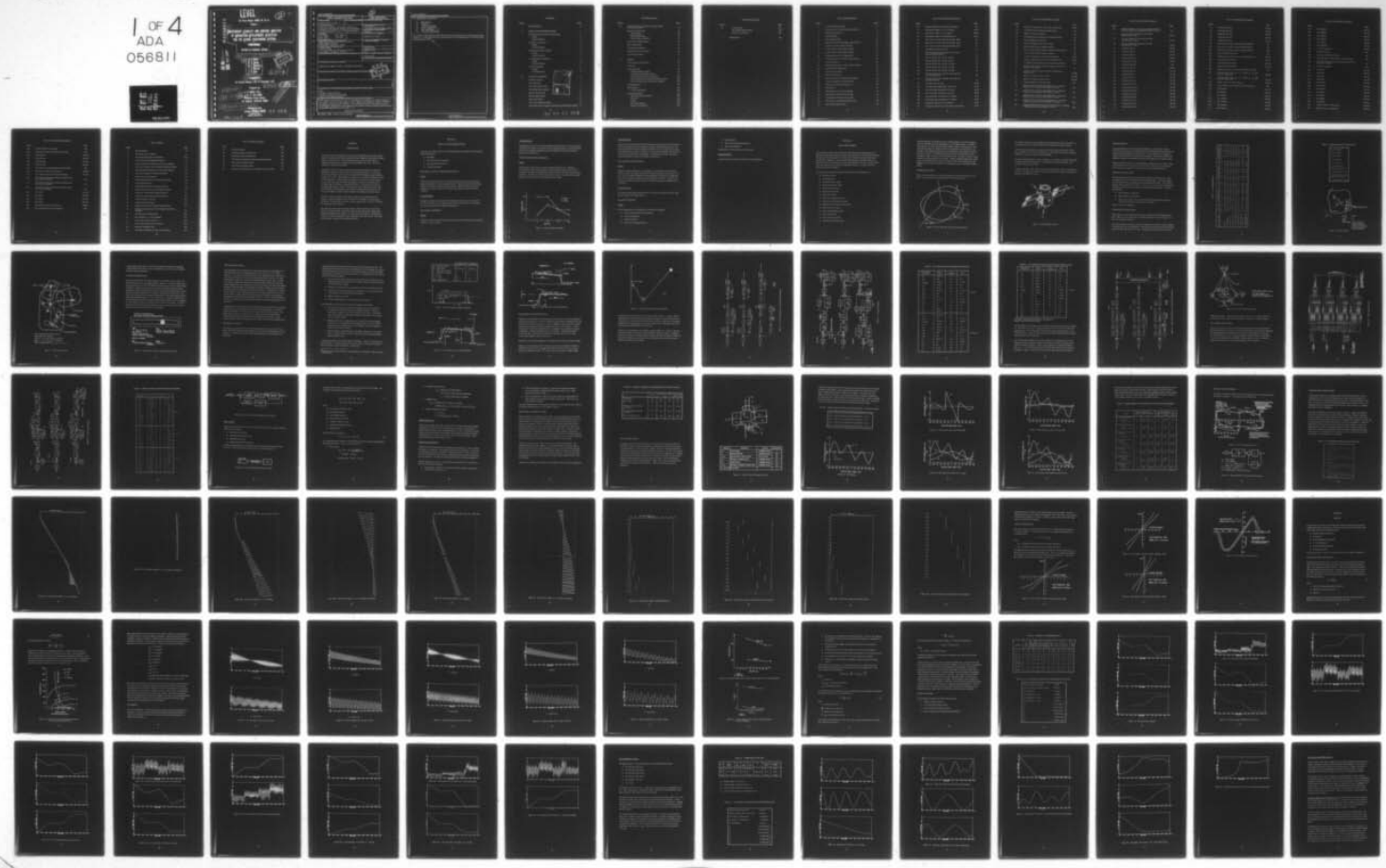

AD A056811

LEVEL II

(2)

Air Force Report SAMSO TR 78-74

Volume I

(6) INDEPENDENT STABILITY AND CONTROL ANALYSIS OF NAVIGATION DEVELOPMENT SATELLITES FOR THE GLOBAL POSITIONING SYSTEM. Volume I.

~~FINAL REPORT~~

VOLUME I: TECHNICAL REPORT.

AD No.
DDC FILE COPY

(9) Final rept 3 Feb 75-9 Sep 77

(10) R. E. POPE,
M. D. WARD,
M. F. BARRETT,
J. G. RUPERT
S. P. KAU

DDC
DRAFTED
JUL 28 1978
F

(12) 355 P.

(11) January 1978

For Period February 1975 to September 1977

(14) 78SRC10-VOL-1

(18) SAMSO

Prepared for

SAMSO (YEZ)
P. O. Box 92960
Worldway Postal Center
Los Angeles, California 90009

(19) TR-78-74-VOL-1

This document has been approved for public release and sale; its distribution is unlimited.

(15) F04701-75-C-0135

Honeywell
SYSTEMS & RESEARCH CENTER
2600 RIDGWAY PARKWAY
MINNEAPOLIS, MINNESOTA 55413

78 08 24 035

402 349

JUB

UNCLASSIFIED

SECURITY CLASSIFICATION OF THIS PAGE (WHEN DATA ENTERED)

(2)

REPORT DOCUMENTATION PAGE		READ INSTRUCTIONS BEFORE COMPLETING FORM
1. REPORT NUMBER SAMSO TR 78-74 VOL. I	2. GOV'T ACCESSION NUMBER	3. RECIPIENT'S CATALOG NUMBER
4. TITLE (AND SUBTITLE) Independent Stability and Control Analysis of Navigation Development Satellites for the Global Positioning System--Vol. I: Technical Report		5. TYPE OF REPORT/PERIOD COVERED Final Report 3 February 1975 to 9 Sept. 1977 6. PERFORMING ORG. REPORT NUMBER 78SRC10
7. AUTHOR(S) R. E. Pope J. G. Rupert M. D. Ward S. P. Kau M. F. Barrett		8. CONTRACT OR GRANT NUMBER(S) F04701-75-C-0135
9. PERFORMING ORGANIZATIONS NAME/ADDRESS Honeywell Systems and Research Center 2600 Ridgway Parkway Minneapolis, Minnesota 55413		10. PROGRAM ELEMENT, PROJECT, TASK AREA & WORK UNIT NUMBERS
11. CONTROLLING OFFICE NAME/ADDRESS SAMSO (YEZ) P.O. Box 92960, Worldway Postal Center Los Angeles, California 90009		12. REPORT DATE January 1978 13. NUMBER OF PAGES 354
14. MONITORING AGENCY NAME/ADDRESS (IF DIFFERENT FROM CONT. OFF.)		15. SECURITY CLASSIFICATION (OF THIS REPORT) Unclassified 15a. DECLASSIFICATION DOWNGRADING SCHEDULE

16. DISTRIBUTION STATEMENT (OF THIS REPORT)

Approved for public release; distribution unlimited.

DDC
RECEIVED
JUL 28 1978
F

17. DISTRIBUTION STATEMENT (OF THE ABSTRACT ENTERED IN BLOCK 20, IF DIFFERENT FROM REPORT)

18. SUPPLEMENTARY NOTES

19. KEY WORDS (CONTINUE ON REVERSE SIDE IF NECESSARY AND IDENTIFY BY BLOCK NUMBER)

GPS
Satellite attitude control
Satellite simulation and modeling
Control and stability analysis

20. ABSTRACT (CONTINUE ON REVERSE SIDE IF NECESSARY AND IDENTIFY BY BLOCK NUMBER)

This report documents the results of an independent stability and control analysis of the control systems and procedures of the navigation development satellite (NDS) for the global positioning system (GPS). The analysis consisted of detailed analytical investigation substantiated with sophisticated satellite system modeling and simulation of the following GPS mission events:

(continued on reverse)

HD-168 REV 11/74

DD FORM 1 JAN 73 1473 EDITION OF 1 NOV 55 IS OBSOLETE

UNCLASSIFIED

SECURITY CLASSIFICATION OF THIS PAGE (WHEN DATA ENTERED)

20. ABSTRACT (concluded)

- Spin phase,
- Despin,
- Earth acquisition,
- Panel deployment,
- Sun acquisition, and
- On-orbit operations.

The results of the analysis indicated satisfactory performance in all mission phases analyzed. A redesign of the jet control system was recommended to facilitate earth acquisition operations.

CONTENTS

Section		Page
I	INTRODUCTION	1
II	RESULTS AND RECOMMENDATIONS	2
	Spin Phase--Nutation Damper Performance	2
	Results	2
	Recommendations	2
	Spin Phase--Precession	2
	Results	2
	Recommendations	3
	Earth Acquisition/Reacquisition	3
	Results	3
	Recommendations	4
	Sun Acquisition/Reacquisition	4
	Results	4
	Recommendations	4
	On-Orbit Conditions	4
	Results	4
	Recommendations	5
III	MODEL DEVELOPMENT	6
	Reference Systems	7
	Mass Properties	9
	One-Body Dynamic Model	9
	Three-Body Dynamic Model	9
	Nutation Damper Model	13
	Spin Sun Sensor Model	14
	Reaction Jet Model	14
	Solar Array Deployment Model	17
	Control Electronics Assembly--Reaction Jet Control System Model	17

ACCESSION for
NTIS White Section
DDC Buff Section
UNANNOUNCED
JUSTIFICATION
BY
DISTRIBUTION/AVAILABILITY CODES
Dist. SPECIAL
A

78 07 24 035

CONTENTS (continued)

Section		Page
III	Control Electronics Assembly--Momentum Wheel Control System Model	22
	Solar Array Drive Model	24
	Motor Torques	28
	Model Simplification	30
	Pulse Frequency Modulator	30
	Solar Array Flexibility Model	31
	Solar Torque Model	32
	Reaction Wheel Dynamics	38
	Combined Earth Sensor Model	39
	Yaw Sun Sensor Model	50
IV	RESULTS	53
	Nutation Damper Performance	53
	Precession	55
	Earth Acquisition	63
	Despin Simulation Analysis	74
	Jet Control Loop Stability Analysis	81
	Earth Acquisition Simulation Analysis	116
	Earth Reacquisition and Despin Simulation Analysis	167
	CEA Jet Control System Preliminary Redesign	168
	Array Deployment	187
	Sun Acquisition	187
	+Y Array Deployment	222
	On-Orbit Operations	222
	Wheel Loop Stability Analysis	230
	Noon Turn	234
	Eclipse	235
	Momentum Dumping	263
	Failed Reaction Wheels	279

CONTENTS (concluded)

Section		Page
IV	Lunar Eclipse	292
	Jet Backup to Wheel Control	294
	Solar Array Autotrack	305
V	CONCLUSIONS	340

LIST OF ILLUSTRATIONS

Figure		Page
1	Earth Acquisition Envelope	3
2	Inertial and Local Vertical Reference Systems	7
3	Body Reference System	8
4	One-Body Model	11
5	Three-Body Structure	12
6	NDS and NTS-2 Nutation Damper Characteristics	13
7	Thruster Dynamic Response Modeling	16
8	0.1 lb Thruster versus Model Response	16
9	5.0 lb Thruster versus Model Response	17
10	Deployment Mechanism Linkage Model	18
11	Jet Control System--Analytical Block Diagram	19
12	Jet Control System	20
13	Wheel Control System--Analytical Block Diagram	23
14	Reaction Wheel Configuration	24
15	Wheel Control Concept	25
16	Wheel Control System	26
17	Solar Array Drive Functional Block Diagram	28
18	Torsional Spring Mass Damper System	28
19	Thermal Control Coating Properties	33
20	GPS Nominal	34
21	GPS Nominal with No Partial Shading	35
22	GPS Nominal and Worst Case C_P Shift	35
23	GPS Nominal and Worst Case C_M Shift	36
24	GPS Nominal and Combination Worst Cases	36
25	Motor Torque-Speed Curves	38

LIST OF ILLUSTRATIONS (continued)

Figure		Page
26	Simulation Model of Reaction Wheel Dynamics	38
27	Earth Sensor Output, p = q = 0.2 deg/sec	40-43
28	Earth Sensor Output, q = 0.2 deg/sec	44-45
29	Earth Sensor Output, Failed Roll Detector	46-49
30	Static Sensor Transfer Function Envelope, 200°K	50
31	Static Sensor Transfer Function Envelope, 220°K	51
32	Static Sensor Transfer Function Envelope, 250°K	51
33	Yaw Sun Sensor Characteristics	52
34	Nutation Damper Time Constant Estimates from Energy Sink Approximation	54
35	Nutation Damper Run, 95 rpm, Launch	56
36	Nutation Damper Run, 40 rpm, Launch	57
37	Nutation Damper Run, 95 rpm, On-Orbit	58
38	Nutation Damper Run, 40 rpm, On-Orbit	59
39	Nutation Damper Run, 20 rpm, On-Orbit	60
40	Nutation Damper Time Constant versus Spin Rate for Launch Condition	61
41	Nutation Damper Time Constant versus Spin Rate for Post AKM Burn	61
42	Precession Run, Nominal	65-66
43	Precession Run, High Thrust, Worst Case	66-67
44	Precession Run, Mismatch, Worst Case	68-69
45a	Precession Run, Low Thrust, Low Spin	69-70
45b	Precession Run, Low Thrust, B = 150 deg	71-72
45c	Precession Run, Low Thrust, B = 130 deg	72-73
46	Despin Run, Worst Case, 20 to 10 rpm	76-77
47	Despin Run, Worst Case, 10 to 6 rpm, Stowed Array	77-78

LIST OF ILLUSTRATIONS (continued)

Figure		Page
48	Despin Run, Worst Case, 16 to 1 rpm, Stowed Array	79-80
49	Jet Control System--Analytical Block Diagram	82
50	Single-Axis Jet Control Loop	83
51	Describing Function Equivalent of Nonlinear Element	84
52	Relay Describing Function Gain	84
53	Linearized Single-Axis Jet Control Loop	85
54	Roll Jet Control Loop Frequency Response	87
55	Pitch Jet Control Loop Frequency Response (Panels Stowed)	87
56	Yaw Jet Control Loop Frequency Response	88
57	Version 2 Acquisition Controller (Nominal Gain)	91-92
58	Version 2 Acquisition Controller (4 x Nominal Gain)	93-94
59	Describing Function Equivalent for Pseudo-Rate Modulator	95
60	Pitch Jet Control Loop Frequency Response with Saturation (Version 2 Acquisition)	97
61	Version 2 Acquisition from 10 Degrees with Saturation (Nominal Gain)	99-100
62	High Gain, 8 Degree, Initial Attitude	101-102
63	High Gain, 5 Degree, Initial Attitude	103-104
64	Coupled Roll/Pitch Jet Control Loops	105
65	Dominant Roll Jet Control Loop Eigenvalues as a Function of Spin Rate for Roll-Axis Control Only, Version 1	106
66	Dominant Roll Jet Control Loop Eigenvalues as a Function of Spin Rate for Roll-Axis Control Only, Version 2	107
67	Dominant Pitch Jet Control Loop Eigenvalues as a Function of Spin Rate for Pitch-Axis Control Only, Version 1	107
68	Dominant Pitch Jet Control Loop Eigenvalues as a Function of Spin Rate for Pitch-Axis Control Only, Version 2	108
69	Dominant Roll/Pitch Jet Control Loop Eigenvalues as a Function of Spin Rate for Roll/Pitch Control, Version 1	108

LIST OF ILLUSTRATIONS (continued)

Figure		Page
70	Dominant Roll/Pitch Jet Control Loop Eigenvalues as a Function of Spin Rate for Roll/Pitch Control, Version 2	109
71	Version 2 Roll/Pitch Acquisition Controller (Nominal Gain, 1 rpm)	110-111
72	Version 2 Roll/Pitch Acquisition Controller (Nominal Gain, 4 rpm)	112-113
73	Version 2 Roll/Pitch Acquisition Controller (Nominal Gain, 8 rpm)	114-115
74	Acquisition Run 1A	118-119
75	Acquisition Run 2A	120-121
76	Acquisition Run 2B	122-123
77	Acquisition Run 4B	124-125
78	Acquisition Run 4AP	126-127
79	Acquisition Run 4BP	128
80	Acquisition Run 7A	129-130
81	Acquisition Run 7B	131-132
82	Acquisition Run 8A	133-134
83	Acquisition Run 9A	135-136
84	Acquisition Run 11A	137-138
85	Acquisition Run 11B	139-140
86	Acquisition Run 11AP	141-142
87	Acquisition Run 11BP	143-144
88	Acquisition Run 12A	145-146
89	Acquisition Run 26A	147-148
90	Acquisition Run 13A	149-150
91	Acquisition Run 15B	151-152
92	Acquisition Run 14A	153-154

LIST OF ILLUSTRATIONS (continued)

Figure		Page
93	Acquisition Run 16A	155-156
94	Acquisition Run 17A	157-158
95	Acquisition Run 18A	159-160
96	Acquisition Run 19A	161-162
97	Acquisition Run 25A	163-164
98	Static Sensor Transfer Function Envelope (200°K)	165
99	Static Sensor Transfer Function Envelope (220°K)	166
100	Static Sensor Transfer Function Envelope (250°K)	166
101	Earth Acquisition Envelope	167
102	Despin Run, Worst Case 6 to 1 rpm, Deployed Array	169-170
103	Reacquisition Run RACQ-1	170-172
104	Reacquisition Run RACQ-2	173-174
105	Reacquisition Run RACQ-3	175-176
106	Preliminary Pitch Jet Loop Redesign (with Saturation)	178
107	Pitch Redesign (2 rpm, $\phi_{ic} = \theta_{ic} = 10$ deg, $\eta_{ic} = 2.3$ deg, ACQ 12A, High Gain)	179-182
108	Pitch Redesign (2 rpm, $\phi_{ic} = \theta_{ic} = 20$ deg, $\eta_{ic} = 2.3$ deg, ACQ 12A', High Gain)	183-186
109	Deploy-Y Panel, 1.0 rpm, Nominal	188-189
110	Sun Line/Spin Vector Orientation for Sun Acquisition	190
111	Run SACQ01A	193-195
112	Run SACQ02	195-197
113	Run SACQ03A	198-200
114	Run SACQ04A	200-202
115	Run SACQ05A	203-205
116	Run SACQ06A	205-206
117	Run SACQ07A	207-209

LIST OF ILLUSTRATIONS (continued)

Figure		Page
118	Run SACQ08A	209-211
119	Run SACQ09A	212-214
120	Run SACQ10A	214-216
121	Run SACQ11A	217-219
122	Run SACQ12A	219-221
123	Run SRACQ01A	223-225
124	+Y Array Deployment	226-229
125	Jet Control System	231
126	Single-Axis Wheel Control Loop	232
127	Roll/Pitch Wheel Control Loop Frequency Response	233
128	Yaw Wheel Control Loop Frequency Response (with Yaw Momentum Feedback)	233
129	Noon Turn Conditions	235
130	Run NT01A	237-240
131	Run NT02A	240-243
132	Run NT03A	244-247
133	Run NT04A	247-250
134	Run ECL01A	252-255
135	Run ECL02A	255-258
136	Run ECL03A	259-262
137	Run MD01A	266-268
138	Run MD02A	269-271
139	Run MD03A	272-274
140	Run MD04A	275-278
141	Wheel 2 Failure, Uncompensated	280-287
142	Wheel 2 Failure, Compensated	288-291

LIST OF ILLUSTRATIONS (concluded)

Figure		Page
143	General Geometry for Eclipses	292
144	Sun Sensor Temperature during Lunar Eclipse	293
145	Run LECL01A	295-296
146	Run LECL02A	297-299
147	Run LECL03A	299-301
148	Run LECL04A	302-304
149	Yaw Attitude for Sun Pointing (Sun in Orbit Plane)	305
150	Post Lunar Eclipse Array Autotrack	306-309
151	Jet Backup to Wheel Loop Transient Response	310-311
152	Pitch Wheel Control Loop Frequency Response (with Solar Panel Flexibility)	313
153	Roll Wheel Control Loop Frequency Response (with Solar Panel Flexibility)	314
154	Yaw Wheel Control Loop Frequency Response (with Solar Panel Flexibility)	315
155	Run SAF01	317-321
156	Run SAF02	321-325
157	Run SAF03	327-331
158	Run SAF04	331-335
159	Sun Acquisition with Flexible Arrays	336-339
160	Body Pitching Moment versus Spin Rate	339

LIST OF TABLES

Table		Page
1	Mass Properties	10
2	Mass Property Uncertainties	11
3	Jet Control Block Diagram Parameters	21-22
4	Wheel Control Block Diagram Parameters	27
5	Natural Frequency Comparisons, Test versus Models	32
6	Worst Case Center of Mass and Center of Pressure Shifts	34
7	Wheel Torque and Momentum for Two Orbit Conditions	37
8	CES Corridor Logic (Acquisition Mode Only)	39
9	Summary of Precession Runs	64
10	Off-Nominal Conditions for Precession Simulation	64
11	Despin Simulation Runs	75
12	Off-Nominal Conditions for Despin Simulation	75
13	Improved Linearized Jet Control Loop Parameters	86
14	Nominal Jet Loop Stability Analysis Summary	89
15	Acquisition and Reacquisition Simulation Runs	117
16	Control Loop Gain Variations	165
17	Reacquisition Run Summary	168
18	Improved Linearized Jet Control Loop Parameters	177
19	Stability Margin Comparison for Preliminary Pitch Loop Redesign	178
20	Sun Acquisition Simulation Runs	191
21	Mass Properties, -Y Array Deployed	192
22	Wheel Control Loop Parameters	232
23	Wheel Loop Stability Analysis Summary	234
24	Noon Turn Simulation Runs	236
25	Off-Nominal Conditions for Noon Turn Simulation	236

LIST OF TABLES (concluded)

Table		Page
26	Eclipse Simulation	251
27	Momentum Dump Jet Firing Times	264
28	Momentum Dump Simulation Runs	265
29	Off-Nominal Conditions for Momentum Dump Simulation	265
30	Wheel Failure Simulation Runs	279
31	Lunar Eclipse Simulation Runs	294
32	Solar Array Drive/Wheel/Array Flexibility Interaction Runs	316

SECTION I

INTRODUCTION

Since February 1975, Honeywell has conducted an independent analysis of the control systems and mission procedures associated with the Navigational Development Satellite (NDS). NDS is part of the NAVSTAR Global Positioning System (GPS) which is designed to ensure precise navigation coverage throughout the world. The prime contractor is Rockwell International.

During the course of the analysis, there have been numerous changes in NDS mass properties, components, characteristics, and mission procedures. The majority of the results presented in this report are based on NDS configuration and procedures defined July 15, 1977. Much of this data definition is the result of qualification testing of NDS components. Since programs of this type are continually in a state of flux, we were extremely concerned about maintaining a consistent, well-defined and, to as large a degree as possible, independent data base. In presenting the results of the independent analysis, we have cited the source and time period of all items that went into NDS model development and control and mission procedure analysis. We have also attempted to define all approximations and assumptions that were made.

Section II contains a summary of the major results and recommendations of the analysis. Model development for the NDS vehicle and components is presented in Section III. Section IV gives results in mission sequence order. Section V reiterates the conclusions of the analysis.

We would like to thank the three project officers, Major Jack Henry, Captain Jeff Quirk, and Captain Ed Butt, who provided the data necessary for the analysis and a thorough questioning of the results. We would also like to thank Dr. Frank Barbera and Mr. Jim Jantz of Rockwell for their enthusiastic cooperation and Mr. Phil Talley of the Aerospace Corporation for keeping us honest.

SECTION II

RESULTS AND RECOMMENDATIONS

In this section, analysis results and recommendations are presented for the following NDS mission phases:

- Spin phase
- Earth acquisition/reacquisition
- Sun acquisition/reacquisition
- On-orbit operations

SPIN PHASE--NUTATION DAMPER PERFORMANCE

Results

Nutation damper performance, as measured by the time constant of an equivalent exponential response, meets design specification (<1200 sec) for both prior and post AKM spin conditions assuming nominal conditions. The specification is violated slightly (time constant ≃ 1500 sec) at 20 rpm, post AKM burn, under worst case conditions.

Recommendations

Although the analysis results indicate a specification violation, we do not consider this to be a problem if it is recognized that time constants of 1500 sec are possible and if mission time lines are adjusted appropriately.

SPIN PHASE--PRECESSION

Results

Simulation results indicated that deviation from a desired 180 deg precession maneuver could be as much as 15 deg.

Recommendations

The magnitude of deviation is a control problem only in the sense that more propellant expenditure is required to achieve the desired 180 deg precession. Our analysis indicated that the propellant expenditure was within budget and that the procedure for precession was satisfactory.

EARTH ACQUISITION/REACQUISITION

Results

From analysis of procedures and control system performance for acquiring or reacquiring the earth, which included a detailed stability analysis, we have determined that acquisition is achievable from the initial attitude and spin conditions shown in Figure 1. Modification of the control system, however, can increase the attitude boundary to the field of view of the earth sensor (24.0 deg).

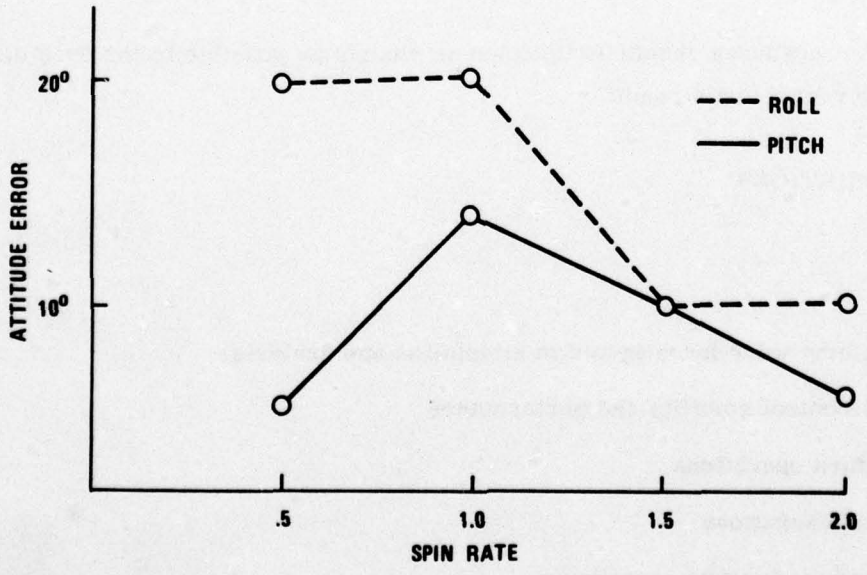

Figure 1. Earth Acquisition Envelope

Recommendations

Because the jet control system has been committed to hardware for the early launches, we do not recommend that it be modified to increase the acquisition envelope. We do recommend that the envelope depicted in Figure 1 be used as a guide for initiating earth acquisition procedures. In addition, we recommend a redesign of the pitch and roll axis jet control loops for future flights. (A preliminary redesign, showing an extended acquisition envelope, is discussed in Section IV.)

SUN ACQUISITION/REACQUISITION

Results

Simulation results indicate that sun acquisition, or reacquisition, is achievable at sun line to spin vector angles of from 45 to 135 deg and at spin rates from 0.5 to 1.0 rpm. We also verified a problem in maintaining solar array position at higher spin rates (for reacquisition) which initially was observed by Rockwell. Time and cost constraints, however, prevented us from verifying the procedures proposed to treat the problem.

Recommendations

Sun acquisition procedures should be initiated as closely as possible to the 90.0 deg sun line to spin vector angle condition.

ON-ORBIT CONDITIONS

Results

The following items were investigated in simulation and analysis:

- Wheel control stability and performance
- Noon turn operations
- Eclipse operations
- Momentum dumping procedures

- Wheel failures
- Solar array autotrack performance
- Solar array flexibility

No problems were observed in any of these areas.

Recommendations

On-orbit operations should be continued as currently defined.

SECTION III

MODEL DEVELOPMENT

In this section we discuss the models of the NDS vehicle and components that were used in the independent analysis of control system performance and mission procedures. The models were constructed on a data base that consisted of all data in-house as of 15 July 1977. Appendix A contains a description of the items comprising the data base, the source of each data item, and the associated time reference. Every attempt was made to obtain the very latest data available; however, we realize that some items have since been modified.

The features of the models developed are discussed in the following order:

- Reference systems
- Mass properties
- One-body dynamic model
- Three-body dynamic model
- Nutation damper model
- Spin sun sensor model
- Reaction jet model
- Solar array deployment model
- Reaction jet control system model
- Momentum wheel control system model
- Solar array drive model
- Solar array flexibility model
- Solar torque model
- Reaction wheel dynamics
- Combined earth sensor model

These models were all incorporated into a satellite dynamics simulation computer program, SATSIM, which was implemented on a CDC 6600 computer. SATSIM is an extension of an earlier general-purpose satellite simulation developed for ATS-6 which has provisions for simulation of four orbiting bodies. Because they are not relevant to the independent stability and control analysis, orbit equations will not be presented. However, SATSIM does contain orbit dynamic models for two bodies orbiting the earth, and the earth's orbit around the sun. This latter feature is important since the NDS satellite is a sun tracker. Details of SATSIM organization, input/output, and use will not be presented. A current version of the program has been supplied to the Air Force Academy and is implemented in their Burroughs computer facility.

REFERENCE SYSTEMS

Three reference systems were used in the analysis: inertial, local vertical, and body. The inertial and local vertical systems are shown in Figure 2.

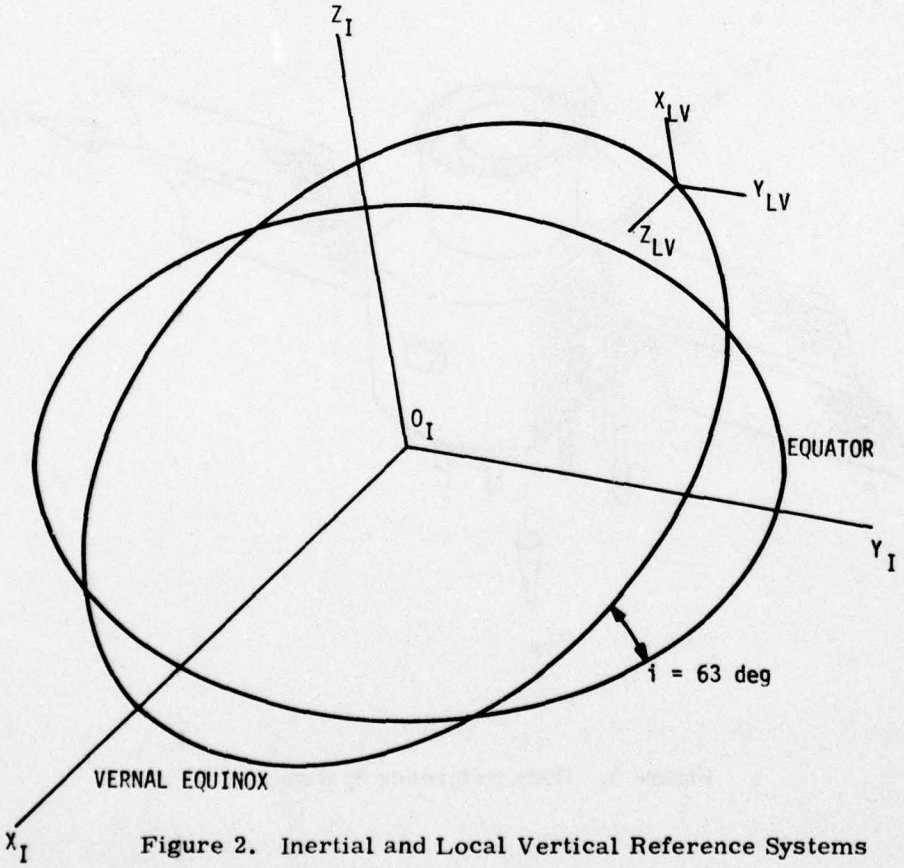

Figure 2. Inertial and Local Vertical Reference Systems

The inertial coordinate system employed has its origin at the center of the earth: Z_I axis points north, and X_I axis is positive in the direction of the vernal equinox.

The local vertical system has its origin at the center of mass of the space vehicle: Z_{LV} axis points at the center of the earth, X_{LV} axis points in the direction of orbital velocity, and Y_{LV} axis is normal to the orbit plane.

The body coordinate system is shown in Figure 3. The origin, as defined by Rockwell, is at the center of the thruster cone; Z_B is positive towards the antennae; Y_B is parallel to the solar array boom.

The Euler angles for either a body-to-inertial or body-to-local vertical transformation assume a yaw, pitch, roll sequence where yaw rotates about Z, pitch rotates about Y, and roll rotates about the X axis.

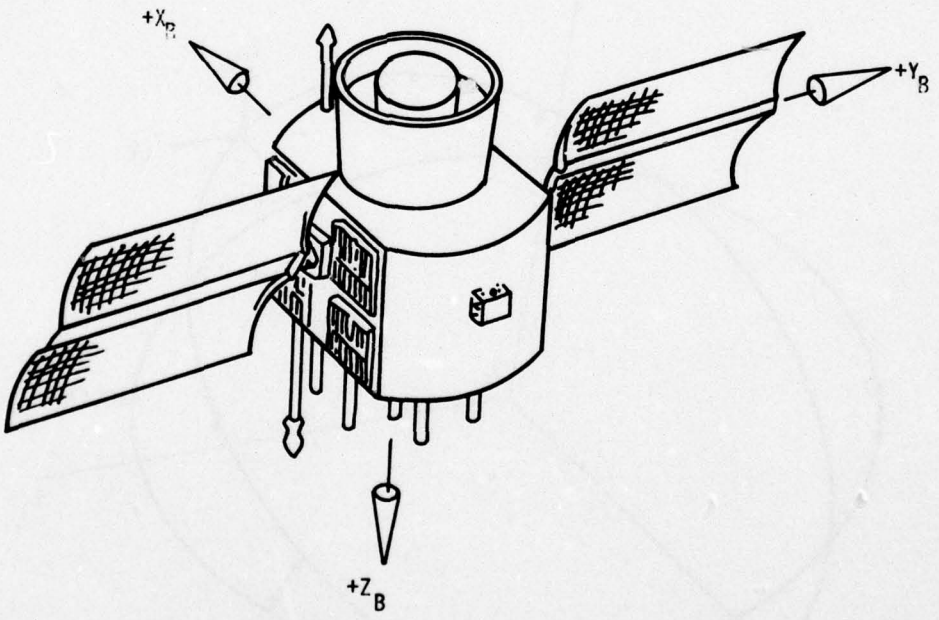

Figure 3. Body Reference System

MASS PROPERTIES

The mass properties for the various mission phases are summarized in Table 1. These have been extracted and condensed from a Rockwell-generated mass properties computer program output dated January 1977. The data shown is for a complete vehicle and was used in the one-body model simulation. The three-body model used individual component mass property data which was supplied in the computer output.

Table 2 presents uncertainties in measuring mass properties prior to launch. These were provided by the contract monitor in June 1977. Center of mass uncertainties were increased to account for center of mass variations during the mission.

ONE-BODY DYNAMIC MODEL

The NDS independent analysis has used two space vehicle models which have come to be known as the one-body model and the three-body model. As the titles suggest, the one-body model is less sophisticated than the three-body model. The one-body model is shown conceptually in Figure 4. It was used in the earth and sun acquisition simulation analysis and in the on-orbit operations simulation analysis. It assumes the following:

- Space vehicle is a rigid body.
- Mass properties are constant.
- There are no dynamic interactions between various components of space vehicle (except wheels and jets on space vehicles).

Details are given in Appendix B.

THREE-BODY DYNAMIC MODEL

This model in its most complete form represents eight spacecraft components (one space vehicle, four reaction wheels, one nutation damper, two solar arrays). It is shown conceptually in Figure 5.

The model provides interaction between all components of the space vehicle in addition to representing solar array flexibility. These interaction effects include time varying inertia and time varying center of mass. Although the one-body model was used for

TABLE 1. MASS PROPERTIES

Mission Phase	Mass	Moments of Inertia			Products of Inertia			Center of Gravity		
		I_{xx}	I_{yy}	I_{zz}	I_{xy}	I_{xz}	I_{yz}	X_{cg}	Y_{cg}	Z_{cg}
Launch	52.31	104.9157	116.4178	126.0639	-0.4479	-0.0072	-0.0079	0	-0.00	35.77
AKM ignition	52.10	104.9081	115.6999	125.3536	-0.4479	-0.0072	-0.0079	0	-0.00	35.76
On-orbit stowed	30.58	94.0642	102.2130	111.3049	-0.4479	-0.0082	-0.0065	0	-0.01	37.03
On-orbit no array	27.04	67.1157	89.8376	86.8442	-0.4479	-0.0082	0.0093	0	-0.011	37.22
On-orbit deployed x-y	30.58	187.8814	94.4581	211.5831	-0.7221	-0.0081	-0.0091	0	-0.01	36.87
On-orbit deployed y-z	30.58	192.03	94.8916	208.0	-0.4485	-0.0147	0.0094	-0.53	-0.01	37.15
On-orbit deployed y-z End mission	29.81	192.0261	92.0261	205.4076	-0.4485	0.0122	0.0093	-0.55	-0.01	37.13
On-orbit deployed x-y End mission	29.81	187.8737	91.8598	208.9923	-0.7221	-0.0080	0.0090	0	-0.00	34.16

TABLE 2. MASS PROPERTY UNCERTAINTIES

$I_{zz} \pm 1.2$ slug ft^2
$I_{xx} \pm 3$ slug ft^2
$I_{yy} \pm 3$ slug ft^2
$I_{xz} \pm 3$ lb inch^2
$I_{yz} \pm 3$ lb inch^2
$I_{xy} + 100$ lb inch^2 (machine accuracies)
$\bar{x} \pm 0.001$ inches $\Rightarrow \pm 0.1$
$\bar{y} \pm 0.001$ inches $\Rightarrow \pm 0.1$ (machine accuracies)
$\bar{z} = \pm 0.10$ inches $\Rightarrow \pm 0.2$

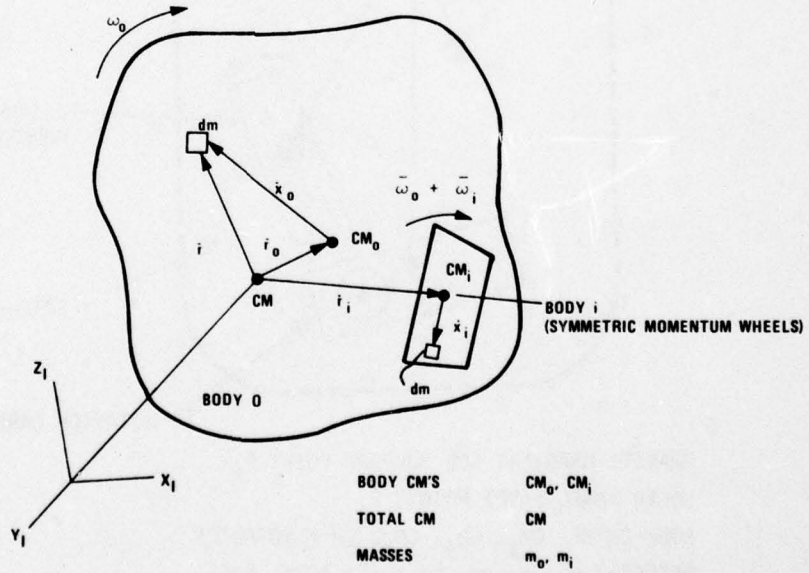

Figure 4. One-Body Model

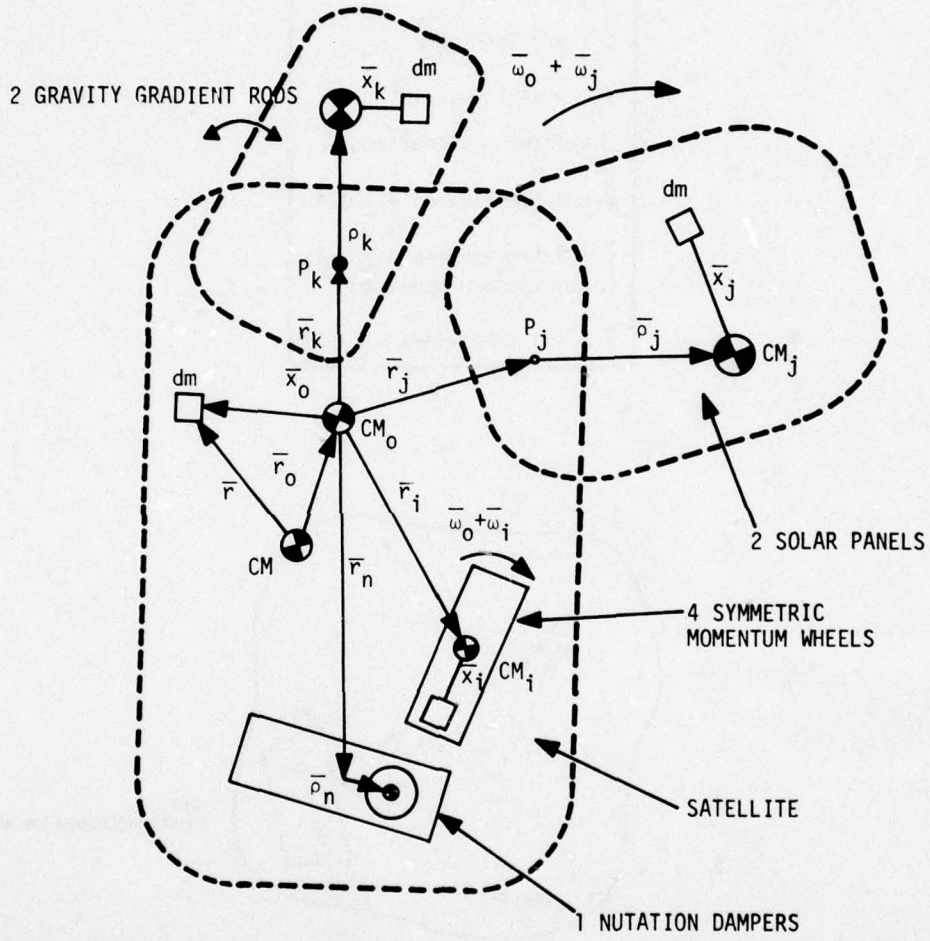

GRAVITY GRADIENT ROD SUPPORT POINT P_k

SOLAR PANEL PIVOT POINTS P_j

BODY CM's: CM_i, CM_j, CM_k; CM = TOTAL CM

MASSES: m_i, m_j, m_k, m_n; m = TOTAL MASS

INERTIA TENSORS (ABOUT CM's) J_o, J_i, J_j, J_k, J_n

Figure 5. Three-Body Structure

a large portion of the analysis, the three-body model was required for analyzing nutation damper performance, solar array deployment, and solar array flexibility. Details are given in Appendix C.

NUTATION DAMPER MODEL

The same type of ball-in-tube nutation damper used in NTS-2 is used in NDS. The physical characteristics are slightly different. Figure 6 is a Rockwell description of the nutation damper for NDS. The numbers in parenthesis refer to the NTS-2 model. For NTS-2, a specification requires that the nutation damper damping coefficient be between .01 and .015 (NRL Nutation Damper Assembly Design Specification, Specification No. NDL-SD-265498, Ford Aerospace Corporation, 25 April 1975). This agrees well with our predicted estimate of performance of the NDS damper which has a predicted damping coefficient of .017 $\pm$ 30 percent. A detailed description of the nutation damper model used for both the NDS and NTS-2 analysis is given in Appendix D. All pertinent data has been modified to reflect NDS characteristics. As will be discussed under nutation damper performance results, the location of the nutation damper does have a significant effect on performance.

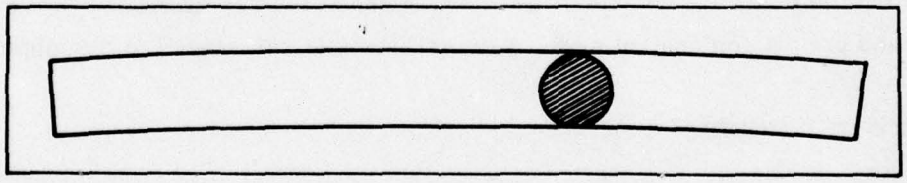

Figure 6. NDS and NTS-2 Nutation Damper Characteristics

SPIN SUN SENSOR MODEL

The digital spin sun sensor provides sun angle measurements by quantizing the sun angle through the use of an appropriately gray coded reticle over a set of photodetectors. The reticle construction provides for 1/4 deg quantization. Construction of the device provides for a narrow fan-shaped 180 deg field of view for scan angle measurement. This slit is oriented at a nominal 90 deg to the spin axis. A small slit oriented at right angles to the field of view (nominally parallel to the spin axis) allows sunlight to fall on a photodetector once each revolution to provide a short pulse; this pulse, called the pipper command pulse, provides an angular reference between the sun and the body coordinate frame about the spin axis. The pipper slit is of fixed width; therefore, as the angle between the sun vector and the spin vector decreases, the sun vector is within the width of the slit for a greater portion of the revolution. This portion of the revolution is proportional to $1/\cos \beta$, where β is the angle between the sun vector and its projection on the plane which is nominally perpendicular to the spin vector.

The pipper pulse, which is output asynchronously to the Control Electronics Assembly (CEA), also causes the angular data to be read from the photocells into a nine-bit register which holds the data until it is interrogated by the telemetry system. The pipper pulse is input to the CEA for use as a timing reference for initiating jet firings for either attitude control or precession control of the spin axis. In the attitude and precession control mode, each jet firing is referenced to the pipper pulse.

REACTION JET MODEL

The dynamics for NDS reaction jets are based on the model used in the 3XATS simulation. Both ATS and GPS use Rocket Research Corporation monopropellant hydrazine thrusters. Any data that was not available from Rockwell was extracted from ATS documents.

The model consists of an initialization section and a normal operation section. The initialization section performs one-time computations and clears outputs and counters. The normal operation section receives jet commands from the controller and outputs total jet force and total jet torque on the spacecraft. The following are system characteristics included in the model:

- Thrust increases with catalyst temperature which increases when the jet is firing and decreases when the jet is not firing. The time constant for heating is less than that for cooling.
- No thrust is developed if the jet command is less than the minimum ON time.
- Thrust start and stop times lag the jet command start and stop times due to valve response time and hydrazine burn response.
- Eighteen thrusters are used.
- Thruster torque depends on variable spacecraft cg location.

The following are jet system characteristics not included in the model:

- Dynamics of the thrust rise at turn-on and thrust decay at turn-off must be considered because of the impact on computer run time. The static model will be adequate for all but difficult limit cycle cases. These limit cycle cases should be studied using a single-axis simulation and correlated with static model results.
- Changes in thrust due to supply pressure reduction with fuel consumption is not modeled. The supply pressure changes will be very slow. Stability should be analyzed with both high and low supply pressure by changing the thrust level initialization inputs.
- Dynamic changes in thruster position and angular alignment are not considered. The spacecraft is very stiff. Cases of extreme position and angular alignment should be run.

A detailed description of the model is given in Appendix F. Model characteristics are shown in Figure 7. Model response and actual test data[1] are compared in Figures 8 and 9 for the 0.1 lb and 5.0 lb thrusters, respectively.

---

[1] Qualification Test Report, GPS 5.0-LBF REA (GPS 0.1-LBF REA), CDRL Item A005, 31 March 1976.

	5 lb THRUSTER	0.1 lb THRUSTER
F_{SS} - STEADY STATE THRUST	5.0	.1
F_{MIN} - MINIMUM THRUST	4.0 (80% F_{SS})	.09 (90% F_{SS})
τ_R - THRUST RISE TIME CONSTANT	[illegible]	0.4
τ_D - THRUST DECAY TIME CONSTANT		0
τ_{ON} - ON DELAY	.02	[illegible]
τ_{OFF} - OFF DELAY	.025	.07
$\tau_{MIN\ ON}$ - MINIMUM ON TIME	.05	.05

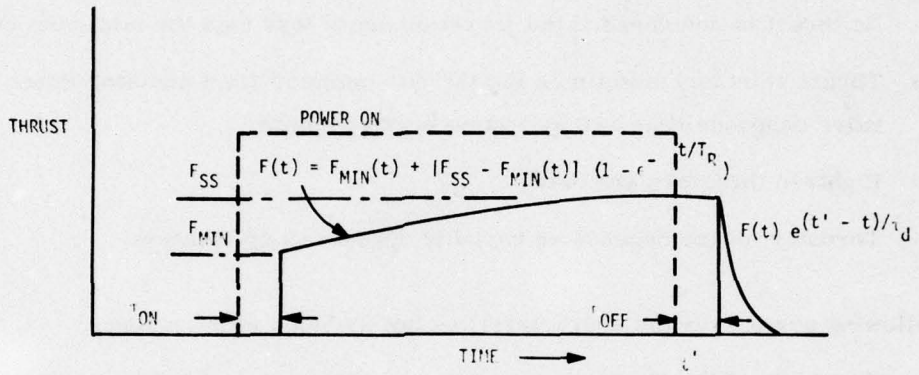

Figure 7. Thruster Dynamic Response Modeling

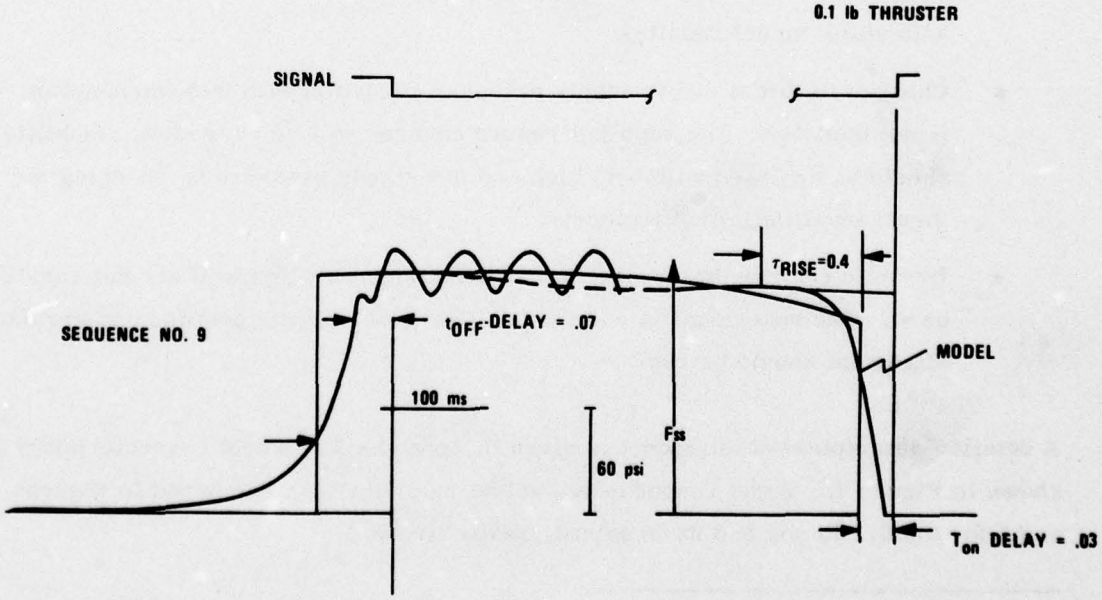

Figure 8. 0.1 lb Thruster versus Model Response

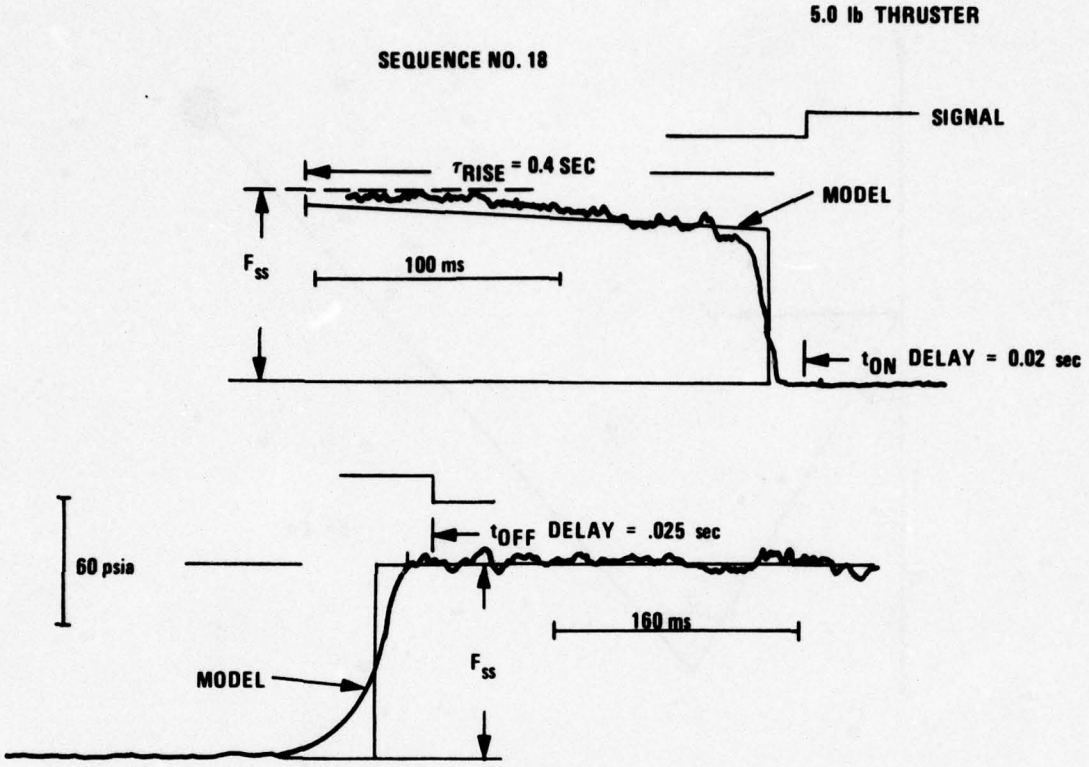

Figure 9. 5.0 lb Thruster versus Model Response

SOLAR ARRAY DEPLOYMENT MODEL

During the early spin phase of the mission, the solar arrays are stowed up against the main body of the spacecraft. After the vehicle has been despun to approximately 1 rpm and has acquired earth tracking, the -y panel is deployed. Figure 10 shows a deployment mechanism linkage geometry assuming a point mass for the panels. Detailed equations for the dynamics describing the array deployment and its effects are given in Appendix G. Nominal deployment rate is 3.0 deg/sec. Full deployment takes 30 sec nominally. The model is constructed so that either the +y or -y or both arrays can be deployed, each at its own rate.

CONTROL ELECTRONICS ASSEMBLY--REACTION JET CONTROL SYSTEM MODEL

Figure 11 is a block diagram for the CEA jet control system provided by Rockwell. There are two versions of it distinguished by different low pass filters in the pitch and roll axis feedforward path. The version represented with the straight-through

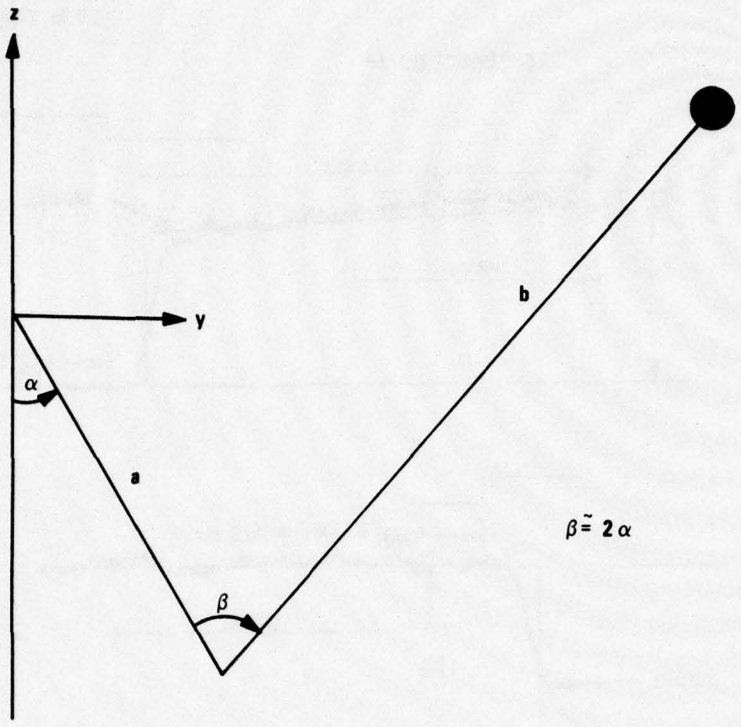

Figure 10. Deployment Mechanism Linkage Model

path will be used on the initial launches and is termed Version 1. Version 2 will be implemented in later launches and is designated in Figure 11 by the dashed lines and elevated boxes. The boxes labeled Horizon Sensor and Array Sun Sensor are approximations of the actual equipment. The actual models of these components which were implemented in SATSIM will be discussed later.

Figure 11 was implemented into SATSIM as shown in Figure 12. Values of constants are given in Table 3 with the values in parenthesis defined for Version 2. Software limits were inserted to simulate amplifier voltage saturation levels shown in Figure 12. Also shown in Table 3 are the Fortran name of the parameters and the input array element as implemented in SATSIM.

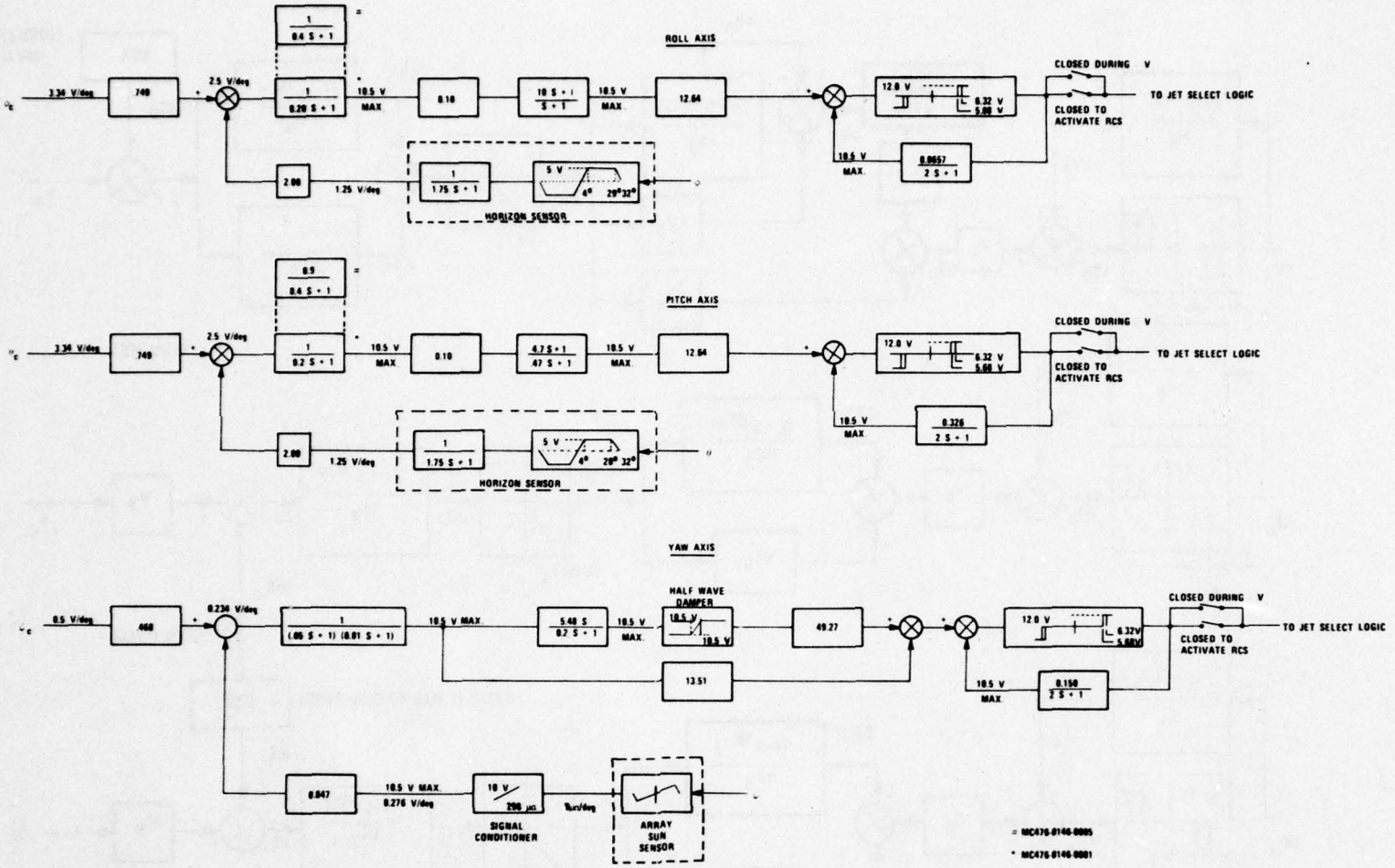

Figure 11. Jet Control System--Analytical Block Diagram

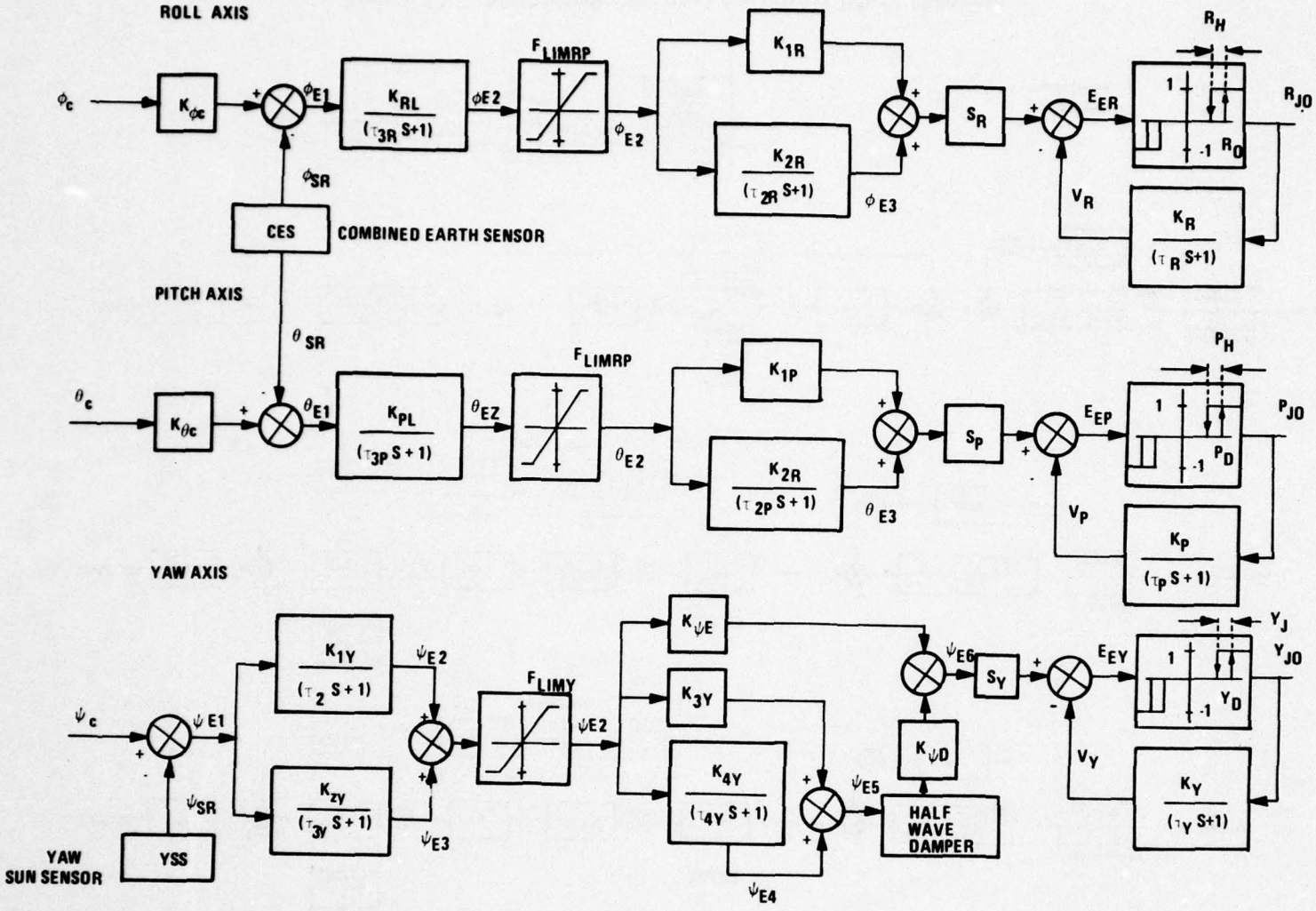

Figure 12. Jet Control System

TABLE 3. JET CONTROL BLOCK DIAGRAM PARAMETERS

Block Diagram Parameter	Fortran Name	AIN Array Index	Value	
$K_{\phi c}$	KPHICM	304	1.0	
K_{RL}	RKL	353	1.0	
F_{LIMRP}	FLIMRP	355	0.07331	
τ_{1R}	TAU1R	307	10.0	
τ_{2R}	TAU2R	308	1.0	
τ_{3R}	TAU3R	309	0.2 (0.4)	
K_{1R}	RK1	---	10.0	Roll Axis
K_{2R}	RK2	---	-9.0	
R_H	ROLHYS	153	0.2025	
S_R	SR	154	57.29577	
K_R	KR	155	0.25	
τ_R	TAUR	156	2.0	
R_D	RDEAD	383	2.0	
$K_{\phi c}$	KTHTCM	305	1.0	
K_{PL}	PKL	354	1.0 (0.9)	
F_{LIMRP}	FLIMRP	355	0.07331	
τ_{1P}	TAU1P	310	4.7	
τ_{2P}	TAU2P	311	0.47	
τ_{3P}	TAU3P	312	0.2 (0.4)	
K_{1P}	PK1	---	10.0	Pitch Axis
K_{2P}	PK2	---	-9.0	
P_H	PITHYS	161	0.225	
S_P	SP	162	57.29577	
K_P	KP	163	1.24	
τ_P	TAUP	164	2.0	
P_D	PDEAD	383	2.0	

TABLE 3. JET CONTROL BLOCK DIAGRAM PARAMETERS (concluded)

Block Diagram Parameter	Fortran Name	AIN Array Index	Value	
τ_{1Y}	TAU1Y	313	5.48	
τ_{2Y}	TAU2Y	314	0.05	
τ_{3Y}	TAU3Y	315	0.01	
τ_{4Y}	TAU4Y	316	0.2	
$K_{\psi S}$	KPSIE	317	1.0	
$K_{\psi D}$	KPSID	318	20.0	
F_{LIMY}	FLIMY	356	0.7332	Yaw Axis
Y_H	YAWHYS	169	0.2025	
S_Y	SY	170	57.29577	
K_Y	KY	171	0.5694	
τ_Y	TAUY	172	2.0	
Y_D	YDEAD	384	2.0	
K_{1Y}	YK1	---	1.25	
K_{2Y}	YK2	---	-0.25	
K_{3Y}	YK3	---	27.4	
K_{4Y}	YK4	---	-27.4	

CONTROL ELECTRONICS ASSEMBLY--MOMENTUM WHEEL CONTROL SYSTEM MODEL

The block diagram of the wheel control system provided by Rockwell is given in Figure 13. As was the case for the jet control system, there are two versions of the wheel control system. The versions differ in two low pass filter implementations in each of the three axes. Version 1 will be defined as the straight-through path and Version 2 will be defined as the elevated path.

The reaction wheel configuration is shown in Figure 14. Blending logic for transforming axis torque commands to wheel torque commands is given in Figure 15 for failed and unfailed conditions. Figure 13 was implemented in SATSIM as shown in Figure 16. Values of constants are given in Table 4 with Version 2 values shown in parentheses. Software limiters have been inserted where appropriate to simulate

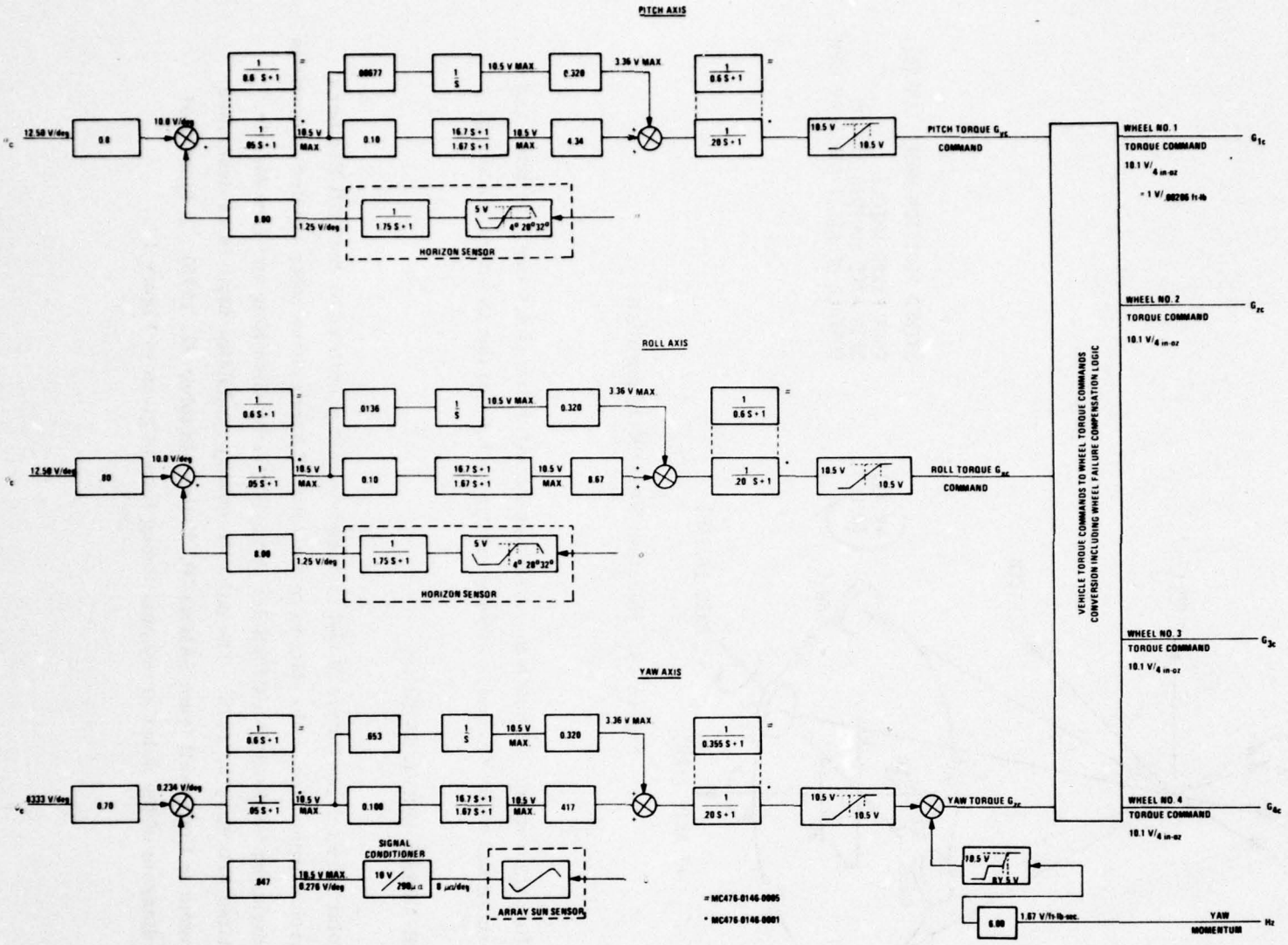

Figure 13. Wheel Control System--Analytical Block Diagram

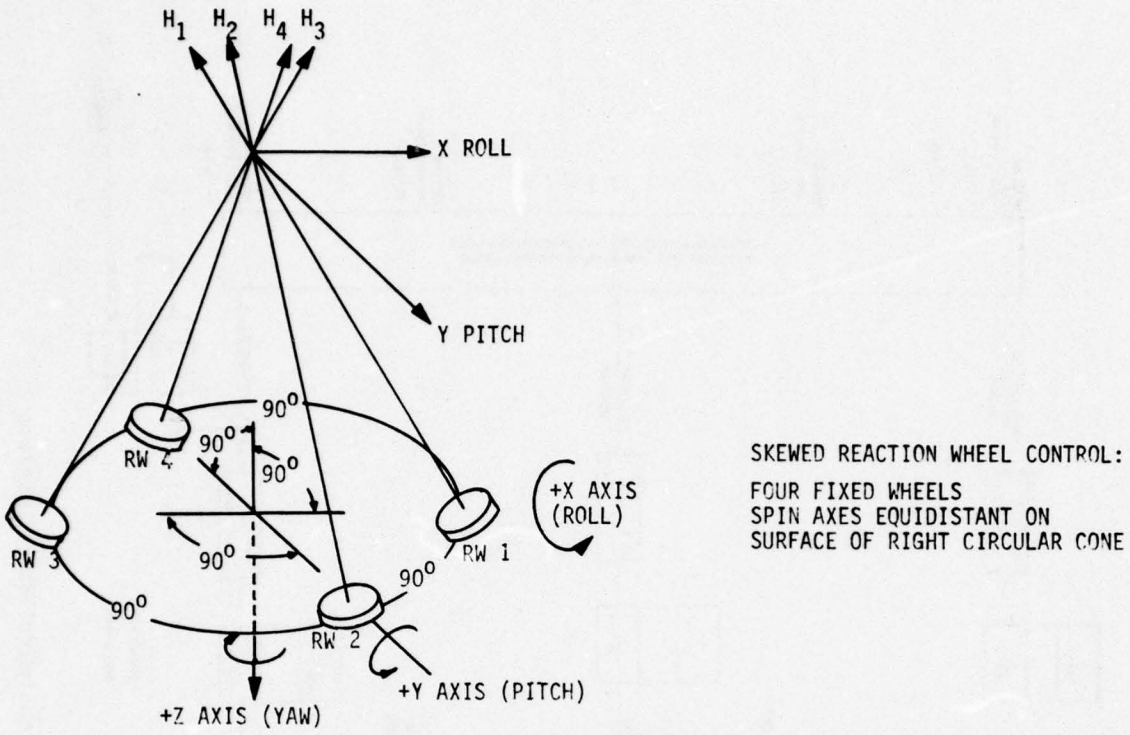

Figure 14. Reaction Wheel Configuration

amplifier saturation. Although the earth sensor saturates at 4.0 deg, the pitch and roll axis of the wheel control system saturates at 1.0 deg due to internal scaling.

SOLAR ARRAY DRIVE MODEL

The solar array drive torque model is based on data generated by the Ball Brothers Research Corporation. The data is in the form of handwritten notes labeled "Equations for Simulating the Rockwell GPS Solar Array Drive by Glen King and Lew Martin." It is dated February 5, 1976. The pulse frequency modulator logic is as described in a memo to Honeywell from SAMSO (P. Talley, October 22, 1975). A functional block diagram of the solar array positioning loop is given in Figure 17.

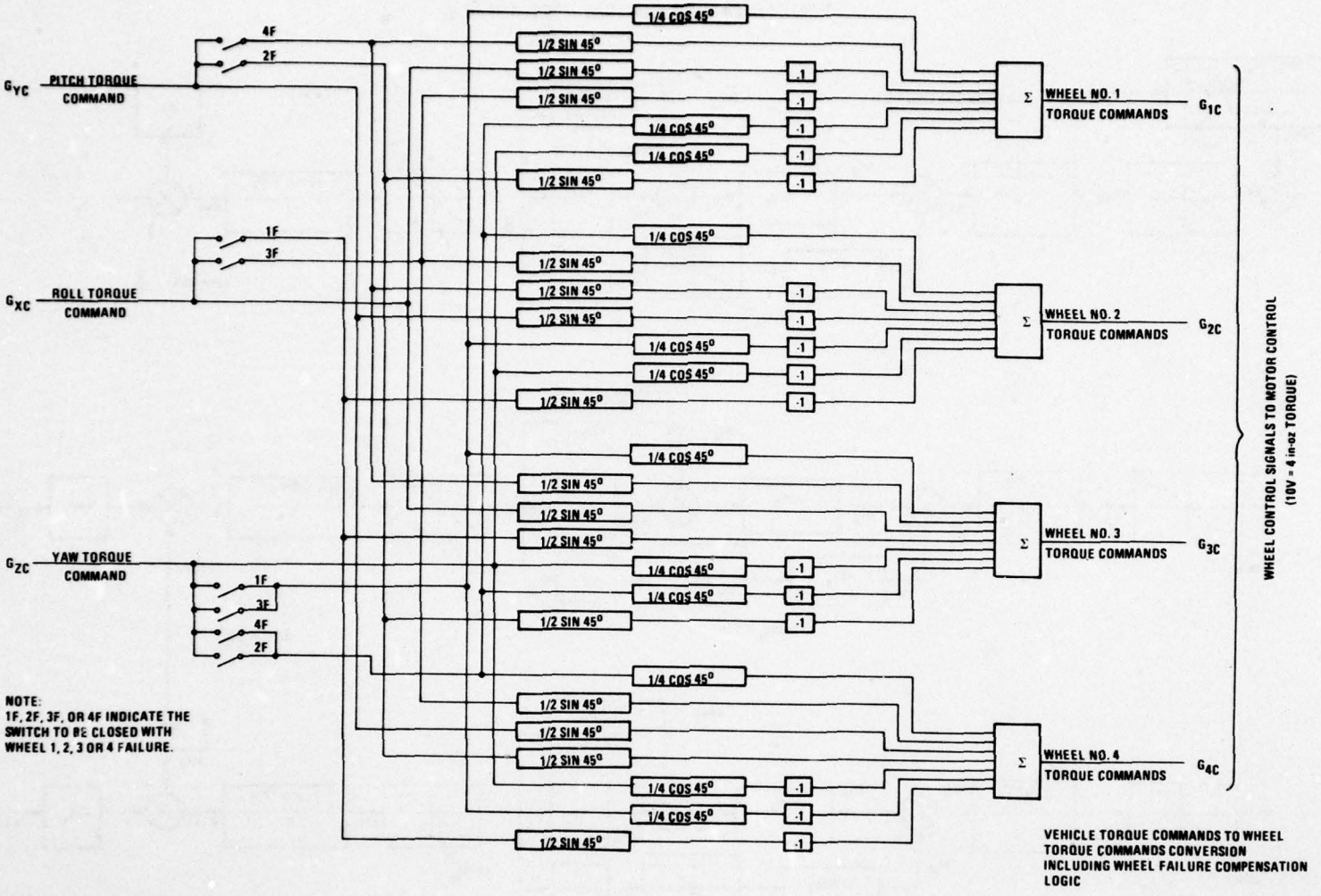

Figure 15. Wheel Control Concept

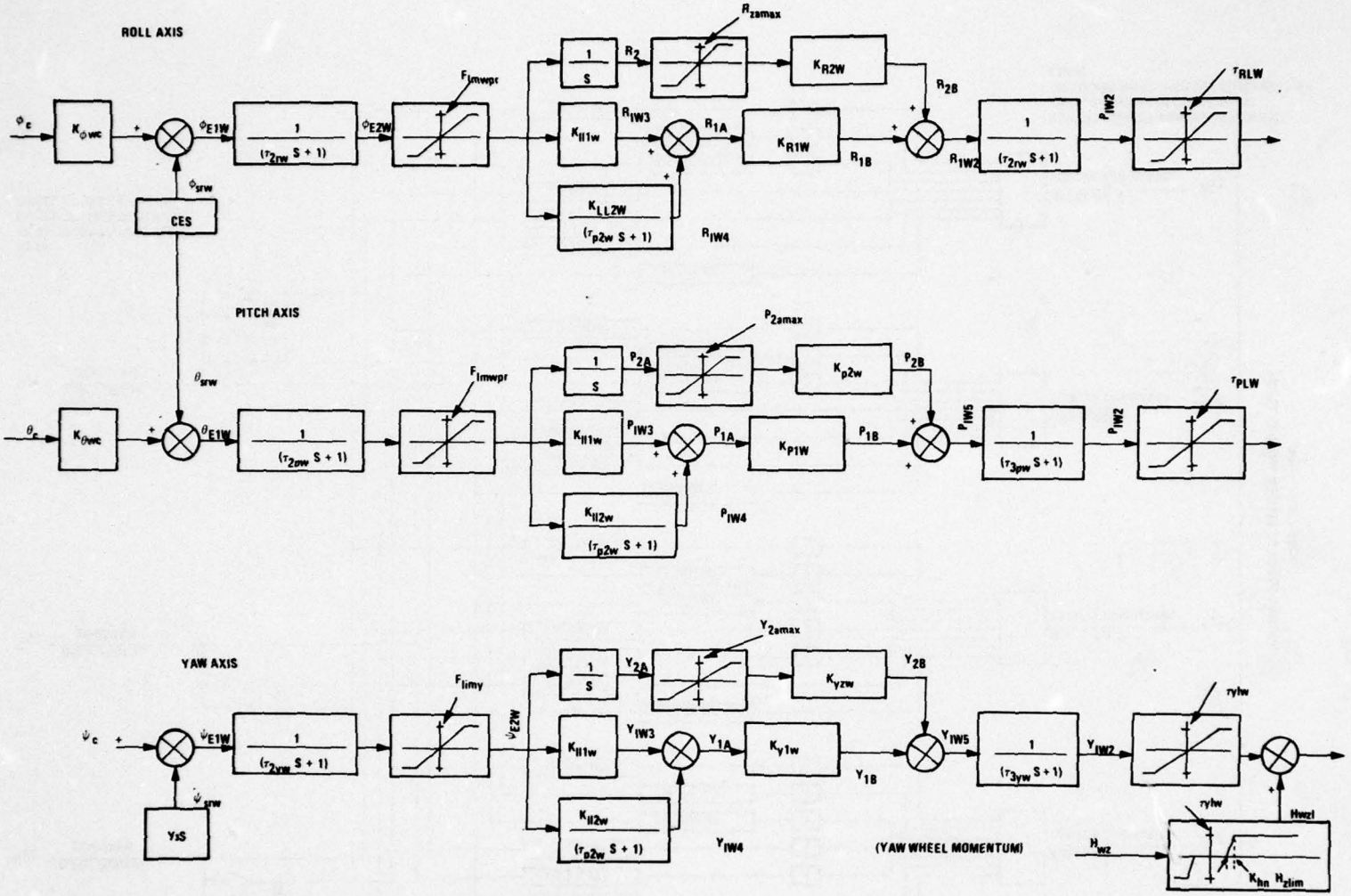

Figure 16. Wheel Control System

TABLE 4. WHEEL CONTROL BLOCK DIAGRAM PARAMETERS

Block Diagram Parameter	Fortran Name	AIN Array Index	Value	
$K_{\phi WC}$	KPHIWC	360	1.0	
τ_{P1W}	TAUP1W	371	16.667	
τ_{P2W}	TAUP2W	372	1.667	
τ_{2RW}	TAU2RW	385	0.05 (0.6)	
τ_{3RW}	TAU3RW	386	0.20 (0.6)	
K_{RW}	KR1W	362	0.984045	
K_{R2W}	KR2W	363	0.004934	Roll Axis
τ_{RLW}	TAULRW	366	0.0208	
FLMWPR	FLMWPR	306	0.018325	
R_{2AMAX}	R2AMAX	---	1.349	
EINTLW	EINTLW	391	0.006656	
KLL1W	KLL1W	---	10.0	
KLL2W	KLL2W	---	-9.0	
$K_{\theta WC}$	KTHTWC	361	1.0	
τ_{P1W}	TAUP1W	371	16.667	
τ_{P2W}	TAUP2W	372	1.6667	
τ_{2PW}	TAU2PW	387	0.05 (0.6)	Pitch Axis
τ_{3PW}	TAU3PW	388	0.20 (0.6)	
K_{P1W}	KP1W	365	0.49259	
K_{P2W}	KP2W	366	0.0024334	
τ_{PLW}	TAULPW	367	0.0208	
FLMWPR	FLMWPR	306	0.018325	
P2AMAX	P2AMAX	---	2.735	
τ_{P1W}	TAUP1W	371	16.667	
τ_{P2W}	TAUP2W	372	1.6667	
τ_{2YW}	TAU2YW	389	0.05 (0.6)	
τ_{3YW}	TAU3YW	390	0.2 (0.355)	
K_{Y1W}	KY1W	368	1.1075	Yaw Axis
K_{Y2W}	KY2W	369	0.0055	
τ_{YLW}	TAUYLW	370	0.0208	
H_{ZLIM}	HZLIM	380	0.9	
K_{HW}	KHW	381	0.8	
FLIMY	FLIMY	356	0.7832	
Y2AMAX	Y2AMAX	---	1.21	

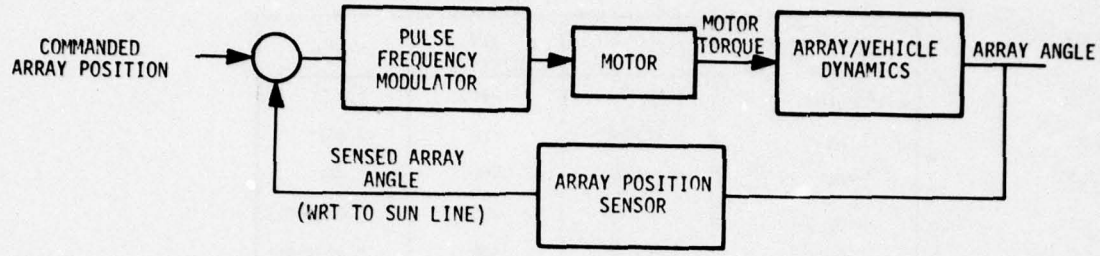

Figure 17. Solar Array Drive Functional Block Diagram

Motor Torques

As given in the Ball Brothers data there are four sources of torque associated with the solar array drive motor:

- Mechanical torque (T_M)
- Coulomb friction torque (T_{CL})
- Cogging torque (T_{CG})
- Magnetic hysteresis torque (T_D)

In addition, Ball Brothers has modeled the interaction between the motor shaft and array as a torsional spring mass damper system as shown in Figure 18.

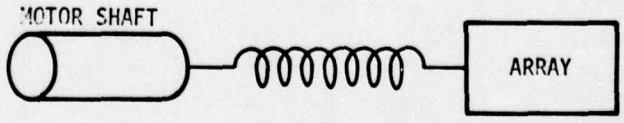

Figure 18. Torsional Spring Mass Damper System

With this model, motor drive shaft angle may be different from array angle. The dynamics representing this interaction are given by

$$T_S = I_S \ddot{\theta}_S - D(\dot{\theta}_A - \ddot{\theta}_S) - K(\theta_A - \theta_S) \quad (1)$$

$$D(\dot{\theta}_S - \dot{\theta}_A) + K(\theta_S - \theta_A) = I_A \ddot{\theta}_A$$

where

T_S = total torque on the drive shaft

θ_S = shaft angular position

θ_A = array angular position

I_S = moment of inertia of shaft

I_A = moment of inertia of array

D = equivalent damping coefficient

K = spring constant

The total torque on the shaft is

$$T_S = T_M - T_{CL} - T_{CG} - T_D \quad (2)$$

The torque-producing components of this equation have been modeled by Ball Brothers from experimental data. They are as follows (oz-in.):

- Motor Torque

$$T_M = (25 - 1.44\ \theta_S)\left(\frac{8.48}{1/800\ S + 1}\right)$$

$$\cong 8.48(25 - 1.44\ \theta_S)$$

$$\text{Minimum } T_M = 5.92(25 - 1.44\ \theta_S)$$

- Coulomb Friction Torque

$$T_{CL} = 65.0 \text{ for } \dot{\theta}_S > 0.007 \text{ rad/sec}$$

$$= 78.0 \text{ for } \dot{\theta}_S < 0.007 \text{ rad/sec (during pulse)}$$

$$= 0 \quad \text{for } \dot{\theta}_S < 0.007 \text{ rad/sec (no pulse)}$$

- Cogging Torque

$$T_{CG} = \{2.3933[\sin 97\ \theta_S + \sin(97\ \theta_S + 0.803)] + 0.3506 \sin (16\ \theta_S + 1.57)\}\{0.0385 + 0.964 \sin^2 (0.5\ \theta_S)\}$$

- Magnetic Hysteresis Torque

$$T_D = \int T_D\, dt$$

$$T_D = 14.6[T_D \text{ SGN } \theta_S - 10.0]^2 \dot{\theta}_S$$

Model Simplification

Values for the spring constant ($K = 1.905 \times 10^5$ oz-in./rad) and equivalent damping coefficient ($D = 352$ oz-in.-sec) are equivalent to a torsional mode frequency of 230.46 rad/sec (36.68 Hz) and a damping coefficient of .213. Preliminary analysis indicated that this frequency is much higher than the highest significant structural mode-frequency of the panels (less than 20 rad/sec). Thus we assumed a rigid connection between the motor and the array.

Pulse Frequency Modulator

The pitch sun sensor signal which is proportional for $\pm$ 30 deg (i.e., input = output) is scaled at 7.2 μamp/deg. This signal rescaled drives an integrator. A test level is established such that the integration of a 10 deg error for .5 sec or a 1 deg error for 5 sec will reach the same test value. (Pulse width for both normal and extended modes, bandwidths, and expected response specifications are given in Appendix A.)

Using the integrator and a timer, variable pulse rates between .2 Hz and 2 Hz are generated with the following logic:

- The integrator and timer are initialized each time a pulse is generated or when the timer reaches 5 sec.

- If the error signal is > 10 deg (i.e., the test level would be reached in <.5 sec), the pulse is inhibited until the timer reaches .5 sec. (This limits the pulse rate to 2 Hz.)
- If the error signal is < 1 deg, the test level will not be reached before the timer reaches 5 sec and, hence, no pulse is generated. This forms a $\pm$ 1 deg deadband around null.

The pulse torque polarity is determined by the pitch sun sensor polarity and is directed to rotate the drive such that the error signal is reduced.

SOLAR ARRAY FLEXIBILITY MODEL

Because of delays in receipt of up-to-date solar array mass properties and structure data, several iterations were performed before reaching the final flexible solar array dynamics model. The progression in model revisions as described by the natural frequencies is shown in Table 5. Column I contains informal ground vibration test data for a prototype array obtained from Rockwell. Column II presents preliminary model natural frequencies with outdated boom and stiffness data. Column III contains natural frequencies with updated boom stiffness. Finally, Column IV contains the natural frequencies of the model that was used in both simulation and stability analysis. Good agreement was obtained for the lowest bending modes, with a frequency difference of only .2 Hz (less than 5 percent) between test and the fine mesh model.

The next two modes are the coupled torsion and X-Y plane bending modes. The STARDYNE-generated finite element, fine mesh model shows the dominant torsion mode at about 5 Hz and X-Y plane bending at 3.9 Hz. The test frequencies show the torsion mode at the lowest frequency. Including a flexible torsion lock in the deployment arm will reduce the fine mesh model torsion frequency. This lock is not used during flight so the array torsion frequency in flight should be higher than the 3.1 Hz test frequency.

Details of the development of the solar array flexibility model are given in Appendix K.

TABLE 5. NATURAL FREQUENCY COMPARISONS, TEST VERSUS MODELS

	Test f_n	Preliminary Models f_n		Fine Mesh Model f_n
Mode Shape	(a)	(b)	(c)	(d)
Description	Hz	Hz	Hz	Hz
Bending, normal to panels, Z direction	4.1	3.07	3.75	3.9133
Bending, inplane of panels, X direction	4.8	3.49	3.75	3.9138
First torsion mode, θ_y	3.1	4.53	6.84	5.086

SOLAR TORQUE MODEL

A detailed model of the torques generated on the spacecraft by solar pressure was developed. Because of their low magnitude, solar torques do not present a stability or control problem. They do, however, influence the wheel momentum buildup and ultimately the frequency of momentum dumps that will occur. The solar torque model was constructed by dividing all spacecraft surfaces into rectangular plates, computing the solar pressure generated on that plate as a function of sun incident angle and the reflectivity and absorptivity of the material of the surface, and then summing the resultant force-moment arm computations. Figure 19 presents a description of the various surfaces and their characteristics. Details of the model are given in Appendix G.

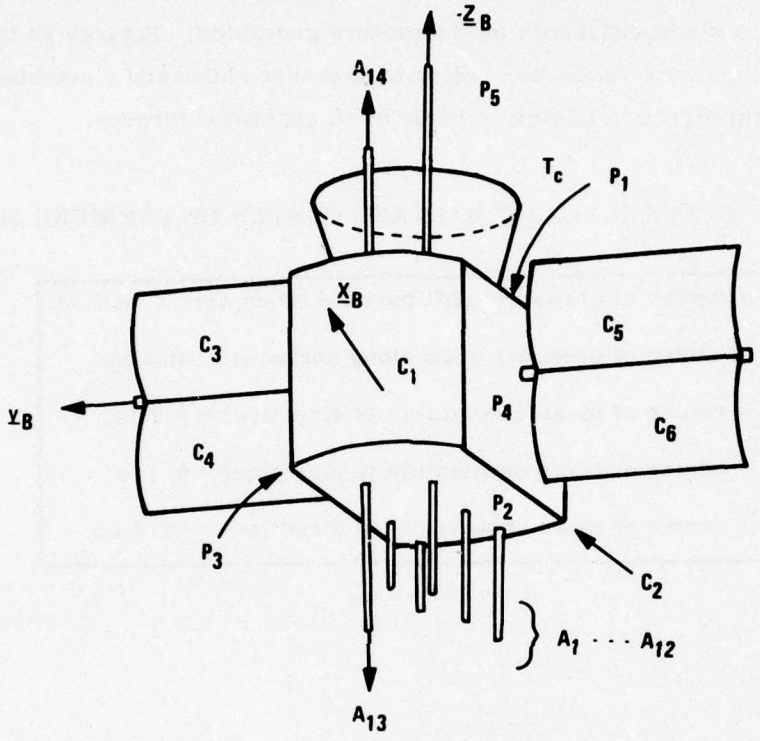

LOCATION	DESCRIPTION	COATING	REFLECTIVITY
P_1	AFT BULKHEAD	ALUMINUM KAPTON	. 7
P_2	FORWARD BULKHEAD	ALUMINUM TEFLON	.88
P_3, P_4	SIDES ADJACENT TO SOLAR PANELS	SILVER TEFLON	.94
P_5	OPEN END OF THRUSTER CONE	ALUMINUM TEFLON	.88
T_c	THRUSTER CONE	ALUMINUM TEFLON	.88
C_1, C_2	MAIN BODY CYLINDRICAL SURFACE SIDES	ALUMINUM TEFLON	.88
C_3, C_4, C_5, C_6	SOLAR PANELS		.15

Figure 19. Thermal Control Coating Properties

Three axis torques generated on the spacecraft due to solar pressure were computed at different panel angles; it was assumed that the panels were pointed at the sun. These computations are shown in Figures 20 through 24. As can be seen from Figures 20 and 21, whether or not shading of one surface by another is included in the model does have a slight difference on the torques generated. Figures 22 through 24 show the effect of center of mass and center of pressure shifts and a combination of the two in the worst direction (shown in Table 6) on generated torques.

TABLE 6. WORST CASE CENTER OF MASS AND CENTER OF PRESSURE SHIFTS

ΔY_{cp}	= center of pressure shift parallel boom axis = -0.5 in.
ΔS_{cp}	= center of pressure shift along surfaces = -0.5 in.
ΔX_{cm}	= center of mass uncertainty (x direction) = 0.1 in.
ΔY_{cm}	= center of mass uncertainty (y direction) = 0.1 in.
ΔZ_{cm}	= center of mass uncertainty (z direction) = -0.2 in.

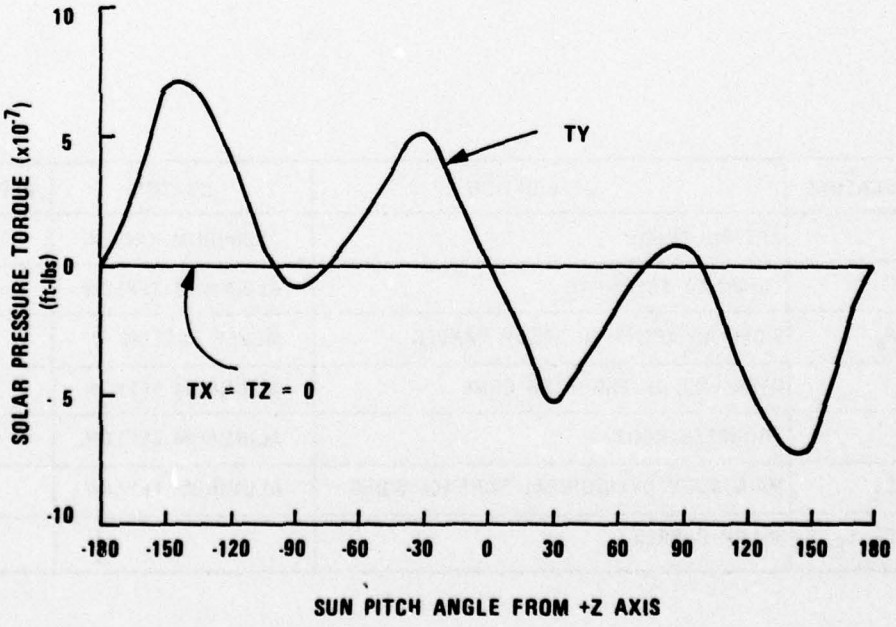

Figure 20. GPS Nominal

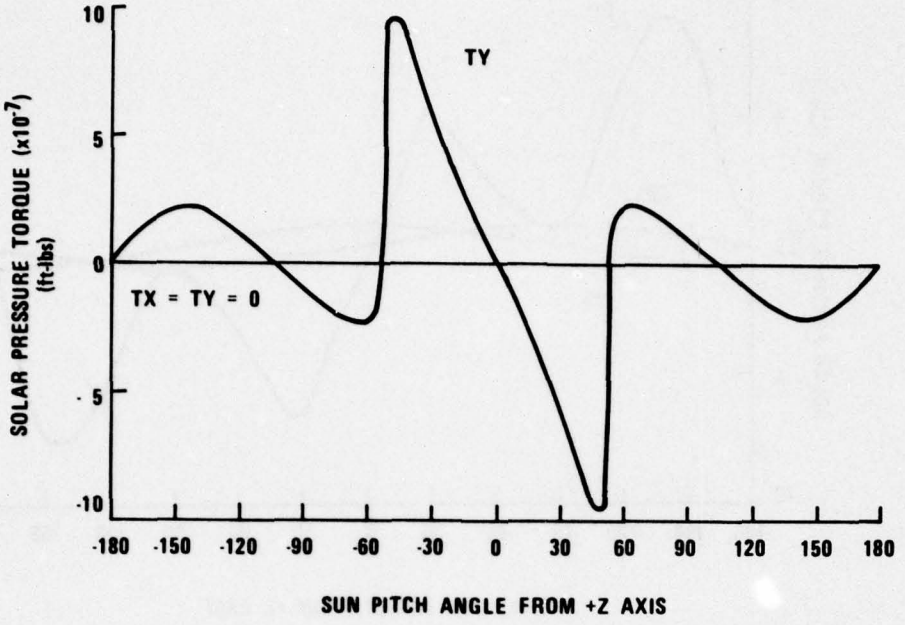

Figure 21. GPS Nominal with No Partial Shading

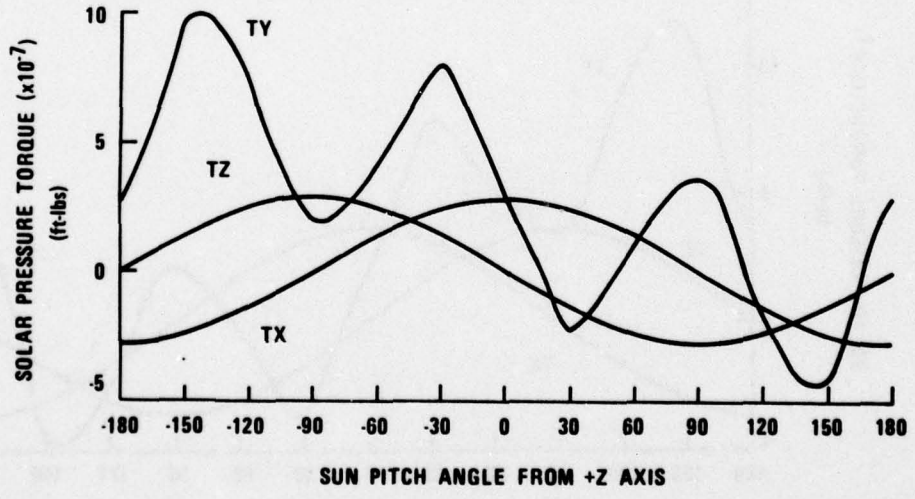

Figure 22. GPS Nominal and Worst Case C_P Shift

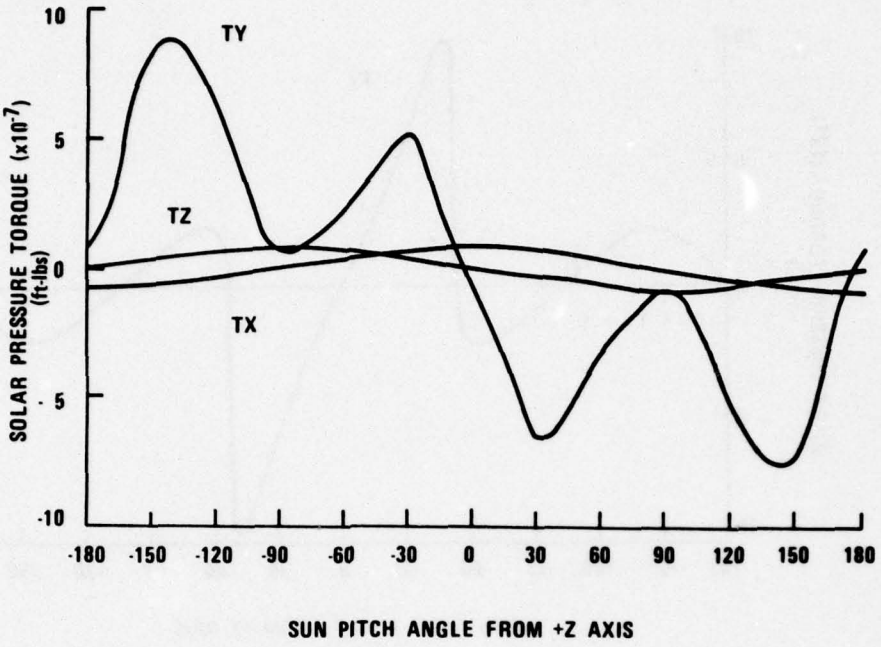

Figure 23. GPS Nominal and Worst Case C_M Shift

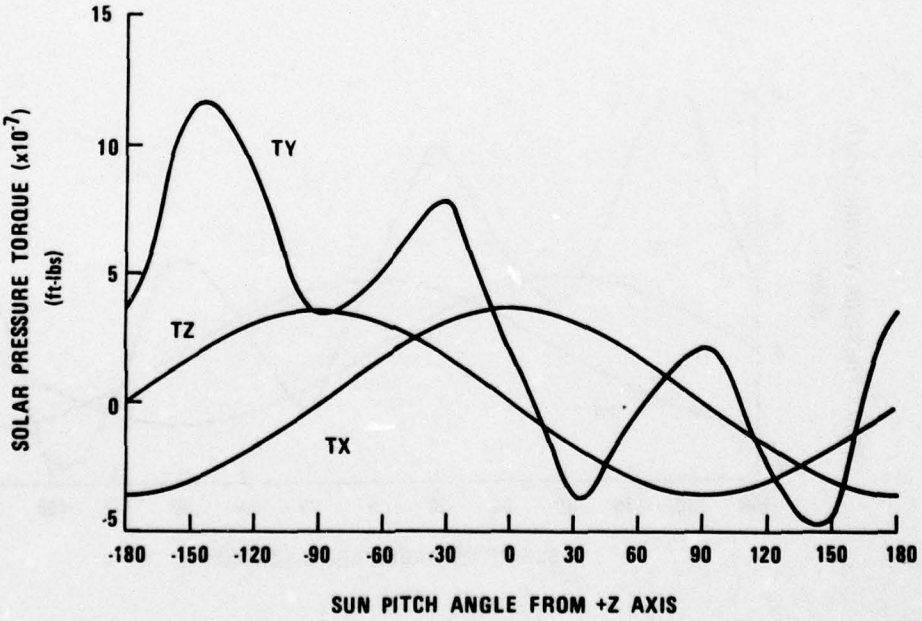

Figure 24. GPS Nominal and Combination Worst Cases

The data shown in Figure 24 was used to determine the momentum buildup due to solar torque that could be expected after five days. These results are shown in Table 7. These results indicate that a worst case momentum dumping frequency would be approximately three to five days with the pitch axis requiring the most attention. Roll axis dumps would be required, worst case, every eight to ten days.

TABLE 7. WHEEL TORQUE AND MOMENTUM FOR TWO ORBIT CONDITIONS

Condition	Sun Line Normal to Orbit			Sun Line in Orbit Plane		
	Roll	Pitch	Yaw	Roll (Peak)	Pitch (Average)	Yaw (Peak)
1) Nominal (with shading)						
T (ft-lb)	0	9×10^{-8}	0	0	3×10^{-7}	0
H_{max} (ft-lb-sec)	0	6×10^{-4}	6×10^{-4}	0	0.13	0
2) Nominal (without shading)						
T (ft-lb)	0	9×10^{-8}	0	0	3×10^{-7}	0
H_{max} (ft-lb-sec)	0	6×10^{-4}	6×10^{-4}	0	0.13	0
3) Nominal plus Worst Case C_P Shift						
T (ft-lb)	0	1.9×10^{-7}	2.8×10^{-7}	2.8×10^{-7}	7×10^{-7}	2.8×10^{-7}
H_{max} (ft-lb-sec)	0	0.0023	0.0023	0.121	0.30	0.12
4) Nominal plus Worst Case C_M Shift						
T (ft-lb)	0	6×10^{-8}	8×10^{-8}	8×10^{-8}	4×10^{-7}	8×10^{-8}
H_{max} (ft-lb-sec)	0	7×10^{-4}	7×10^{-4}	0.035	0.17	0.035
5) Nominal plus Combination Worst Cases						
T (ft-lb)	0	3.4×10^{-7}	3.6×10^{-7}	3.6×10^{-7}	7×10^{-7}	3.6×10^{-7}
H_{max} (ft-lb-sec)	0	0.0034	0.0034	0.16	0.30	0.16
6) Nominal plus Maximum Panel Deadband						
T (ft-lb-sec)	0	0	5.5×10^{-7}	0	9×10^{-7}	0
H_{max} (ft-lb-sec)	0	0.0038	0.0038	0	0.39	0
7) Nominal plus Maximum Windmilling						
T (ft-lb)	0	9×10^{-8}	2.8×10^{-7}	2.8×10^{-7}	3×10^{-7}	2.8×10^{-7}
H_{max} (ft-lb-sec)	0	0.0019	0.0019	0.12	0.13	0.12

REACTION WHEEL DYNAMICS

The torque versus speed characteristics of the reaction wheel were based on the test data shown in Figure 25. The model is shown in Figure 26.

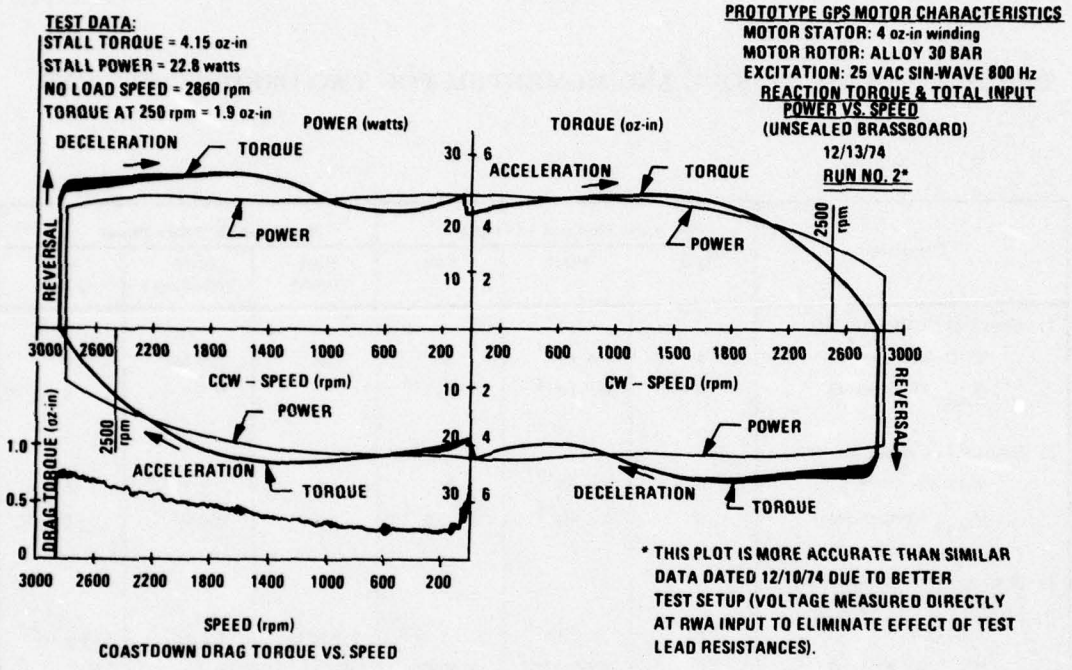

Figure 25. Motor Torque-Speed Curves

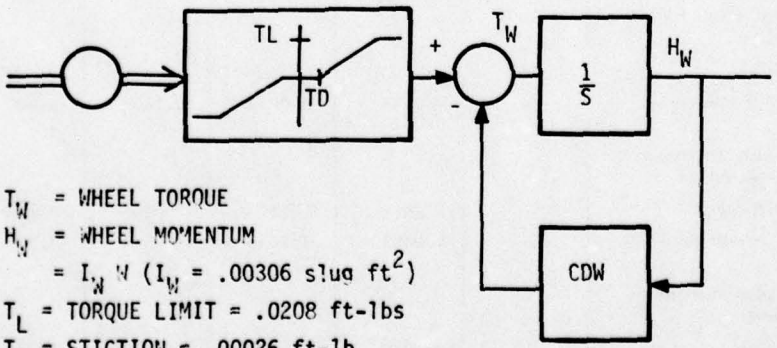

T_W = WHEEL TORQUE
H_W = WHEEL MOMENTUM
= $I_W \omega$ (I_W = .00306 slug ft^2)
T_L = TORQUE LIMIT = .0208 ft-lbs
T_0 = STICTION = .00026 ft-lb
CDW = VISCOUS DRAG = .022 ft-lb/ft-lb-sec

Figure 26. Simulation Model of Reaction Wheel Dynamics

COMBINED EARTH SENSOR MODEL

A mathematical model of the combined earth sensor which includes both a horizon crossing indicator for use in the spin phase and an earth radiation detector for on-orbit generation was developed for the NDS verification. The model includes a filter with a 1.4 sec time constant representing thermopile image processor fade lag. The sampling strategy for computing pitch and roll errors is also included. A complete description is given in Appendix J.

A summary of CES fault detection logic is given in Table 8. Figures 27 through 29 show earth sensor behavior for various simulated conditions. Figure 27 shows the sensor tracking pitch and roll attitude errors due to a .2 deg/sec pitch and roll rate. As can be seen, the pitch output saturates at 5.7 deg while roll saturates at 3.0 deg. This is in good agreement with the earth sensor data referenced in Appendix A. Figure 28 shows earth sensor pitch output for only a pitch rate initial condition. In this case saturation is at 4.0 deg as is nominally predicted. Figure 29 shows the effect of a failure (seen in field of view of detector) in the roll attitude computation occurring at 2 sec into the sun. Roll computations are updated at .5 sec intervals versus the .25 sec nominal. Pitch computations are unaffected.

TABLE 8. CES CORRIDOR LOGIC (Acquisition Mode Only)

1. Calculate R_{1A}
   a. Calculate $C_{2A} = 0.25 + 0.2\{|R_{2A}| + |P_{2A}|\}$
   b. If $\{|P_{1A} - P_{2A}| \leq C_{2A}$ or $|R_{1A} - R_{2A}| \leq C_{2A}\}$ output P_{2A}
   c. Otherwise output P_{1A}

2. Calculate P_{1A}
   a. Calculate $C_{2A} = 0.25 + 0.2\{|R_{2A}| + |P_{2A}|\}$
   b. If $\{|R_{1A} - R_{2A}| \leq C_{2A}$ or $|P_{1A} - P_{2A}| > C_{2A}\}$ output R_{1A}
   c. Otherwise output R_{2A}

3. Calculate R_{2A}
   a. Calculate $C_{1A} = 0.25 + 0.2\{|P_{1A}| + |R_{1A}|\}$
   b. If $\{|P_{1A} - P_{2A}| \leq C_{1A}$ or $|R_{1A} - R_{2A}| > C_{1A}\}$ output P_{1A}
   c. Otherwise output P_{2A}

4. Calculate P_{2A}
   a. Calculate $C_{1A} = 0.25 + 0.2\{|P_{1A}| + |R_{1A}|\}$
   b. If $\{|R_{1A} - R_{2A}| \leq C_{1A}$ or $|P_{1A} - P_{2A}| \leq C_{1A}\}$ output R_{2A}
   c. Otherwise output R_{1A}

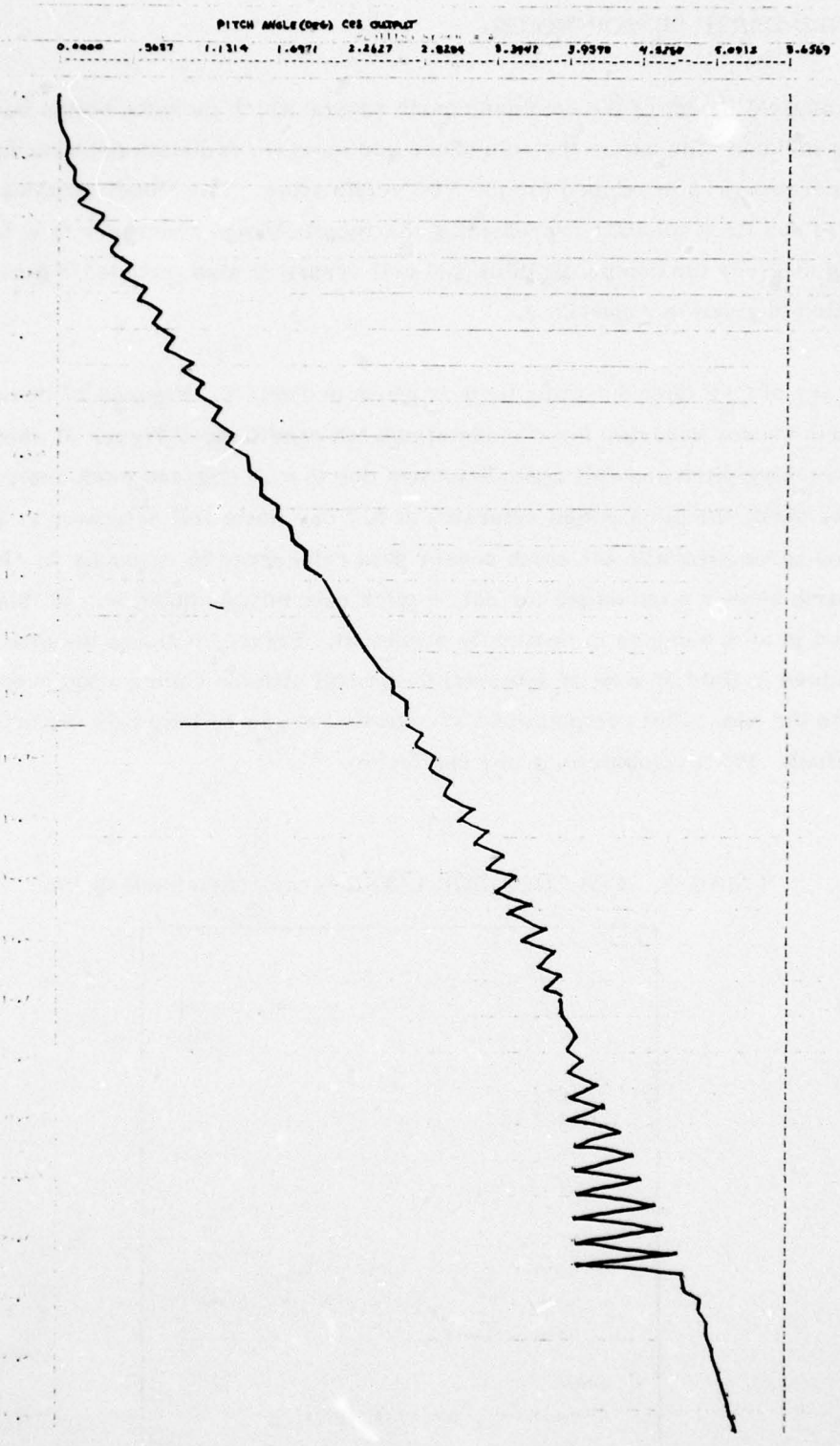

Figure 27a. Earth Sensor Output, p = q = 0.2 deg/sec

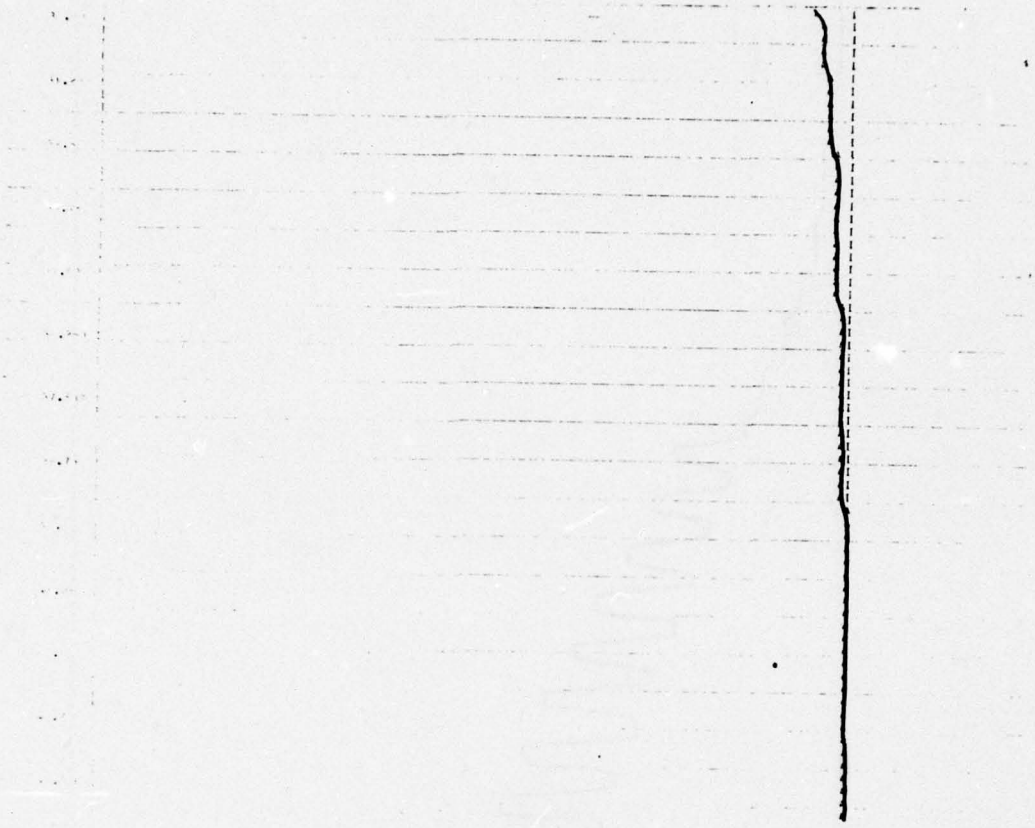

Figure 27a. Earth Sensor Output, p = q = 0.2 deg/sec (concluded)

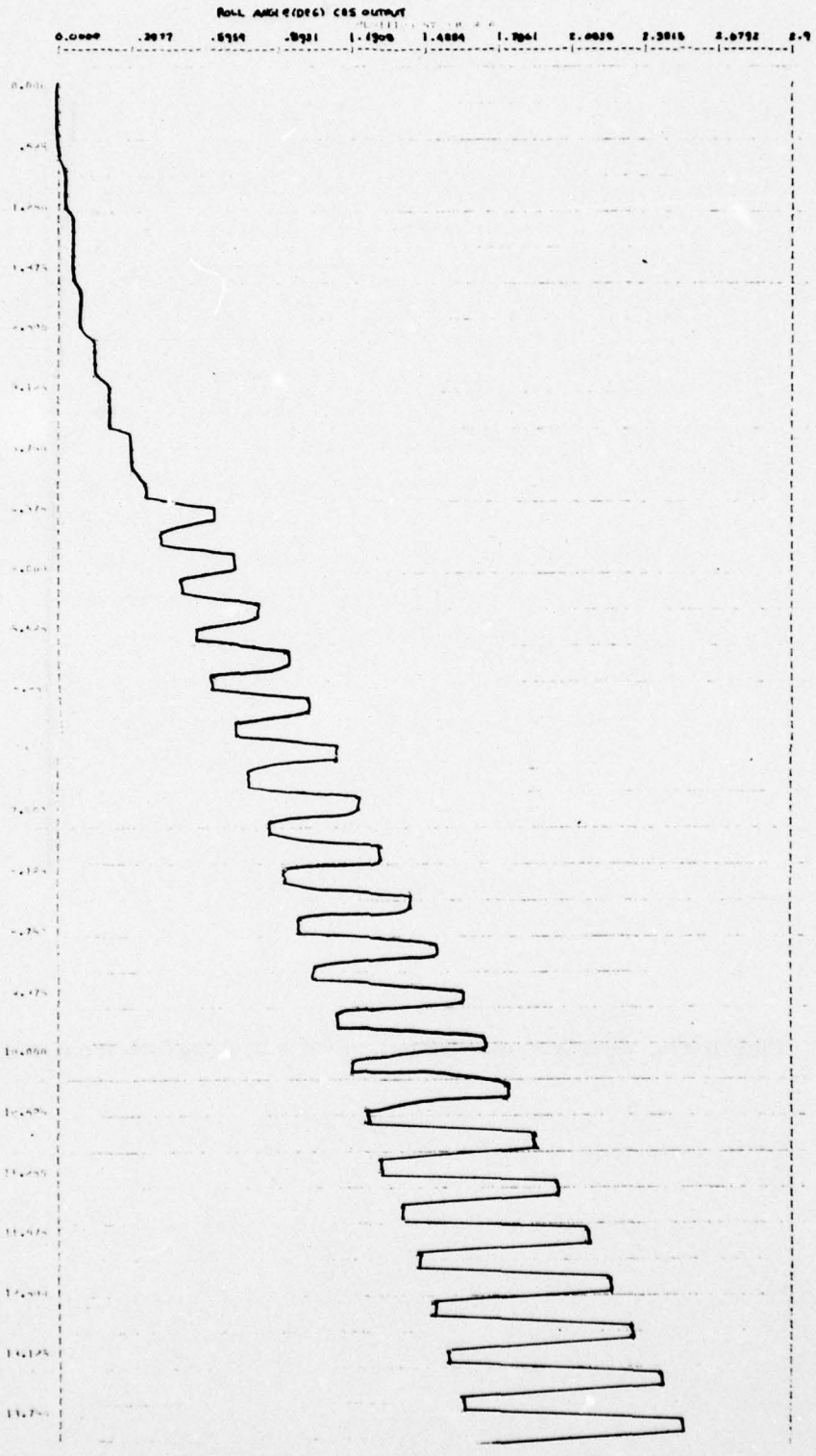

Figure 27b. Earth Sensor Output, p = q = 0.2 deg/sec

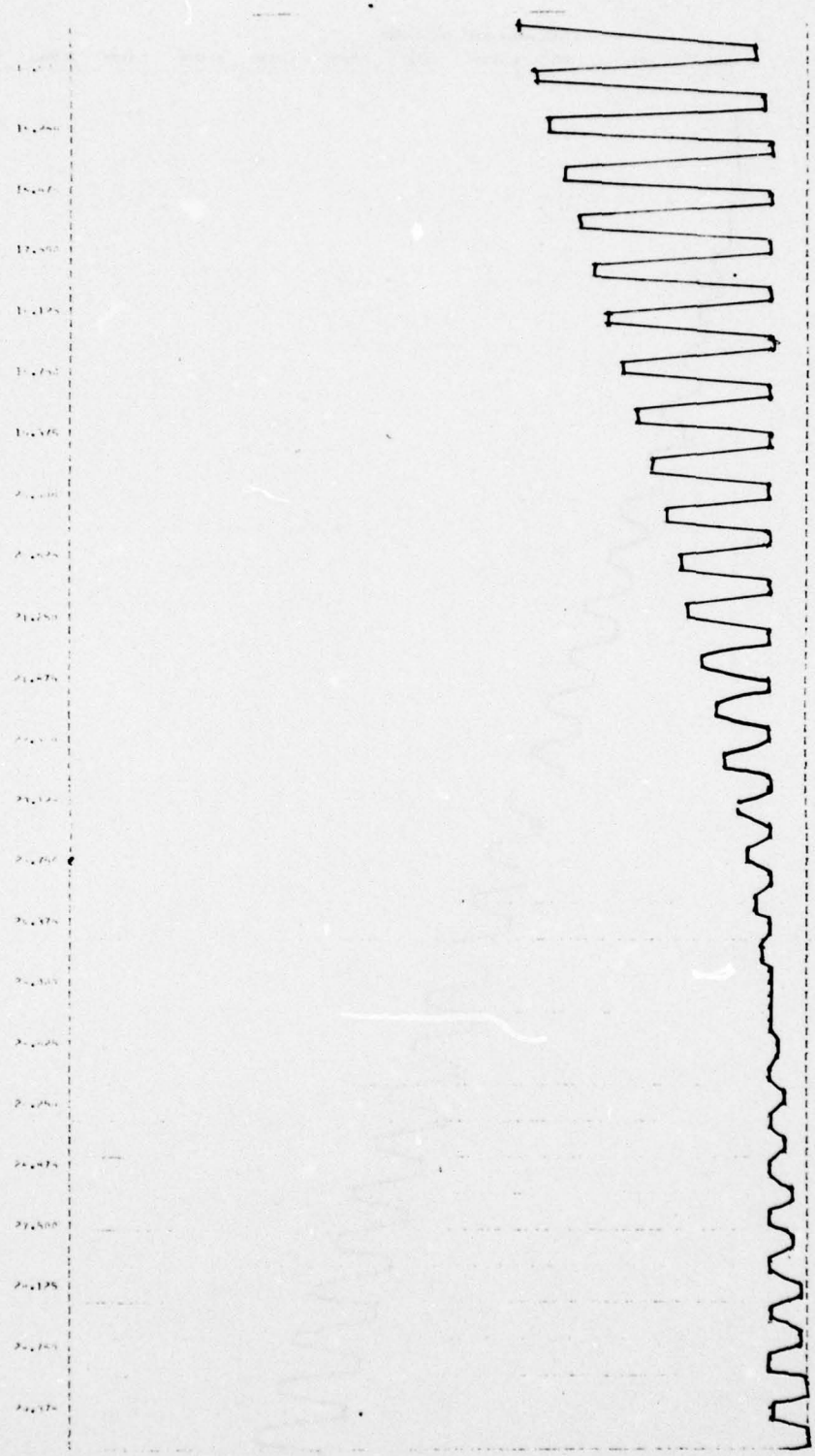

Figure 27b. Earth Sensor Output, p = q = 0.2 deg/sec (concluded)

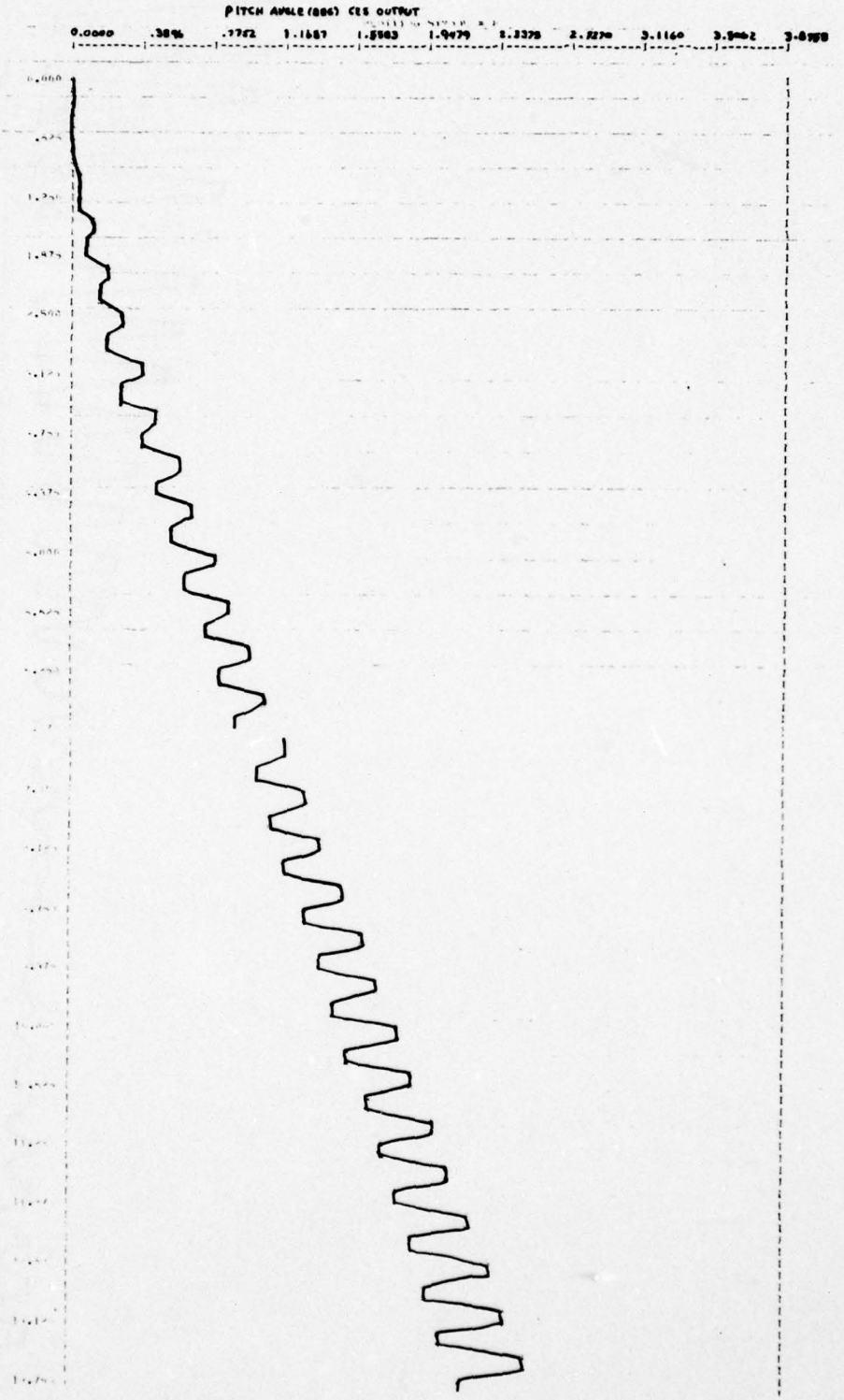

Figure 28. Earth Sensor Output, q = 0.2 deg/sec

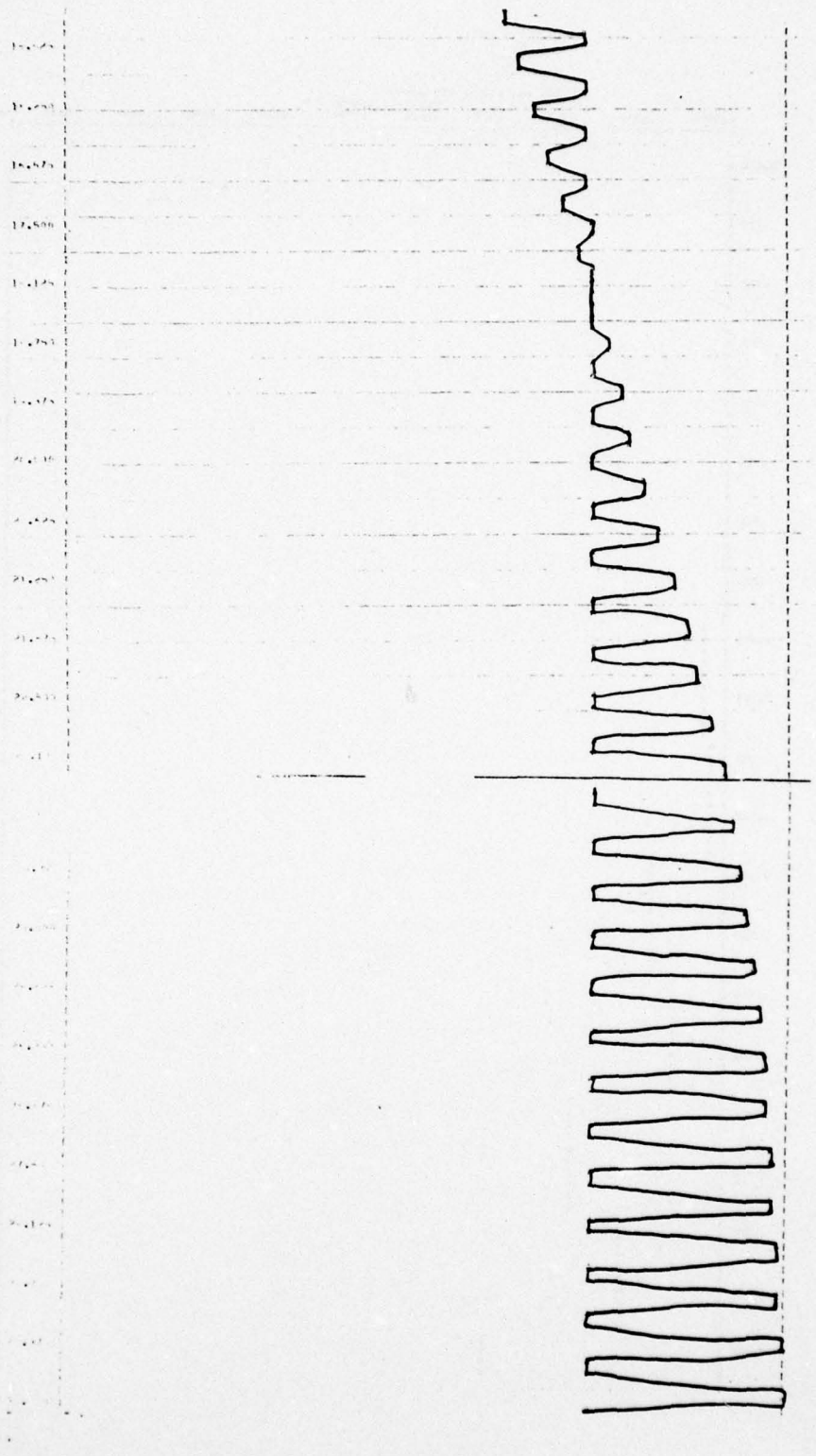

Figure 28. Earth Sensor Output, q = 0.2 deg/sec (concluded)

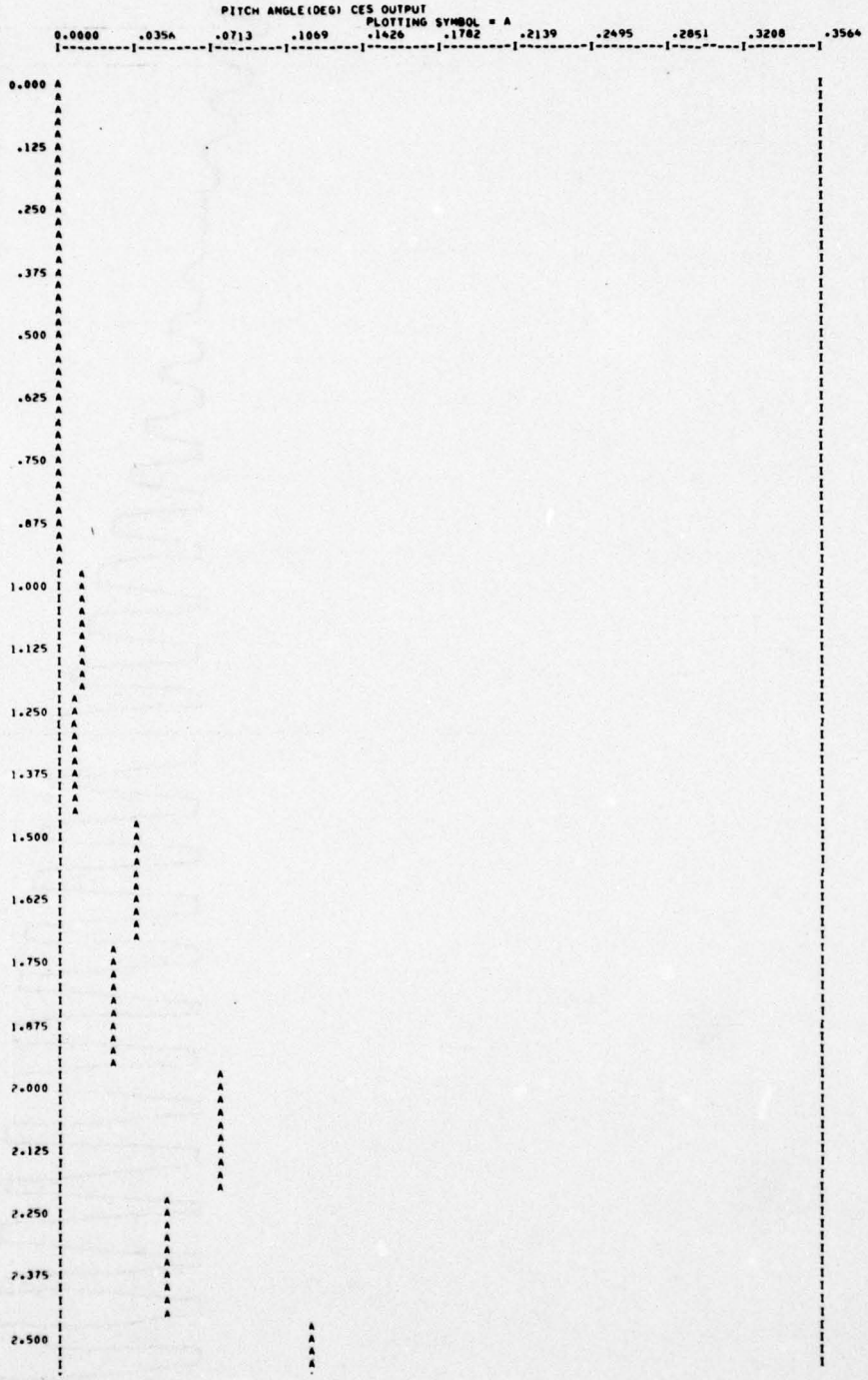

Figure 29a. Earth Sensor Output, Failed Roll Detector

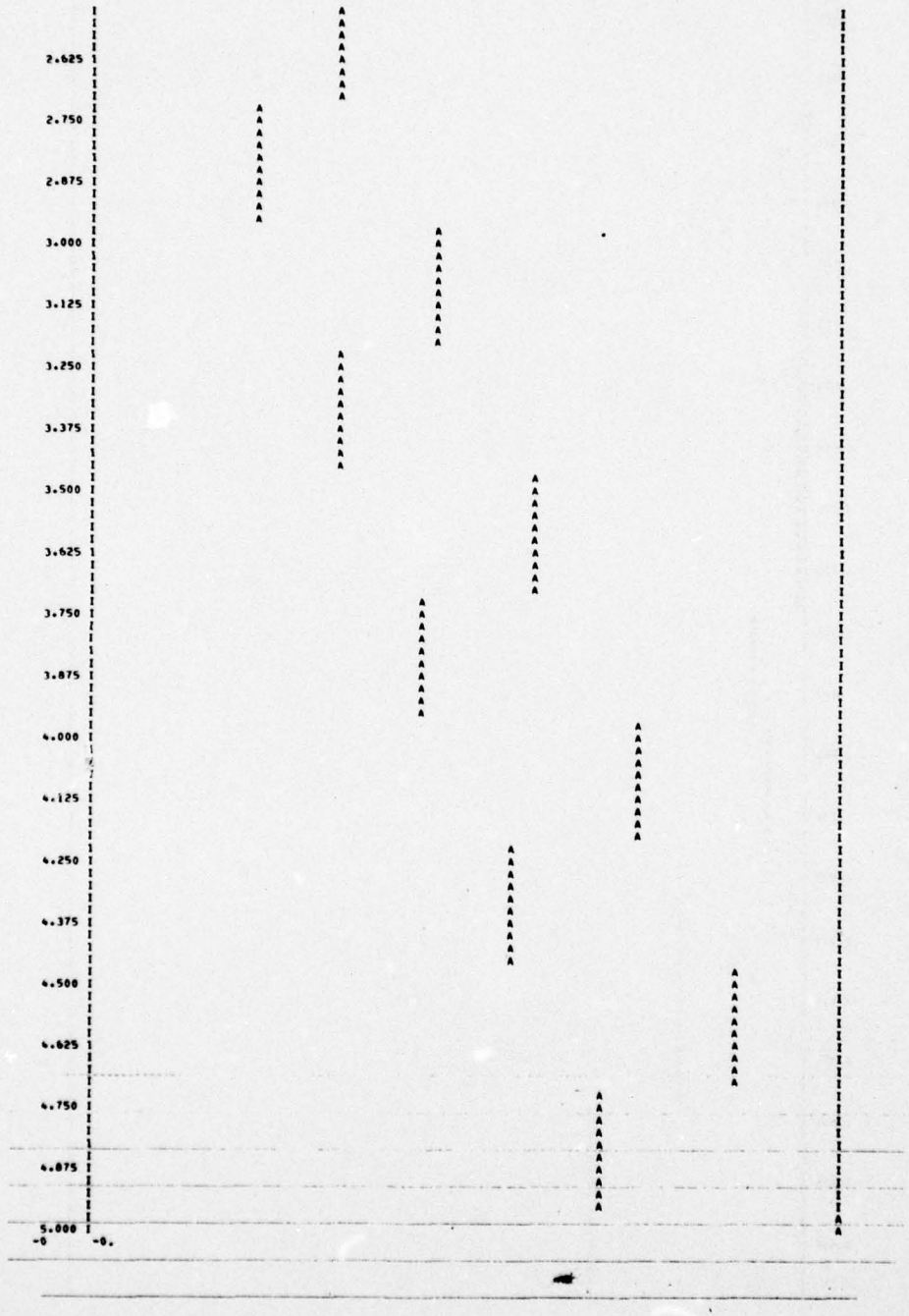

Figure 29a. Earth Sensor Output, Failed Roll Detector (concluded)

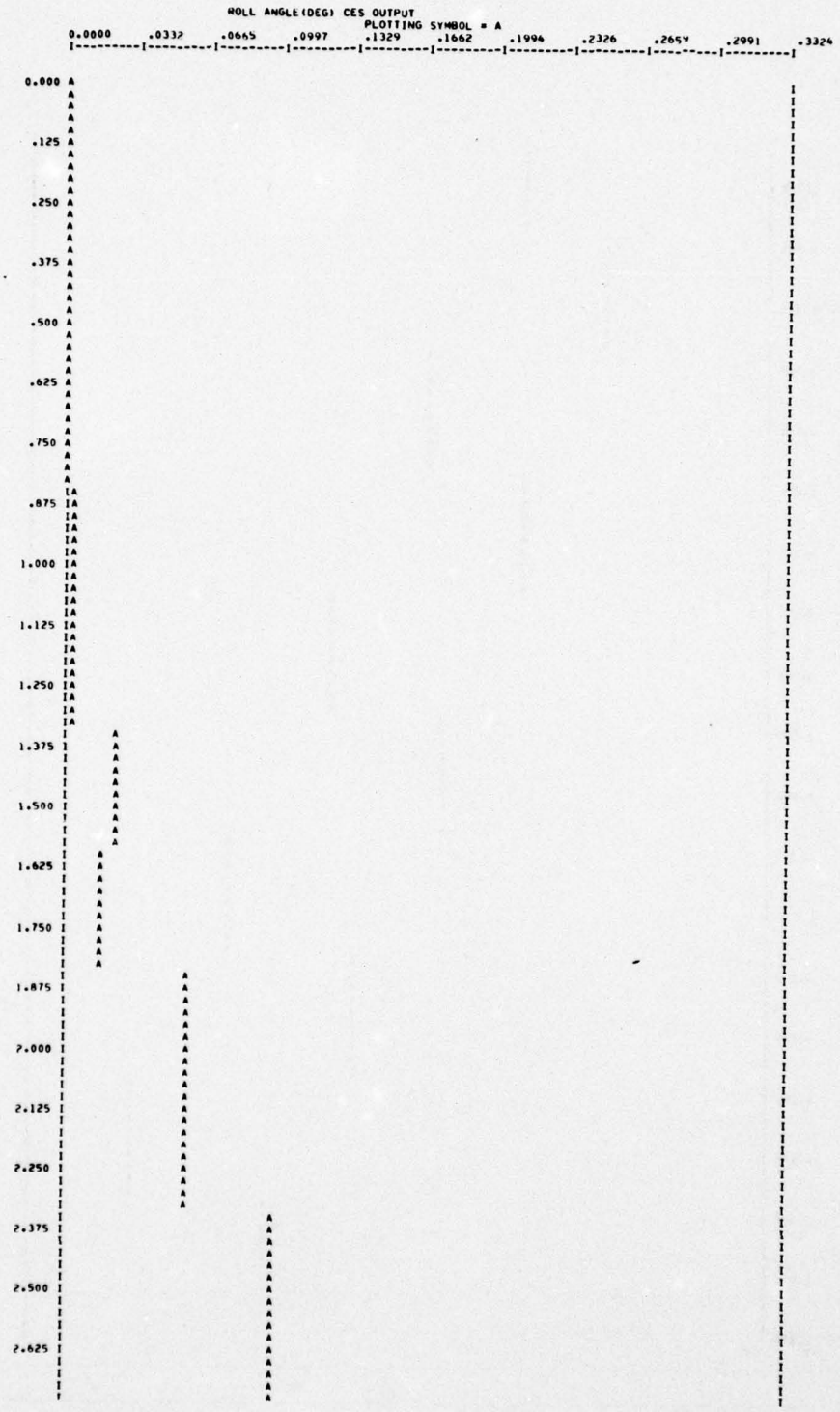

Figure 29b. Earth Sensor Output, Failed Roll Detector

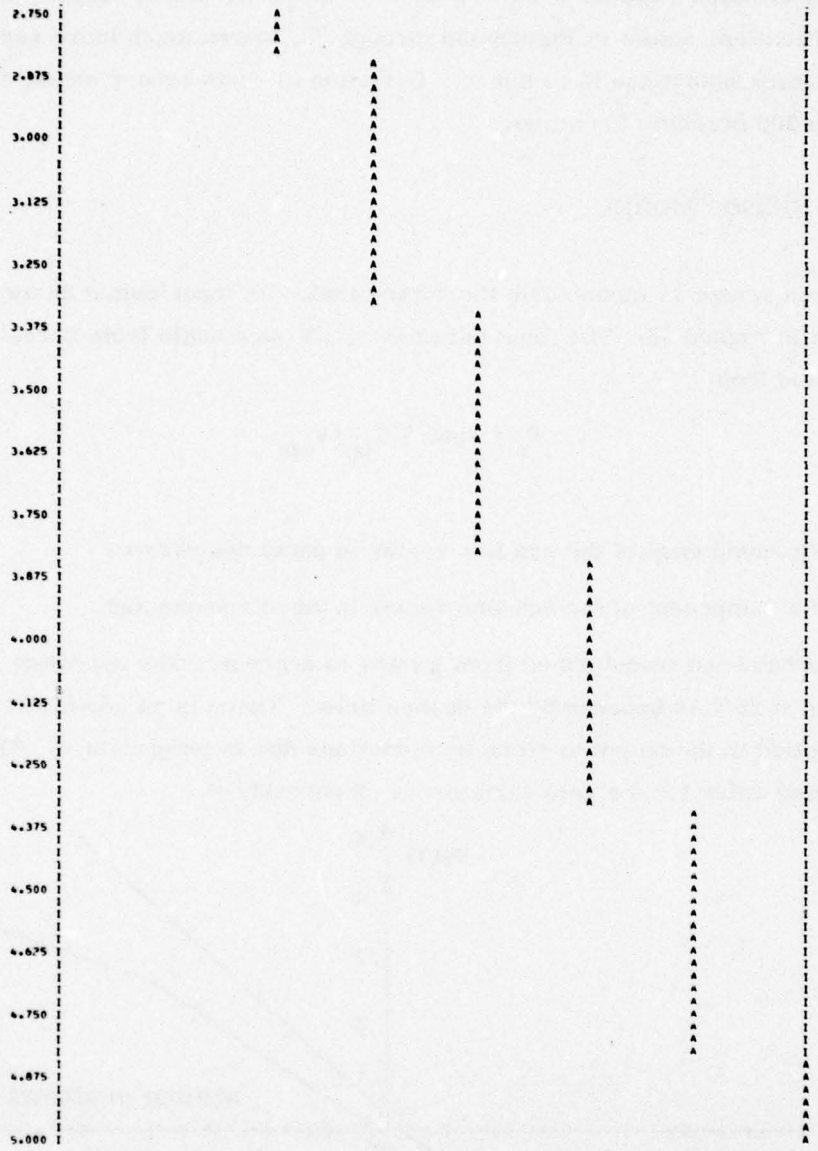

Figure 29b. Earth Sensor Output, Failed Roll Detector (concluded)

Appendix J contains a model of earth radiance effects on sensor output. However, a CES specification, shown in Figures 30 through 32, shows much more serious deviation in earth sensor output due to radiance. Deviation in earth sensor output could range from 40 to 200 percent of nominal.

YAW SUN SENSOR MODEL

The yaw sun sensor is mounted on the solar panel. Its input/output characteristics are shown in Figure 33. The input parameter, rotation angle from boresight (Ψ_s), is calculated from

$$\Psi_s = -\tan^{-1} V_{yp}/V_{zp}$$

where

V_{yp} = y component of the sun line vector in panel coordinates

V_{zp} = z component of the sun line vector in panel coordinates

The output has been transformed from μamps to degrees. The operating accuracy of the sensor at 25°C is bounded by the dashed lines. There is an additional scale factor that is applied to the output to simulate variations due to temperature. The current specification value for the gain variation is .6 percent/°C.

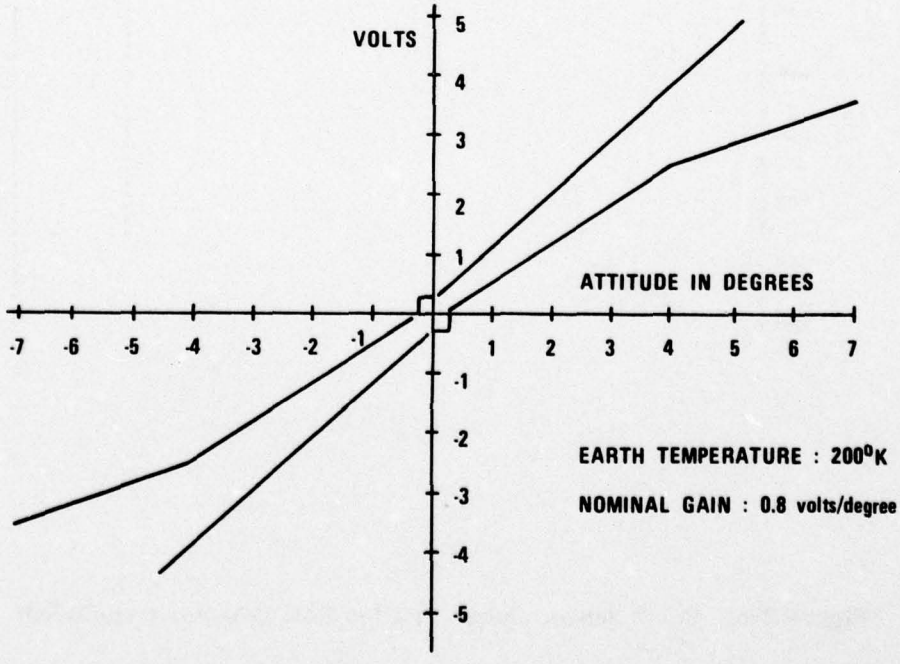

Figure 30. Static Sensor Transfer Function Envelope, 200°K

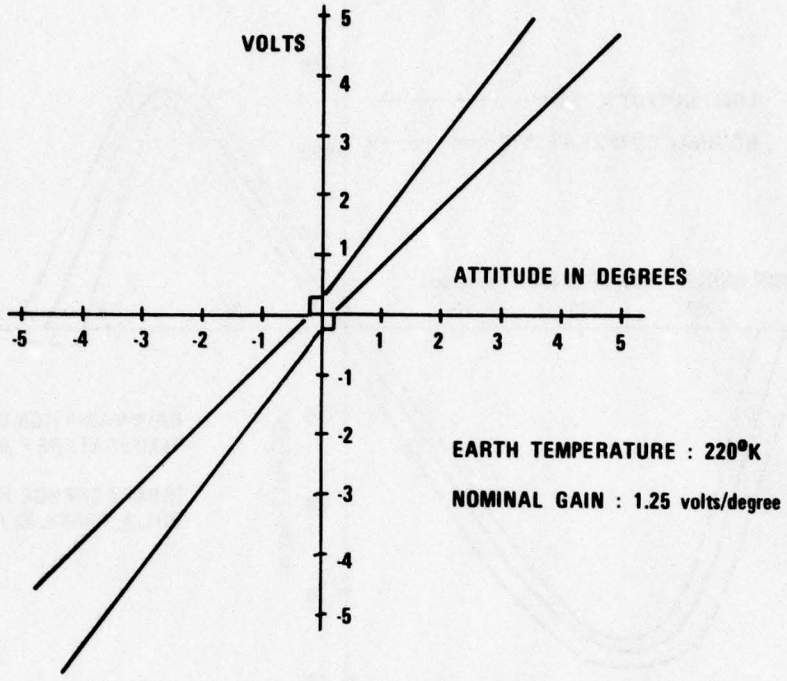

Figure 31. Static Sensor Transfer Function Envelope, 220°K

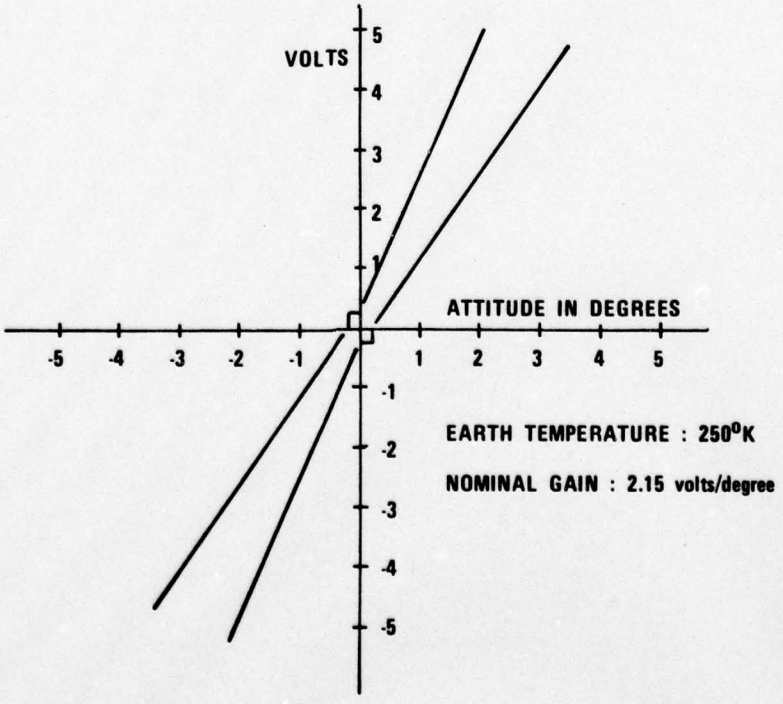

Figure 32. Static Sensor Transfer Function Envelope, 250°K

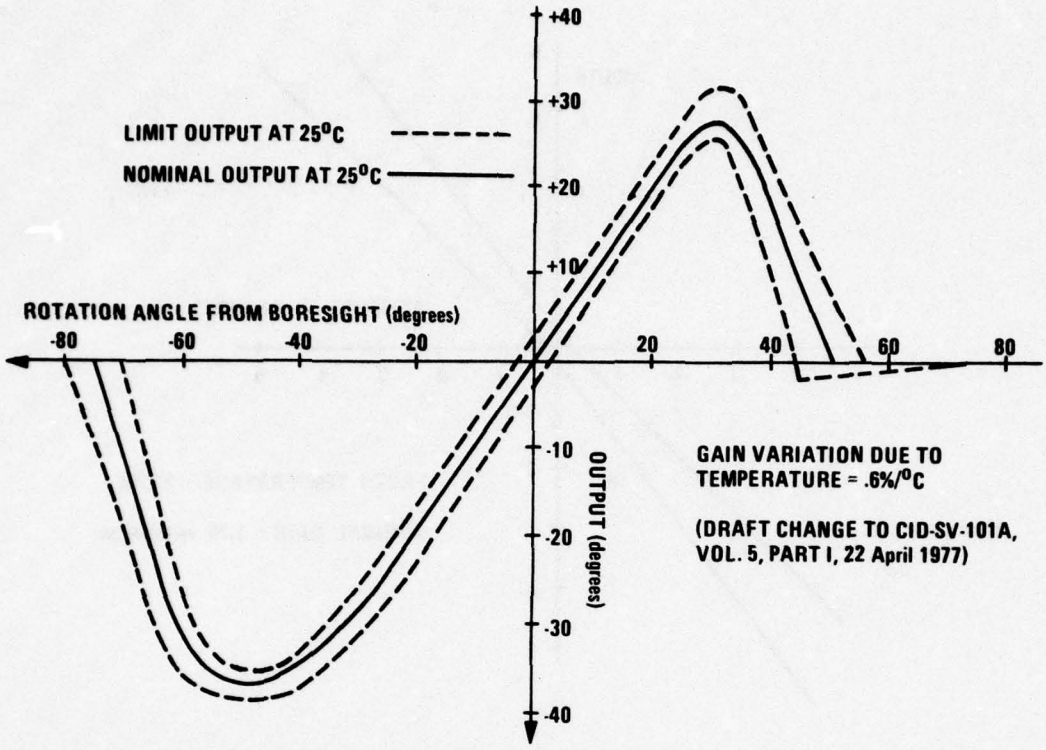

Figure 33. Yaw Sun Sensor Characteristics

SECTION IV

RESULTS

In this section, the results of the independent analysis of NDS control systems and mission procedures are presented. The results are presented as they relate to the GPS mission sequence in the following order:

- Nutation damper performance
- Precession
- Earth acquisition/reacquisition
- -Y array deployment
- Sun acquisition/reacquisition
- On-orbit operations

As stated in Section I, results are referenced to a data base defined in Appendix A.

NUTATION DAMPER PERFORMANCE

Nutation damper performance is evaluated in terms of an equivalent time constant which represents the time required to achieve a 63 percent reduction in nutation angle. The design specification is 1200 sec. The two most significant parameters affecting nutation damper performance are inertia ratio and the distance of the ball in the tube damper from the spin axis. As shown in Appendix D, the motion of the ball in the tube can be modeled with spring damper equations where the frequency of the response is given by

$$\omega_{nd} = \frac{5}{7} \frac{\ell}{R} \omega_z \tag{3}$$

where

ℓ = distance of nutation damper from spin axis

R = radius of curvature of the tube

ω_z = spin rate

Optimum performance of the nutation damper will occur when the nutation damper frequency is tuned to the nutation frequency which is given by

$$\omega_n = \left(\frac{I_{zz} - I_{yy}}{I_{xx}} \right) \omega_z \qquad (4)$$

Combining Equations (3) and (4),

$$\frac{5\ell}{7R} \omega_z = \left(\frac{I_{zz}}{I_{xx}} - 1 \right) \omega_z$$

which when canceling ω_z is independent of spin rate. Figure 34 presents plots of equivalent time constant versus ℓ for different inertia ratios. The time constants were computed using the "energy sink" approximation described in Appendix D. Also shown is the location of the NDS damper at 2.25 ft from the spin axis. At that location, the damper will perform optimally for inertia ratios between 1.3 and 1.4 and performance will degrade as the inertia ratio is reduced from 1.3.

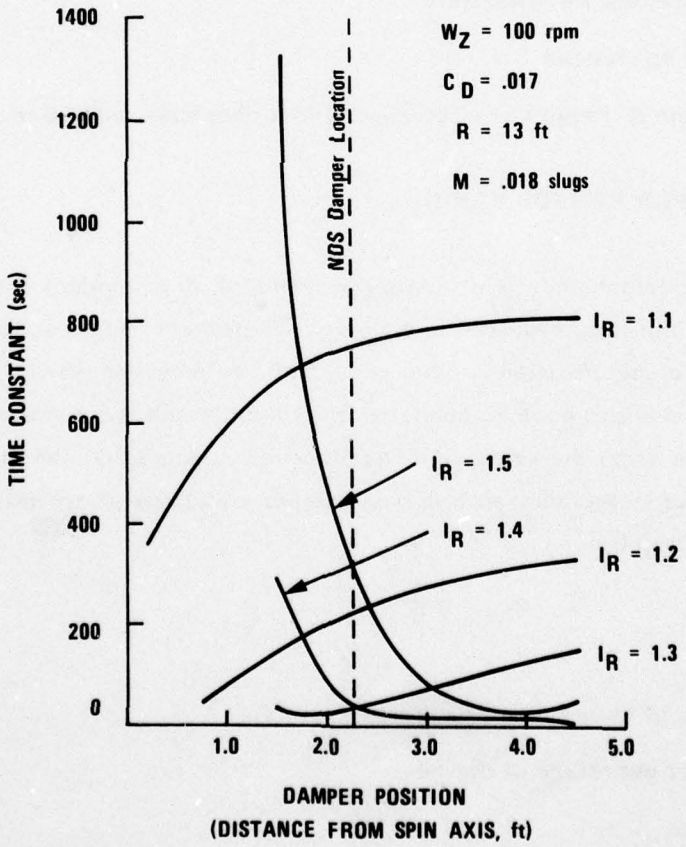

Figure 34. Nutation Damper Time Constant Estimates from Energy Sink Approximation

NDS damper performance was evaluated at two mission conditions: (1) post separation or launch condition, and (2) post AKM burn condition. Mass properties for the two conditions are given in Section III. Performance was evaluated under both nominal and off-nominal conditions. The off-nominal conditions represented variations in the mass properties and in damper characteristics. They may be summarized as follows:

$\Delta I_{zz} = -1.2$ slug ft^2

$\Delta I_{xx} = +3.0$ slug ft^2

$\Delta I_{xx} = +3.0$ slug ft^2

$\Delta I_{xz} = 3.0$ lb-in^2

$\Delta I_{yz} = 3.0$ lb-in^2

$\Delta I_{xy} = 100$ lb-in^2

$\Delta x_{cg} = 0.1$ in

$\Delta y_{cg} = 0.1$ in

$\Delta z_{cg} = 0.2$ in

C_d (damper dissipation coefficient) = 0.012 (-30 percent)

R (damper radius of curvature) = 158.25 in + 10 in

Spin rates were assumed to range from 40 to 95 rpm for the launch condition and from 20 to 95 rpm for post AKM burn. Plots of nutation damper angle for the conditions simulated are given in Figures 35 through 39. Time constants which were extracted from the plots are summarized in Figures 40 and 41. As can be seen, nominal performance does satisfy specification requirements; however, off-nominal performance does exceed the specification requirement slightly at low rpm in the post AKM condition. This fact should be considered in the mission time line particularly in the despin sequence, but we do not consider it to be a problem.

PRECESSION

Prior to the AKM burn, a 180 deg precession maneuver is performed using the 5 lb thrusters. The thruster firing is referenced to the pipper pulse produced by the spin sun sensor when it detects the sun. Details of the precession maneuver are summarized as follows:

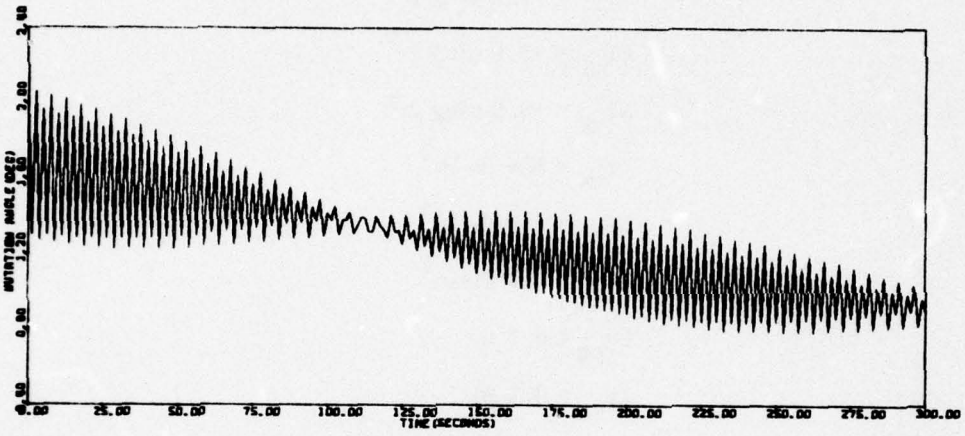

a. Nominal

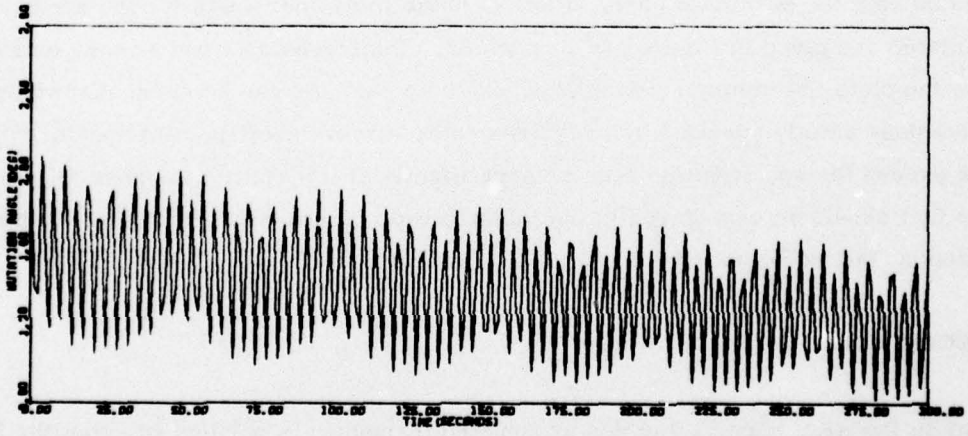

b. Worst Case

Figure 35. Nutation Damper Run, 95 rpm, Launch

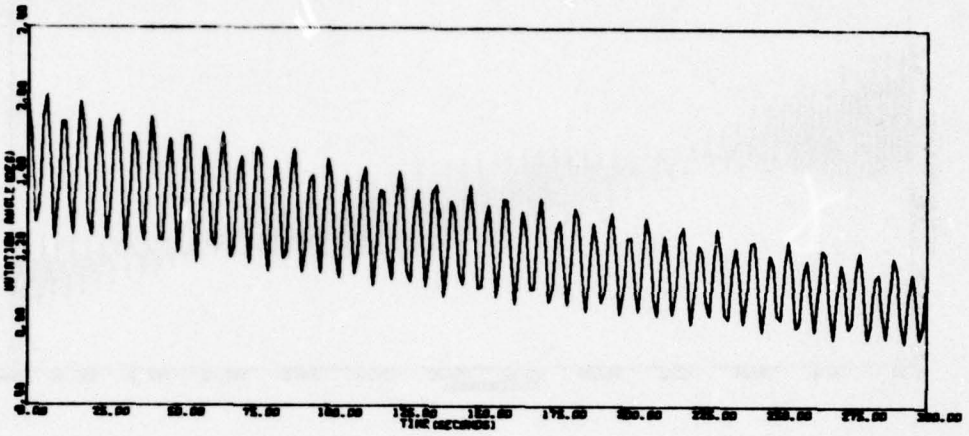

a. Nominal

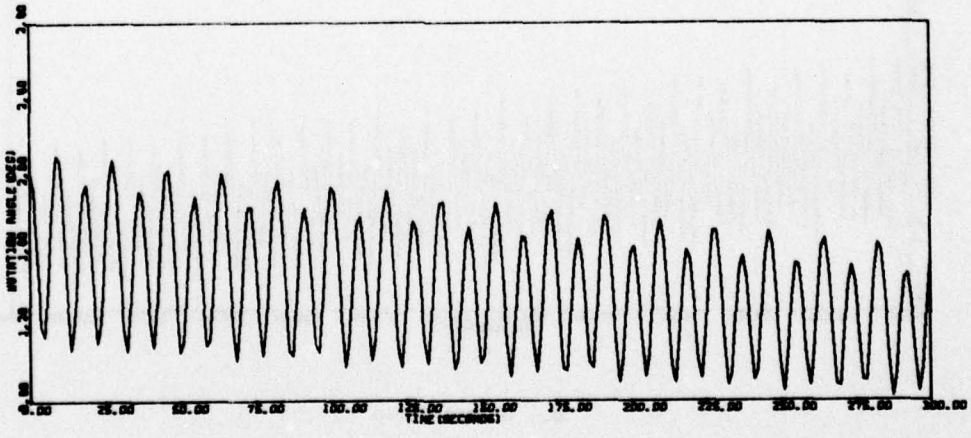

b. Worst Case

Figure 36. Nutation Damper Run, 40 rpm, Launch

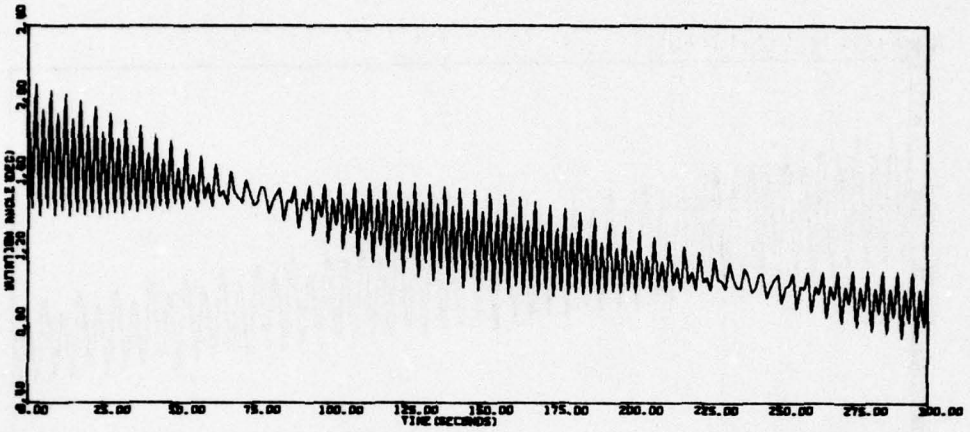

a. Nominal

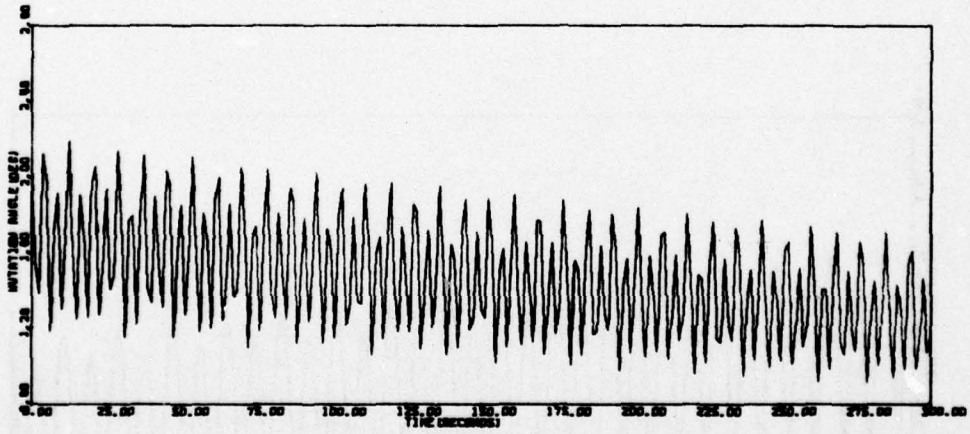

b. Worst Case

Figure 37. Nutation Damper Run, 95 rpm, On-Orbit

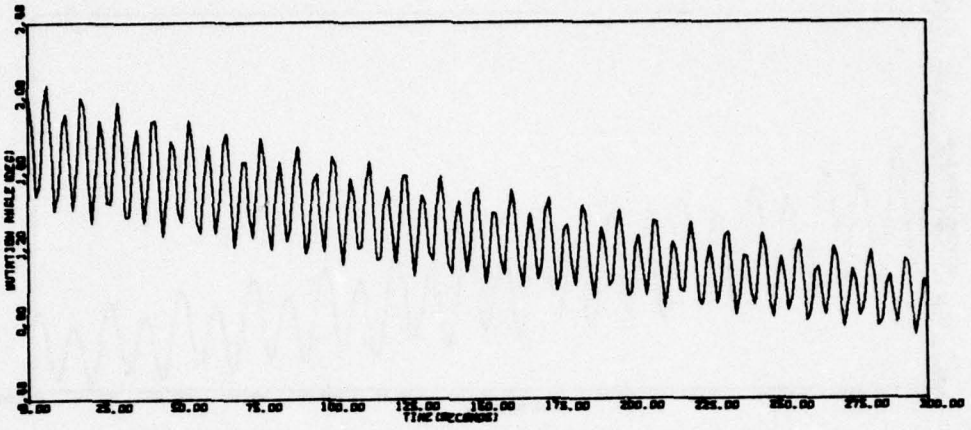

a. Nominal

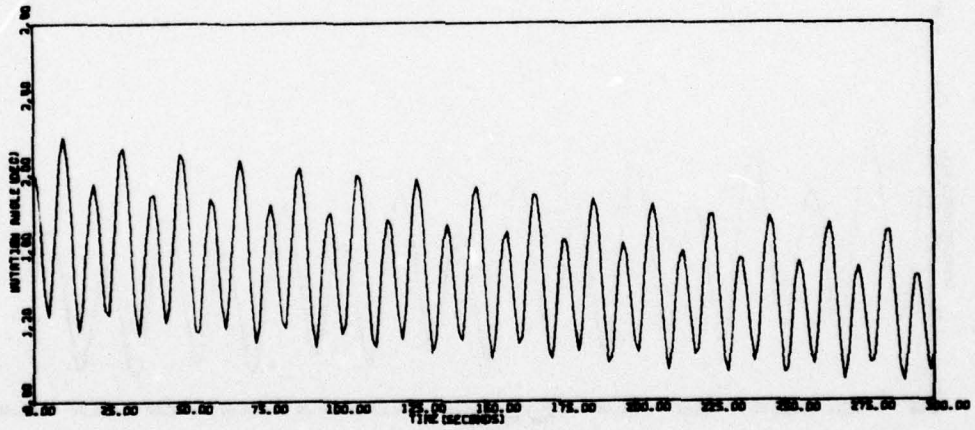

b. Worst Case

Figure 38. Nutation Damper Run, 40 rpm, On-Orbit

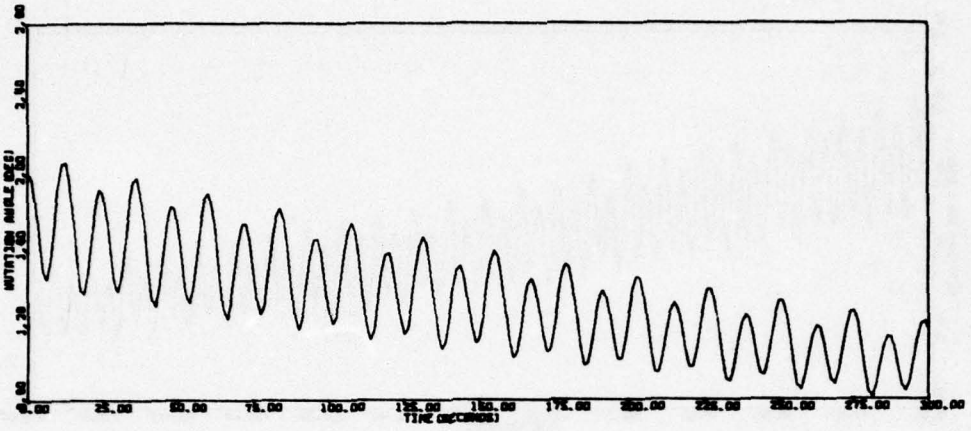

a. Nominal

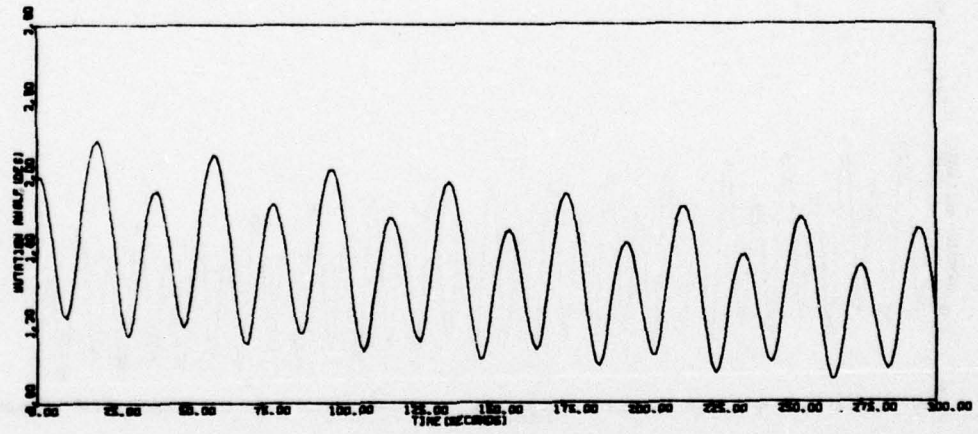

b. Worst Case

Figure 39. Nutation Damper Run, 20 rpm, On-Orbit

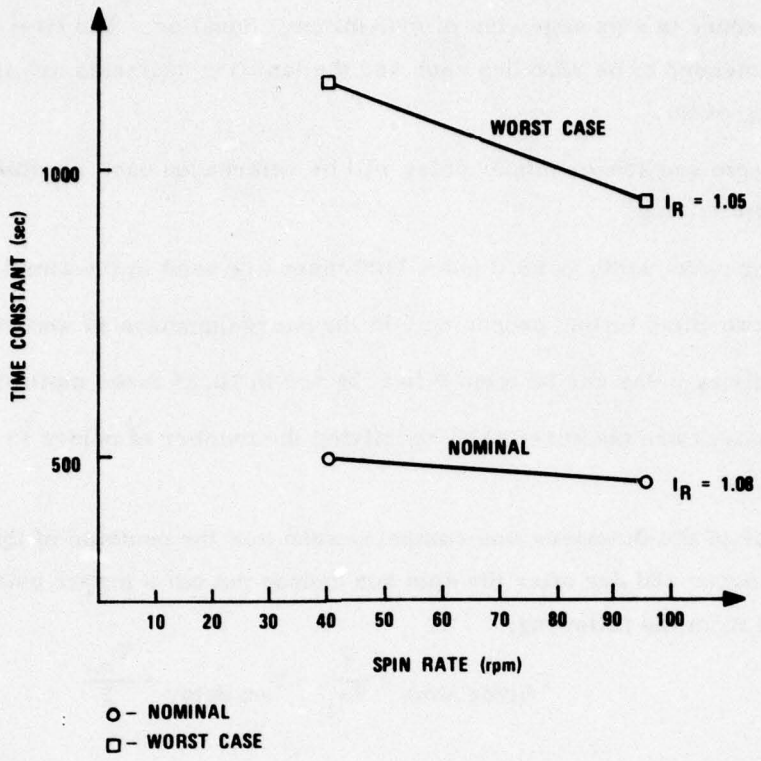

Figure 40. Nutation Damper Time Constant versus Spin Rate for Launch Condition

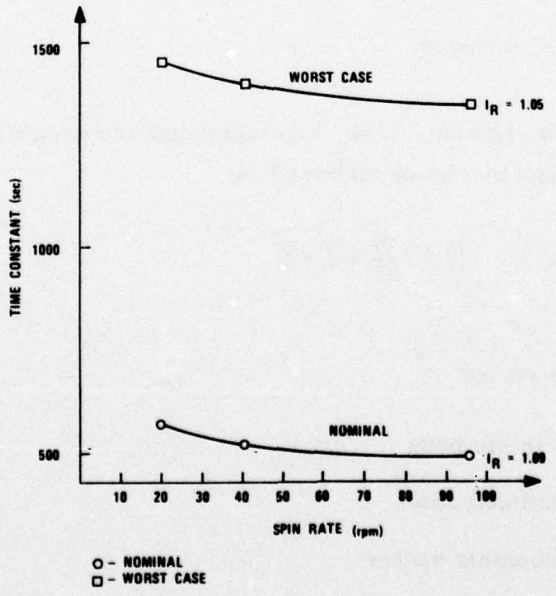

Figure 41. Nutation Damper Time Constant versus Spin Rate for Post AKM Burn

- Procedure is nine segments of four minutes duration. The first four segments are intended to be 22.5 deg each and the last five segments are intended to be 18 deg each.
- The spin sun sensor pipper pulse will be referenced each revolution for thruster firing.
- Firing pulse width is 93.6 msec (100 msec are used in the simulation).
- The two-pitch torque producing 5 lb thrusters (numbers 17 and 18) will be used.
- The firing delay can be from 0 to 5.24 sec in 10.25 msec multiples.
- Thrusters are commanded by specifying the number of pulses in multiples of four.

The firing time of the thrusters was computed such that the centroid of the thrust profile would occur 180 deg after the spin sun sensor put out a pipper pulse. This was computed from the following:

$$T_{\text{firing time}} = \frac{1}{2\omega_z} - T_{\text{on delay}} - \frac{T_{on}}{2}$$

where

ω_z = spin rate

$T_{\text{on delay}}$ = on delay of the thrusters

T_{on} = pulse width of thruster

At the beginning of each segment, $1/2\omega_z$ was computed and used throughout that segment. The number of pulses can be computed based on

$$\vec{T} = \frac{\delta h}{\delta T} + \vec{\omega} \times \vec{h} \qquad (5)$$

where

$\vec{T}$ = inertial torque vector

$\frac{\delta h}{\delta T}$ = torque vector in the body

$\vec{\omega}$ = spacecraft rotational rates

$\vec{h}$ = spacecraft momentum vector

Since spacecraft momentum is mainly in the z axis and since pitch thrusters are being used, Equation (5) reduces to

$$\frac{\delta h}{\delta t} = \omega_x I_{zz} \omega_z$$

The incremental precession attitude change, γ, can then be computed from

$$\gamma = \omega_x T_{on} = T_y / I_{zz} \omega_z T_{on}$$

where

$T_y = \delta h_y / \delta T$ = 5 lb thruster torque

The number of pulses is then computed by dividing the desired precession attitude change per segment by γ.

Table 9 presents a summary of the precession simulation runs. Because of the need to use small integration steps and consequent computer cost, only the first two segments were simulated and the results were extrapolated to nine segments. Plots of the precession maneuver in terms of total precession angle, in-plane precession (roll), out-of-plane precession (pitch), and nutation angle are given in Figures 42 through 45. The off-nominal conditions are defined in Table 10. The results of Table 10 indicate a maximum of 13.2 deg differential in predicted precision angle versus precession angle extrapolated from simulation at 96 rpm. The 150 deg solar aspect angle case exceeds the constraints of 50 deg < β < 130 deg. We were not aware of these constraints at the time of the run. The 150 deg case is shown for information purposes. The 130 deg case shows an extrapolated precession angle of 164 deg which indicates that the 90 deg solar aspect angle would be desirable for precession accuracy purposes.

EARTH ACQUISITION

Earth acquisition analysis was divided into four areas:

1. Despin simulation analysis
2. Jet control loop stability analysis
3. Earth acquisition simulation analysis
4. Earth reacquisition and despin simulation analysis

TABLE 9. SUMMARY OF PRECESSION RUNS

Run Description	Spin Rate (rpm)	Maximum Precession Angle (2 segments)	Extrapolation Precession Angle	Maximum Nutation Angle	Number of Pulses Each Segment	Maximum Pitch	Maximum Roll	Solar Aspect Angle	Pulse Width	Propellant (lbs)
Nominal	96	43.4	173.6	0.71	177	6.9	42.5	90	0.1	1.65
Low Thrust	96	41.7	166.8	0.44	177	6.2	40.9	90	0.1	1.57
High Thrust	96	46.1	184.4	0.49	177	7.9	45.1	90	0.1	1.73
Mismatch	96	43.9	175.6	0.47	177	7.0	43.0	90	0.1	1.65
Low Thrust, Low Spin Rate	75	42.4	169.6	0.98	138	4.4	41.9	90	0.1	1.23
Low Thrust B = 150°	96	36.8	147.2	0.45	177	24.8	23.9	150	0.1	1.57
Low Thrust B = 130°	96	40.9	163.6	0.49	177	19.9	34.8	130	0.1	1.57

TABLE 10. OFF-NOMINAL CONDITIONS FOR PRECESSION SIMULATION

Nutation damper coefficient	0.0119
Nutation damper radius of curvature	14.021 ft
Jet misalignment	1.5 deg
cg misalignment--x axis	0.00833 ft
cg misalignment--y axis	0.00833 ft
cg misalignment--z axis	-0.0775 ft
I_{xx}	107.92 slug ft^2
I_{yy}	119.42 slug ft^2
I_{zz}	124.86 slug ft^2
I_{xy}	-0.4698 slug ft^2
I_{xz}	-0.0078 slug ft^2
I_{yz}	0.0085 slug ft^2

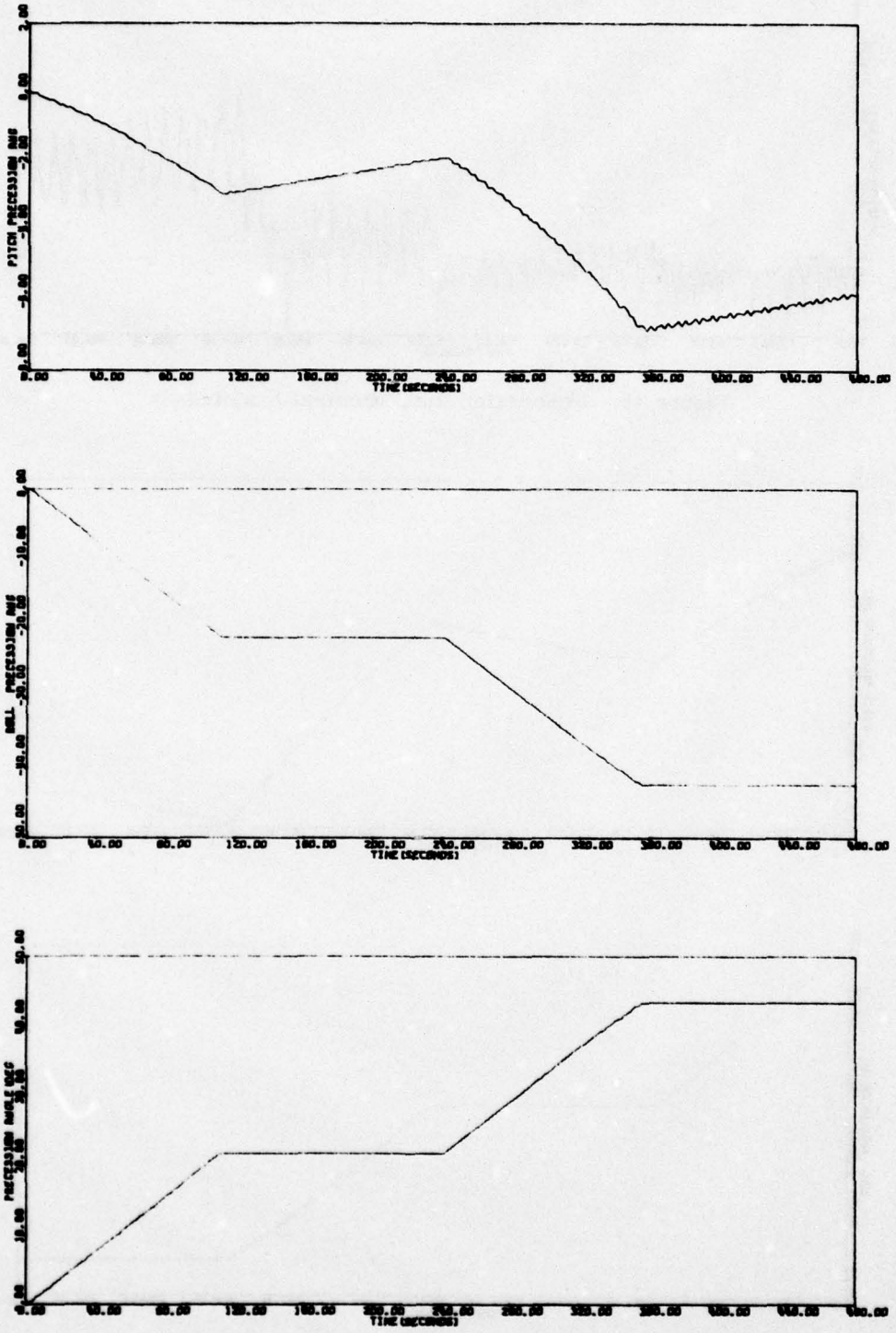

Figure 42. Precession Run, Nominal

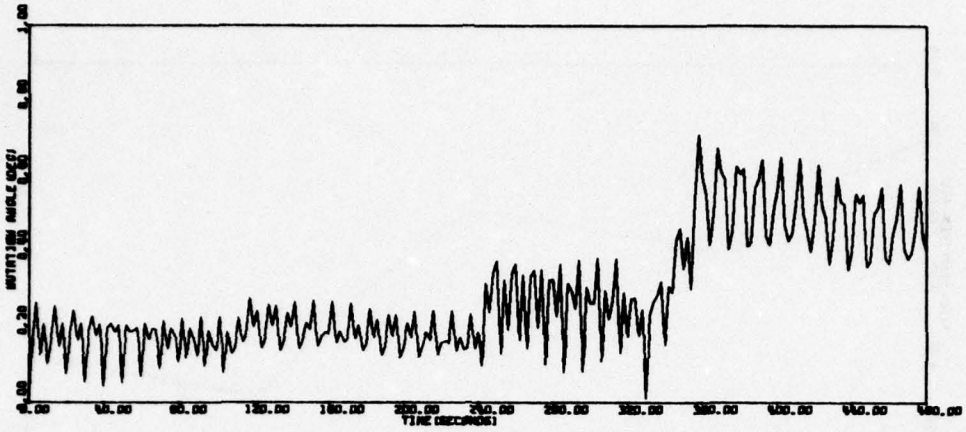

Figure 42. Precession Run, Nominal (concluded)

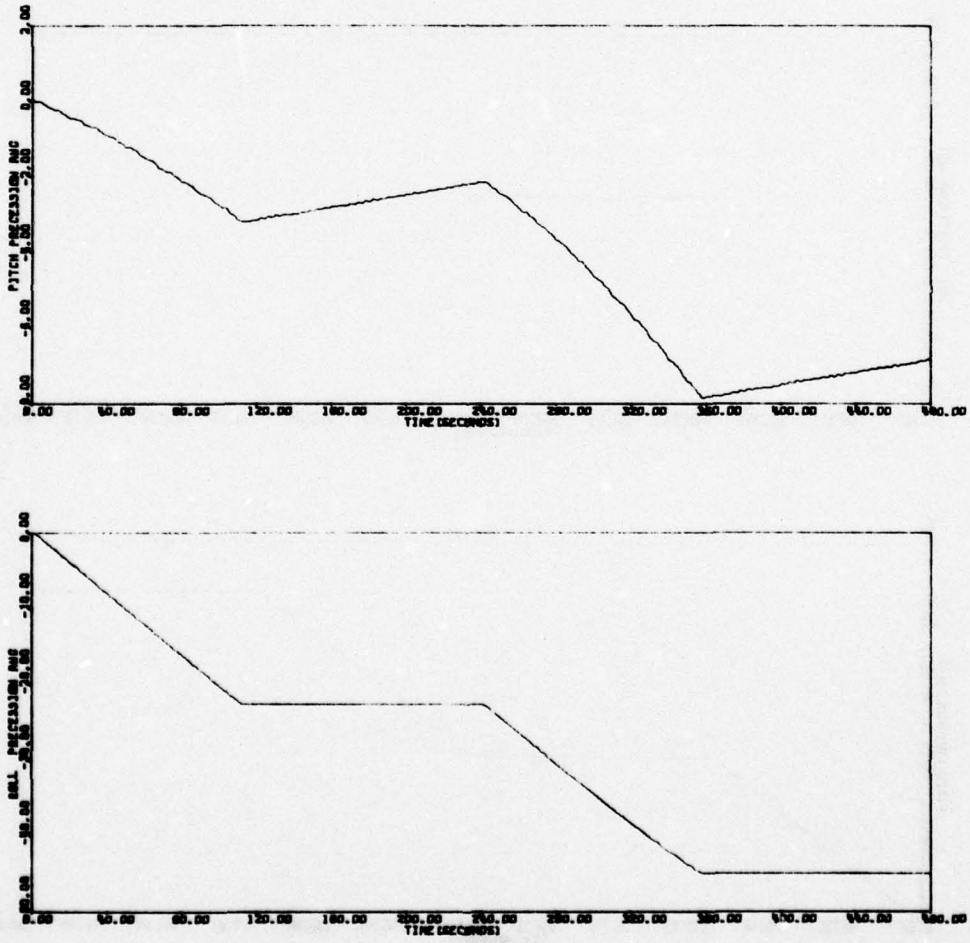

Figure 43. Precession Run, High Thrust, Worst Case

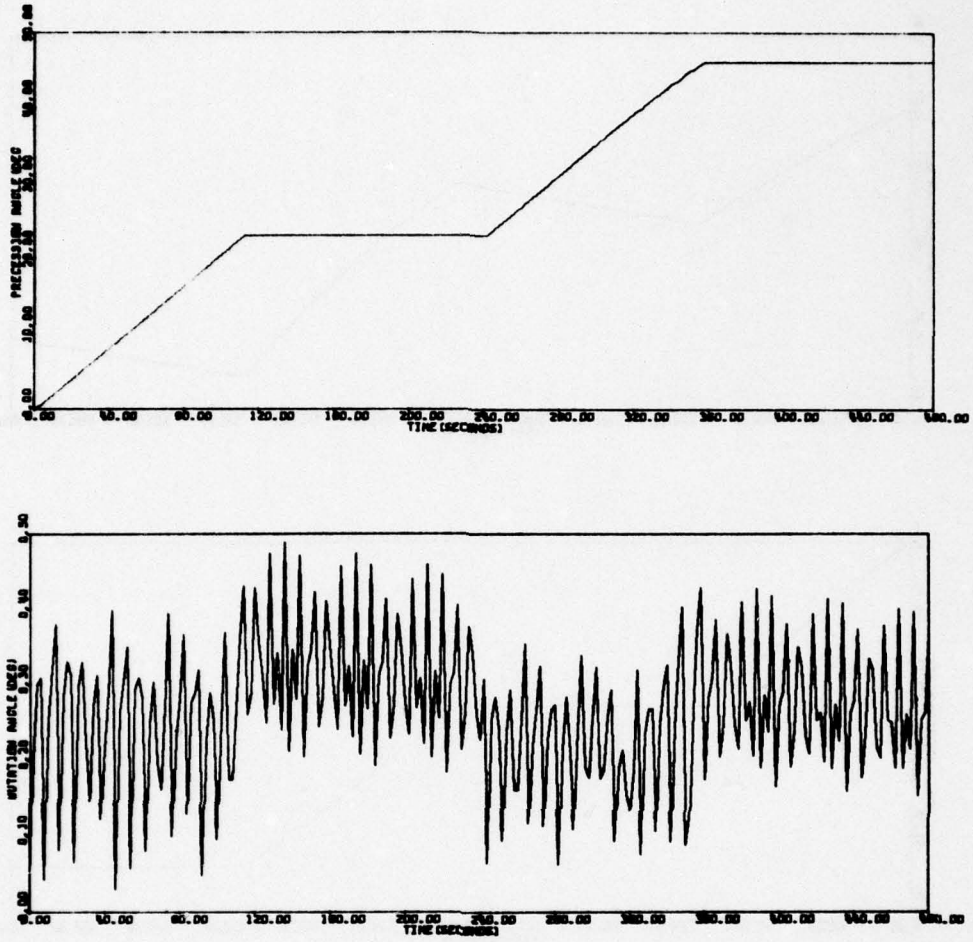

Figure 43. Precession Run, High Thrust, Worst Case (concluded)

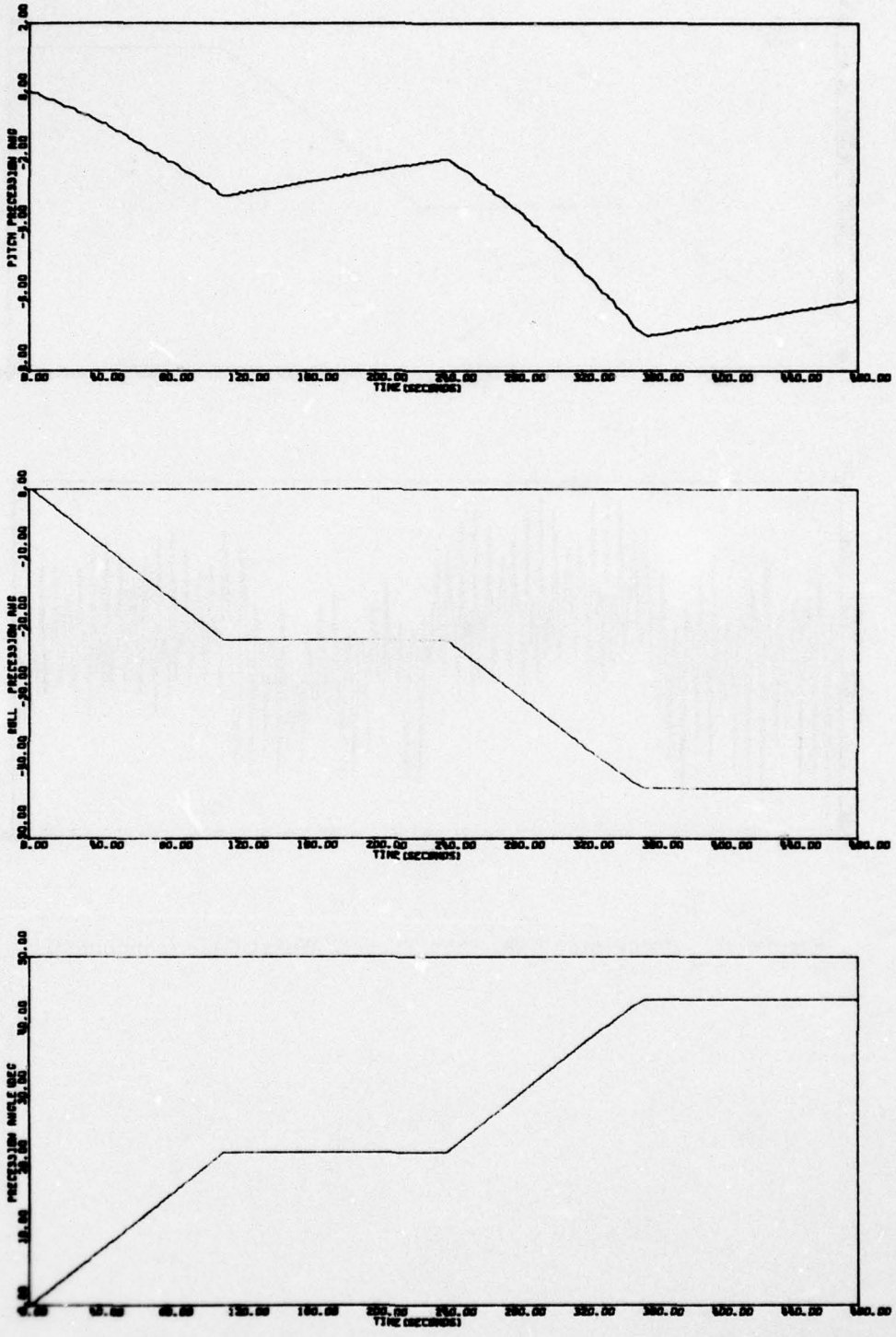

Figure 44. Precession Run, Mismatch, Worst Case

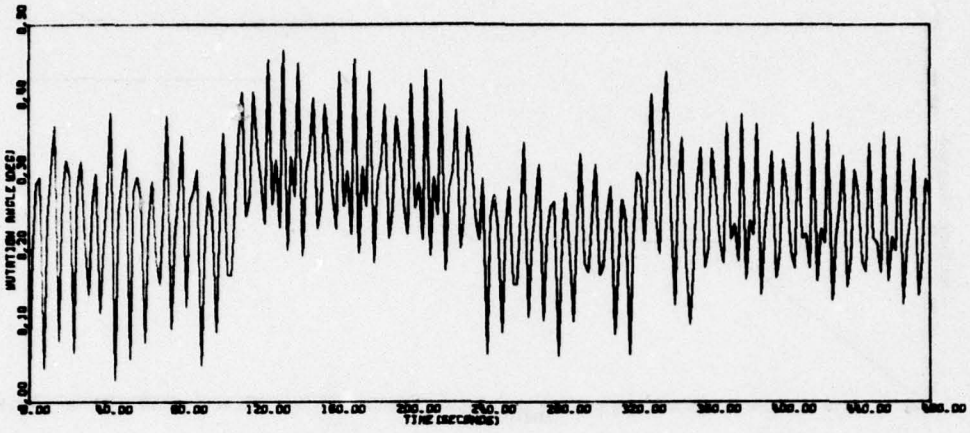

Figure 44. Precession Run, Mismatch, Worst Case (concluded)

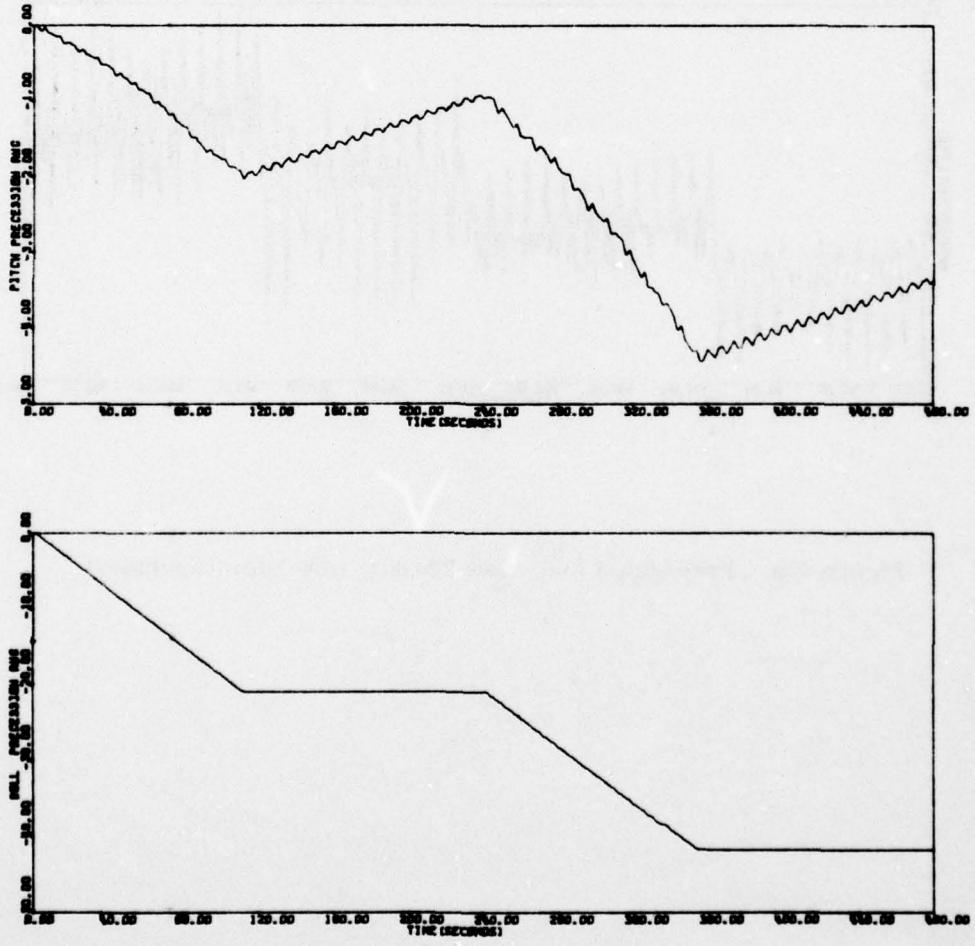

Figure 45a. Precession Run, Low Thrust, Low Spin

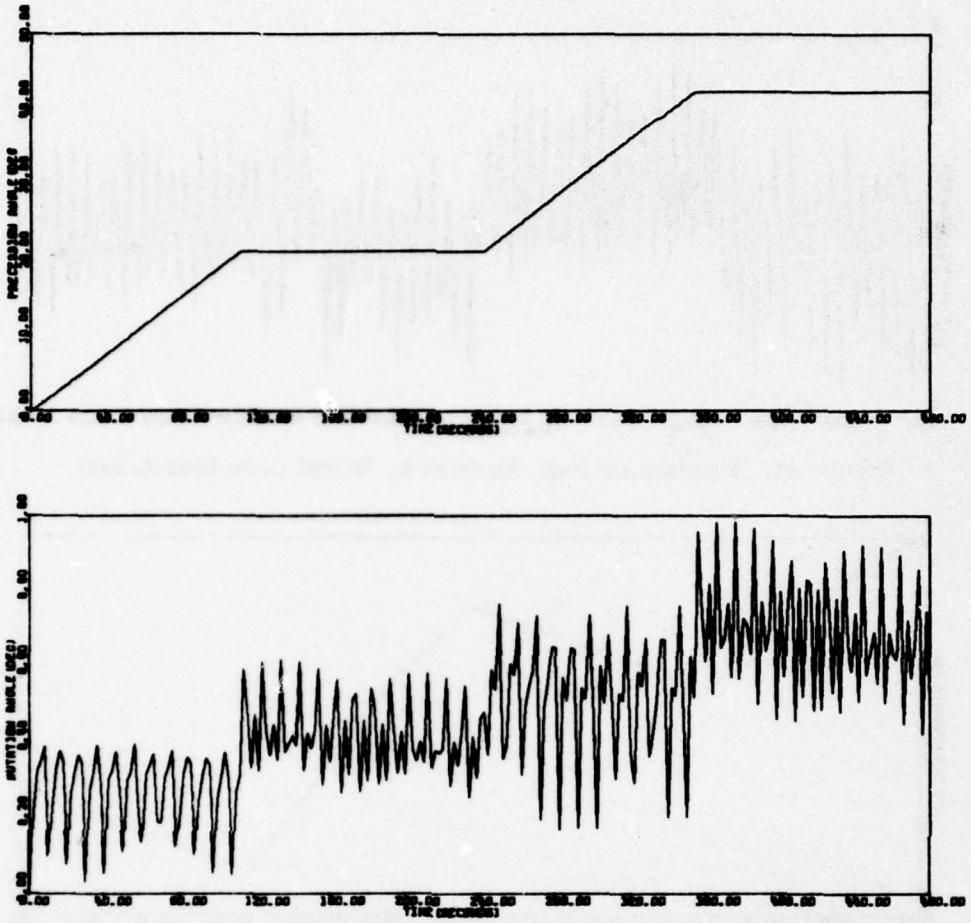

Figure 45a. Precession Run, Low Thrust, Low Spin (concluded)

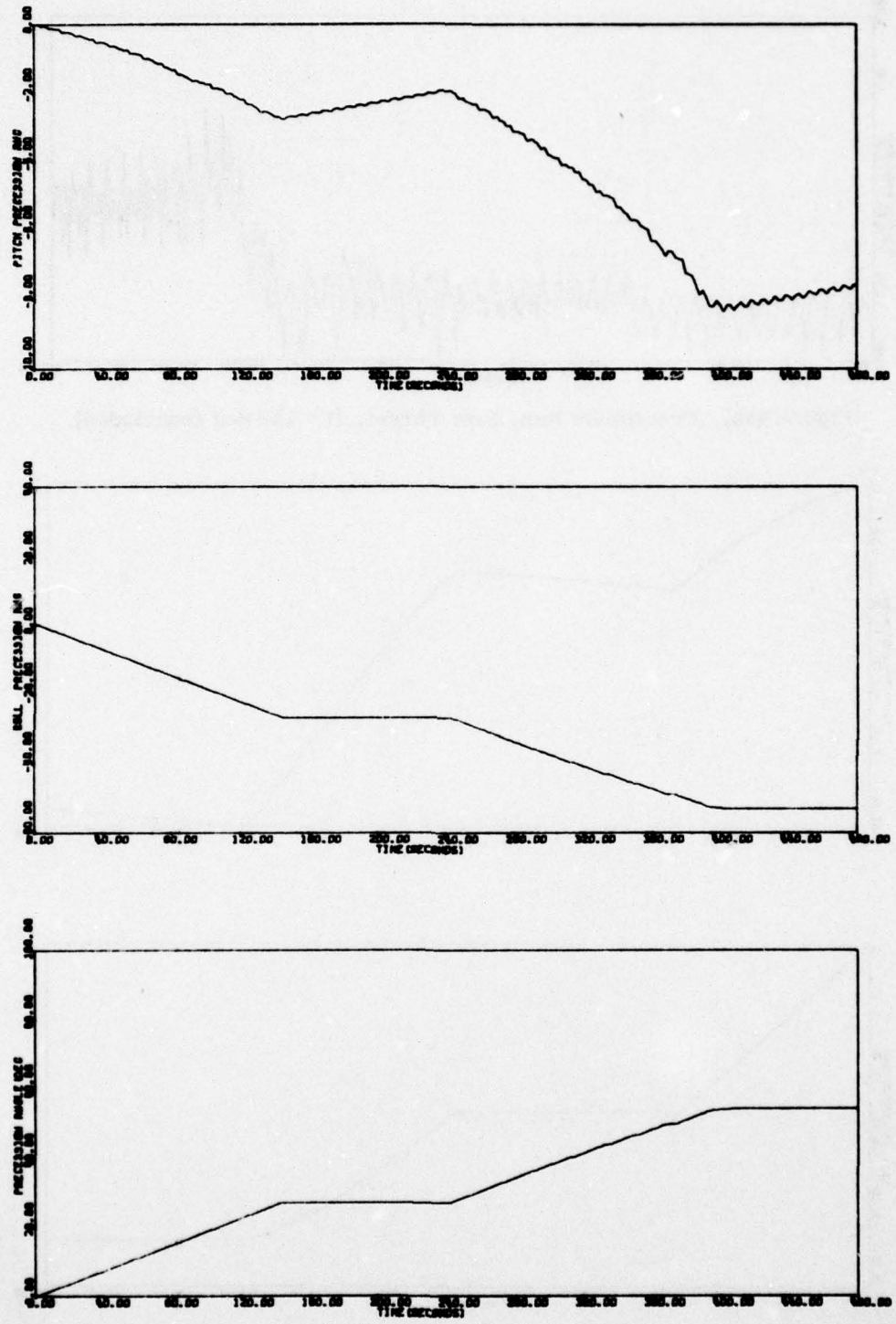

Figure 45b. Precession Run, Low Thrust, B = 150 deg

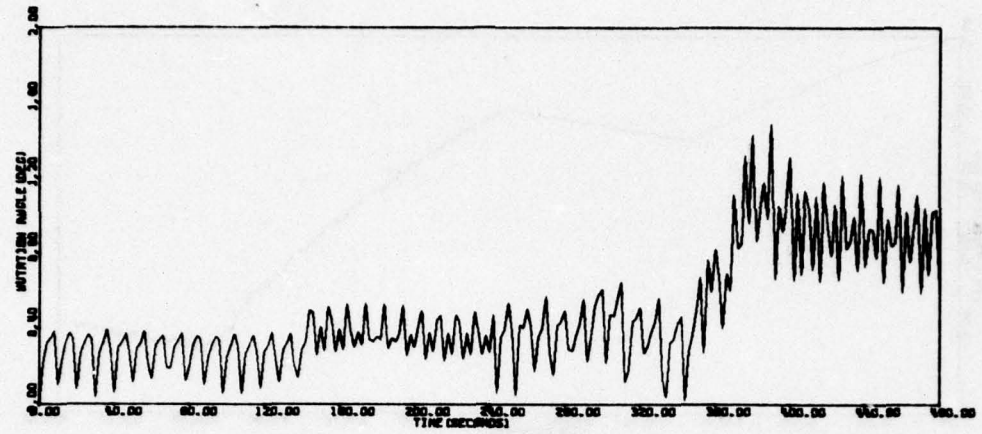

Figure 45b. Precession Run, Low Thrust, B = 150 deg (concluded)

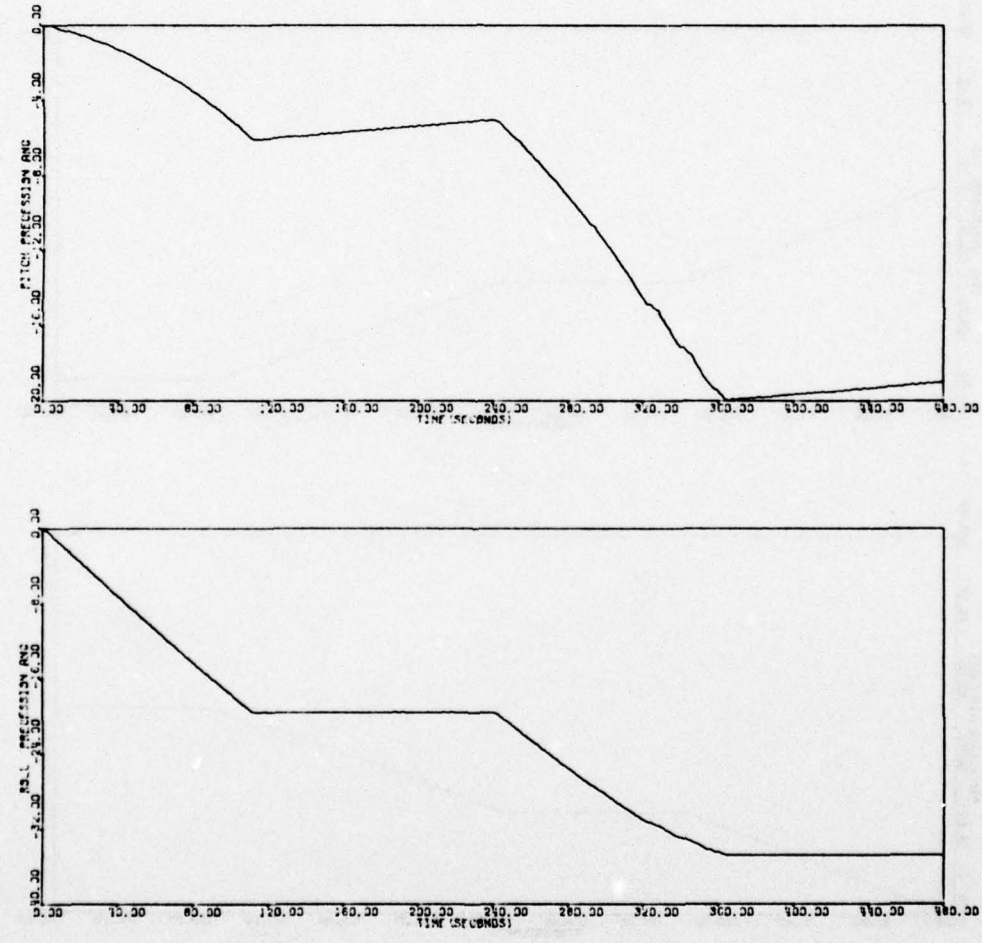

Figure 45c. Precession Run, Low Thrust, B = 130 deg

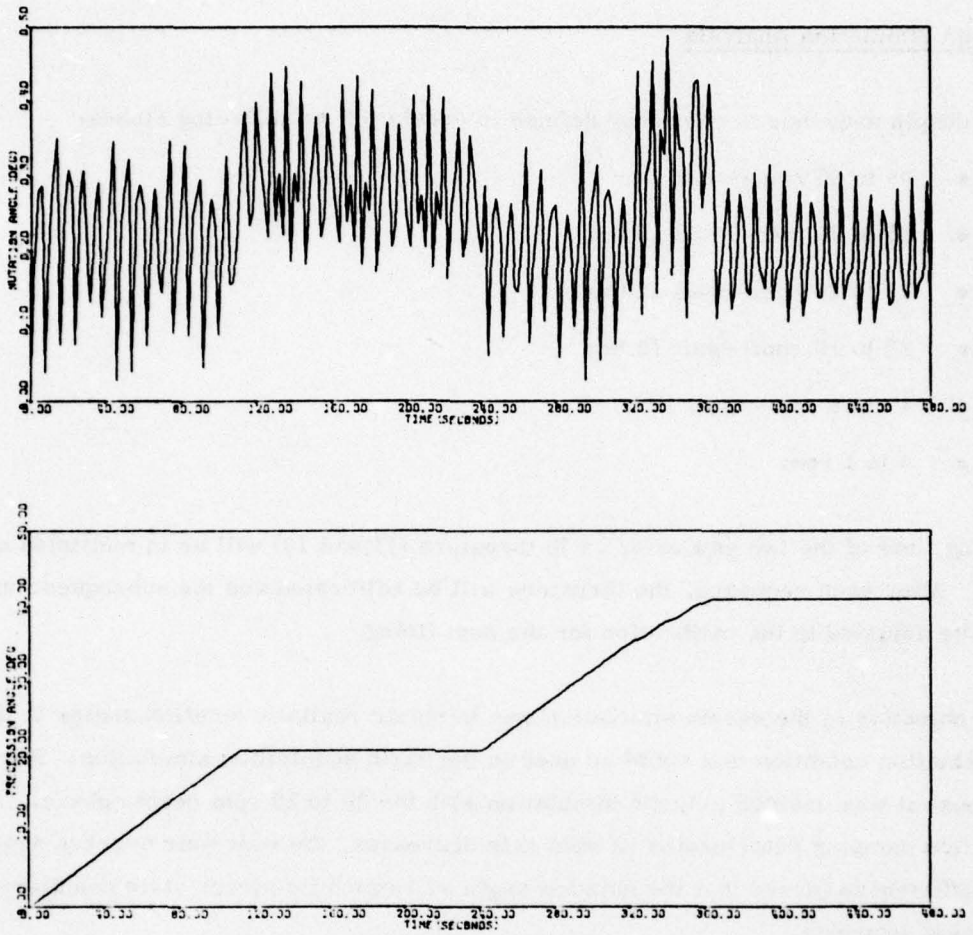

Figure 45c. Precession Run, Low Thrust, B = 130 deg (concluded)

Despin Simulation Analysis

The despin sequence is currently defined to consist of the following stabes:

- 95 to 85 rpm--wait 1 hr
- 85 to 75 rpm--wait 12 hrs
- 75 to 20 rpm--wait 12 hrs
- 20 to 10 rpm--wait 12 hrs
- 10 to 6 rpm--wait 1 hr
- 6 to 1 rpm

Firing time of the two yaw axis, .1 lb thrusters (11 and 13) will be in multiples of 5.27 sec. After each sequence, the thrusters will be calibrated and the subsequent on time will be adjusted to the calibration for the next firing.

The objective of the despin simulation was to obtain realistic nutation angles at the 1 rpm termination condition that could be used in the earth acquisition simulation. For this purpose it was decided to begin simulation with the 20 to 10 rpm despin phase. Although nutation damping deteriorates as spin rate decreases, the wait time between sequences is sufficient to insure that the nutation angle will reach its steady state condition before the next sequence.

The simulated despin runs are summarized in Table 11. All runs were made under worst case conditions, which are defined in Table 12. Jet thrust variations due to the off-nominal conditions were calibrated and on time was adjusted accordingly between each sequence. Plots of vehicle rates and nutation angle for the three runs are given in Figures 46 through 48. As can be seen from Table 12, the worst case nutation angle expected at 1 rpm is 2.5 deg. Final spin rate was in error by approximately 0.17 rpm.

TABLE 11. DESPIN SIMULATION RUNS

Run	Range (rpm)	η_{1c} (deg)	η_T (deg)	τ_{1c} (sec)	τ_T	On Time (sec)	Propellant (lbs)
DS1	20 - 9.95	0.06	0.36	1200	---	174	0.09
DS2	9.95 - 6.00	0.36	0.98	---	1300 sec	68.5	0.034
DS3	6.00 - 0.83	0.11	2.55	1300	3 hrs	89.62	0.045

η_{1c} = nutation angle at start of run

η_T = nutation angle at termination of run

τ_{1c} = time constant of damper at start of run

τ_T = time constant of damper at termination of run

TABLE 12. OFF-NOMINAL CONDITIONS FOR DESPIN SIMULATION

Nutation damper coefficient	0.0119
Nutation damper radius of curvature	14.021 ft
Jet 11 thrust at temperature	0.12188 lbs
Jet 13 thrust at temperature	0.12813 lbs
Jet misalignment	1.0 deg
I_{xx}	97.064 slug ft^2
I_{yy}	105.21 slug ft^2
I_{zz}	110.10 slug ft^2
I_{xy}	-0.4095 slug ft^2
I_{xz}	-0.0078 slug ft^2
I_{yz}	-0.0085 slug ft^2

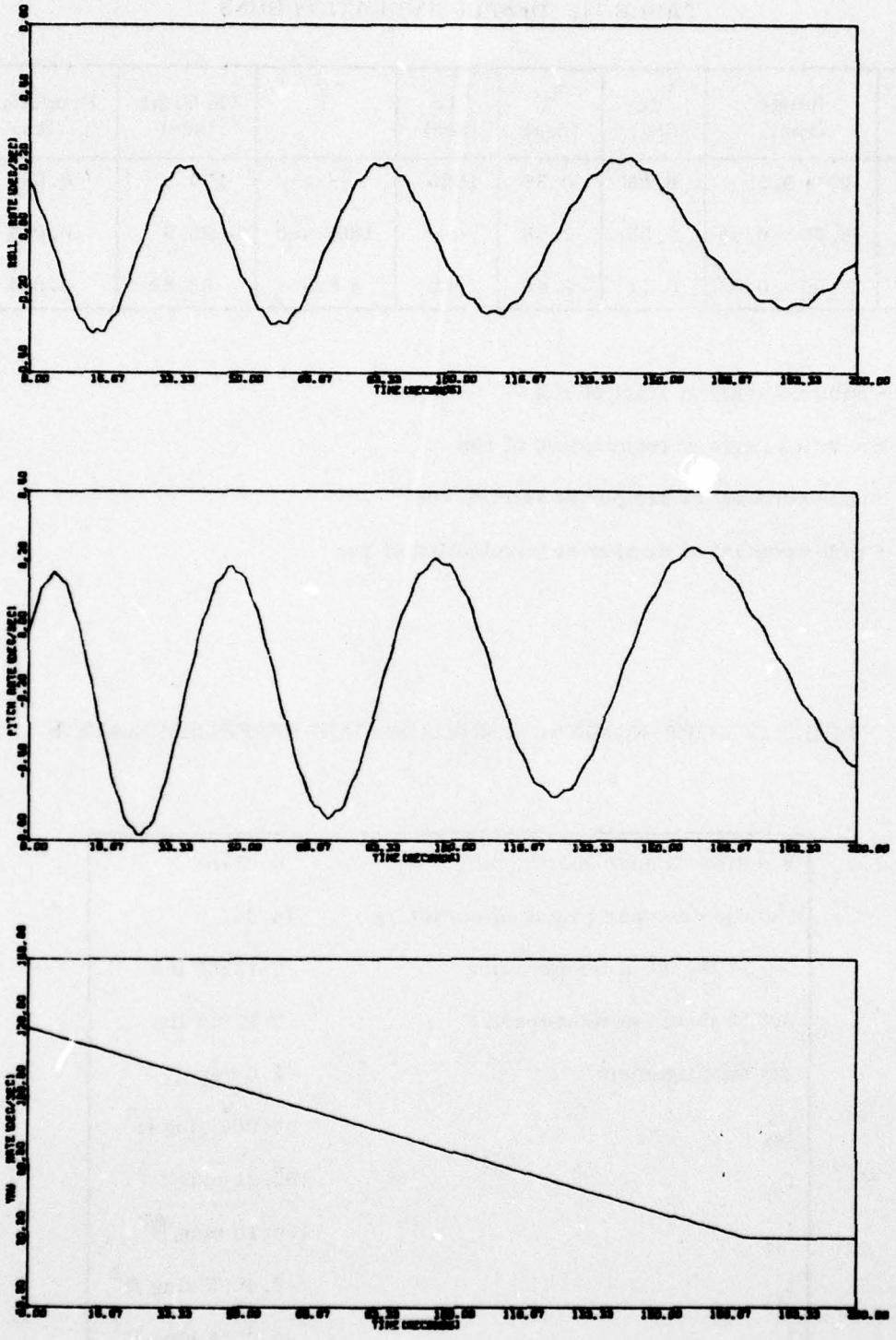

Figure 46. Despin Run, Worst Case, 20 to 10 rpm

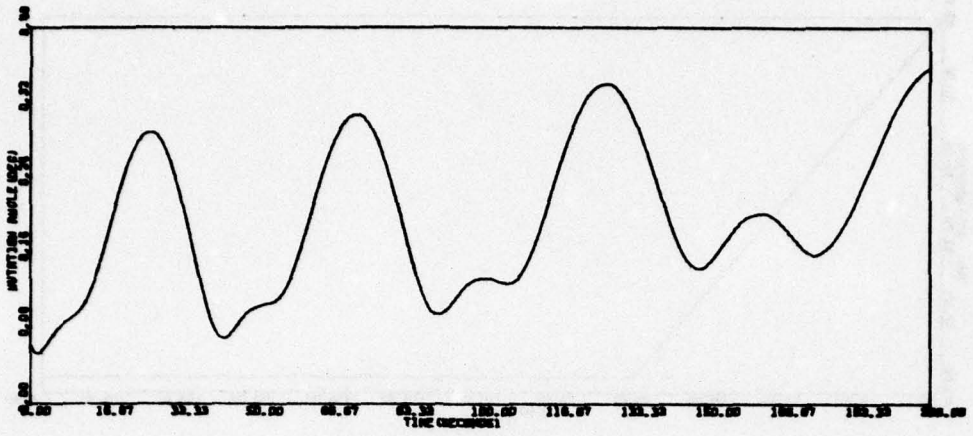

Figure 46. Despin Run, Worst Case, 20 to 10 rpm (concluded)

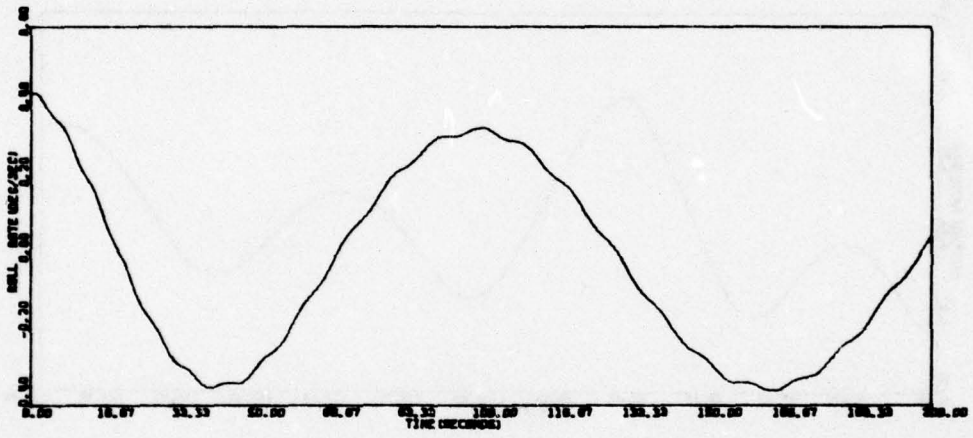

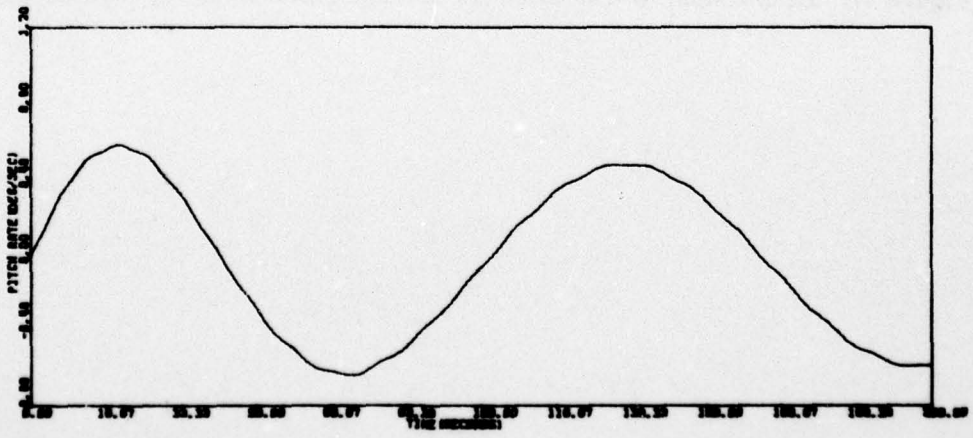

Figure 47. Despin Run, Worst Case, 10 to 6 rpm, Stowed Array

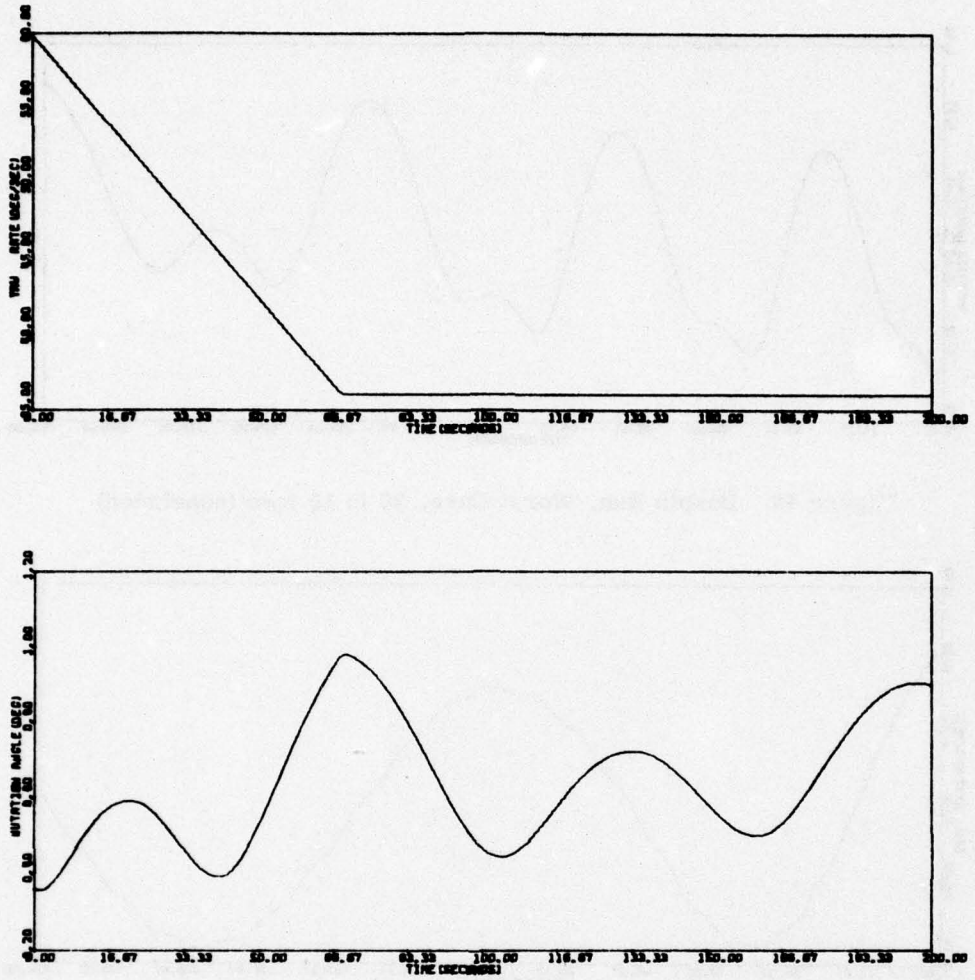

Figure 47. Despin Run, Worst Case, 10 to 6 rpm, Stowed Array (concluded)

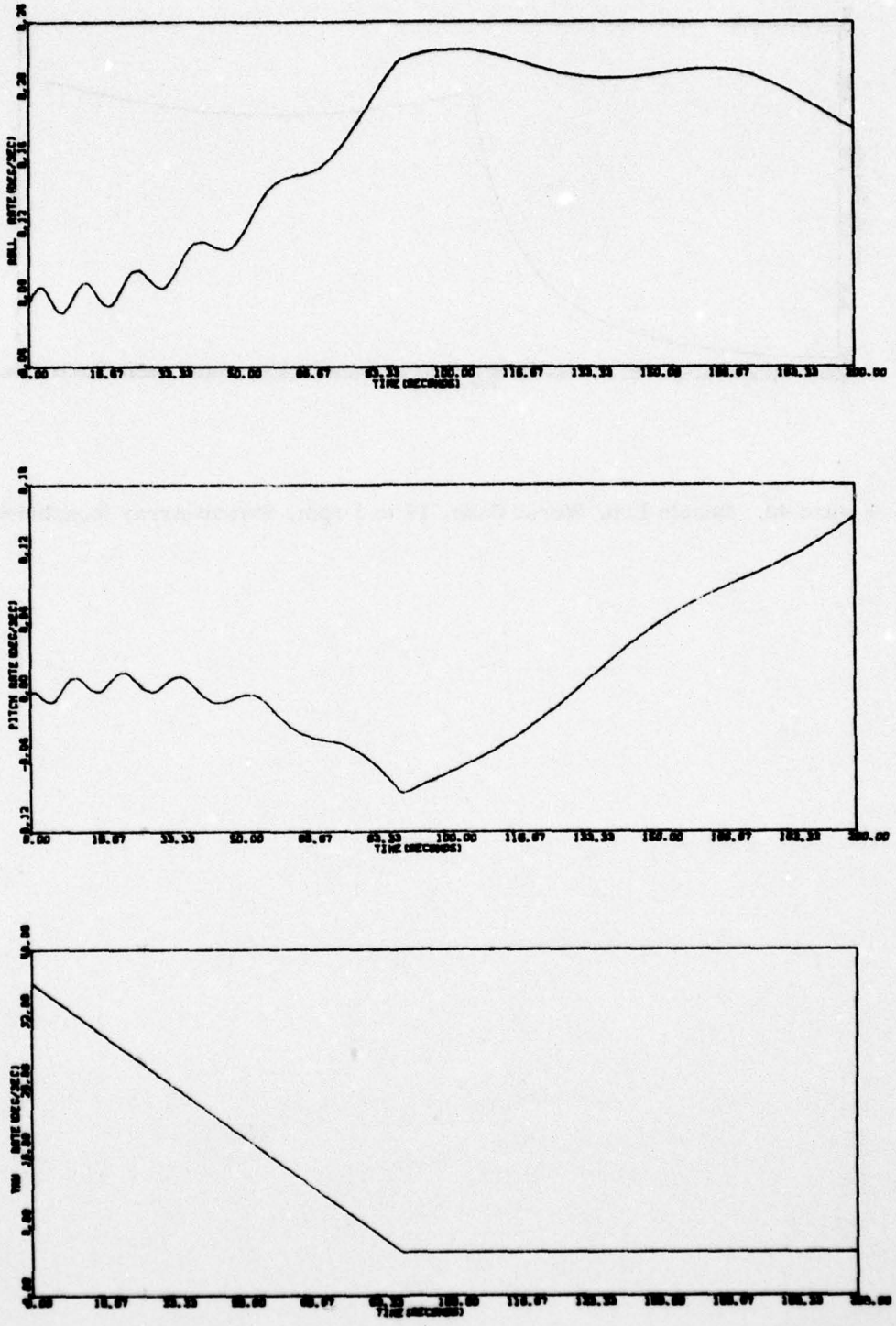

Figure 48. Despin Run, Worst Case, 16 to 1 rpm, Stowed Array

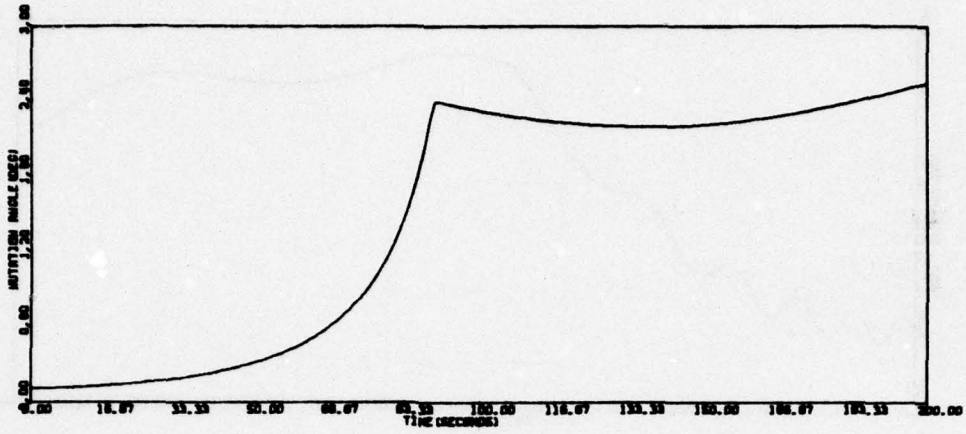

Figure 48. Despin Run, Worst Case, 16 to 1 rpm, Stowed Array (concluded)

Jet Control Loop Stability Analysis

The jet control system shown in Figure 49 was analyzed using frequency domain techniques to determine stability for both acquisition and reacquisition. This analysis was conducted for the two versions of the control system. Version 1 (denoted by *) represents the control system being used for the first NDS satellite; Version 2 (denoted by #) represents the design to be used on the remaining NDS satellites.

The technique used to examine stability is open-loop frequency response analysis. To apply this technique, the control system must be linearized. This is accomplished using describing function analysis. Next, we examine stability of each of the linearized control loops by neglecting spin rate about the z body axis to remove coupling between roll and pitch. This is done first for small attitudes below sensor saturation and later for large attitudes well above saturation. Large attitudes are typical of what may be encountered during acquisition. Finally, we examine the effects of spin rate on control system stability.

Linearized Single-Axis Jet Control Loops--Starting with the block diagram in Figure 49, and neglecting spin rate about the z axis, each axis of the jet control system can be examined independently. By collecting scale factors, each loop can be redrawn in a form more convenient for analysis (Figure 50). Note that the jet relay has been normalized to unite output with input trip levels specified in degrees.

In order to apply frequency domain techniques, each loop must be linearized. For small attitudes (< 4 deg) we can ignore the saturation element. The jet relay, however, cannot be ignored since it is an integral part of the jet control system. Using describing function analysis we can replace the relay by a linear equivalent gain and phase.

Describing function analysis is based on the fact that the output of any nonlinear element in response to sinusoidal input can be expressed as a Fourier series consisting of constant, fundamental, and higher order harmonics of the input frequency. The equivalent gain is simply the amplitude ratio of the fundamental component of the output to that of the input; the equivalent phase is the corresponding phase shift of the fundamental component of the output relative to the input. The general procedure for computing the describing function equivalent is illustrated mathematically in

AD-A056 811 HONEYWELL INC MINNEAPOLIS MINN SYSTEMS AND RESEARCH --ETC F/G 17/7
INDEPENDENT STABILITY AND CONTROL ANALYSIS OF NAVIGATION DEVELO--ETC(U)
JAN 78 R E POPE, M D WARD, M F BARRETT F04701-75-C-0135

UNCLASSIFIED 78SRC10-VOL-1 SAMSO-TR-78-74-VOL-1 NL

2 OF 4
ADA
056811

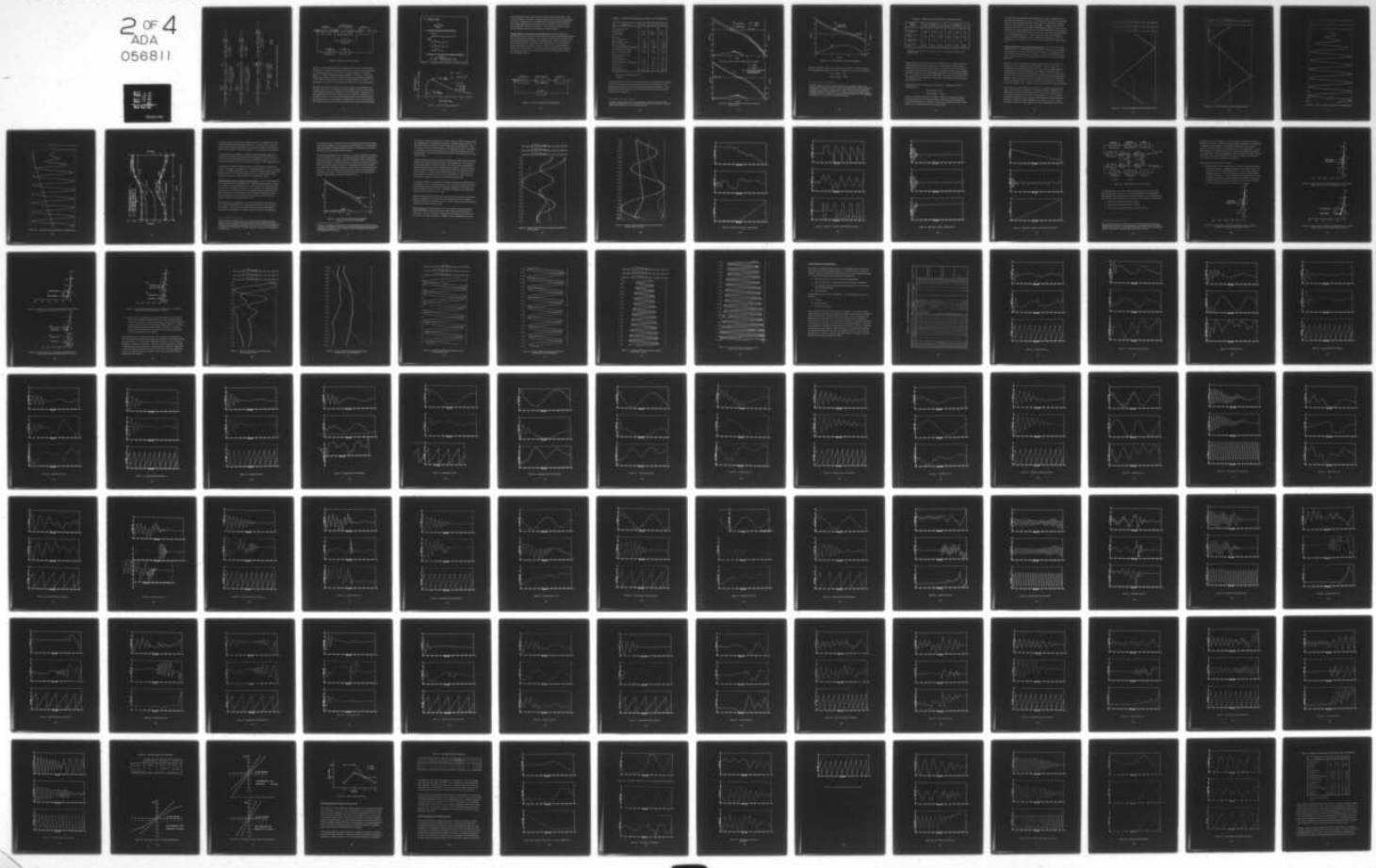

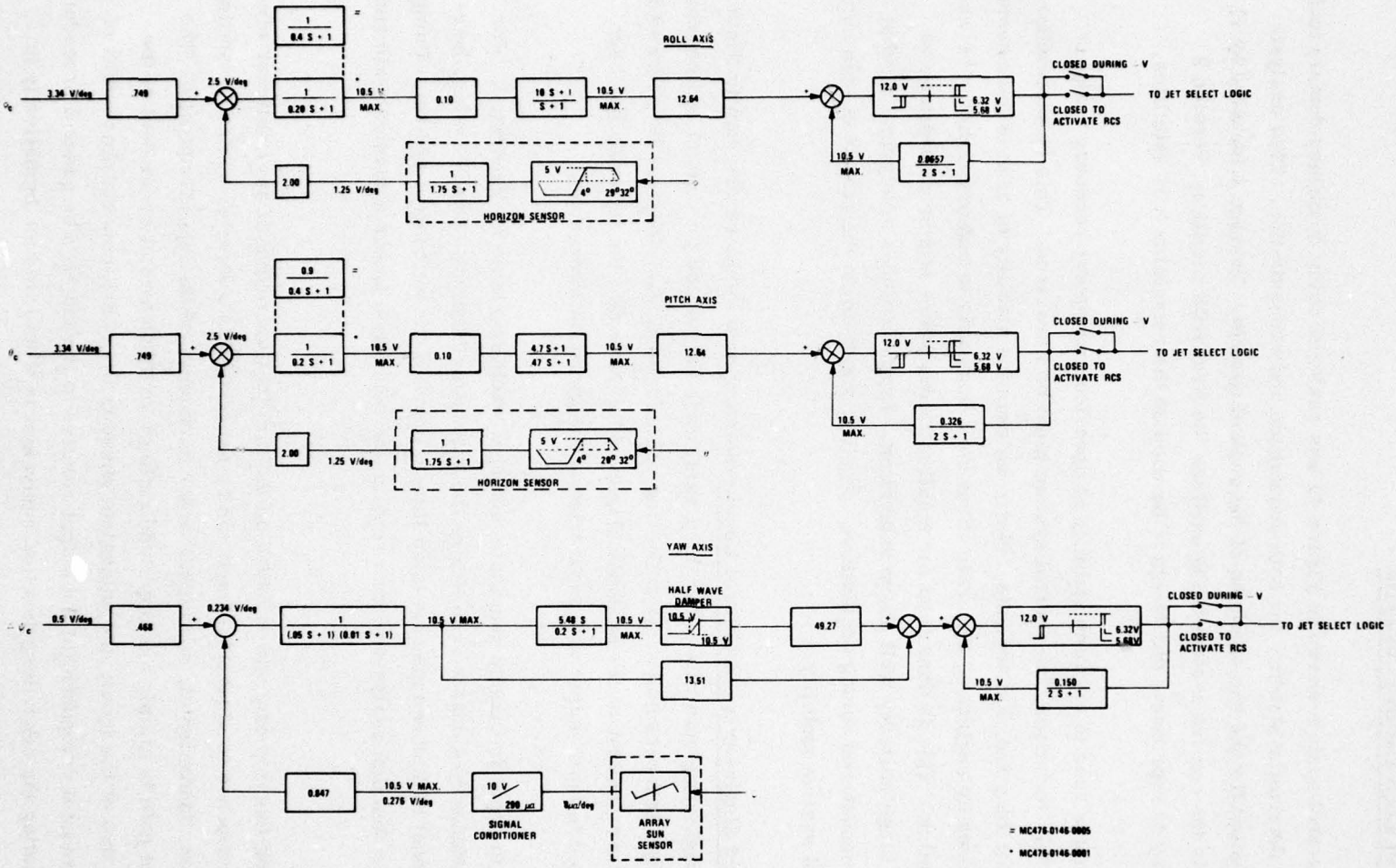

Figure 49. Jet Control System--Analytical Block Diagram

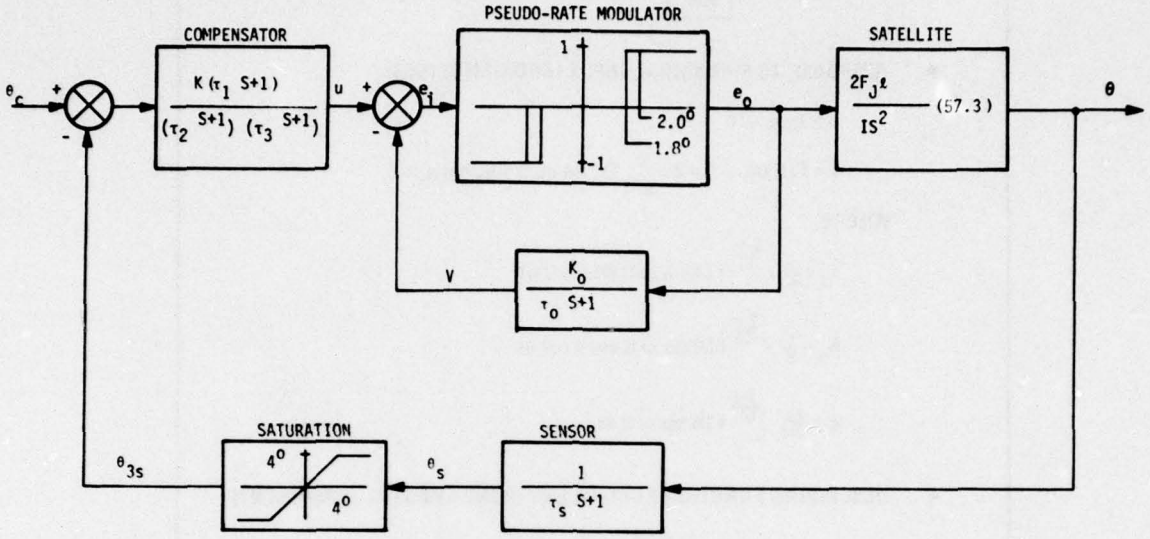

Figure 50. Single-Axis Jet Control Loop

Figure 51. Describing functions for most simple nonlinearities can be computed analytically and are tabulated in many books on the subject. For the jet relay in Figure 50, the describing function gain as a function of relay input amplitude (A) is shown in Figure 52. Analytical expressions for gain and phase are also given. Note that the equivalent gain approaches $4\pi/A$ for large input amplitudes, while phase approaches $-0.1/A$. Note also that relay gain reaches a maximum of 0.335 at an input of A = 2.7 deg. Phase at this point is -2.99 deg and can be neglected for all practical purposes.

We will use the worst-case maximum relay gain for stability analysis purposes for the simple reason that the relay input must pass through the region of maximum gain during acquisition and hence the loop must be stable at this point. Furthermore, for relay inputs below peak relay gain, phase lag of the relay becomes significant and can no longer be ignored. Thus, as control loop gain increases, the corresponding lower phase margin forces the relay to operate at a higher gain in order to reduce its phase lag. Ultimately, this will force the relay to operate in the negative slope region where

- **NONLINEAR ELEMENT**

- **RESPONSE TO SINUSOIDAL INPUT (FOURIER SERIES)**

$$u = A \sin \omega t$$

$$v = f(A \sin \omega t) = c + \sum_{n=1}^{\infty} (f_n \sin n\omega t + h_n \cos n \omega t)$$

WHERE

$$f_n = \frac{\omega}{\pi} \int_0^{\frac{2\pi}{\omega}} f(A \sin \omega t) \sin n \omega t \, dt$$

$$h_n = \frac{\omega}{\pi} \int_0^{\frac{2\pi}{\omega}} f(A \sin \omega t) \cos n \omega t \, dt$$

$$c = \frac{\omega}{2\pi} \int_0^{\frac{2\pi}{\omega}} f(A \sin \omega t) \, dt$$

- **DESCRIBING FUNCTION EQUIVALENT (FUNDAMENTAL COMPONENT)**

$$N(A) = \frac{f_1 + jh_1}{A} = \frac{\sqrt{f_1^2 + h_1^2}}{A} \angle \sin^{-1}(h_1/f_1) = Keq \angle d$$

Figure 51. Describing Function Equivalent of Nonlinear Element

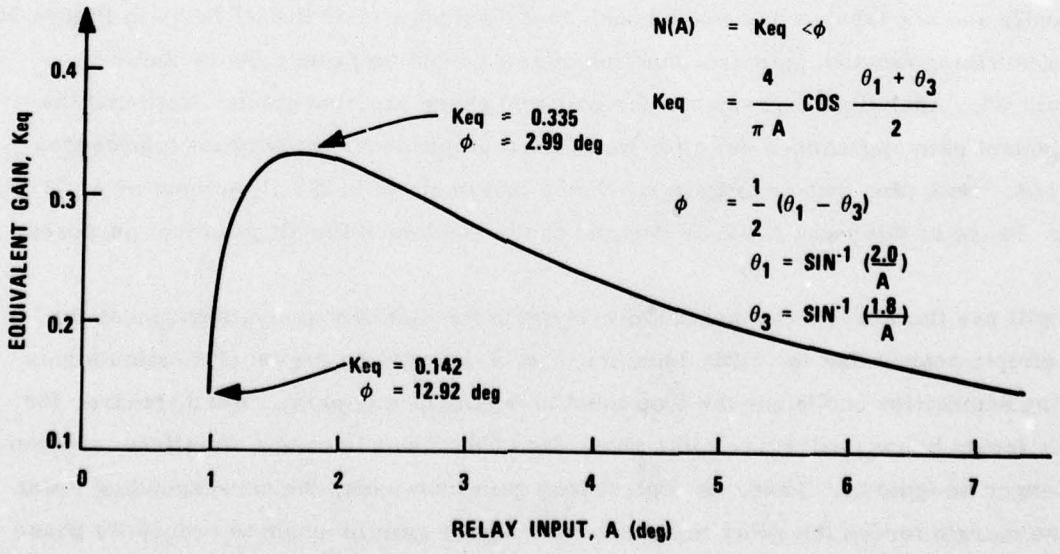

Figure 52. Relay Describing Function Gain

relay input becomes large enough to make the control loop (neutrally) stable. Thus the use of maximum relay gain for stability analysis cannot be considered unreasonably pessimistic. Replacing the relay in Figure 50 with its maximum describing function gain and ignoring the phase shift, the pseudo-rate jet modulator can be reduced to a lead-lag element as illustrated in Figure 53. Thus we have reduced the jet control loop to a linearized equivalent form suitable for stability analysis.

Stability Analysis for Attitudes below Sensor Saturation--Stability analyses were performed for two versions of the control system and for both acquisition (panels stowed) and reacquisition (panels deployed). These analyses neglect spin rate about the z axis. Effects of spin rate will be examined in a later subsection. Nominal parameters for each axis of the linearized jet loop are summarized in Table 13. Note that the yaw loop has no sensor time constant. However, it does have an extra roll-off filter which in effect takes the place of the earth sensor filter in pitch and roll. Note also that nominal jet thrust has been reduced to 0.09 lb from the design value of 0.1 lb used for earlier analyses.

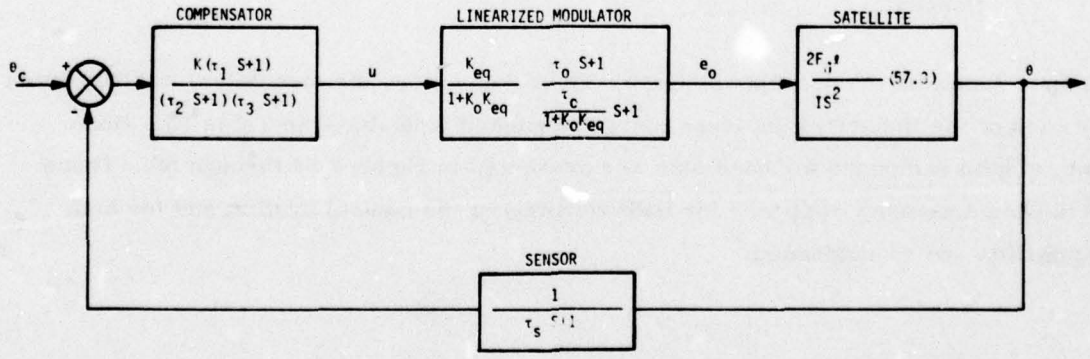

Figure 53. Linearized Single-Axis Jet Control Loop

TABLE 13. IMPROVED LINEARIZED JET CONTROL LOOP PARAMETERS

Parameter	Roll	Pitch	Yaw
Inertias (slug ft^2)			
• Stowed	94.1	102.2	111.3
• Deployed	187.9	94.5	211.6
Gains			
• Loop Gain, K	1.0	1.0	1.0
• Pseudo-rate, K_0	0.25	10.0	0.57
• Relay,* K_{EQ}	0.335	0.335	0.335
• Modulator, $K_{EQ}/(1+K_0K_{EQ})$	0.309	0.077	0.281
• Moment Arm, ℓ (ft)	0.4	2.8	2.8
• Jet Thrust, F_J (lb)	0.09	0.09	0.09
Time Constants (sec)			
• Sensor, τ_S	1.75	1.75	0.01
• Pseudo-lead, τ_0	2.0	5.0	2.0
• Pseudo-lag, $\tau_0/(1+K_0K_{EQ})$	1.85	1.15	1.7
• Lead, τ_1	10.0	5.0	20.2
• Lag, τ_2	1.0	1.0	0.2
• Roll-off, τ_3	0.2 (0.4)†	0.4†	0.05

*Maximum describing function gain

†Version 2

An open-loop frequency response (with loop broken before the modulator) was computed for each of the linearized jet loops using the parameters shown in Table 13. Bode plots of gain and phase for each axis are presented in Figures 54 through 56. These plots show frequency response for both versions of the control system and for both acquisition and reacquisition.*

*The upper curves show gain on the left-hand scale, while the lower curves show phase on the right-hand scale. In each plot the 0 dB gain line is shown for reference; phase of -180 deg occurs at the bottom of each plot.

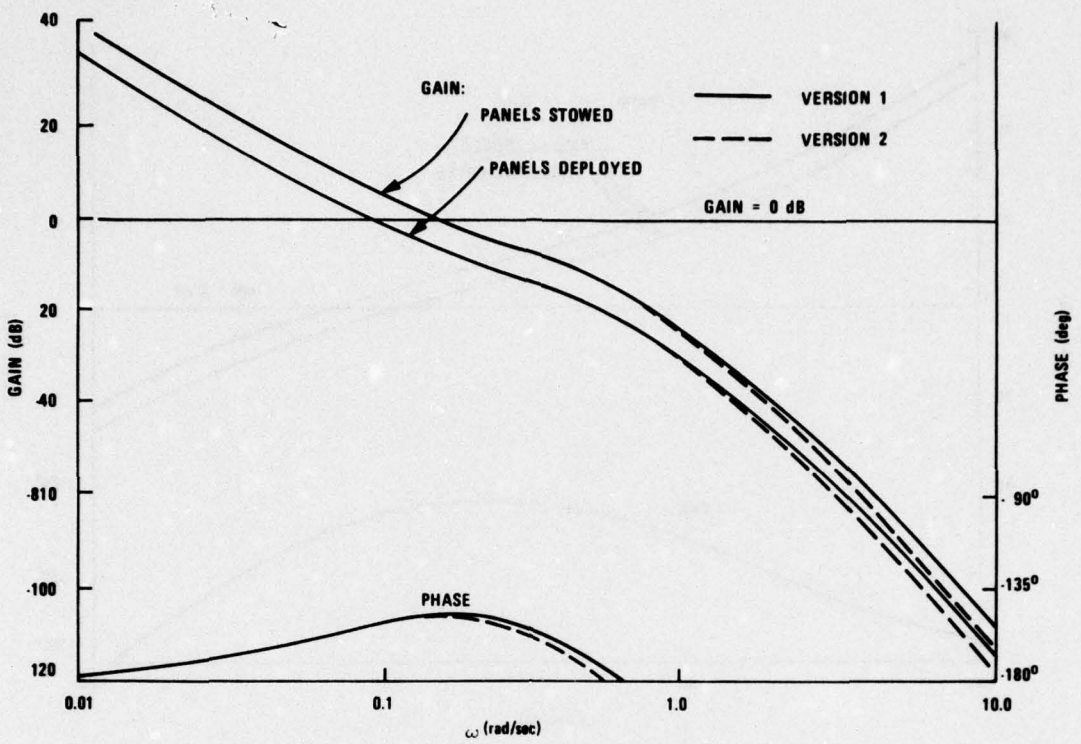

Figure 54. Roll Jet Control Loop Frequency Response

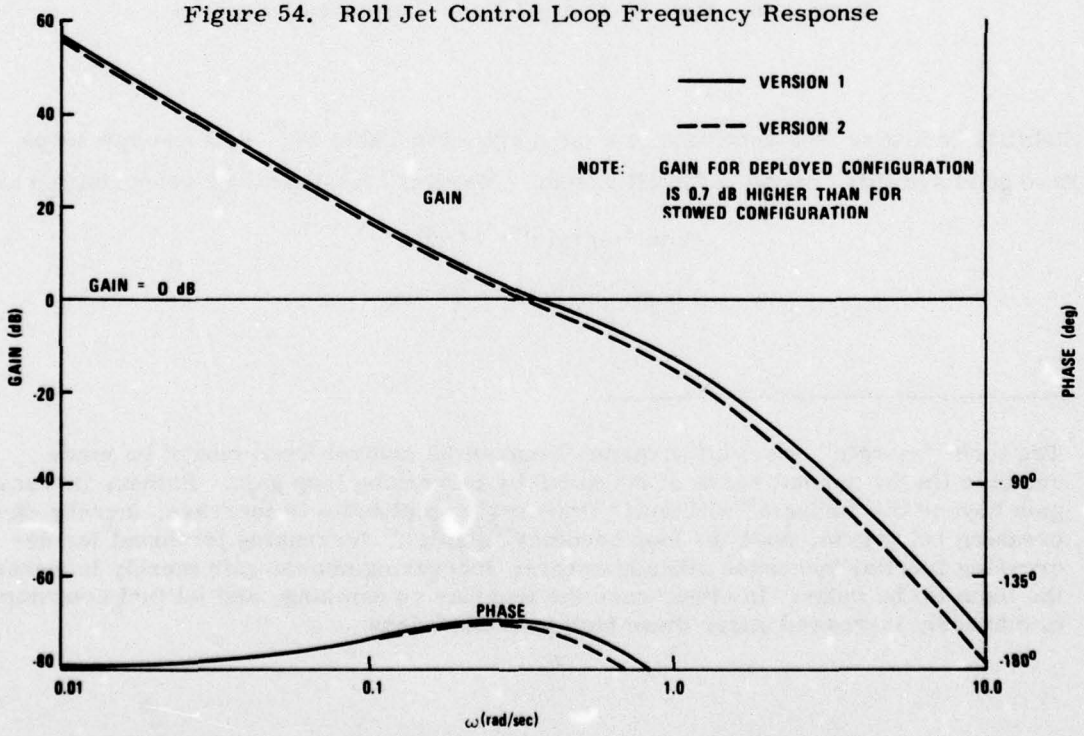

Figure 55. Pitch Jet Control Loop Frequency Response (Panels Stowed)

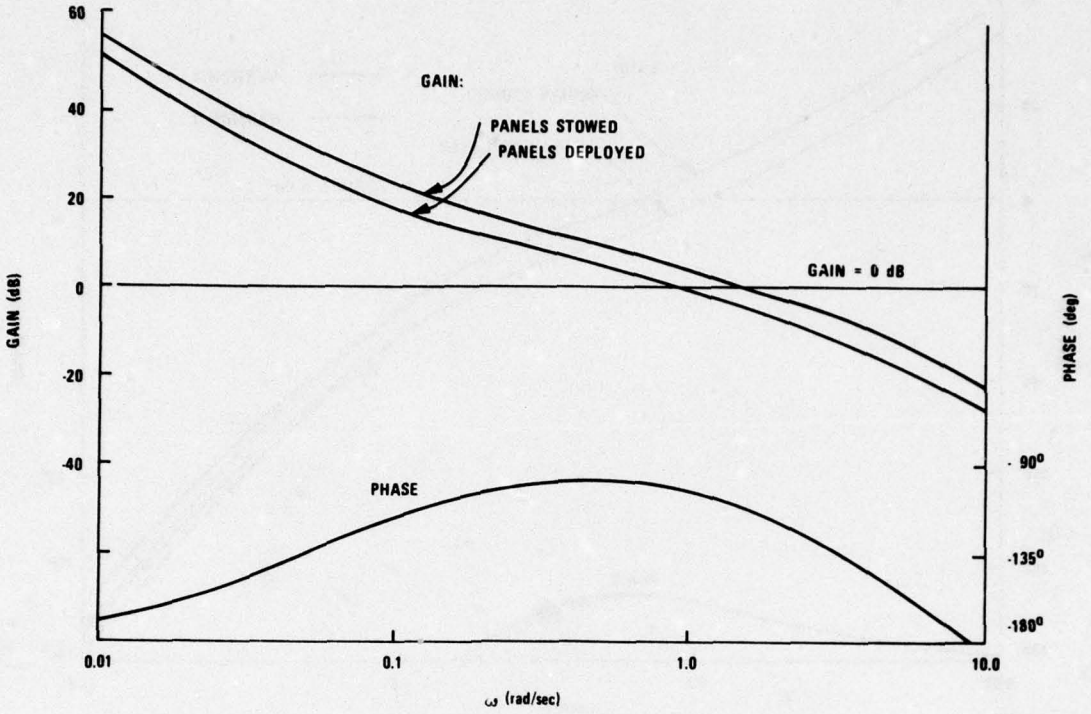

Figure 56. Yaw Jet Control Loop Frequency Response

Stability "margins" for each axis are summarized in Table 14.* Roll and yaw loops have good stability "margins" in all cases. "Margins" for Version 2 reacquisition are

Gain "margin" = 14 dB

Phase "margin" = 27 deg

---

*The term "margin" is set off in quotes because jet control loops cannot be made unstable (in the normal sense of the word) by increasing loop gain. Rather, increasing gain beyond the "margin" will cause limit cycle amplitudes to increase, thereby decreasing relay gain, until the loop becomes "stable." Increasing jet thrust (or decreasing inertia) increases attitude errors; increasing sensor gain merely increases the input to the relay. In either case the loop has no damping, and jet fuel consumption is markedly increased under these high gain conditions.

TABLE 14. NOMINAL JET LOOP STABILITY ANALYSIS SUMMARY*

Stability Margins	Version 1			Version 2		
	Roll	Pitch	Yaw	Roll	Pitch	Yaw
Gain crossover (rad/sec)	0.15 (0.09)	0.36 (0.38)	1.6 (0.9)	0.15 (0.09)	0.33 (0.35)	1.6 (0.9)
Phase "margin" (deg)	33.0 (27.0)	22.0 (21.0)	67.0 (79.0)	31.0 (27.0)	19.0 (18.0)	67.0 (79.0)
Phase crossover (rad/sec)	0.58	0.80	9.2	0.52	0.68	9.2
Gain "margin" (dB)	+16.0 (+22.0)	+10.0 (+9.0)	+21.0 (+26.0)	+14.0 (+20.0)	+10.0 (+9.0)	+21.0 (+26.0)

*Numbers not in parentheses are for stowed panels. Numbers in parentheses are for deployed panels.

These "margins" are more than adequate for any expected gain and phase variations. Known earth sensor gain variations of a factor of 2 ($\pm$ 6 dB) can be expected due to temperature variations of the earth's horizon. Jet thrust over the mission can vary by $\pm$ 30 percent ($\pm$ 2 dB) from nominal. Inertia variations are expected to be negligible compared to those due to the stowed/deployed panels which have already been accounted for. Phase shifts due to earth sensor time constant variations of as much as a factor of two would not cause instabilities in either axis, even if coupled with the worst-case gain variations above.

Stability margins for the pitch axis are less adequate. "Margins" for Version 2 reacquisition are

Gain "margin" = 9 dB

Phase "margin" = 18 deg

Version 1 reacquisition is better only in phase. Worst-case known gain variations alone can account for 8 dB of the gain "margin." This leaves 1 dB of "margin" (or 10 percent) for unknown gain variations. A 10 percent increase in earth sensor time constant at this condition would cause instability in pitch.

To verify that actual "margins" agree with predicted "margins," loop gains (between the sensor and modulator) of 1.0, 2.0, 2.6, and 4.0 times the nominal were simulated for the Version 2 acquisition controller. These gains correspond to gain increases of 0, 6, 8, and 12 dB over the nominal, respectively. As expected, the simulation shows that the first three cases maintain small amplitude stable limit cycles; the last case grows to a large amplitude limit cycle, with corresponding large fuel consumption. Jet on time for the nominal case is 2.3 sec for a 200 sec run, while that for the worst case (4 x nominal gain) is 171 sec. These results agree well with the predicted "margin" of 10 dB. Simulation traces of attitude, relay input, and jet on time for the nominal and 4 x nominal gain cases are summarized in Figures 57 and 58, respectively.

Improved Jet Modulator Describing Function Equivalent--A more accurate but more complex approach is to use describing function analysis on the pseudo-rate modulator (relay plus pseudo-rate feedback) rather than the jet relay. The improved accuracy stems from the fact that the pseudo-rate feedback around the relay involves only one order of filtering, while the outer-loop feedback involves five orders of filtering (see Figure 50).

With this in mind we computed the describing function equivalent for the relay with feedback (i.e., the describing function between points u and e_0 in Figure 50). Describing function equivalents for the pitch axis are compared for both approaches in Figure 59 at several input amplitudes. At first glance, there appears to be a sizeable difference between the two approaches at low frequencies for an input amplitude of 2.7. The exact approach appears to have 4 dB less gain than the approximate approach. This would lower pitch-axis gain crossover to 0.3 rad/sec and increase phase margin by about 9 deg. However, near phase crossovers (0.7 to 0.8 rad/sec) for both describing functions are within a degree, while gain differs by less than 0.5 dB.

Aside from these apparent differences, there is a more fundamental difference that makes comparison of both approaches more difficult. The input amplitude for the approximate approach corresponds to the input to the relay (e_i), while that for the exact approach corresponds to the input to the modulator ($u = e_i - v$). In order to compare both approaches on the same basis, input amplitude to the modulator must be adjusted to produce the proper amplitude at the relay (i.e., $A = 2.7$). At low frequencies the modulator input amplitude (A_u) must be approximately 4.0 in order

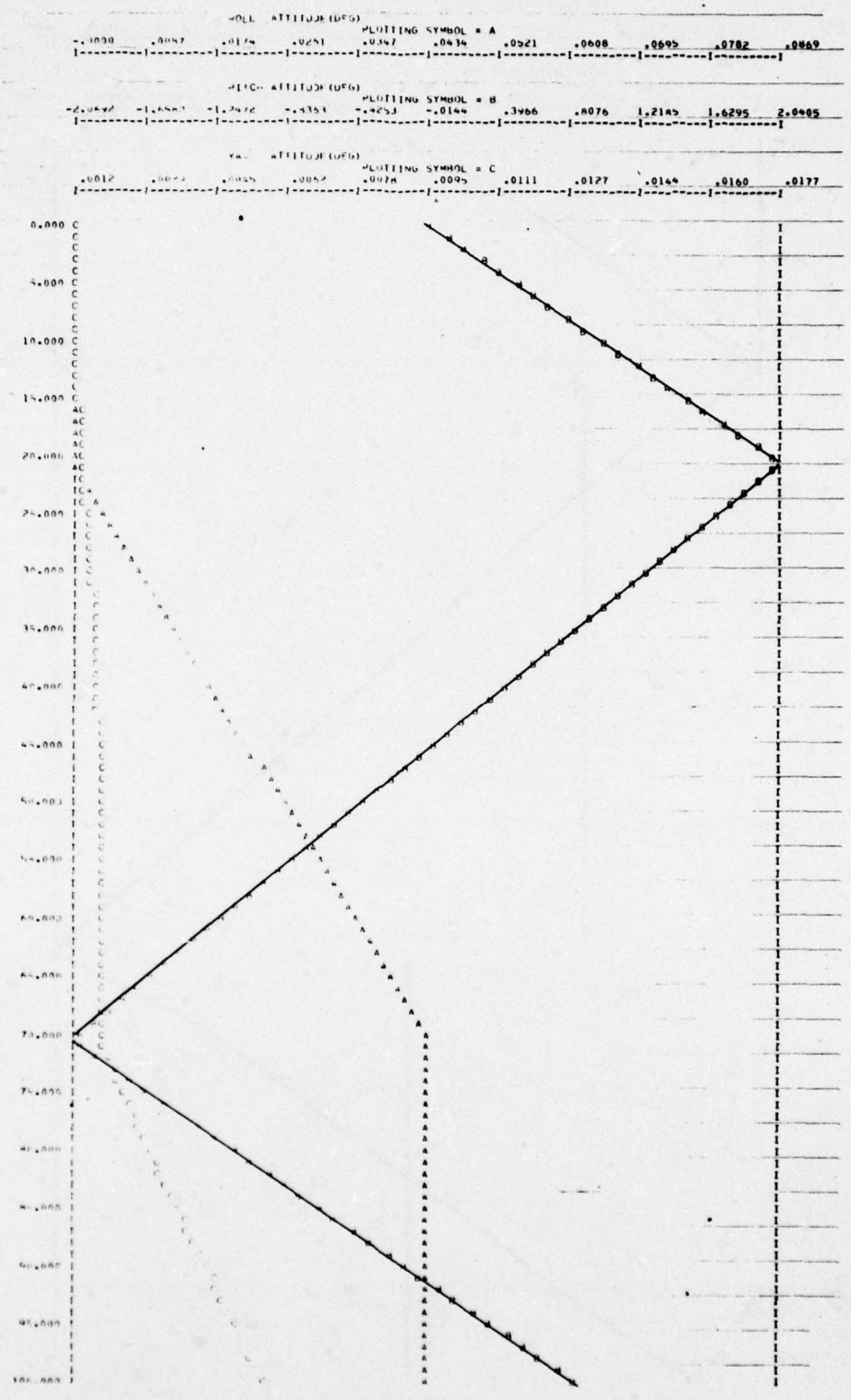

Figure 57a. Version 2 Acquisition Controller (Nominal Gain)

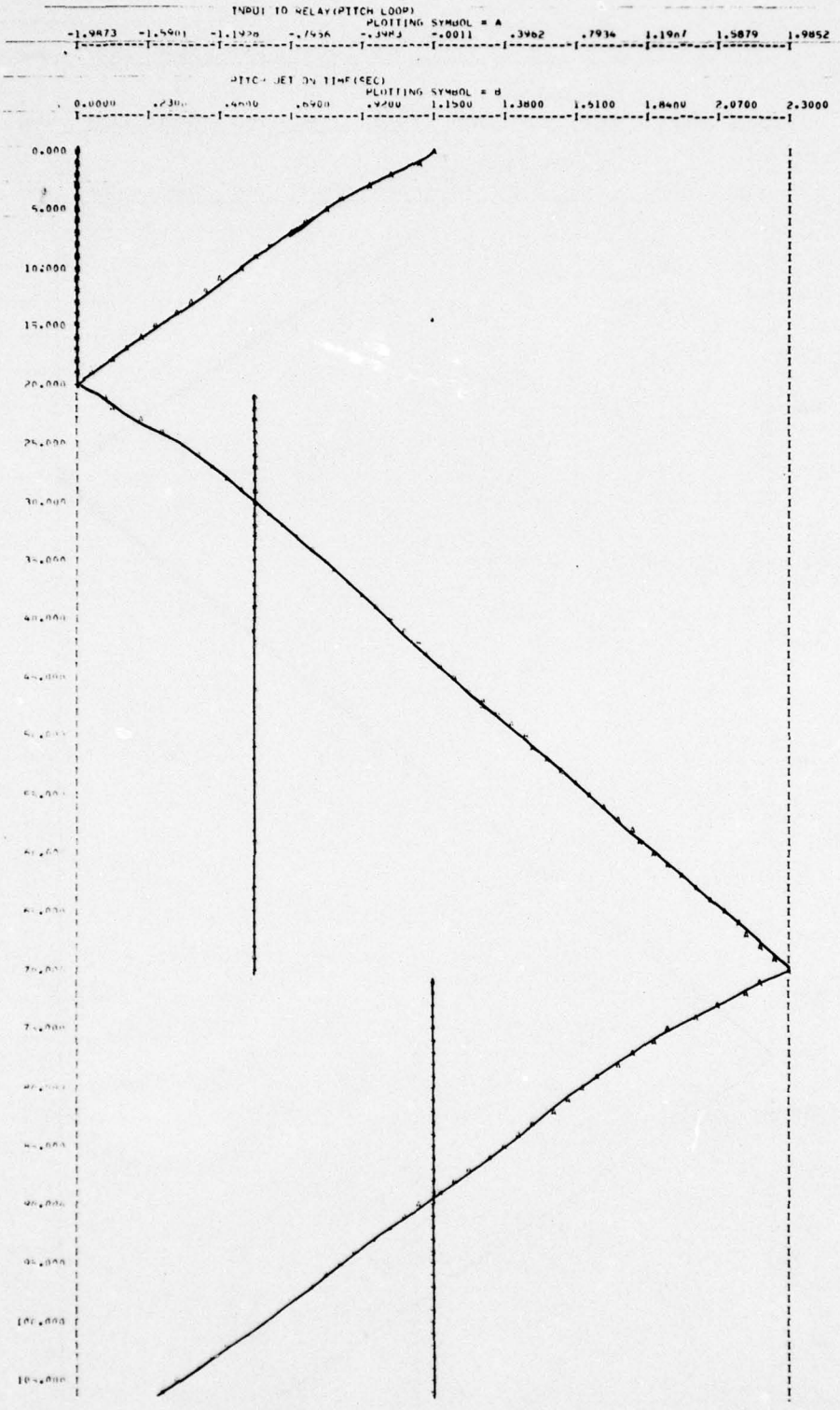

Figure 57b. Version 2 Acquisition Controller (Nominal Gain)

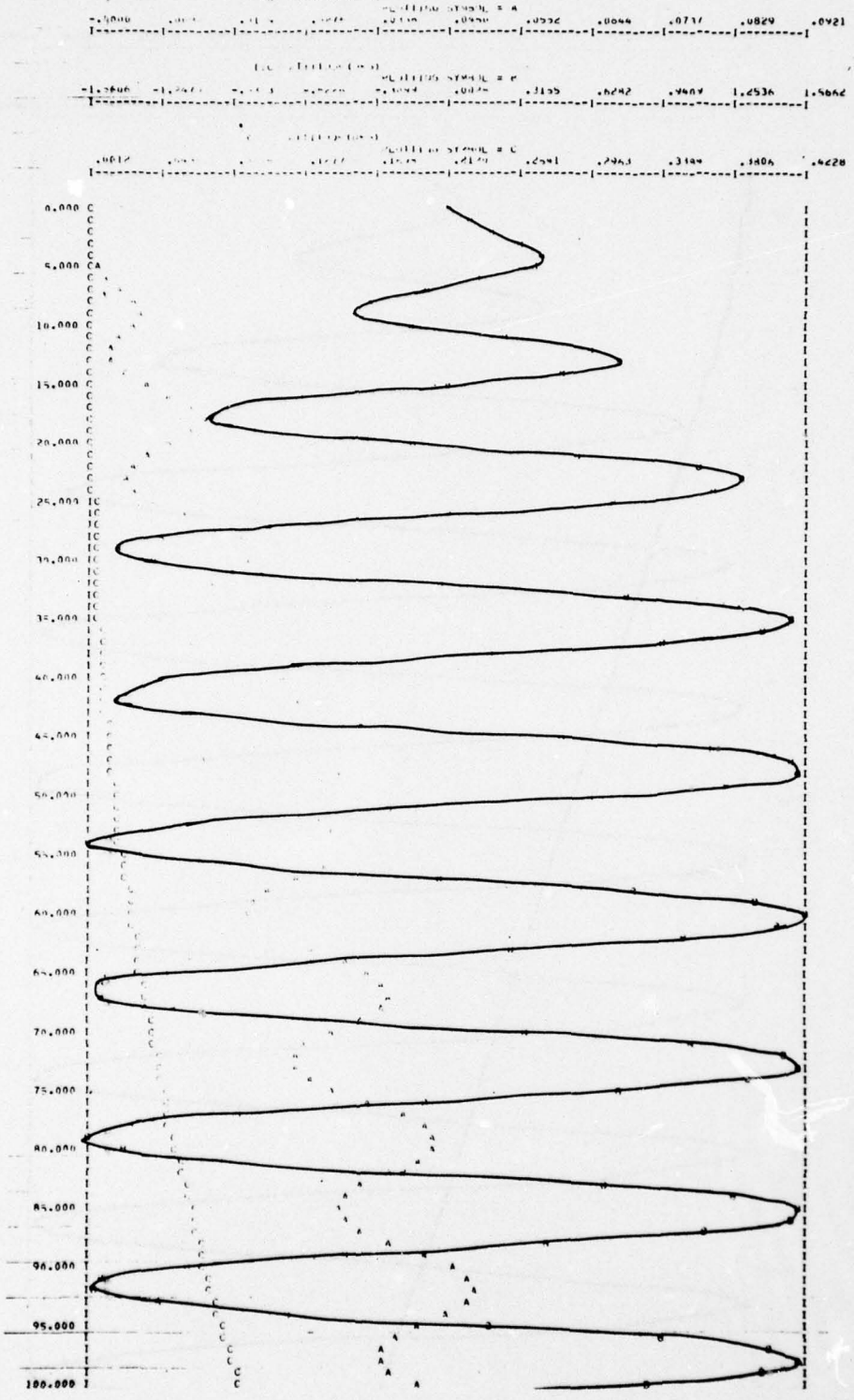

Figure 58a. Version 2 Acquisition Controller (4 x Nominal Gain)

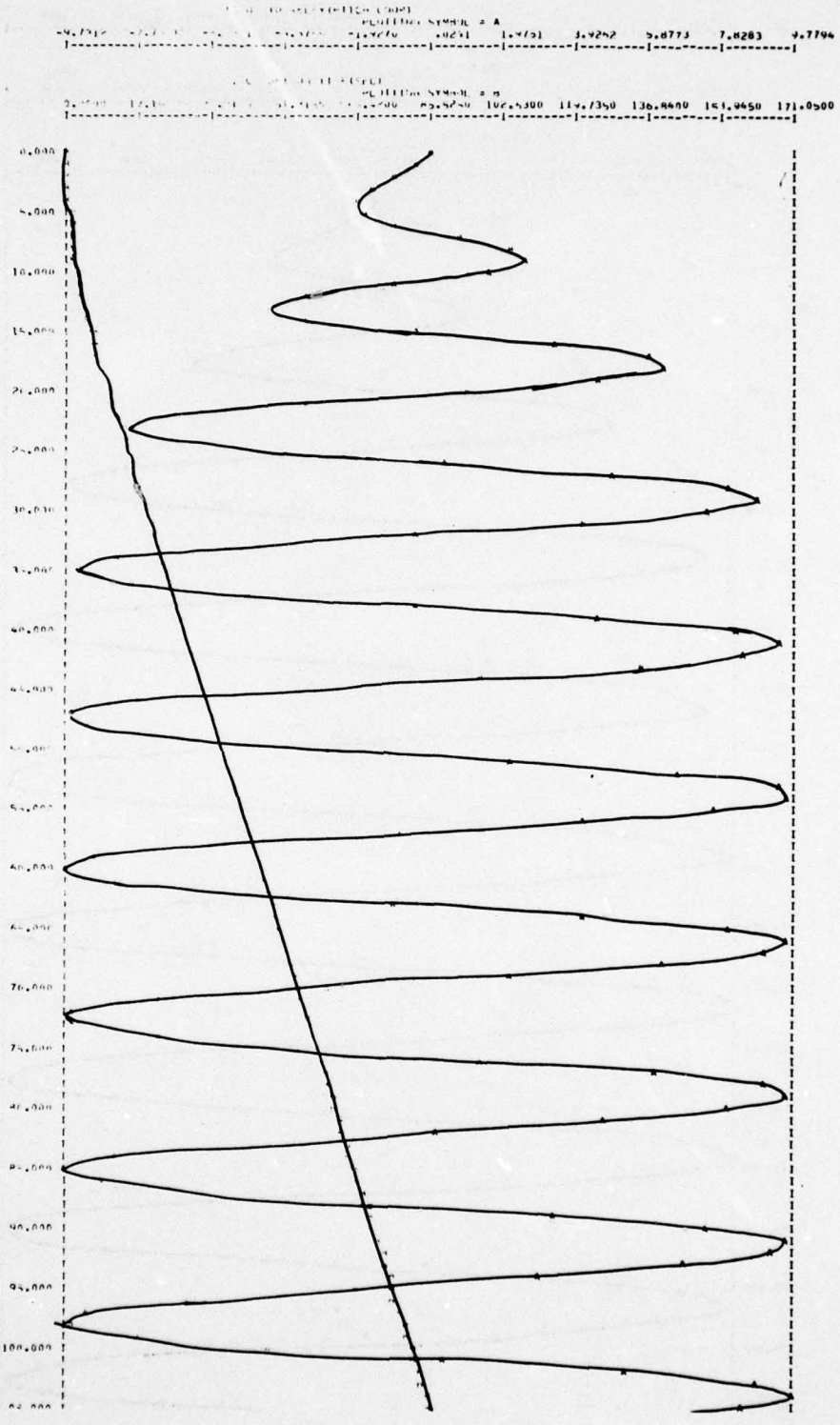

Figure 58b. Version 2 Acquisition Controller (4 x Nominal Gain)

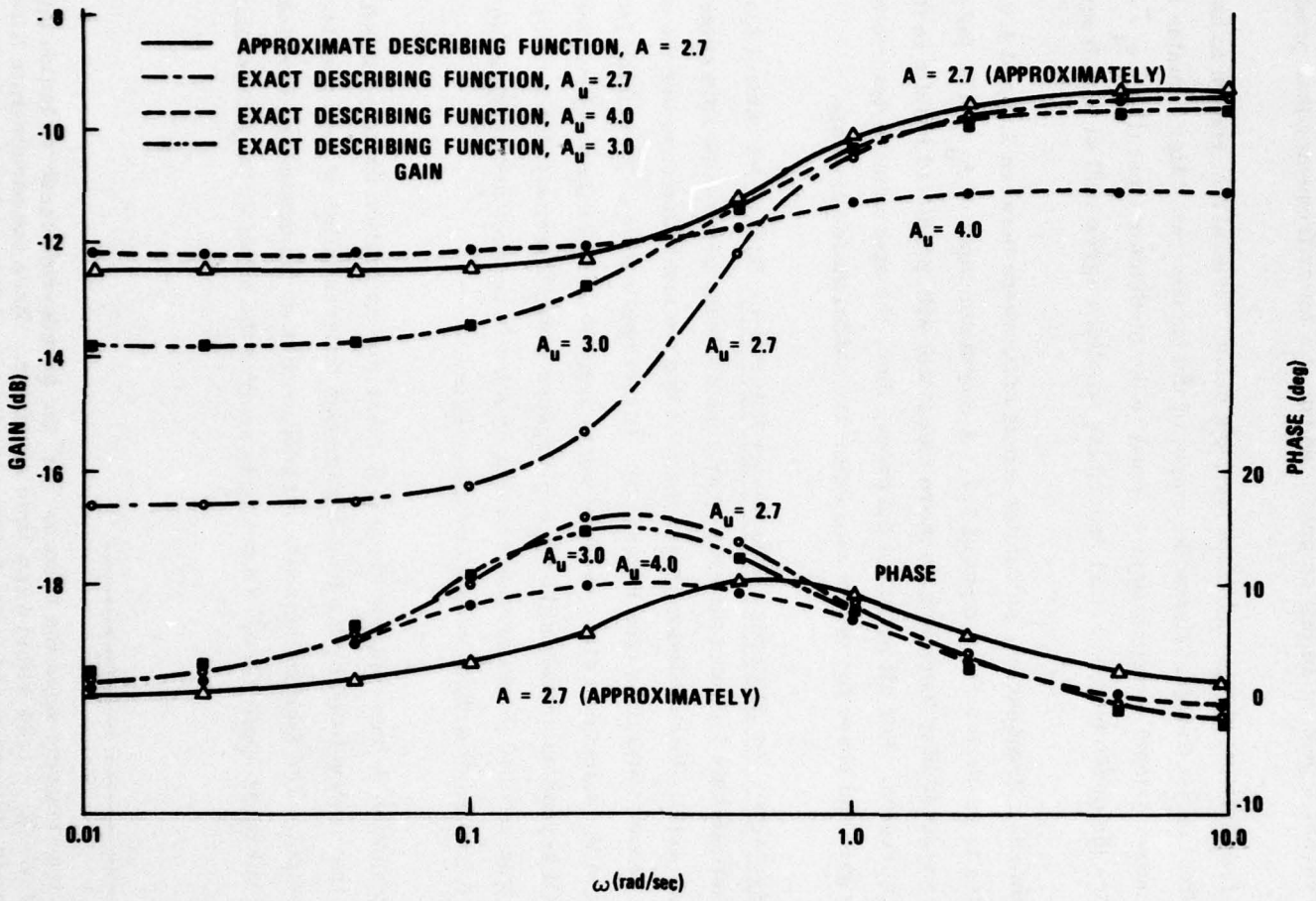

Figure 59. Describing Function Equivalent for Pseudo-Rate Modulator

to produce an input to the relay with amplitude (A) near 2.7.* Modulator describing function gain and phase for modulator input of $A_u = 4.0$ is also shown in Figure 57. Note that modulator gain is now much nearer the predicted value at low frequencies. Phase reaches a peak of 10 deg as predicted but at a lower frequency than predicted.

At high frequencies, the pseudo-rate feedback cannot respond fast enough to have much effect on jet firings. Hence the output of the pseudo-rate filter remains near zero, and relay input is approximately equal to the modulator input (i.e., $e_i \tilde{=} u$). Therefore the predicted and actual describing functions agree well at high frequencies.

At intermediate frequencies, modulator inputs somewhere between 2.7 and 4.0 are necessary to produce a relay input of 2.7. A modulator input of $A_u = 3.0$, for example, produces a describing function gain more consistent with predicted results in the mid-frequency region. For all practical purposes, then, the approximate describing function gain and phase for the jet modulator are sufficient for analysis.

Stability Analysis for Attitudes above Sensor Saturation--So far, jet control loops have been examined only for local stability near zero attitudes (neglecting spin rates about the z body axis). For attitudes larger than ~ 4 deg we must also consider the effects of earth sensor saturation (see Figure 50). Direct application of describing function analysis to the saturation element alone would suggest no stability problems for attitudes well beyond saturation although convergence would be expected to be slower. This is true because the saturation element effectively reduces sensor gain (and therefore loop gain) without adding any phase shift.

This explanation is unacceptable since it is clear that saturation destroys much of the lead that is developed by the lead-lag through differentiation of the (saturated) sensor output. The fault in the above explanation lies not in describing function analysis but in its application. To properly analyze the effect of the jet modulator

---

*This is true because when the relay is "on" the pseudo-rate feedback builds up to a value of $V = K_o = 1.24$ within a few time constants. Since the pseudo-rate filter response is fast compared to the frequency of the modulator input (at low frequencies), the input to the relay reaches a peak value of $e_i = 4.0 - 1.24 = 2.76$ when the modulator input is at its peak. Thus, the input amplitude to the relay is near the point of peak relay gain.

and sensor saturation, we must determine the describing function between the input to the saturation element (θ_s) and the output of the modulator (e_o).* To simplify subsequent computation of open-loop frequency response, we may just as well include the sensor lag in the describing function analysis.

The above describing function was computed as a function of amplitude and frequency of the attitude input to the sensor. The resulting open-loop frequency response for the Version 2 pitch axis acquisition controller (including the effects of saturation) is presented in Figure 60. Note that this frequency response was obtained by adding the effect of the satellite (double integrator) to the describing function gain and phase. The solid line shows frequency response for attitude input to the sensor below saturation (A_s = 3 deg). The dashed line shows frequency response for attitudes above saturation (A_s = 10 deg). The broken line shows the same for attitude adjusted to produce a relay input near maximum relay gain ($A \cong 2.7$).

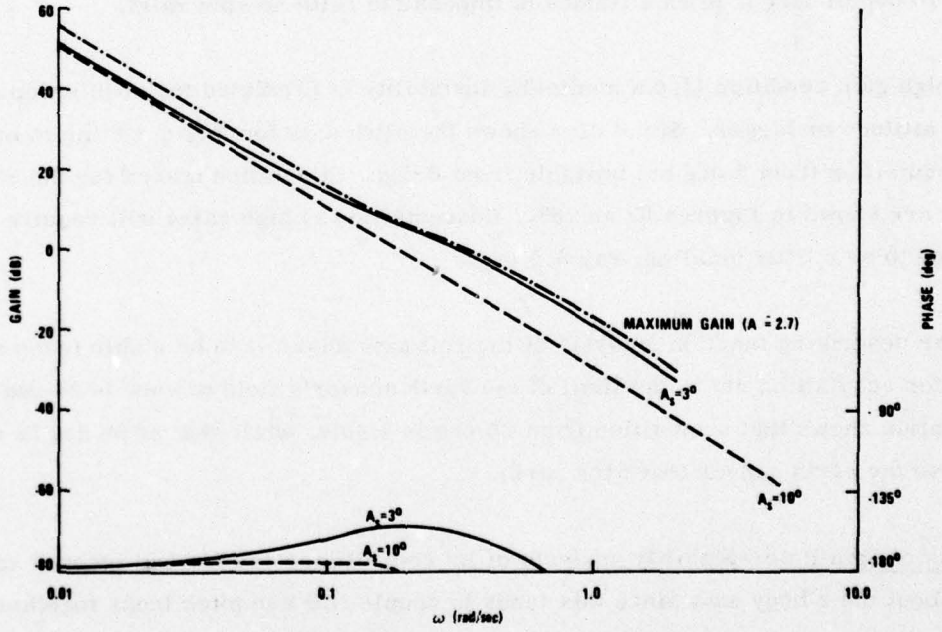

Figure 60. Pitch Jet Control Loop Frequency Response with Saturation (Version 2 Acquisition)

*In general, describing function analysis of multiple nonlinearities requires that we include all nonlinearities as well as any linear elements between them in the analysis. In many cases, however, it may be valid to replace each nonlinear element by its describing function equivalent.

This last gain curve lies within 1 dB of the earlier pitch axis results which were based upon "approximated" describing function analysis. The high amplitude case (A_s = 10 deg) shows that gain is reduced by ~9 dB from nominal near gain crossover. Thus gain crossover occurs at a lower frequency. More important, however, is that phase is substantially reduced from the nominal case so that phase crossover occurs near gain crossover. The loop is nearly unstable with about 1 dB of gain margin and 1 deg of phase margin.

Simulation actually shows the pitch axis to be unstable for acquisition from 10 deg with attitude growing until the earth sensor loses the earth (Figure 61). The roll axis, on the other hand, acquires nicely from 10 deg. The yaw axis, which is uncontrolled, responds only to pitch and roll jet misalignments and cg offsets. Note that the earth sensor model used for this run is an ideal one with 1.75 sec time constant and saturation at 4 deg (i.e., identical to that assumed for analysis). Use of the true earth sensor model would result in loss of the earth at about 150 sec. Hence acquisition from 10 deg or larger pitch attitudes is impossible (with no spin rate).

At a high gain condition (2.6 x nominal), instability is predicted for acquisition from 7 deg attitude or larger. Simulation shows the pitch axis for this condition to be stable for acquisition from 5 deg but unstable from 8 deg. Simulation traces for these two cases are shown in Figures 62 and 63. Reacquisition at high gains will require pitch attitude to be a little smaller, say 6.5 deg.

Similar describing function analysis of the roll axis shows it to be stable (even at high gain) for acquisition out to the limit of the earth sensor's field of view (~ 24 deg). Simulation shows that acquisition from 20 deg is stable, while that at 28 deg is unstable because the earth sensor loses the earth.

Effects of Spin Rate--Stability analysis of jet control loops so far has ignored spin rate about the z body axis since this tends to couple roll and pitch loops together (Figure 64). Notice that attitudes are coupled at the spin frequency, ω_s, while rates are coupled at the nutation frequency, $\Omega = \sqrt{\Omega_1 \Omega_2}$, which is proportional to spin rate.

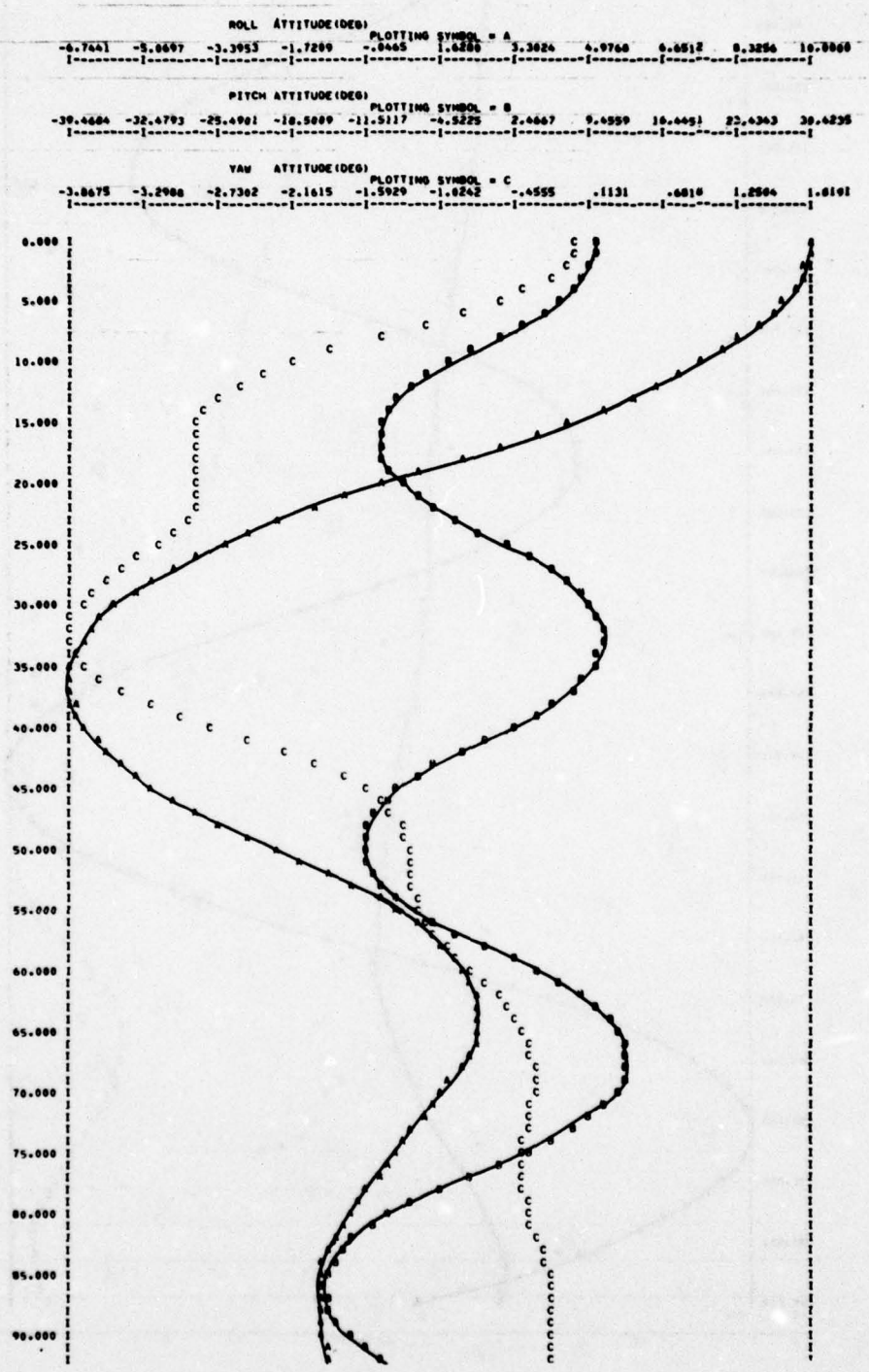

Figure 61. Version 2 Acquisition from 10 Degrees with Saturation (Nominal Gain)

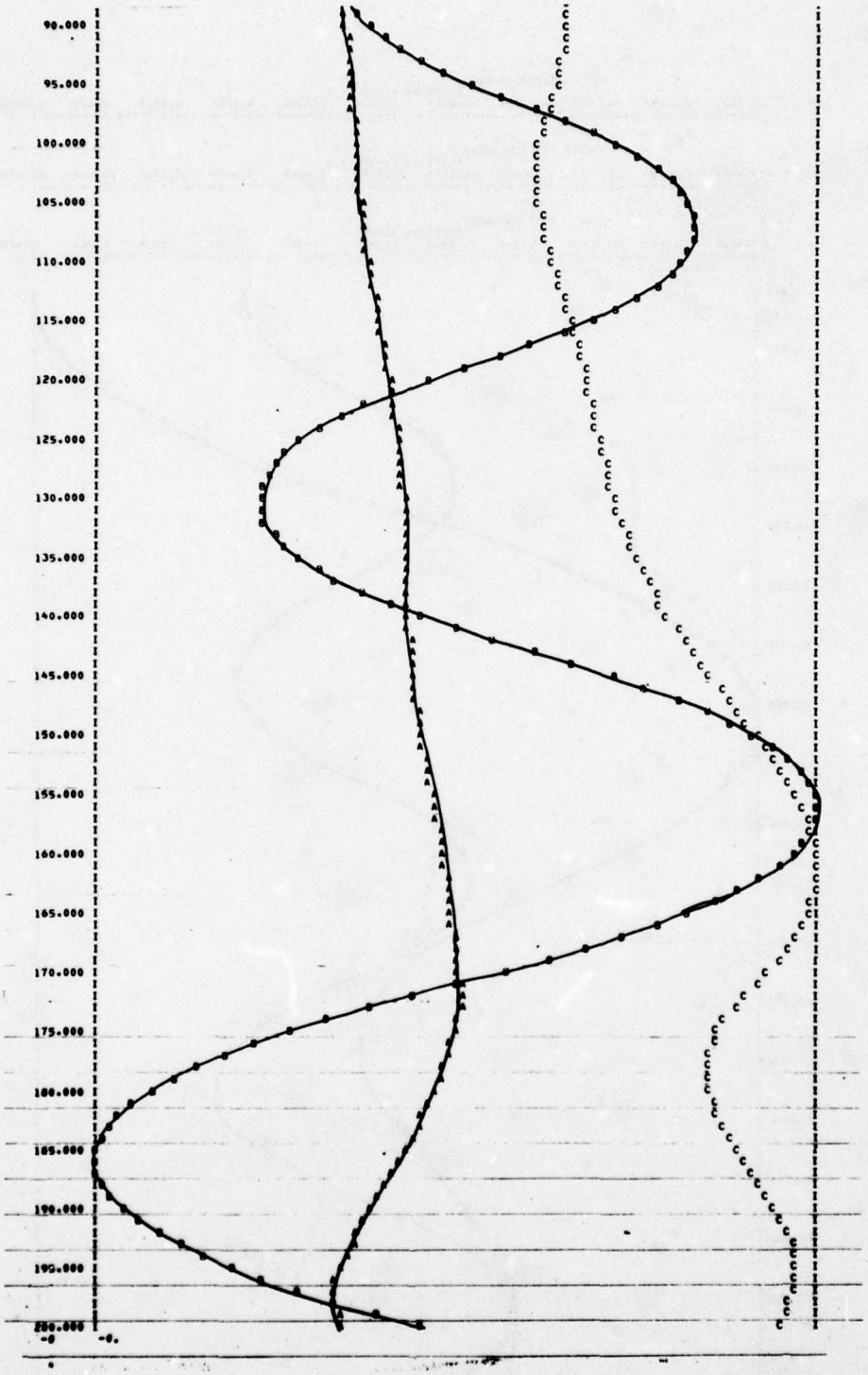

Figure 61. Version 2 Acquisition from 10 Degrees with Saturation (Nominal Gain) (concluded)

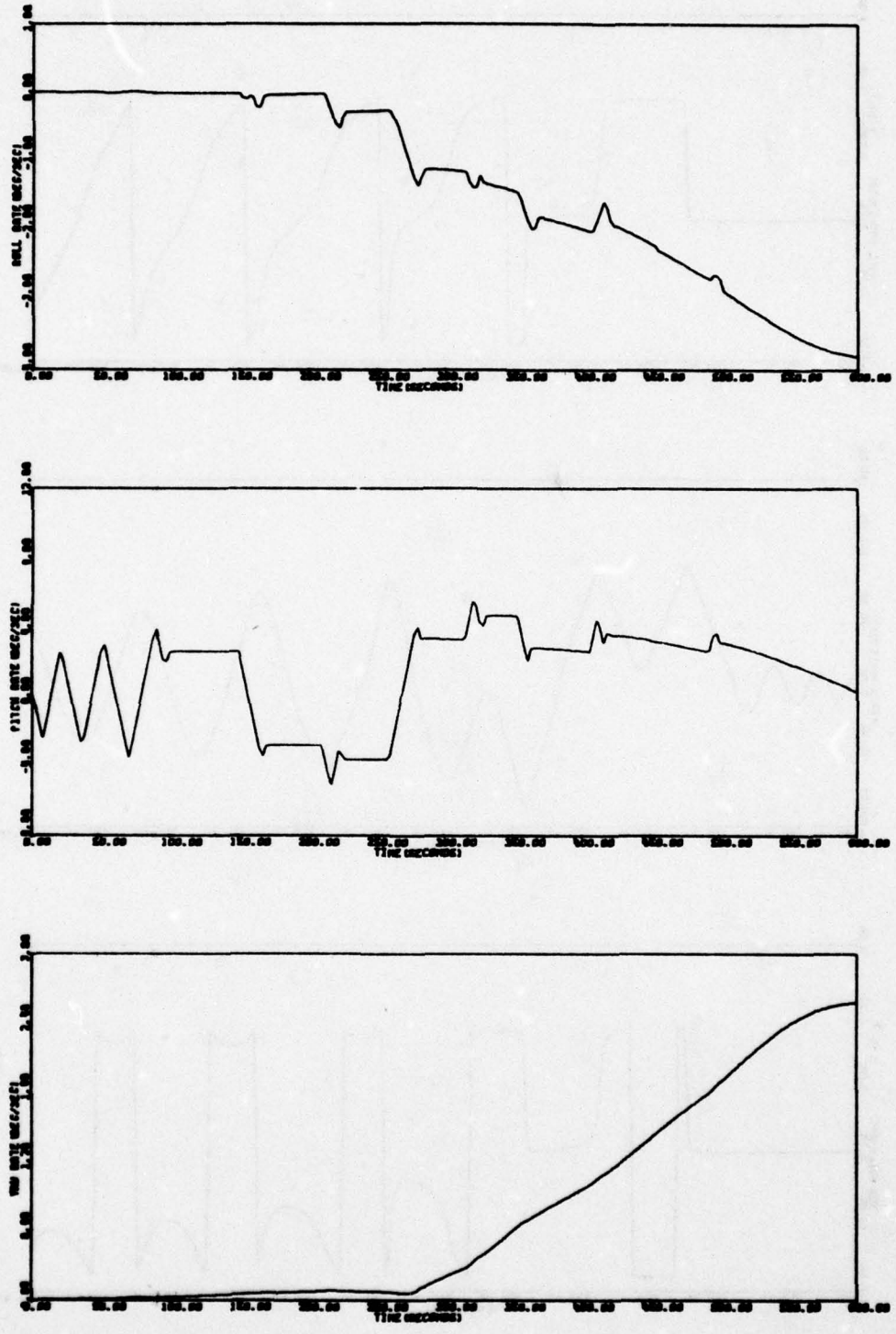

Figure 62. High Gain, 8 Degree, Initial Attitude

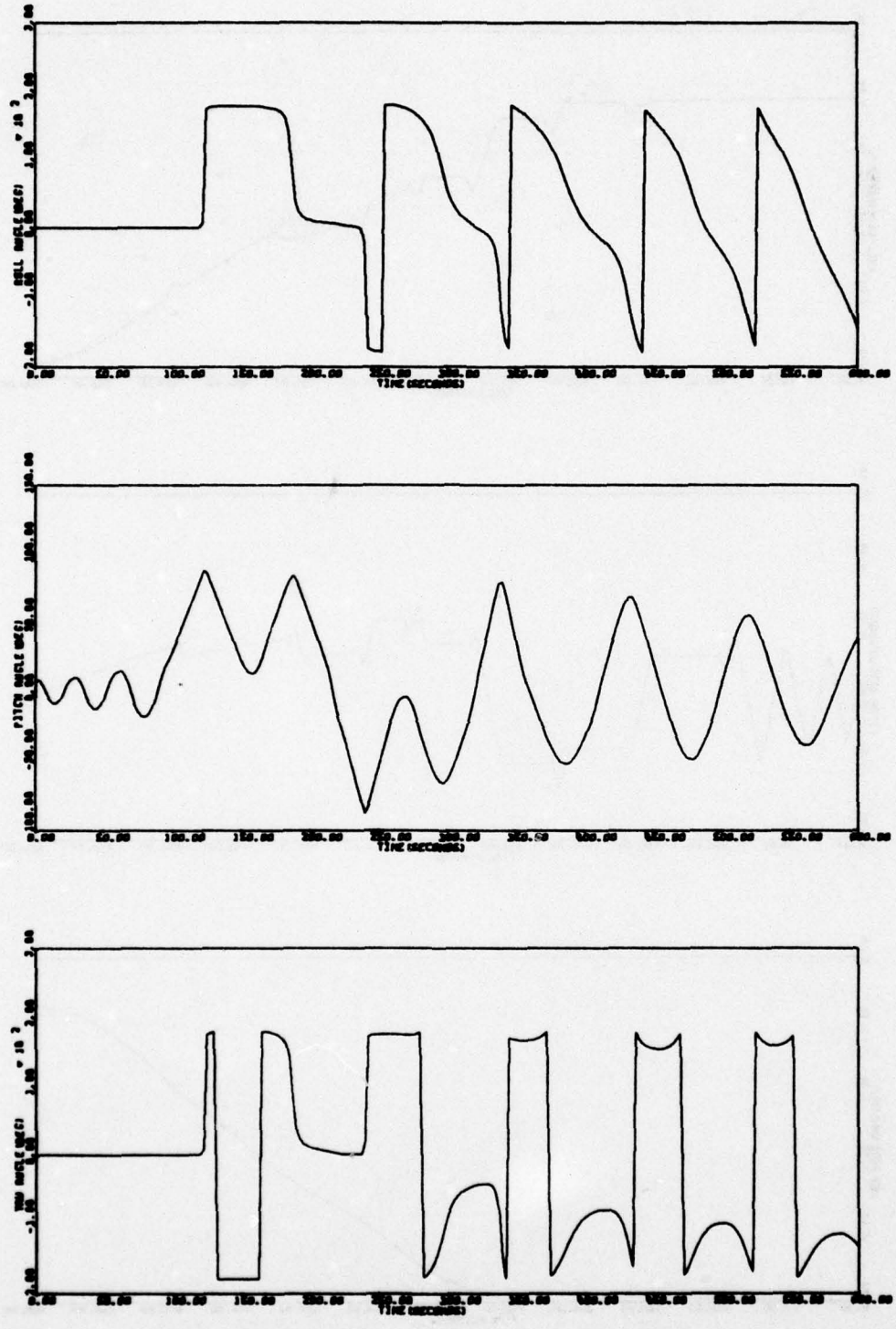

Figure 62. High Gain, 8 Degree, Initial Attitude (concluded)

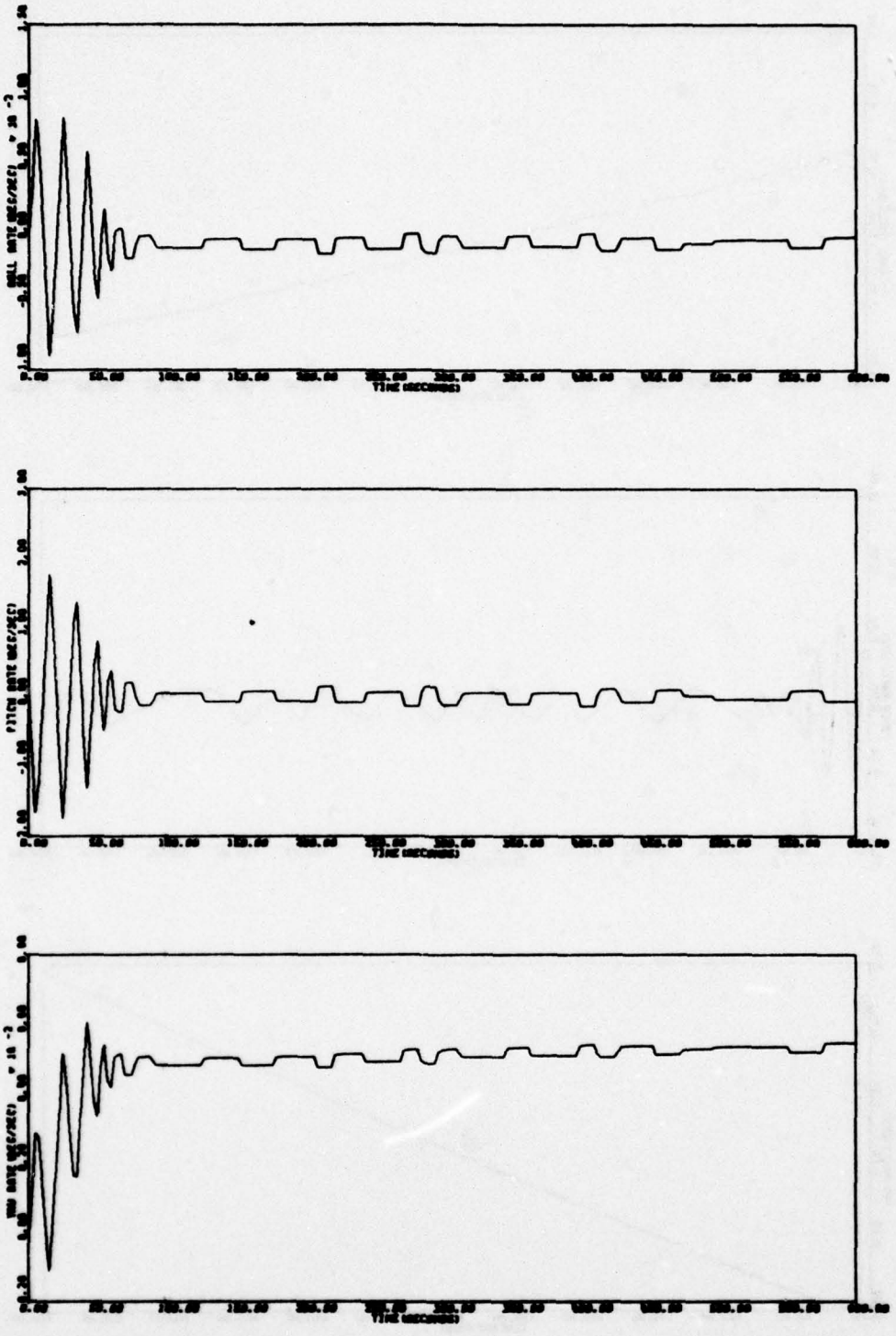

Figure 63. High Gain, 5 Degree, Initial Attitude

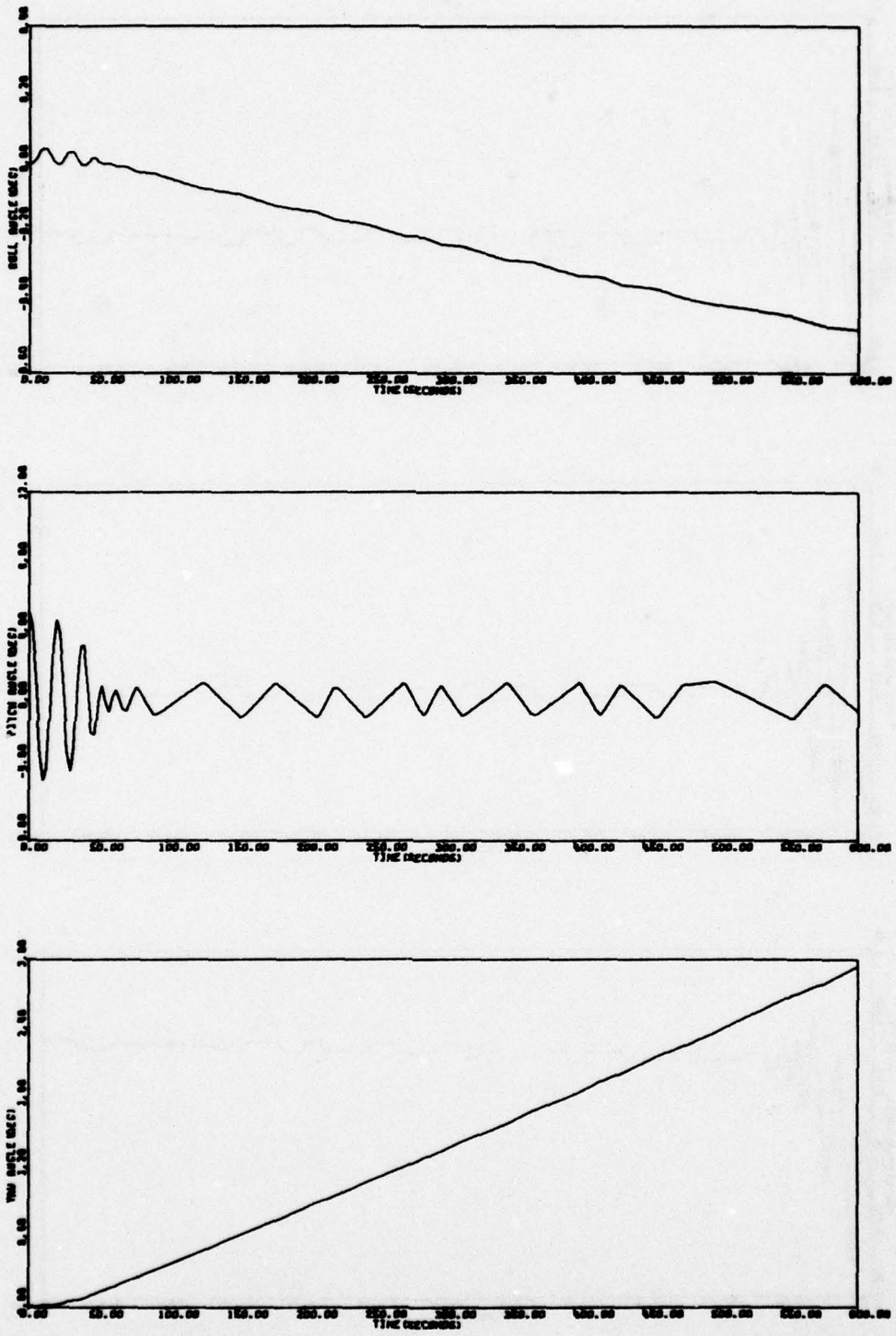

Figure 63. High Gain, 5 Degree, Initial Attitude (concluded)

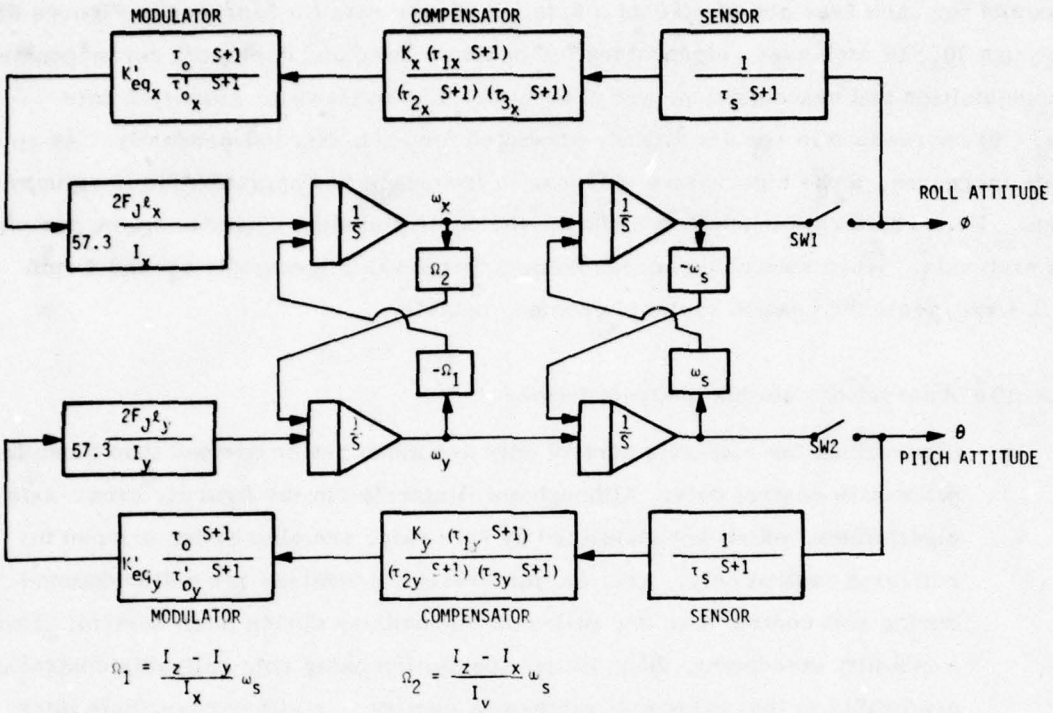

Figure 64. Coupled Roll/Pitch Jet Control Loops

This coupling due to spin rate has a destabilizing influence on pitch and roll axis stability.* The effects of spin rate on control loop stability can be determined by examining closed-loop eigenvalues of the coupled roll/pitch loop as a function of spin rate. This was done for both versions of the control system under three conditions:

1. Roll-axis control only (Switch SW 1 closed)
2. Pitch-axis control only (Switch SW 2 closed)
3. Roll and pitch control (Switches SW 1 and SW 2 closed)

*For attitudes beyond saturation, however, simulation shows that spin rates up to approximately 1 rpm have a stabilizing influence, presumably because they prevent the pitch earth sensor from remaining saturated due to interchange of roll and pitch errors. This analysis, however, neglects effects of saturation.

Results for each case are plotted as a function of spin rate (in rad/sec) in Figures 65 through 70. In each case, eigenvalues for panels stowed and deployed, corresponding to acquisition and reacquisition, are presented. Eigenvalues for zero spin rate ($\omega_s = 0$) correspond to results already predicted for each axis independently. As spin rate increases, these eigenvalues increase in frequency and approach the imaginary axis. Hence spin rate tends to destabilize the control system by reducing the damping in each axis. When spin rate exceeds some critical value (generally around 4 rpm $\tilde{=}$ 0.4 rad/sec), the control system becomes unstable.

Specific observations on this analysis follow:

- Eigenvalues for roll-axis control only are much better damped than those for pitch-axis control only. Although not illustrated in the figures, cross-axis eigenvalues, which are stabilized by spin rate, are also better damped for roll-axis control only. That is, pitch-axis eigenvalues are better damped during roll control than are roll-axis eigenvalues during pitch control. From a stability standpoint, then, initial acquisition using only roll-axis control is preferable to that using only pitch-axis control. In either case, both pitch and roll control would be needed to complete earth acquisition.

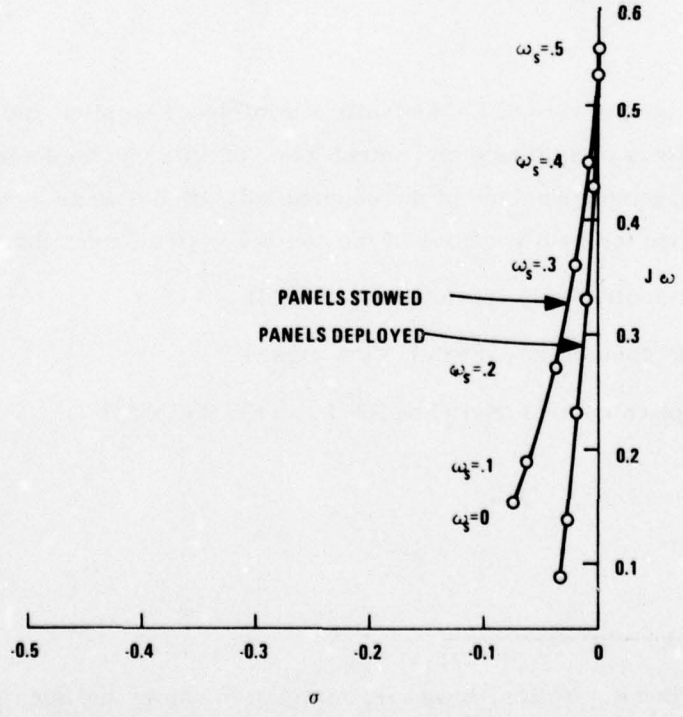

Figure 65. Dominant Roll Jet Control Loop Eigenvalues as a Function of Spin Rate for Roll-Axis Control Only, Version 1

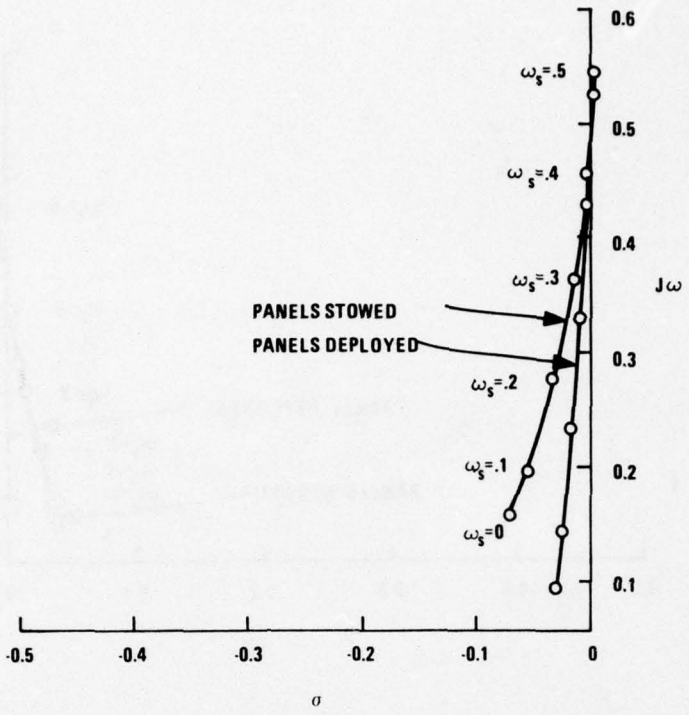

Figure 66. Dominant Roll Jet Control Loop Eigenvalues as a Function of Spin Rate for Roll-Axis Control Only, Version 2

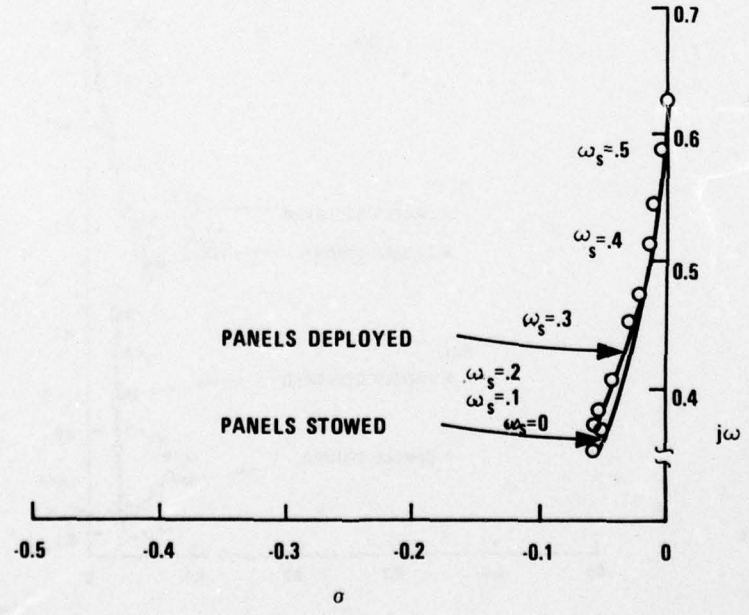

Figure 67. Dominant Pitch Jet Control Loop Eigenvalues as a Function of Spin Rate for Pitch-Axis Control Only, Version 1

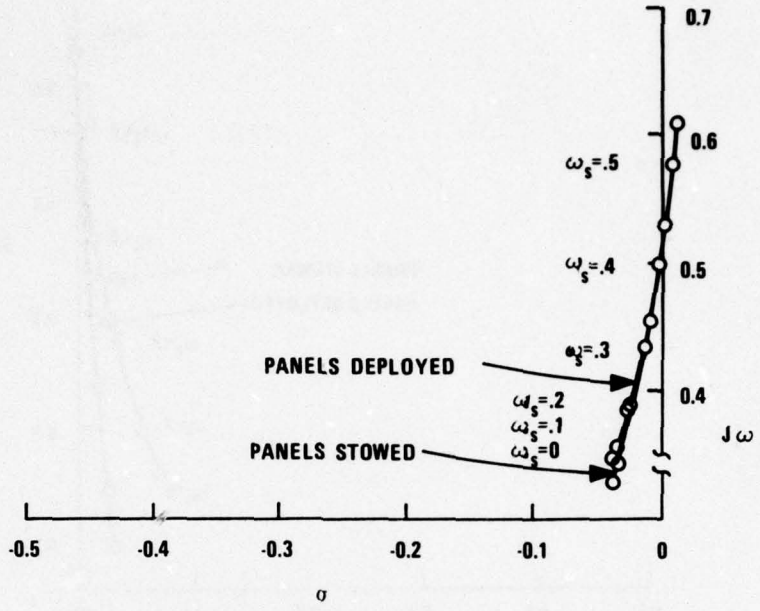

Figure 68. Dominant Pitch Jet Control Loop Eigenvalues as a Function of Spin Rate for Pitch-Axis Control Only, Version 2

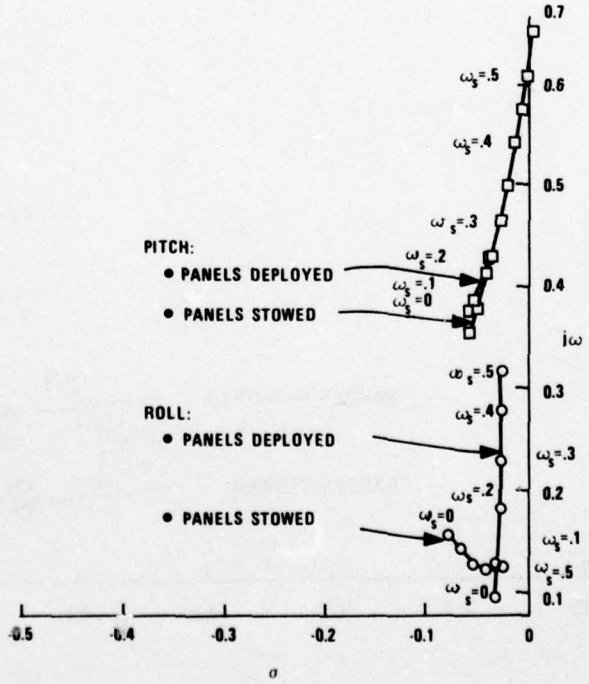

Figure 69. Dominant Roll/Pitch Jet Control Loop Eigenvalues as a Function of Spin Rate for Roll/Pitch Control, Version 1

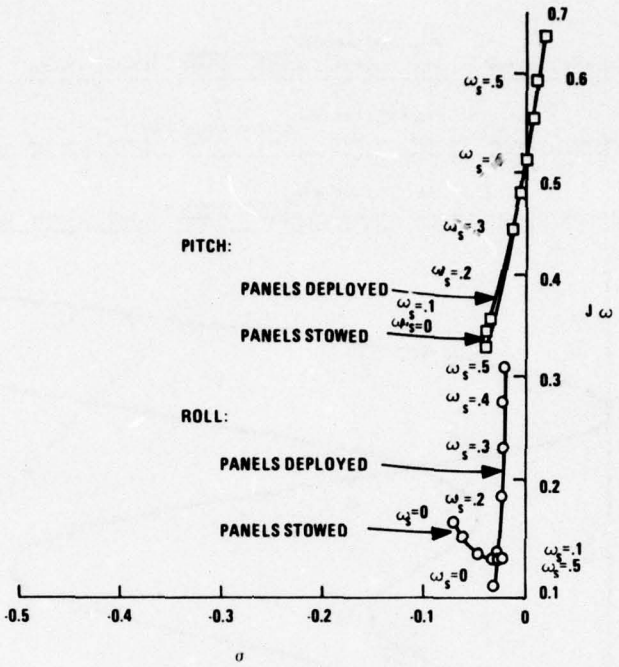

Figure 70. Dominant Roll/Pitch Jet Control Loop Eigenvalues as a Function of Spin Rate for Roll/Pitch Control, Version 2

- Simultaneous roll- and pitch-axis control would probably be most desirable from a fuel consumption standpoint since time to acquire should be shortest for this case. However, because of the difficulties associated with acquisition in pitch for large attitudes, the first approach appears safest (i.e., roll-axis control only followed by roll and pitch control). Of course, care must be taken to insure that pitch errors are within the critical attitude before pitch-axis control is enabled to ensure stability.

The effects of spin rate on closed-loop stability were verified via simulation for the Version 2 acquisition controller (nominal gain) using simultaneous roll and pitch control for spin rates of 0, 1, 2, 4, and 8 rpm. Simulation results for 1, 4, and 8 rpm are summarized in Figures 71 through 73. Earth sensor saturation limits were removed to isolate the effects of spin rate alone, as was assumed in the analysis. Results indicate that the control loop is stable for spin rates at or below 4 rpm and unstable above 4 rpm. The 4 rpm case is just barely stable. Again, these results agree closely with predictions in Figure 70.

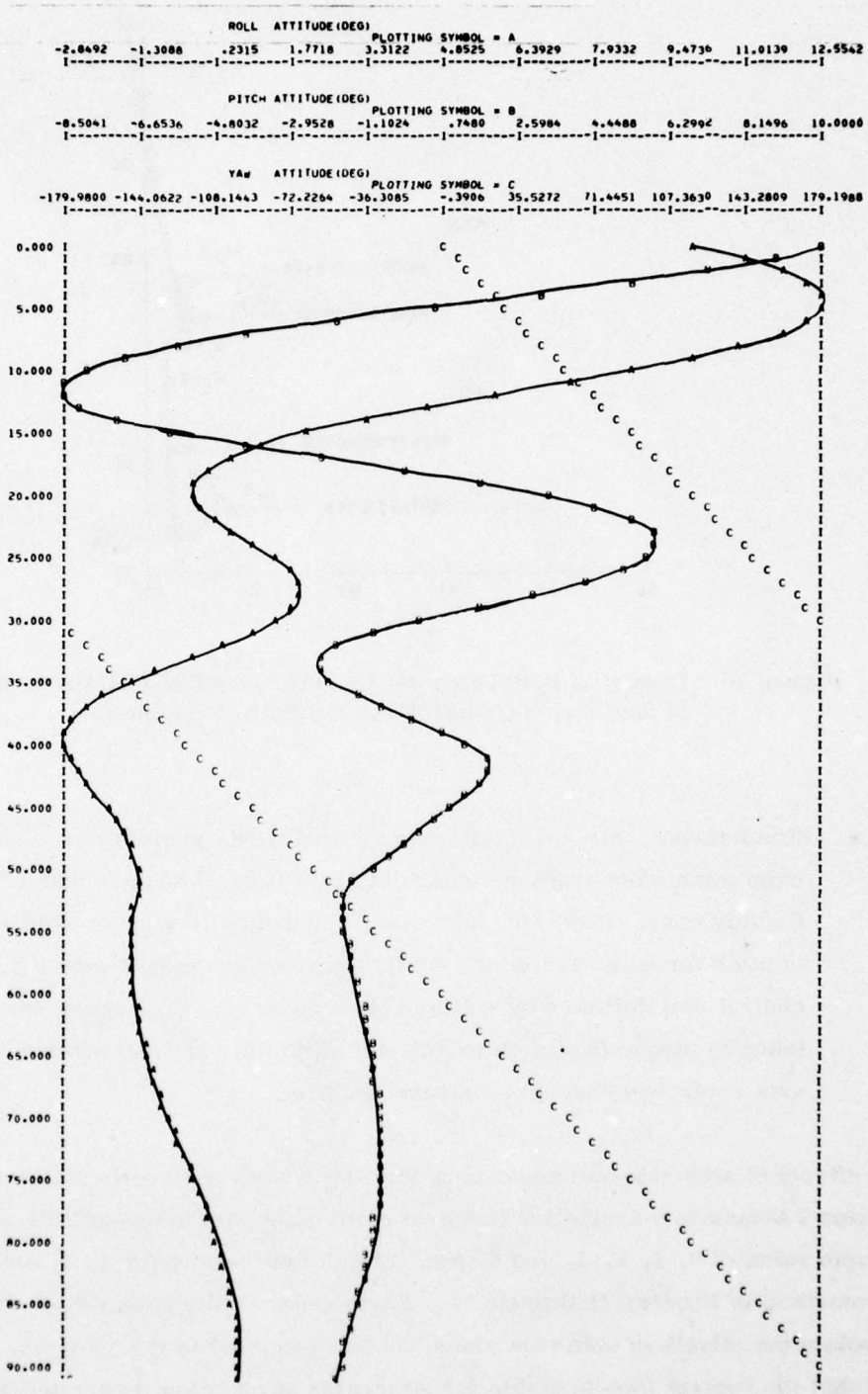

Figure 71. Version 2 Roll/Pitch Acquisition Controller (Nominal Gain, 1 rpm)

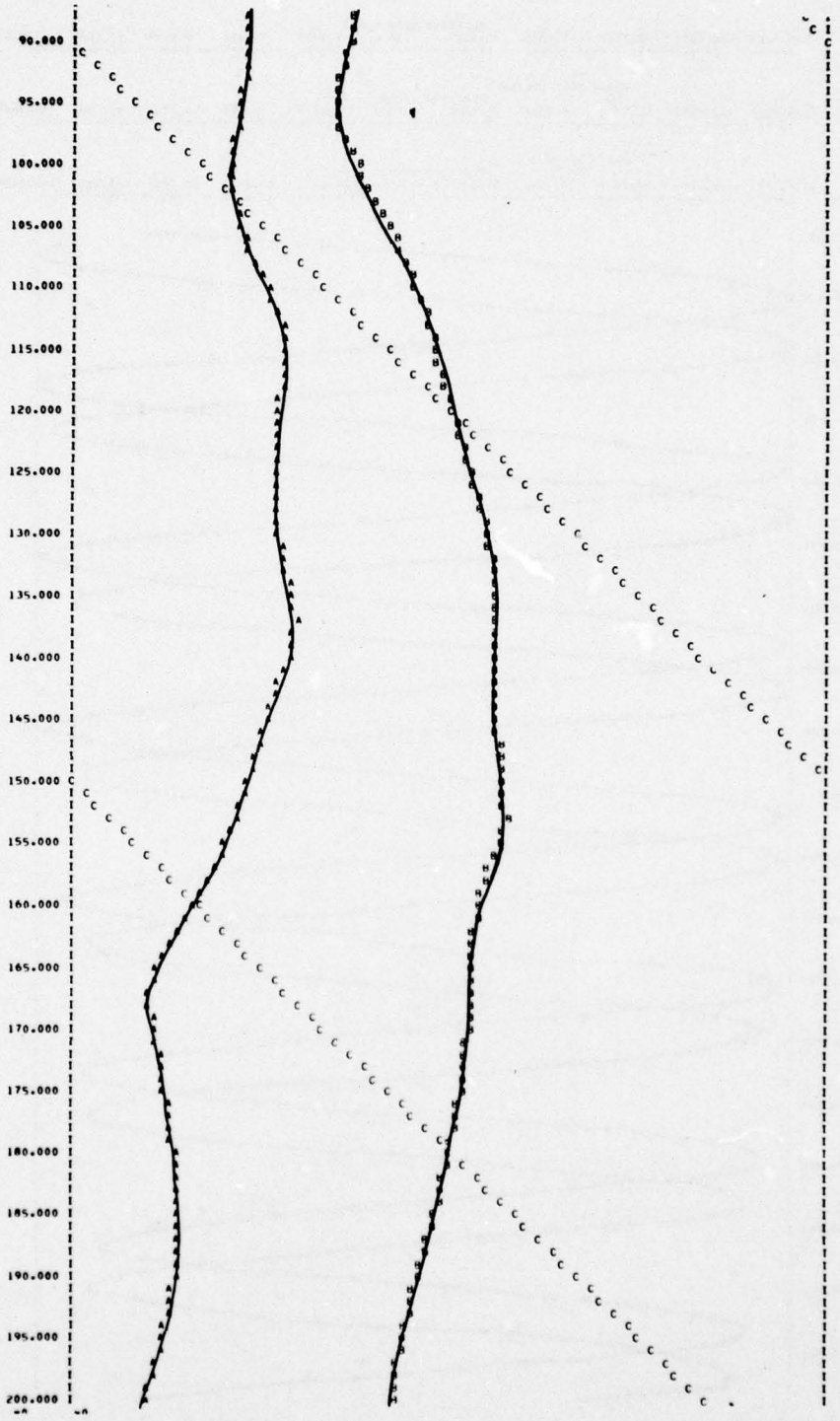

Figure 71. Version 2 Roll/Pitch Acquisition Controller (Nominal Gain, 1 rpm) (concluded)

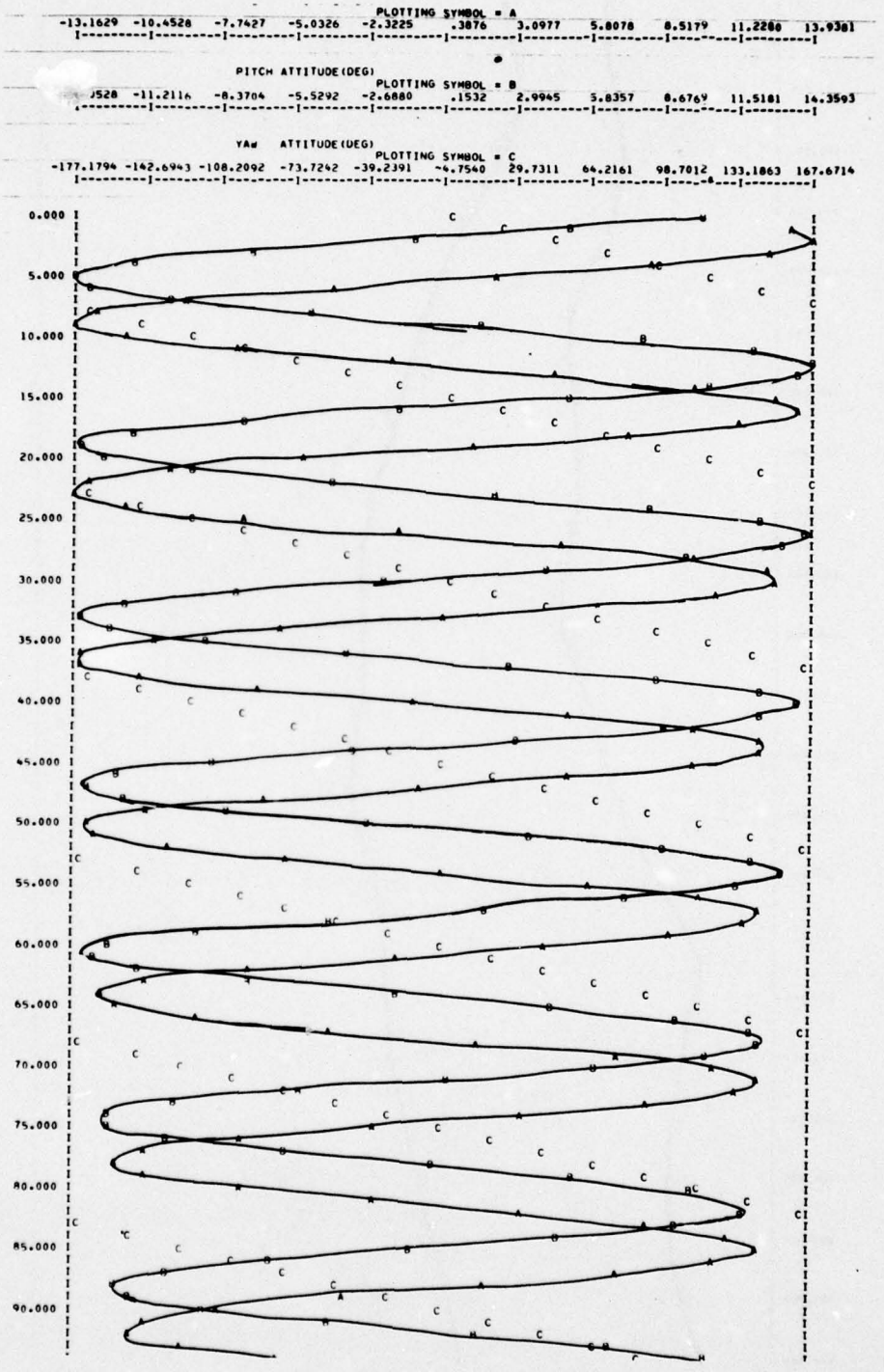

Figure 72. Version 2 Roll/Pitch Acquisition Controller (Nominal Gain, 4 rpm)

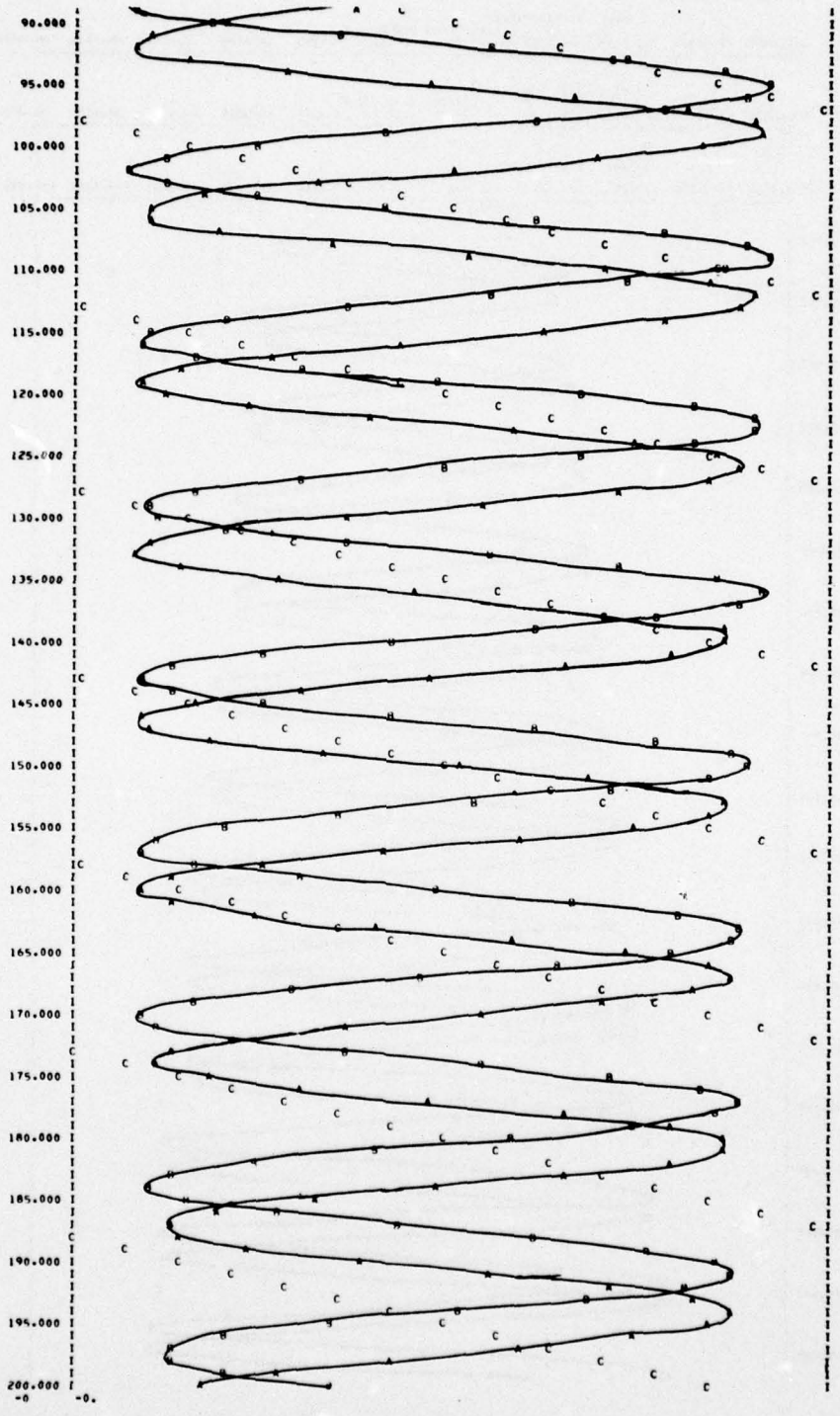

Figure 72. Version 2 Roll/Pitch Acquisition Controller (Nominal Gain, 4 rpm) (concluded)

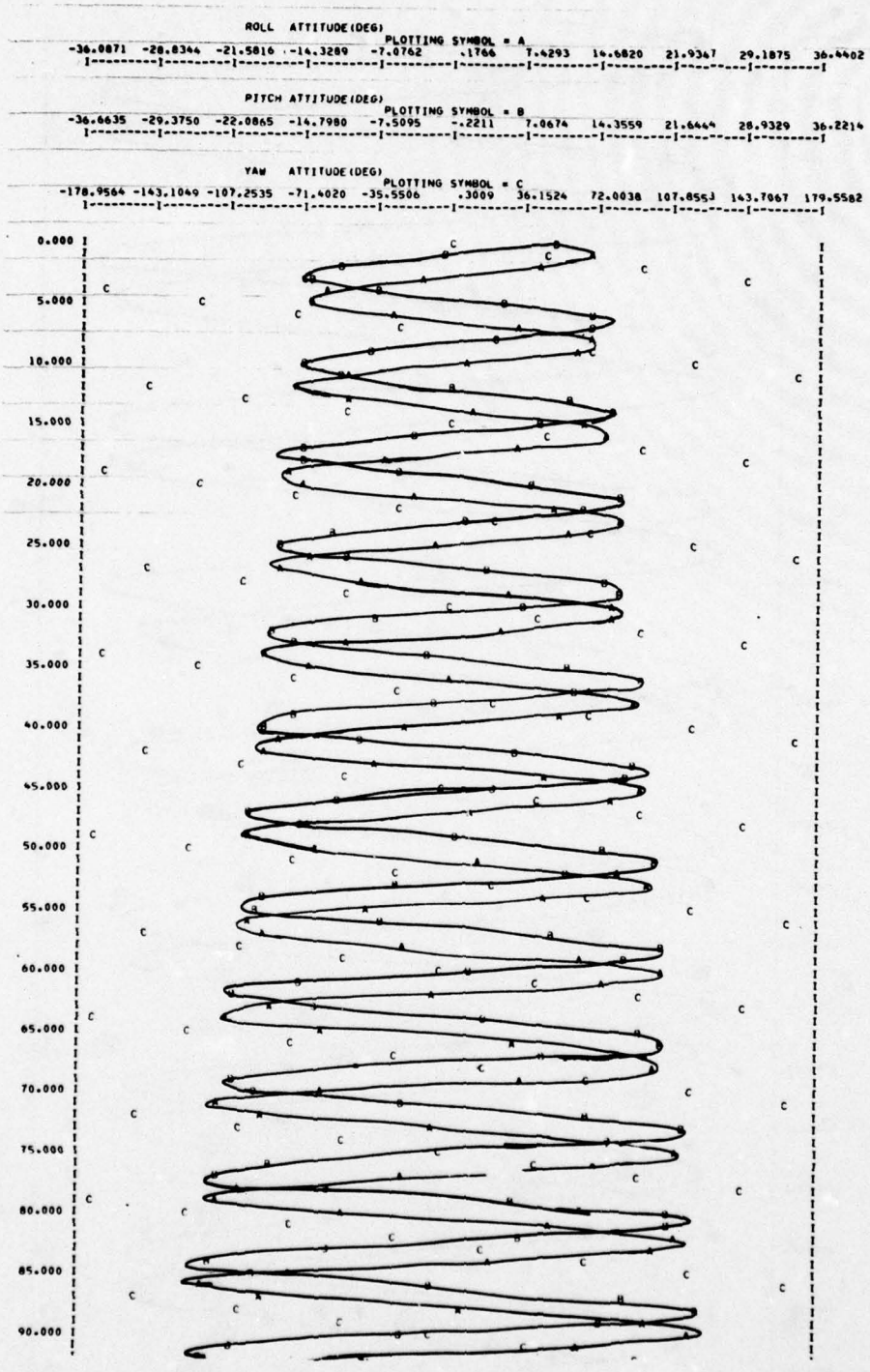

Figure 73. Version 2 Roll/Pitch Acquisition Controller (Nominal Gain, 8 rpm)

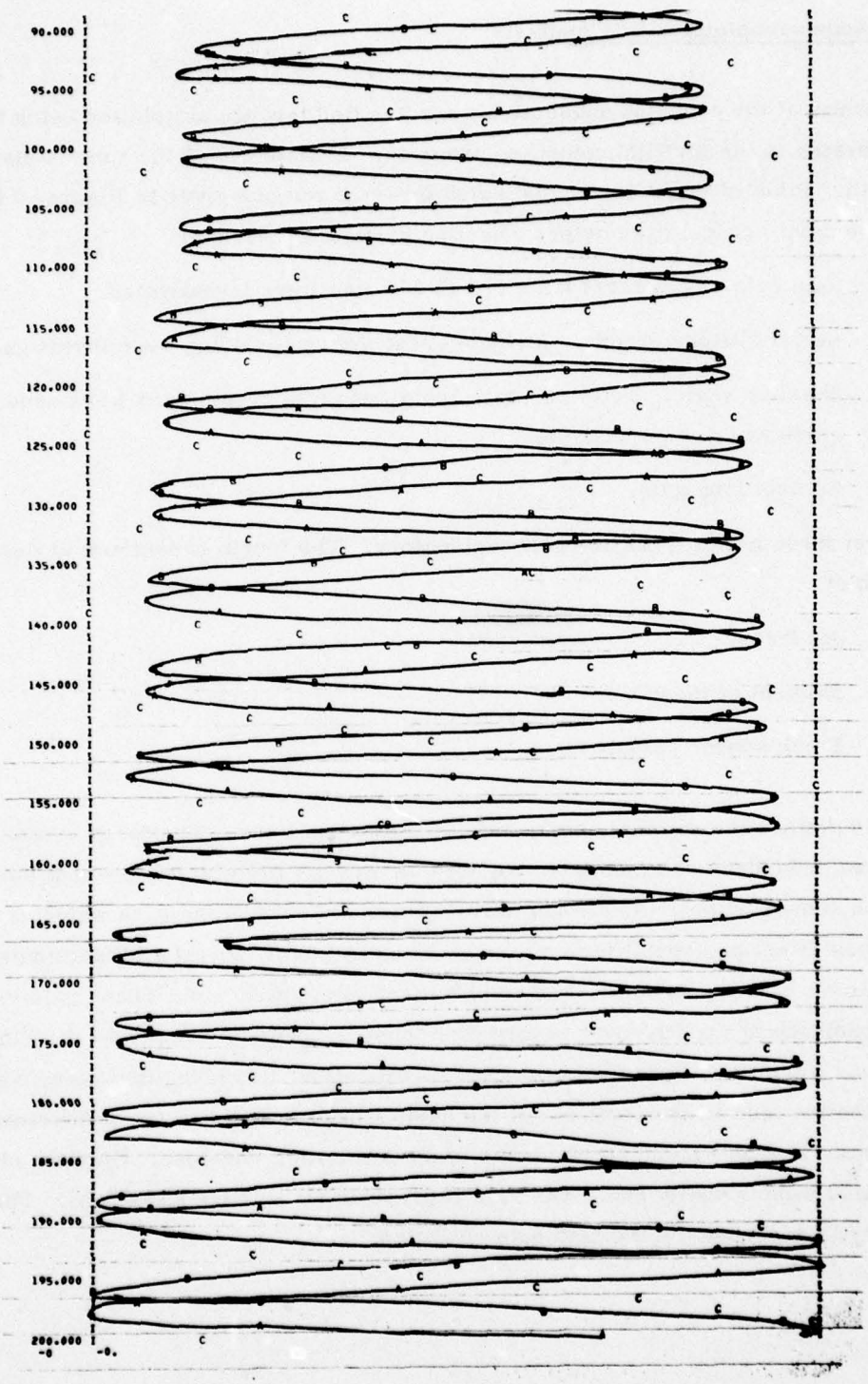

Figure 73. Version 2 Roll/Pitch Acquisition Controller (Nominal Gain, 8 rpm) (concluded)

Earth Acquisition Simulation Analysis

The results of the previous subsection were verified through simulation using the one-body version of the SATSIM computer program. A summary of the runs is given in Table 15. Plots of the attitudes and rates for each run are given in Figures 74 through 97. The most critical parameters affecting earth acquisition are

- Spin rate. Spin rates from 0.5 to 2.0 rpm were investigated.
- Initial attitude errors. Attitude errors of up to 20 deg were investigated.
- Nutation angle. Nutation angles obtained from despin runs were used in the earth acquisition analysis.
- Control loop gain.

The first three parameters are self explanatory. The fourth parameter varies as a function of

- Jet thrust
- Moment of inertia
- Earth sensor variations

Table 16 defines the nominal, high, and low gain conditions. The earth sensor gain variations have been obtained from Figures 98 through 100 which represent the radiance effect on sensor output. Additional uncertainties included in the runs which have the significant effect on acquisition are center of mass offset, thruster misalignment, earth sensor biases and noise, and earth sensor misalignments. These gain variations due to radiance are much more severe than those described in Appendix J. Since these variations were to be included in the CES specification, however, they were considered to be possible operating conditions of the earth sensor. The results of the simulation are summarized in Figure 101 in terms of an acquisition envelope. Only the circled data points were actually run. The data represents worst case conditions. The pitch boundary is generated by the high gain condition.

TABLE 15. ACQUISITION AND REACQUISITION SIMULATION RUNS

Run Number	Controller	Spin Rate (rpm)	ϕ_{ic} (deg)	θ_{ic} (deg)	ψ_{ic} (deg)	Loop Gain	Propellant		Uncertainties	Figure Number	Comment
							Roll	Pitch			
Acq-1A	2	1.0	5.0	5.0	0.11	Nominal	0.03	0.0004	No	74	Converged
Acq-2A	2	1.0	10.0	10.0	0.11	Nominal	0.06	0.0001	No	75	Converged
Acq-2B	1	1.0	10.0	10.0	0.11	Nominal	0.06	0.001	No	76	Converged
Acq-4A	2	1.0	10.0	10.0	2.3	Nominal	0.08	0.0001	No		Converged
Acq-4B	1	1.0	10.0	10.0	2.3	Nominal	0.07	0.0005	No	77	Converged
Acq-4AP	2	1.0	10.0	10.0	2.3	Nominal	---	0.02	No	78	Converged, pitch control only
Acq-4BP	1	1.0	10.0	10.0	2.3	Nominal	---	0.02	No	79	Converged, pitch control only
Acq-7A	2	1.0	10.0	10.0	2.3	Low	0.04	0.0	Yes	80	Converged
Acq-7B	1	1.0	10.0	10.0	2.3	Low	0.05	0.0003	Yes	81	Converged
Acq-8A	2	2.0	10.0	10.0	2.3	Low	0.09	0.0007	Yes	82	Converged
Acq-9A	2	0.5	10.0	10.0	4.0	Low	0.03	0.001	Yes	83	Converged
Acq-11A	2	1.0	10.0	10.0	2.3	High	0.19	0.04	Yes	84	Converged
Acq-11B	1	1.0	10.0	10.0	2.3	High	0.16	0.007	Yes	85	Converged
Acq-11AP	2	1.0	10.0	10.0	2.3	High	---	0.09	Yes	86	Converged, pitch control only
Acq-11BP	1	1.0	10.0	10.0	2.3	High	---	0.09	Yes	87	Converged, pitch control only
Acq-12A	2	2.0	10.0	10.0	2.3	High	---	---	Yes	88	Diverged
Acq-26A	2	2.0	5.0	5.0	2.3	High	0.2	0.02	Yes	89	Converged
Acq-13A	2	0.5	10.0	10.0	4.0	High	---	---	Yes	90	Diverged
Acq-15B	1	0.5	10.0	10.0	4.0	High	---	---	Yes	91	Diverged
Acq-14A	2	0.5	5.0	5.0	4.0	High	0.05	0.001	Yes	92	Converged
Acq-16A	2	0.5	10.0	10.0	4.0	High	0.12	---	Yes	93	Converged, roll control only
Acq-17A	2	1.0	20.0	20.0	2.3	High	---	---	Yes	94	Diverged
Acq-18A	2	1.0	15.0	15.0	2.3	High	0.26	0.05	Yes	95	Converged
Acq-19A	2	1.0	20.0	0.0	2.3	High	---	---	Yes	96	Converged in roll
Acq-25A	2	1.5	10.0	10.0	2.3	High	0.29	0.1	Yes	97	Converged
Racq-1A	2	1.0	10.0	10.0	4.0	Low	0.08	0.007	Yes	103	Converged
Racq-2A	2	2.0	10.0	10.0	4.0	Low	0.15	0.02	Yes	104	Converged
Racq-3A	2	0.5	10.0	10.0	6.0	Low	0.05	0.007	Yes	105	Converged

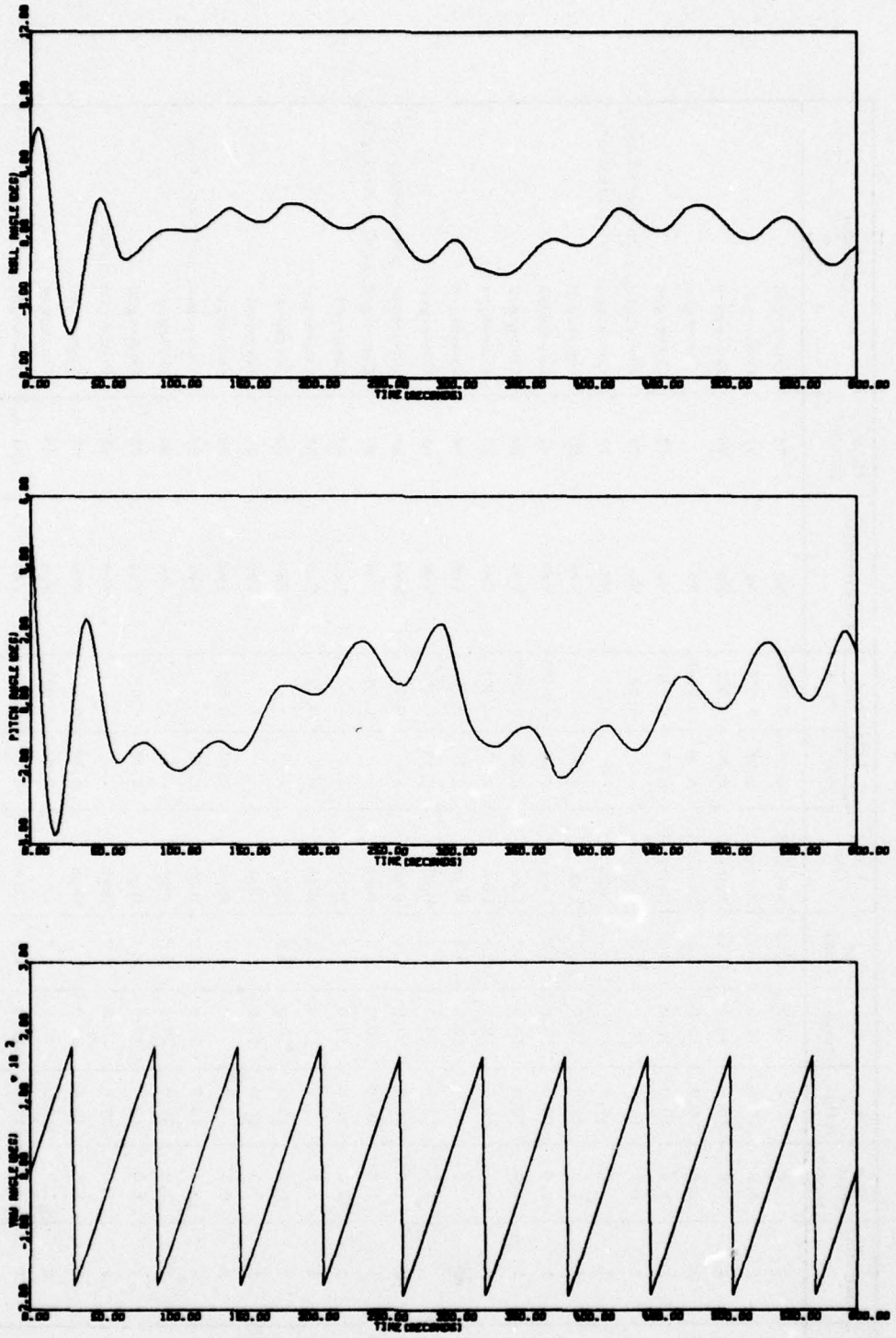

Figure 74. Acquisition Run 1A

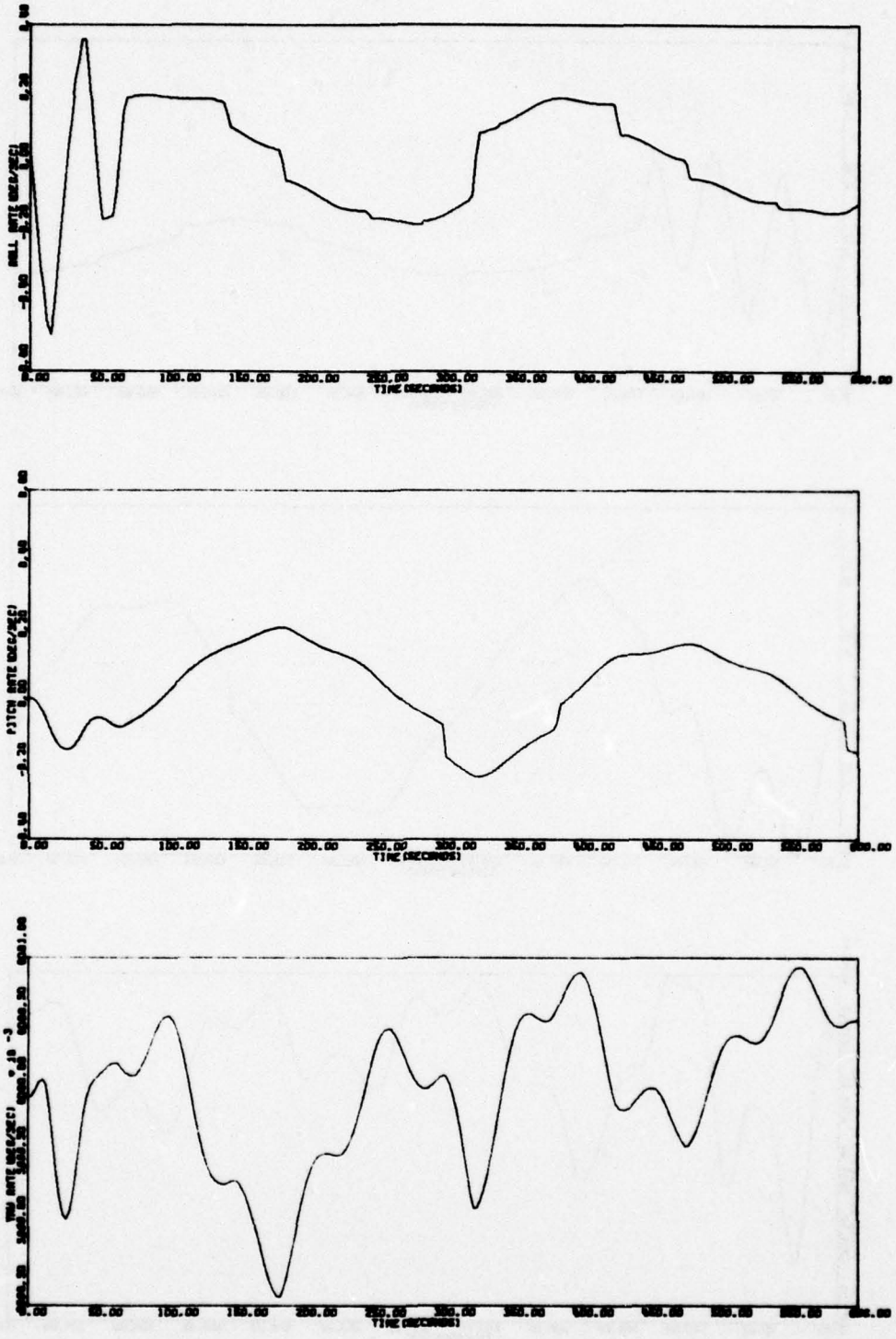

Figure 74. Acquisition Run 1A (concluded)

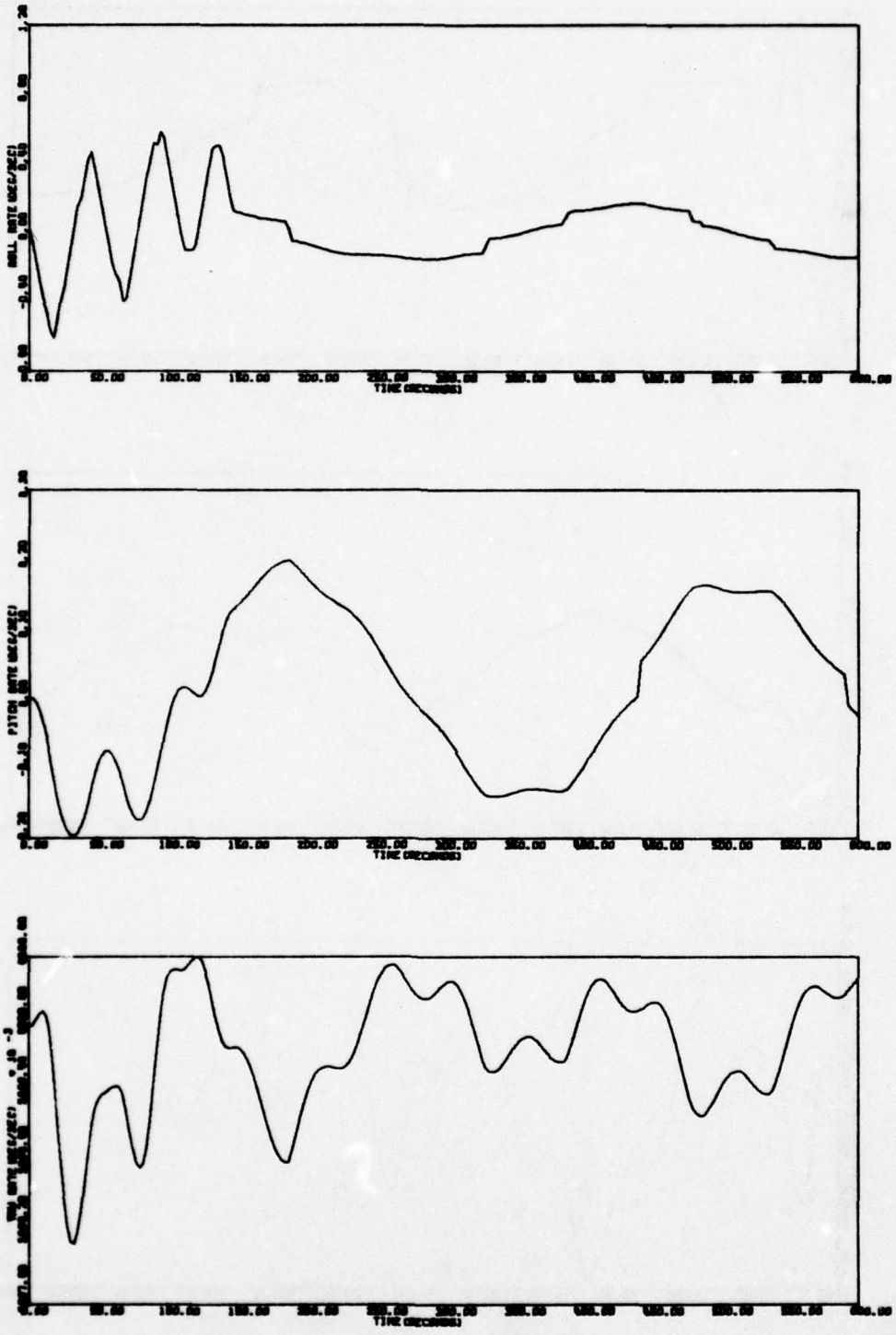

Figure 75. Acquisition Run 2A

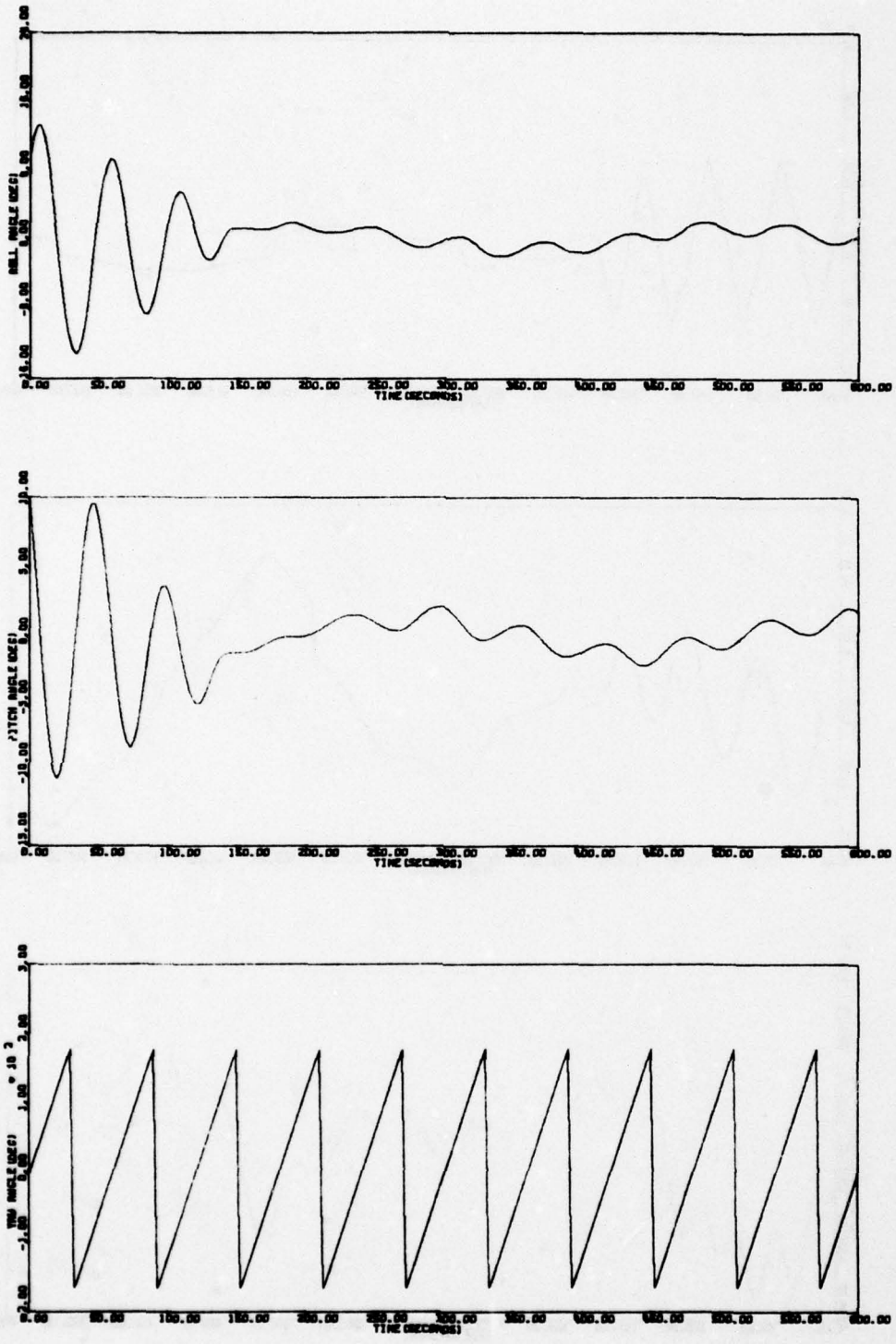

Figure 75. Acquisition Run 2A (concluded)

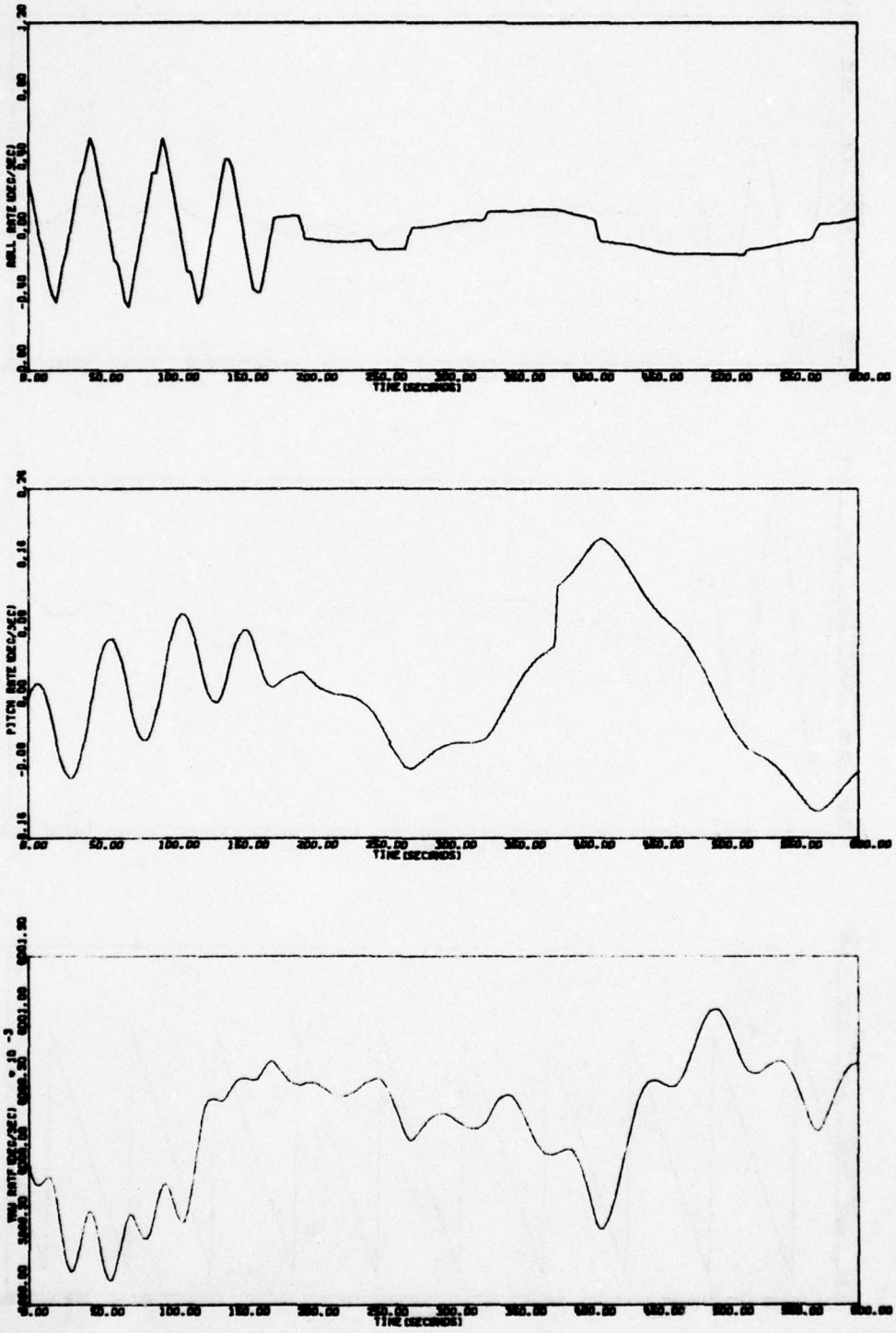

Figure 76. Acquisition Run 2B

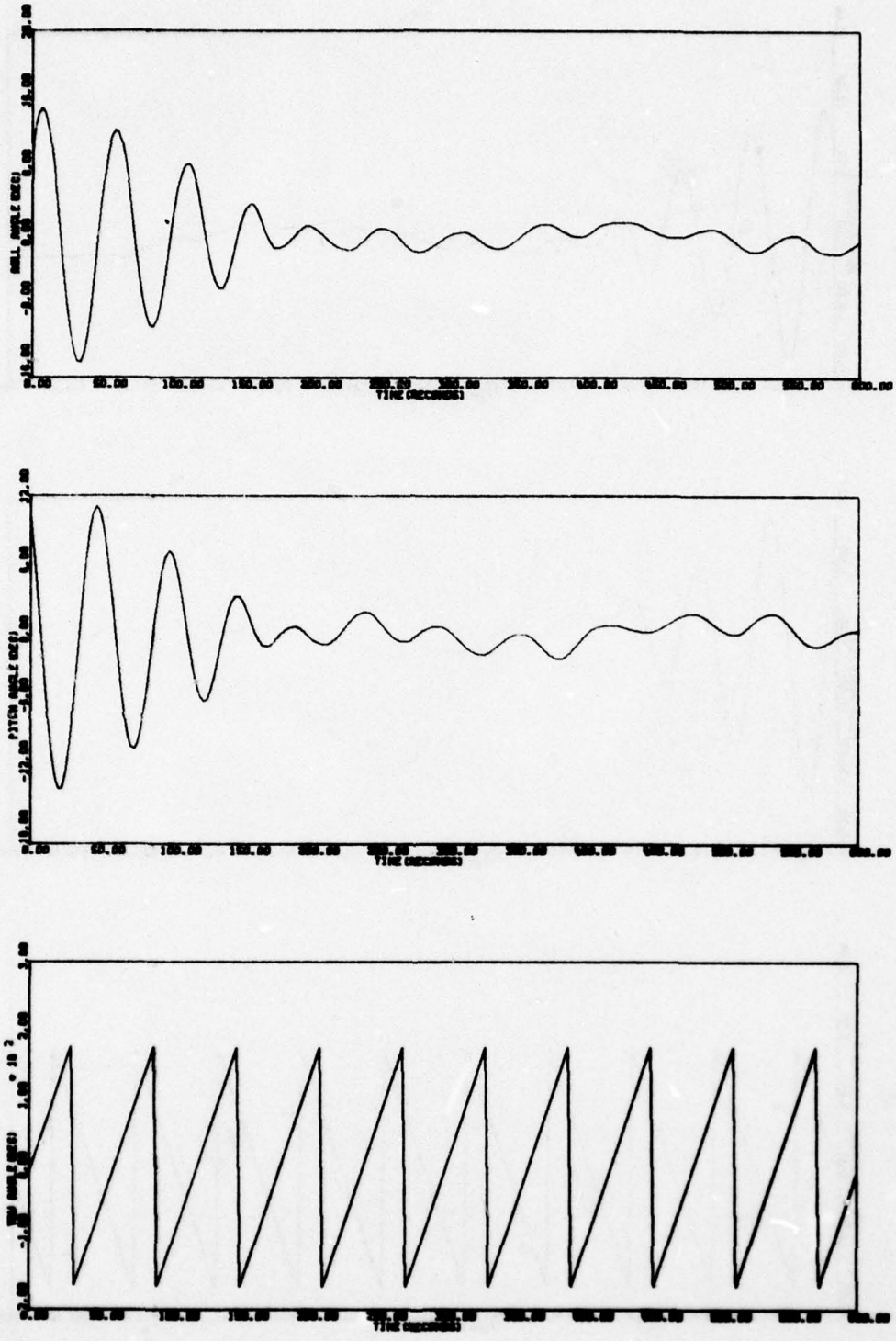

Figure 76. Acquisition Run 2B (concluded)

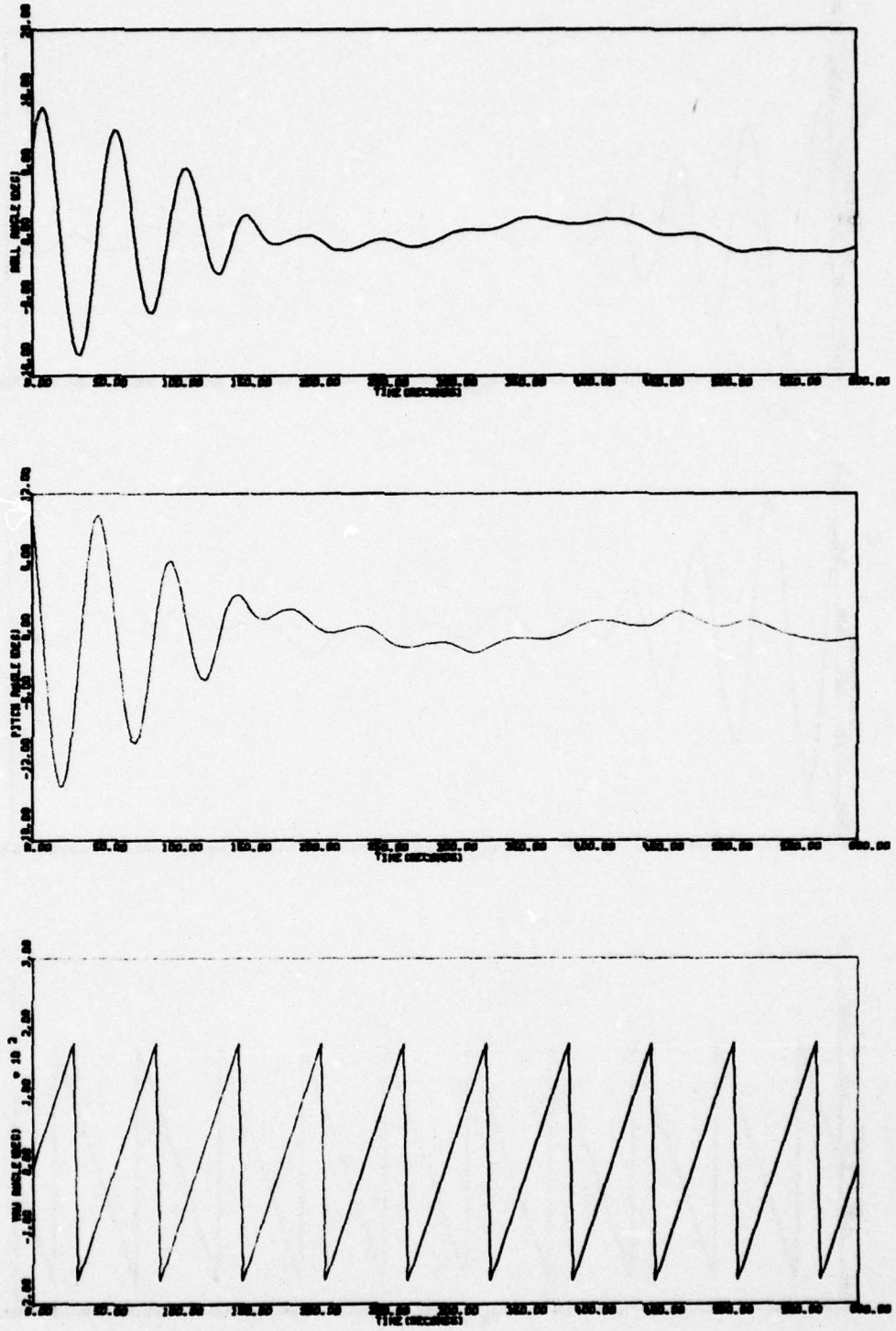

Figure 77. Acquisition Run 4B

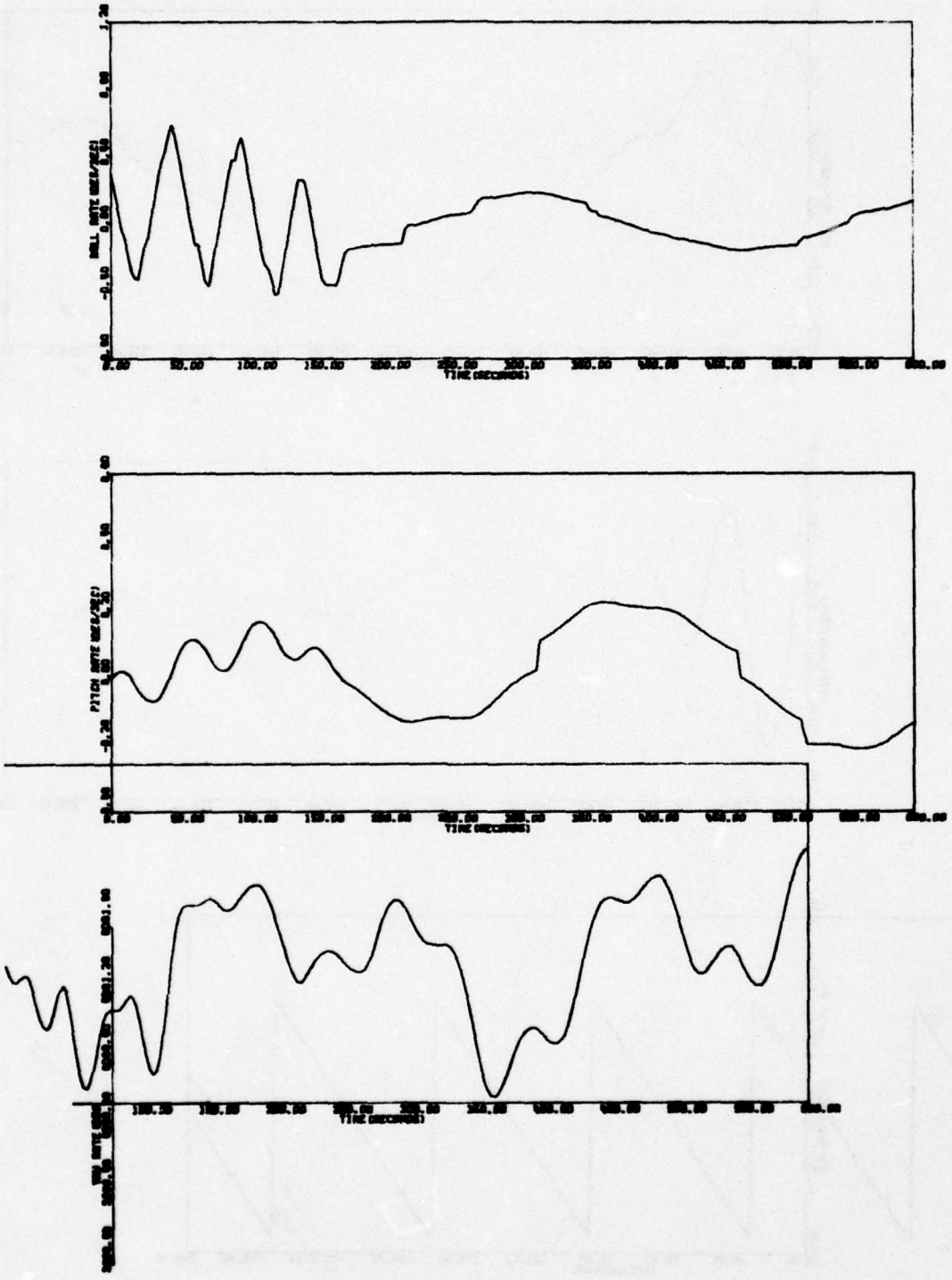

Figure 77. Acquisition Run 4B (concluded)

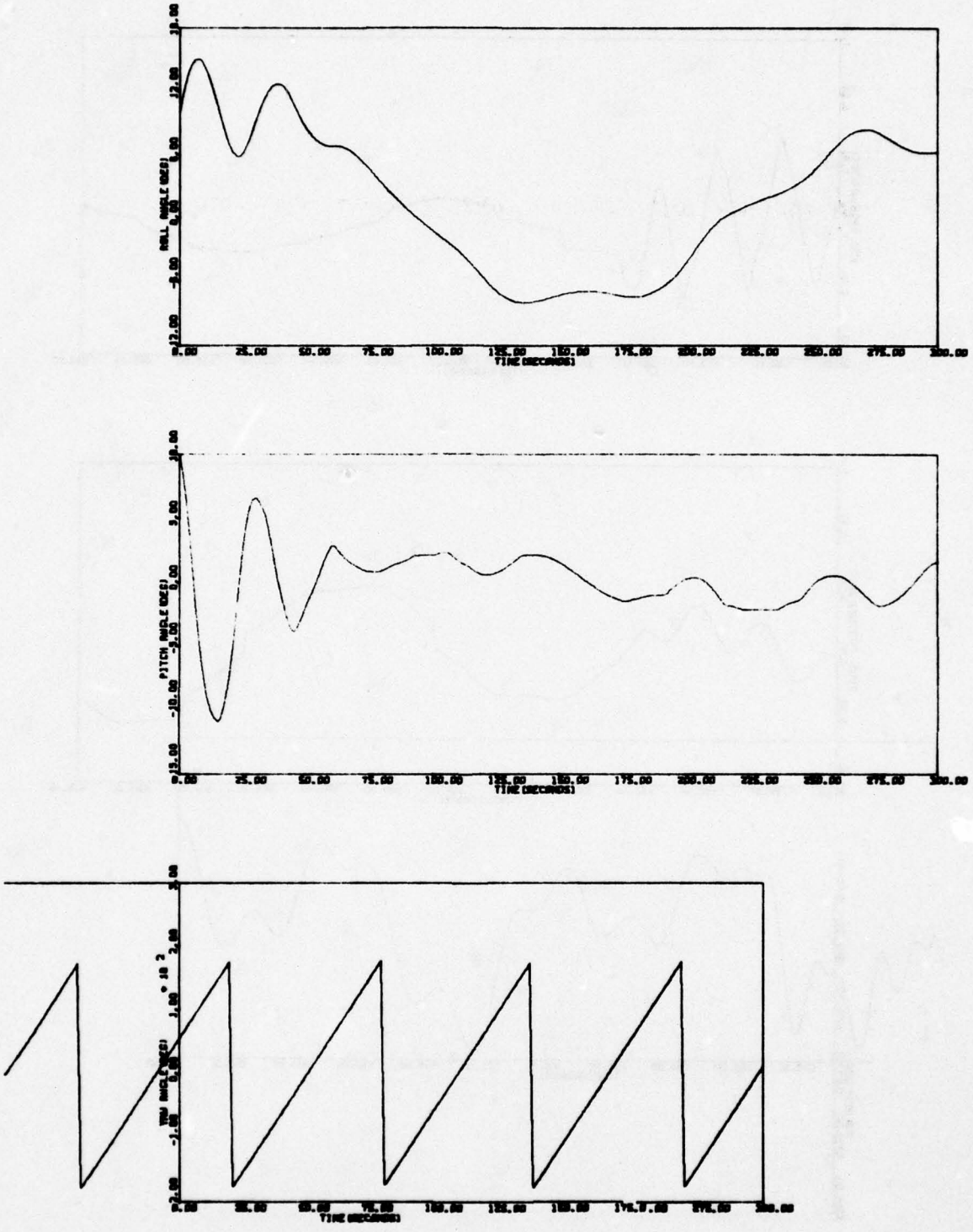

Figure 78. Acquisition Run 4AP

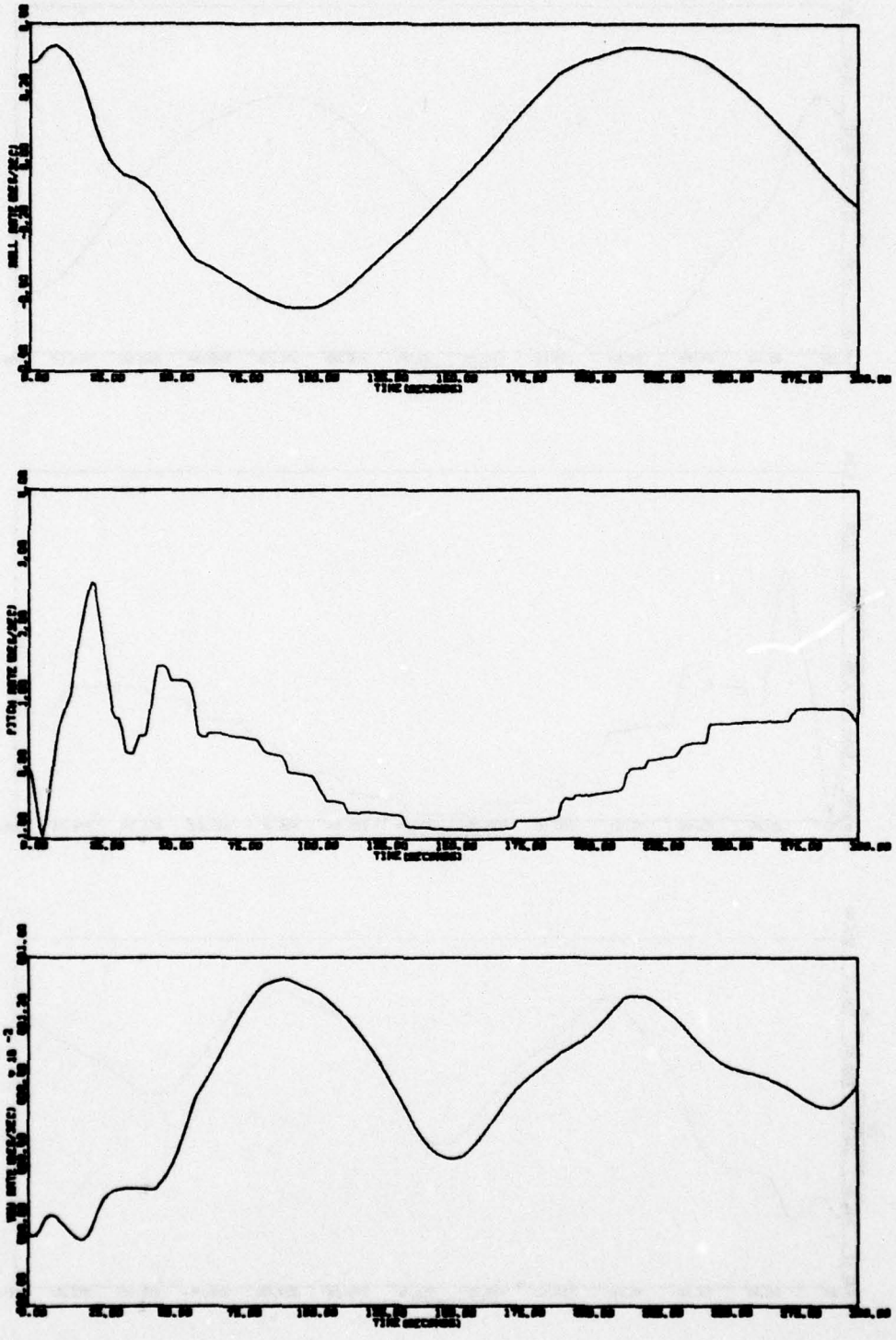

Figure 78. Acquisition Run 4AP (concluded)

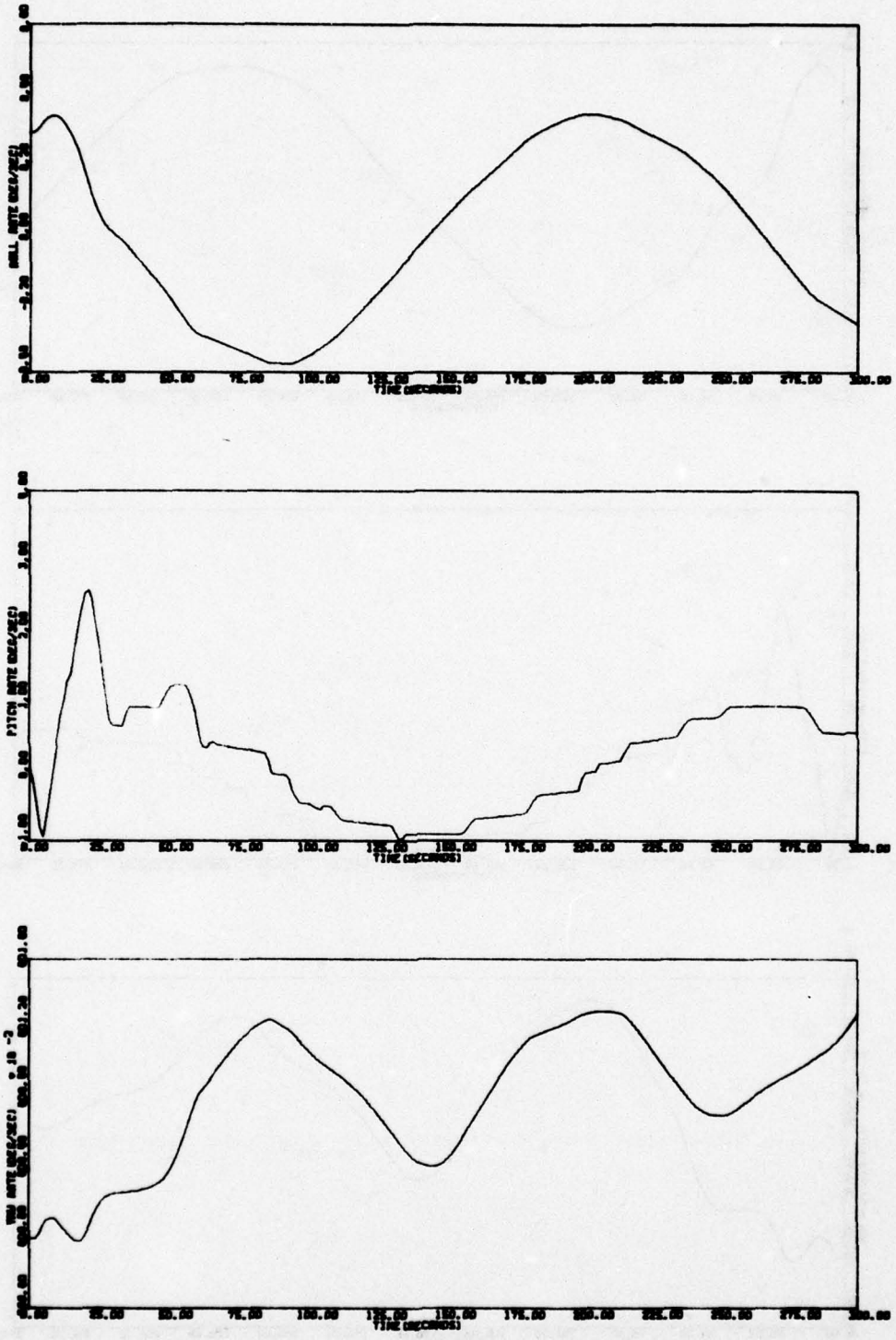

Figure 79. Acquisition Run 4BP

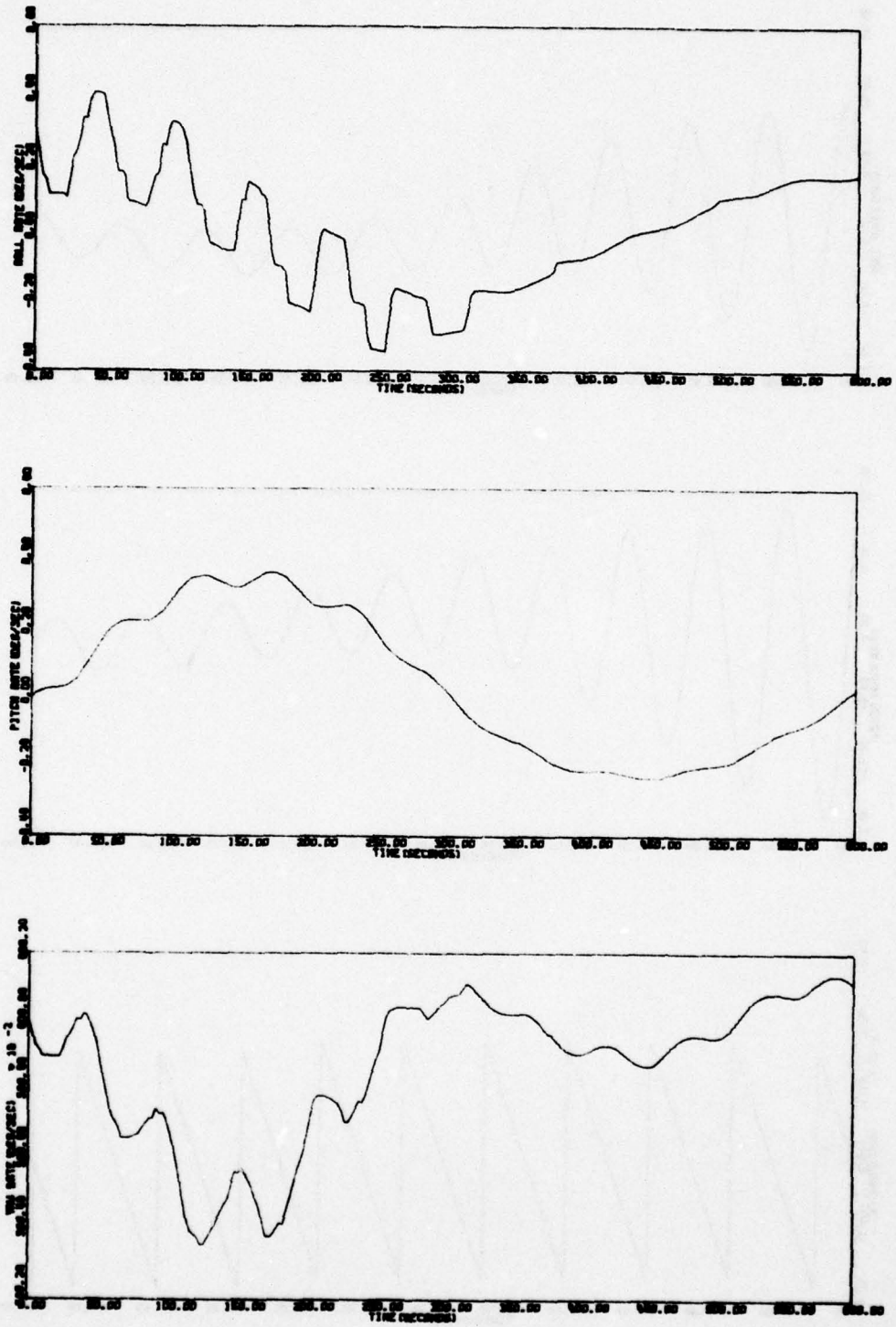

Figure 80. Acquisition Run 7A

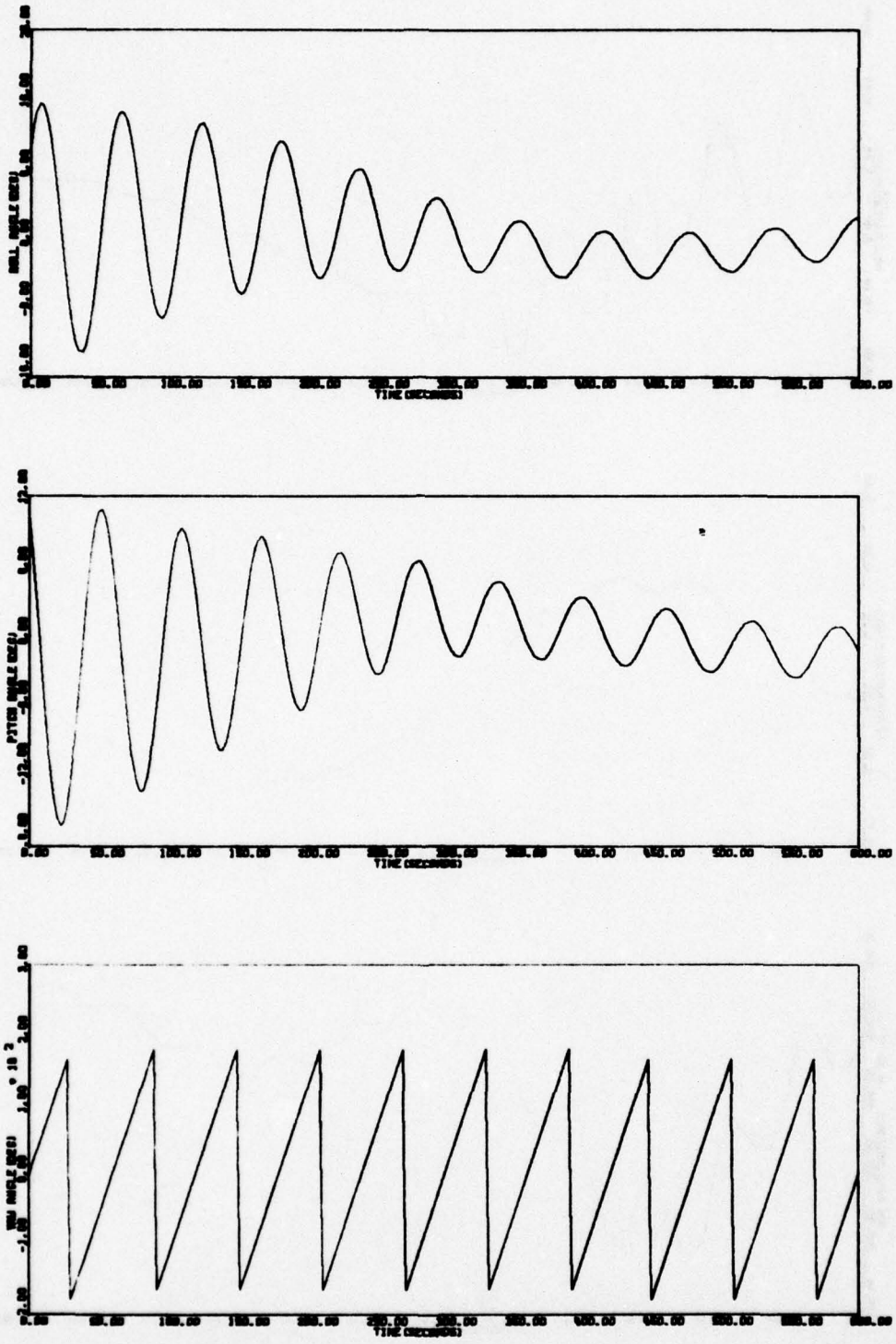

Figure 80. Acquisition Run 7A (concluded)

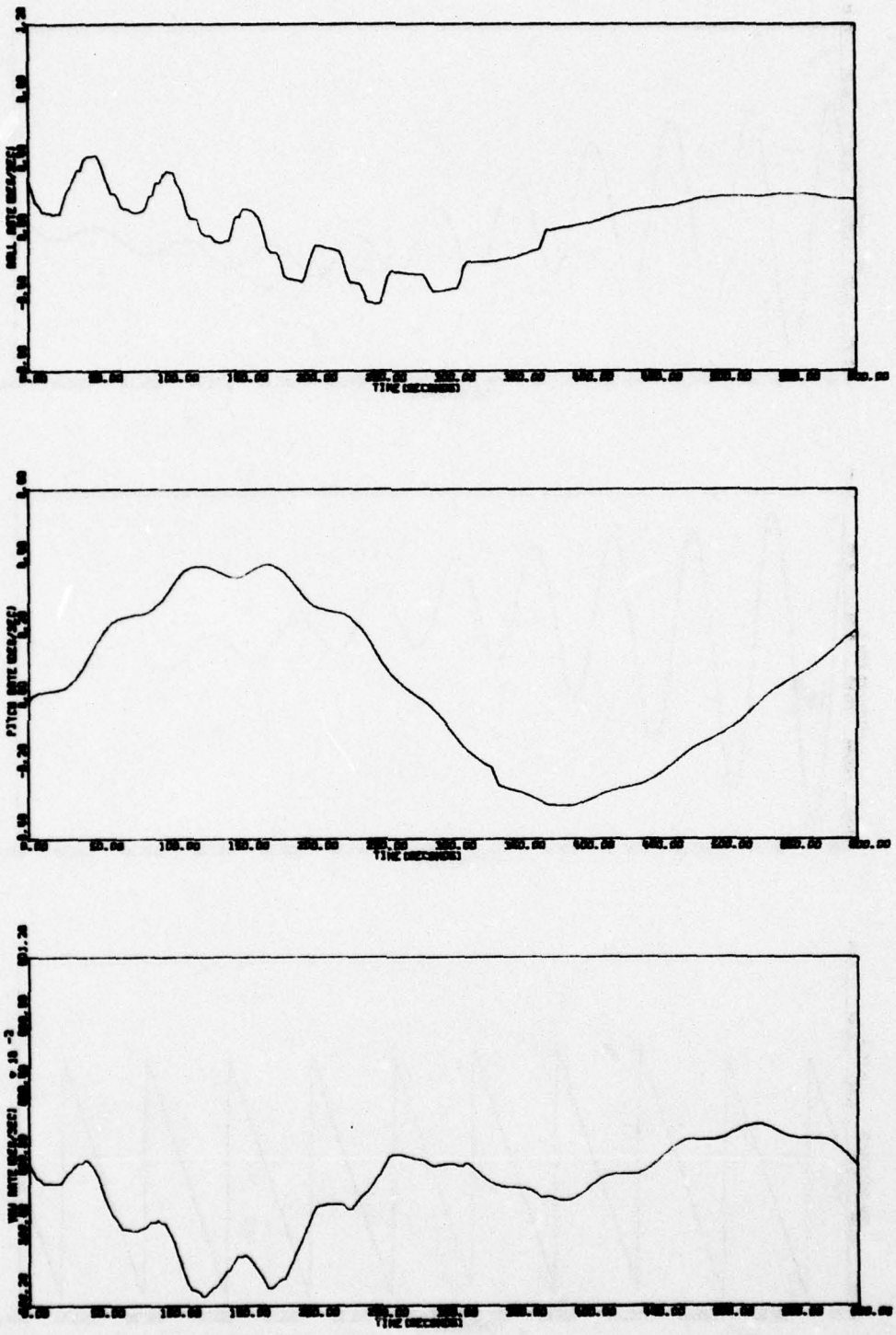

Figure 81. Acquisition Run 7B

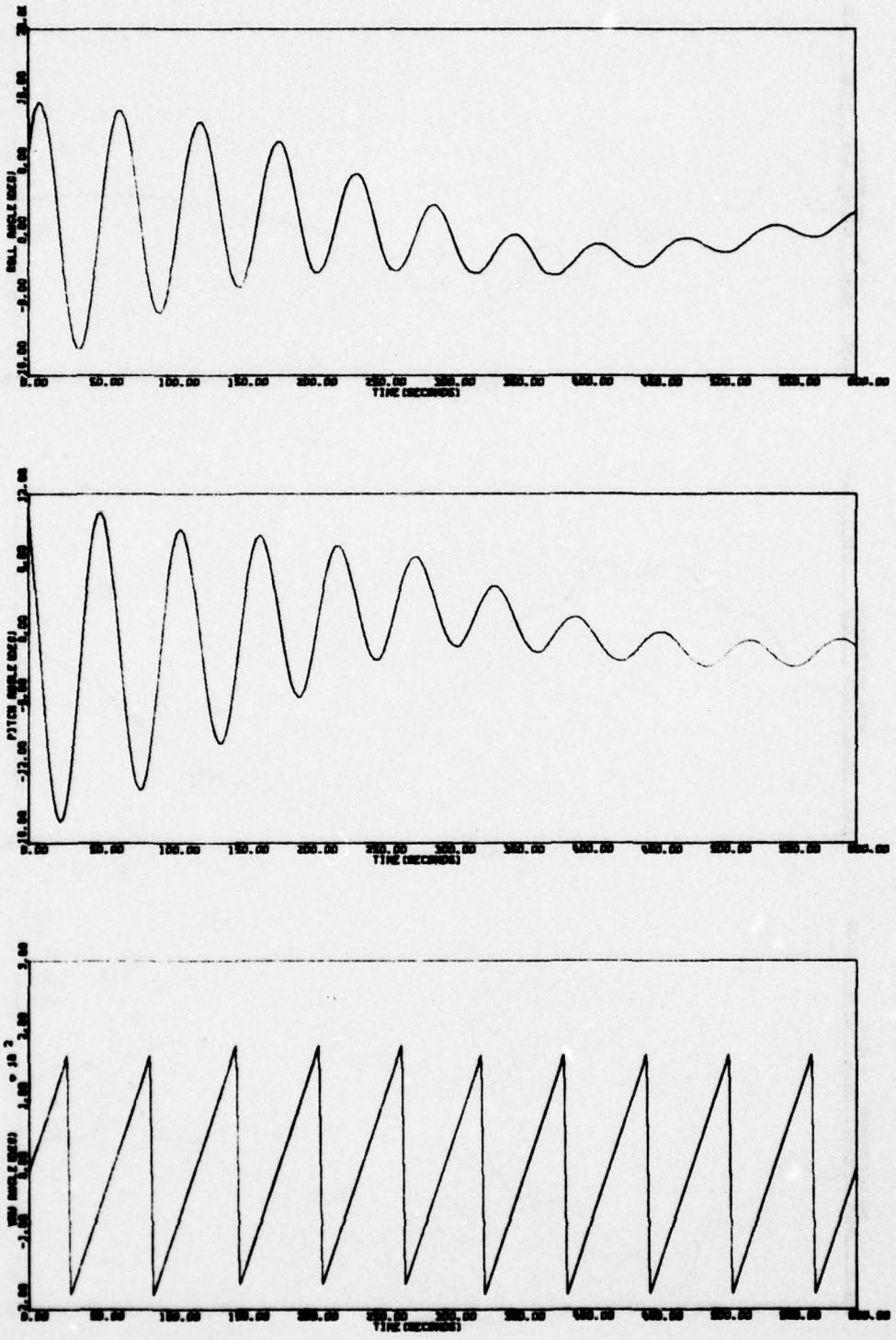

Figure 81. Acquisition Run 7B (concluded)

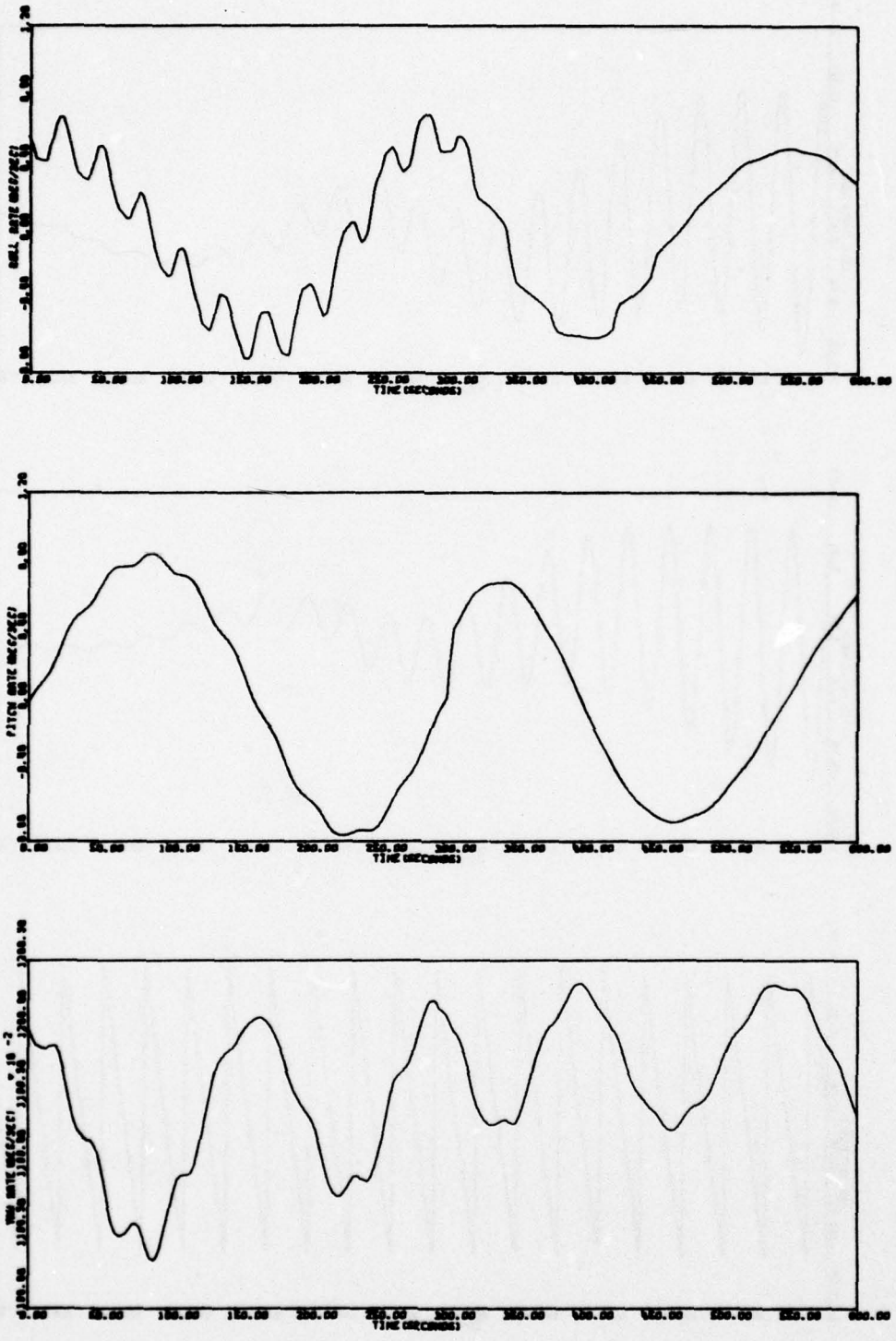

Figure 82. Acquisition Run 8A

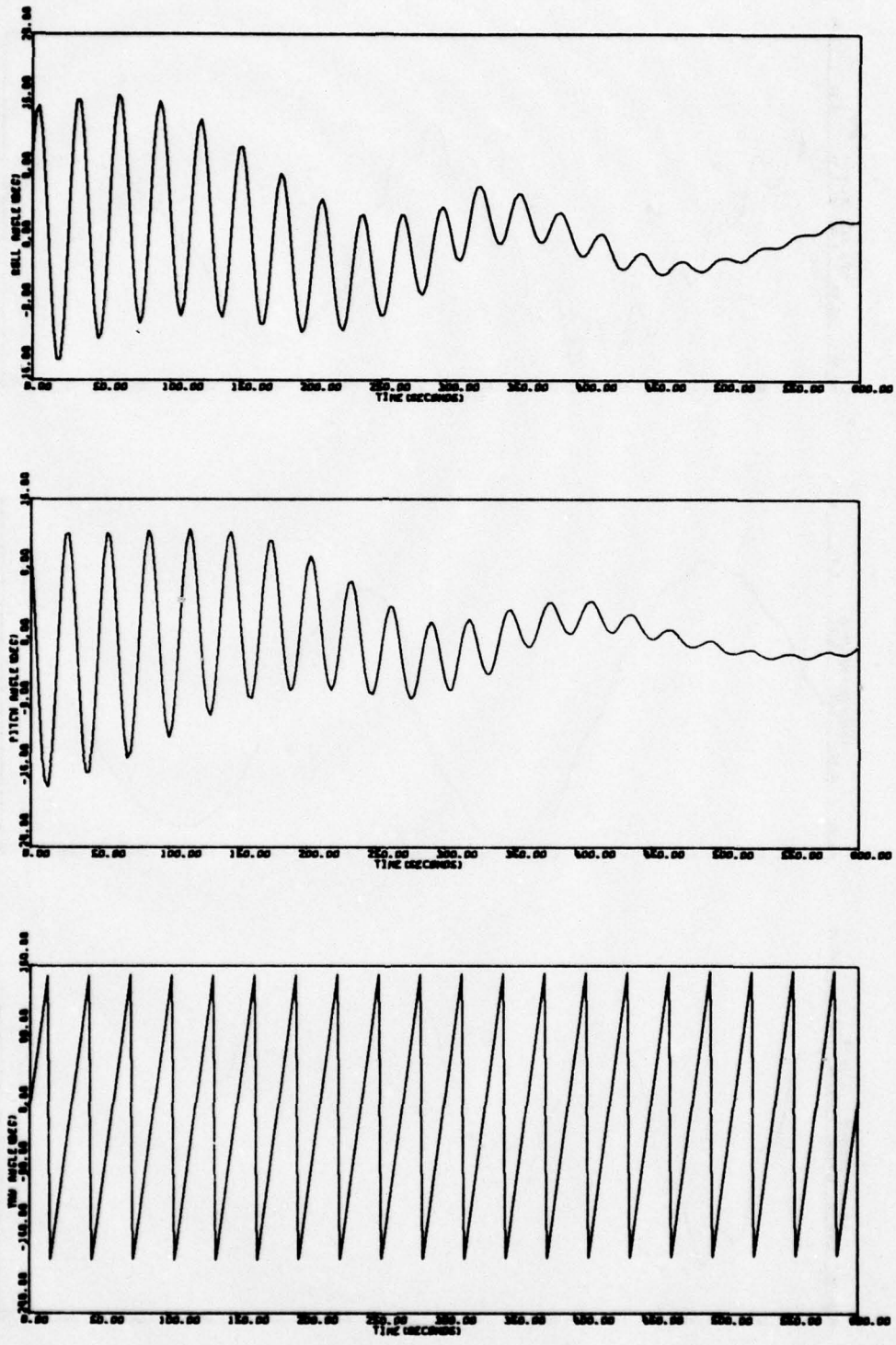

Figure 82. Acquisition Run 8A (concluded)

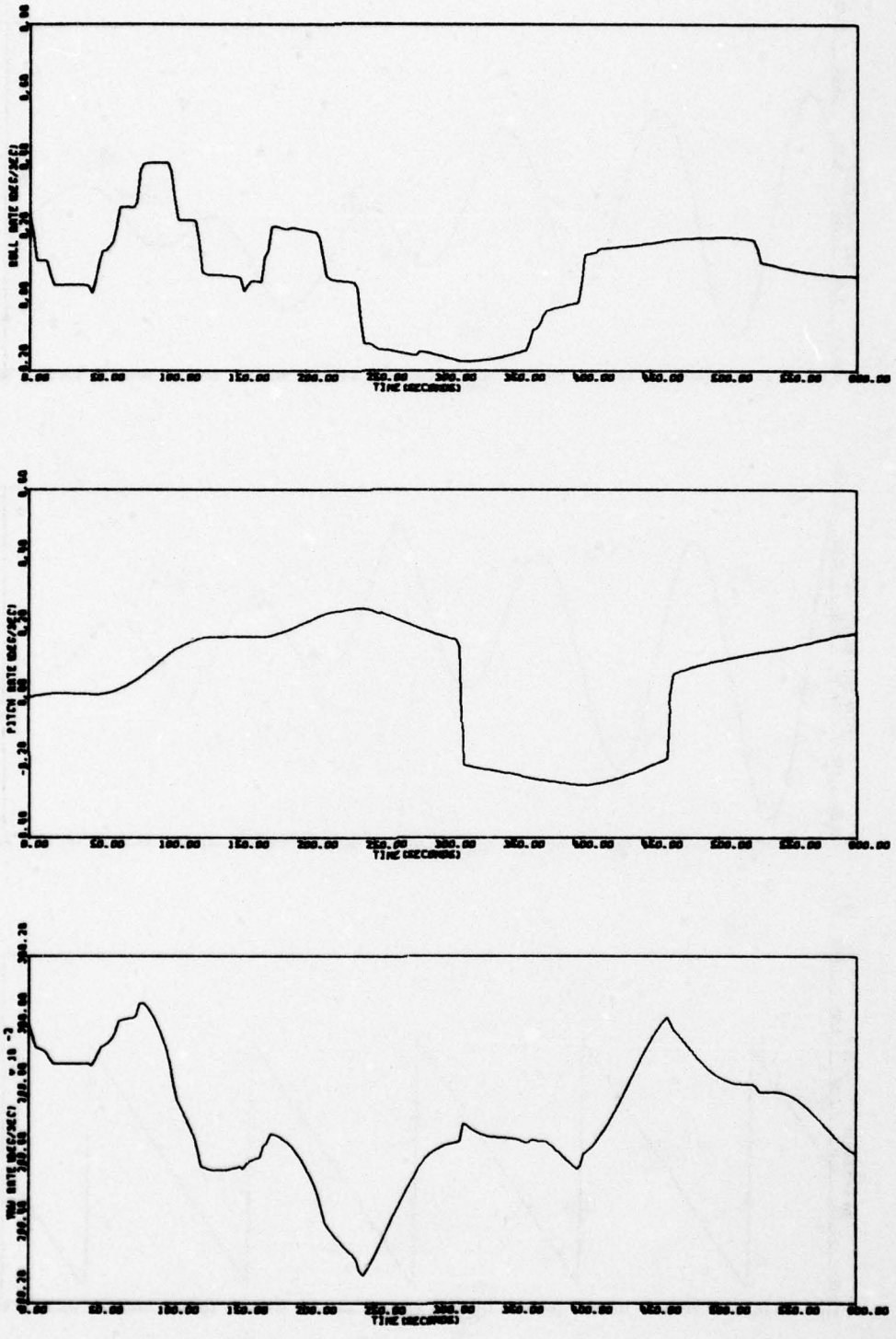

Figure 83. Acquisition Run 9A

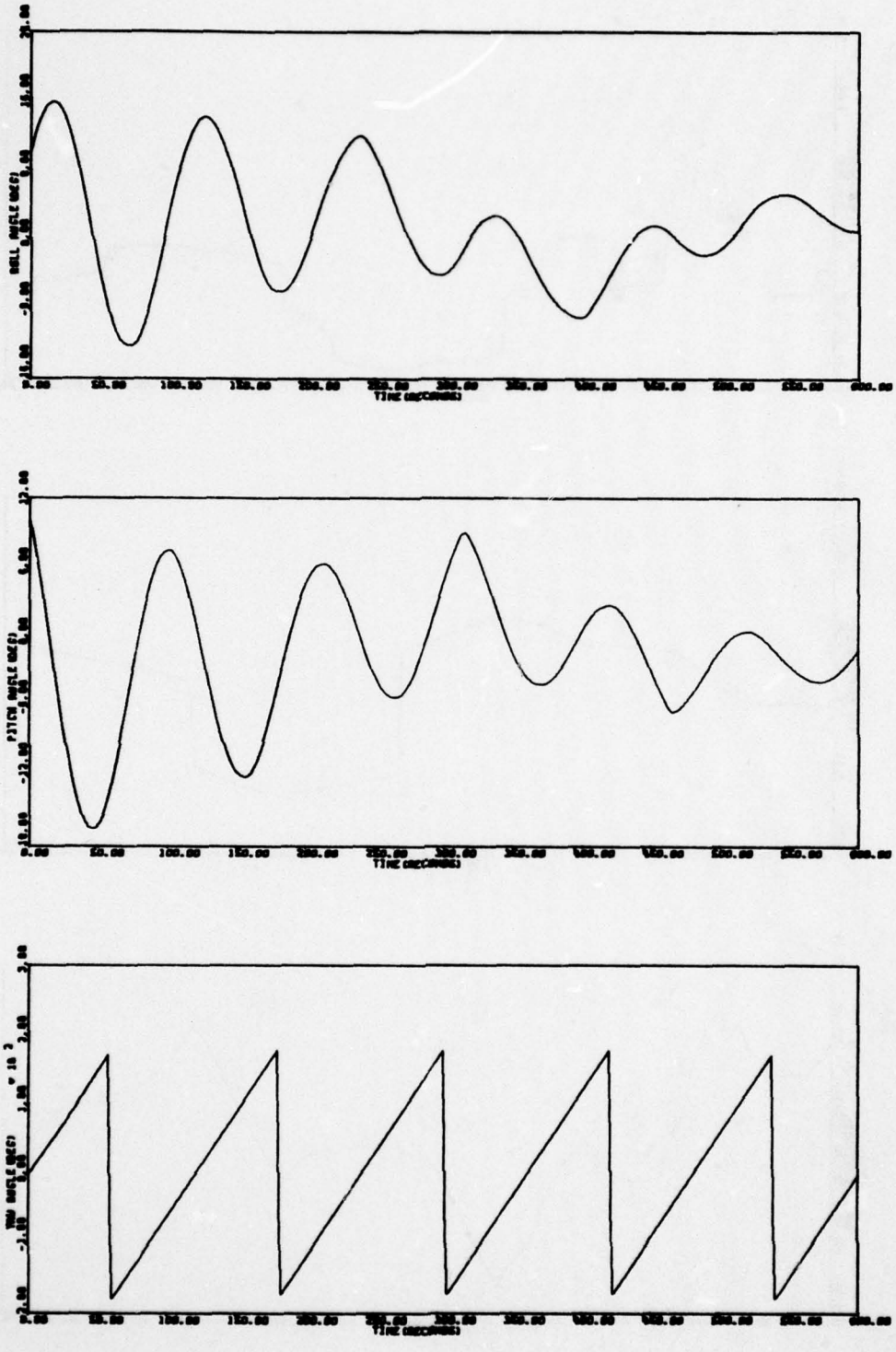

Figure 83. Acquisition Run 9A (concluded)

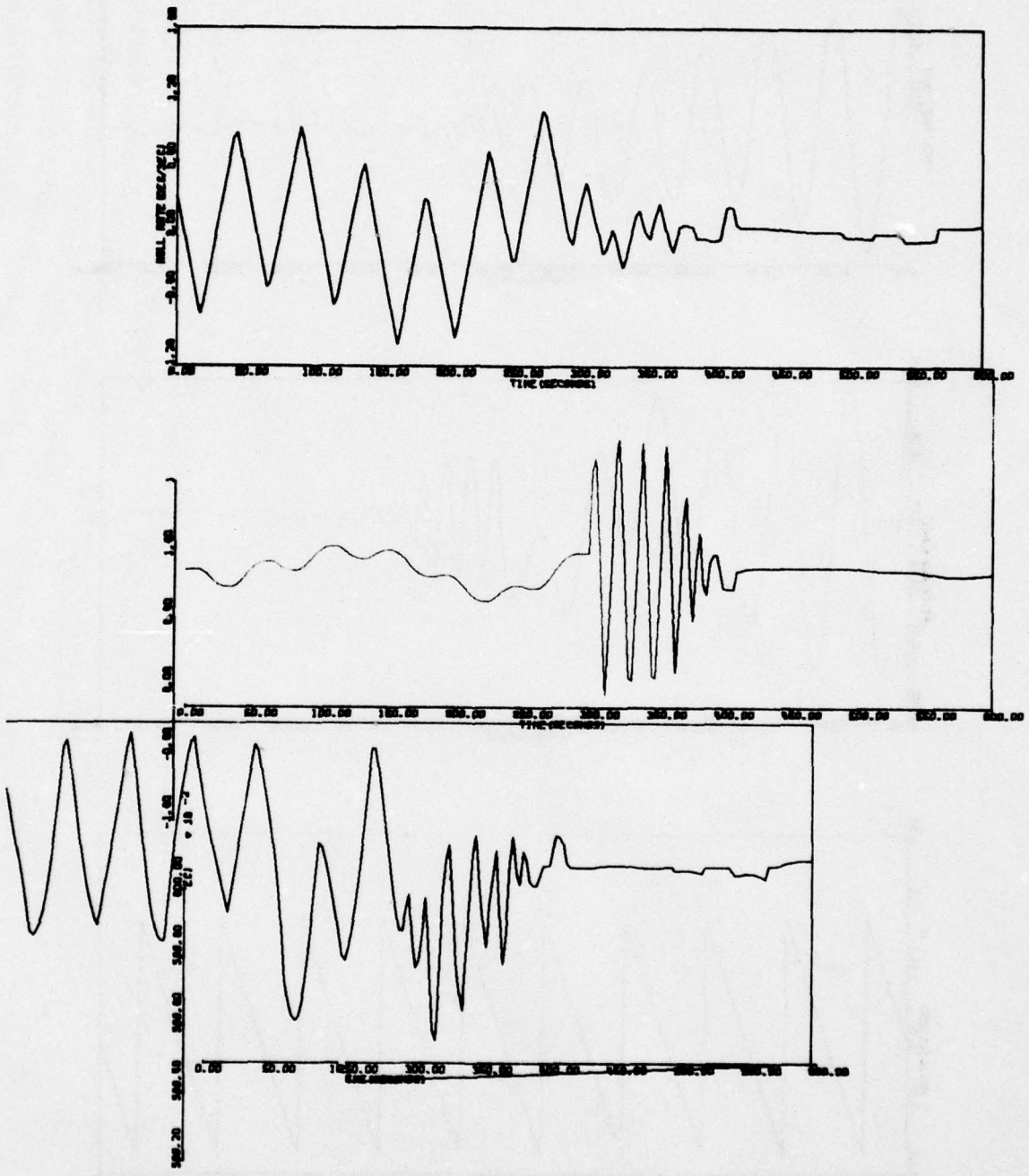

Figure 84. Acquisition Run 11A

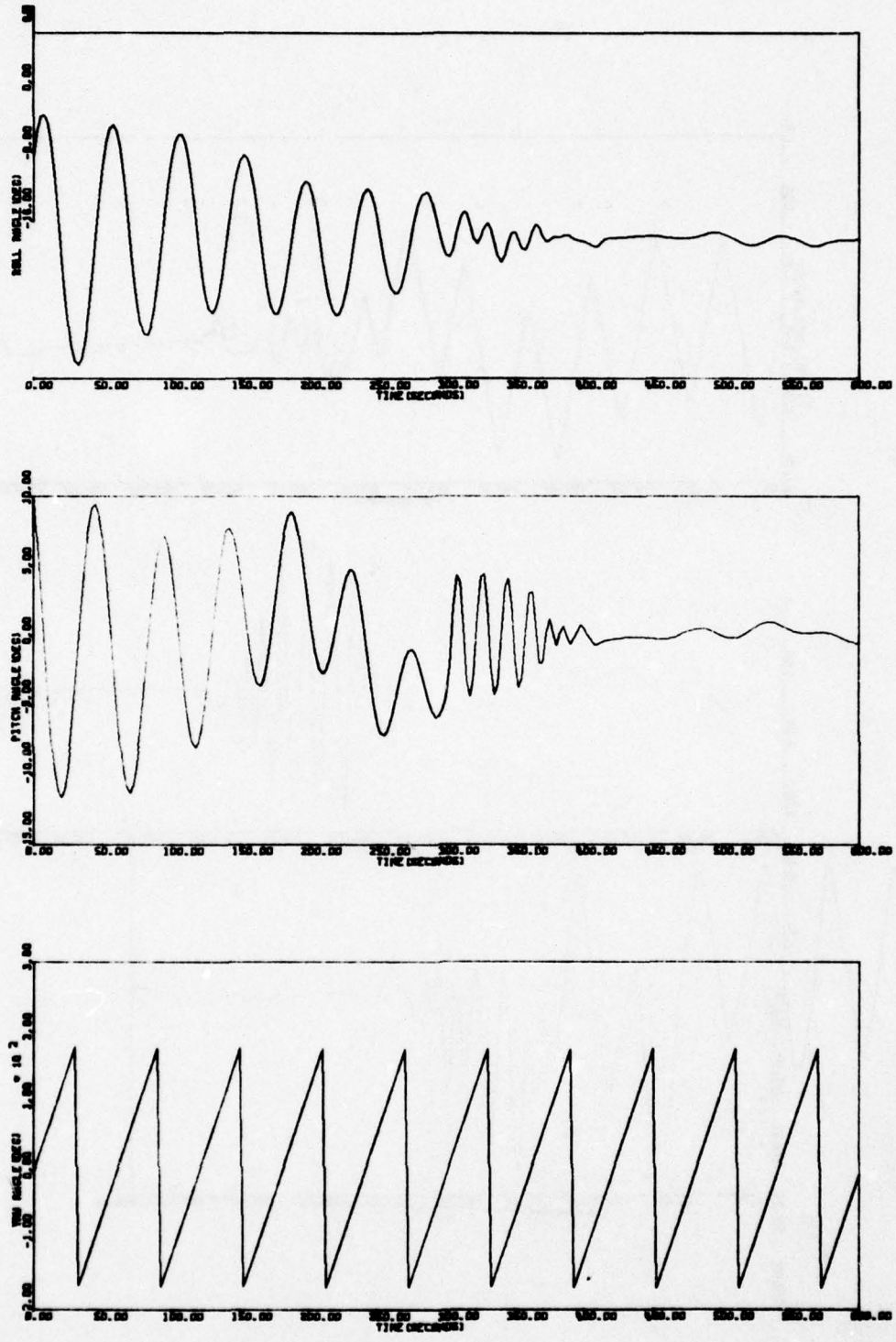

Figure 84. Acquisition Run 11A (concluded)

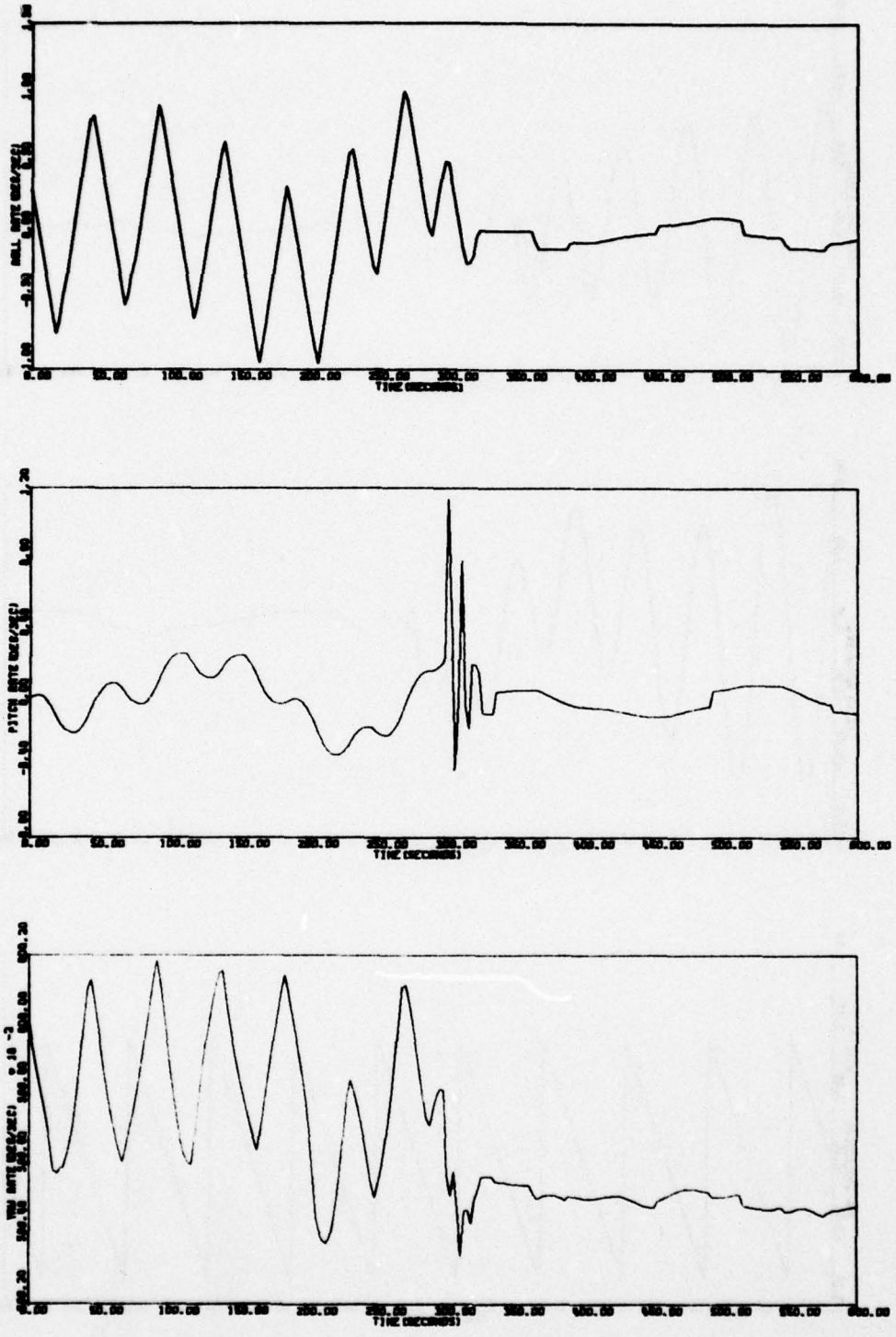

Figure 85. Acquisition Run 11B

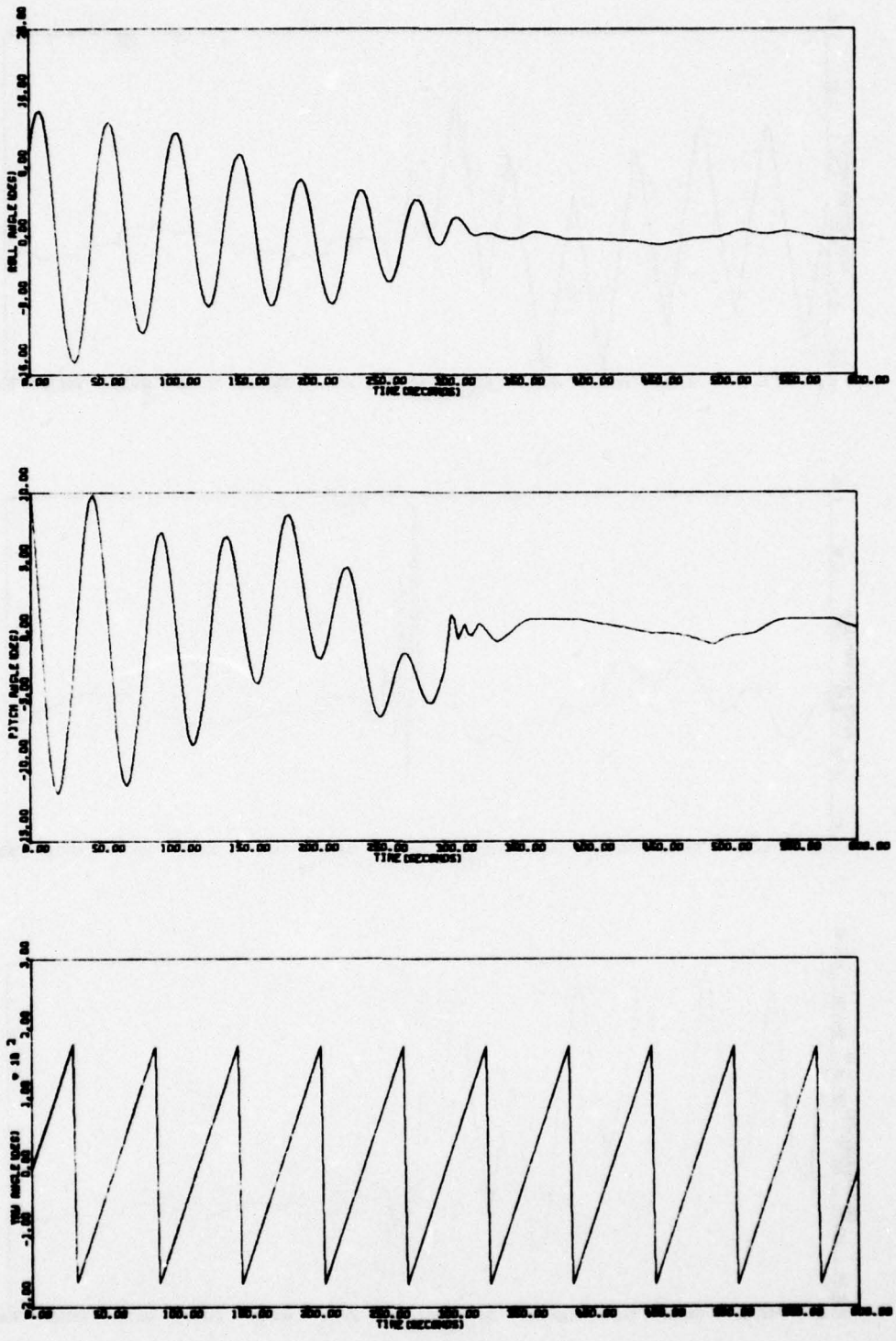

Figure 85. Acquisition Run 11B (concluded)

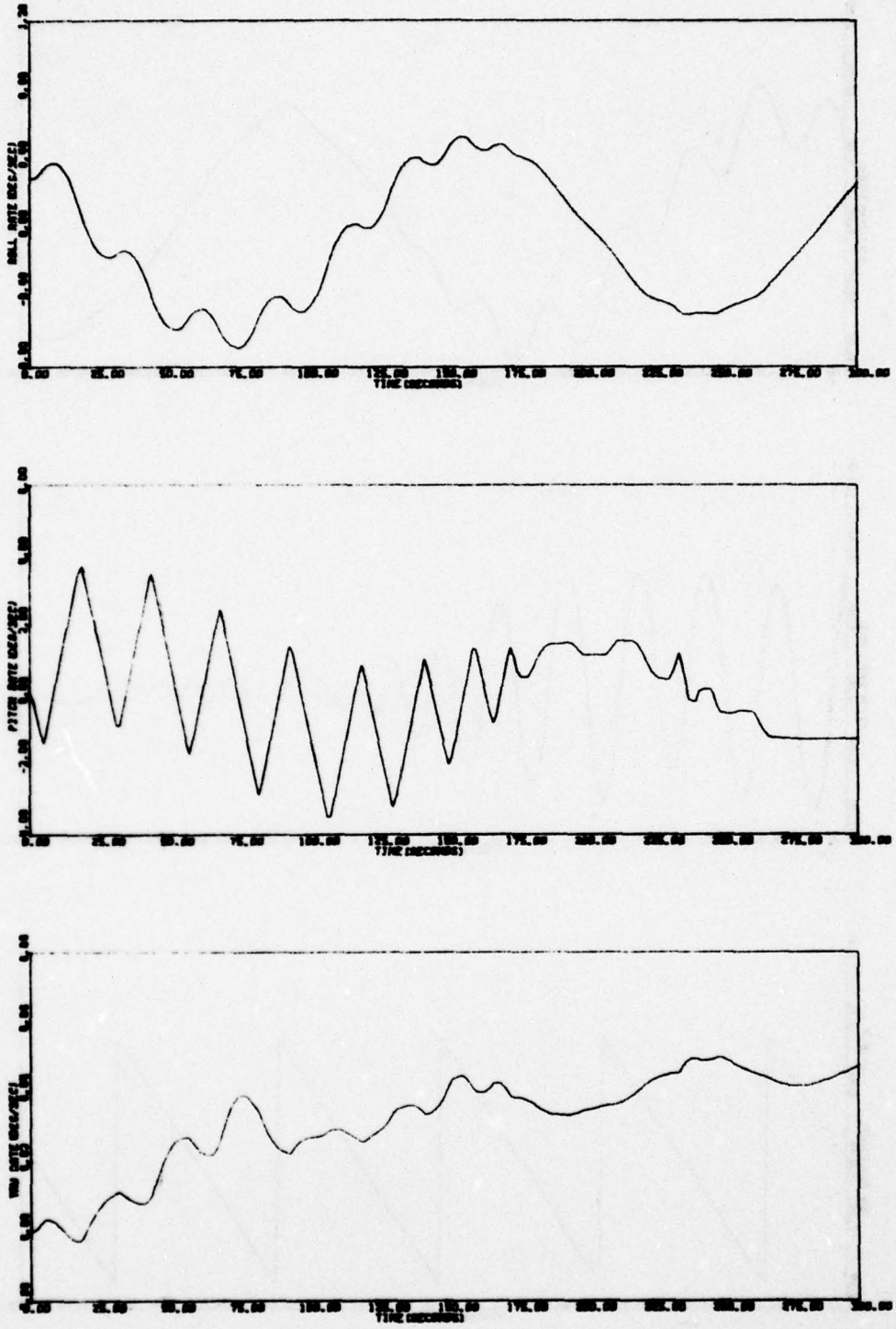

Figure 86. Acquisition Run 11AP

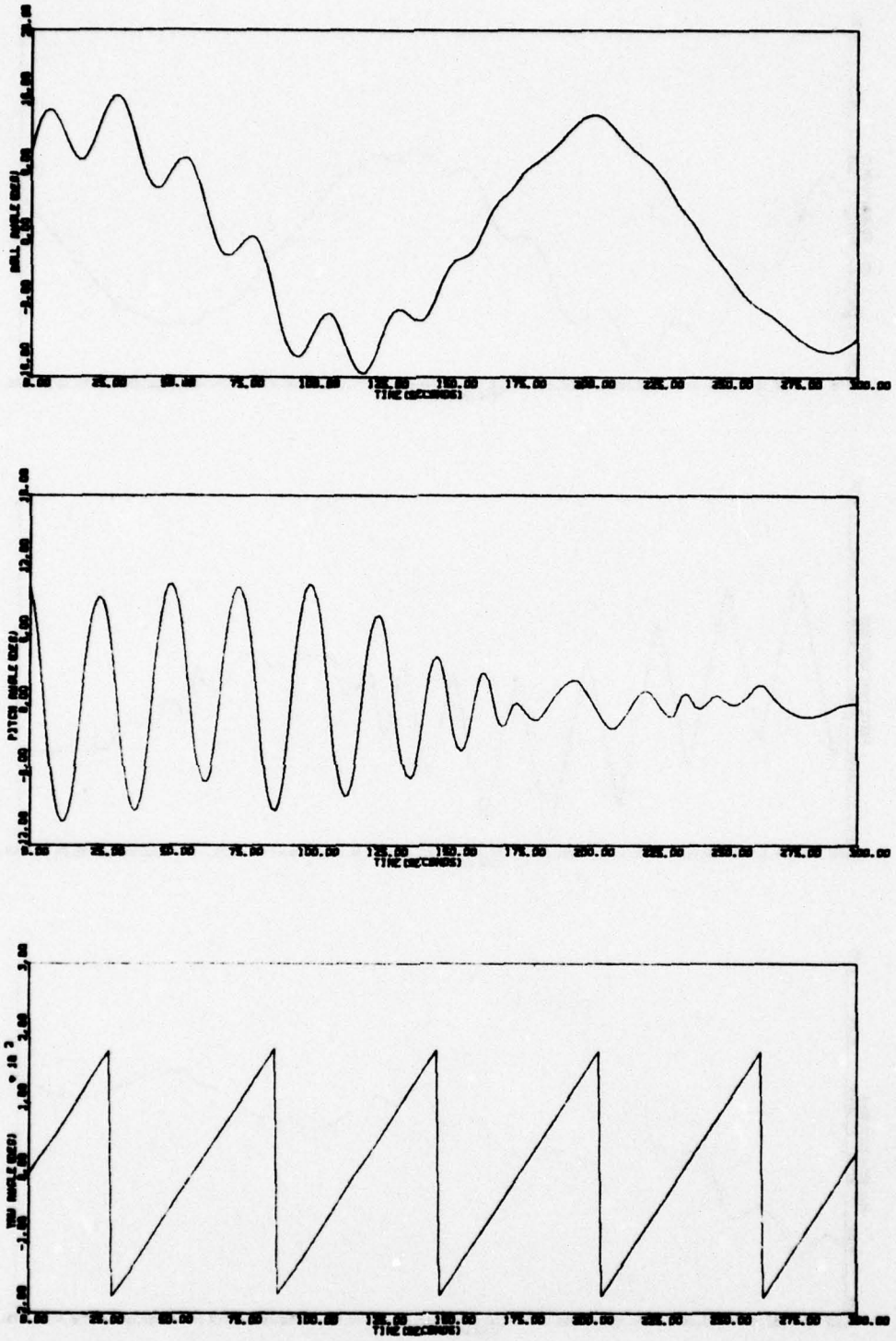

Figure 86. Acquisition Run 11AP (concluded)

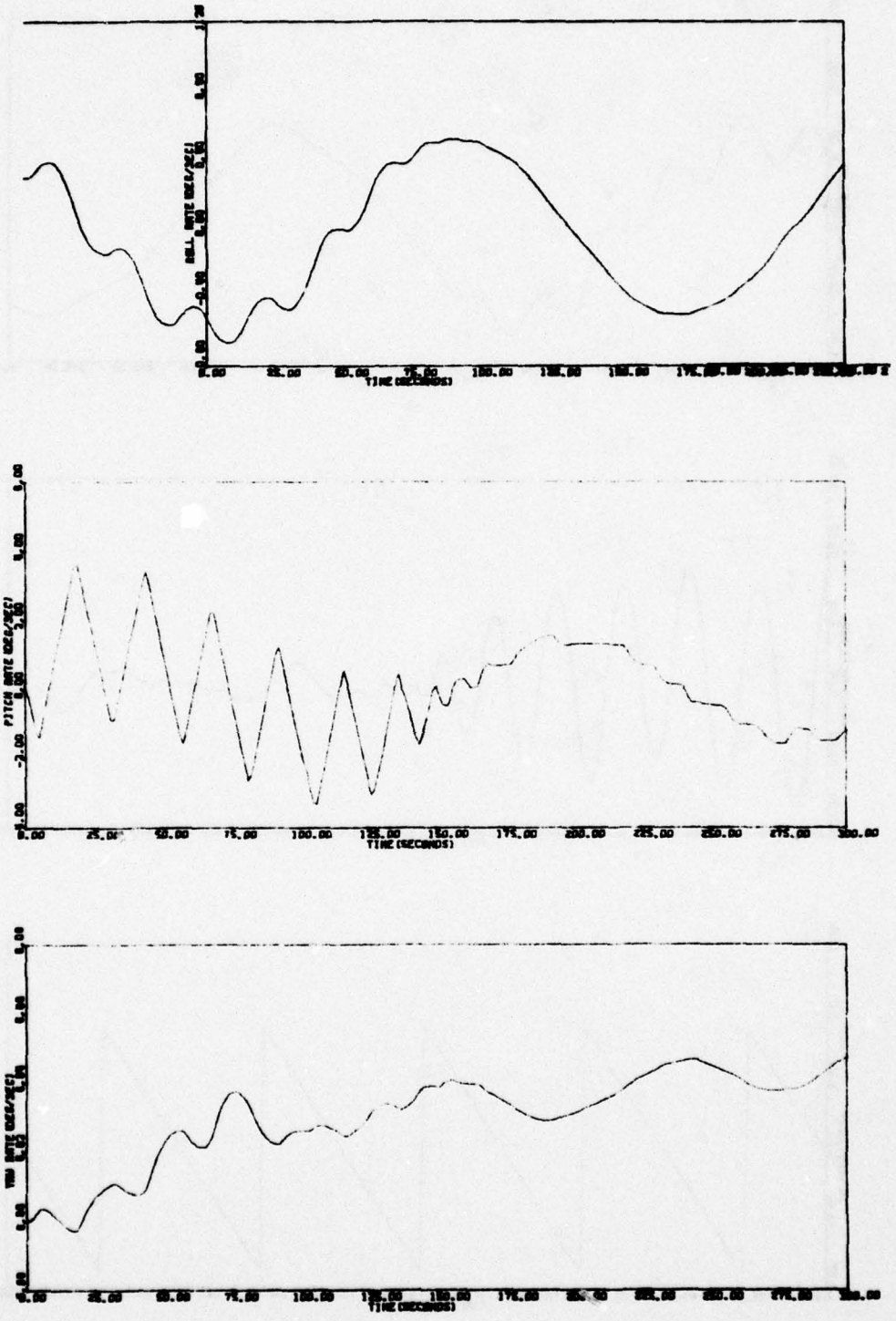

Figure 87. Acquisition Run 11BP

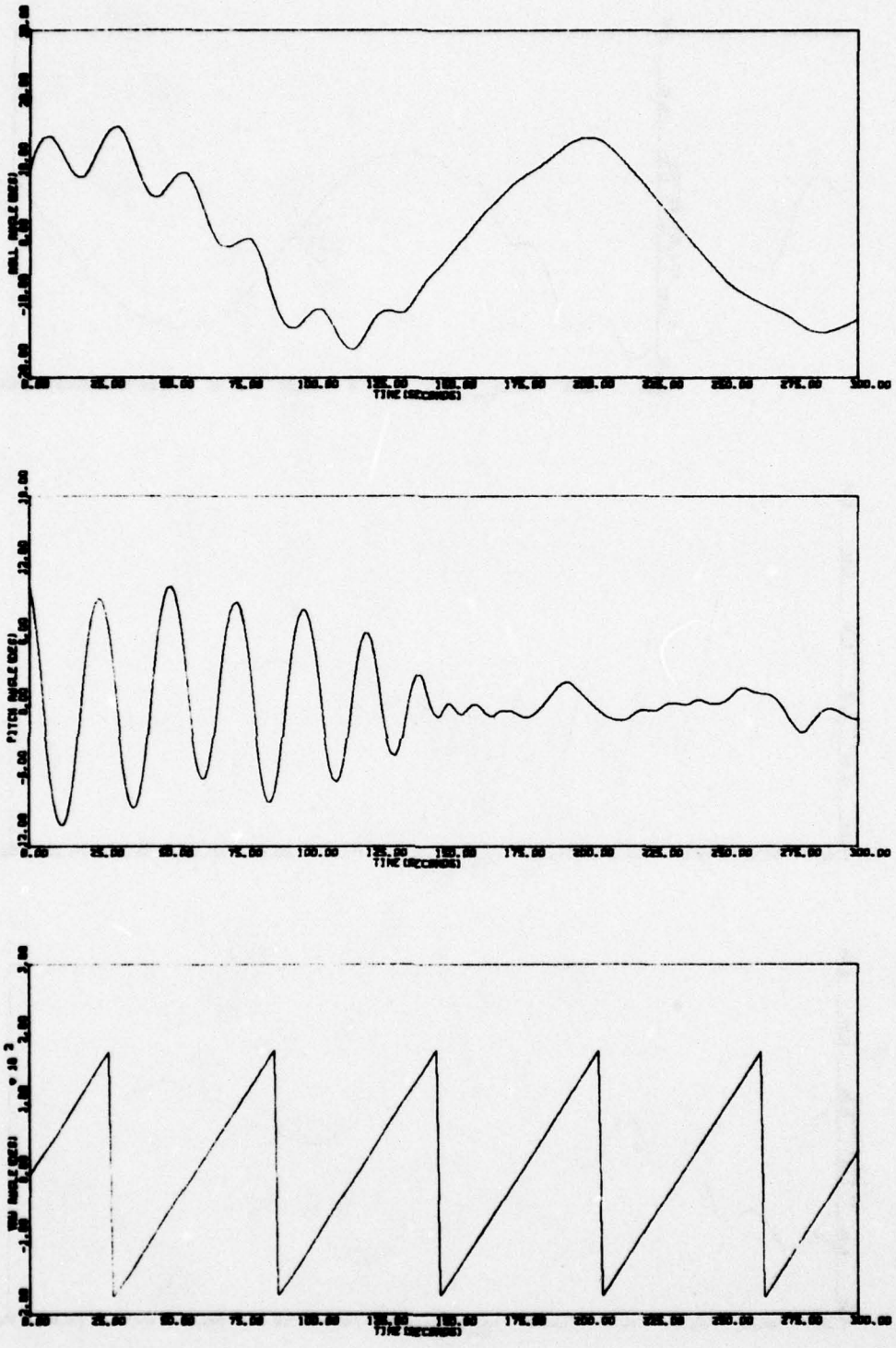

Figure 87. Acquisition Run 11BP (concluded)

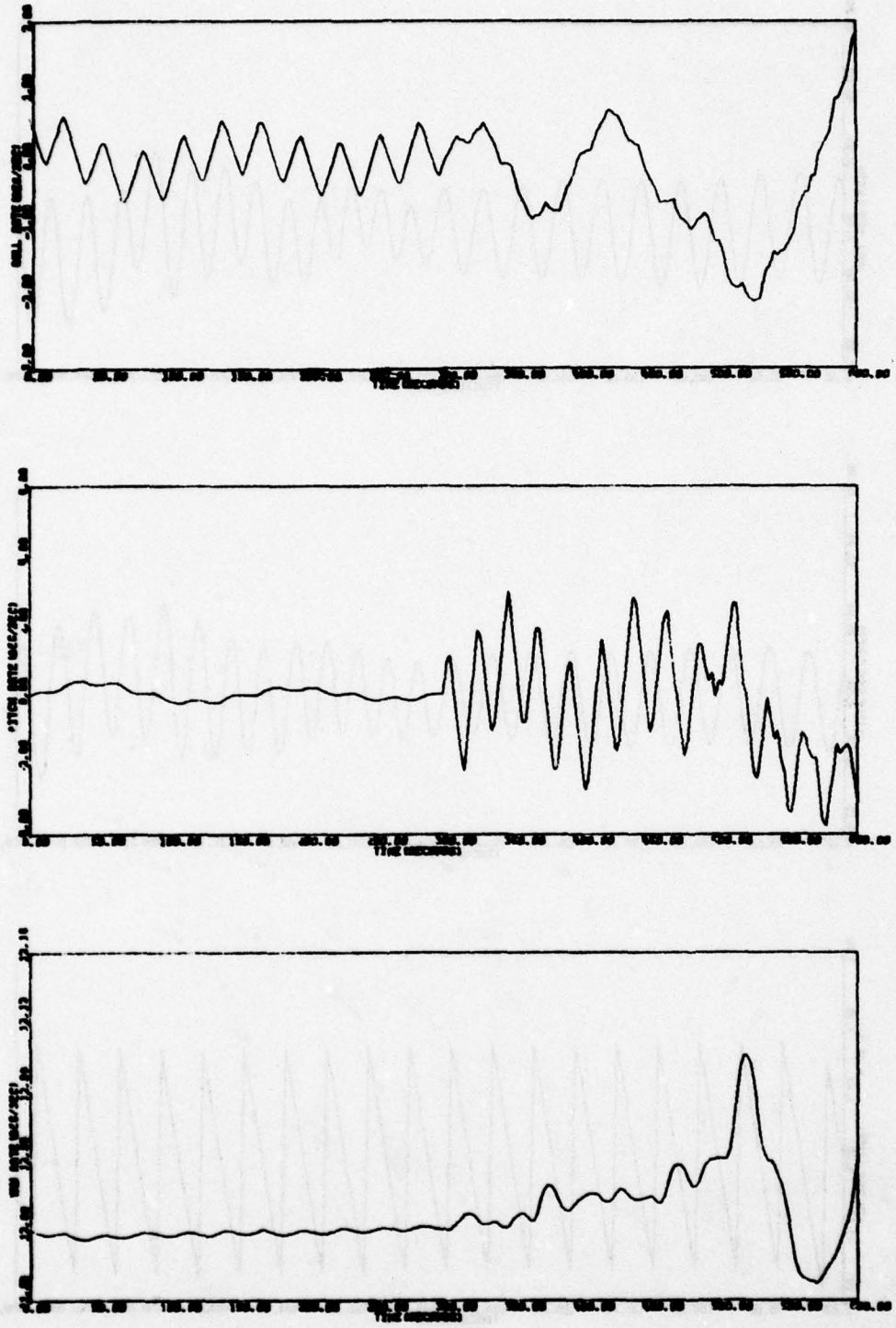

Figure 88. Acquisition Run 12A

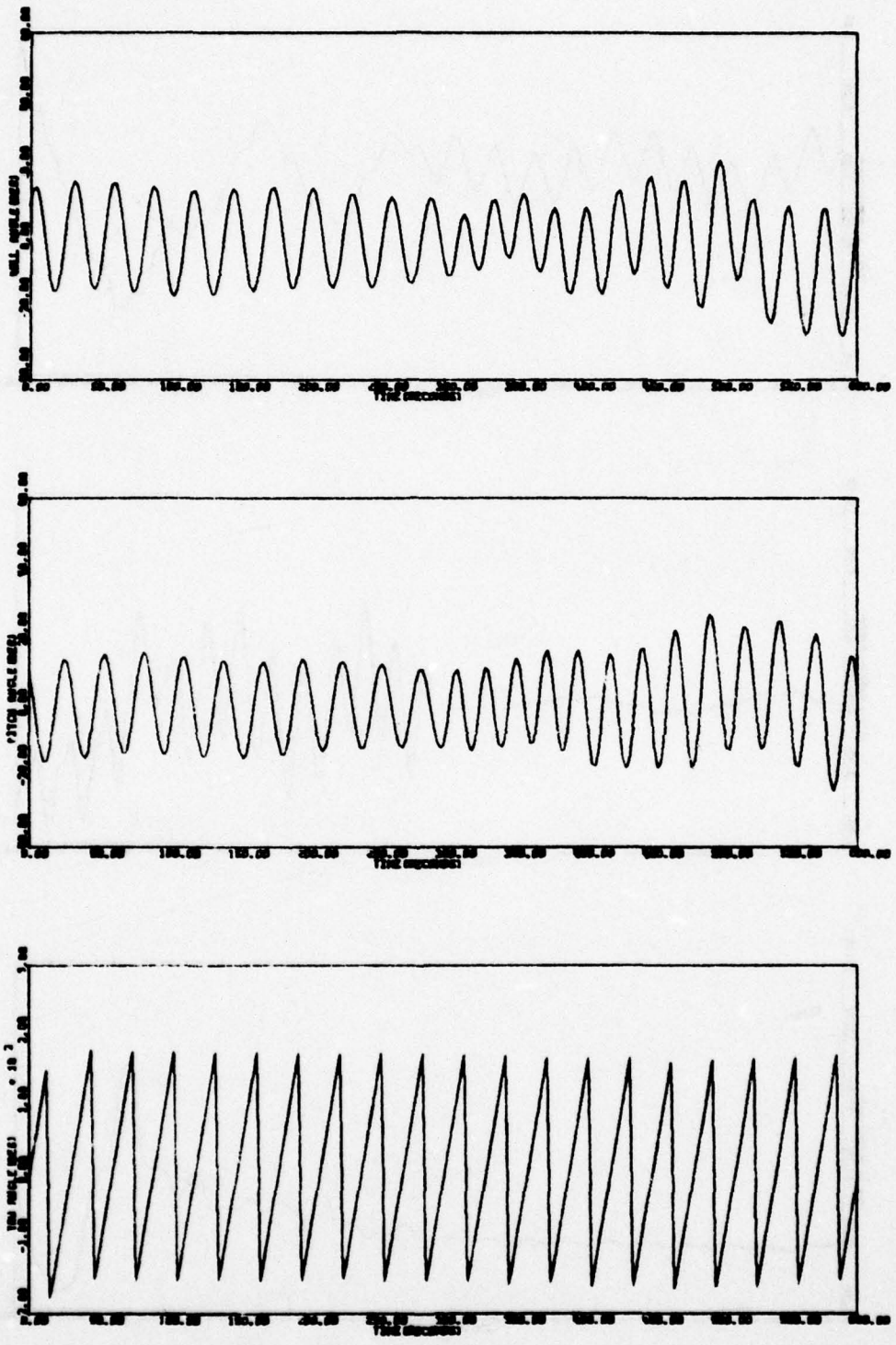

Figure 88. Acquisition Run 12A (concluded)

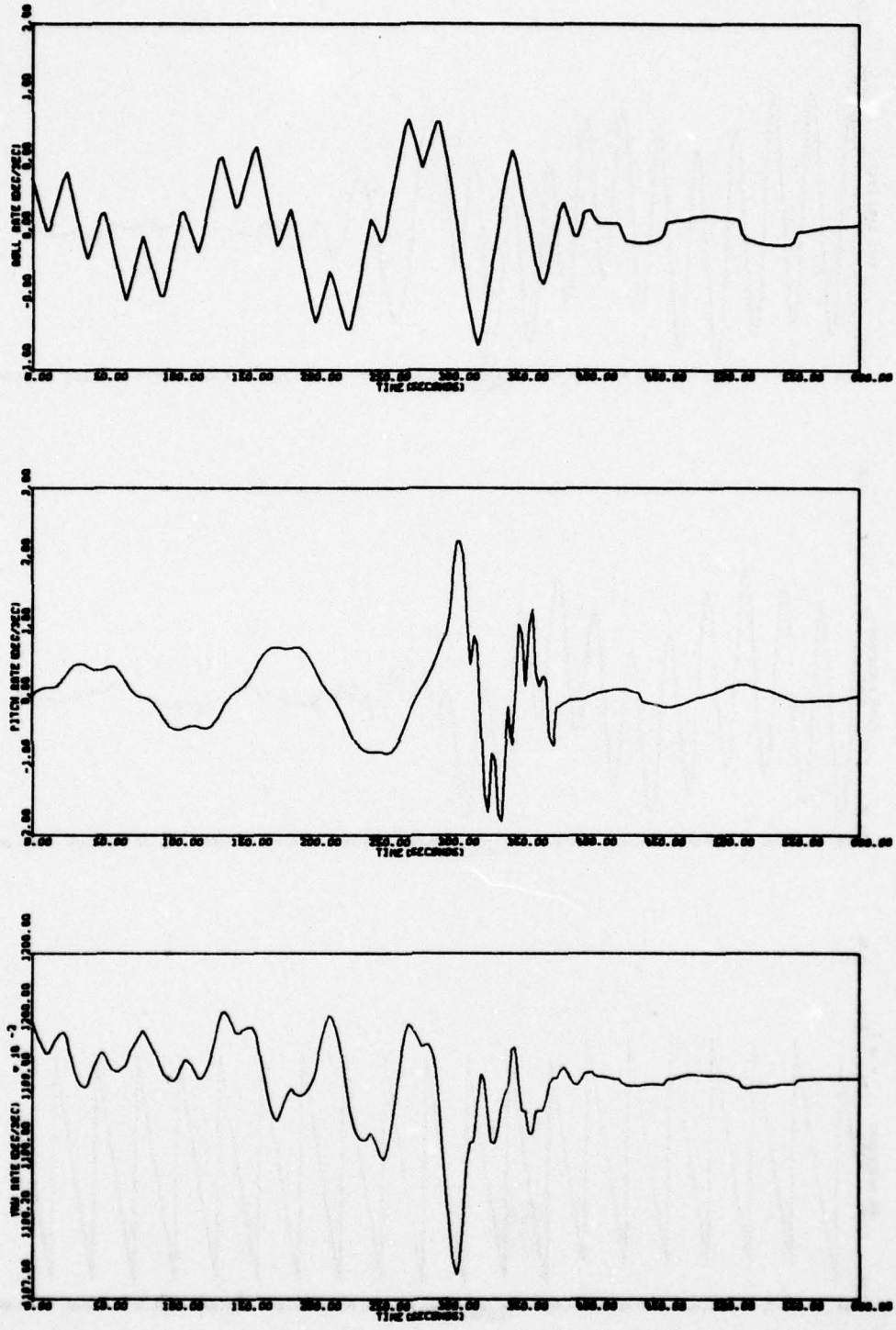

Figure 89. Acquisition Run 26A

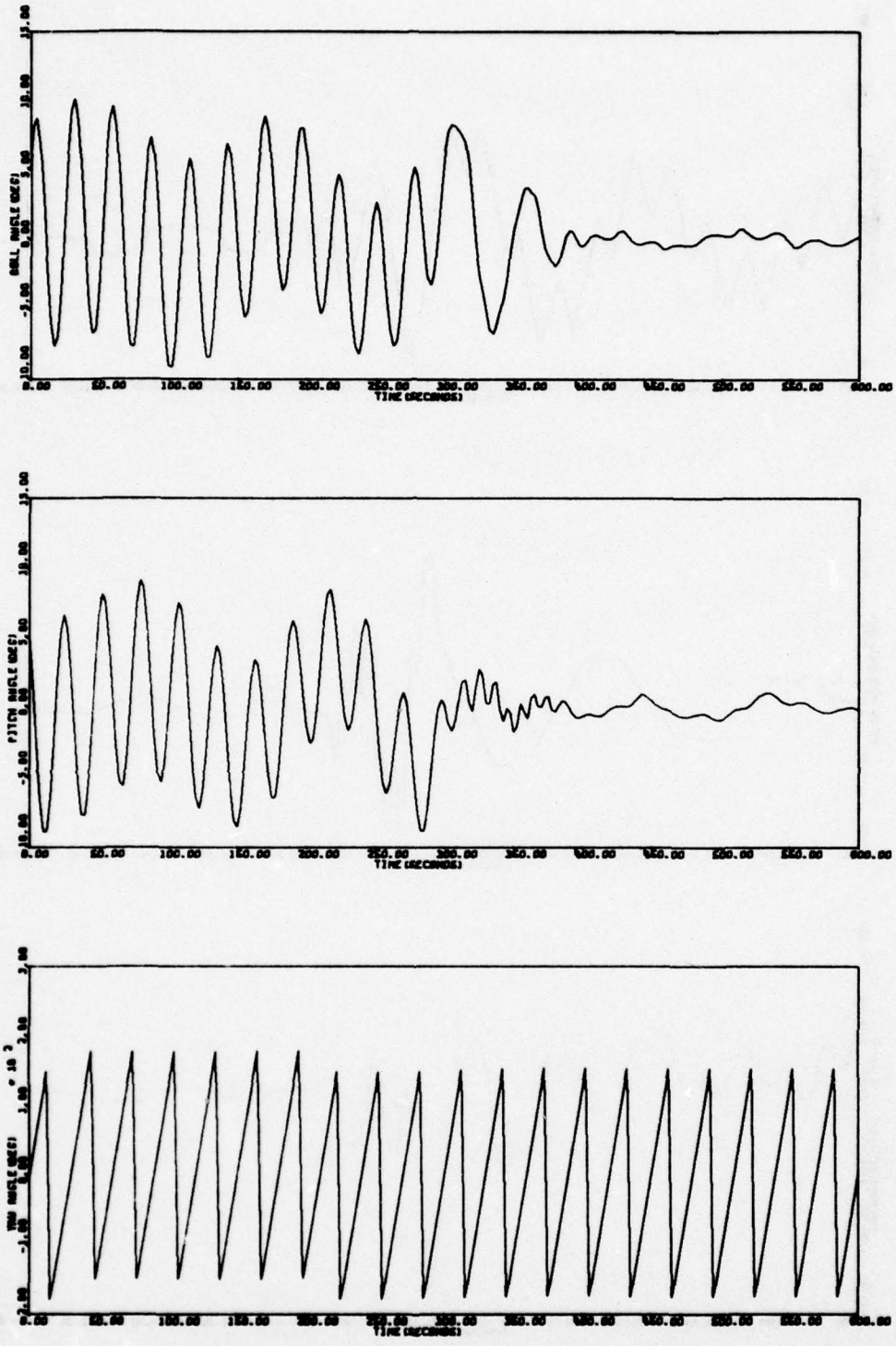

Figure 89. Acquisition Run 26A (concluded)

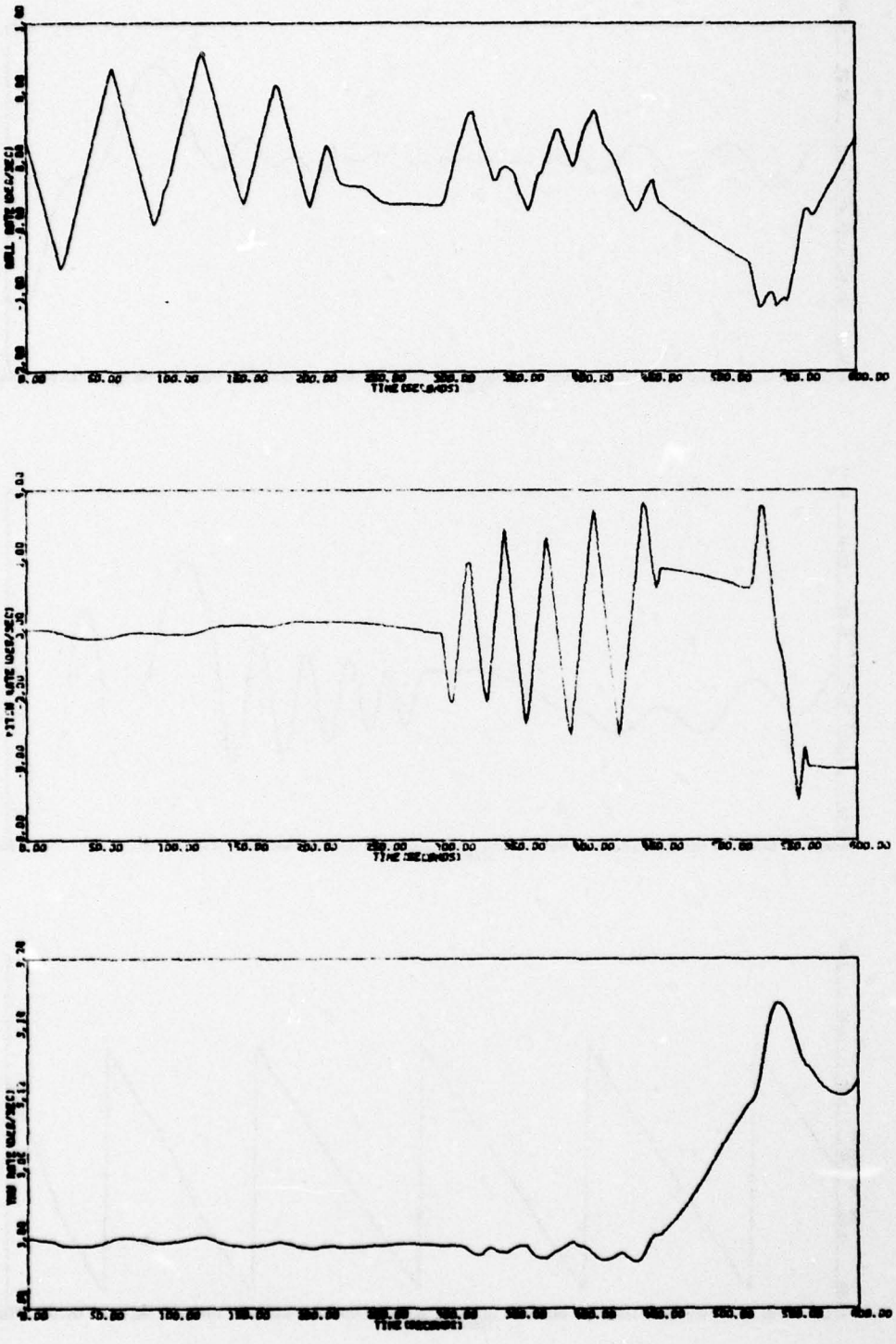

Figure 90. Acquisition Run 13A

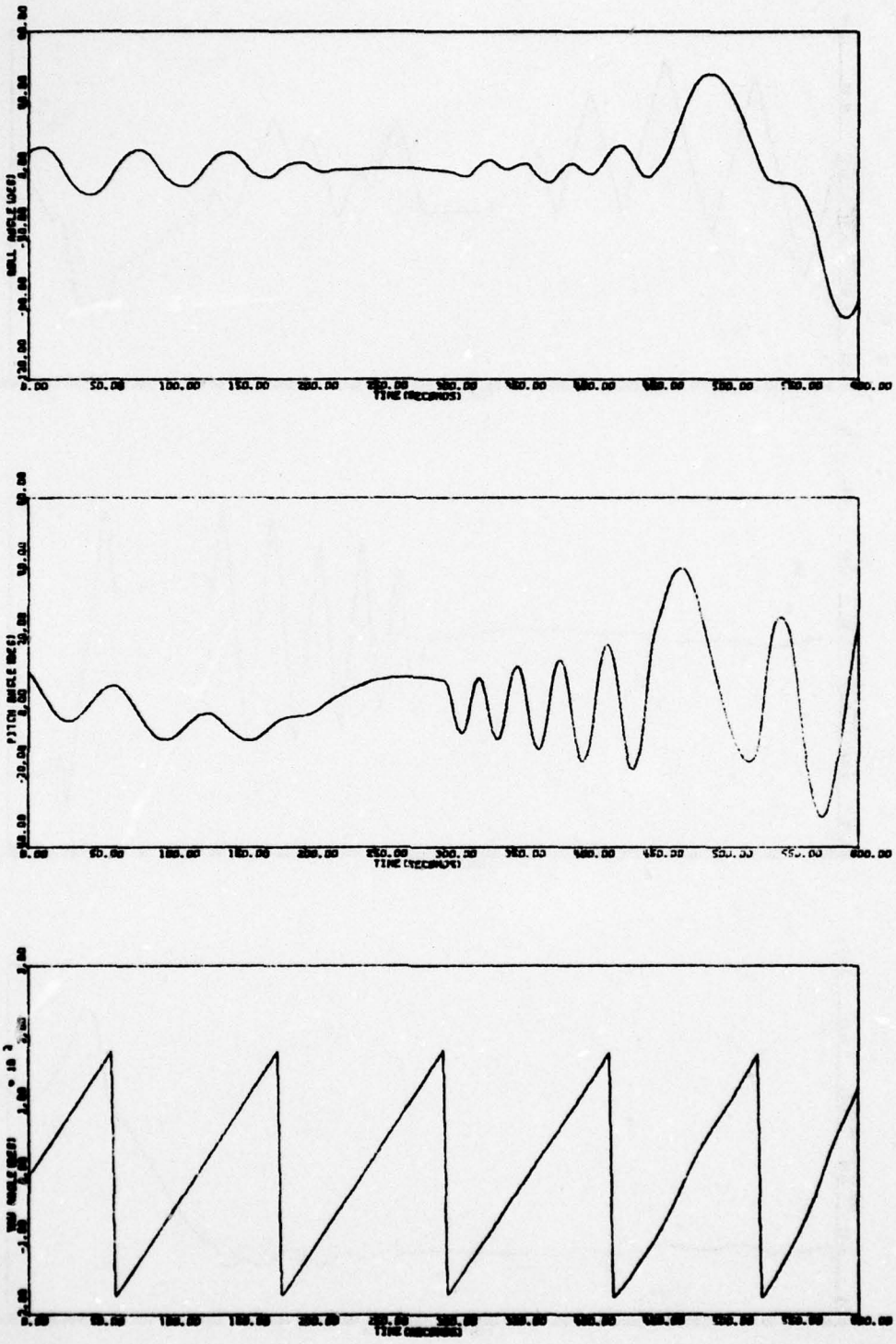

Figure 90. Acquisition Run 13A (concluded)

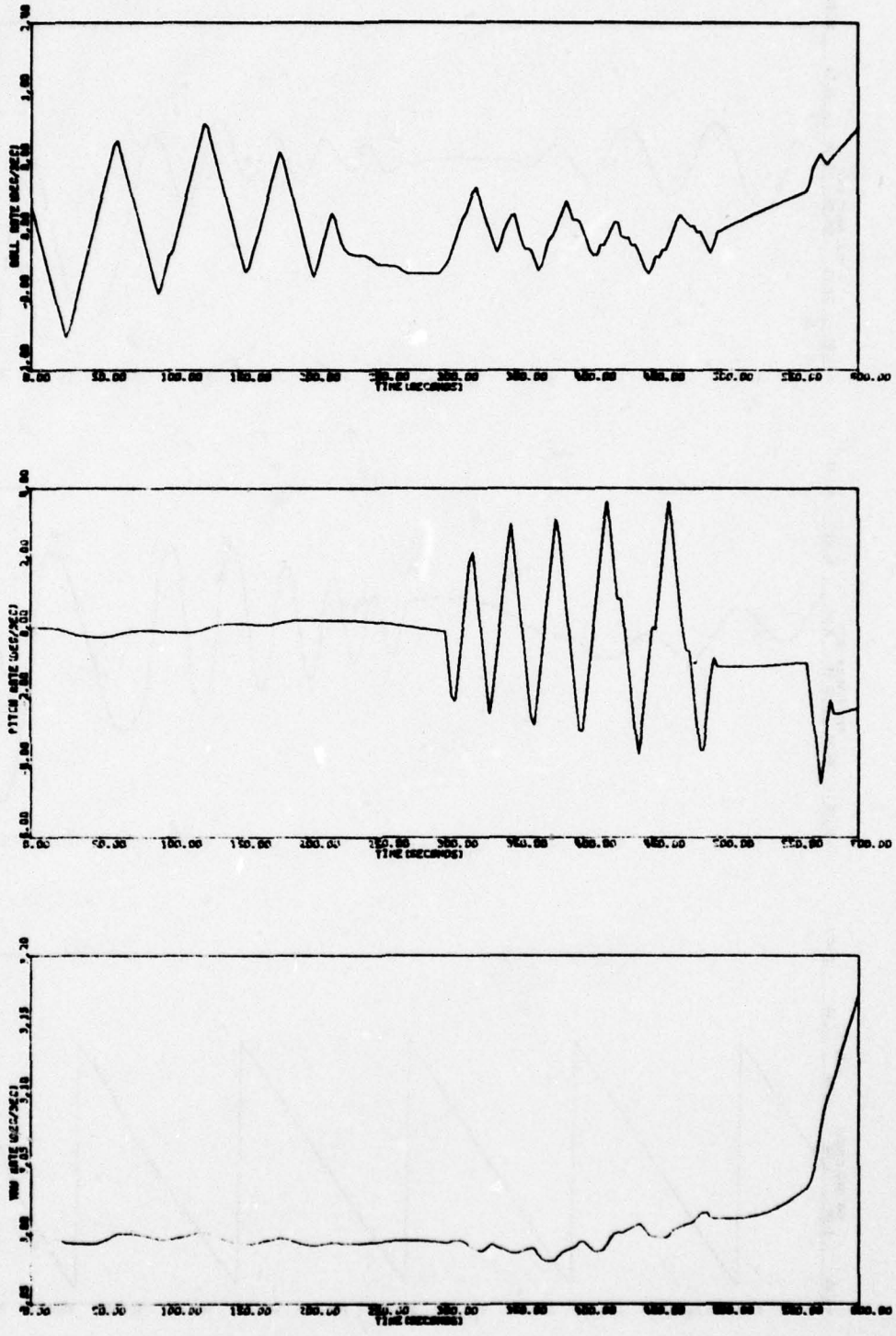

Figure 91. Acquisition Run 15B

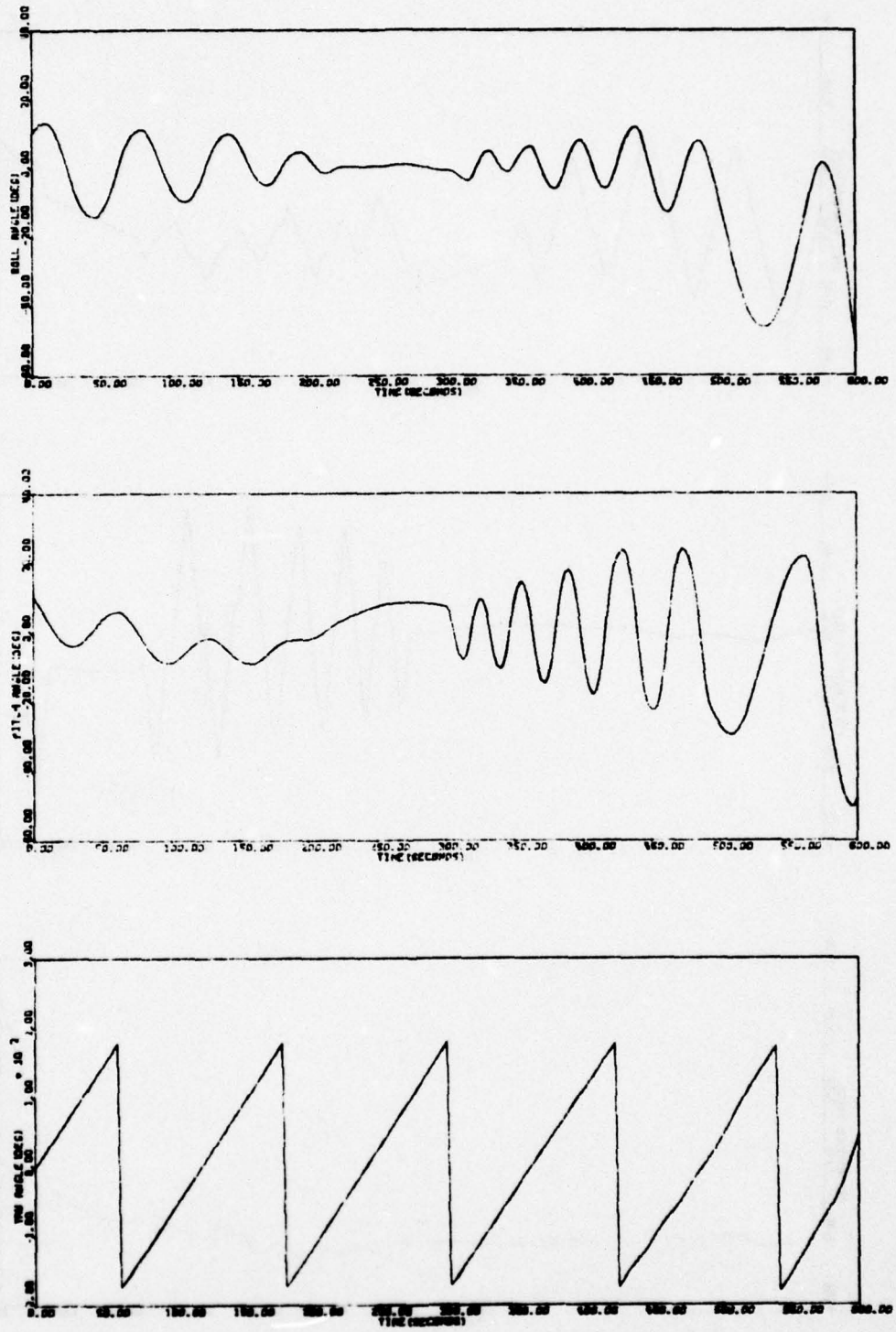

Figure 91. Acquisition Run 15B (concluded)

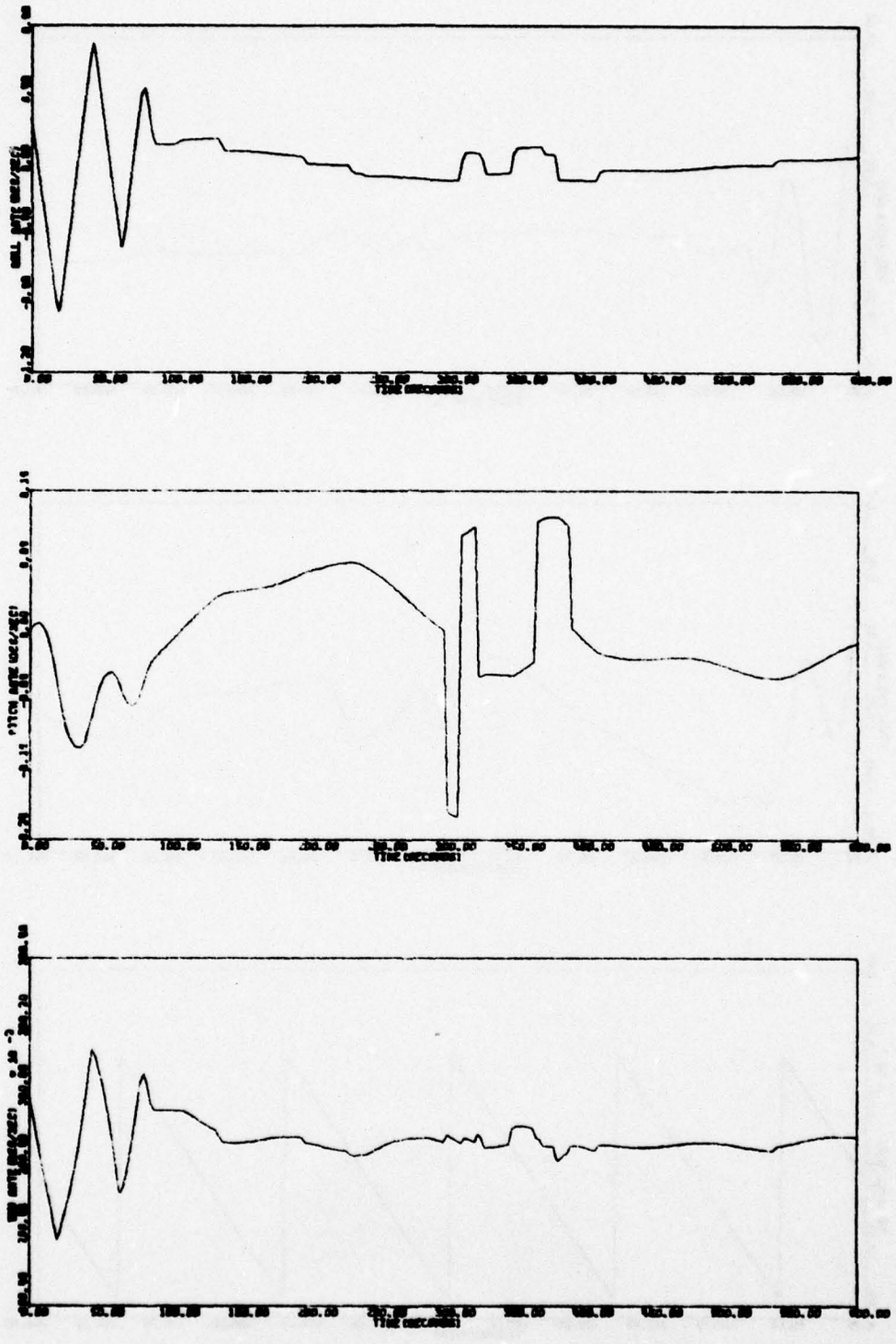

Figure 92. Acquisition Run 14A

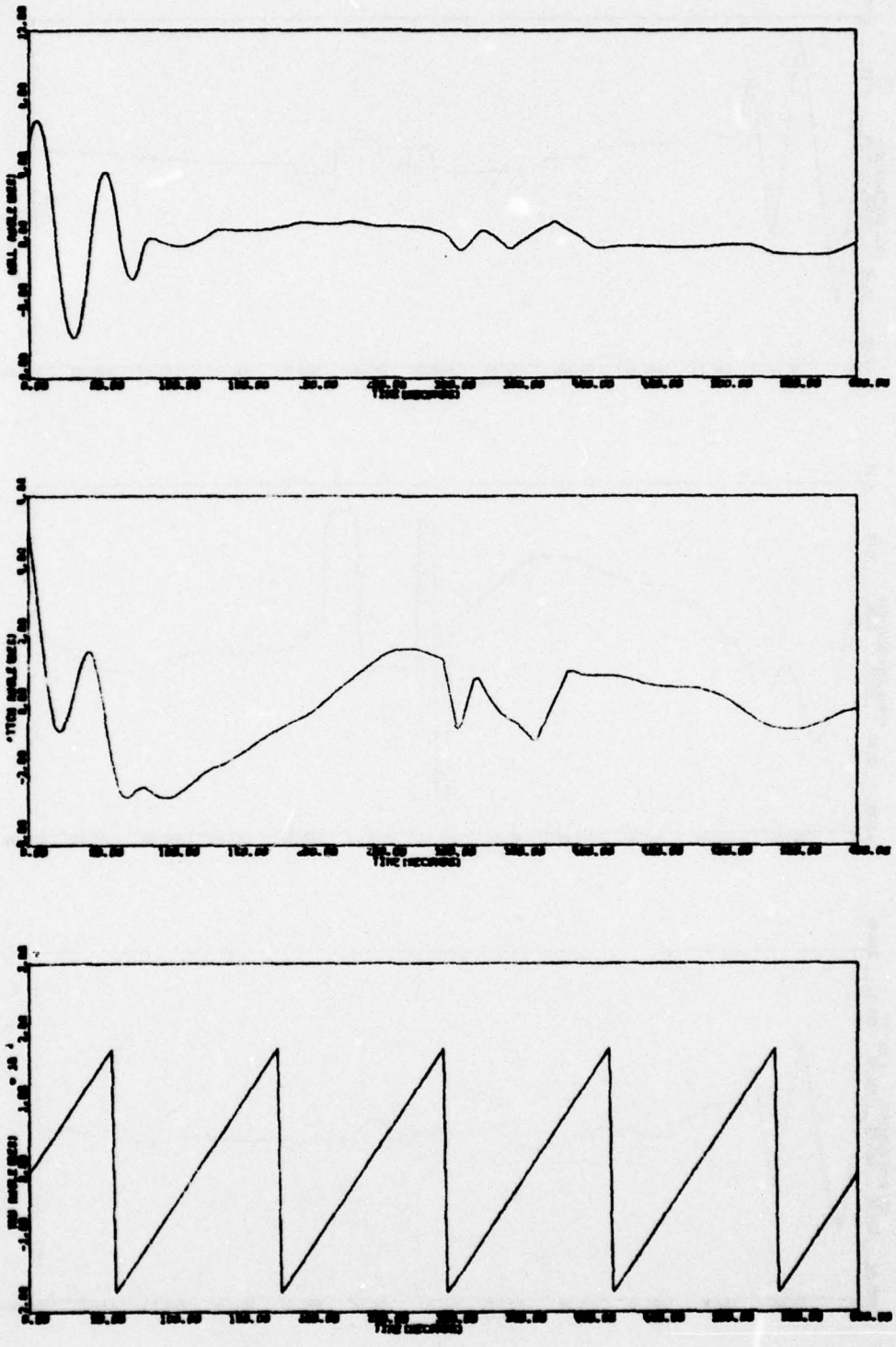

Figure 92. Acquisition Run 14A (concluded)

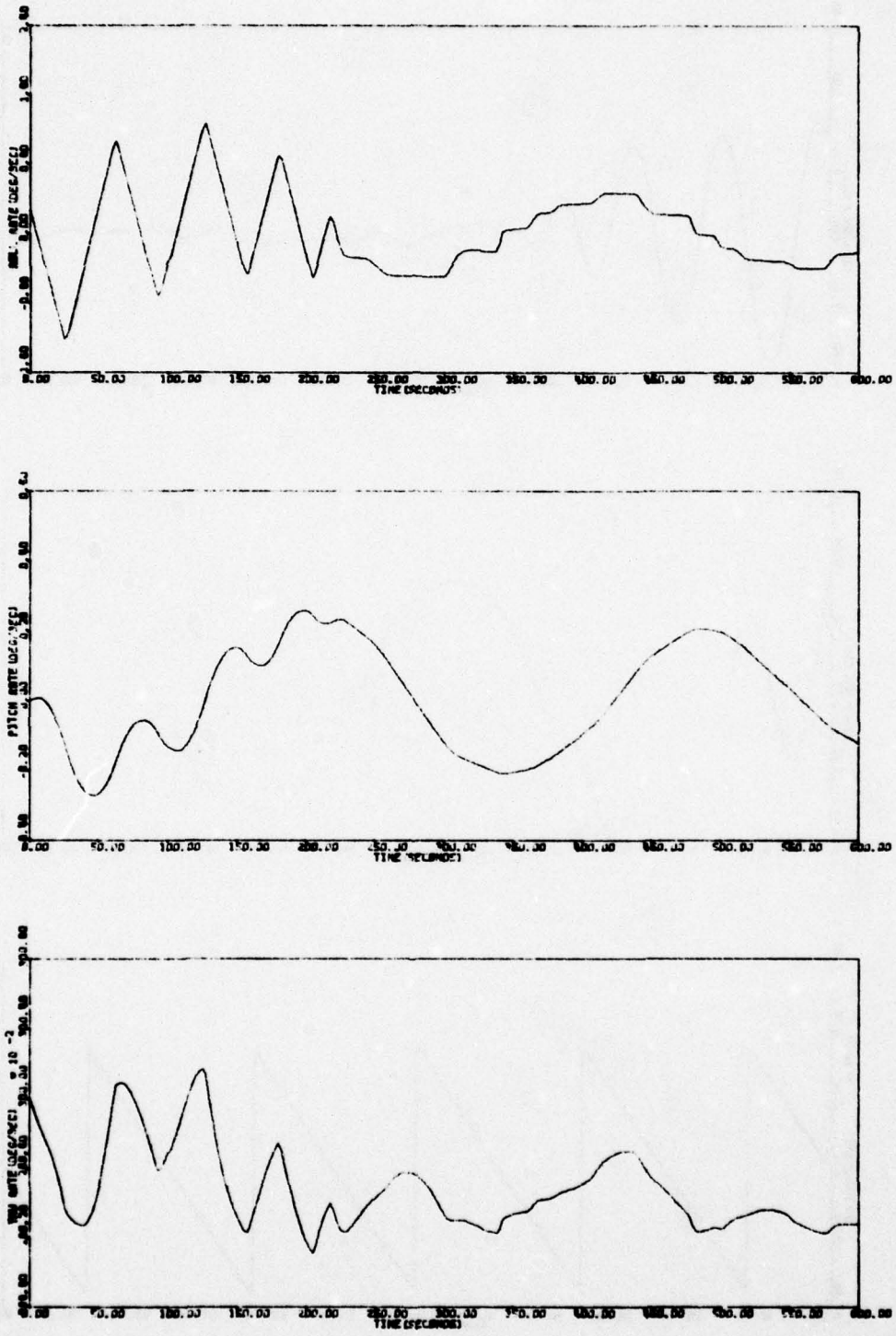

Figure 93. Acquisition Run 16A

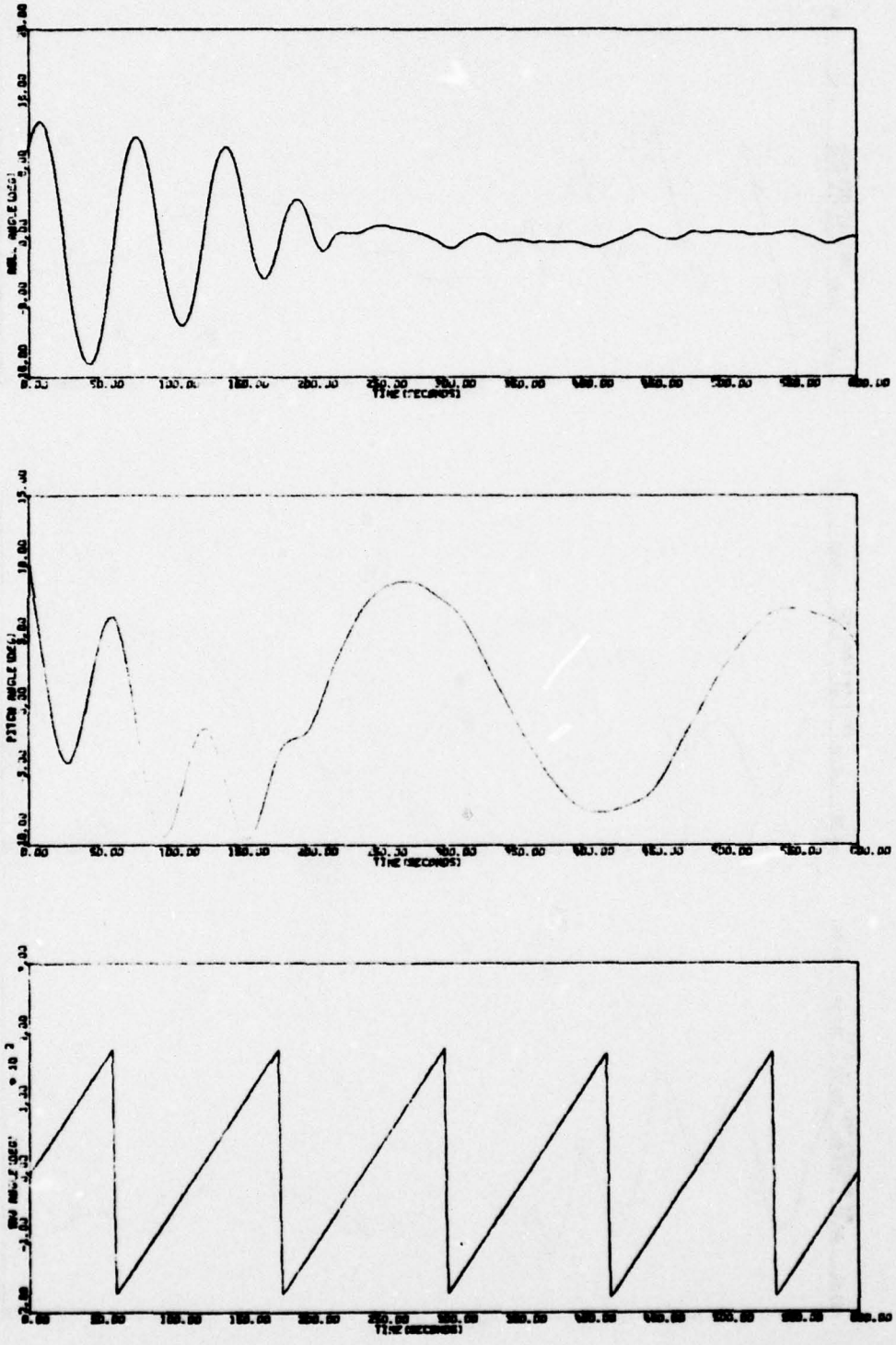

Figure 93. Acquisition Run 16A (concluded)

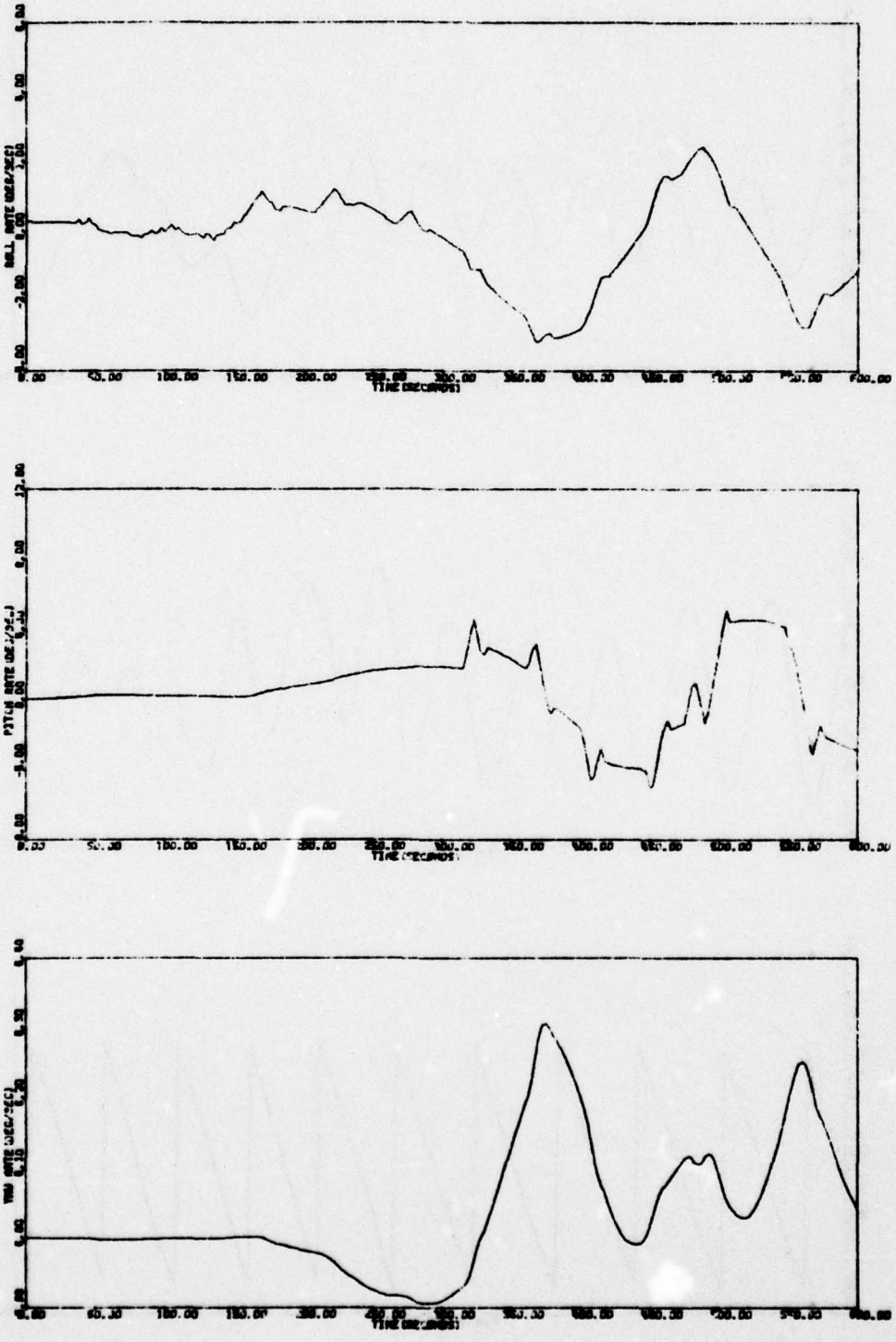

Figure 94. Acquisition Run 17A

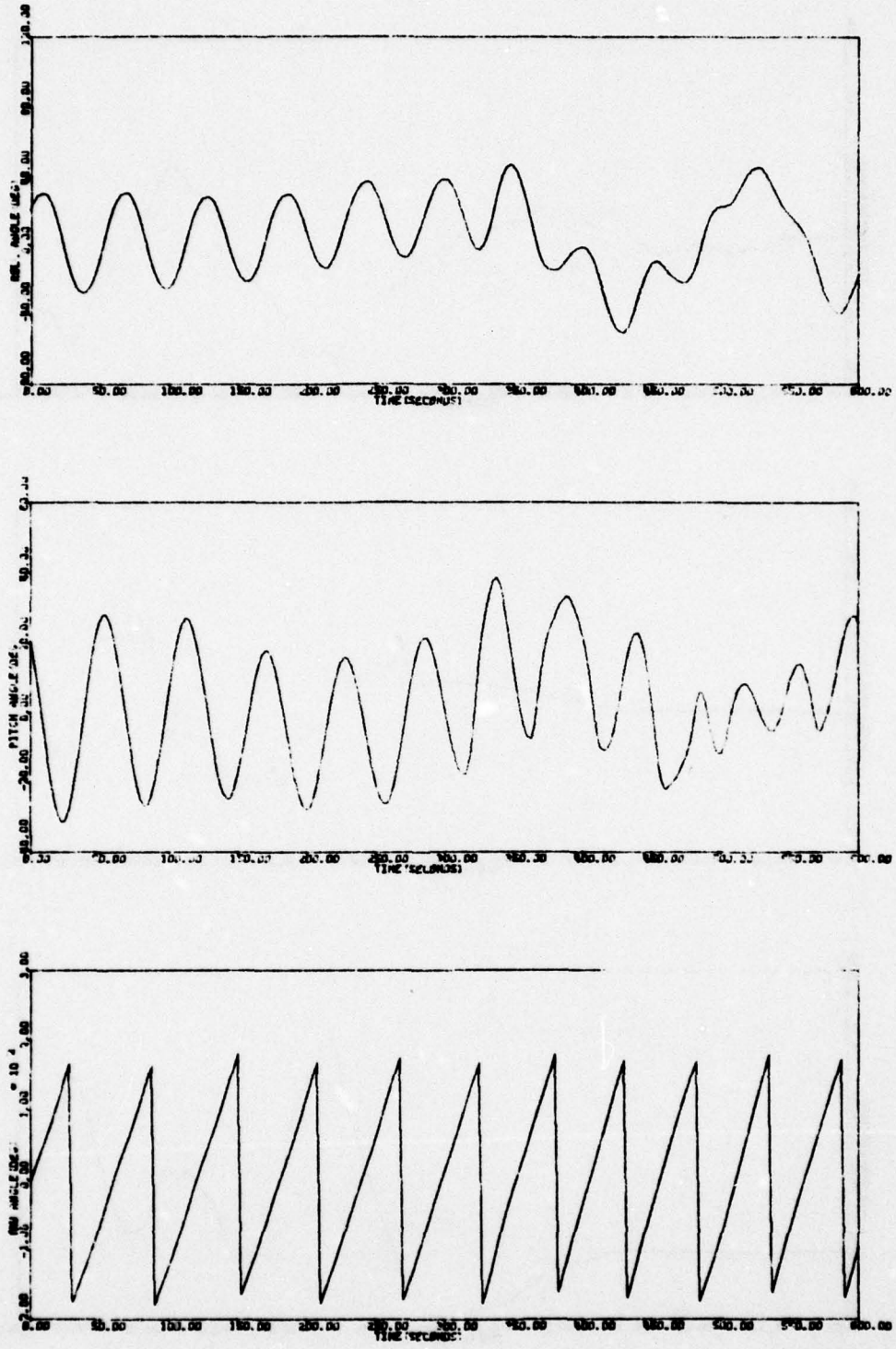

Figure 94. Acquisition Run 17A (concluded)

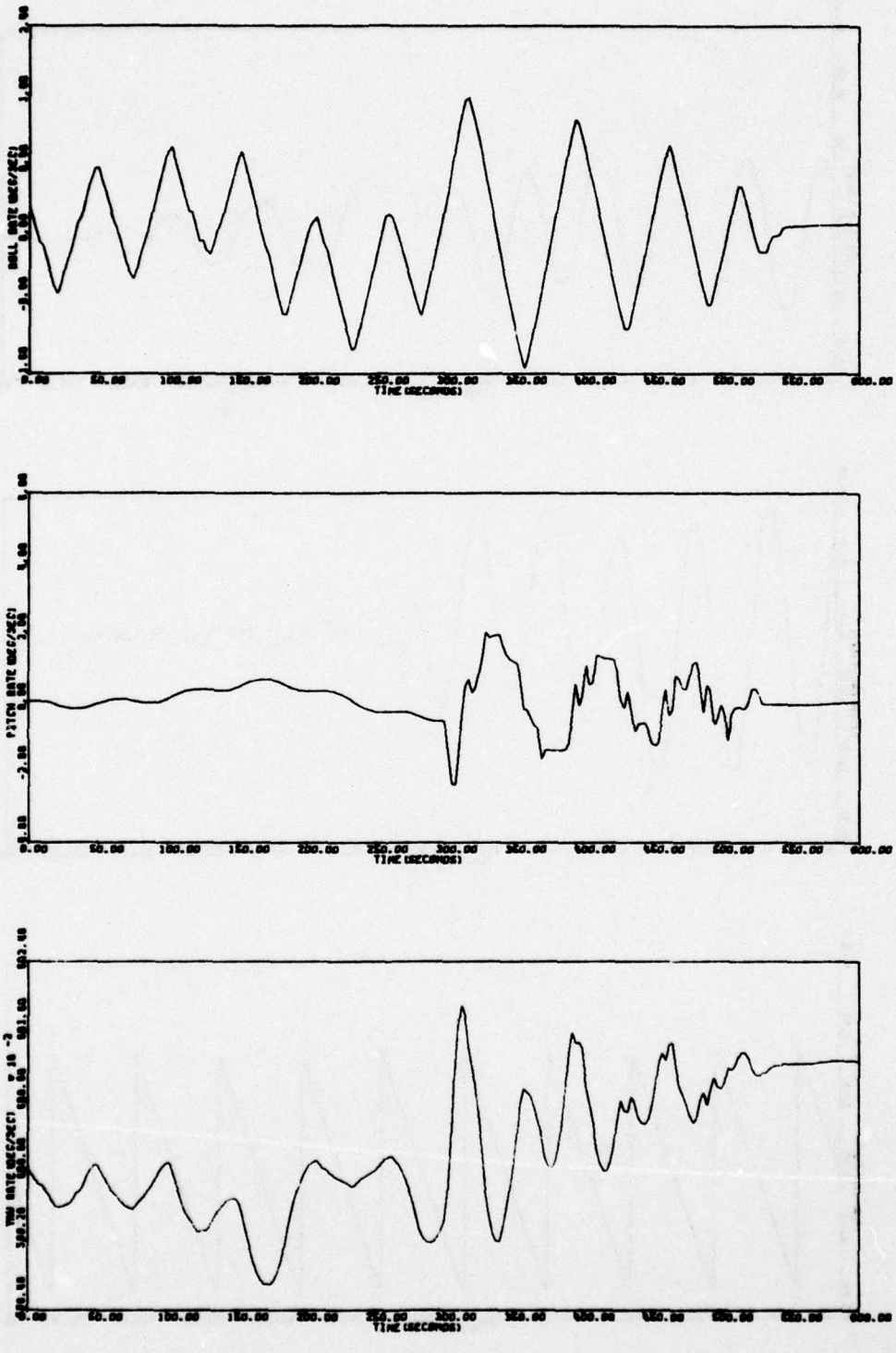

Figure 95. Acquisition Run 18A

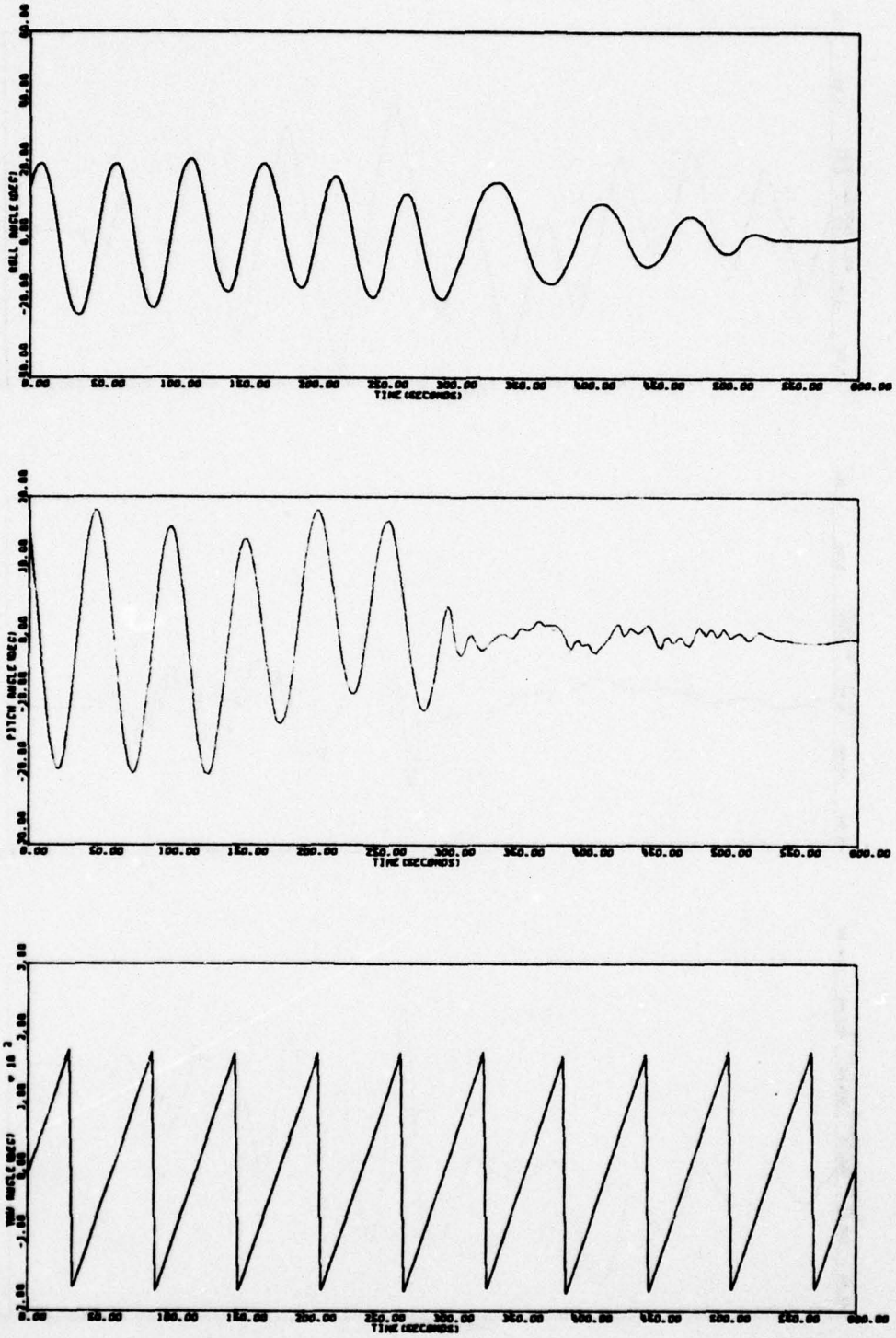

Figure 95. Acquisition Run 18A (concluded)

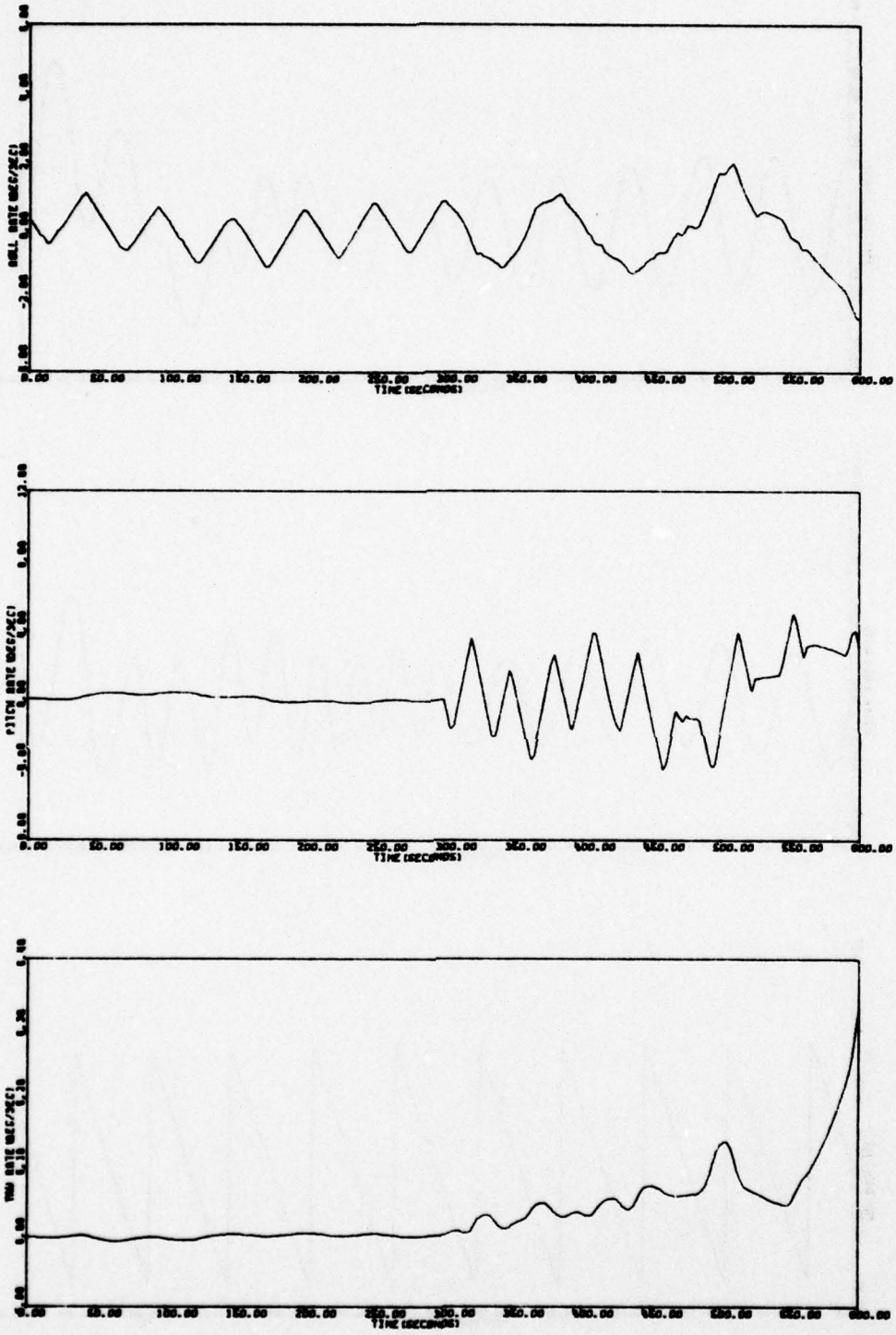

Figure 96. Acquisition Run 19A

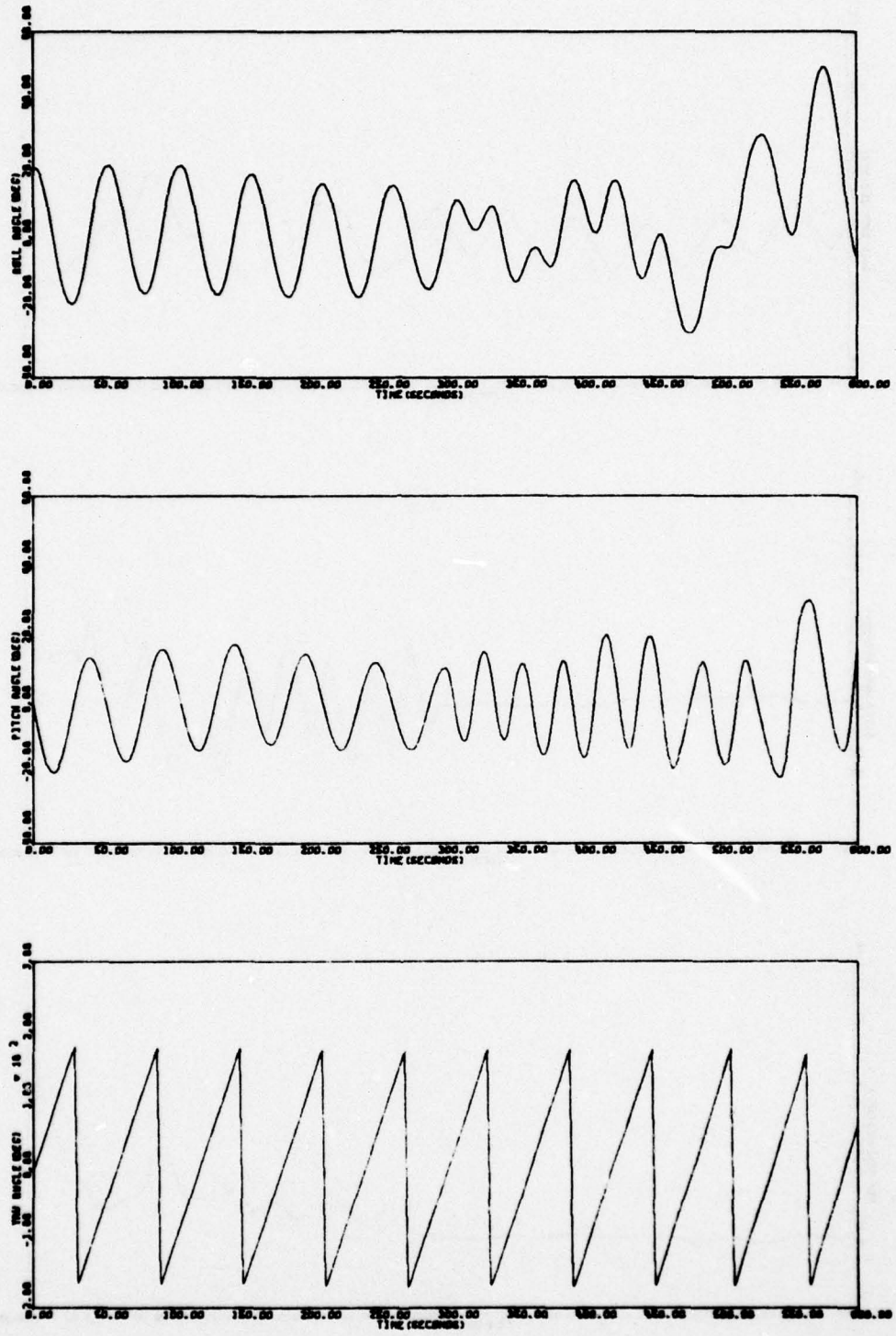

Figure 96. Acquisition Run 19A (concluded)

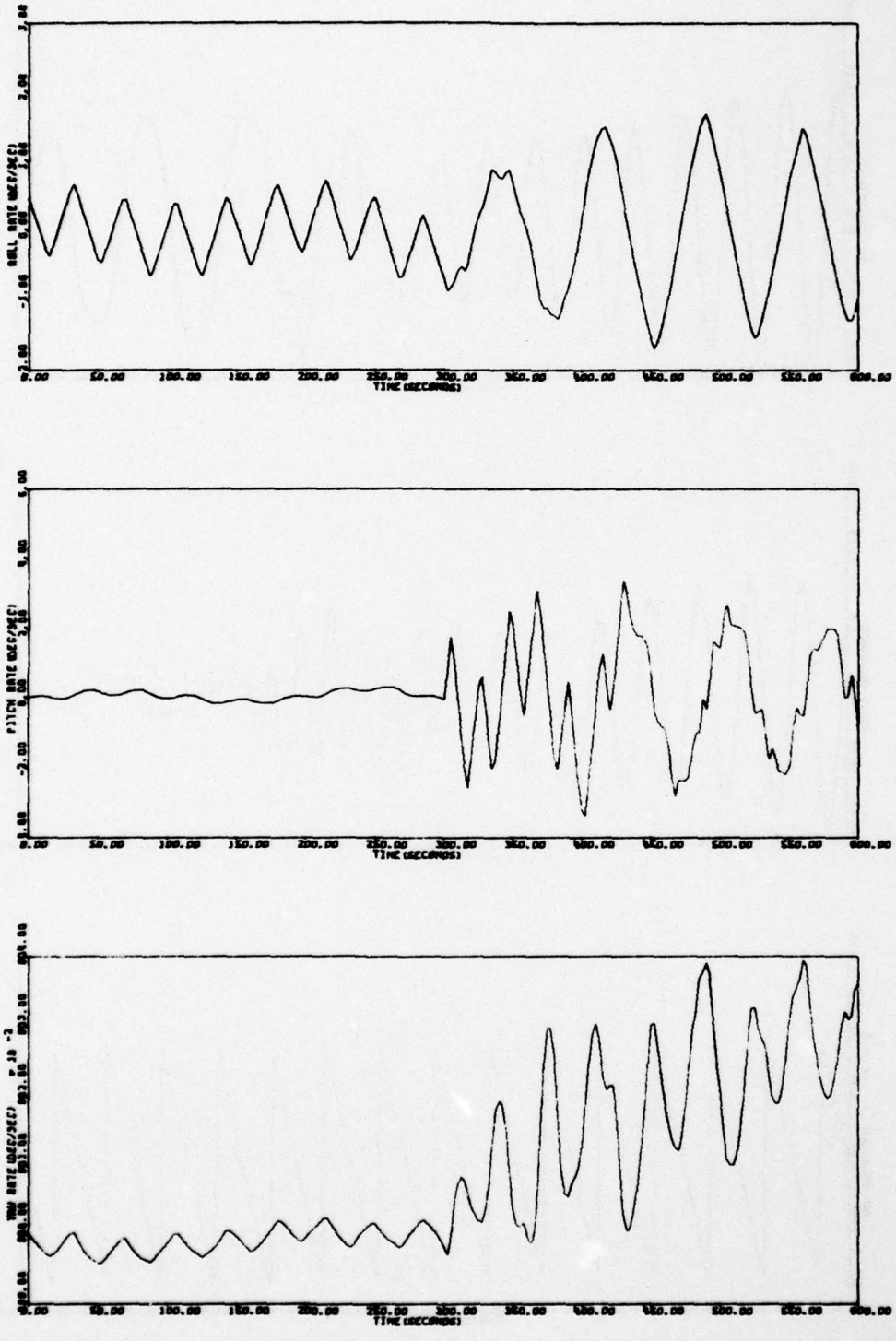

Figure 97. Acquisition Run 25A

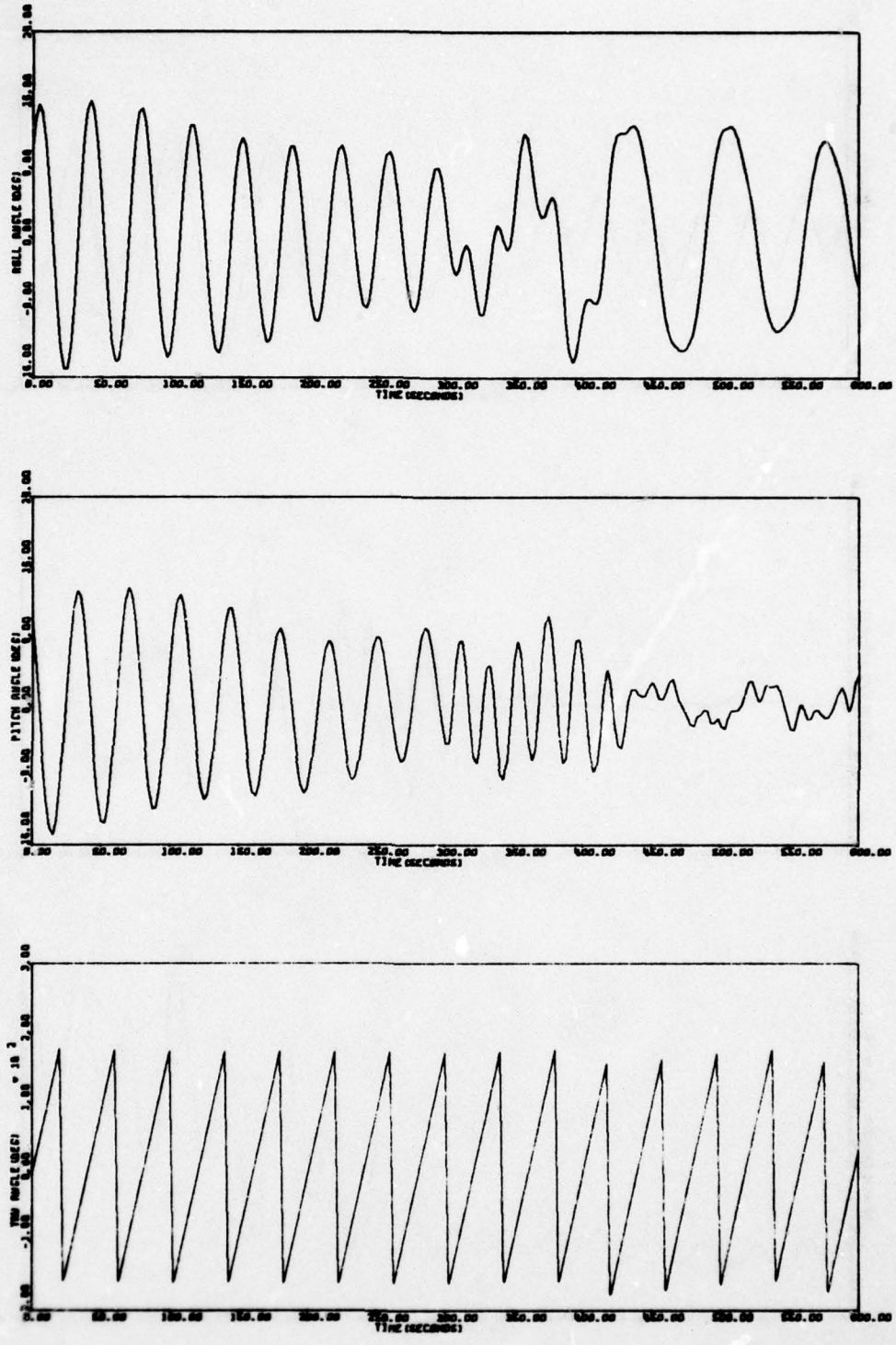

Figure 97. Acquisition Run 25A (concluded)

TABLE 16. CONTROL LOOP GAIN VARIATIONS

	Nominal Gain	High Gain	Low Gain
Jet Thrust	0.09 lb	0.119 lb	0.076 lb
$\Delta I_{xx} = \Delta I_{yy}$	0.0	-3.0 slug ft^2	+3.0 slug ft^2
Sensor Gain	1.0	2.0	0.4

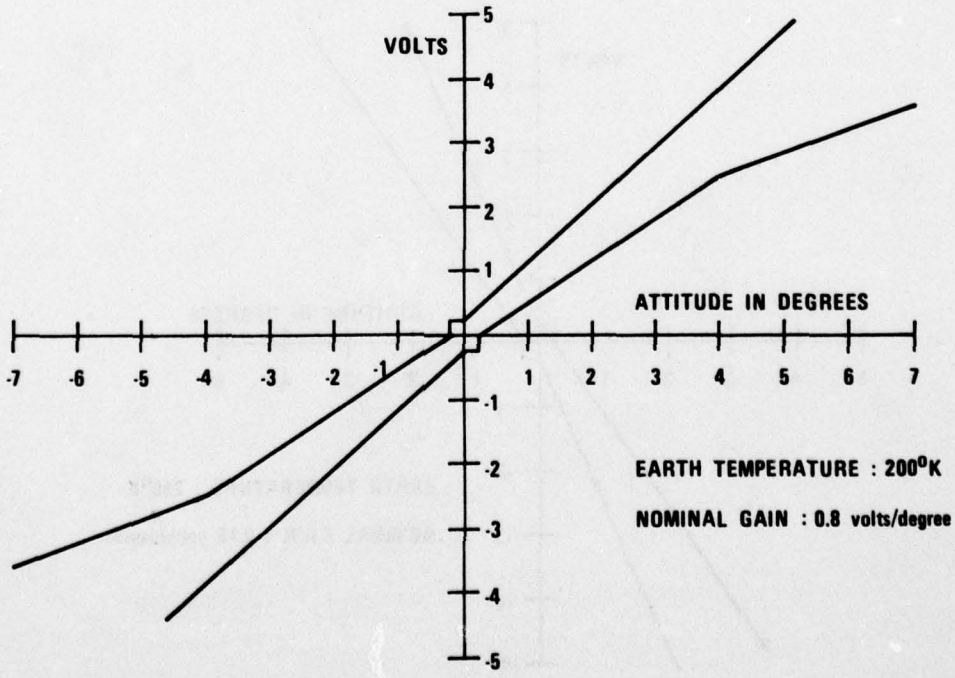

Figure 98. Static Sensor Transfer Function Envelope (200°K)

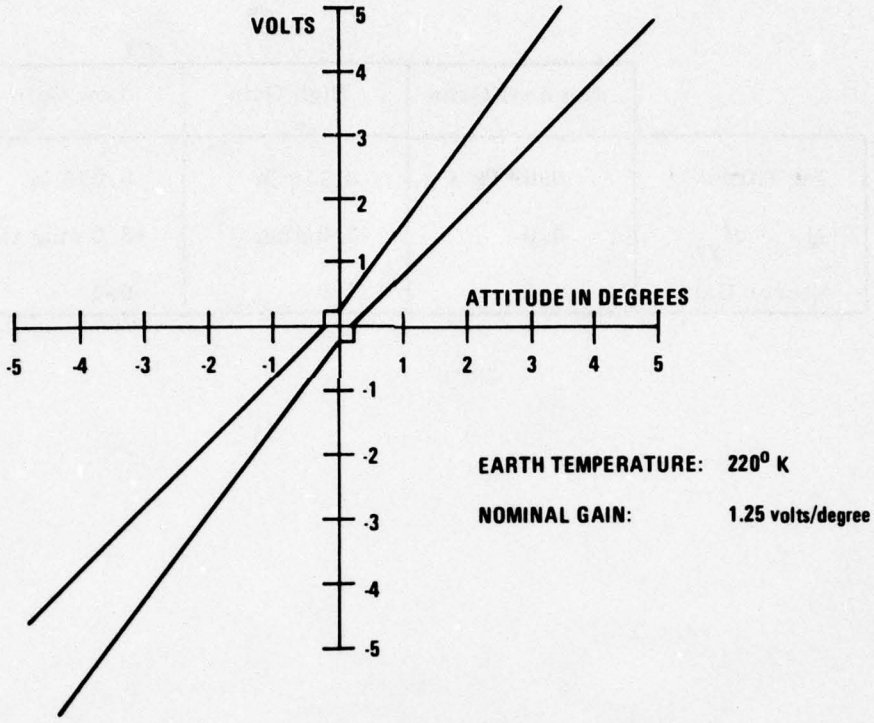

Figure 99. Static Sensor Transfer Function Envelope (220°K)

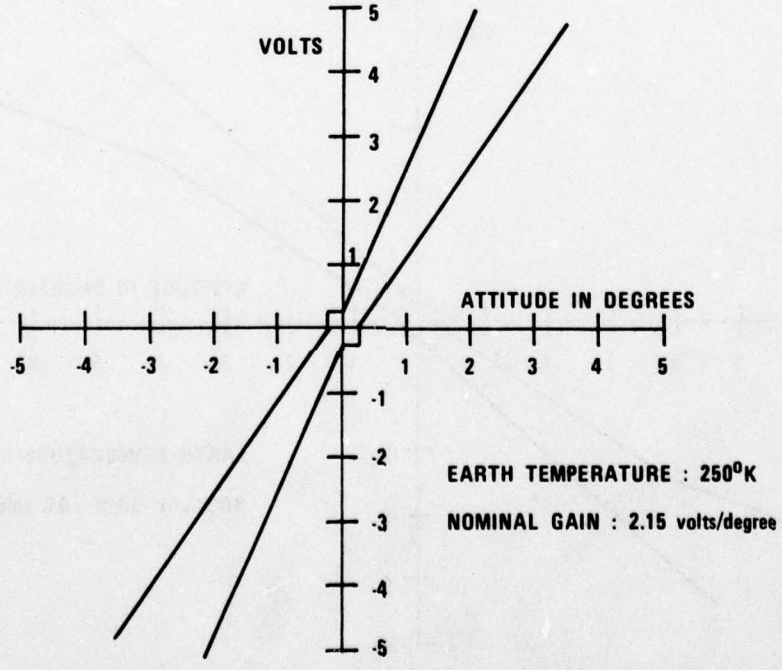

Figure 100. Static Sensor Transfer Function Envelope (250°K)

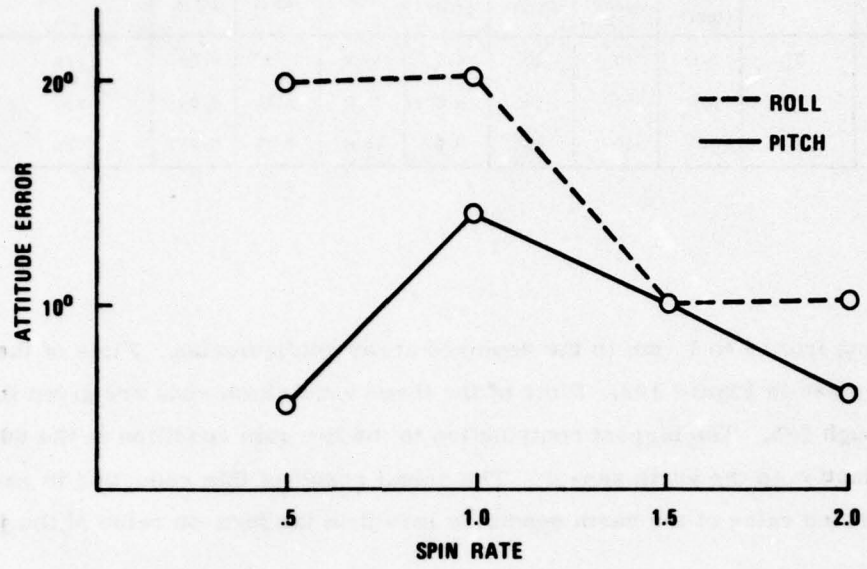

Figure 101. Earth Acquisition Envelope

Earth Reacquisition and Despin Simulation Analysis

The results of the earth reacquisition stability analysis were also verified in simulation. The mass properties used in the earth reacquisition are for the deployed array condition and are given in Appendix A. The major difference between the two sets of mass properties (stowed condition versus deployed array condition) is in I_{xx} and I_{zz} which are both approximately doubled. The axis found to be most critical in the acquisition analysis was the pitch axis. I_{yy} remains approximately the same for back stowed and deployed conditions. Because the pitch axis characteristics remain approximately the same, it is felt that the pitch axis results of acquisition also hold for reacquisition. Hence, only roll axis potential problems were investigated.

The low gain condition has the most potential for problems and would be accentuated by the doubling of the roll inertia. Only the low roll gain condition was investigated in simulation as is shown in Table 17. The initial nutation angle used was obtained by

TABLE 17. REACQUISITION RUN SUMMARY

Run Number	Controller	Spin Rate (rpm)	ϕ_{1c} (deg)	θ_{1c} (deg)	η_{1c} (deg)	Loop Gain	Propellant		Uncertainties	Comments
							Roll	Pitch		
RACQ-1	2	1.0	10	10	4.0	Low	0.08	0.007	Yes	Converged
RACQ-2	2	2.0	10	10	4.0	Low	0.15	0.02	Yes	Converged
RACQ-3	2	0.5	10	10	6.0	Low	0.05	0.007	Yes	Converged

despinning from 6 to 1 rpm in the deployed array configuration. Plots of the despin run are given in Figure 102. Plots of the three acquisition runs are given in Figures 103 through 105. The biggest contribution to the low gain condition is the 60 percent gain reduction in the earth sensor. The actual result of this reduction in gain is that the saturated value of the earth sensor is less than the turn-on value of the jets.

If there were no roll in the loop and if the vehicle were not spinning (i.e., transferring pitch and roll errors), the pitch and roll jet would never turn on. The transient response of Figures 103 through 105 indicates that, although performance is sloppy, attitudes do converge from the initial condition. The 0.5 rpm condition appears to be converging slightly; however, because of the sensor saturation, convergence deteriorates as spin rate decreases. To summarize, it appears that the acquisition envelope can be substituted for the reacquisition envelope with the exception of greater than 10 deg initial roll errors at 0.5 rpm.

CEA Jet Control System Preliminary Redesign

Since we had developed a sophisticated computerized tool for analyzing the stability characteristics of the jet control system, it was a simple task to use that tool to determine whether the jet control system design, particularly in the pitch axis, could be improved. A preliminary redesign was conducted and the results showed dramatic improvement in extending the earth acquisition envelope. Since it has been determined that the pitch axis has the poorest stability characteristics, redesign was limited to that axis. The structure of the control system was maintained. Table 18 shows the changes in pitch control loop parameters that led to improved stability characteristics.

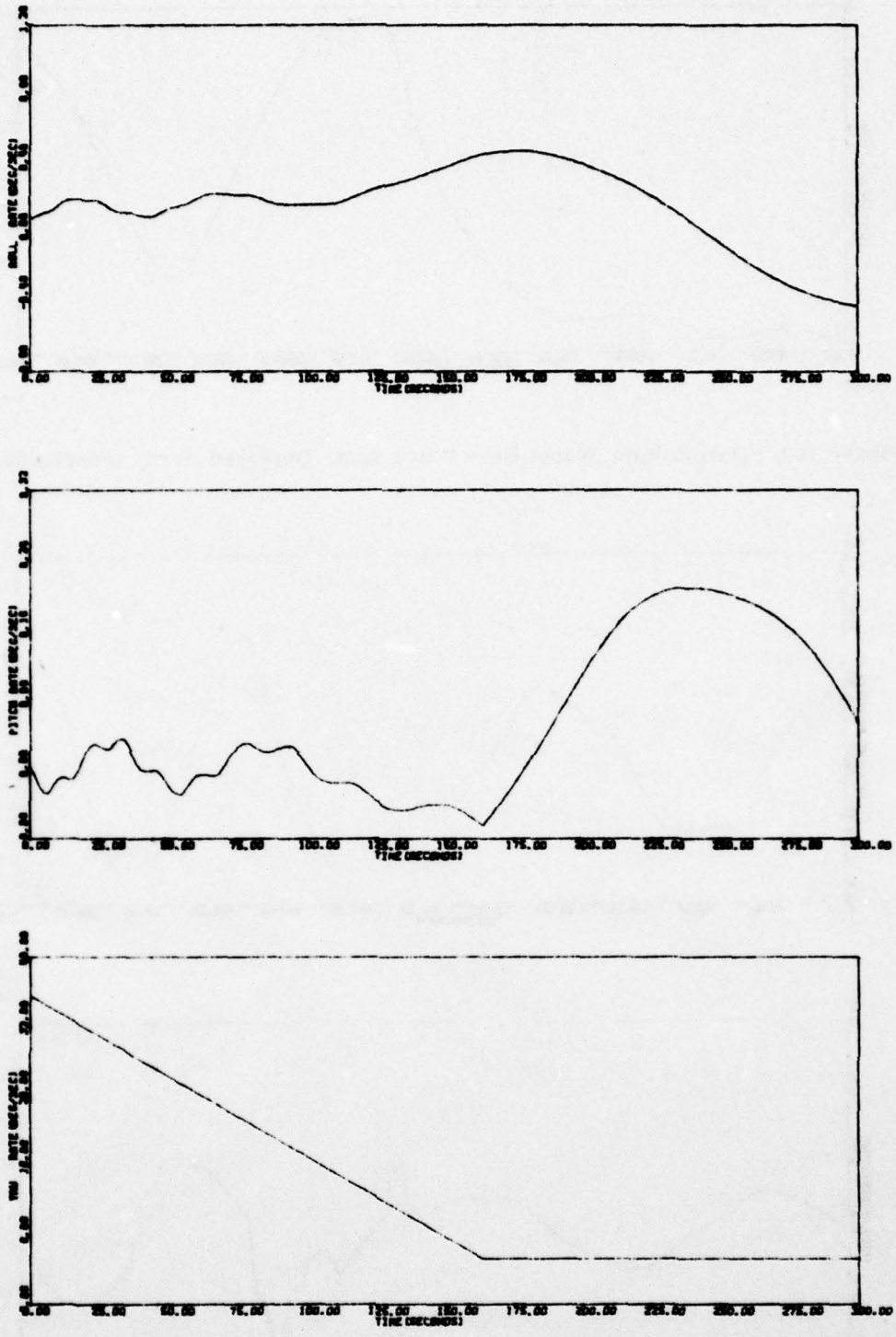

Figure 102. Despin Run, Worst Case 6 to 1 rpm, Deployed Array

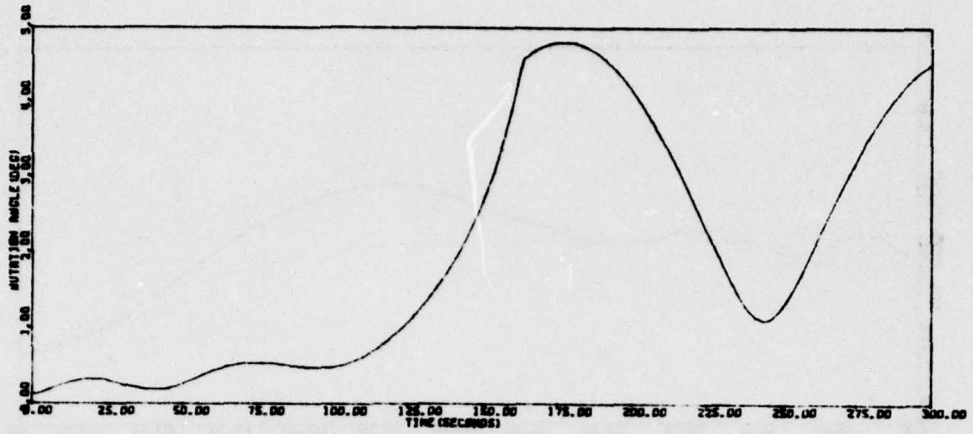

Figure 102. Despin Run, Worst Case 6 to 1 rpm, Deployed Array (concluded)

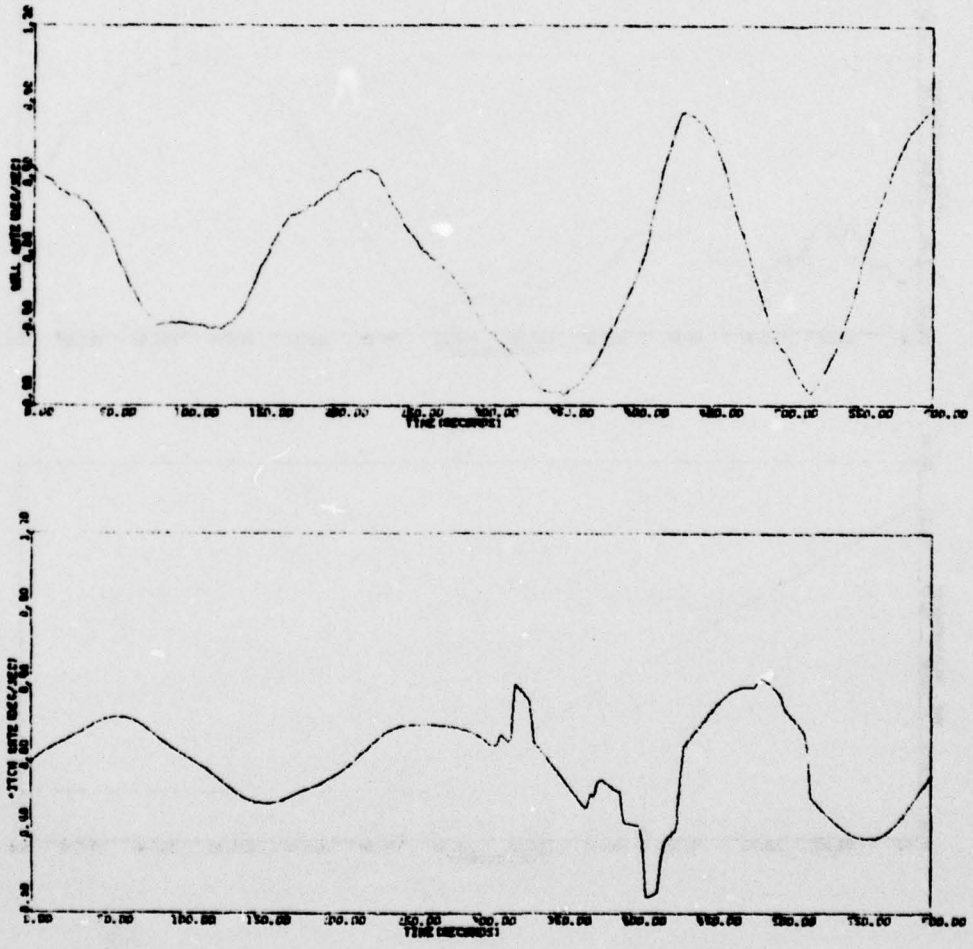

Figure 103. Reacquisition Run RACQ-1

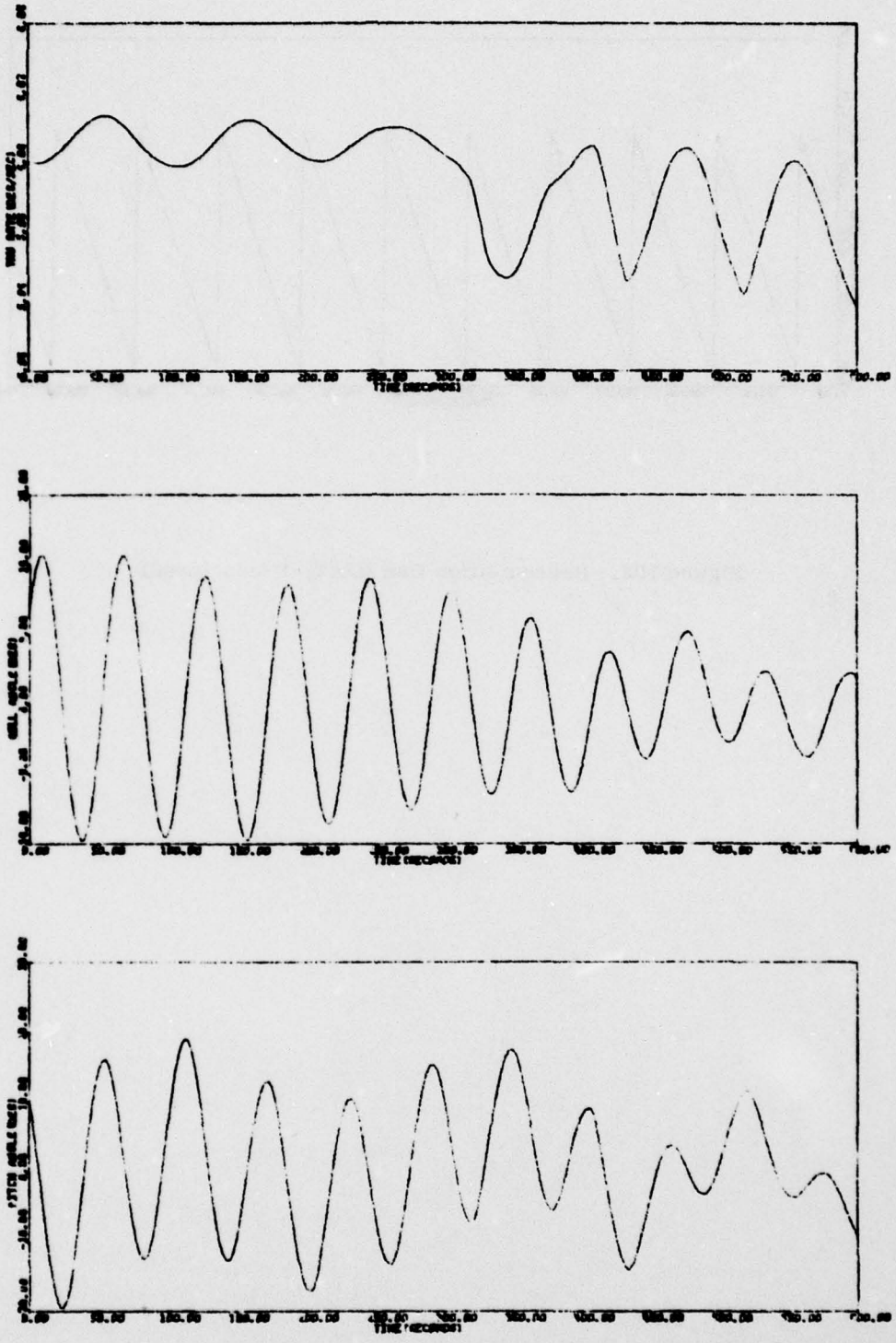

Figure 103. Reacquisition Run RACQ-1
(continued)

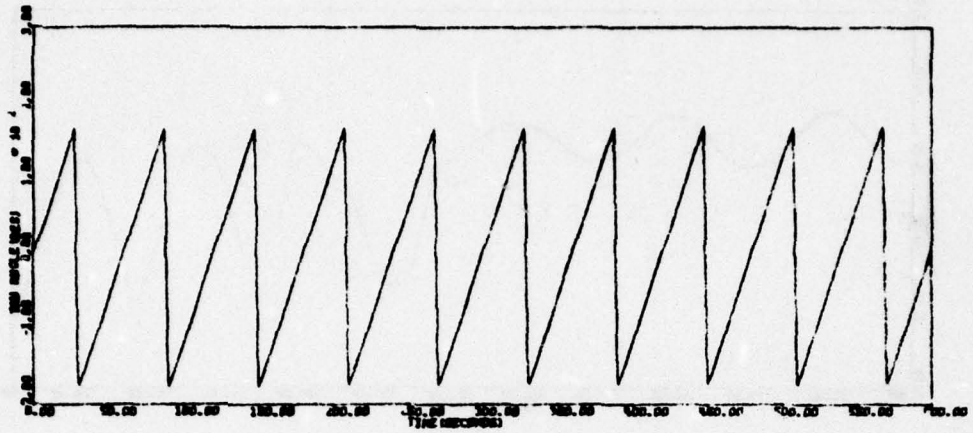

Figure 103. Reacquisition Run RACQ-1 (concluded)

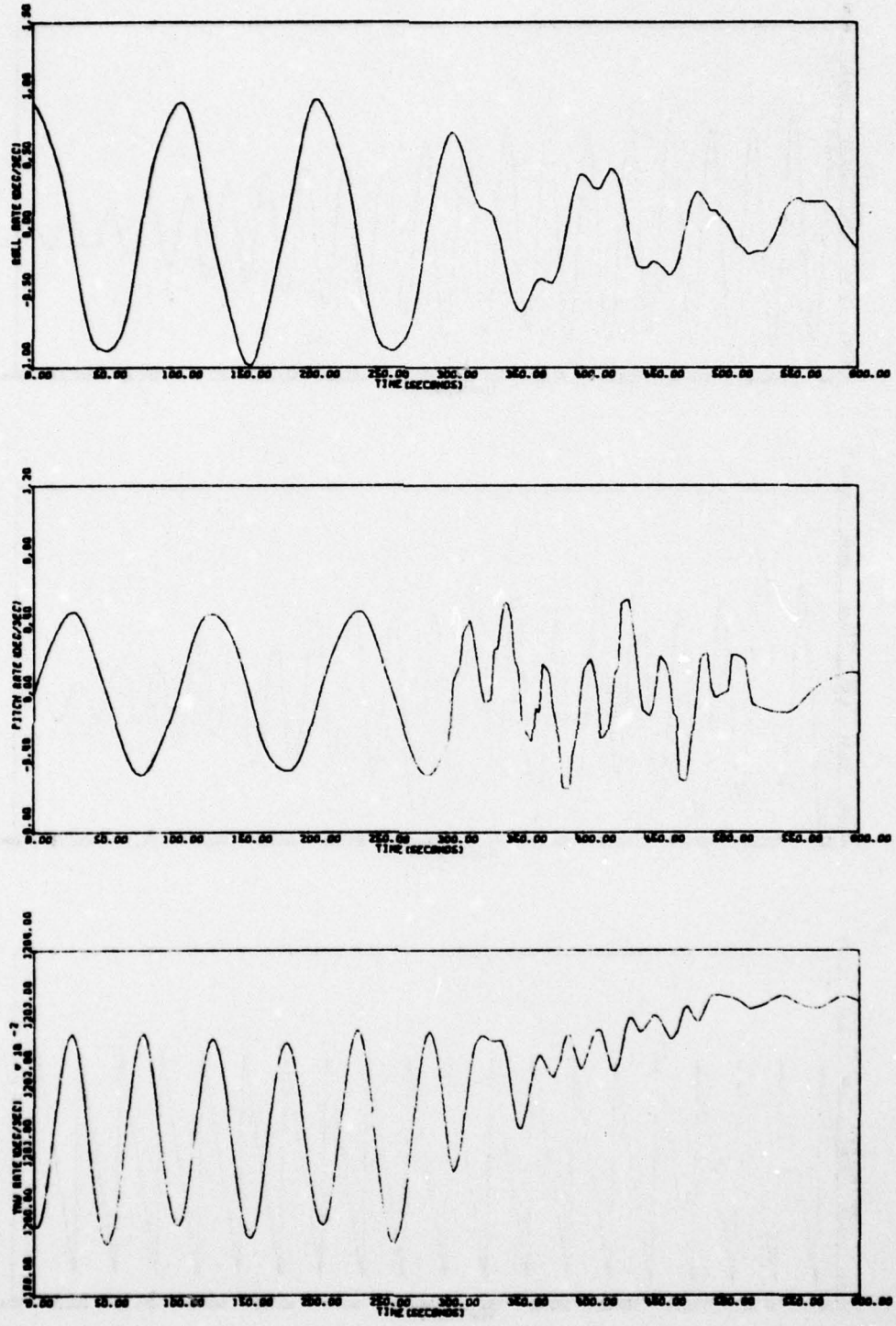

Figure 104. Reacquisition Run RACQ-2

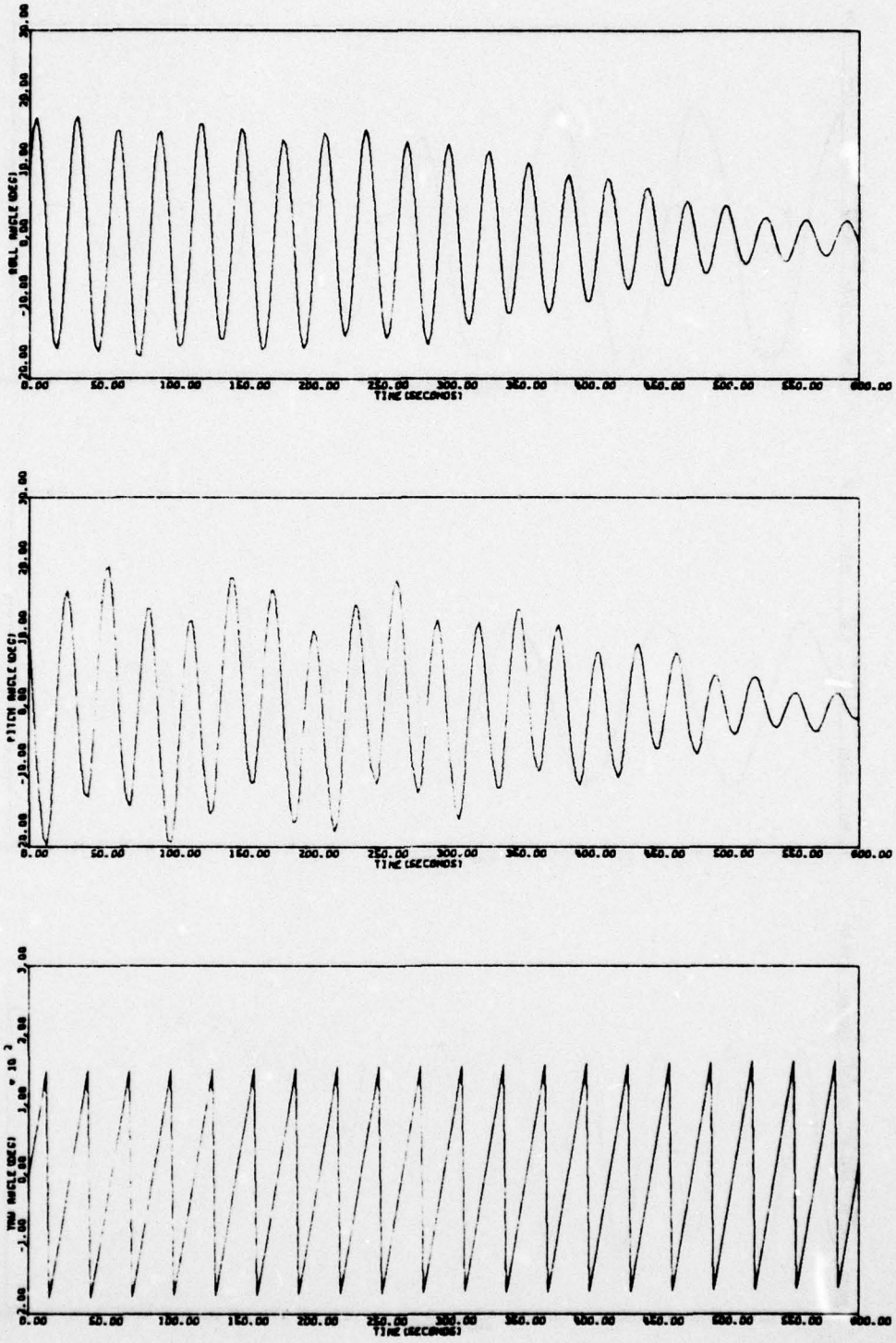

Figure 104. Reacquisition Run RACQ-2 (concluded)

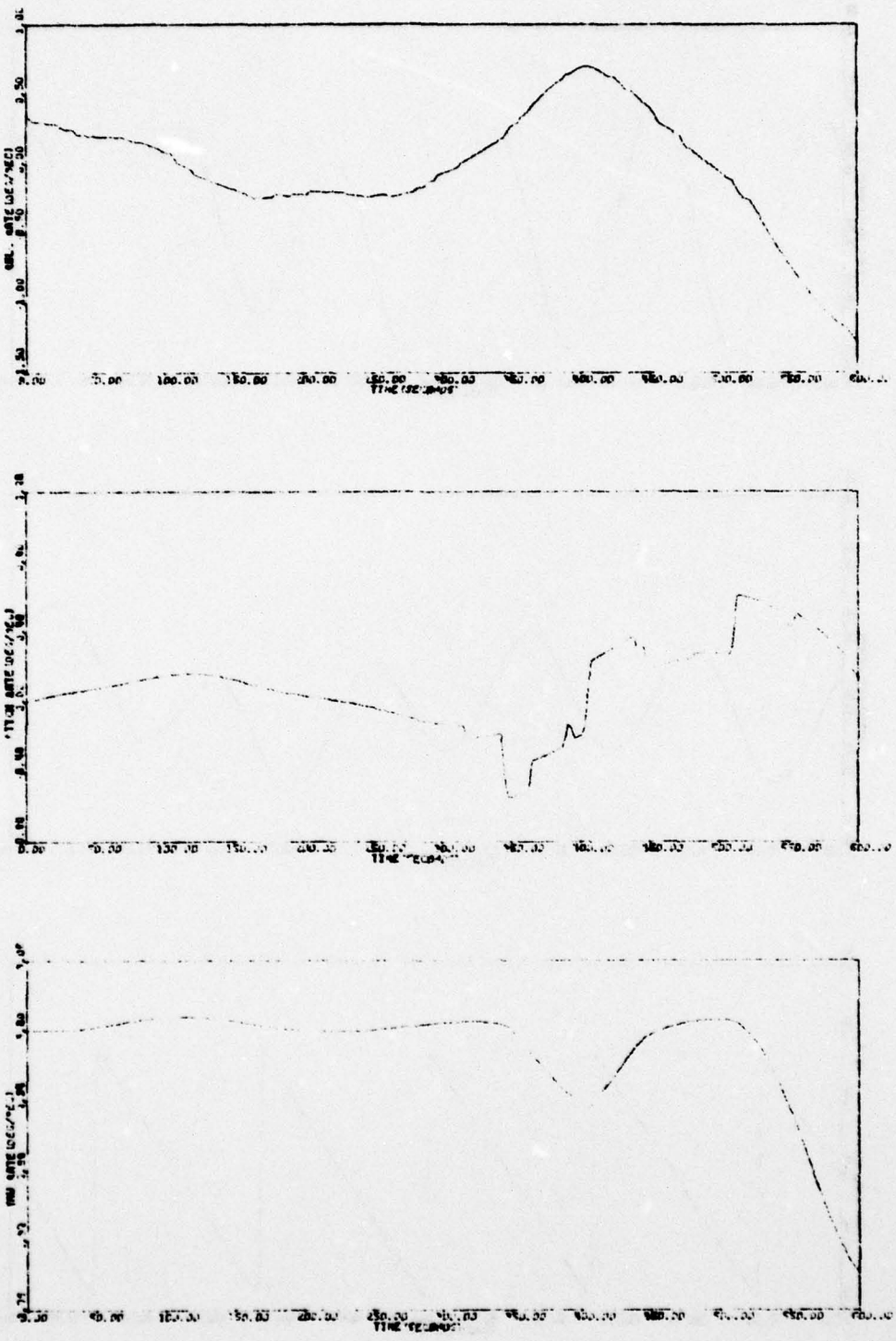

Figure 105. Reacquisition Run RACQ-3

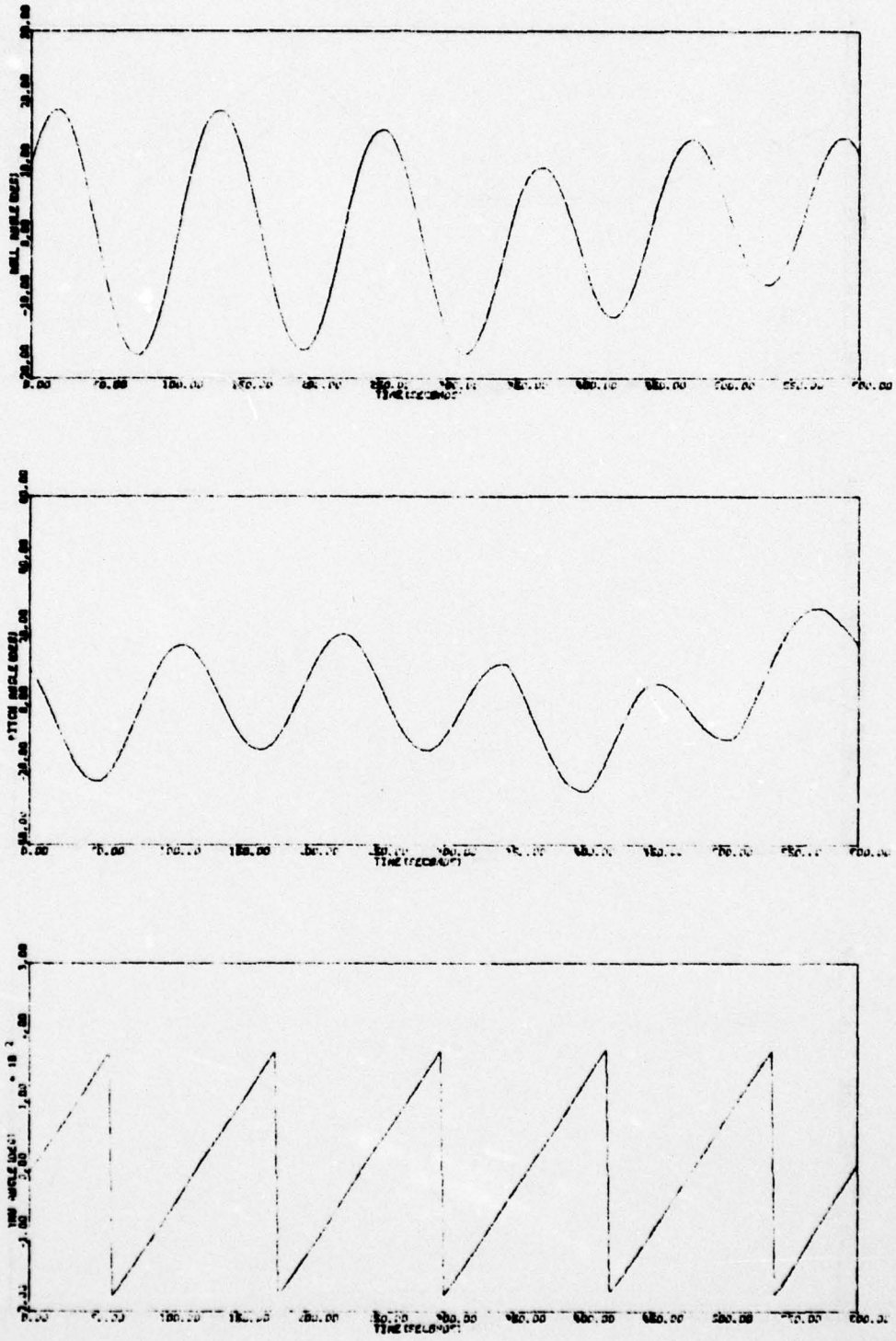

Figure 105. Reacquisition Run RACQ-3 (concluded)

TABLE 18. IMPROVED LINEARIZED JET CONTROL LOOP PARAMETERS

Parameter	Roll	Pitch	Yaw
Inertias (slug ft^2)			
• Stowed	94.1	102.2	111.3
• Deployed	187.9	94.5	211.6
Gains			
• Loop Gain, K	1.0	1.0	1.0
• Pseudo-rate, K_0	0.25	10.0	0.57
• Relay, K_{EQ}	0.335	0.335	0.335
• Modulator, $K_{EQ}/(1+K_0K_{EQ})$	0.309	0.077	0.281
• Moment Arm, ℓ (ft)	0.4	2.8	2.8
• Jet Thrust, F_J (lb)	0.09	0.09	0.09
Time Constants (sec)			
• Sensor, τ_S	1.75	1.75	0.01
• Pseudo-lead, τ_0	2.0	5.0	2.0
• Pseudo-lag, $\tau_0/(1+K_0K_{EQ})$	1.85	1.15	1.7
• Lead, τ_1	10.0	5.0	20.2
• Lag, τ_2	1.0	1.0	0.2
• Roll-off, τ_3	0.2 (0.4)†	0.4†	0.05

*Maximum describing function gain

†Version 2

These improved stability characteristics are shown in a frequency response in Figure 106 for three levels of attitude error. The results are summarized in Table 19. As can be seen, the improvement is substantial. At a 10 deg initial pitch attitude error, phase "margin" increased from 1.0 to 33.0 deg and gain "margin" increased from 1 to 20 dB with approximately the same control system bandwidth (0.17 to 0.1). At 20 deg initial pitch attitude error, the Version 2 controller has a nonconvergent limit cycle, whereas the redesigned version still has good "margins." These analytical results were verified in simulation at two earth acquisition conditions from which acquisition was not possible with Version 2 (or Version 1) of the jet control system.

Simulation results are shown in Figures 107 and 108. Figure 107 can be compared with Figure 88 which diverged from the same initial conditions. As can be seen, the redesigned pitch axis not only easily acquires pitch from the same condition (θ_{1C} = 10.0 deg) but also brings in roll (pitch acquisition is initiated 300 sec into the run).

AD-A056 811 HONEYWELL INC MINNEAPOLIS MINN SYSTEMS AND RESEARCH --ETC F/G 17/7
INDEPENDENT STABILITY AND CONTROL ANALYSIS OF NAVIGATION DEVELO--ETC(U).
JAN 78 R E POPE, M D WARD, M F BARRETT F04701-75-C-0135

UNCLASSIFIED 78SRC10-VOL-1 SAMSO-TR-78-74-VOL-1 NL

3 OF 4
ADA
056811

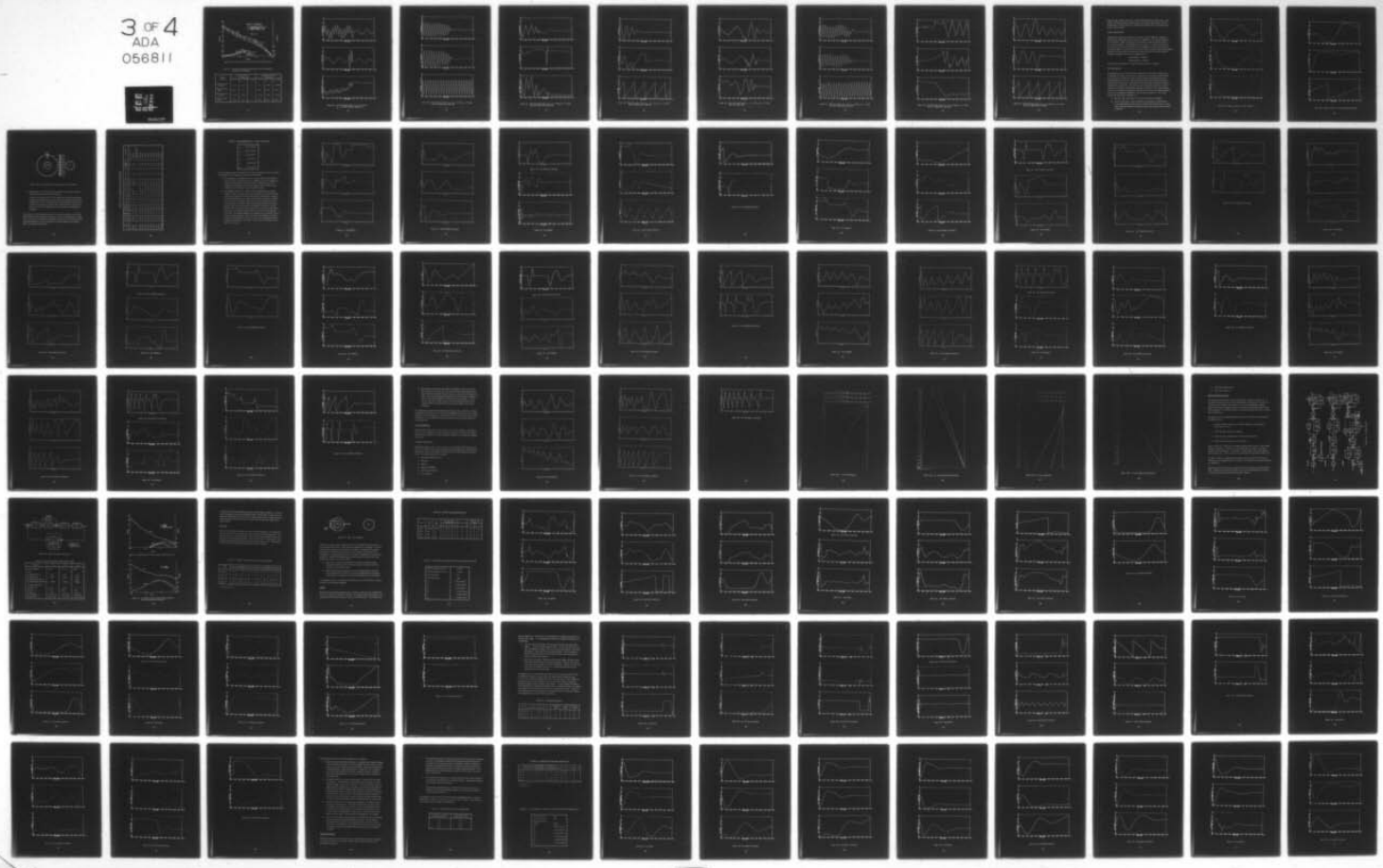

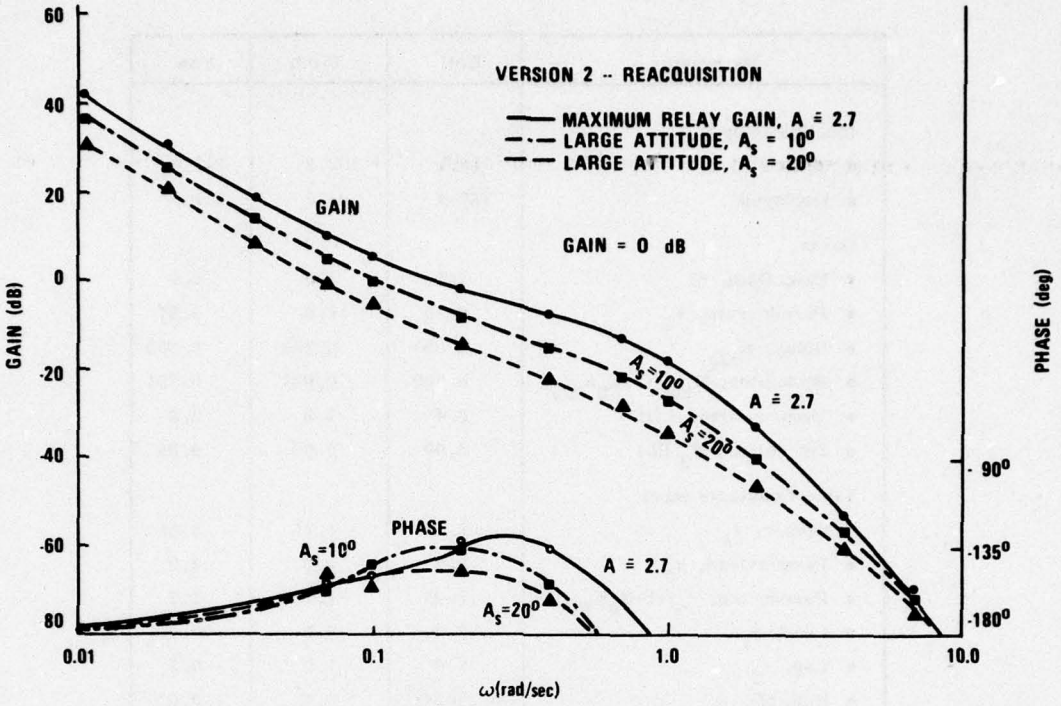

Figure 106. Preliminary Pitch Jet Loop Redesign (with Saturation)

TABLE 19. STABILITY MARGIN COMPARISON FOR PRELIMINARY PITCH LOOP REDESIGN

Stability Margins	Original Version 2 Acquisition			Redesigned Version 2 Acquisition		
	A = 2.7	A_S = 10°	A_S = 20°	A = 2.7	A_S = 10°	A_S = 20°
Gain crossover (rad/sec)	0.33	0.17	---	0.5	0.095	0.062
Phase "margin" (deg)	19.0	1.0	---	37.0	33.0	21.0
Phase crossover (rad/sec)	0.68	0.20	---	0.86	0.58	0.56
Gain "margin" (dB)	10.0	1.0	---	16.0	20.0	27.0

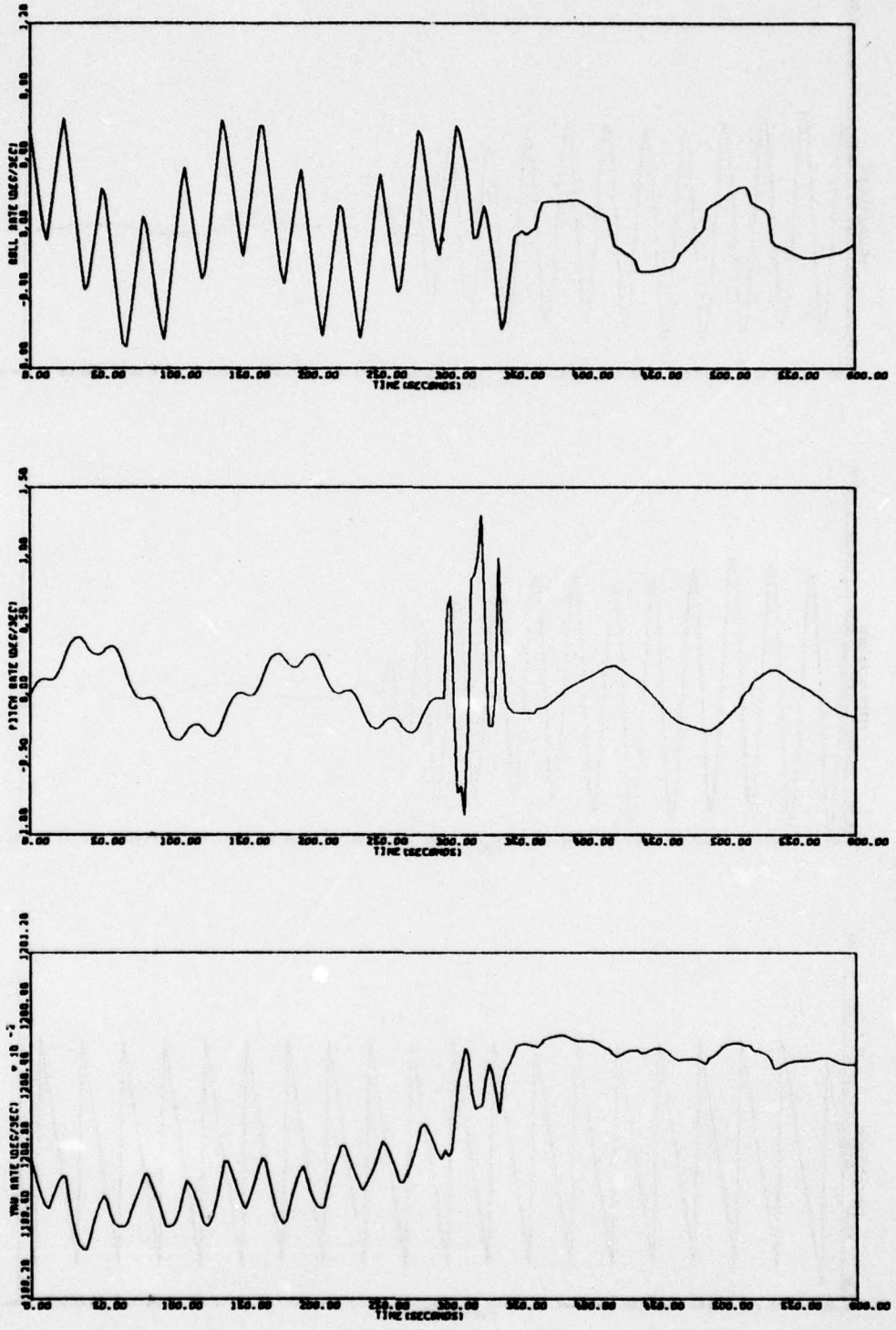

Figure 107. Pitch Redesign (2 rpm, $\phi_{ic} = \theta_{ic} = 10$ deg, $\eta_{ic} = 2.3$ deg, ACQ 12A, High Gain)

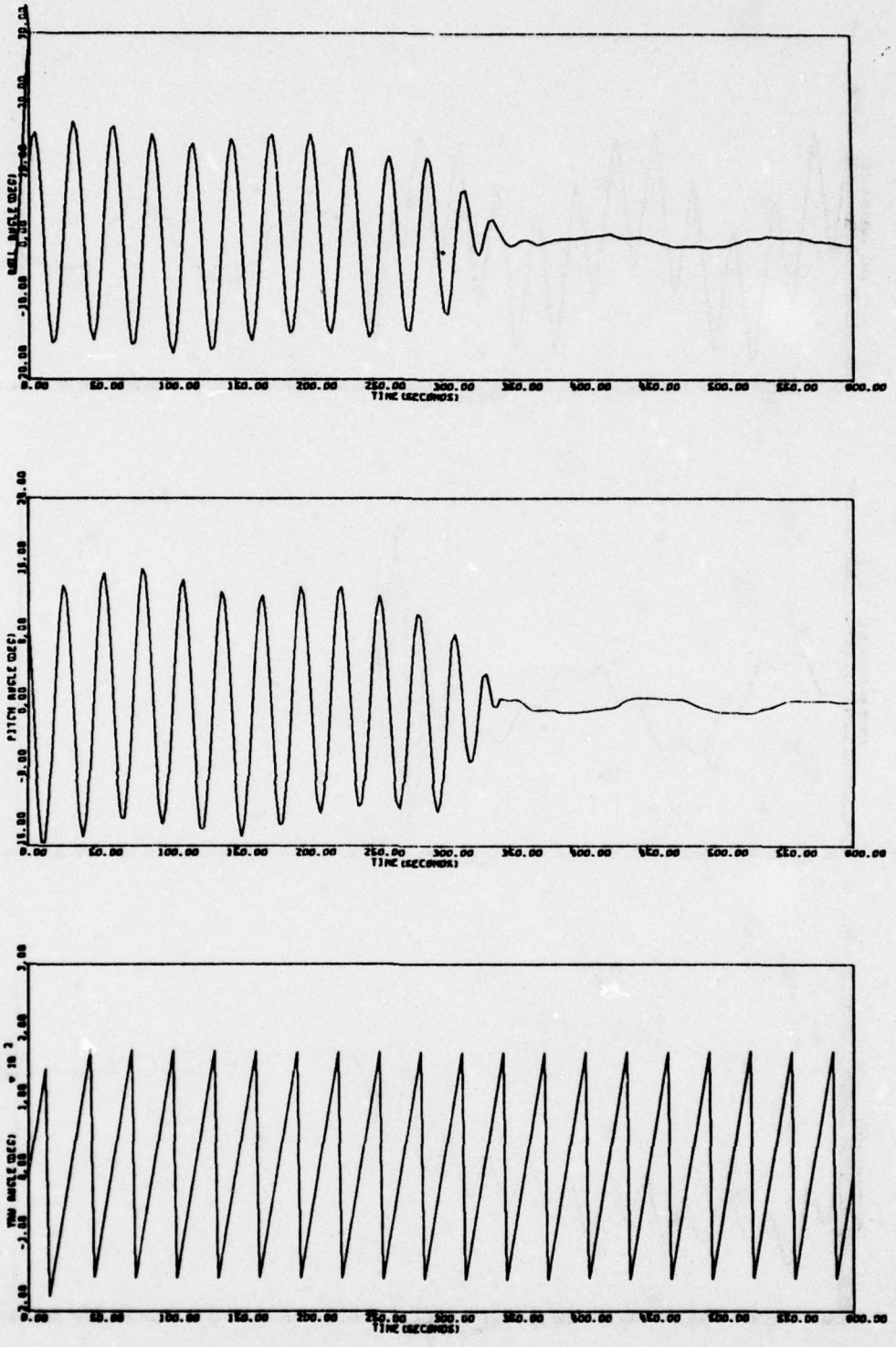

Figure 107. Pitch Redesign (2 rpm, $\phi_{ic} = \theta_{ic} = 10$ deg, $\eta_{ic} = 2.3$ deg, ACQ 12A, High Gain) (continued)

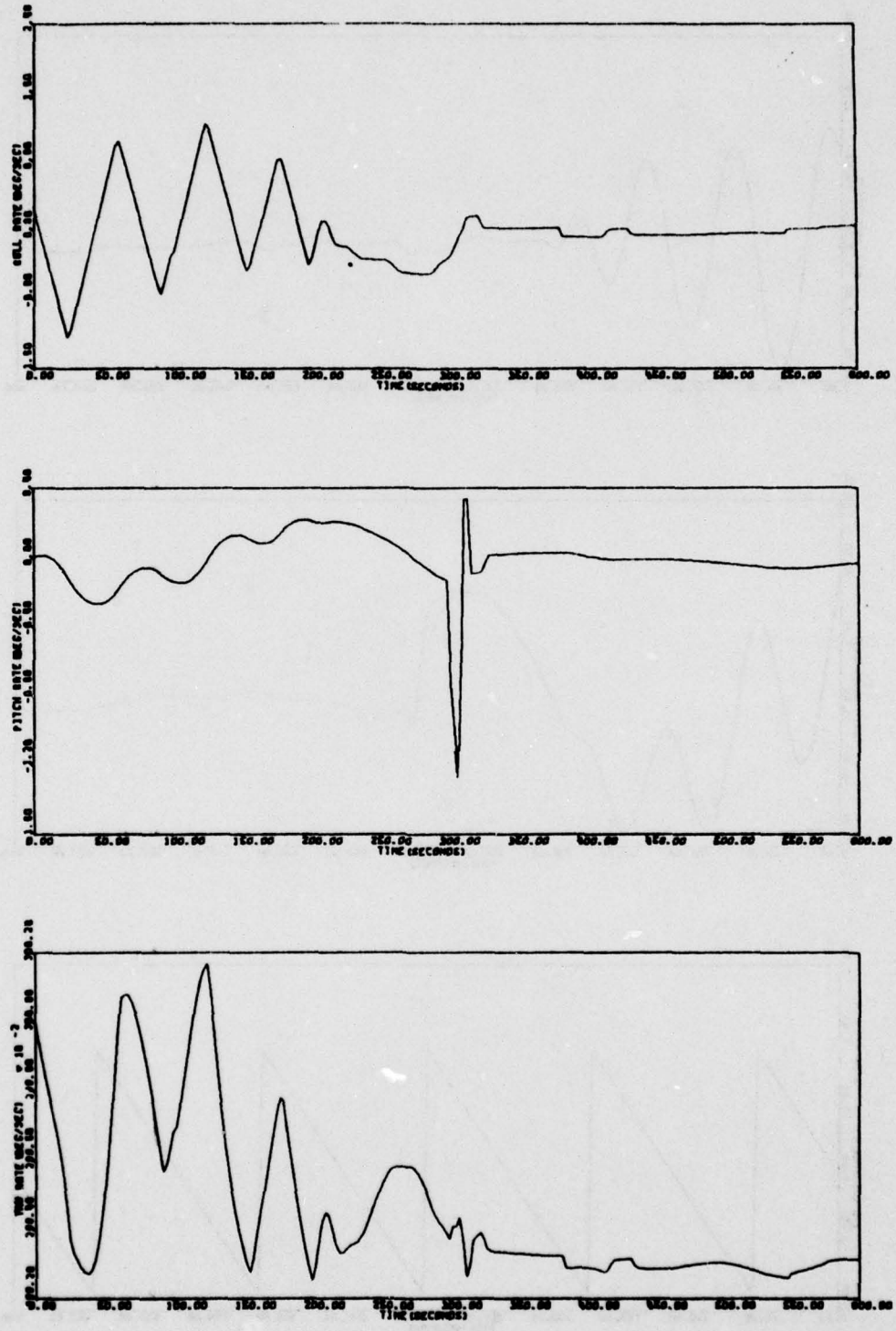

Figure 107. Pitch Redesign (2 rpm, $\phi_{ic} = \theta_{ic} = 10$ deg, $\eta_{ic} = 2.3$ deg, ACQ 12A, High Gain) (continued)

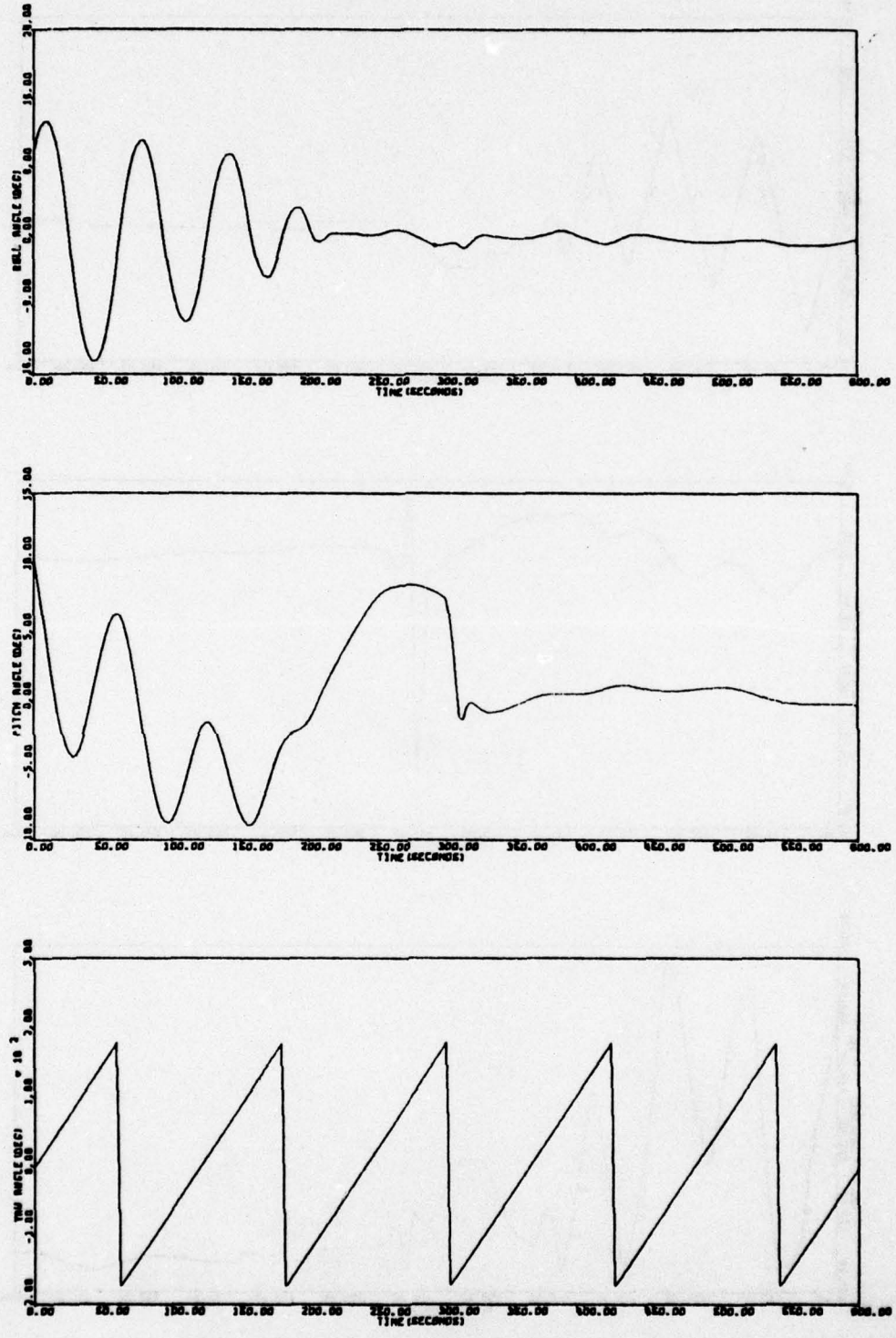

Figure 107. Pitch Redesign (2 rpm, $\phi_{ic} = \theta_{ic} = 10$ deg, $\eta_{ic} = 2.3$ deg, ACQ 12A, High Gain) (concluded)

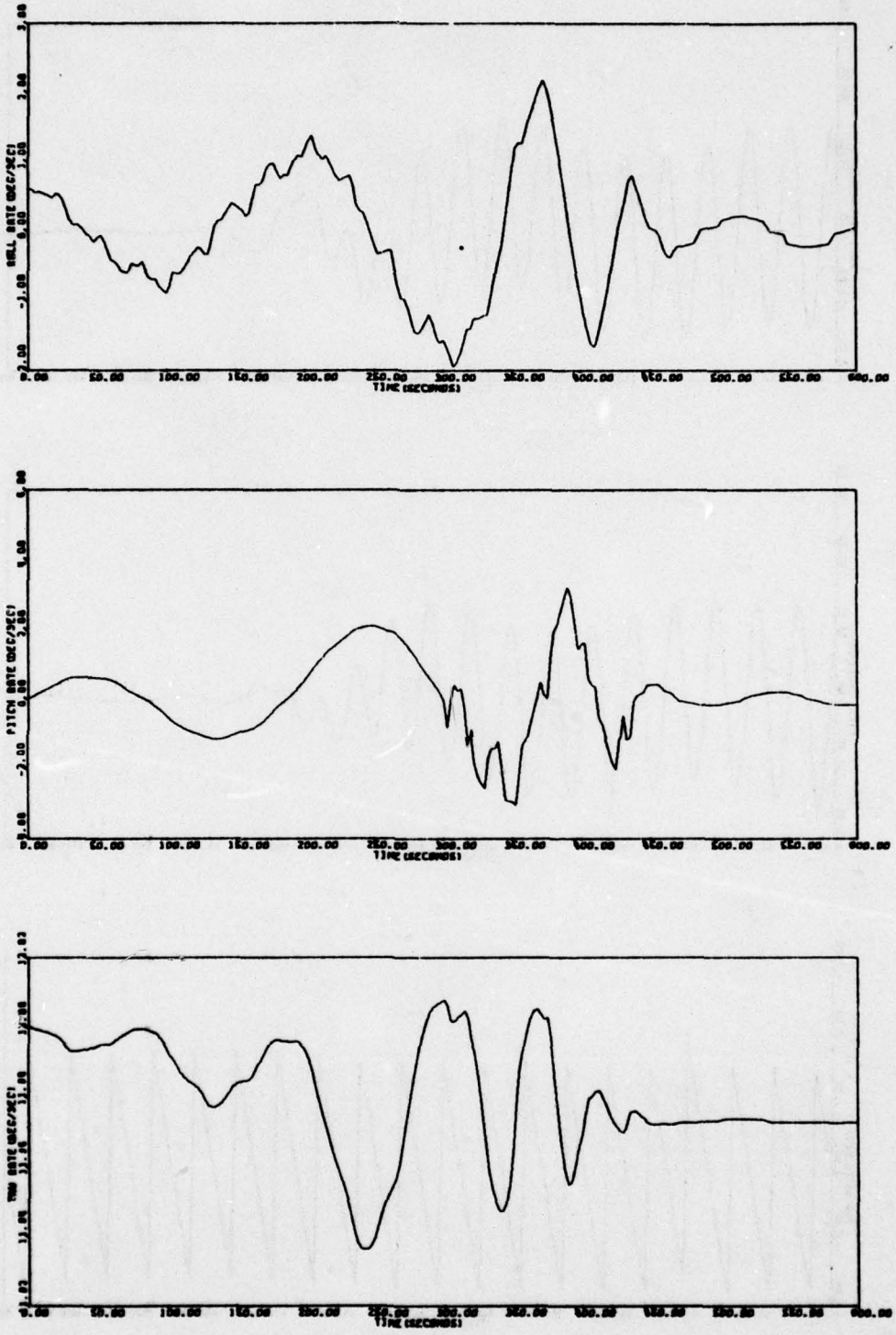

Figure 108. Pitch Redesign (2 rpm, $\phi_{ic} = \theta_{ic} = 20$ deg, $\eta_{ic} = 2.3$ deg, ACQ 12A', High Gain)

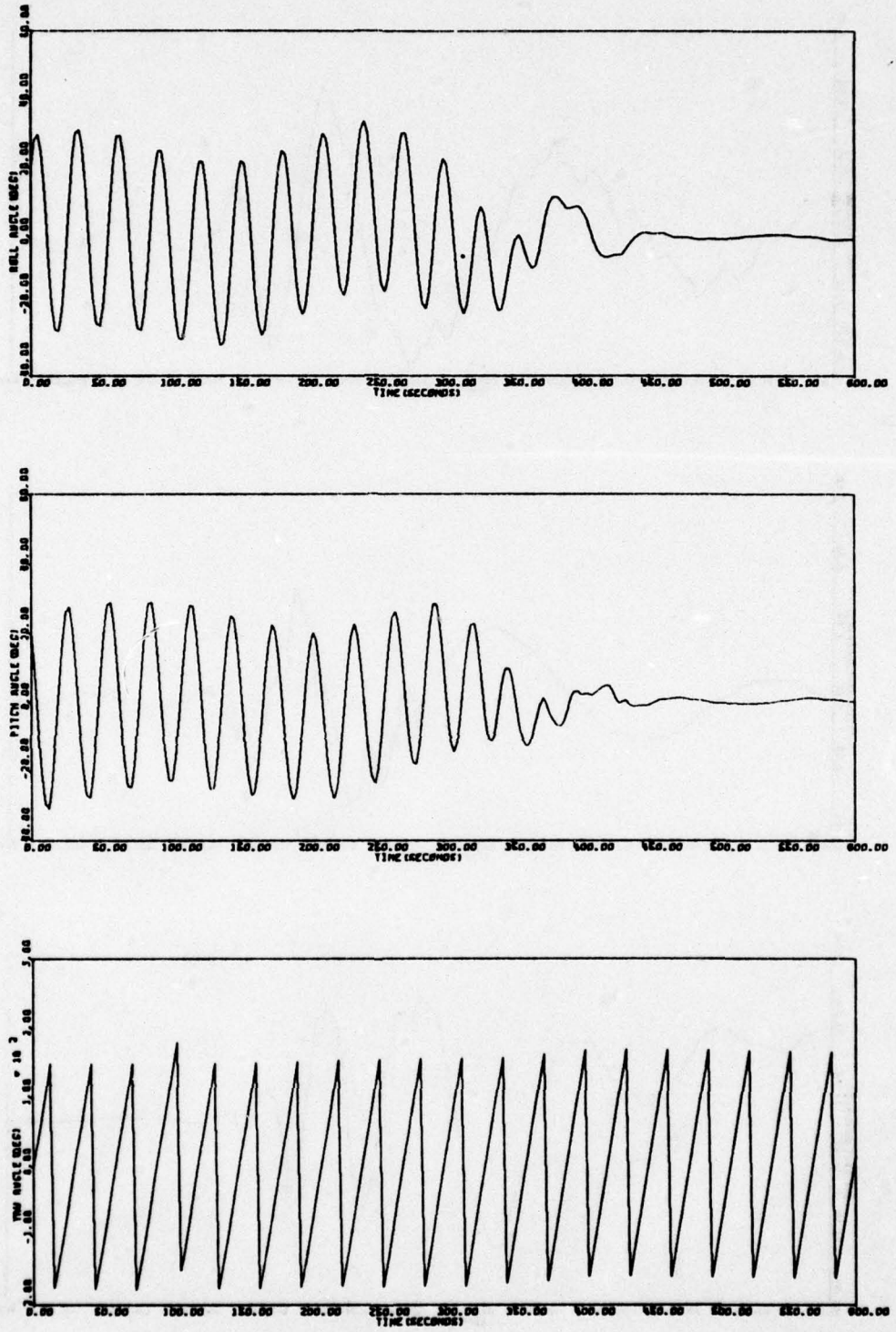

Figure 108. Pitch Redesign (2 rpm, $\phi_{ic} = \theta_{ic} = 20$ deg, $\eta_{ic} = 2.3$ deg, ACQ 12A', High Gain) (continued)

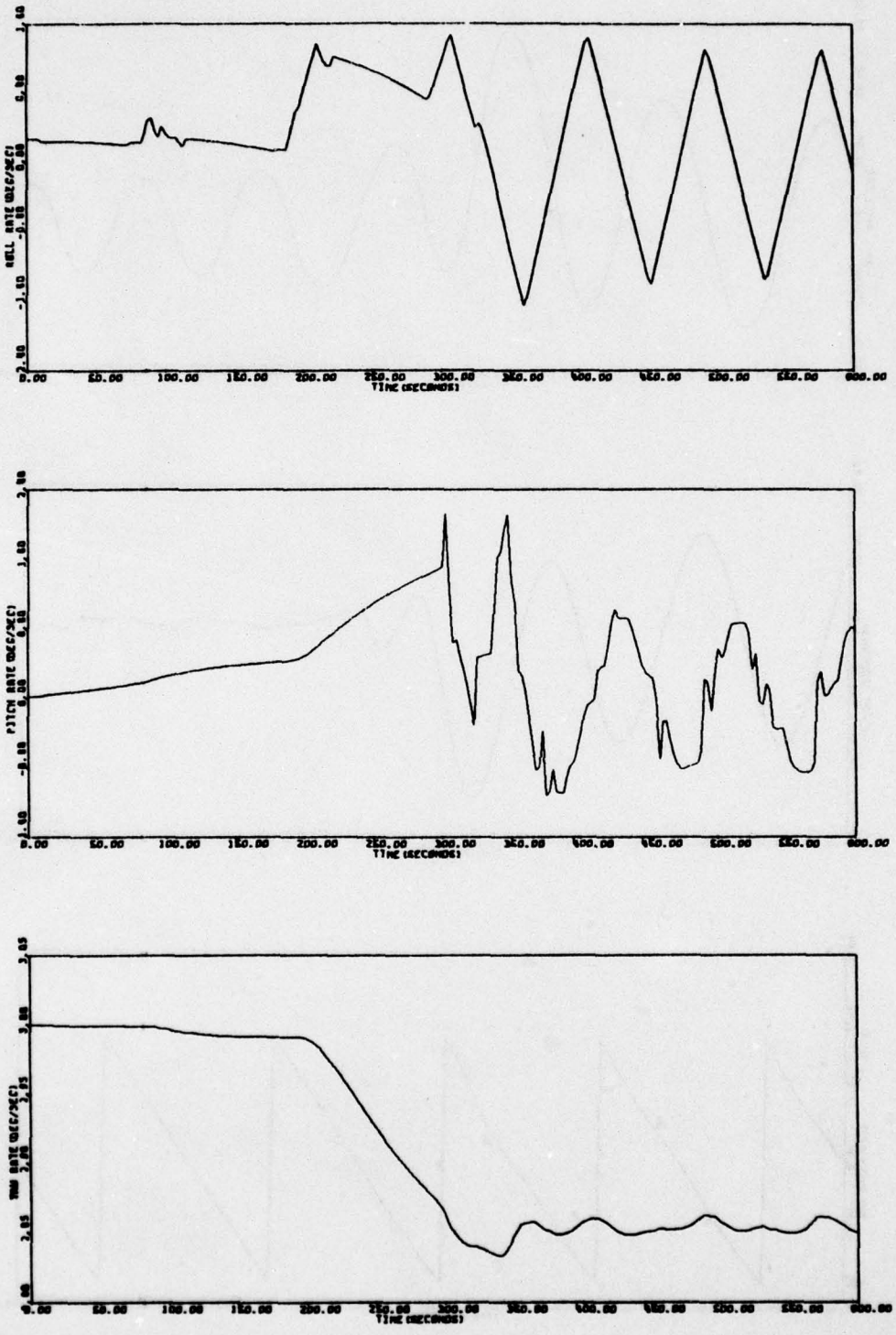

Figure 108. Pitch Redesign (2 rpm, $\phi_{ic} = \theta_{ic} = 20$ deg, $\eta_{ic} = 2.3$ deg, ACQ 12A', High Gain) (continued)

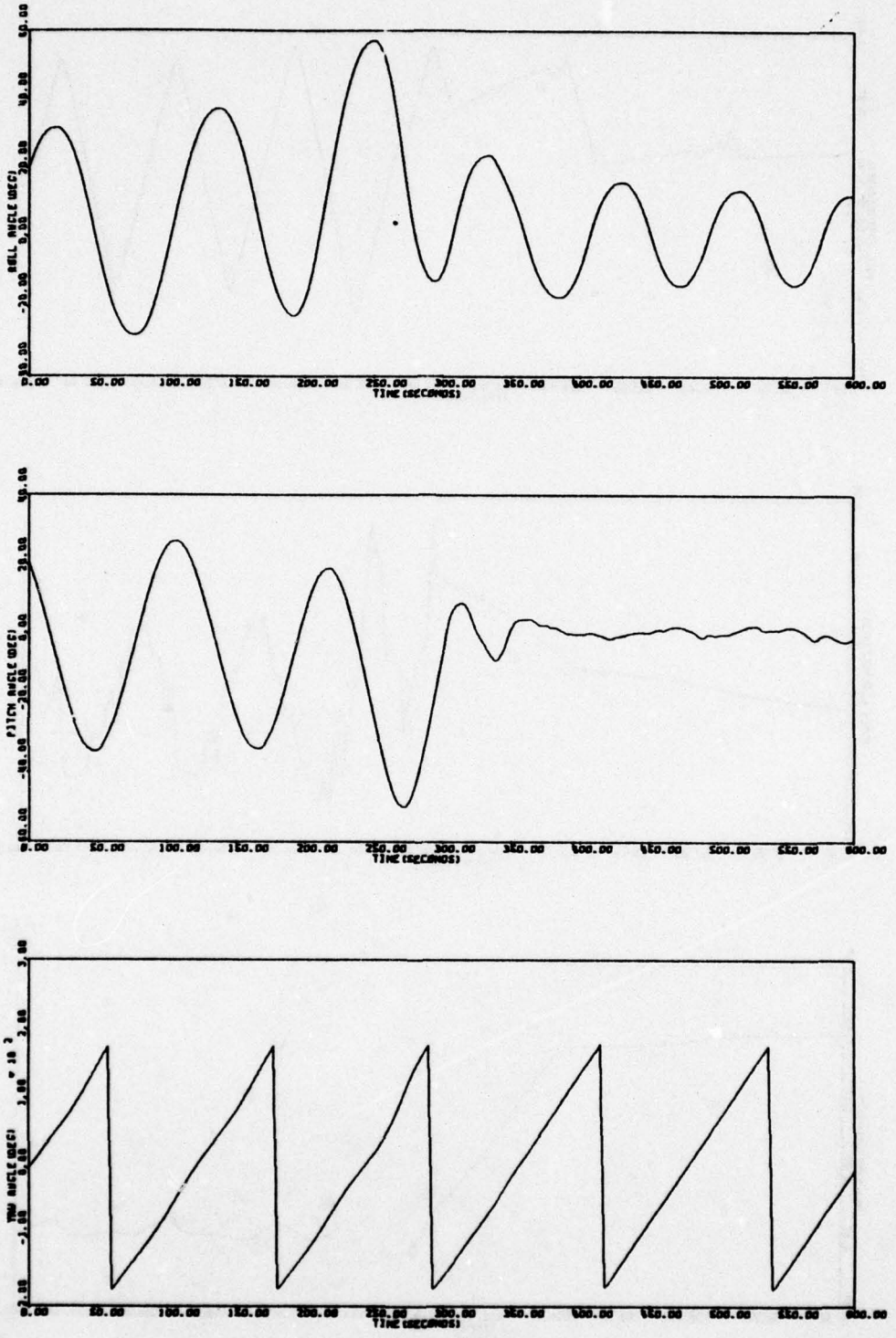

Figure 108. Pitch Redesign (2 rpm, $\phi_{ic} = \theta_{ic} = 20$ deg, $\eta_{ic} = 2.3$ deg, ACQ 12A', High Gain) (concluded)

Figure 108 also easily acquires from an initial pitch attitude error of 20.0 deg. These results, although preliminary, clearly indicate that improved performance is indeed possible with a redesign; therefore, Honeywell recommends that a redesign be considered for future launches.

ARRAY DEPLOYMENT

Following earth acquisition, the solar array on the -y axis is deployed. Equations describing the deployment dynamics are given in Appendix H. The nominal deployment rate is 3 deg/sec. Figure 109 presents time histories of vehicle attitudes and rates as -y array is deployed. Full deployment occurs at 30 sec. As can be seen from the rate traces, yaw rate decreases from the initial condition of 1 rpm (6 deg/sec) to 0.74 rpm (4.435 deg/sec). There is some reaction jet activity, and pitch angle eventually hangs up on the +2.0 deg deadband of reaction jet control (Version 2 of the control system). Propellant expenditure for the 100 sec simulation was

Roll propellant = 0.0047 lb

Pitch propellant = 0.0067 lb

No attitude control problems are expected when the -y array is deployed.

SUN ACQUISITION

Sun acquisition is to be initiated when the angle between the sun line and spin vector is approximately 90 deg. This is shown in Figure 110. At this point, with the panels in the yz plane of the vehicle, the yaw sun sensor output is essentially vehicle yaw angle misalignment to the sun. This condition also represents maximum equivalent yaw gain in the control loop. The stability analysis of Section III indicated satisfactory margins in the yaw jet loop. (There is only one version of the yaw jet loop.) These results were verified by the simulation runs shown in Table 20. The mass properties for the -y array deployed condition were generated by the three-body computer program in the -y array deployment simulation. They are given in Table 21. The critical parameters affecting sun acquisition are

- Spin rate. Spin rates of 0.5, 0.75, and 1.0 rpm were investigated.
- Yaw sun sensor gain. Sensor temperature at acquisition is approximately -37.0°C which produces a 40 percent reduction in sun sensor output. An additional 10 percent reduction was added to construct the low gain condition shown in Table 20.

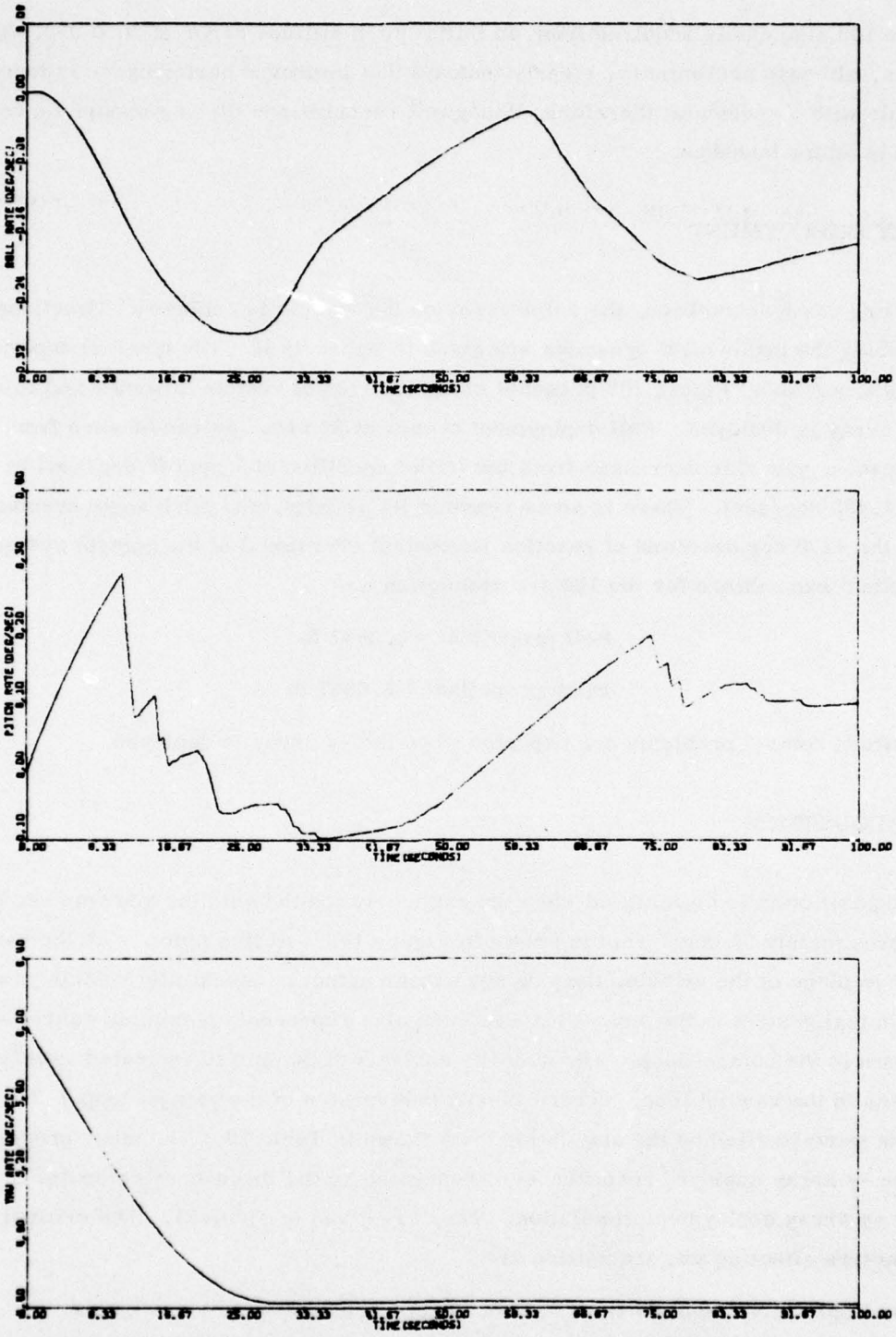

Figure 109. Deploy-Y Panel, 1.0 rpm, Nominal

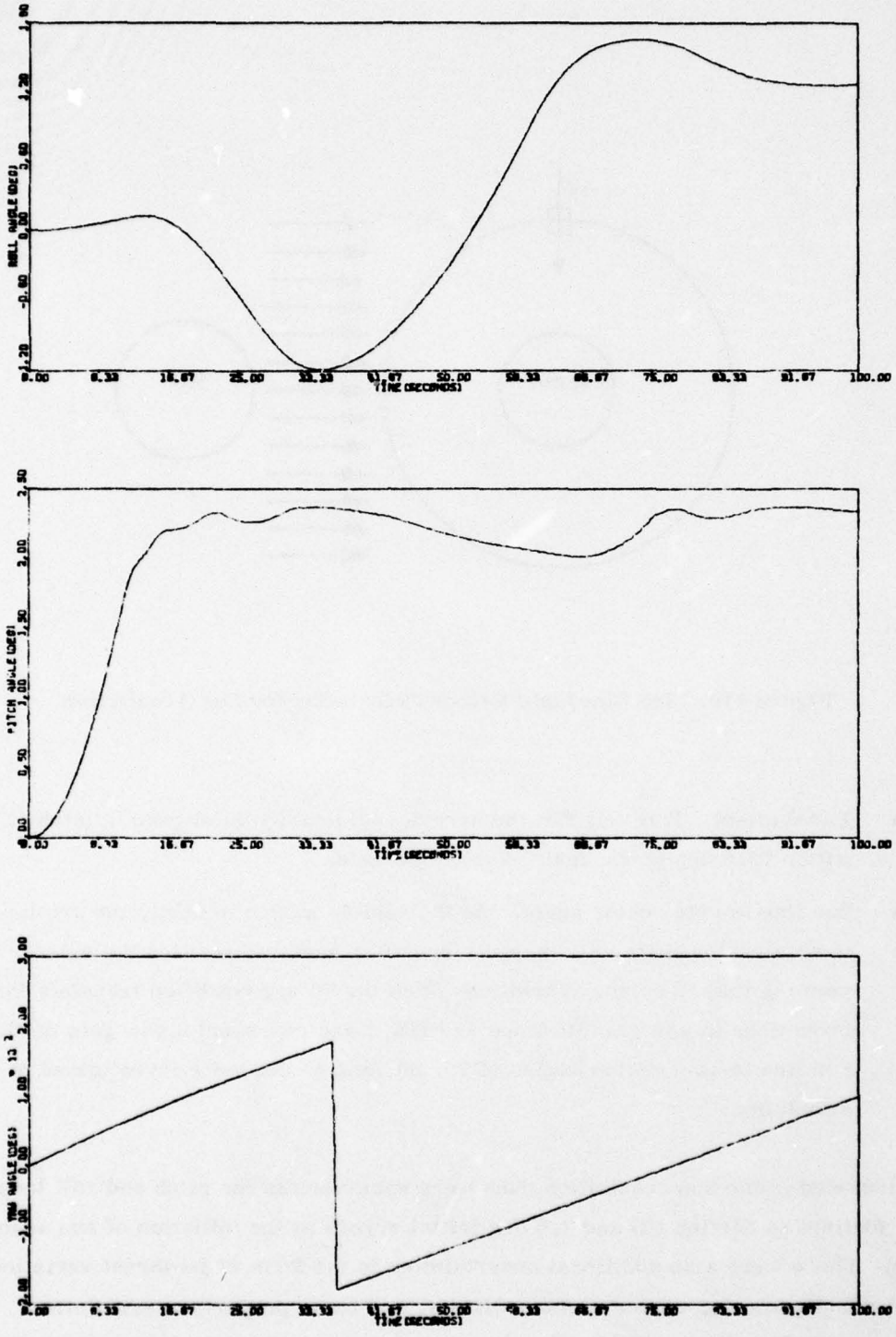

Figure 109. Deploy-Y Panel, 1.0 rpm, Nominal (concluded)

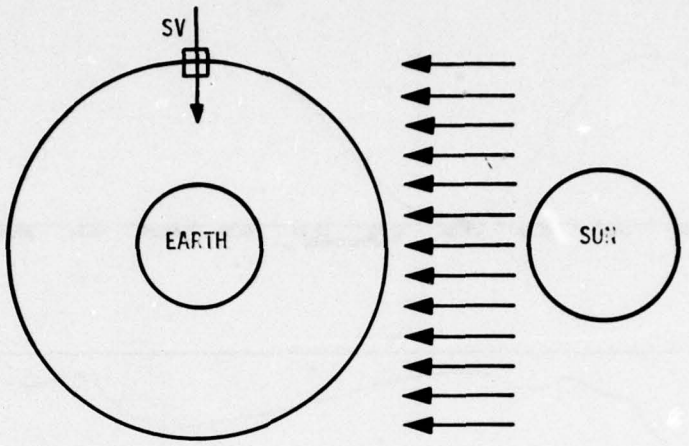

Figure 110. Sun Line/Spin Vector Orientation for Sun Acquisition

- Panel offset. It is felt that the arrays could easily be aligned in pitch to within 10.0 deg of the desired array attitude.
- Sun line to spin vector angle. As the vehicle moves in orbit, the sun line to spin vector angle will change since after earth acquisition the vehicle is pointing toward earth. Variations from the 90 deg condition translate into reductions in yaw gain (0.0 deg and 180.0 deg represent a yaw gain of 0). Sun line to spin vector angles of 90, 60, and 45 deg were investigated in simulation.

Also included in the sun acquisition runs were variations in the pitch and roll loop gains (defined in Section III) and 2.0 deg initial errors at the initiation of sun acquisition. There were also additional uncertainties in the form of jet thrust variations, thrust misalignments, center of mass offsets, and mass property uncertainties. These are summarized in Table 21.

TABLE 20. SUN ACQUISITION SIMULATION RUNS

Run Number	SI./SV (deg)	Spin Rate (rpm)	Panel Offset (deg)	ϕ_{1c} (deg)	θ_{1c} (deg)	Roll, Pitch Gain	Yaw Gain	Uncertainties	Yaw Propellant (lbs)	Comments
SACQ01A	90.0	0.75	0.0	2.0	2.0	Nominal	Nom	No	0.05	Acquired
SACQ02	90.0	0.75	10.0	2.0	2.0	High	High	Yes	0.04	Acquired
SACQ03A	90.0	0.75	10.0	2.0	2.0	Low	Low	Yes	0.06	Acquired yaw, lost pitch and roll
SACQ04A	90.0	0.75	10.0	2.0	2.0	Nominal	Low	Yes	0.06	Acquired
SACQ05A	90.0	0.75	10.0	2.0	2.0	High	Low	Yes	0.06	Acquired
SACQ06A	90.0	0.75	10.0	2.0	2.0	Med-Low	Low	Yes	0.06	Acquired
SACQ07A	60.0	0.75	10.0	2.0	2.0	Med-Low	Low	Yes	0.06	Acquired
SACQ08A	45.0	0.75	10.0	2.0	2.0	Med-Low	Low	Yes	0.14	Acquired
SACQ10A	45.0	0.5	10.0	2.0	2.0	Med-Low	Low	Yes	0.09	Acquired
SACQ11A	45.0	1.0	10.0	2.0	2.0	Med-Low	Low	Yes	0.18	Acquired
SACQ12A	45.0	1.0	45.0	2.0	2.0	Med-Low	Low	Yes	0.07	Acquired
SRACQ01A	45.0	1.0	10.0	2.0	2.0	Med-Low	Low	Yes	0.19	Acquired

TABLE 21. MASS PROPERTIES, -y ARRAY DEPLOYED

I_{xx}	=	150.22 slug ft^2
I_{yy}	=	104.60 slug ft^2
I_{zz}	=	159.68 slug ft^2
I_{xy}	=	1.25 slug ft^2
I_{xz}	=	-0.0168 slug ft^2
I_{yz}	=	3.78 slug ft^2

Transient response of the sun acquisition runs shown in Table 20 are given in Figures 111 through 122. The following are results of the simulation:

- Sun acquisition is achievable in the 0.5 to 1 rpm range at SL/SV angles of 90 deg $\pm$ 45 deg. Since acquisition was achievable over such a large SL/SV range, we did not attempt to find the boundary condition (January 1976 acquisition simulations in the two-array deployed condition indicated that acquisition was not achieved at the 30 deg SL/SV angle).
- Run SACQ03A, Figure 113, resulted in sun acquisition but loss of earth pointing. This was attributed to the low sensor gain (0.4 of nominal) which results in a peak signal of 1.6 deg output from the earth sensor. Since the turn-on signal of the jets is 2.0 deg, the controller can get into a condition where the sensor is saturated; this destroys the lead in the loop, and the jets remain off. We had been advised by the contract monitor of the interpretation of the earth sensor output as described in Section III. We felt, however, that use of the raw data as given in the curves was too pessimistic and, hence, we increased the low gain from 0.4 to 0.6 for the remainder of the runs. Interestingly enough, earth acquisition was achievable at the 0.4 earth sensor gain condition. This was because the spinning of the vehicle resulted in continual desaturation of the sensor, thus allowing some control through the lead network. This effect is removed in sun acquisition as the spin rate is reduced.

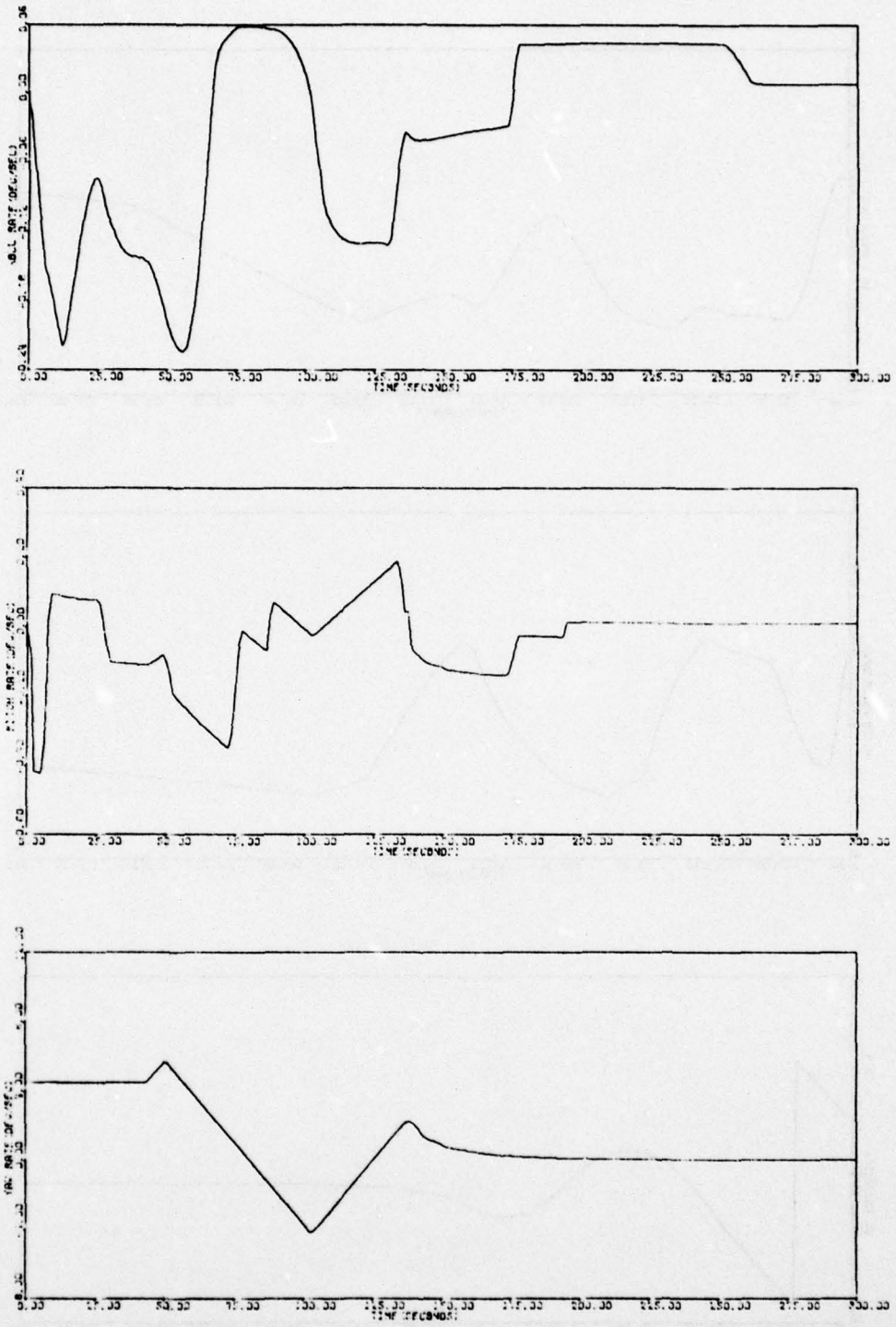

Figure 111. Run SACQ01A

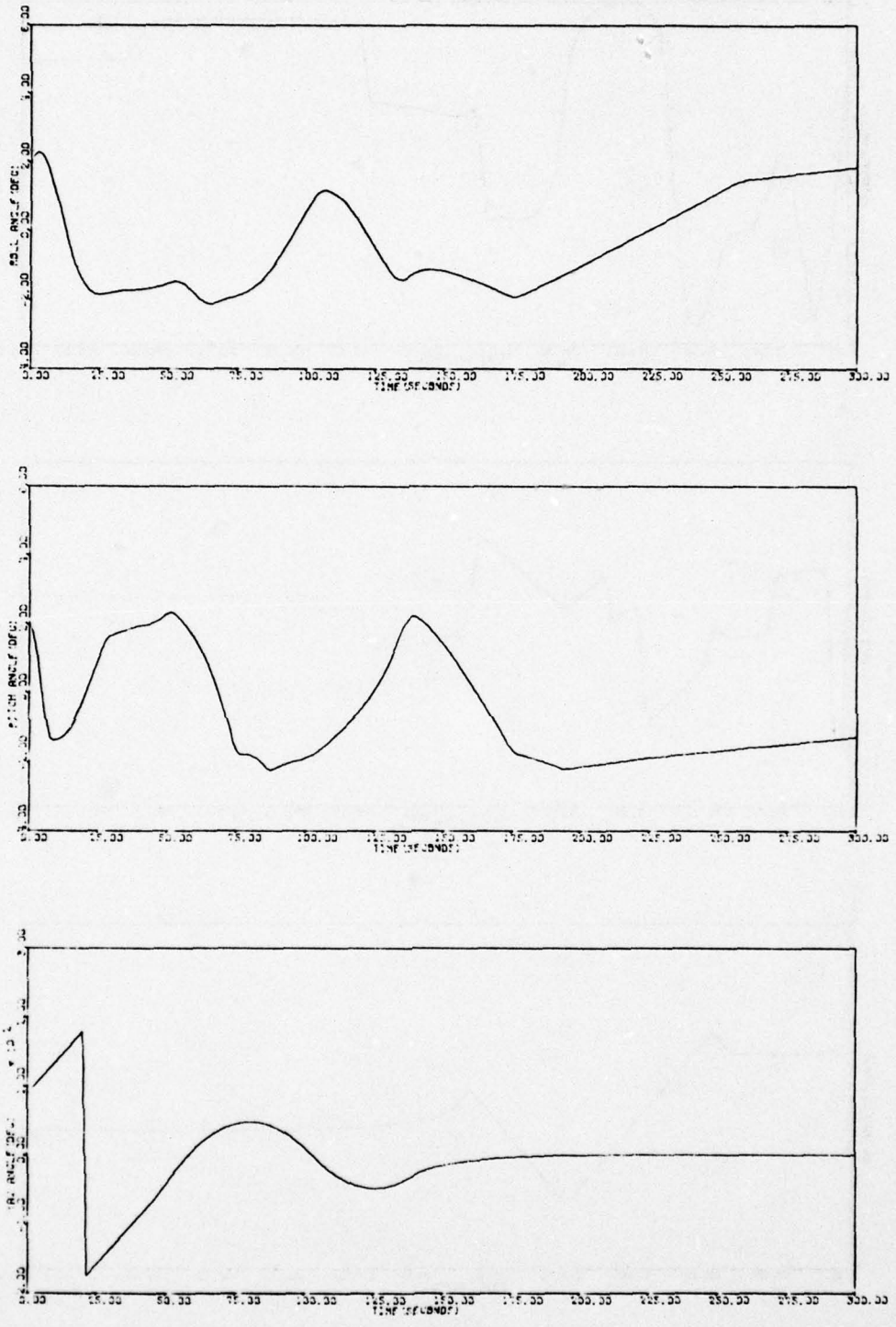

Figure 111. Run SACQ01A (continued)

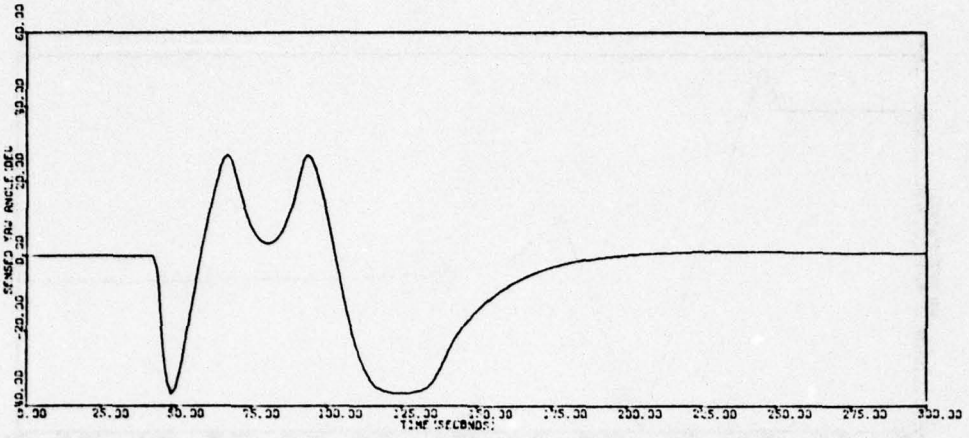

Figure 111. Run SACQ01A (concluded)

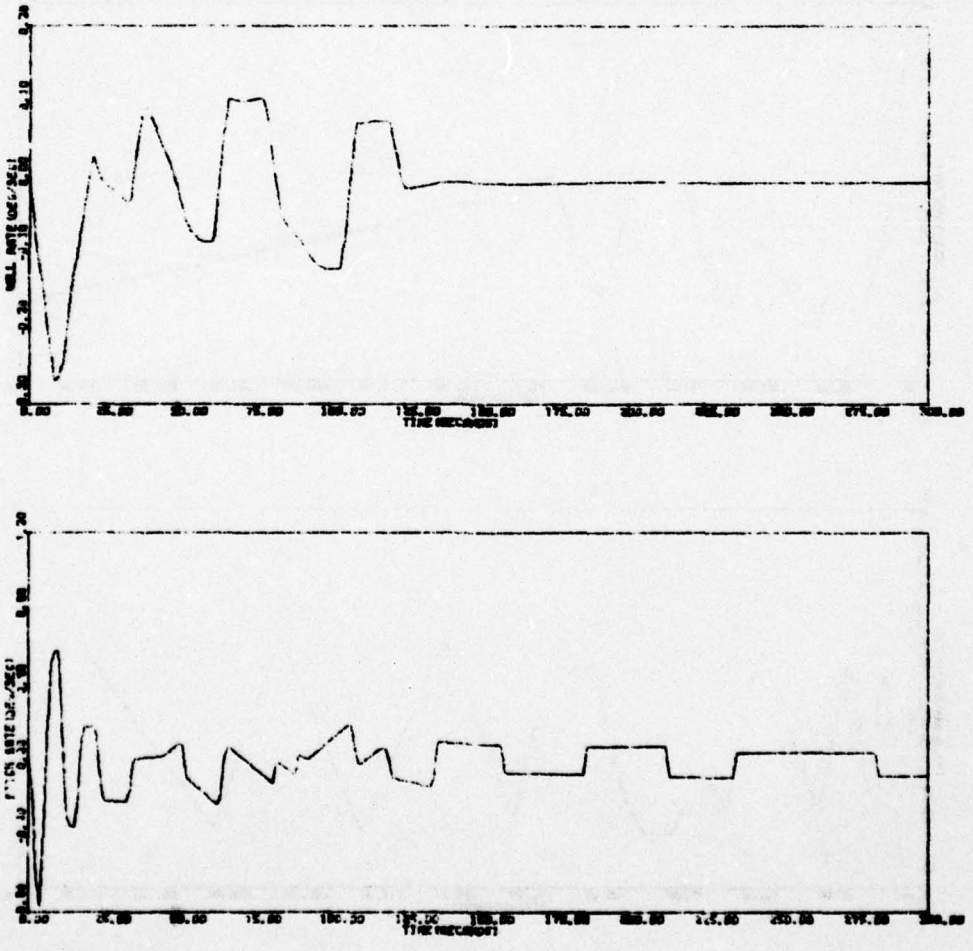

Figure 112. Run SACQ02

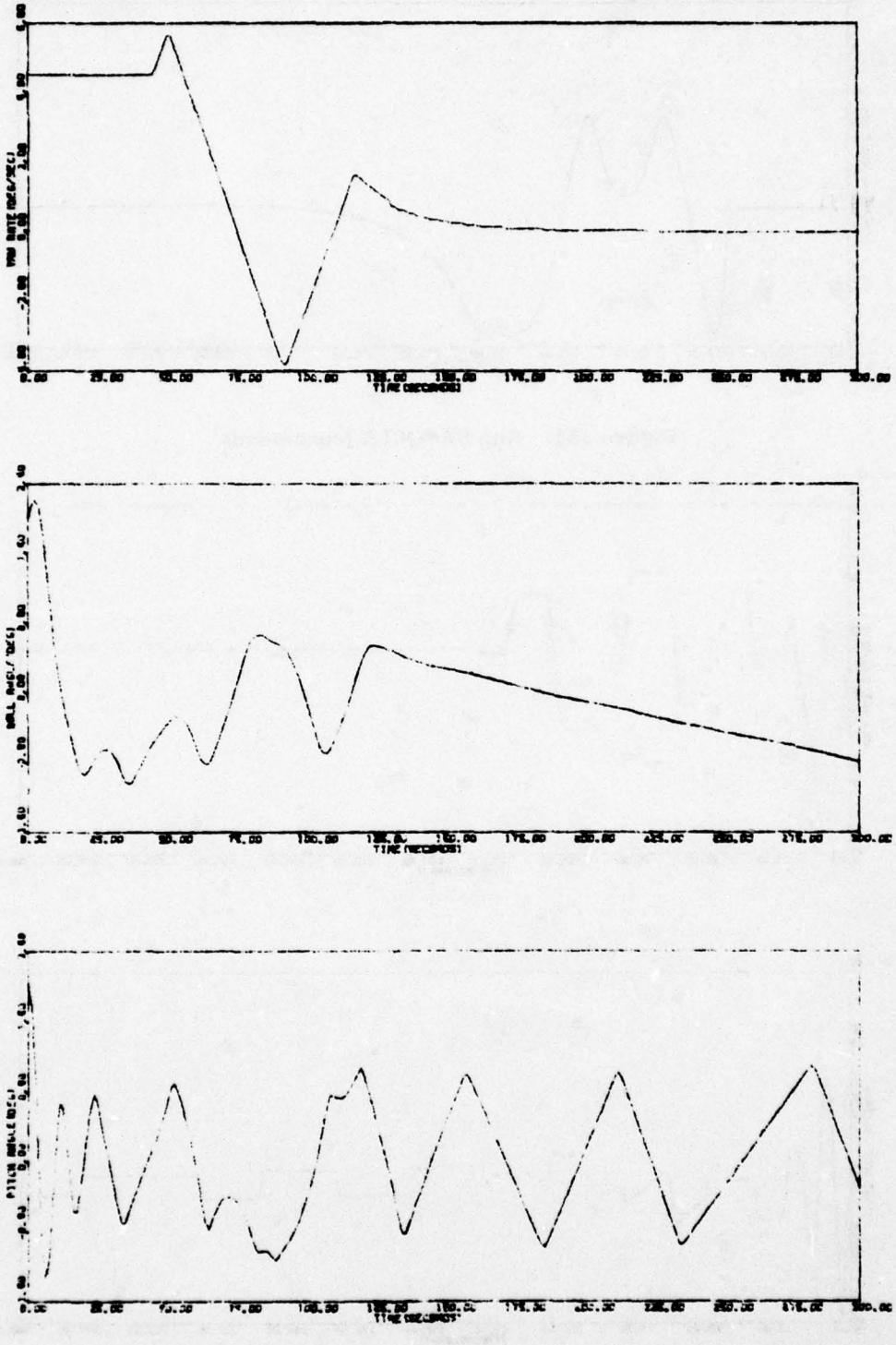

Figure 112. Run SACQ02 (continued)

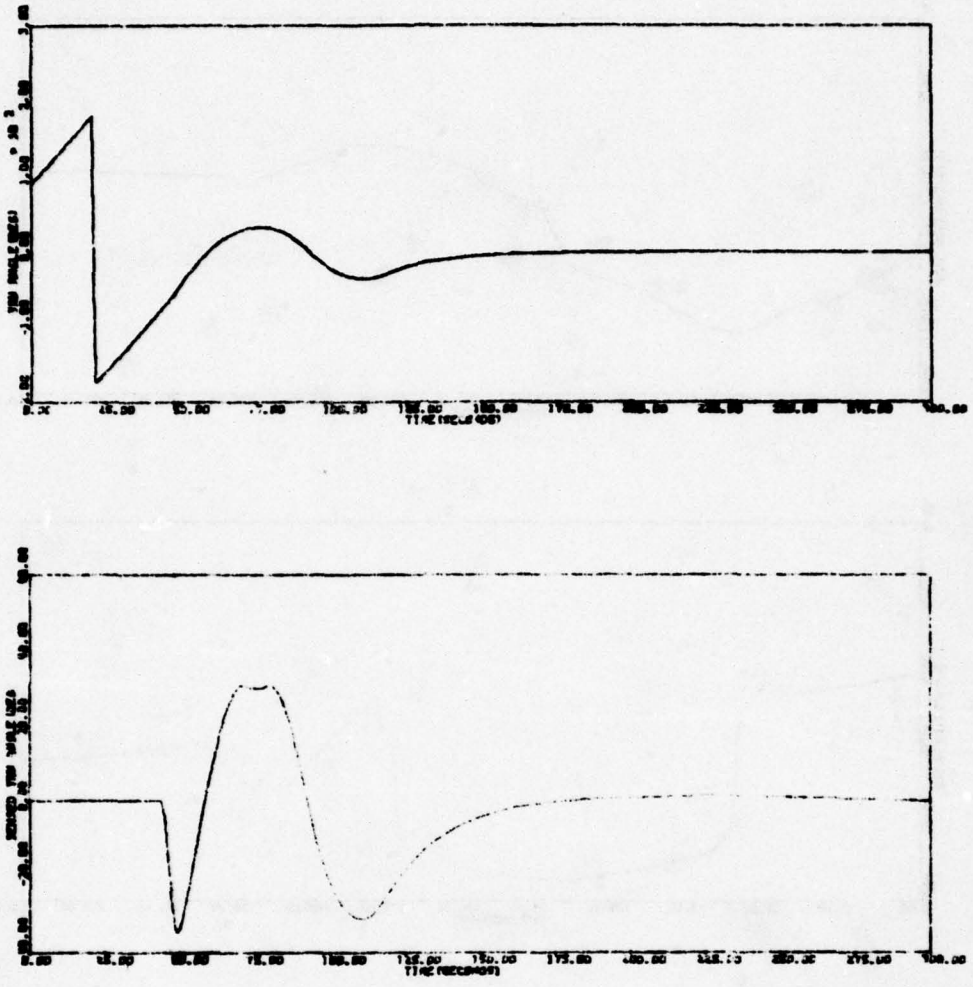

Figure 112. Run SACQ02 (concluded)

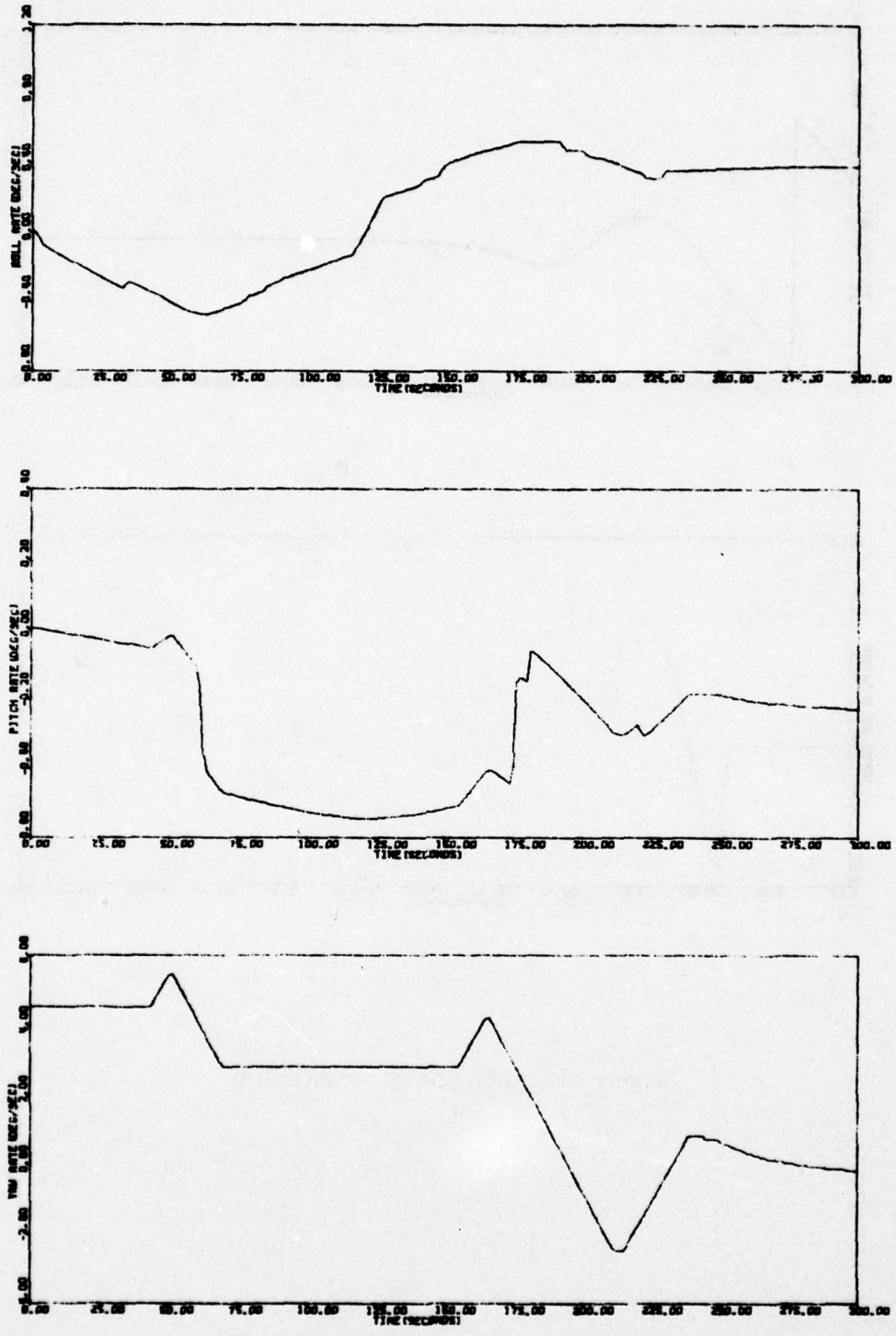

Figure 113. Run SACQ03A

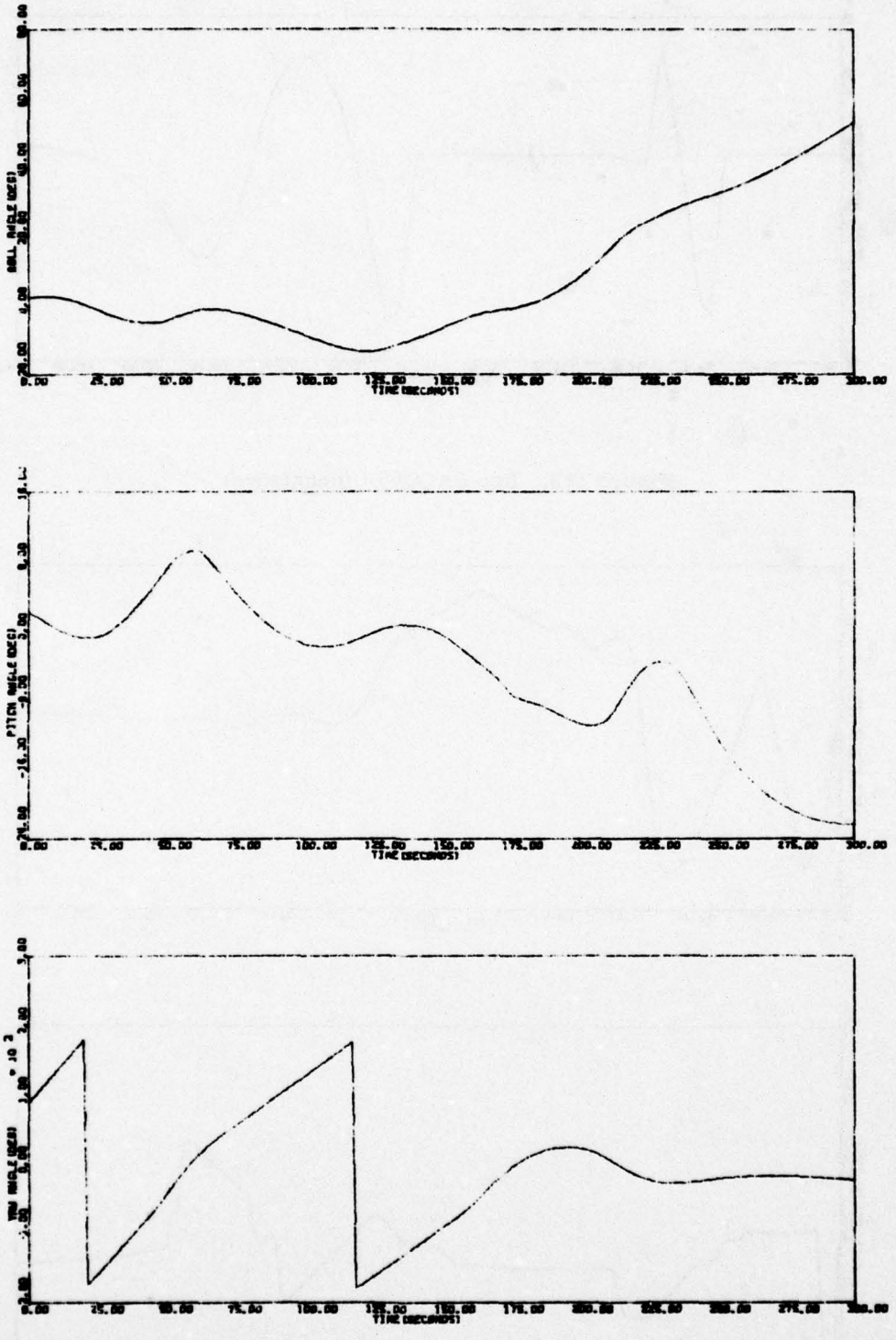

Figure 113. Run SACQ03A (continued)

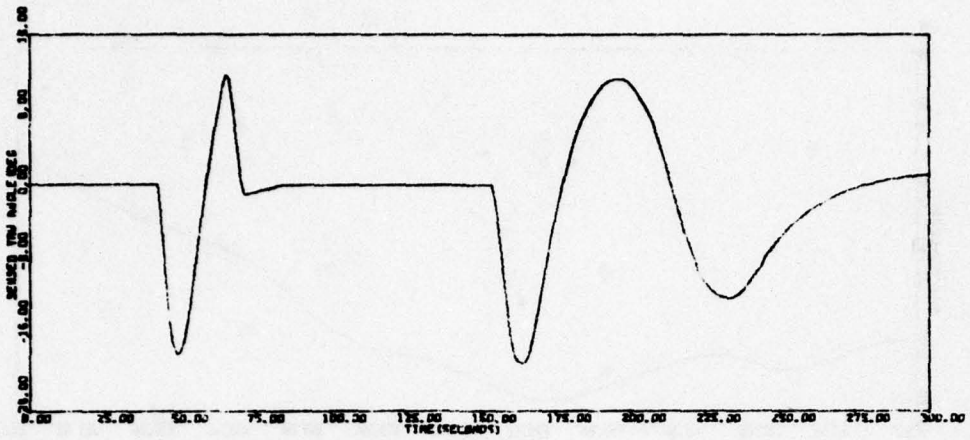

Figure 113. Run SACQ03A (concluded)

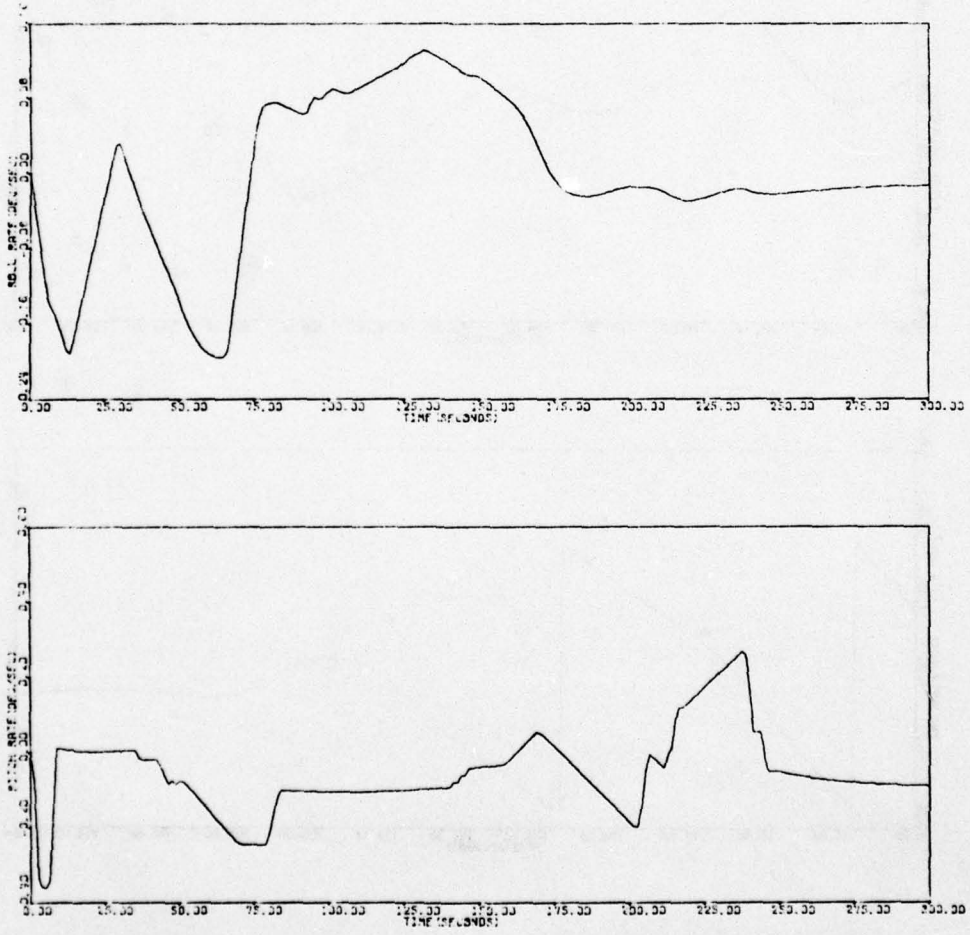

Figure 114. Run SACQ04A

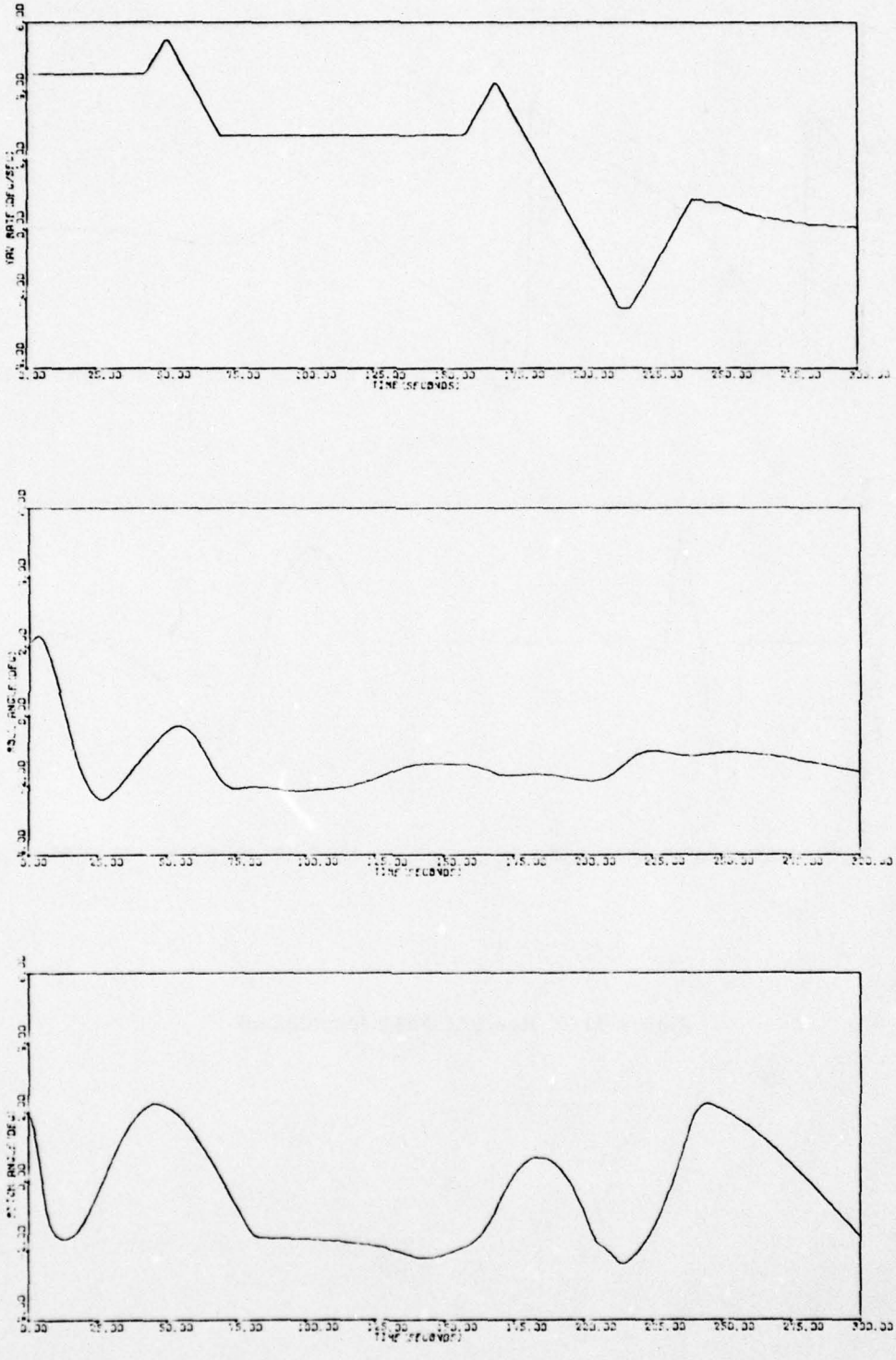

Figure 114. Run SACQ04A (continued)

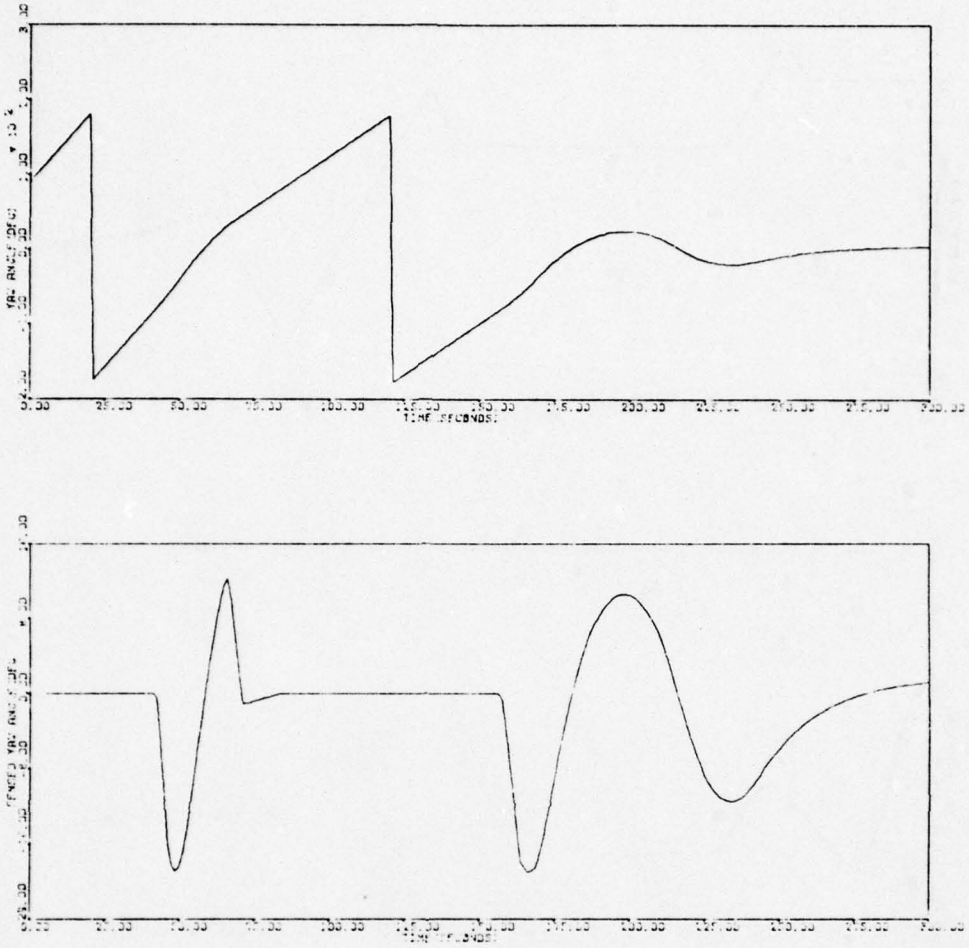

Figure 114. Run SACQ04A (concluded)

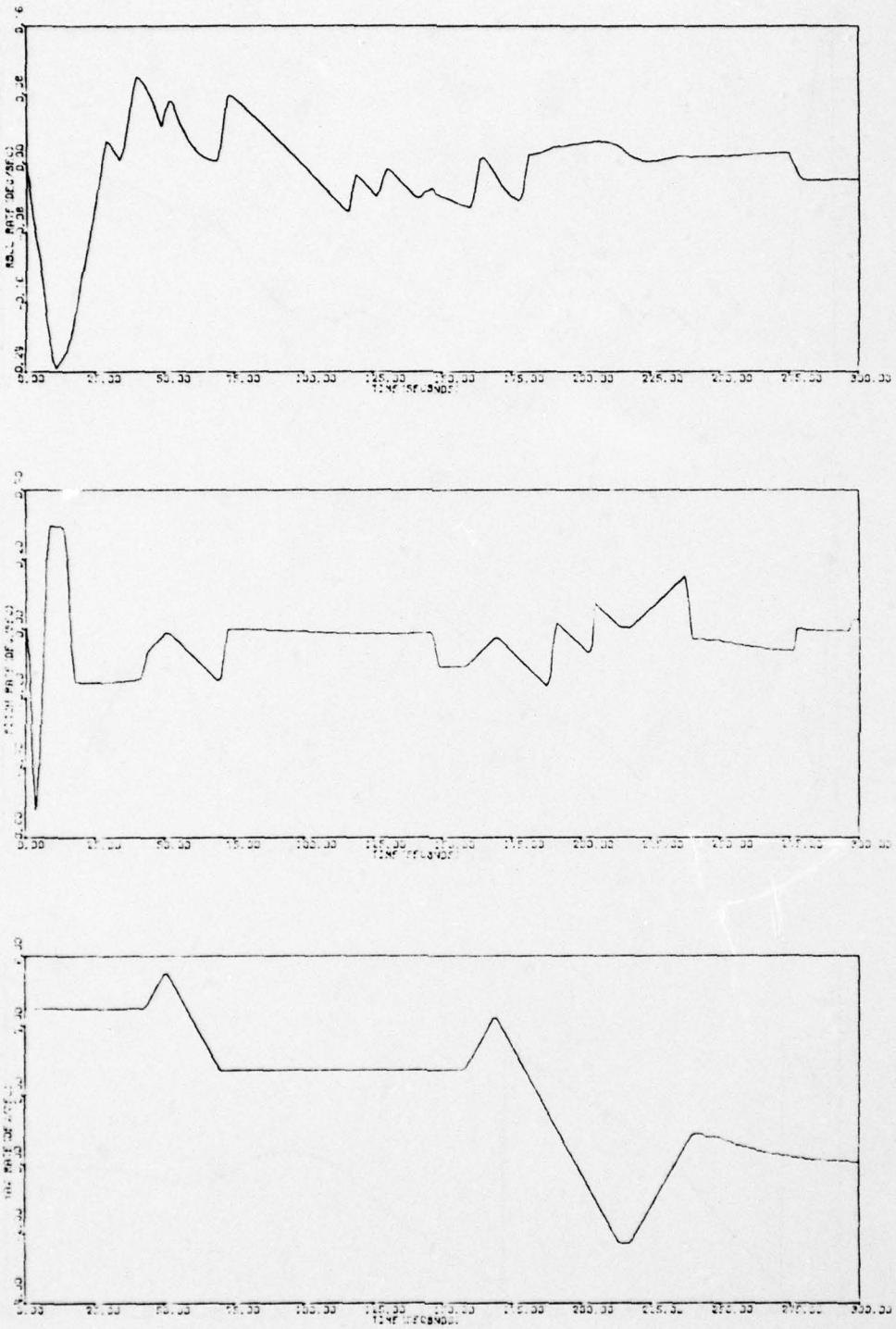

Figure 115. Run SACQ05A

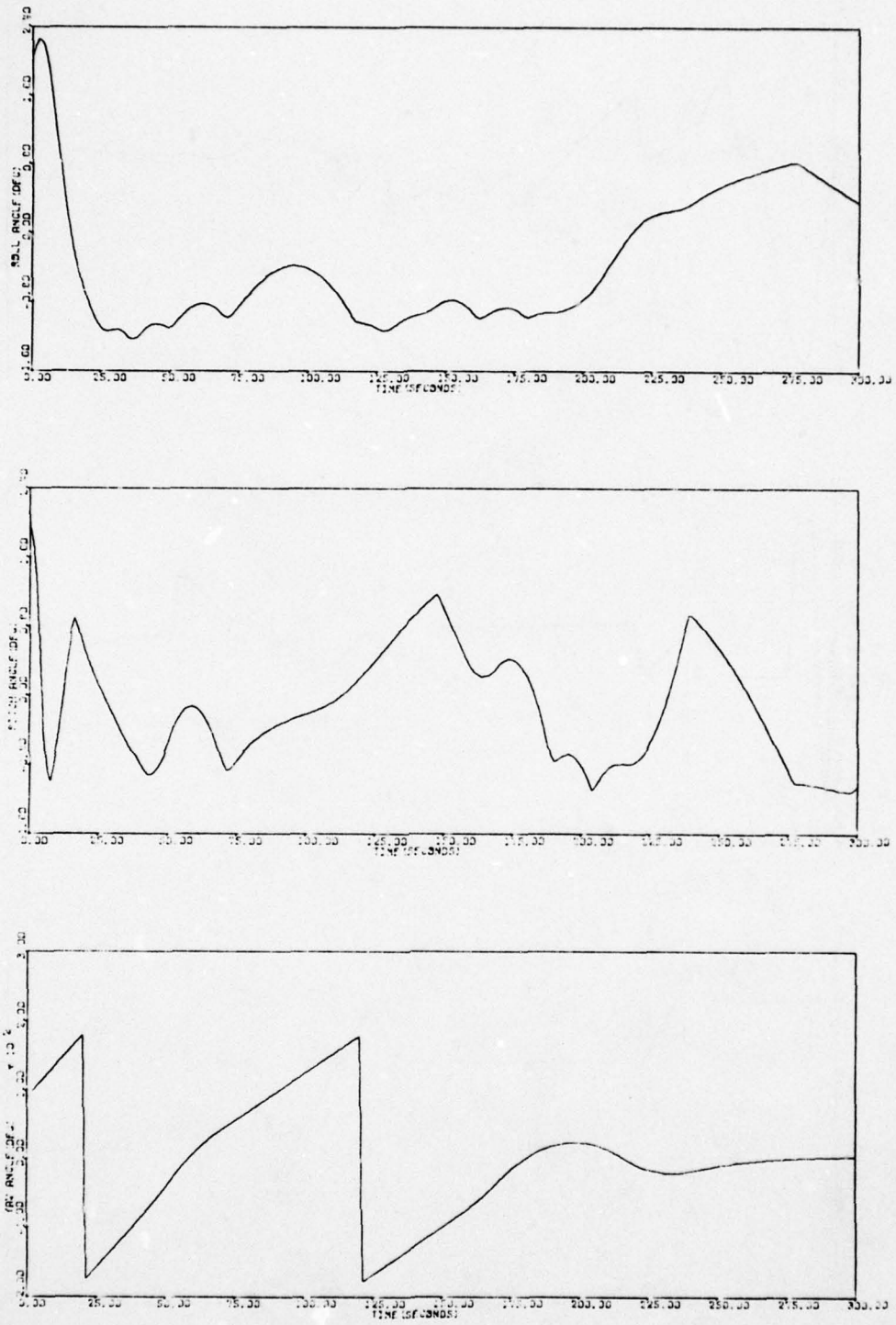

Figure 115. Run SACQ05A (continued)

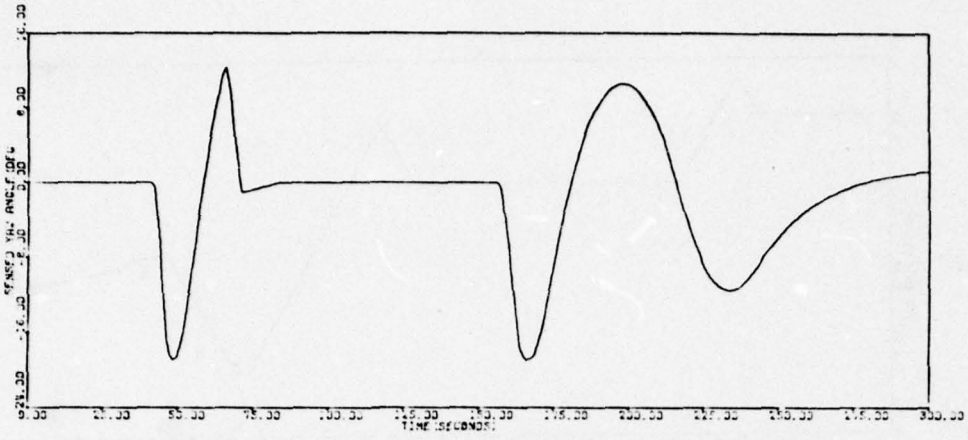

Figure 115. Run SACQ05A (concluded)

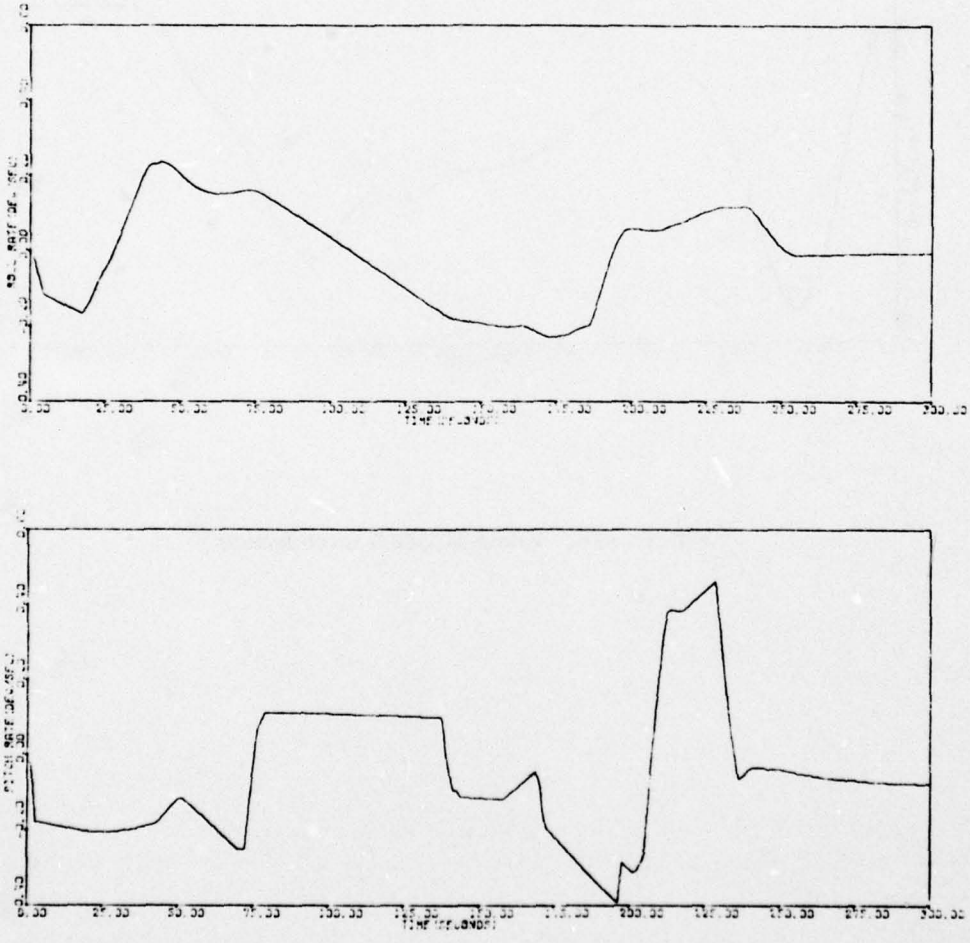

Figure 116. Run SACQ06A

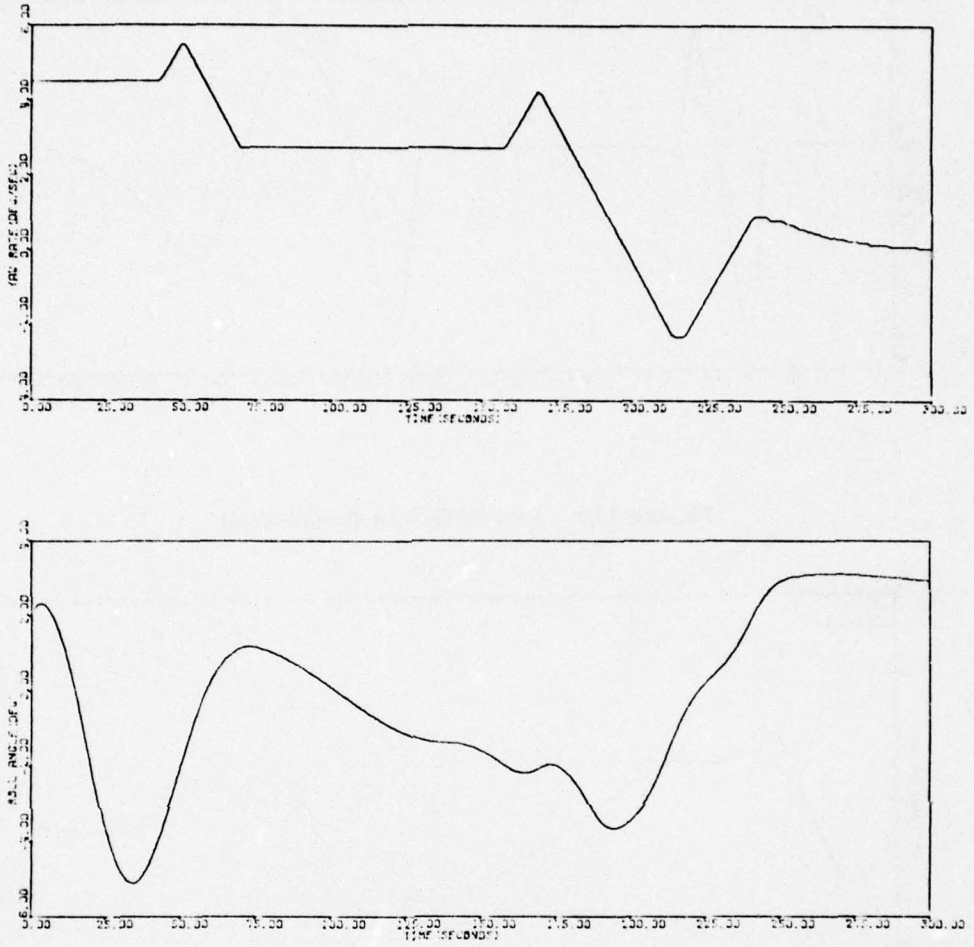

Figure 116. Run SACQ06A (concluded)

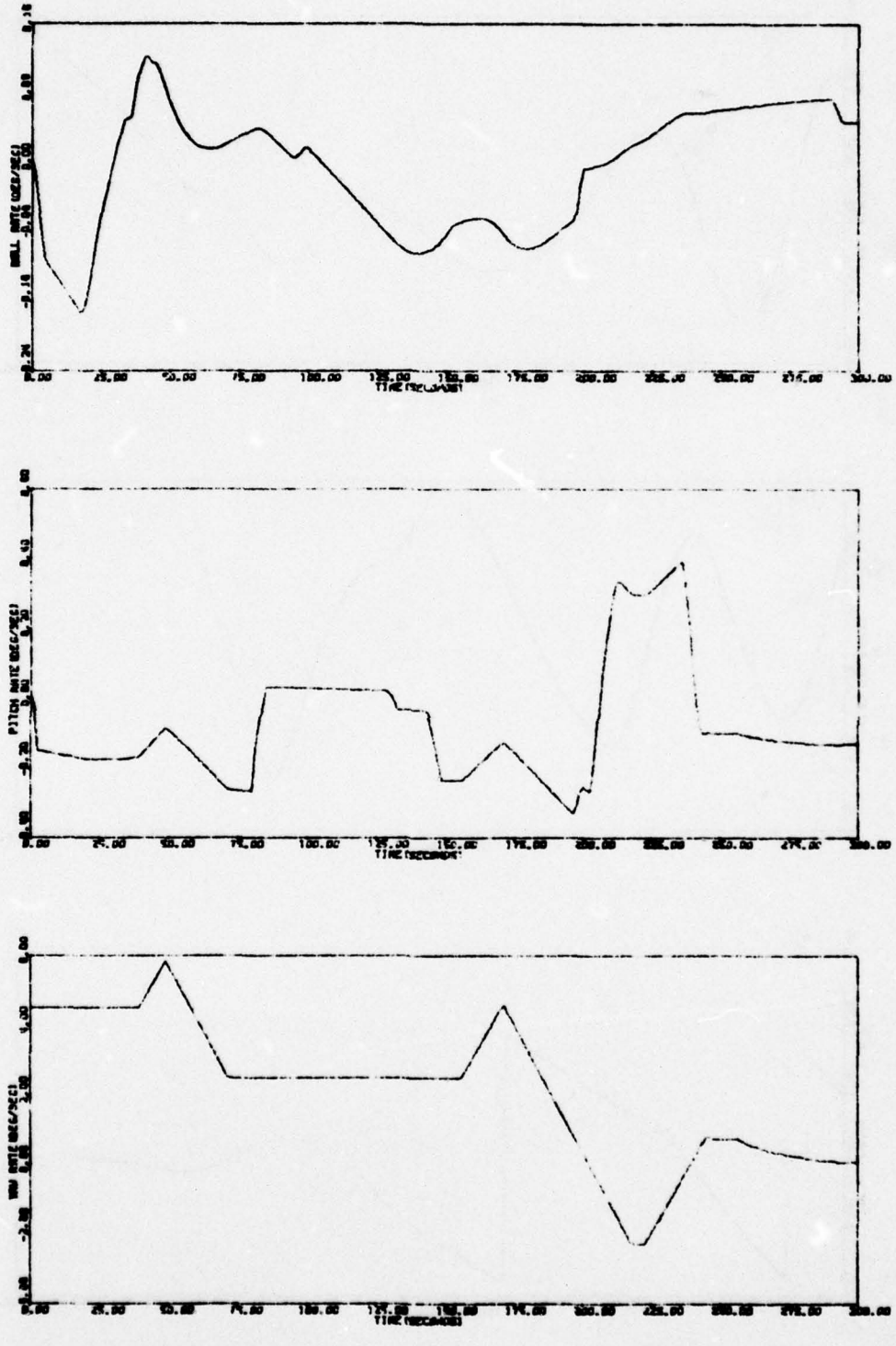

Figure 117. Run SACQ07A

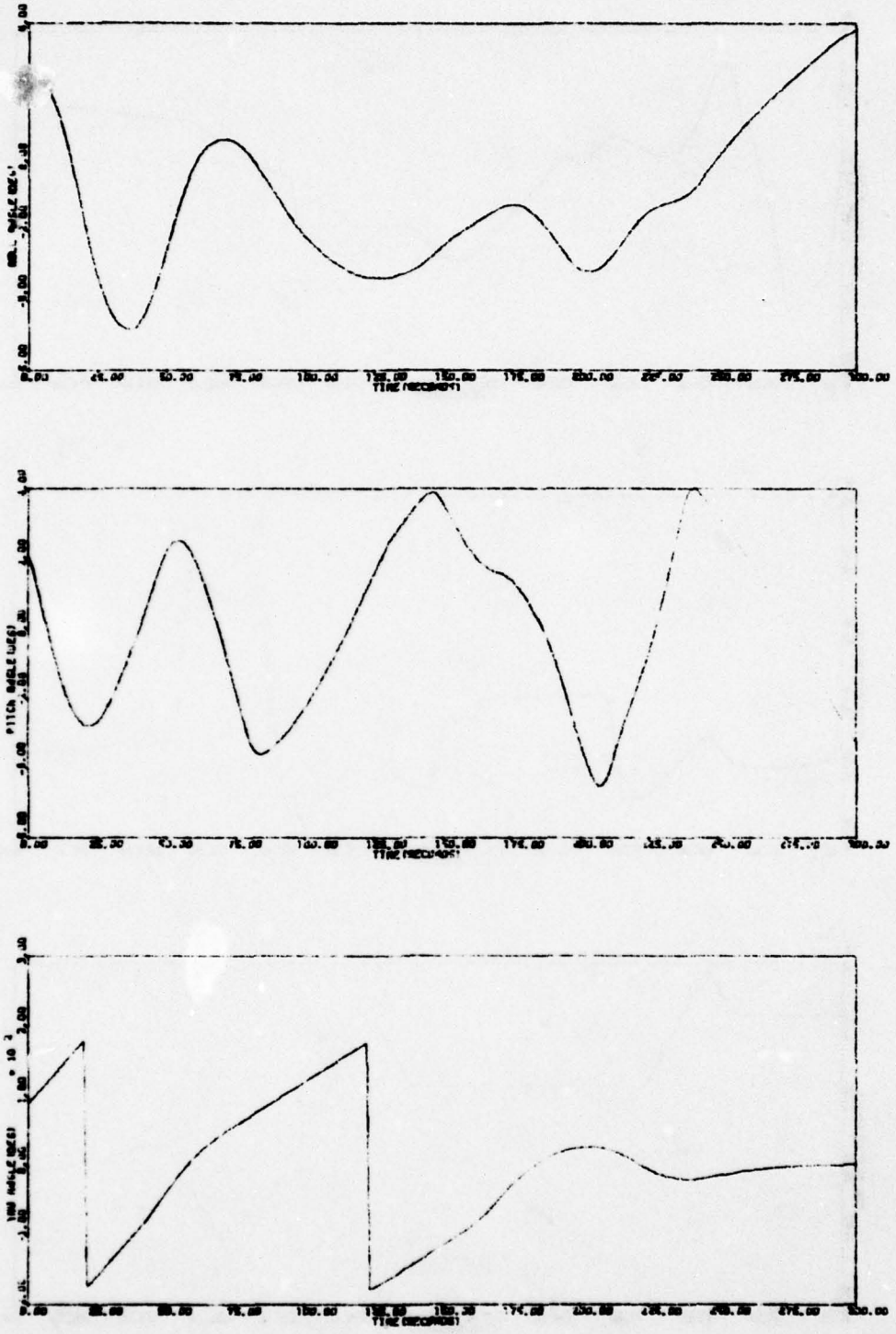

Figure 117. Run SACQ07A (continued)

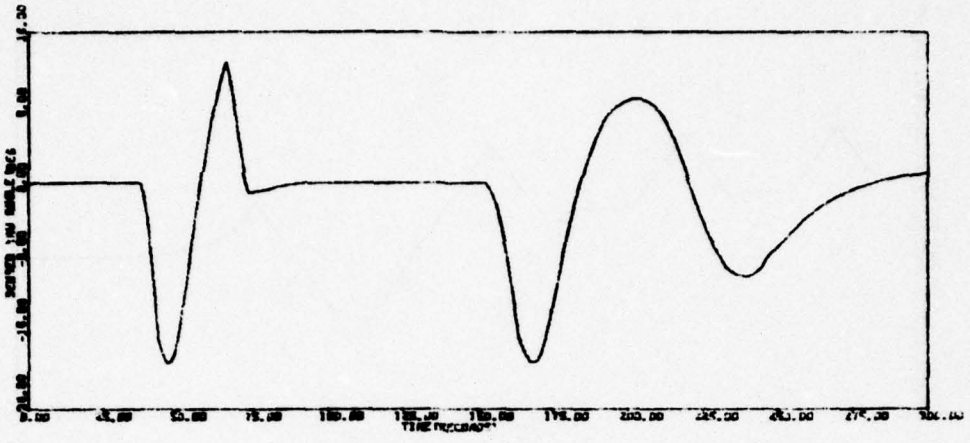

Figure 117. Run SACQ07A (concluded)

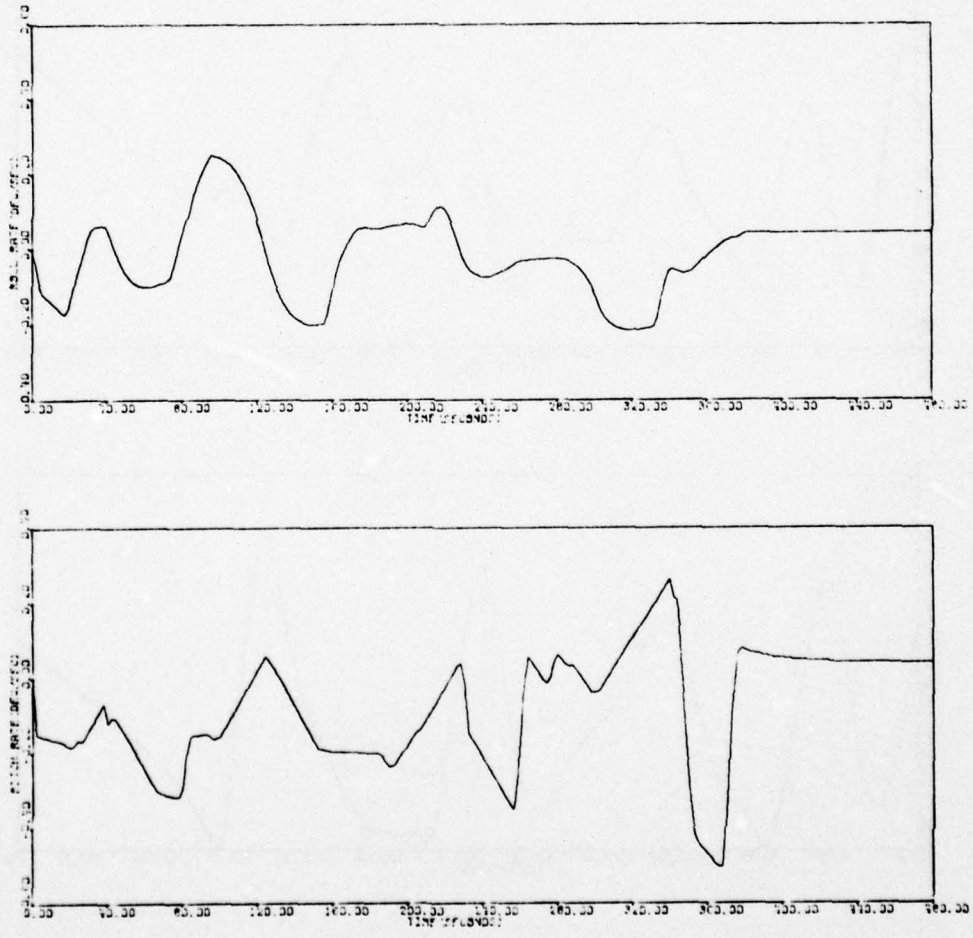

Figure 118. Run SACQ08A

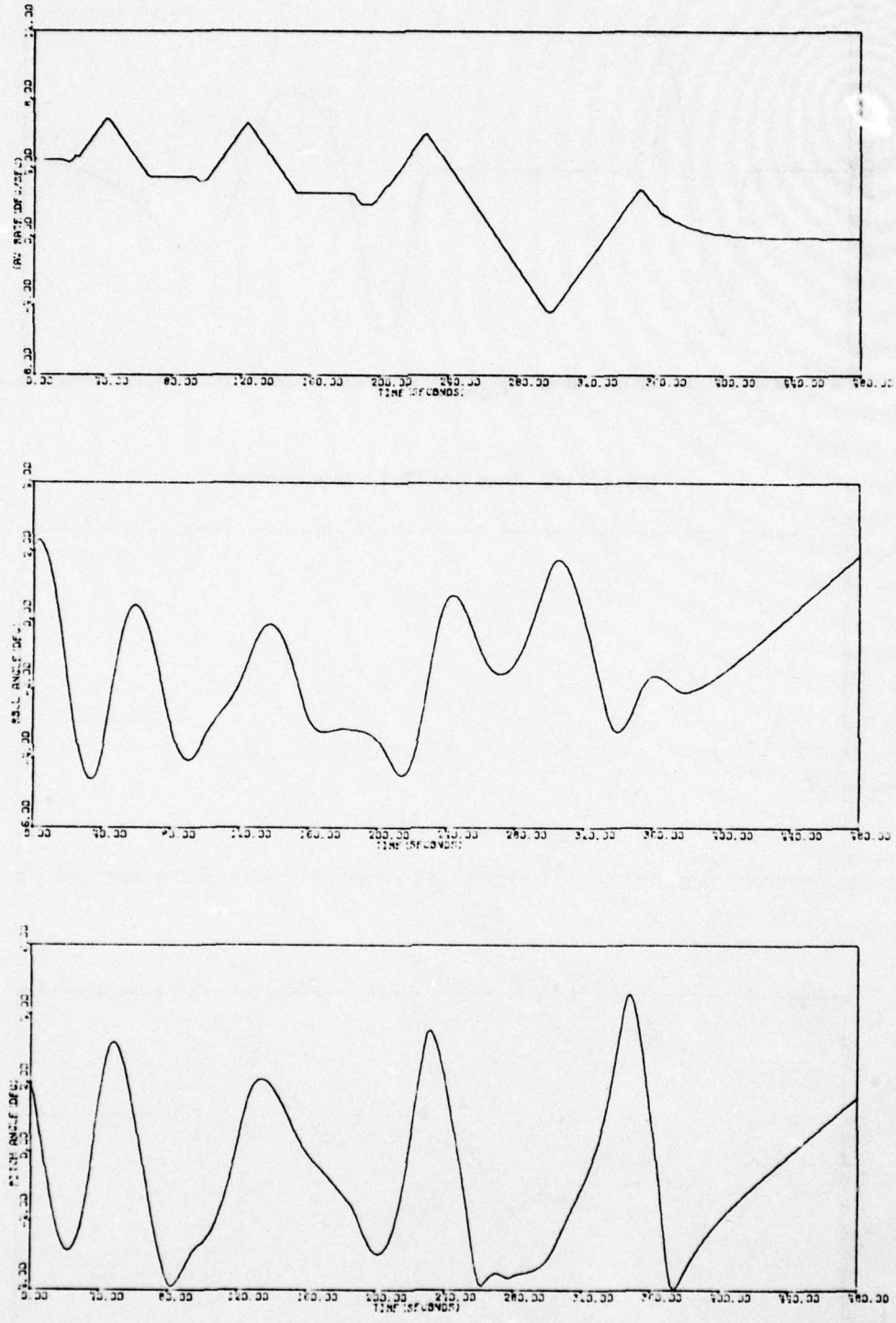

Figure 118. Run SACQ08A (continued)

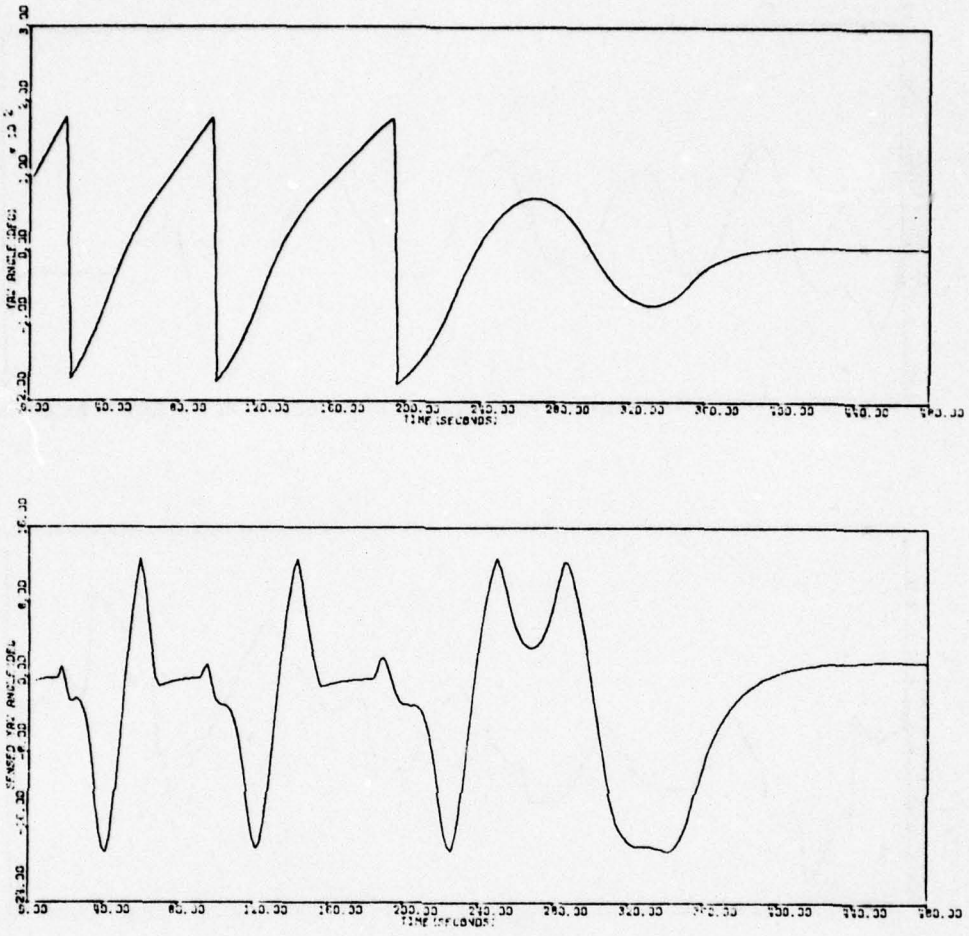

Figure 118. Run SACQ08A (concluded)

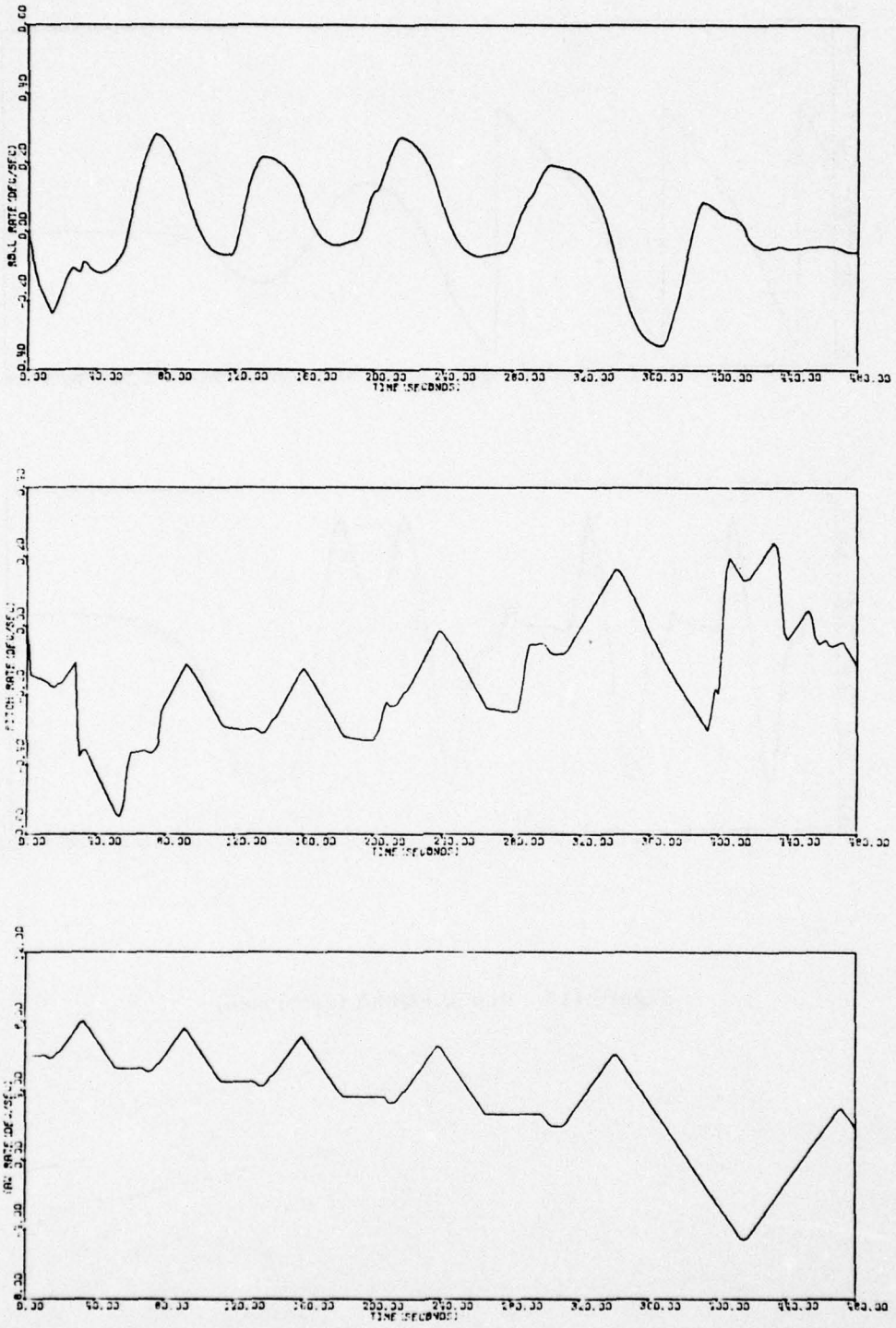

Figure 119. Run SACQ09A

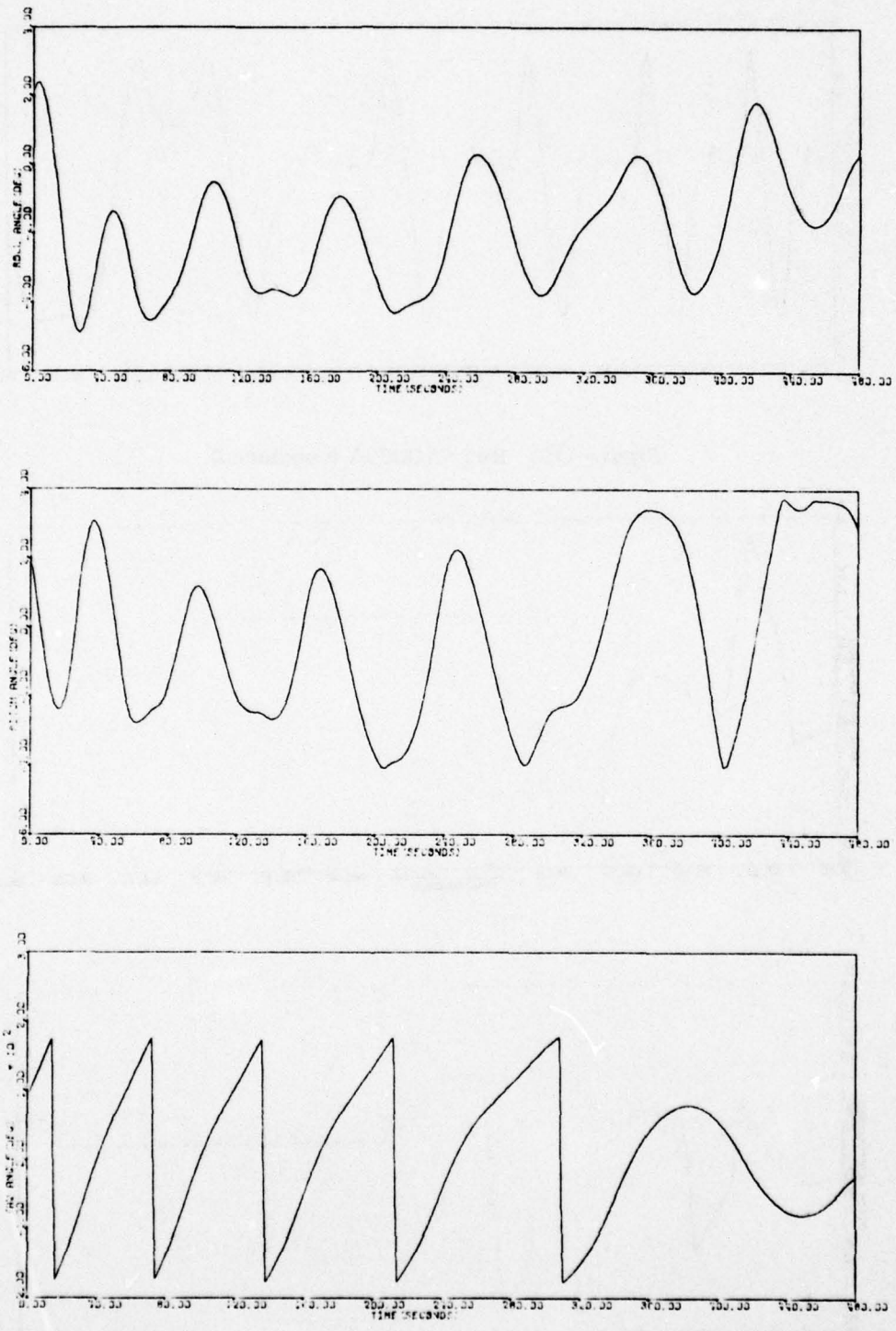

Figure 119. Run SACQ09A (continued)

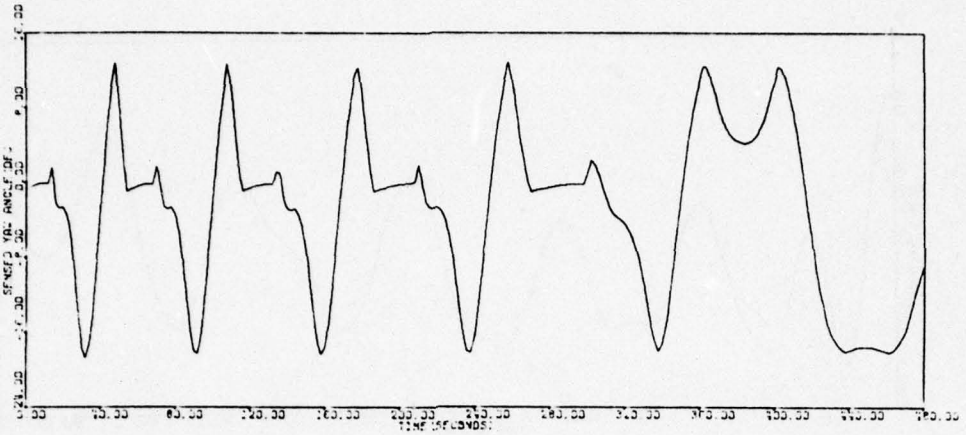

Figure 119. Run SACQ09A (concluded)

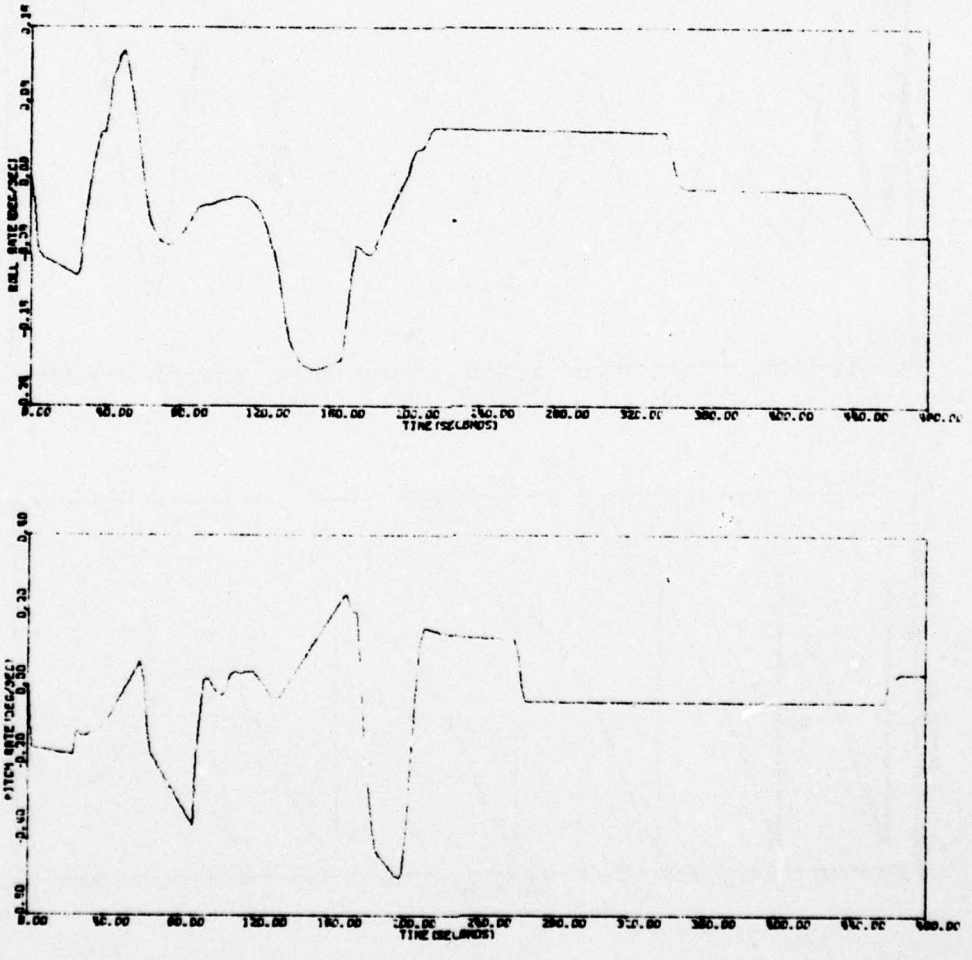

Figure 120. Run SACQ10A

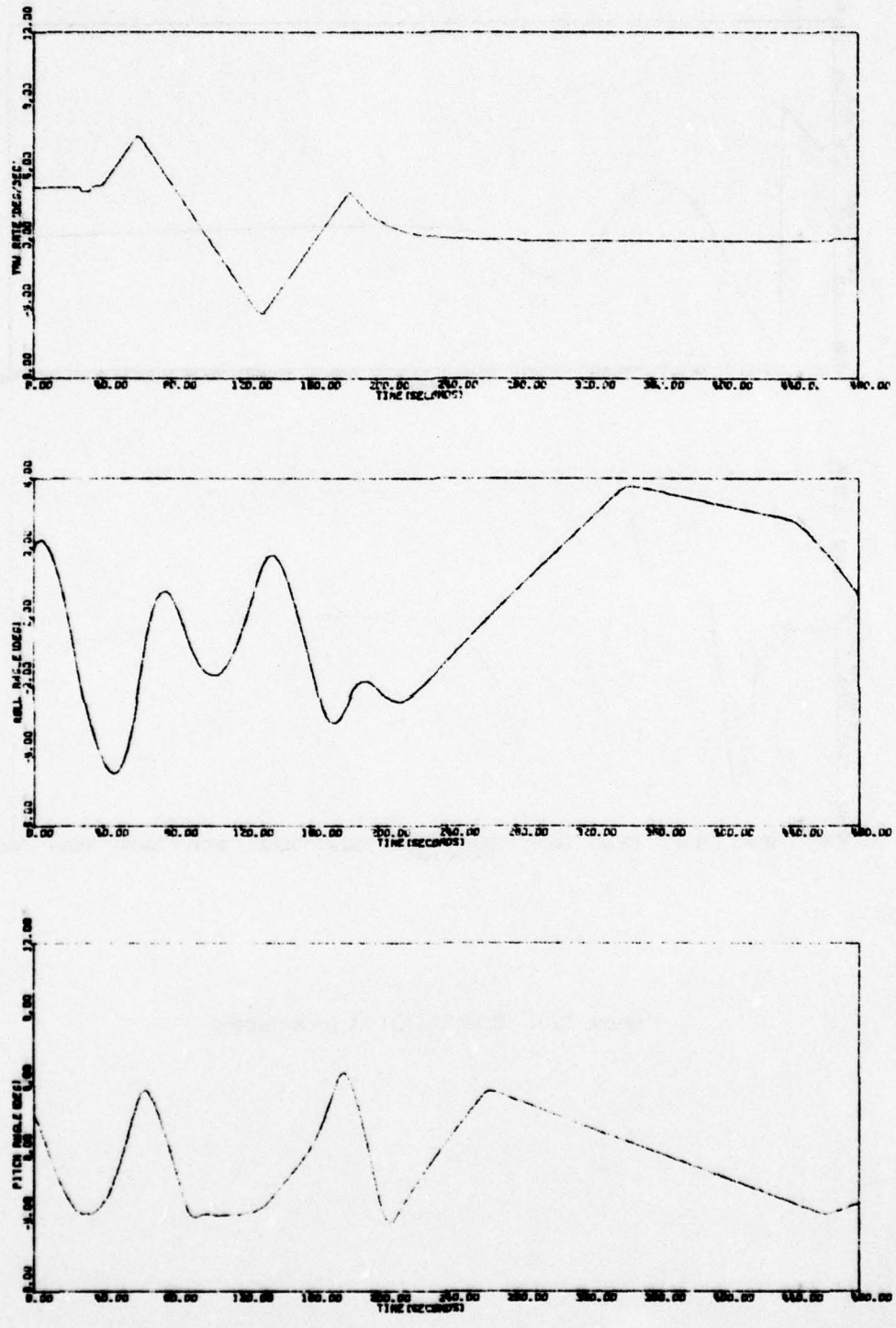

Figure 120. Run SACQ10A (continued)

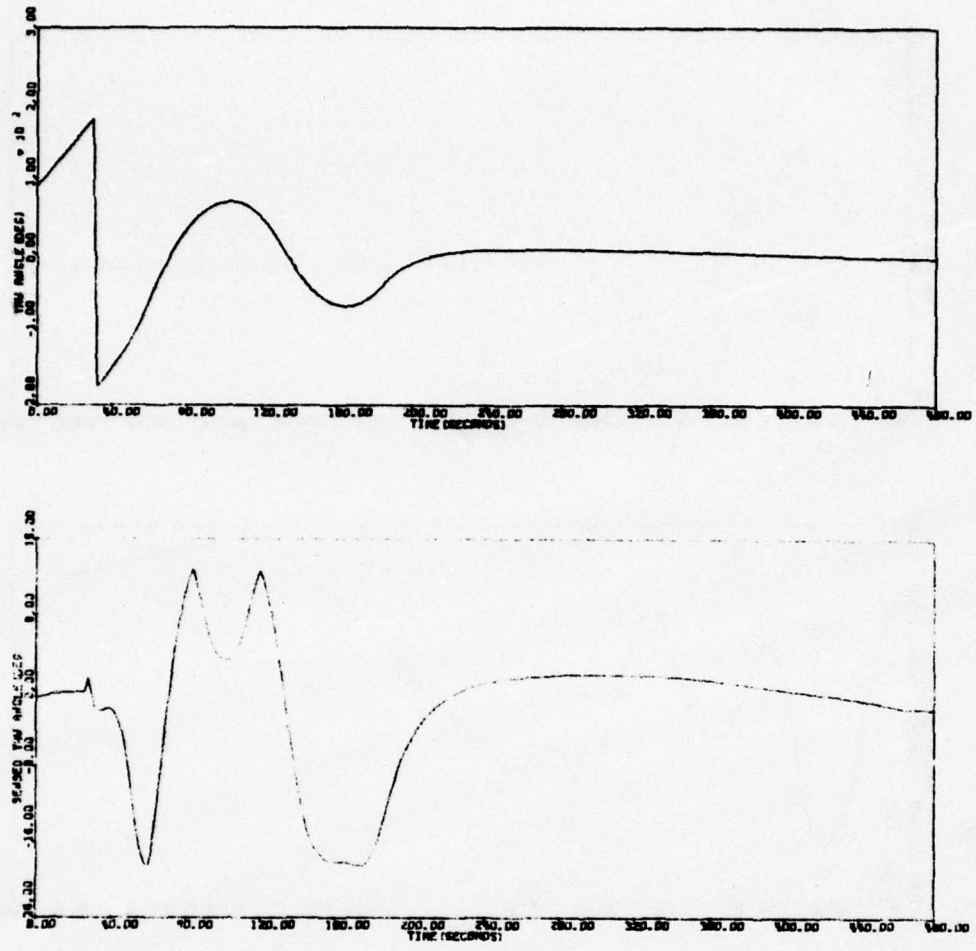

Figure 120. Run SACQ10A (concluded)

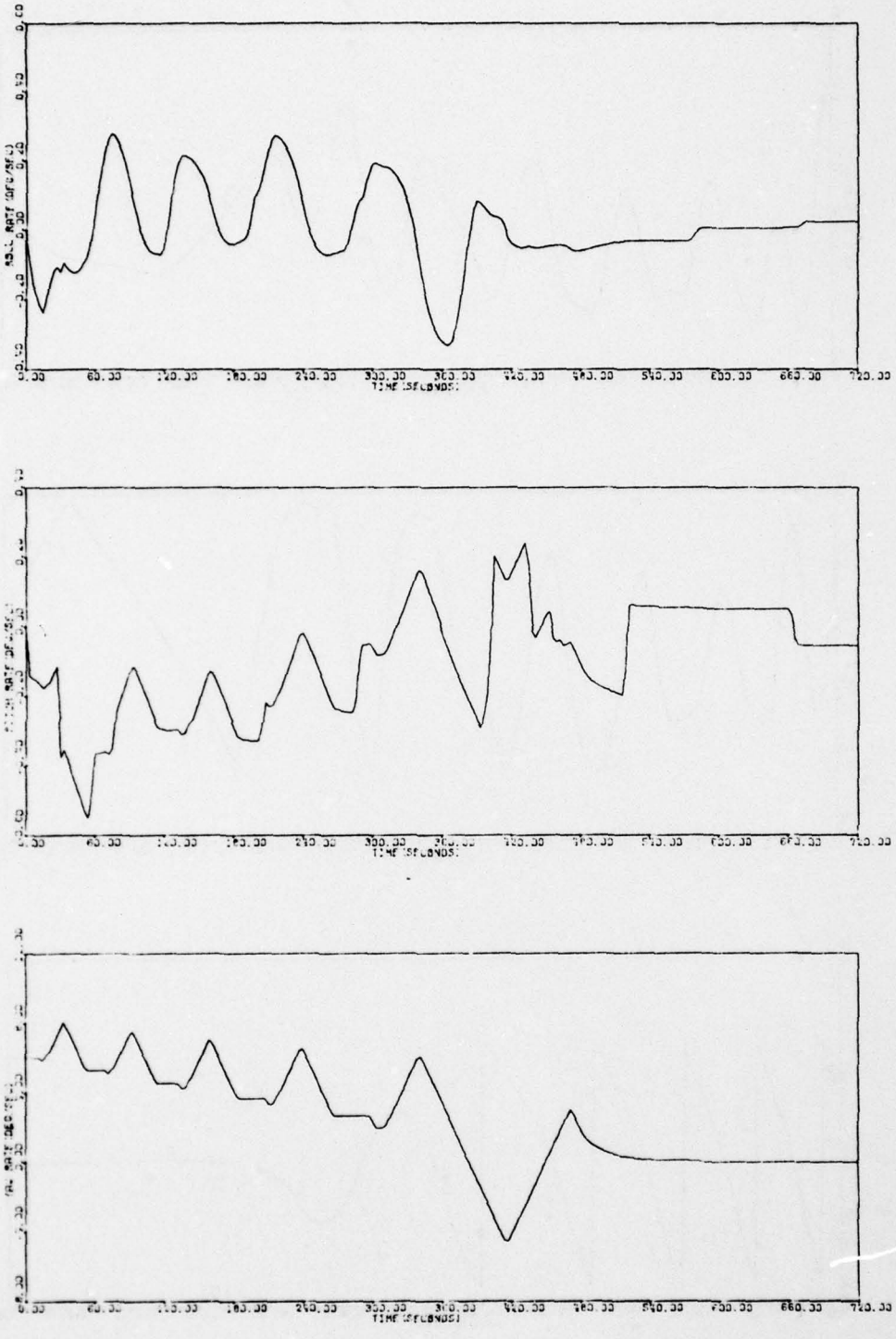

Figure 121. Run SACQ11A

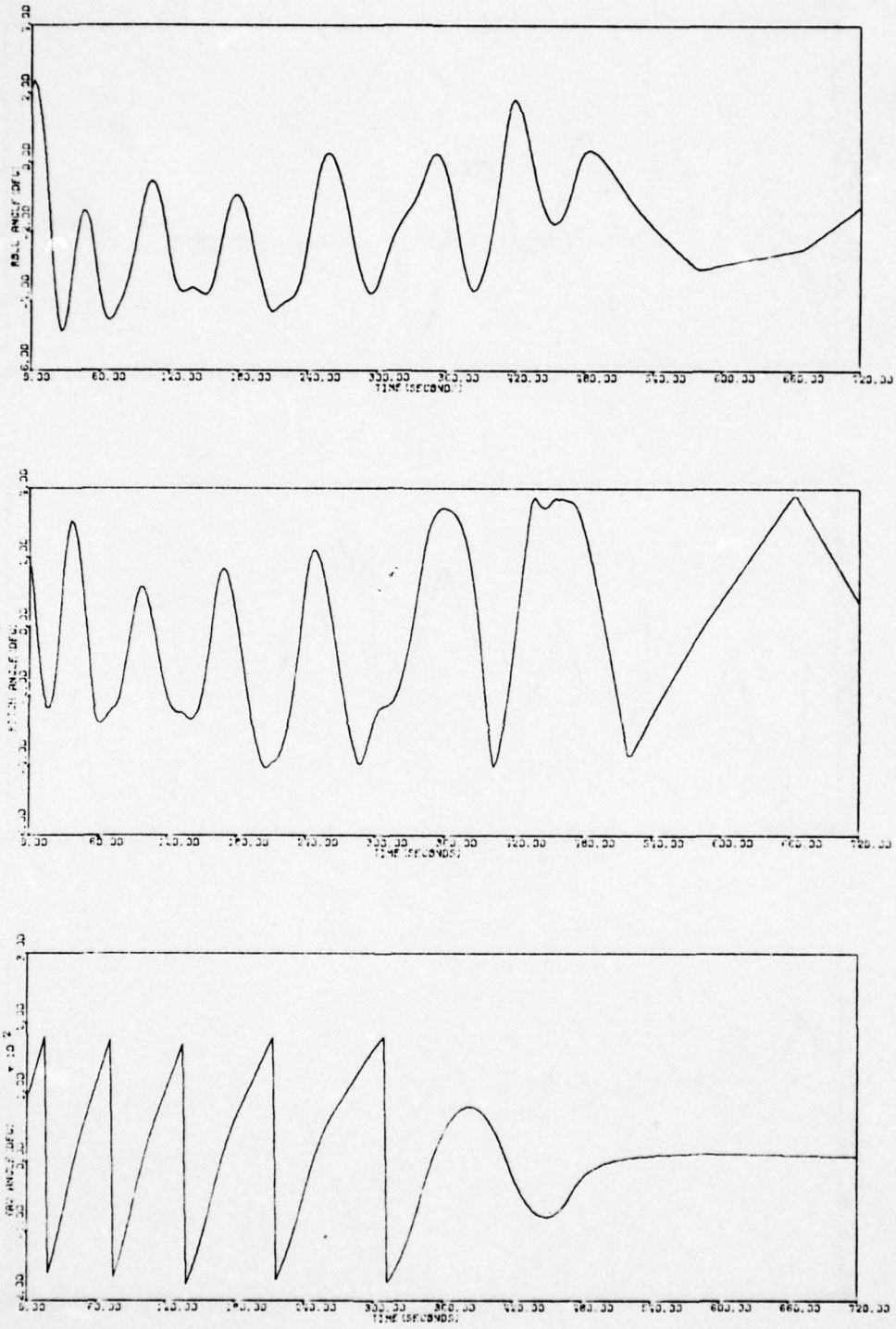

Figure 121. Run SACQ11A (continued)

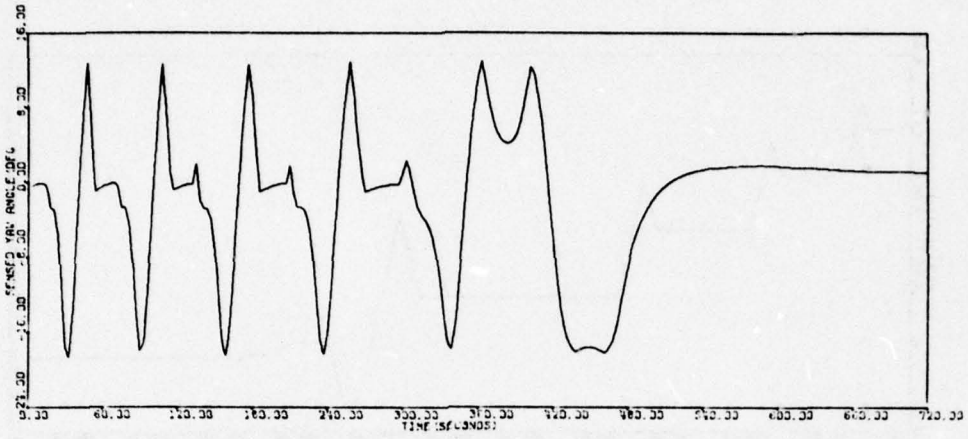

Figure 121. Run SACQ11A (concluded)

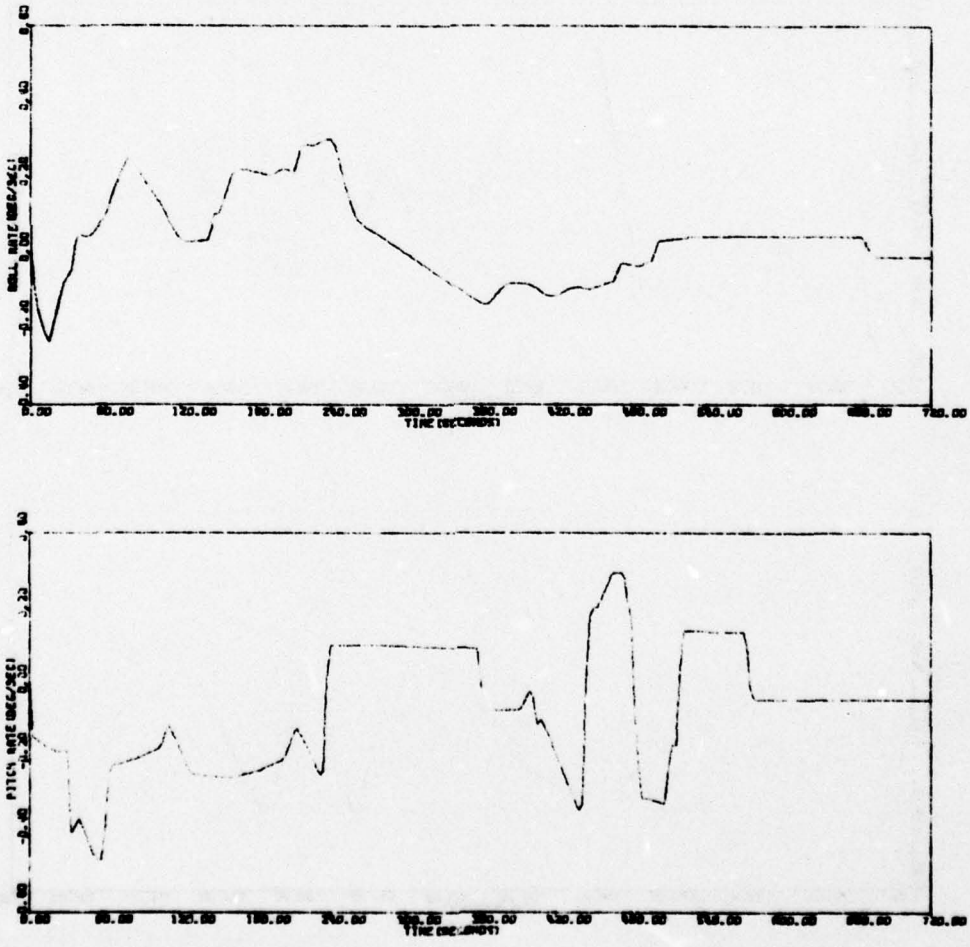

Figure 122. Run SACQ12A

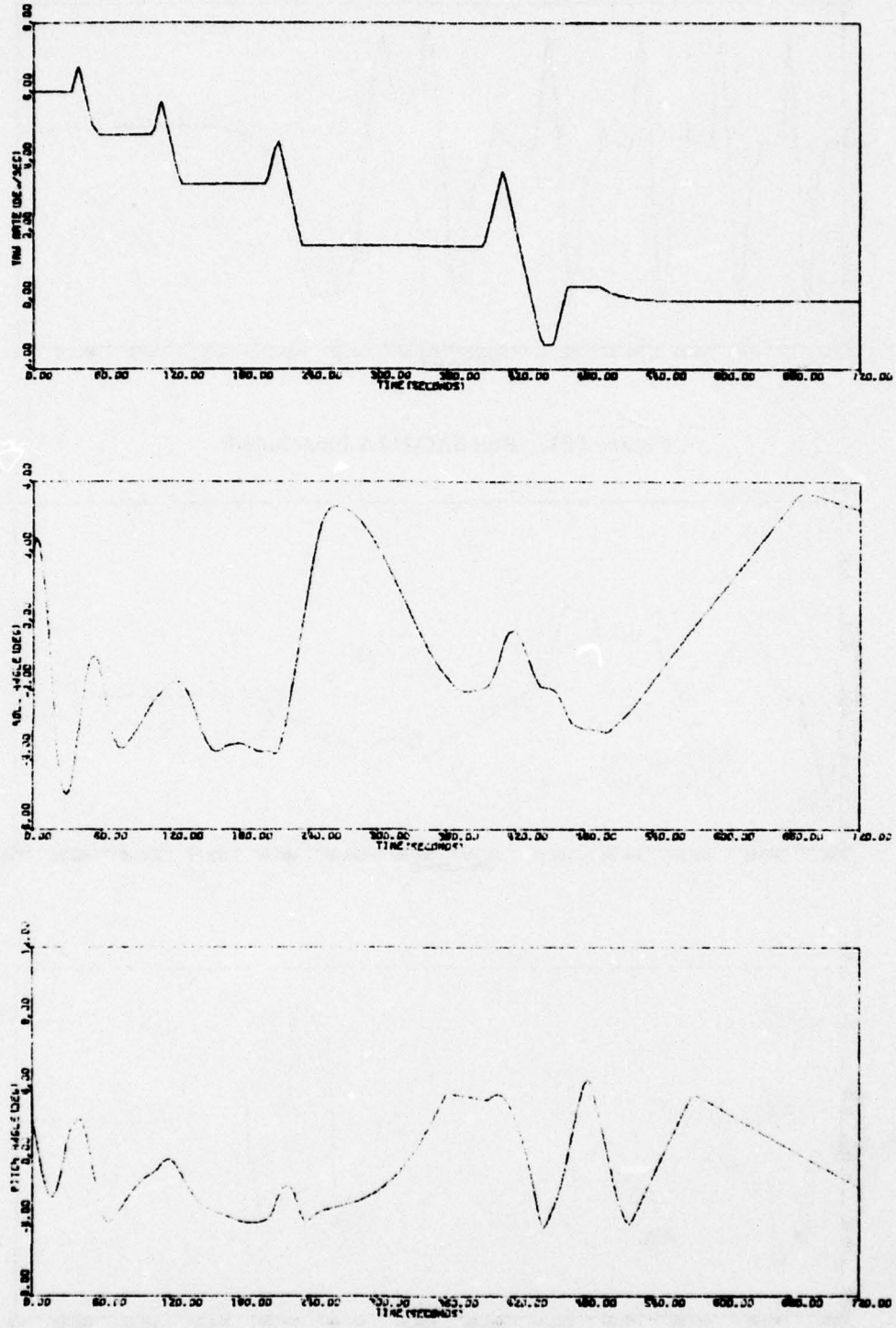

Figure 122. Run SACQ12A (continued)

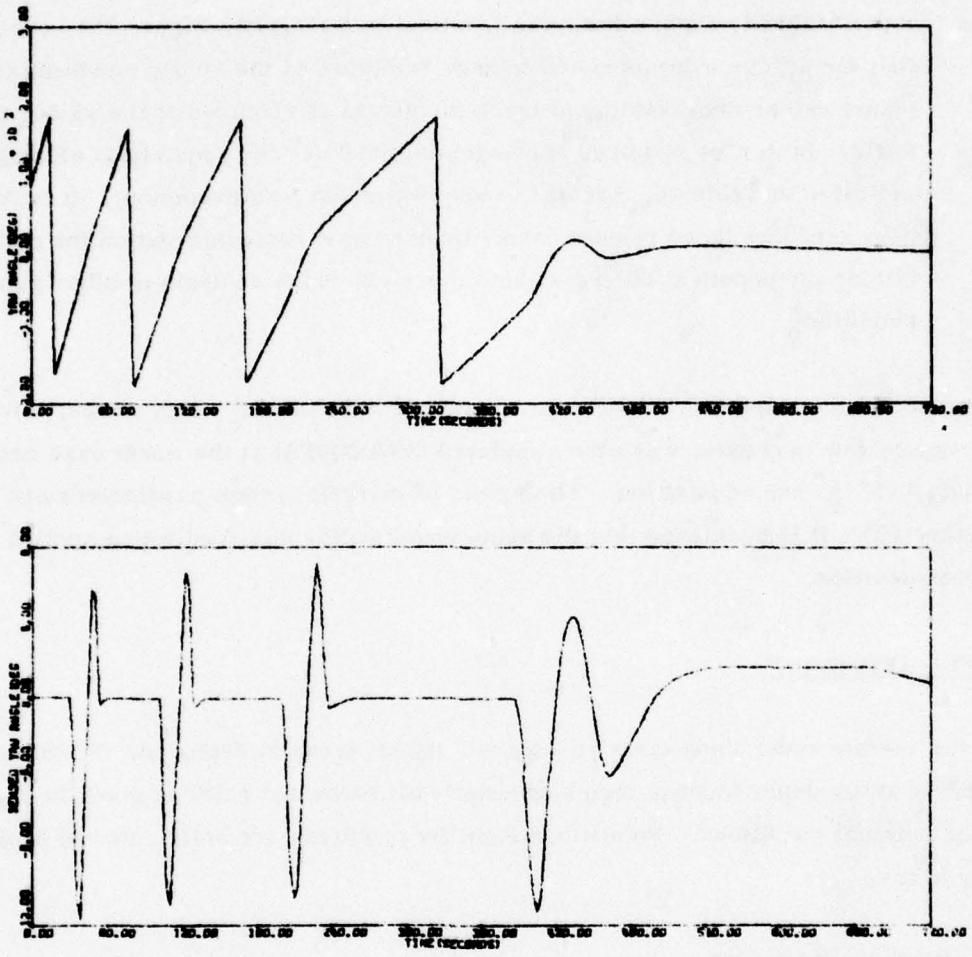

Figure 122. Run SACQ12A (concluded)

- Run SACQ12A, Figure 122, was identical to SACQ11A, Figure 121, except that the arrays were assumed to have remained at the 90 deg condition (in yz plane) rather than rotating to track the sun as is required at the 45 deg SL/SV angle. Both runs required approximately 500 sec for acquisition although, as indicated in Table 20, SACQ12A took 50 percent less propellant. It is felt, however, that these results cannot be used as a recommendation for maintaining the panels at 90 deg without more extensive analysis of other gain conditions.

The reacquisition condition, which represents an increase in I_{zz} and, hence, a further reduction in yaw loop gain, was also simulated (SRACQ01A) at the worst case condition (SACQ11A) of the sun acquisition. Time plots of critical system parameters are shown in Figure 123. It is concluded that the same envelope for sun acquisition applies for sun reacquisition.

+Y Array Deployment

With the vehicle under three-axis jet control, the +y array is deployed. Time history for the +y array deployment in terms of vehicle attitudes and rates is given in Figure 124 for nominal conditions. No attitude stability problems are anticipated in deploying the +y array.

ON-ORBIT OPERATIONS

Following deployment of the +y solar array, the reaction wheel control system is activated. The satellite is then in the on-orbit operational configuration. This subsection presents the results of the analyses of critical events that occur during on-orbit operation. The order of discussion is as follows:

- Wheel loop stability analysis
- Noon turn
- Eclipse
- Momentum dumping
- Failed reaction wheels
- Lunar eclipse

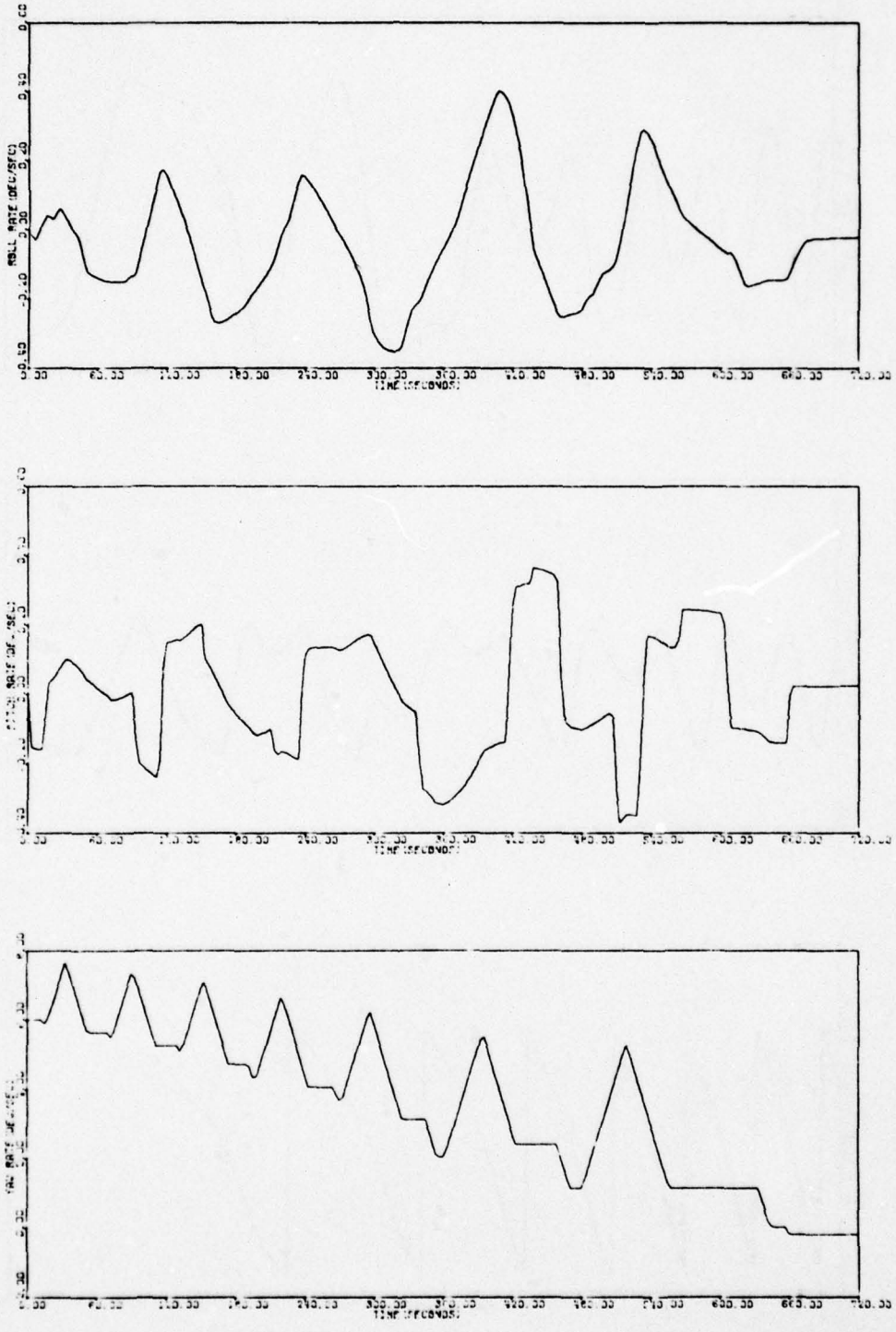

Figure 123. Run SRACQ01A

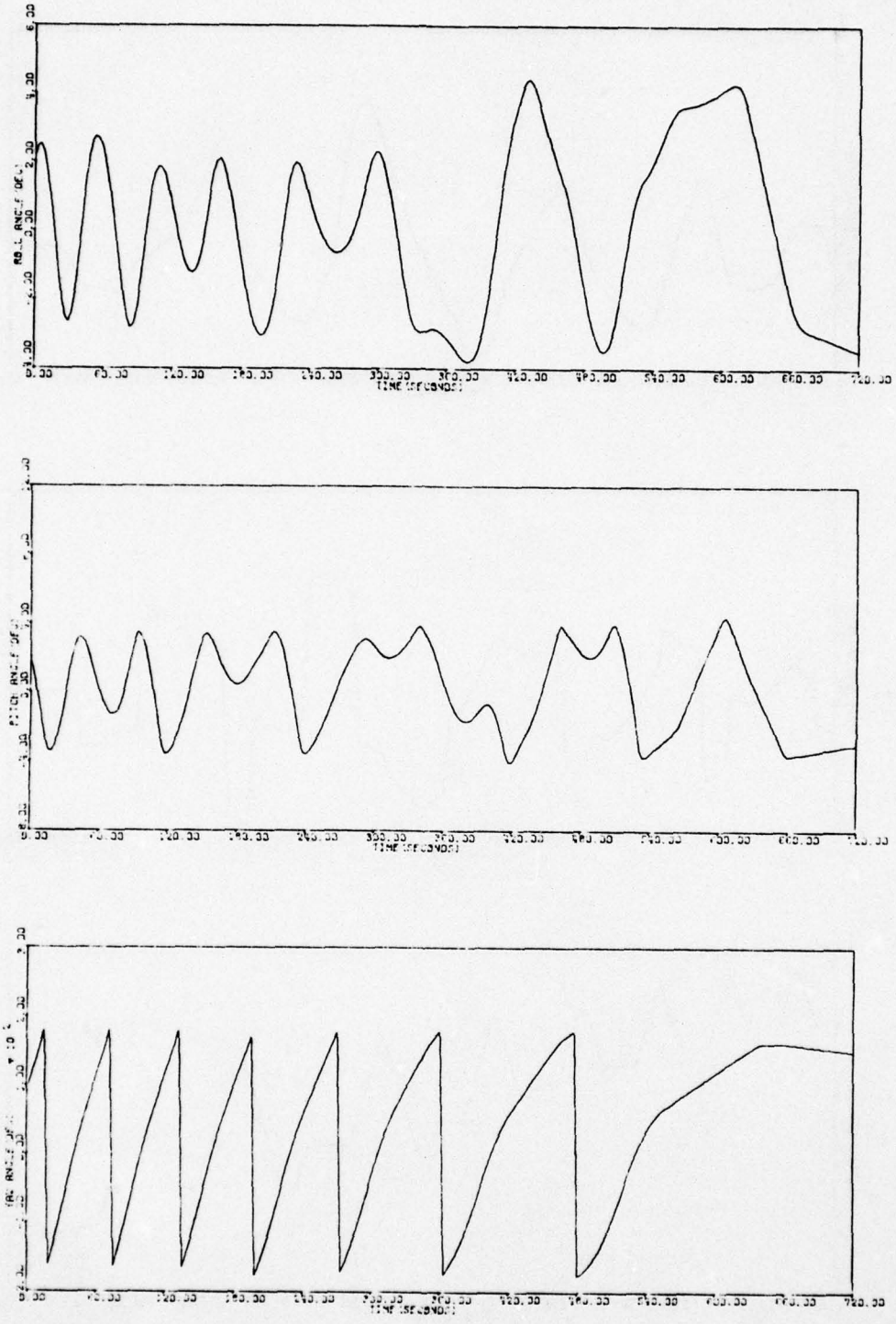

Figure 123. Run SRACQ01A (continued)

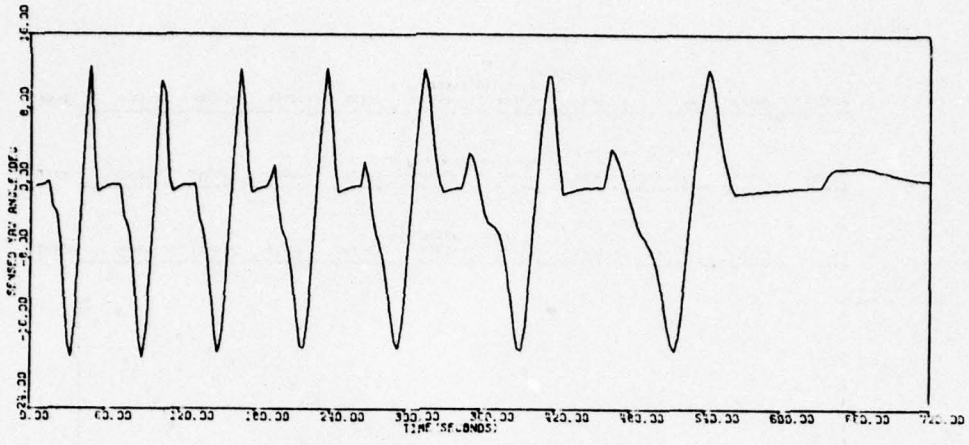

Figure 123. Run SRACQ01A (concluded)

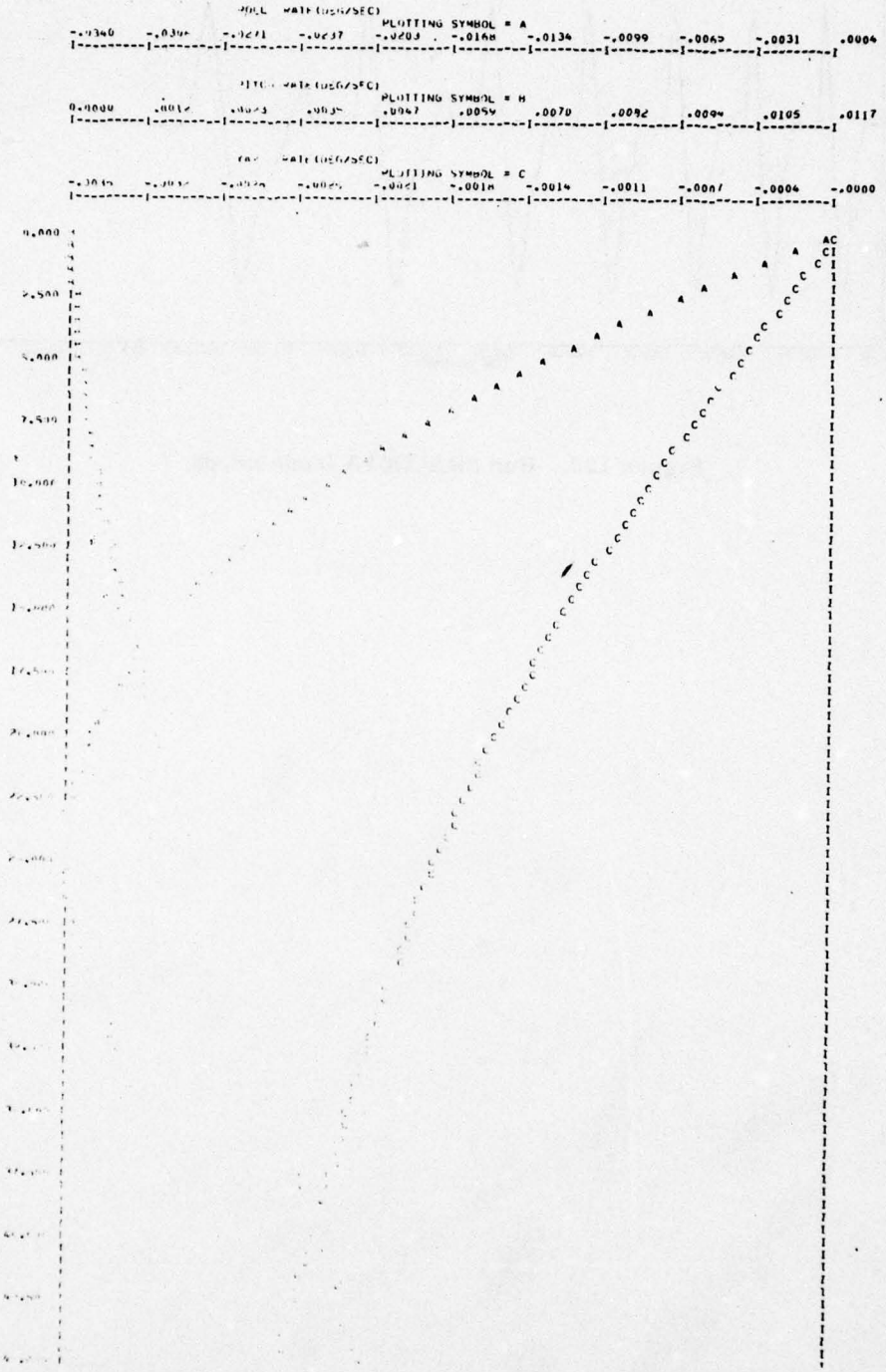

Figure 124a. +Y Array Deployment

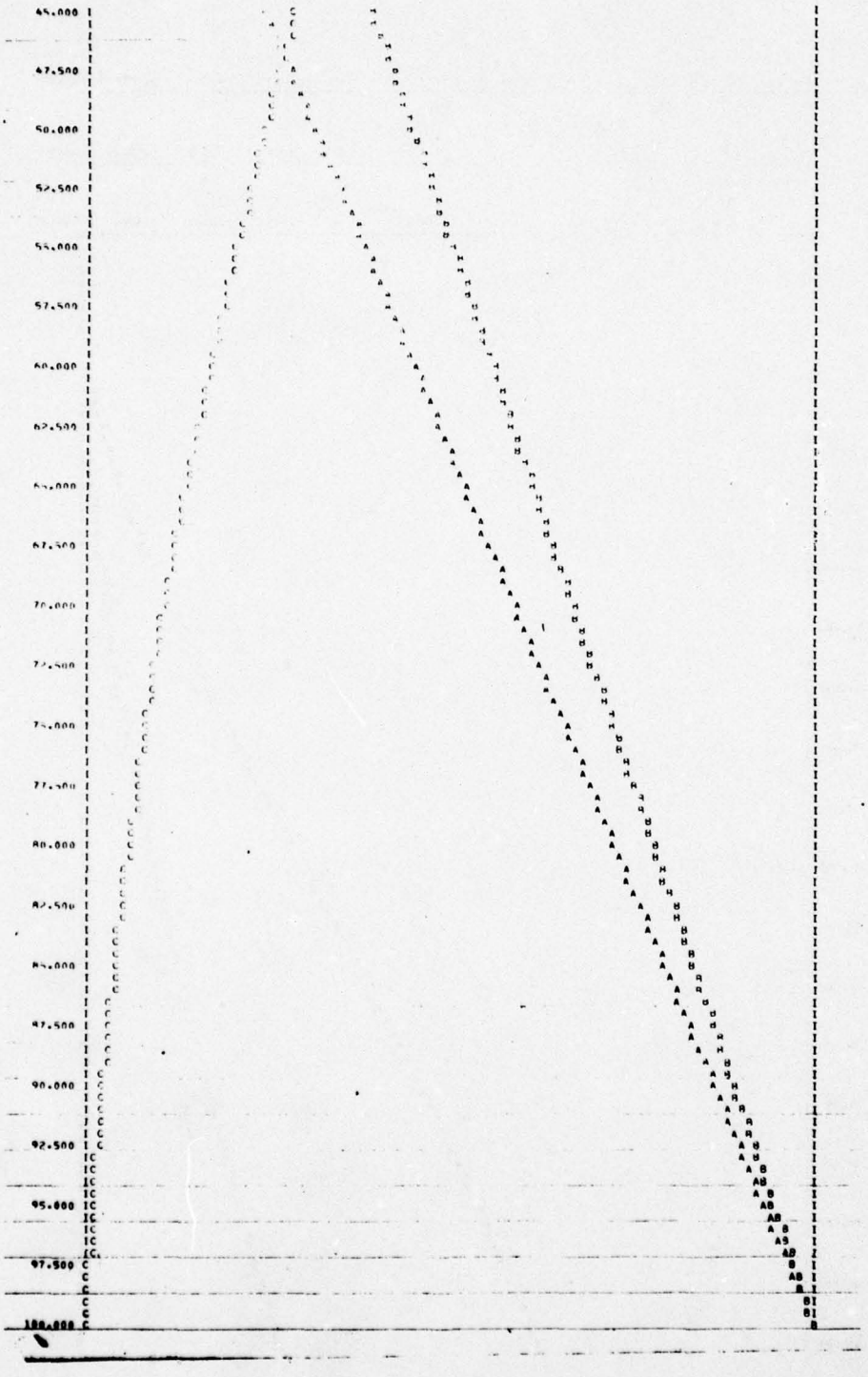

Figure 124a. +Y Array Deployment (concluded)

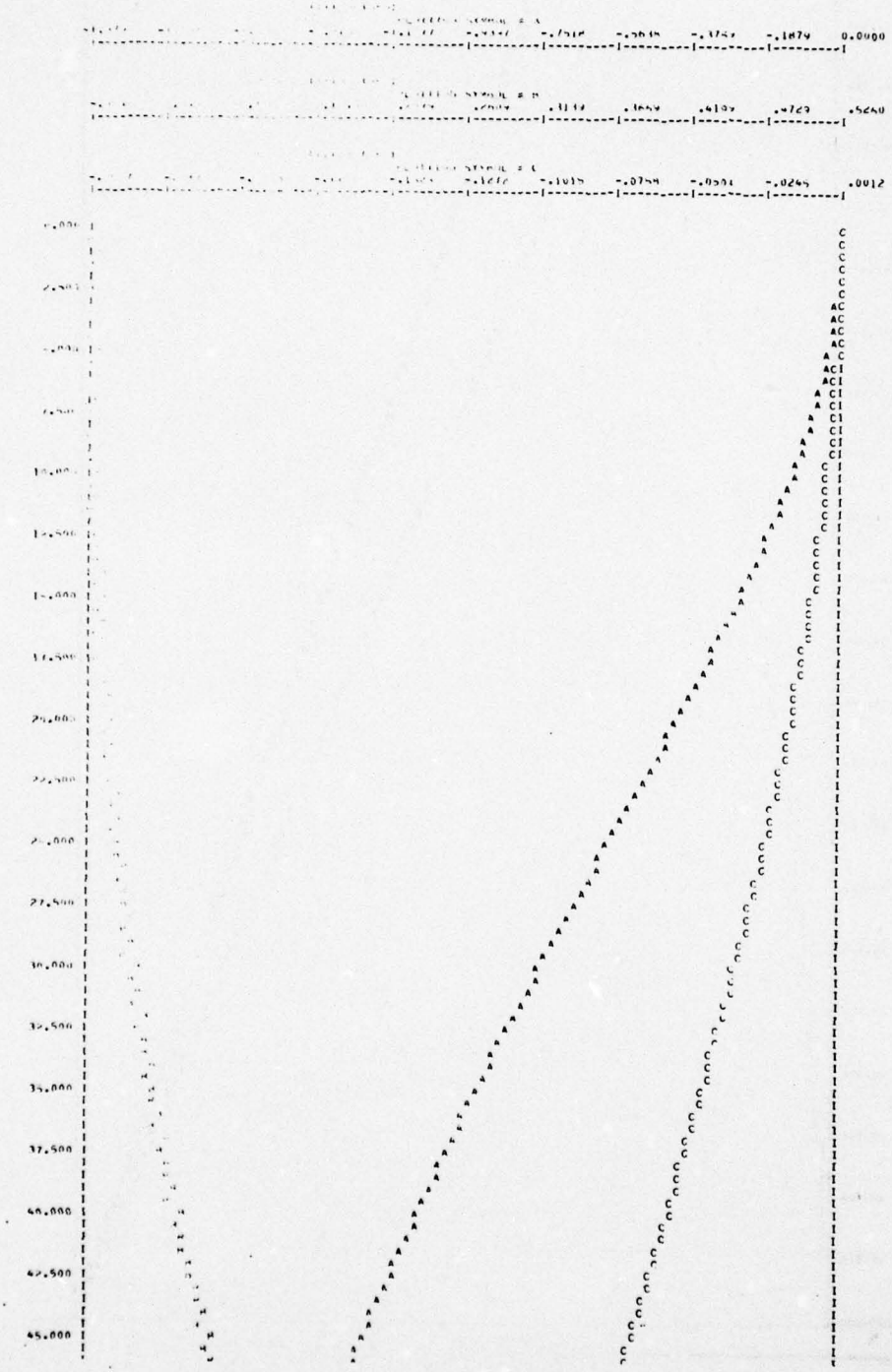

Figure 124b. +Y Array Deployment

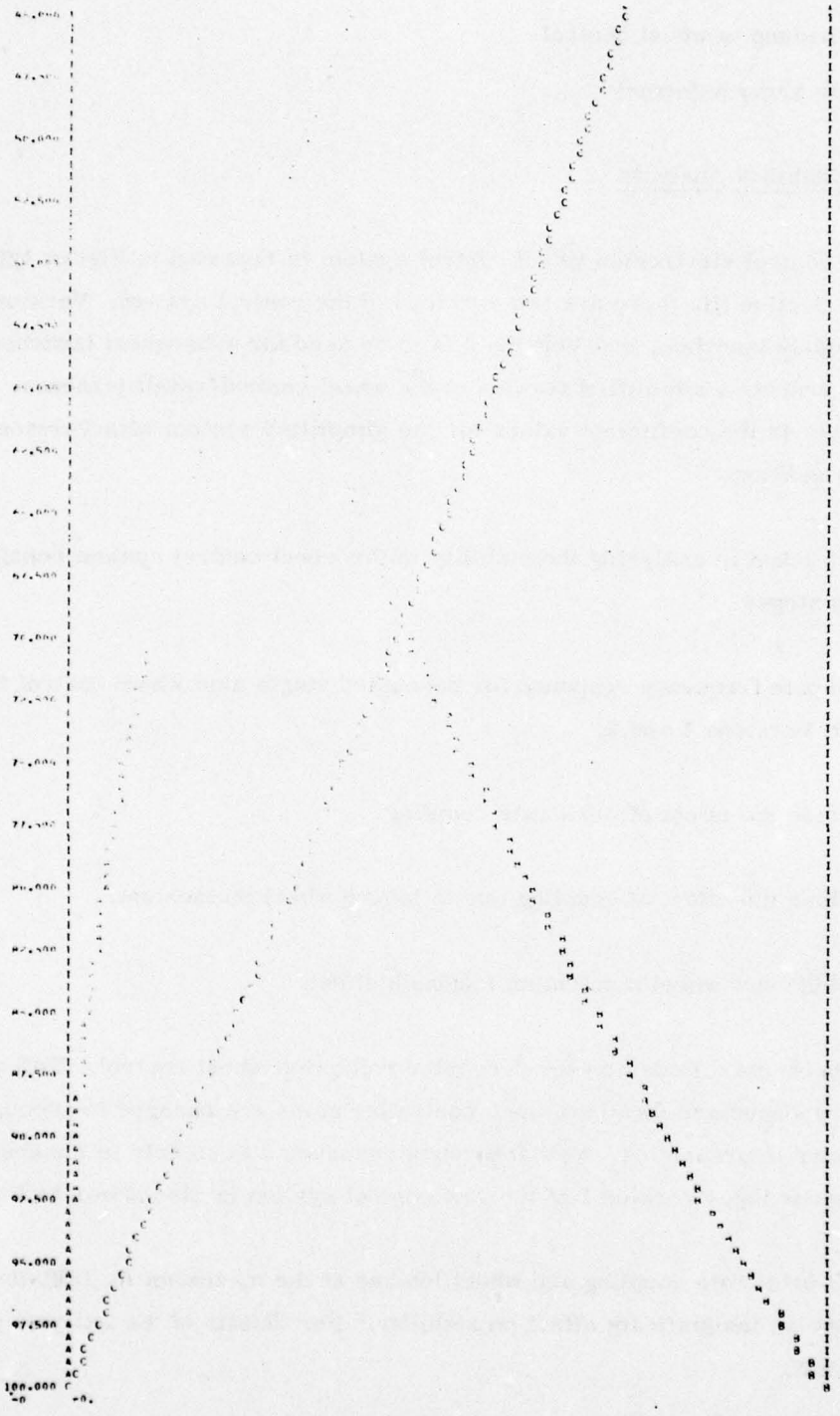

Figure 124b. +Y Array Deployment (concluded)

- Jet backup to wheel control
- Solar array autotrack

Wheel Loop Stability Analysis

The attitude control electronics wheel control system is repeated in Figure 125. As discussed in Section III, there are two versions of the control system: Version 1 is to be used for early launches, and Version 2 is to be used for subsequent launches. Figure 126 presents a simplified version of the wheel control/satellite/sensor system. Table 22 presents the coefficient values for the simplified system with Version 2 values shown in parentheses.

The approach taken in analyzing the stability of the wheel control system consisted of the following steps:

1. Compute frequency response for decoupled single axis wheel control for both Versions 1 and 2.

2. Include the effect of orbit rate coupling.

3. Include the effect of coupling due to loaded wheel momentum.

4. Include yaw wheel momentum feedback effect.

Figure 127 presents a Bode plot for decoupled roll/pitch wheel control. Roll and pitch frequency responses are identical since controller gains are changed to account for changes in inertia properties. Yaw frequency response differs only in the absence of the earth sensor lag. Version 1 of the yaw control system is also shown in Figure 127.

The effect of orbit rate coupling and wheel loading at the maximum (0.25 ft-lb-sec) condition have an insignificant effect on stability. For details of the analysis procedure, see Appendix K.

Figure 128 presents the frequency response for the yaw axis with yaw momentum feedback. Although yaw momentum feedback is used to limit wheel loading, there will be a transient initiated which should be analyzed for stability.

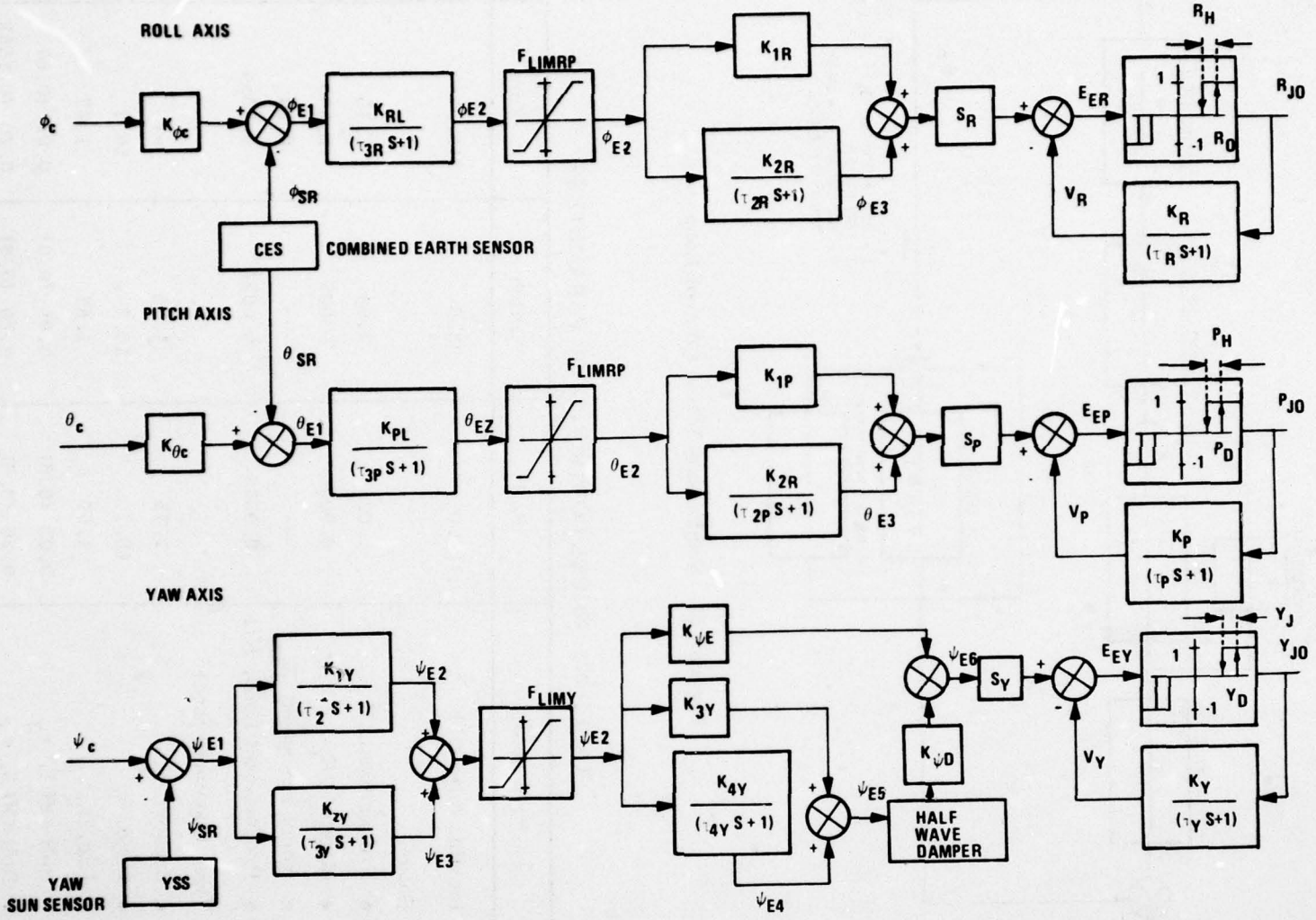

Figure 125. Jet Control System

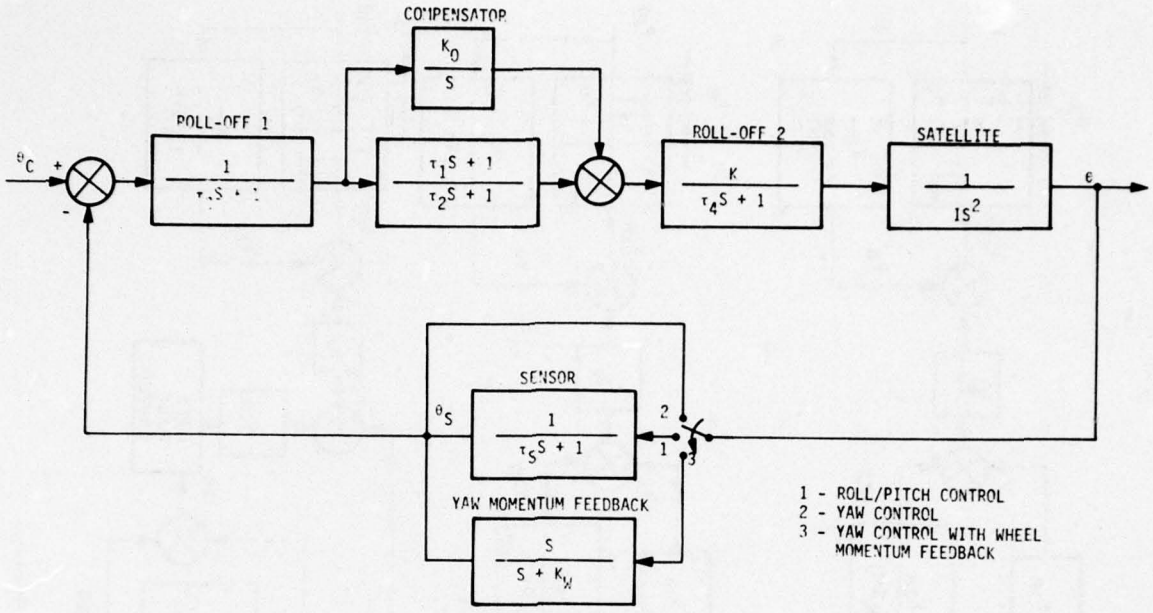

Figure 126. Single-Axis Wheel Control Loop

TABLE 22. WHEEL CONTROL LOOP PARAMETERS

Parameter	Roll	Pitch	Yaw
Inertias (slug ft^2)	190.0	95.0	210.0
Gains			
• Proportional, K	1.02	2.04	1.13
• Integral, K_0	0.005	0.005	0.005
• Wheel Feedback, K_W	---	---	0.22
• Proportional Loop, K/I	0.0054	0.0054	0.0054
Time Constants (sec)			
• Sensor, τ_S	1.75	1.75	---
• Lead, τ_1	16.7	16.7	16.7
• Lag, τ_2	1.67	1.67	1.67
• Roll-Off 1, τ_3	0.05 (0.6)	0.05 (0.6)	0.05 (0.6)
• Roll-Off 2, τ_4	0.20 (0.6)	0.20 (0.6)	0.20 (0.355)

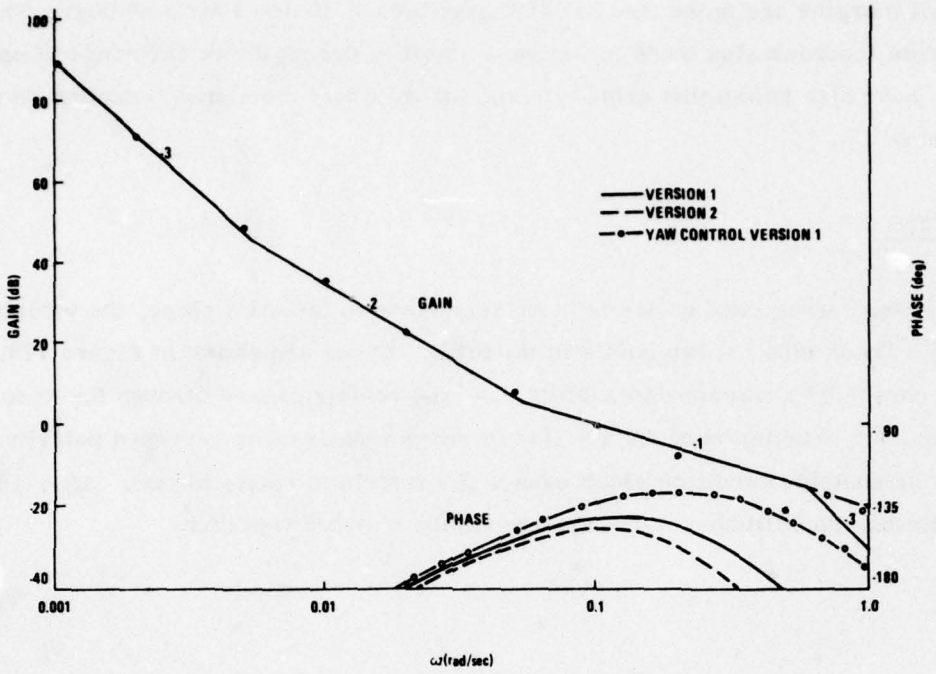

Figure 127. Roll/Pitch Wheel Control Loop Frequency Response

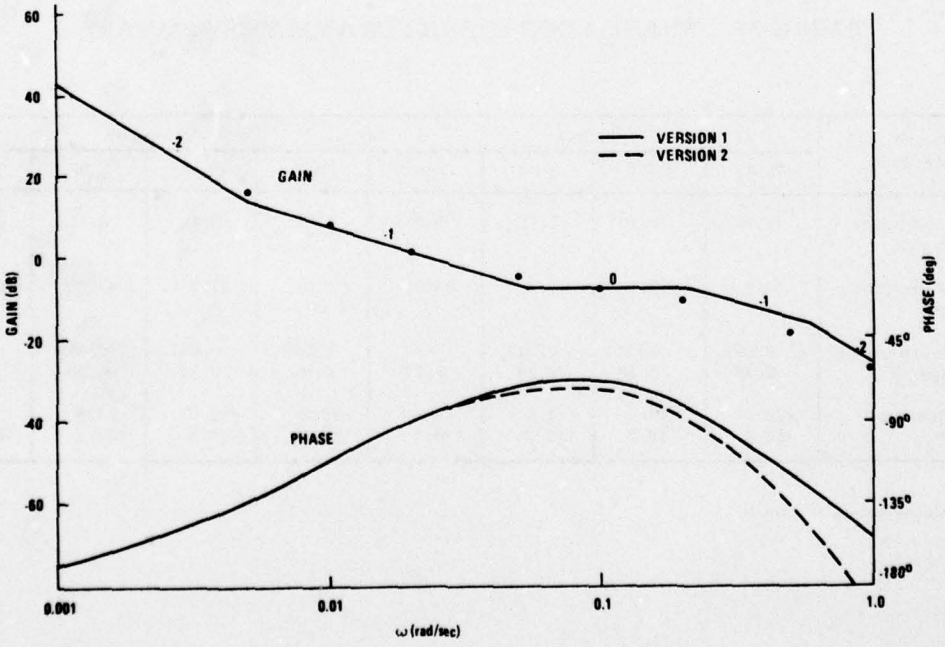

Figure 128. Yaw Wheel Control Loop Frequency Response (with Yaw Momentum Feedback)

A summary of the wheel loop stability analysis results is given in Table 23. As can be seen, all margins are more than satisfactory (GMs > 30 dB, PMs > 30 deg). The yaw momentum feedback also tends to increase stability during the linear range of operation. Results have also shown that orbit rate and loaded wheel momentum coupling do not affect stability.

Noon Turn

Twice a year, when the sun line is in or very close to the orbit plane, the vehicle will execute a "noon turn" at two points in the orbit. These are shown in Figure 129. The turn is caused by a transient instability. As the vehicle passes through the noon turn condition, the orientation of the sun line to the yaw sun sensor reverses polarity. This creates an unstable condition which causes the vehicle to rotate in yaw. After 180 deg yaw rotation, the attitude control system attains a stable condition.

TABLE 23. WHEEL LOOP STABILITY ANALYSIS SUMMARY

Stability Margins	Version 1				Version 2			
	Roll	Pitch	Yaw	Yaw*	Roll	Pitch	Yaw	Yaw*
Gain crossover (rad/sec)	0.10	0.10	0.10	0.025	0.10	0.10	0.10	0.025
Phase margin (deg)	37.2	37.2	47.3	93.0	31.7	31.7	43.2	91.9
Phase crossover (rad/sec)	0.020 0.46	0.020 0.46	0.018 1.44	--- 1.74	0.021 0.32	0.021 0.32	0.019 0.69	--- 0.87
Gain margin (dB)	-23.0 +18.2	-23.0 +18.2	-24.0 +32.8	--- +36.1	-22.2 +13.5	-22.3 +13.5	-23.6 +22.2	--- +26.4

* With momentum feedback.

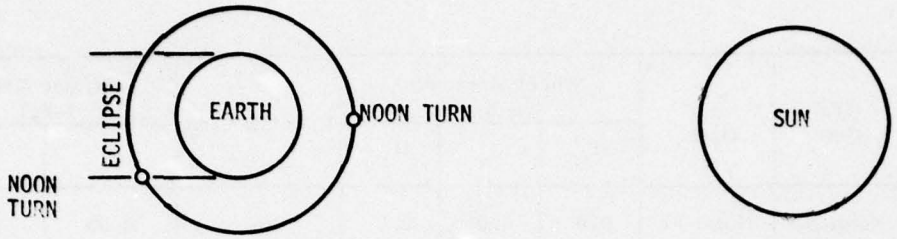

Figure 129. Noon Turn Conditions

A very low yaw gain is characteristic of the noon turn condition since the arrays are in the xy plane of the vehicle. Four noon turn conditions were investigated. The critical parameters of each run are summarized in Table 24. The high and low sensor gains have been defined in previous sections. Uncertainties in the form of wheel misalignments, mass property variations, and sensor misalignments are summarized in Table 25. Figures 130 through 133 present time histories of the noon turn runs. Results of the noon turn runs are as follows:

- There are no attitude stability problems in pitch and roll while turning. Peak pitch and roll errors occur when the wheels are loaded at their peak values and are less than 0.2 deg.
- Wheel loop momentum is limited in each run at approximately 1 ft-lb-sec. This is equivalent to a steady state yaw rate of approximately 0.25 deg/sec which indicates that all noon turns will take approximately 12 to 20 minutes.

It is possible to execute a momentum dump during noon turn and this will be discussed in the section on momentum dumping.

Eclipse

When the sun line is within approximately $\pm$ 12 deg of the orbit plane, the satellite will be in earth eclipse for a portion of each orbit. The longest duration of eclipse is 55.47 minutes and occurs when the sun line is directly in the orbit plane. This condition was

TABLE 24. NOON TURN SIMULATION RUNS

Run	CES Gain	y_{ss} Gain	Wheel Momentum (ft-lb-sec)			Uncertainties	Attitude Errors (deg)	
			H_x	H_y	H_z		ϕ	θ
NT01A	Nominal	Nominal	0.0	0.0	0.0	No	0.05	0.06
NT02A	High	Low	0.0	0.0	0.0	Yes	0.06	0.1
NT03A	High	Low	0.25	0.25	0.0	Yes	0.14	0.15
NT04A	High	High	0.0	0.0	0.0	Yes	0.04	0.1

TABLE 25. OFF-NOMINAL CONDITIONS FOR NOON TURN SIMULATION

Wheel misalignments (cant)	1.0 deg
Wheel misalignments (cone)	1.0 deg
Yaw sensor gain	Low
Earth sensor gain	High
I_{xx}	187.88 slug ft^2
I_{yy}	94.458 slug ft^2
I_{zz}	211.58 slug ft^2
I_{xy}	-0.72210 slug ft^2
I_{xz}	-0.0081 slug ft^2
I_{yz}	-0.0091 slug ft^2

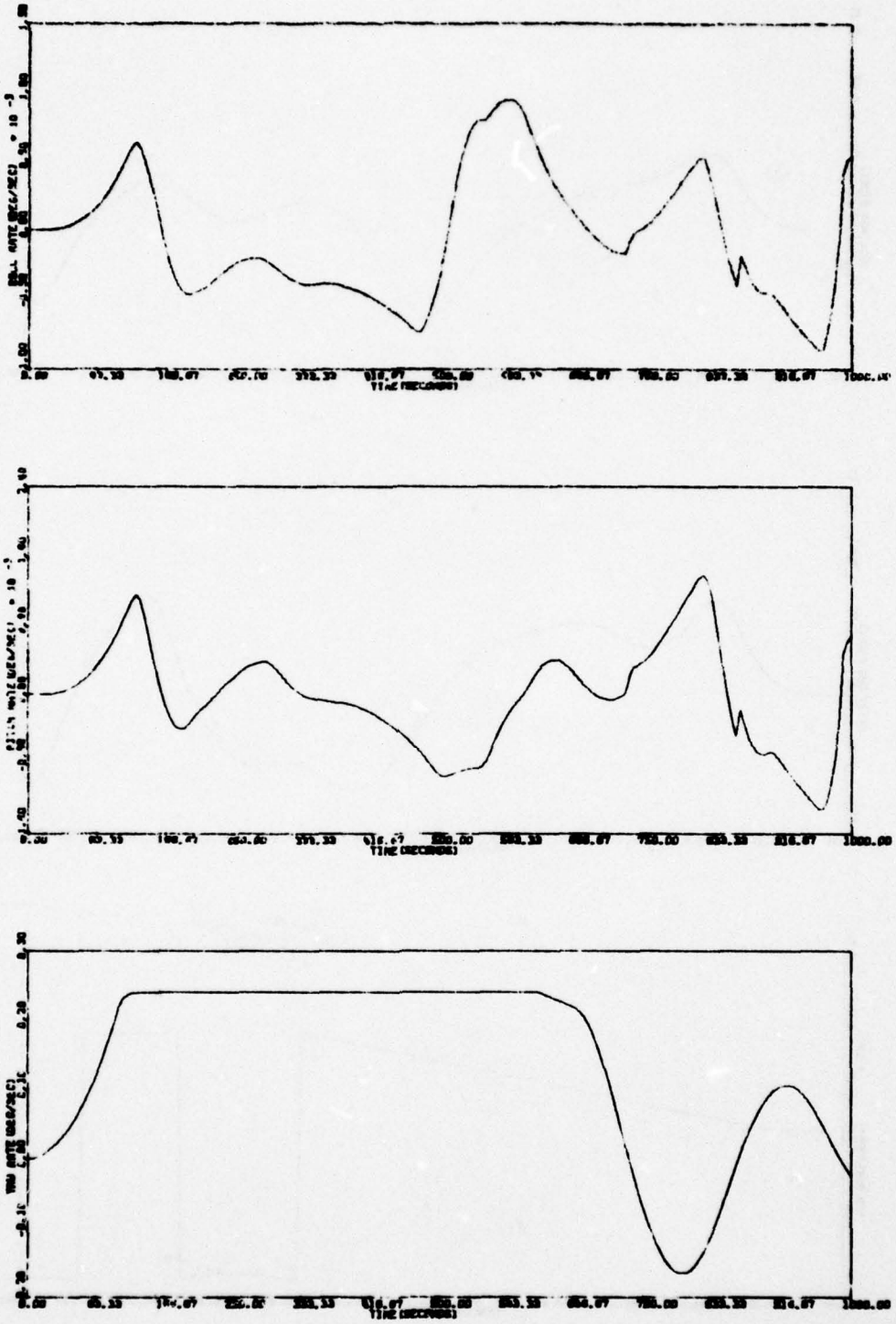

Figure 130. Run NT01A

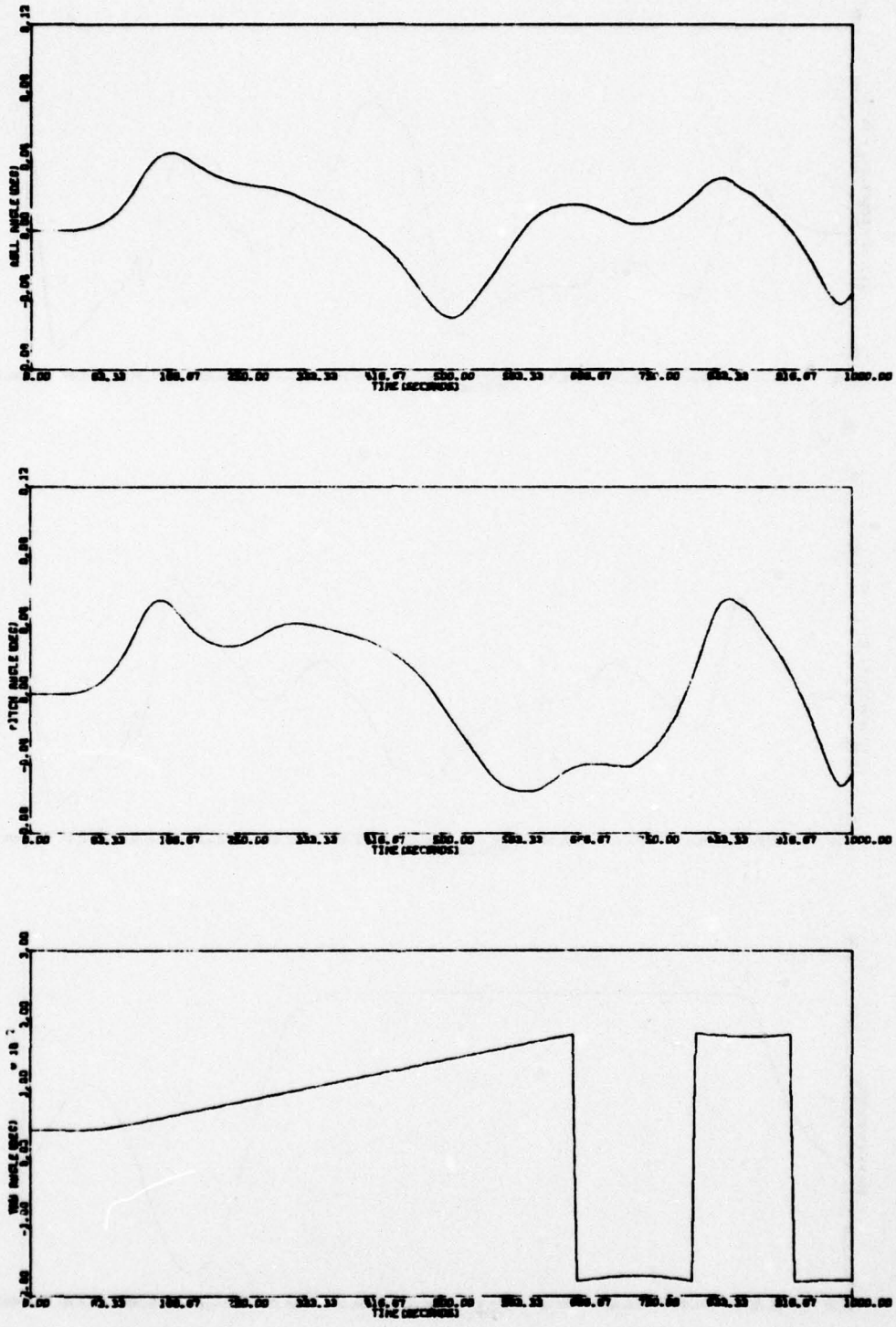

Figure 130. Run NT01A (continued)

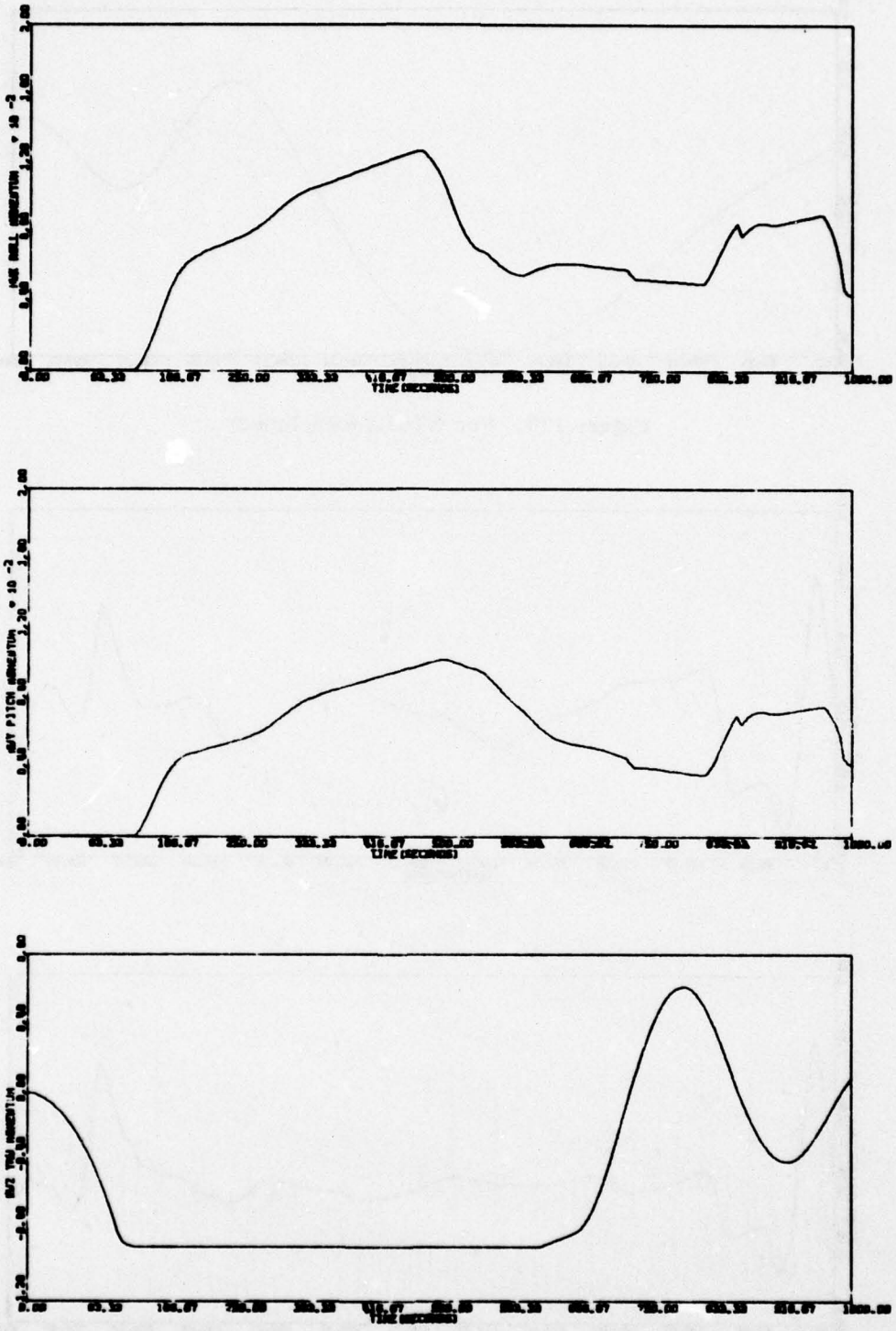

Figure 130. Run NT01A (continued)

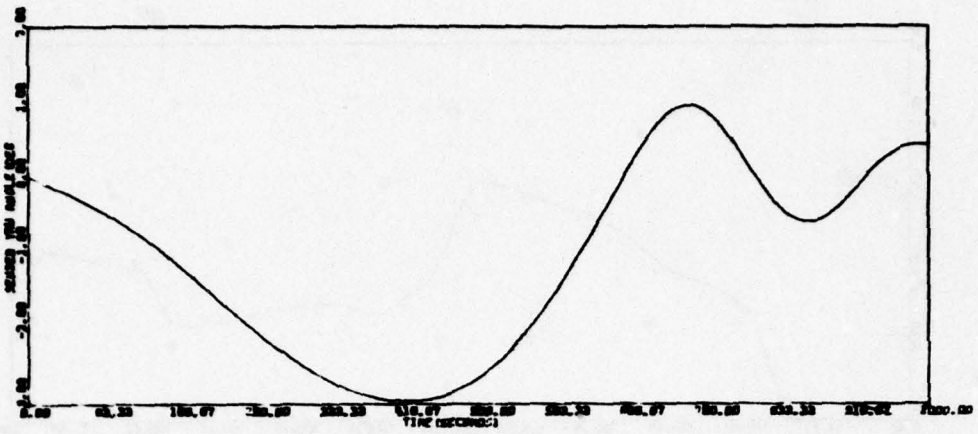

Figure 130. Run NT01A (concluded)

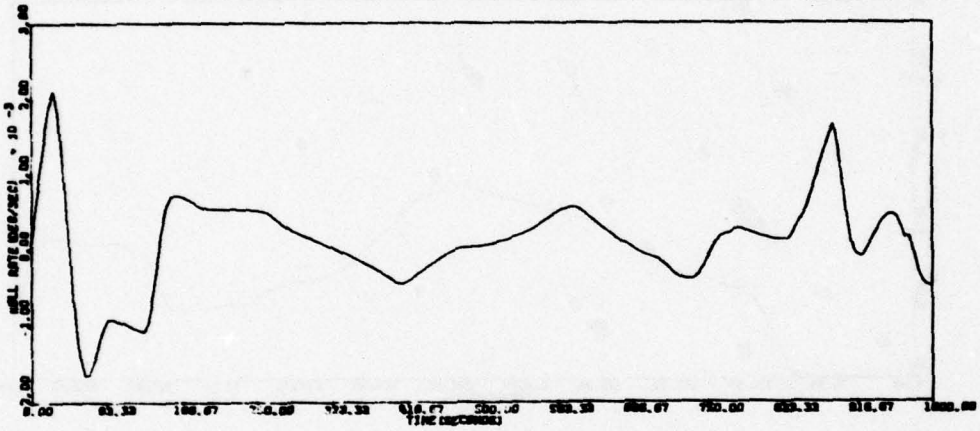

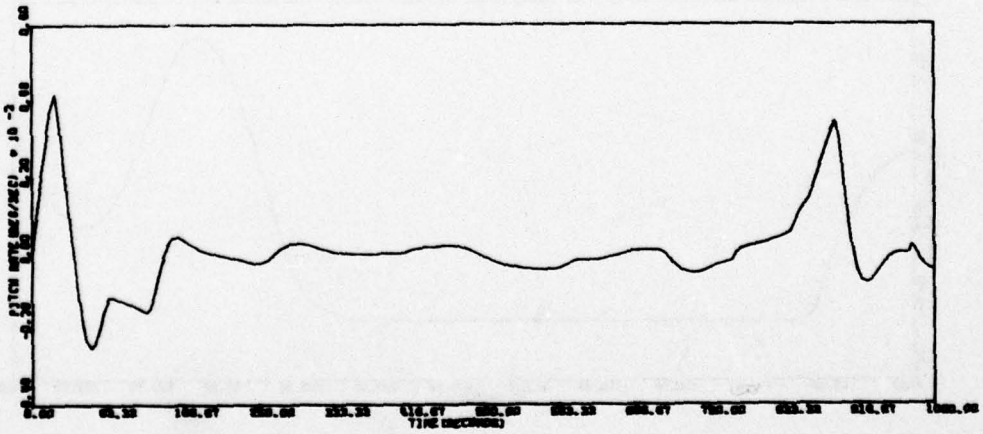

Figure 131. Run NT02A

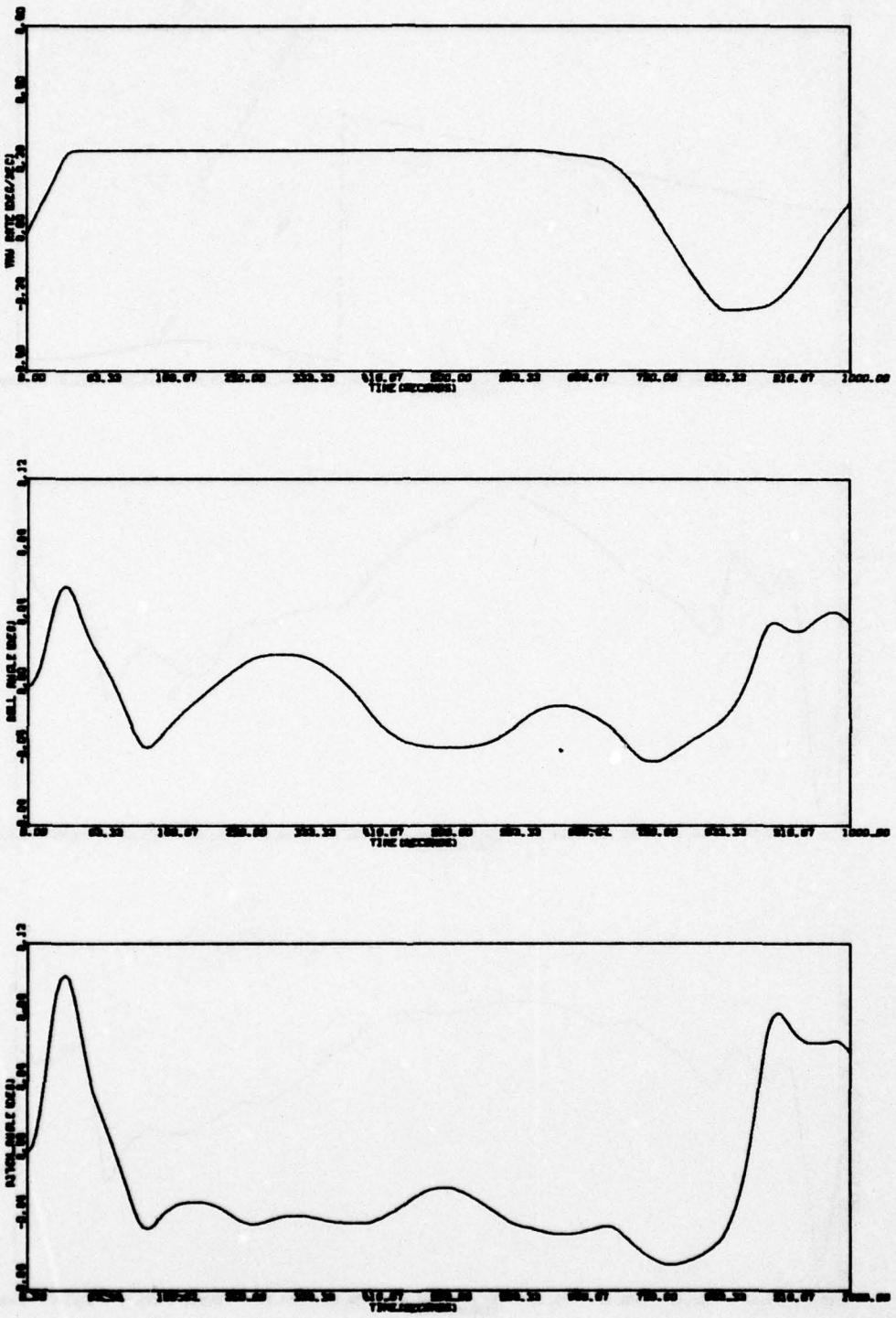

Figure 131. Run NT02A (continued)

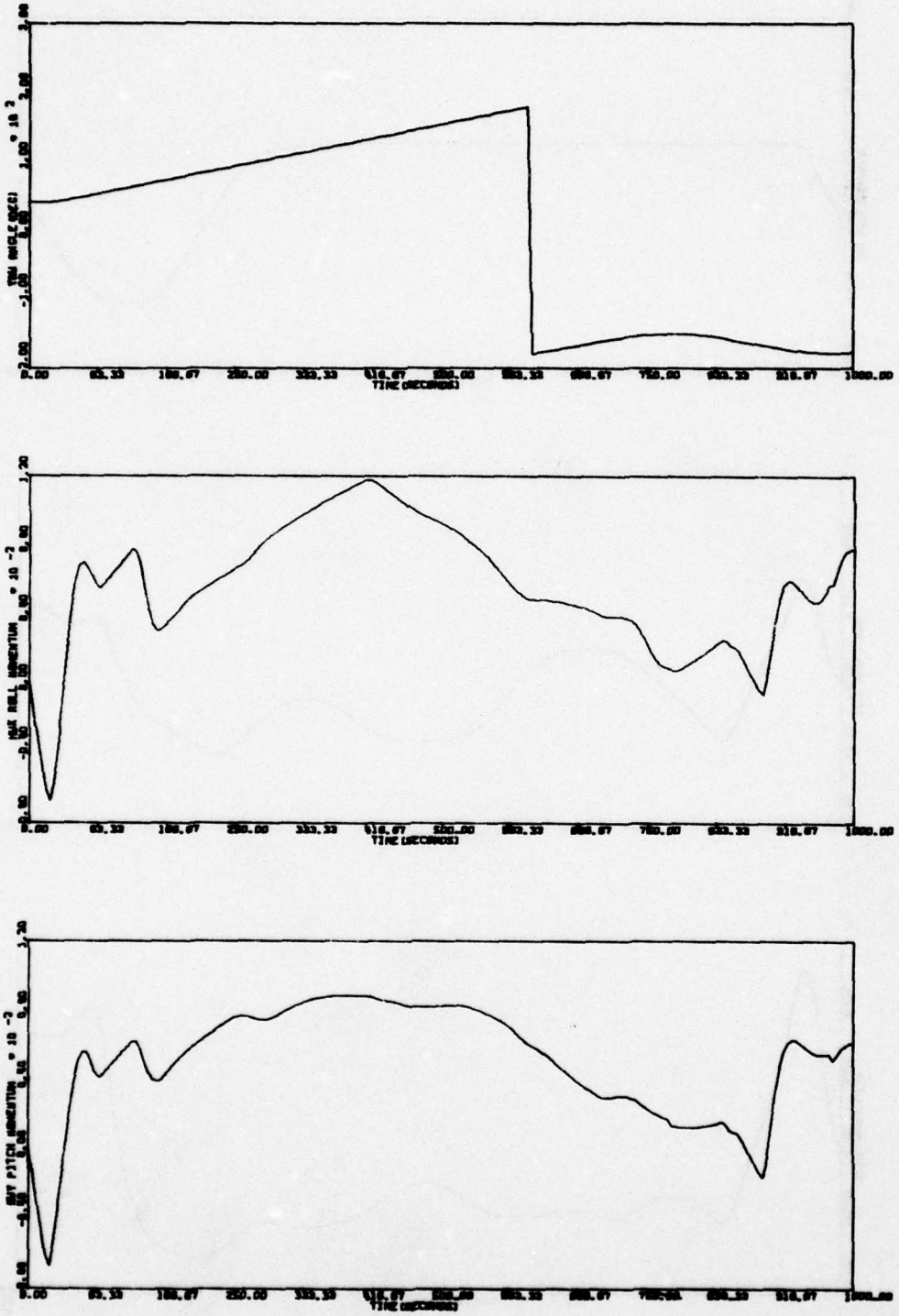

Figure 131. Run NT02A (continued)

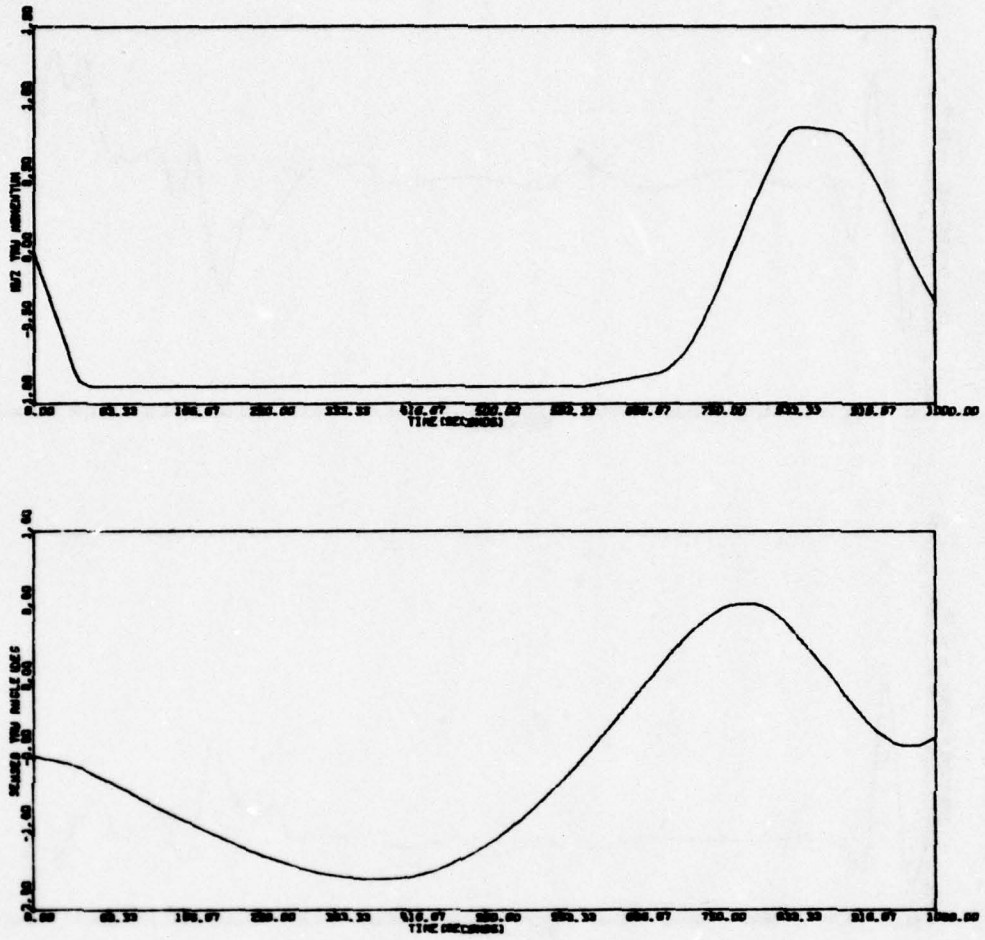

Figure 131. Run NT02A (concluded)

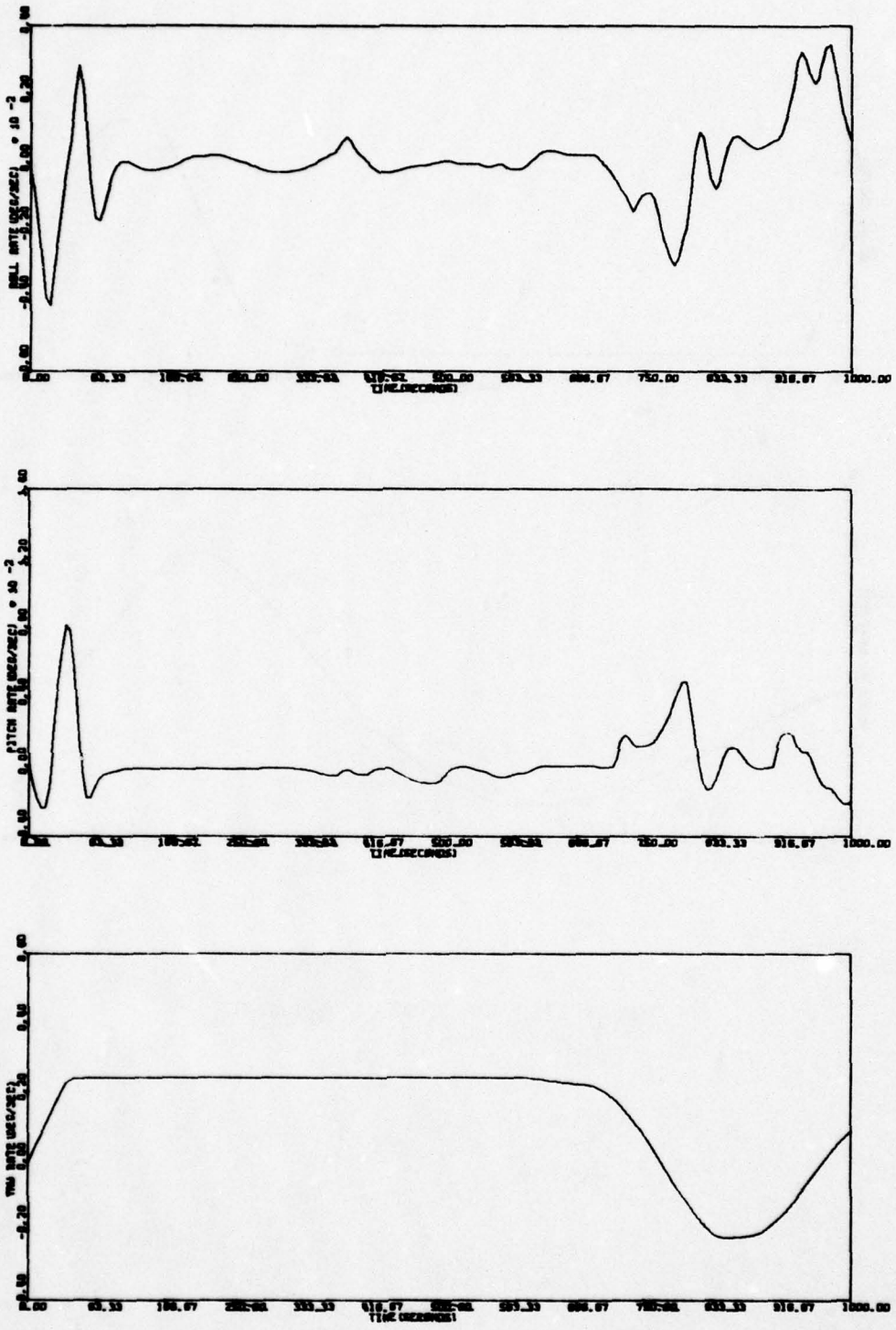

Figure 132. Run NT03A

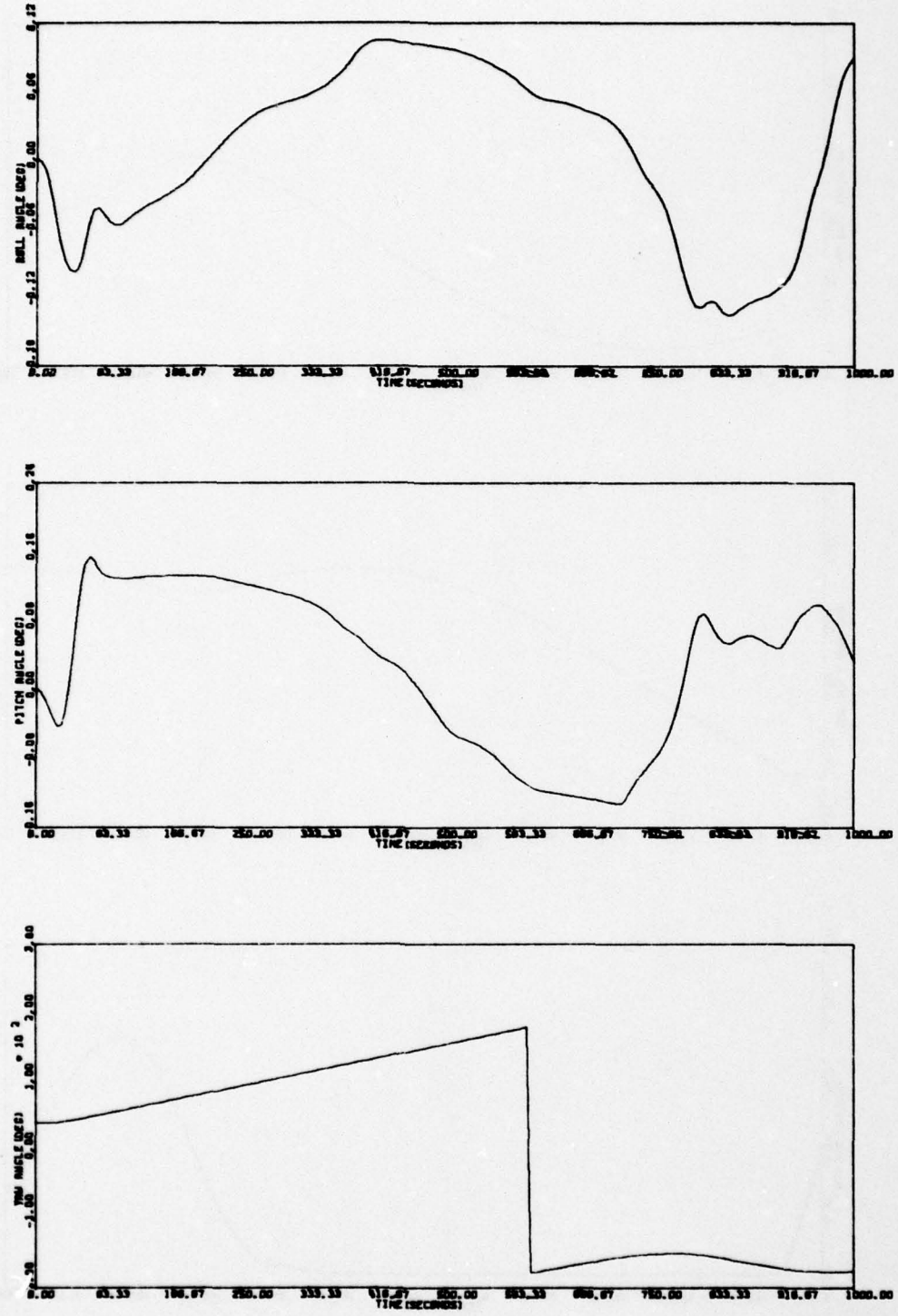

Figure 132. Run NT03A (continued)

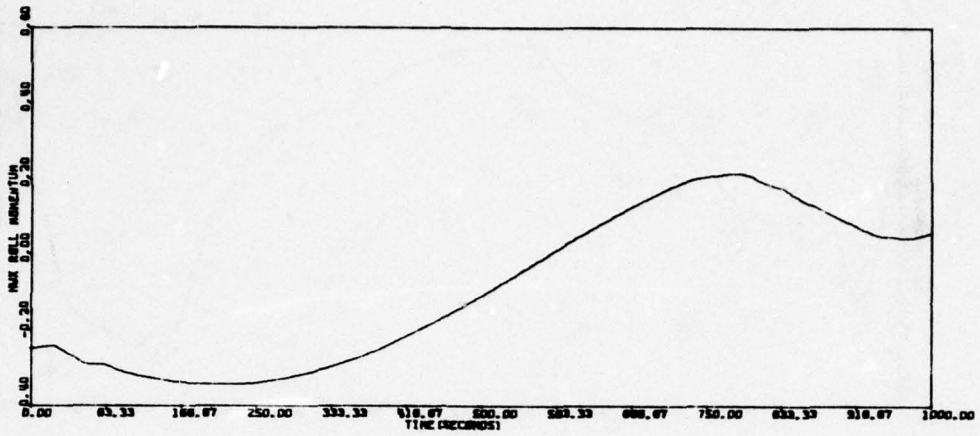

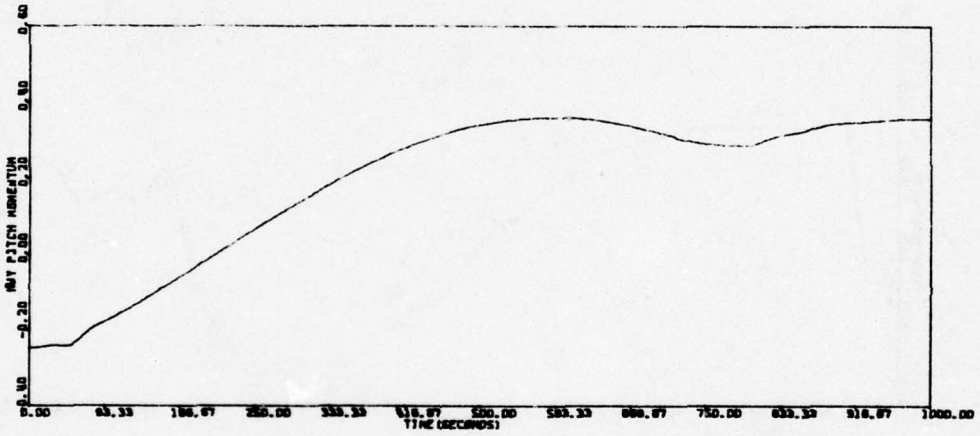

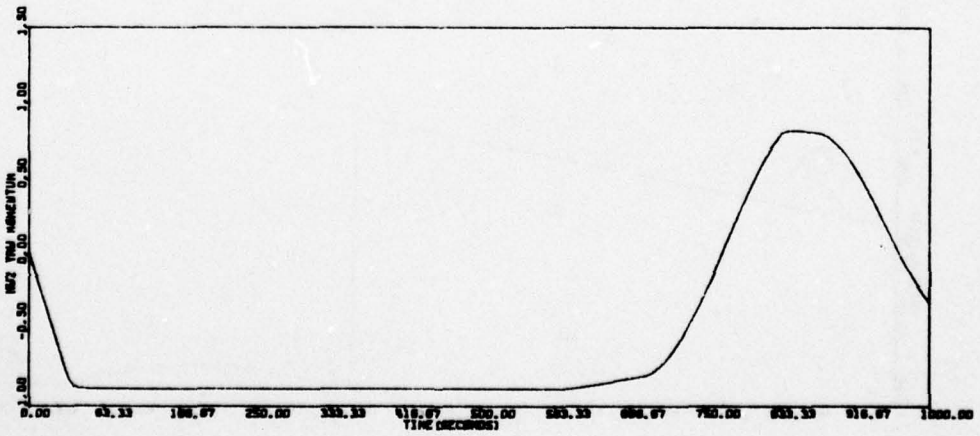

Figure 132. Run NT03A (continued)

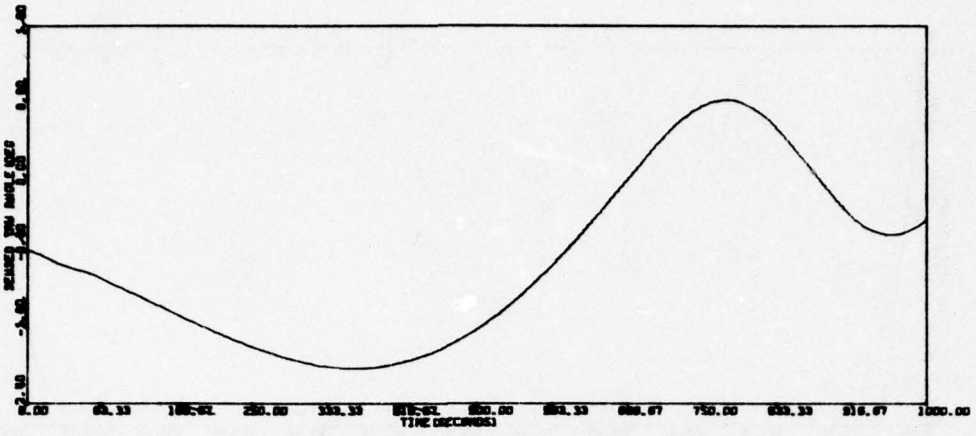

Figure 132. Run NT03A (concluded)

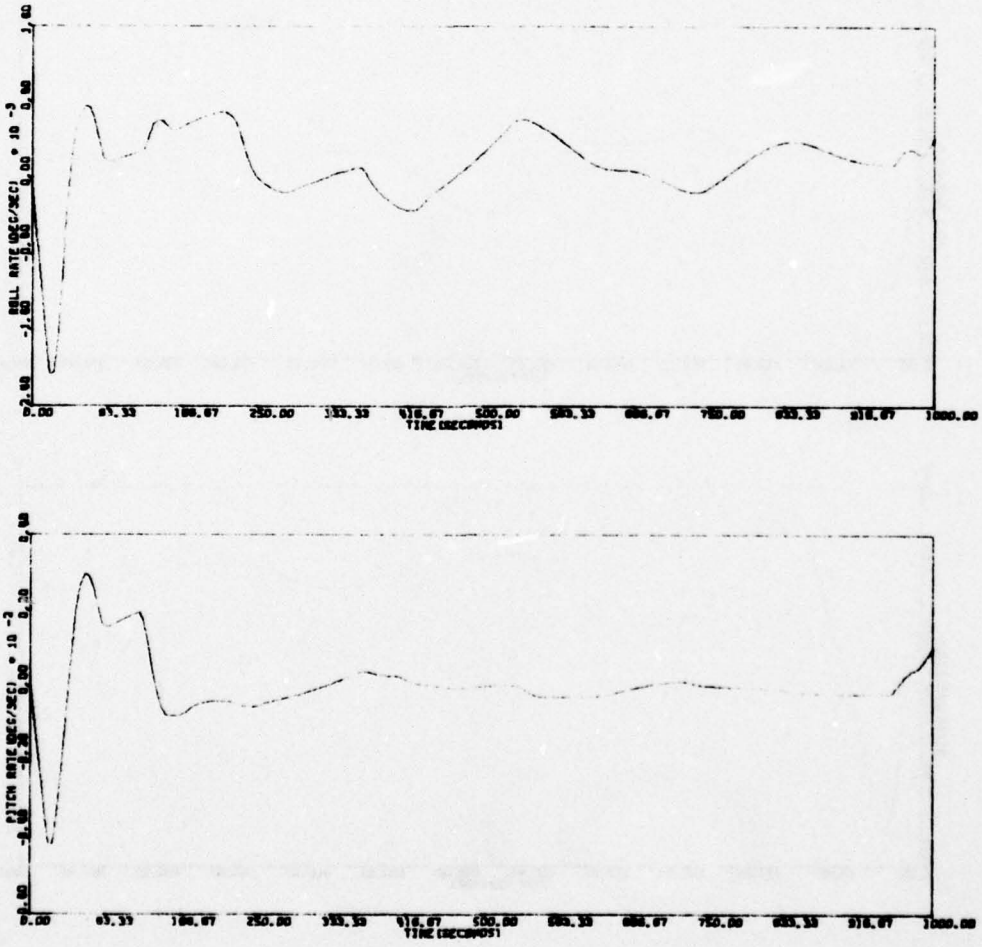

Figure 133. Run NT04A

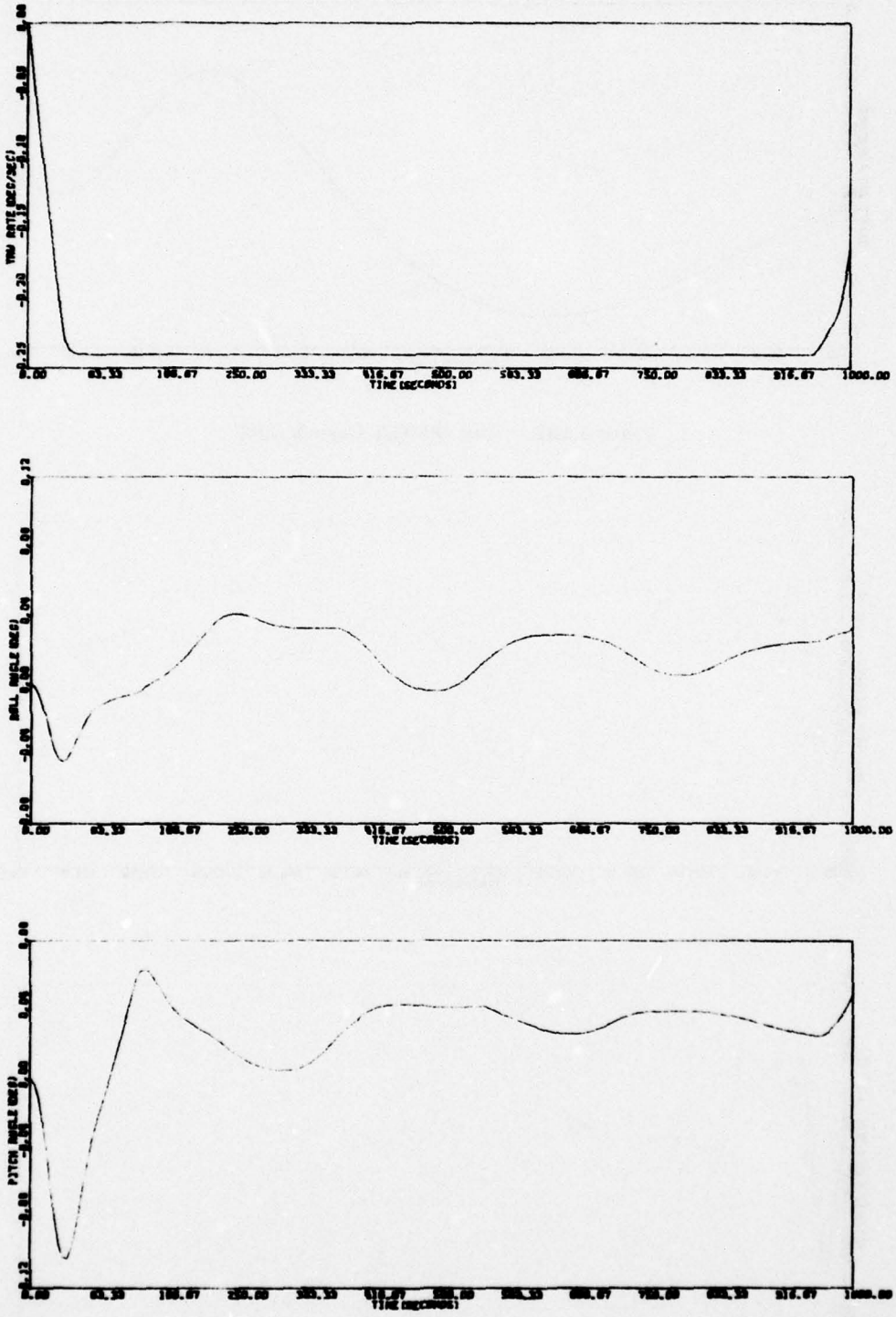

Figure 133. Run NT04A (continued)

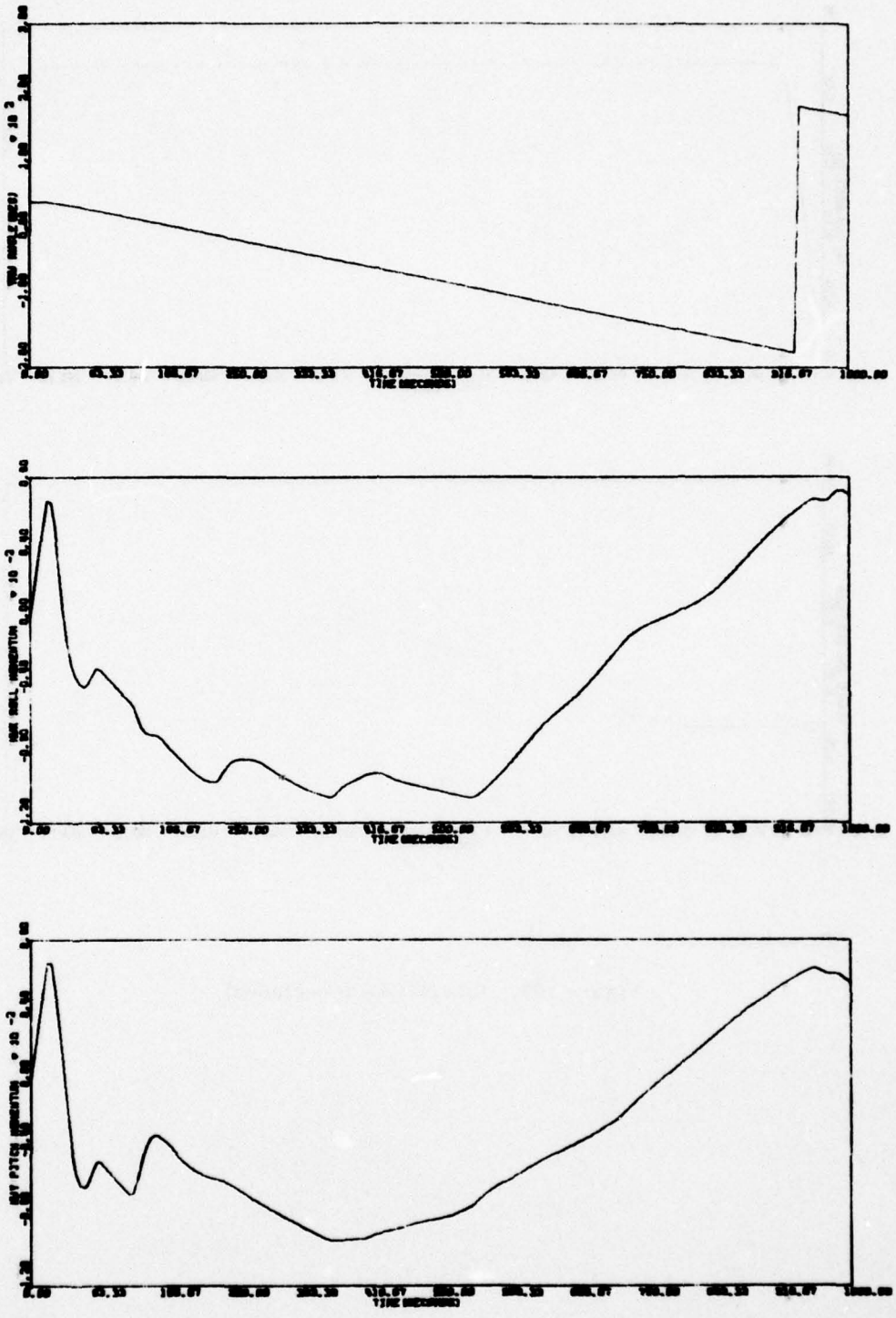

Figure 133. Run NT04A (continued)

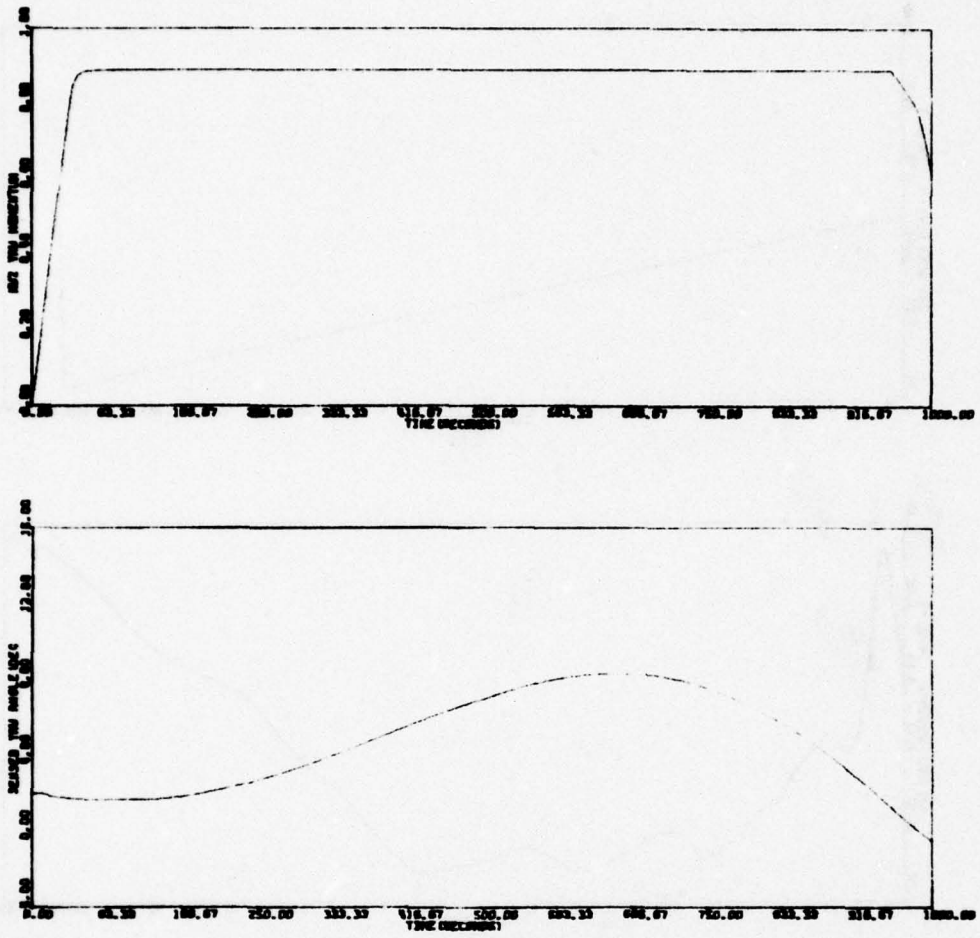

Figure 133. Run NT04A (concluded)

shown in Figure 114. The critical area of investigation is satellite performance as it emerges from eclipse. In investigating that condition, the significant parameters are the following:

- Yaw sun sensor bias and gain. The yaw sun sensor bias was chosen from Figure at the 0.0 deg yaw input condition. At 25°C it amounts to $\pm$ 1.58 deg. Emerging from eclipse, the yaw sun sensor temperature is -45°C which will produce a 42 percent reduction in sensor output. For the simulation, a bias of 1.0 deg and a 50 percent reduction in yaw sun sensor output for the low gain condition were assumed.
- Solar array orientation. When the satellite enters eclipse, both the yaw sun sensor and array pitch sun sensor emit bias signals. Whereas the reaction wheel yaw loop will respond to the bias and generate a constant rate, the solar array drive will maintain the array at a constant position because of the deadband in the drive control loop.

Two approaches were used to simulate the affects of solar array orientation. These avoided the need to simulate long eclipse runs using the small integration steps (Δt = 0.025 sec) required to simulate the solar array drive loop. The first approach assumes that the array is pointing at the sun as it goes into eclipse and holds the position throughout eclipse and upon leaving eclipse. The second approach initializes vehicle parameters as obtained from approach one at a condition just prior to emerging from eclipse and then allows the solar array drive to position the panel. A summary of the simulation runs exercising these two approaches is given in Table 26. Figures 134 through 136 present histories for the three runs.

TABLE 26. ECLIPSE SIMULATION

Run	y_{ss} Gain	p_{ss} Gain	y_{ss} Bias (deg)	Panels	Panel Angle at Emergence (deg)	Yaw Angle at Emergence (deg)	Sensed Yaw at Emergence (deg)
ECL01A	Nominal	---	0.0	Fixed	14.0	180.0	-0.23
ECL02A	Low	---	1.0	Fixed	14.0	96.16	6.05
ECL03A	Low	Low	1.0	Track	14.0	105.15	6.00

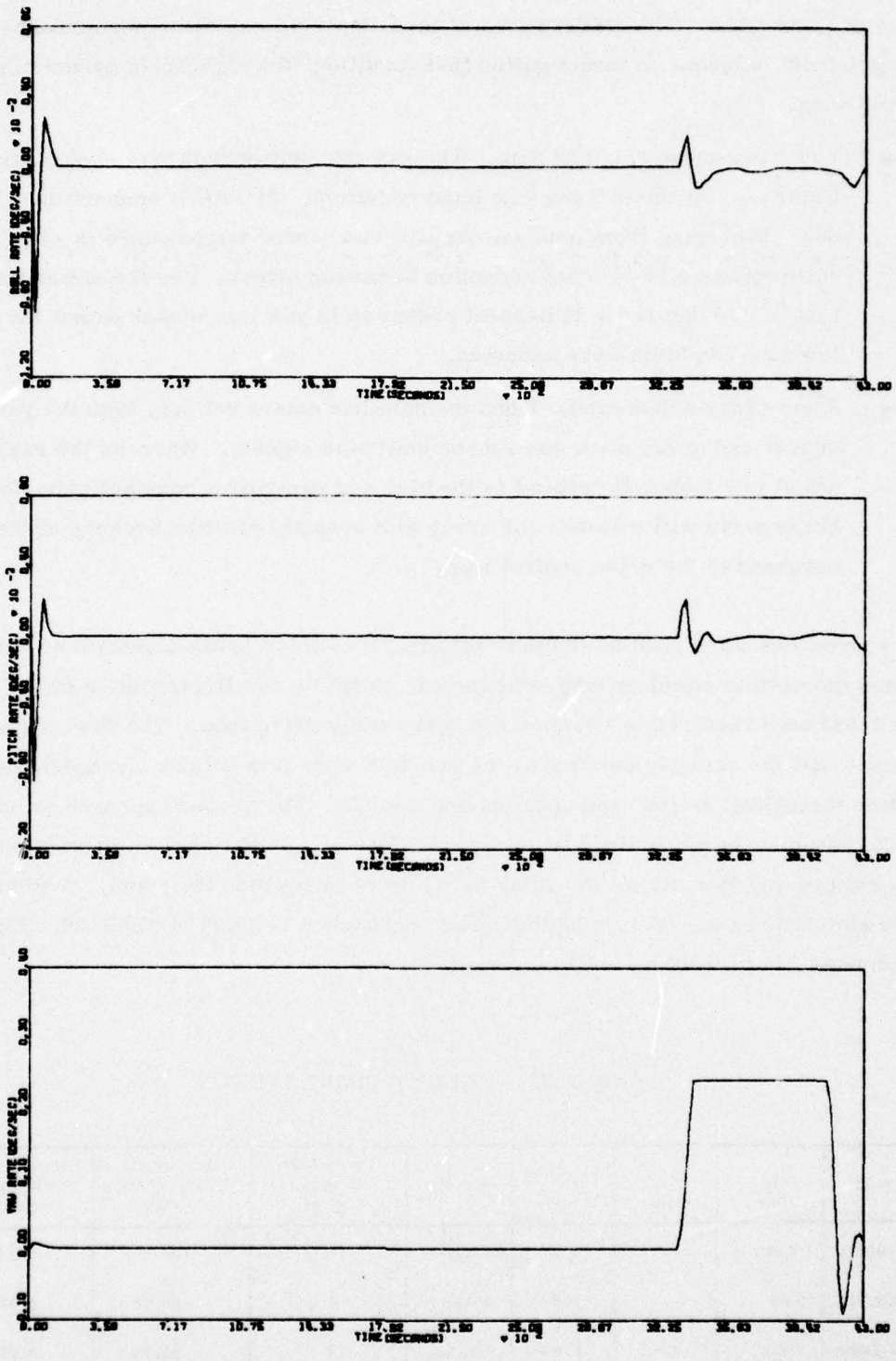

Figure 134. Run ECL01A

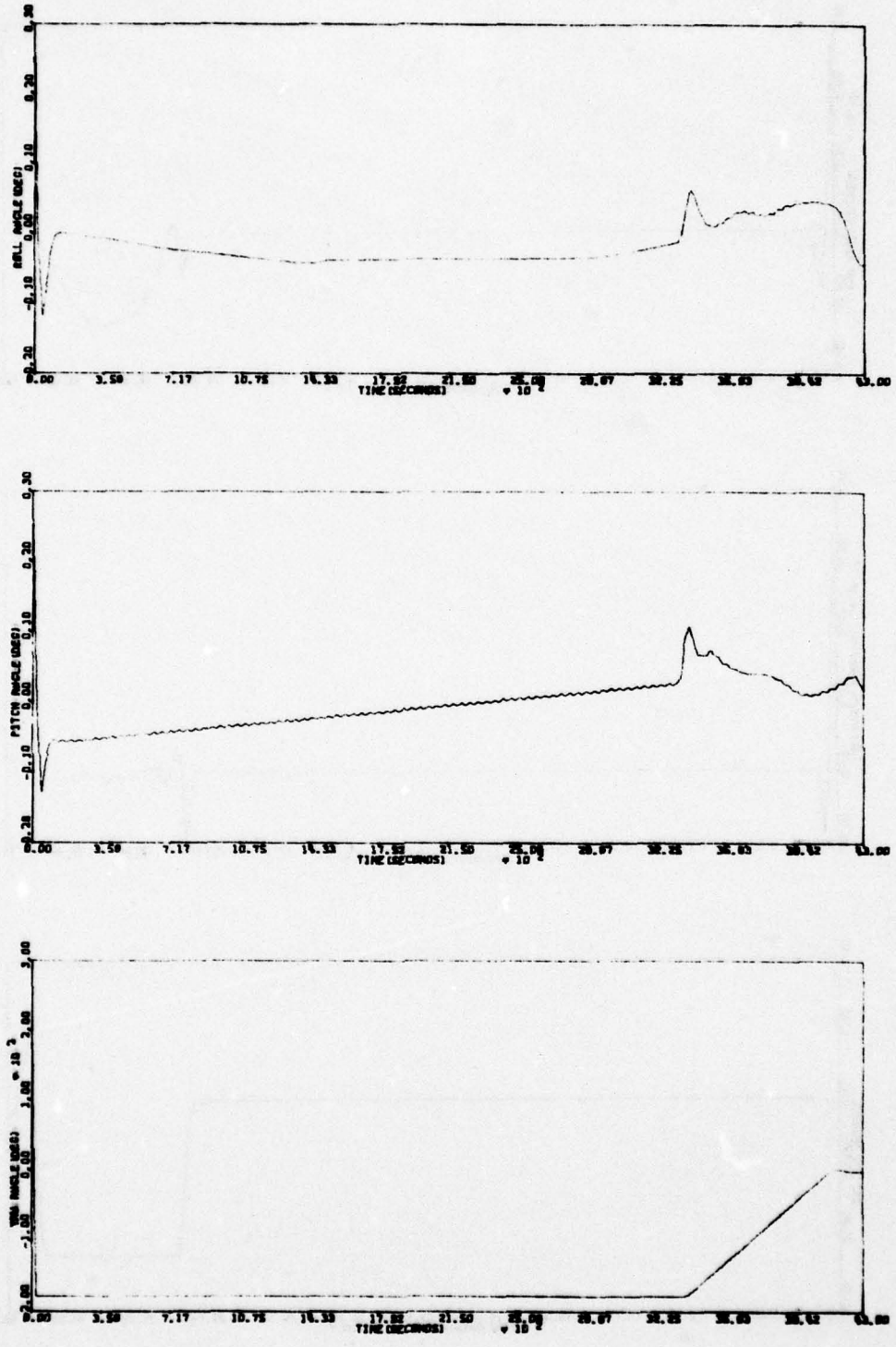

Figure 134. Run ECL01A (continued)

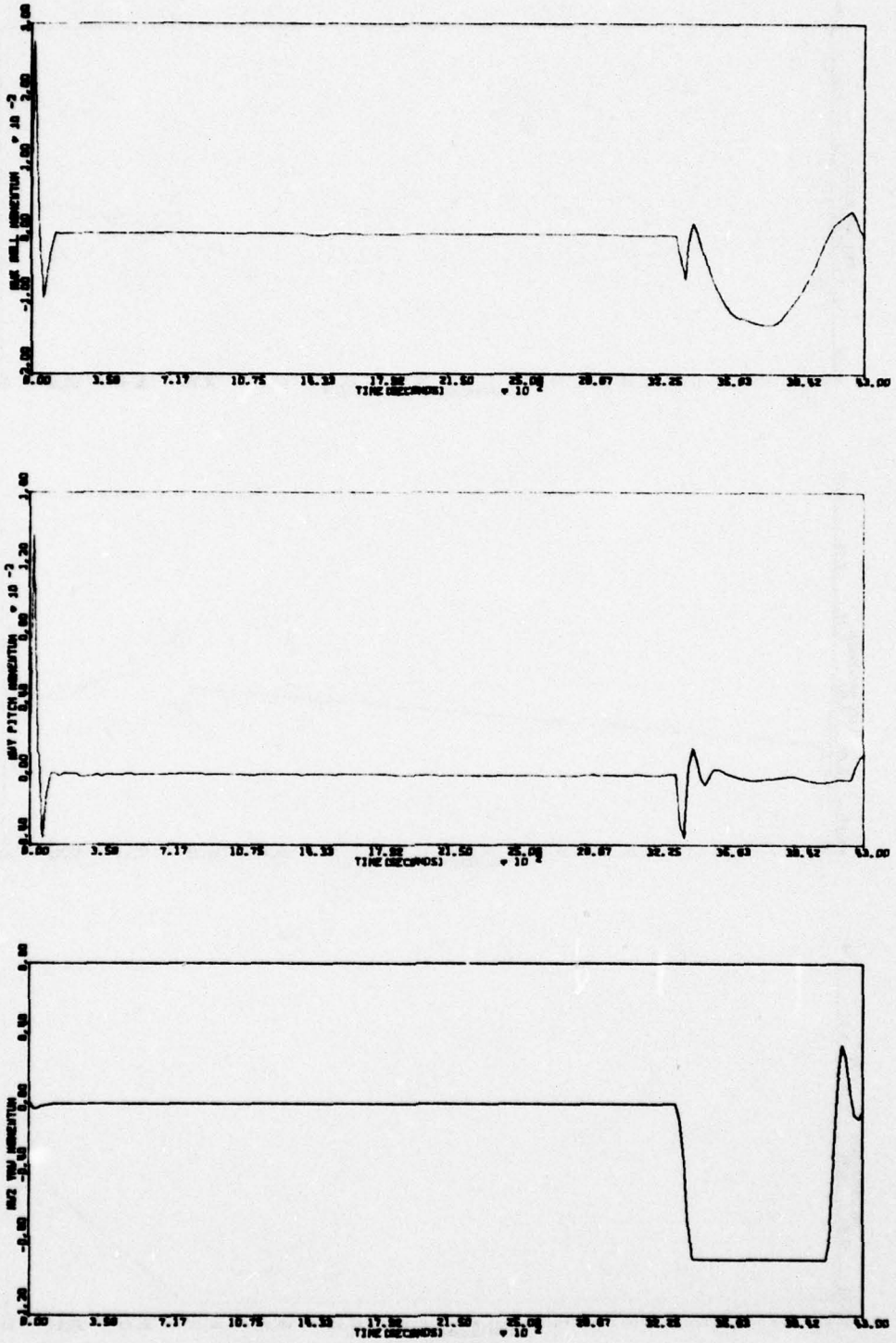

Figure 134. Run ECL01A (continued)

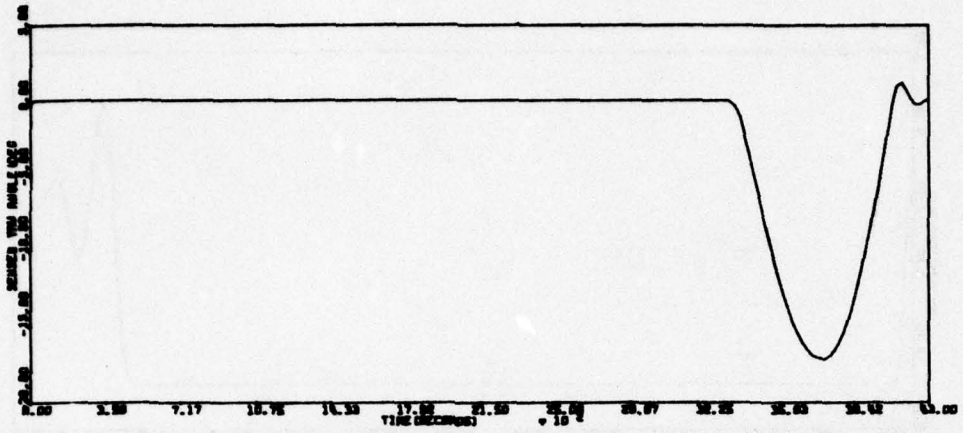

Figure 134. Run ECL01A (concluded)

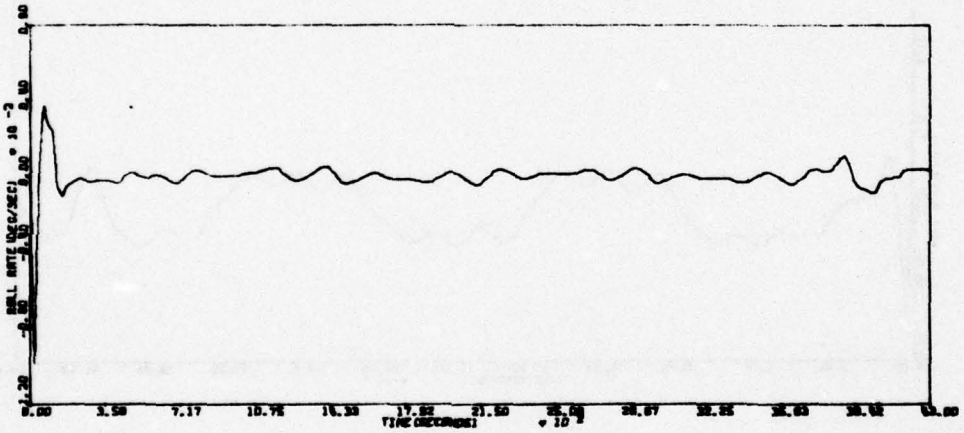

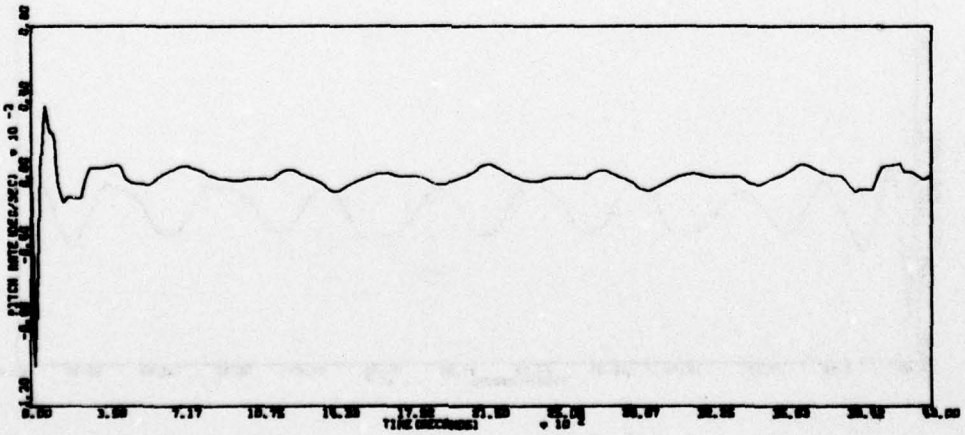

Figure 135. Run ECL02A

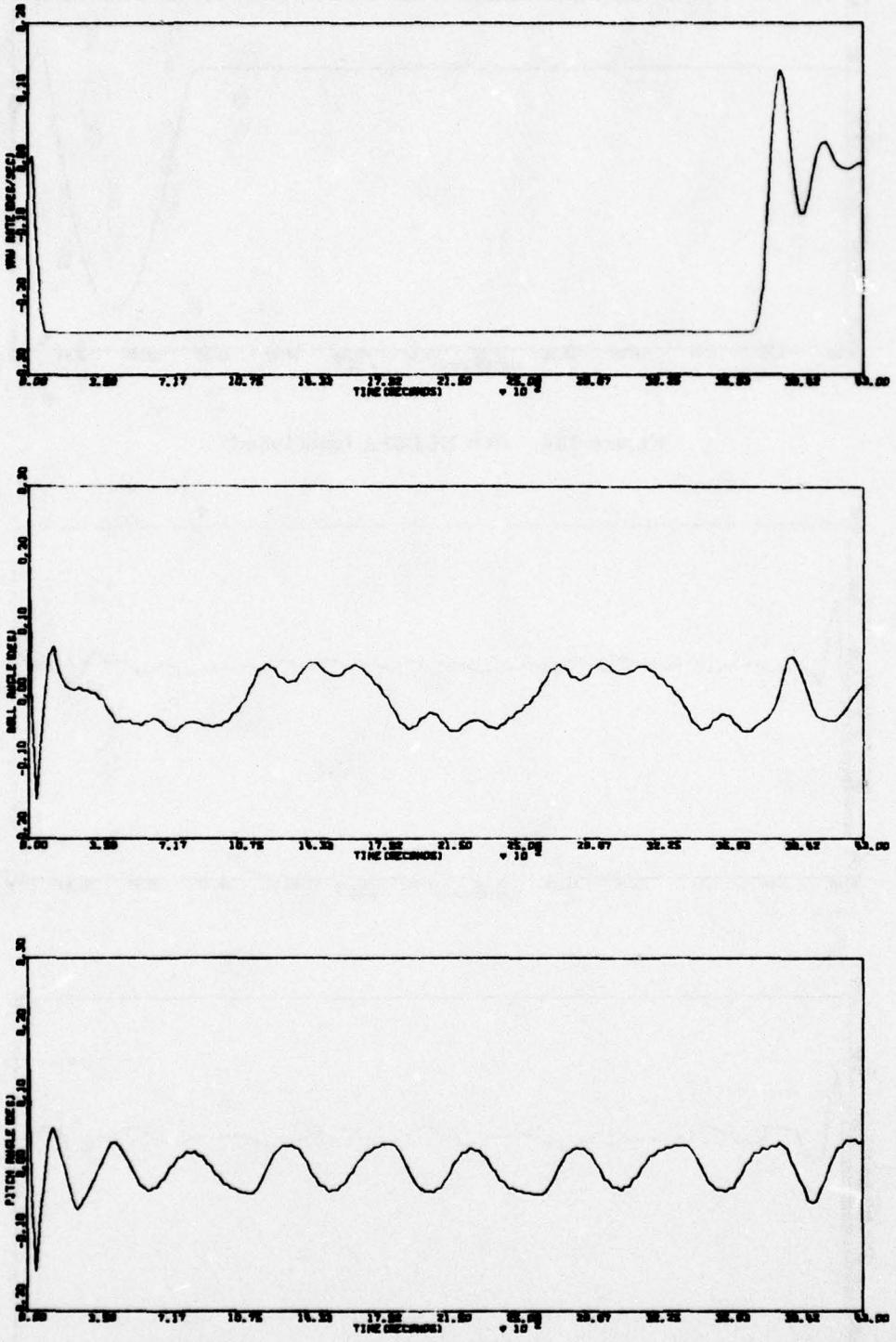

Figure 135. Run ECL02A (continued)

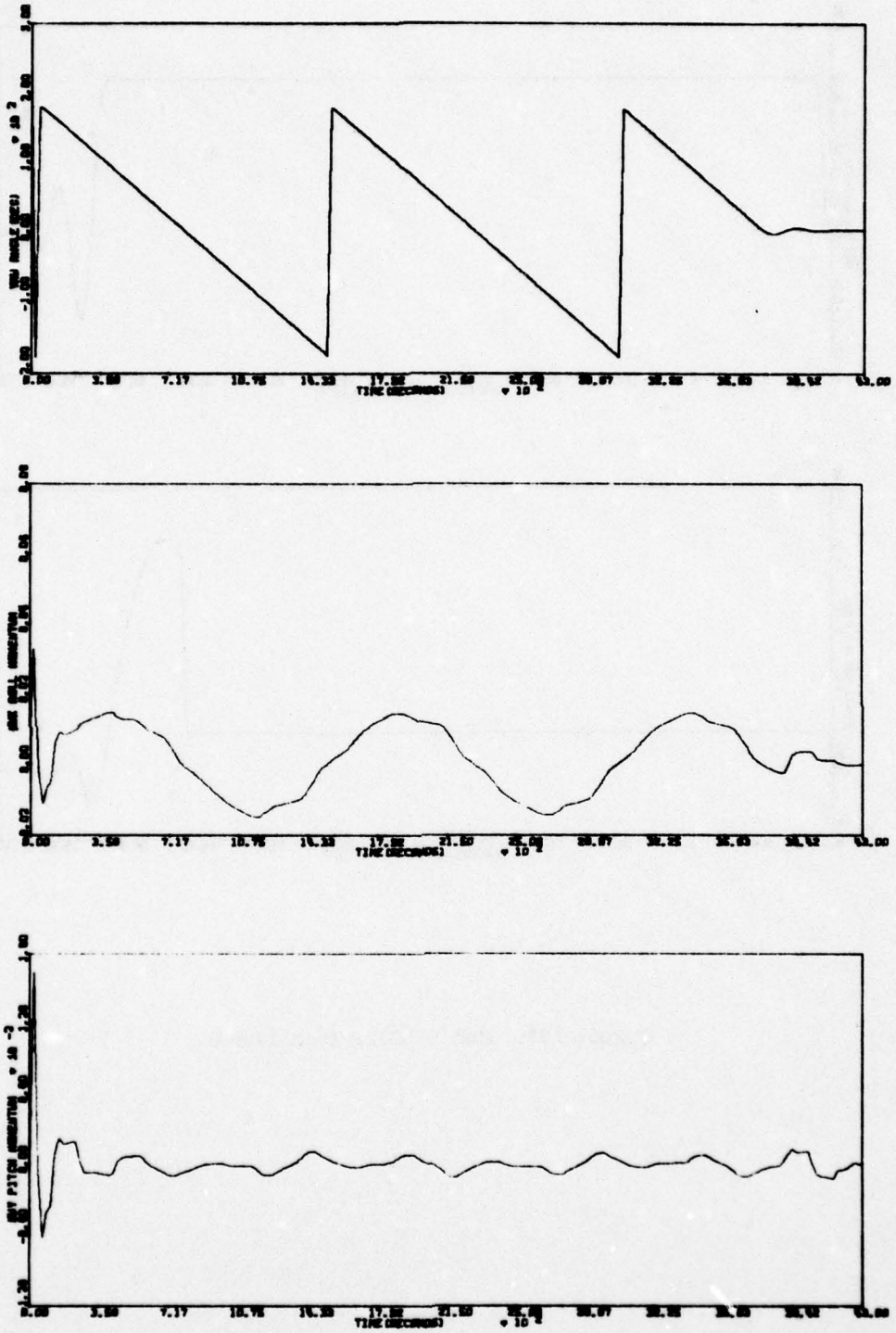

Figure 135. Run ECL02A (continued)

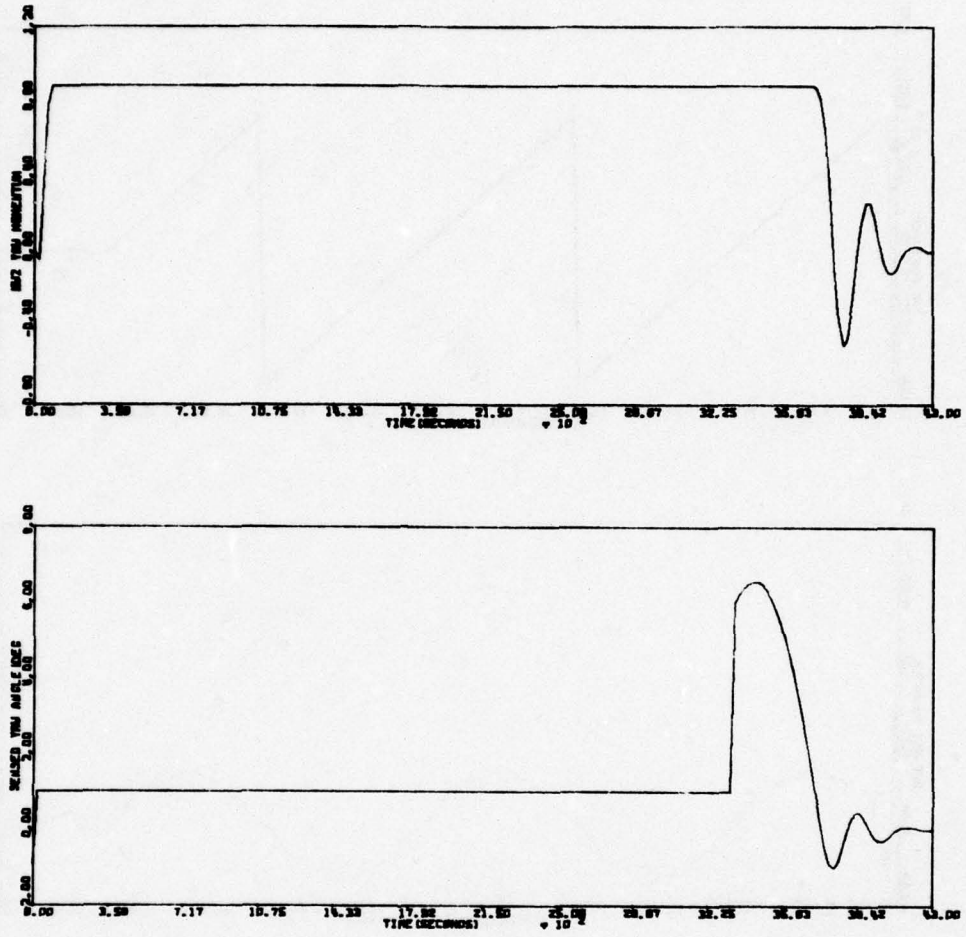

Figure 135. Run ECL02A (concluded)

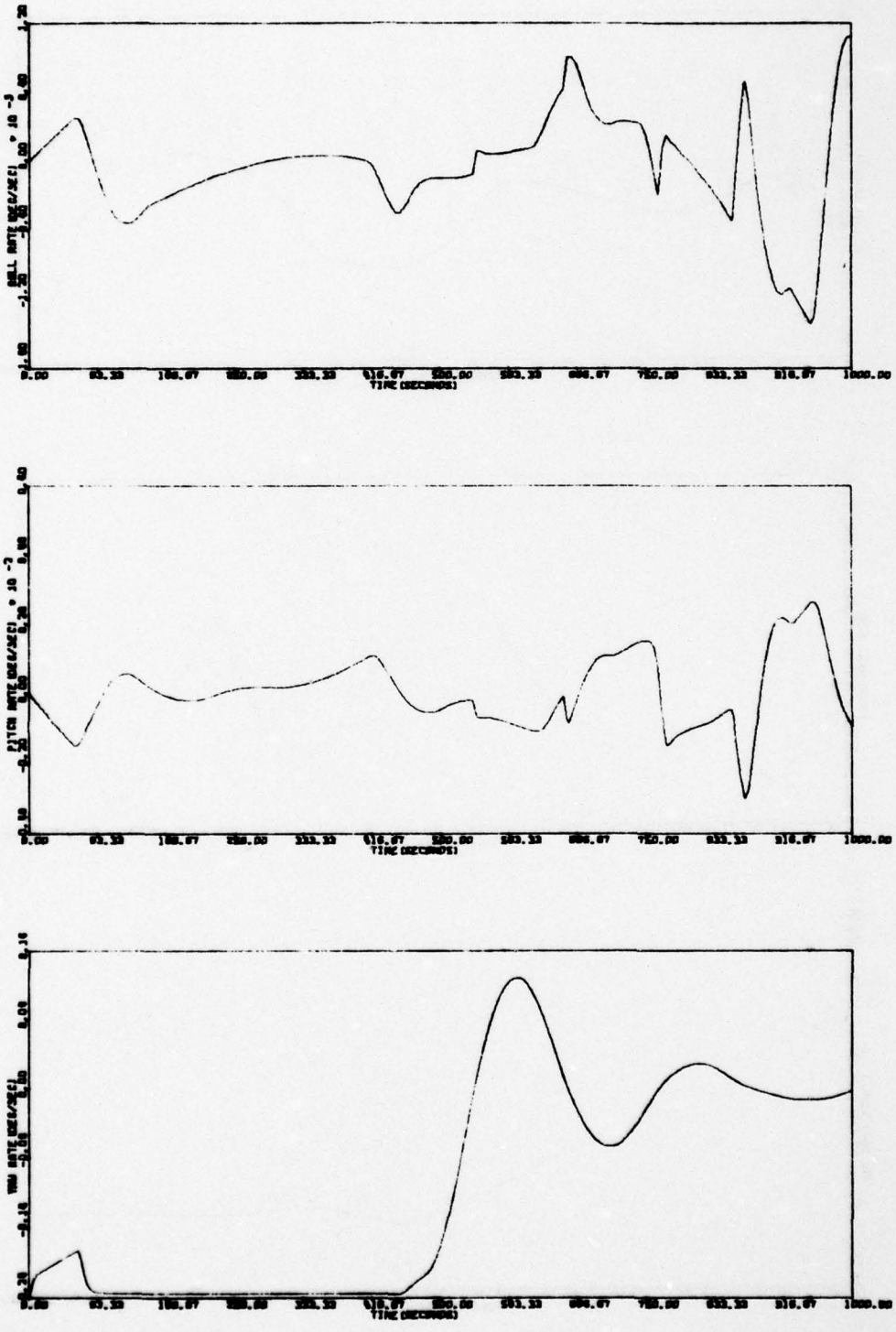

Figure 136. Run ECL03A

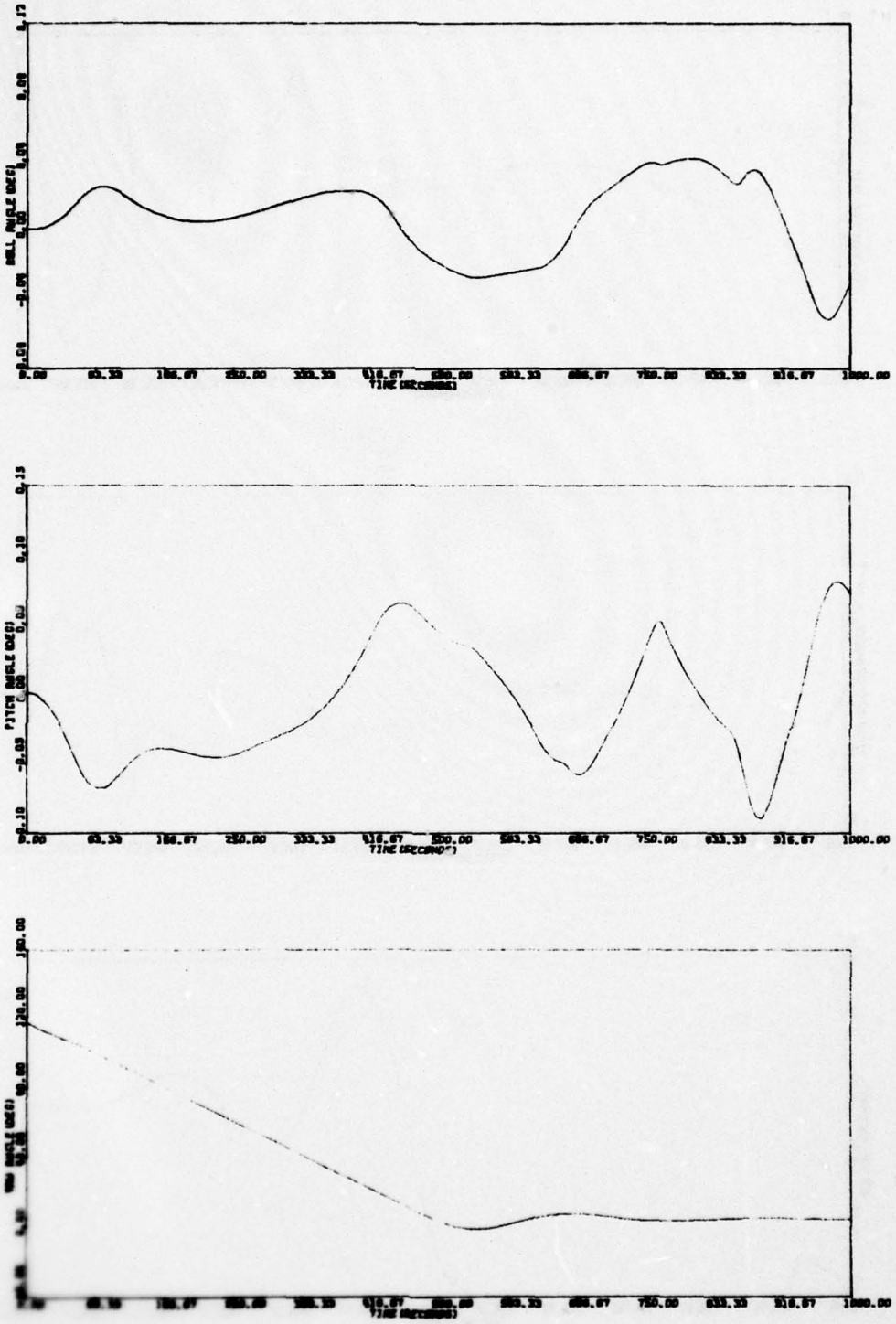

Figure 136. Run ECL03A (continued)

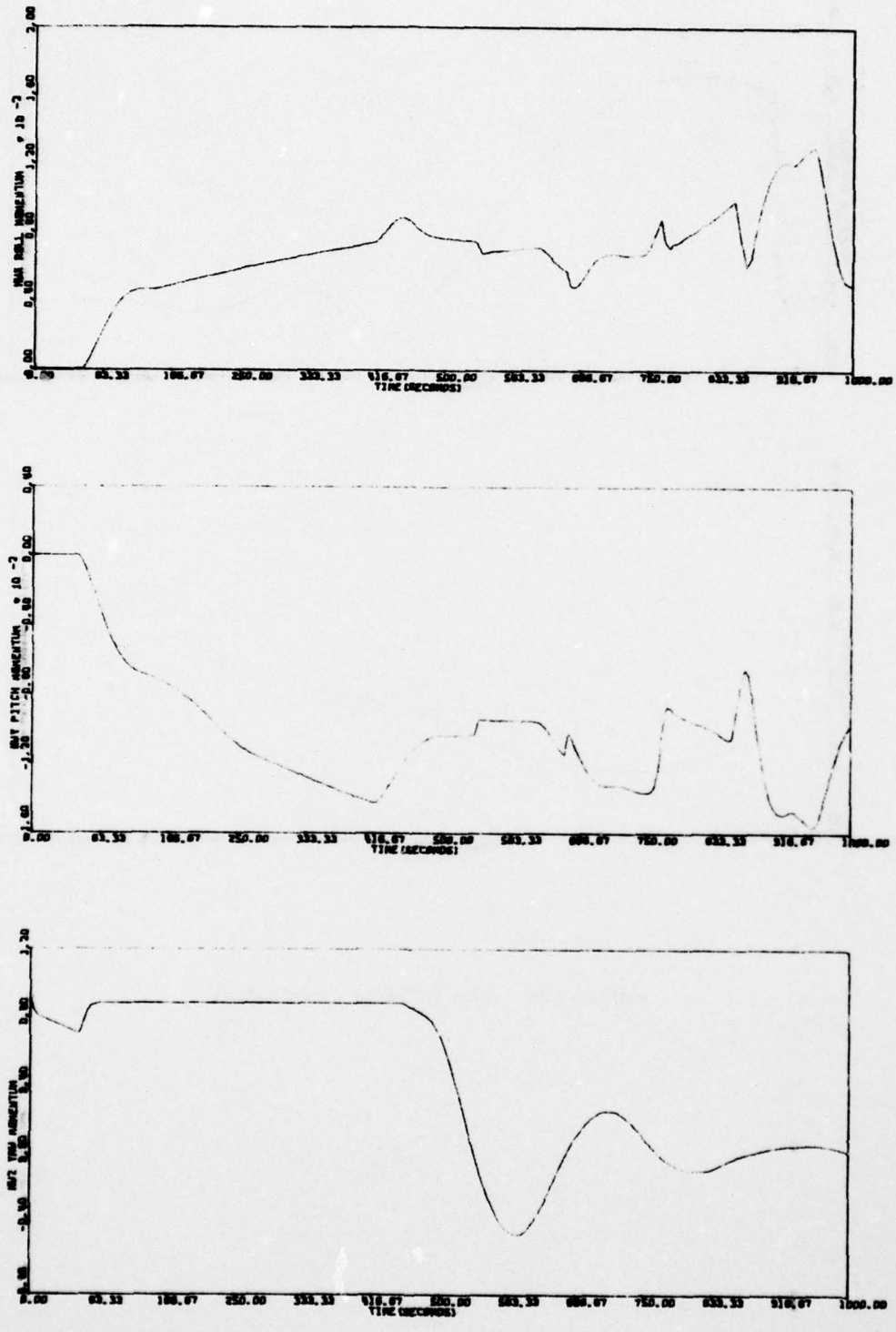

Figure 136. Run ECL03A (continued)

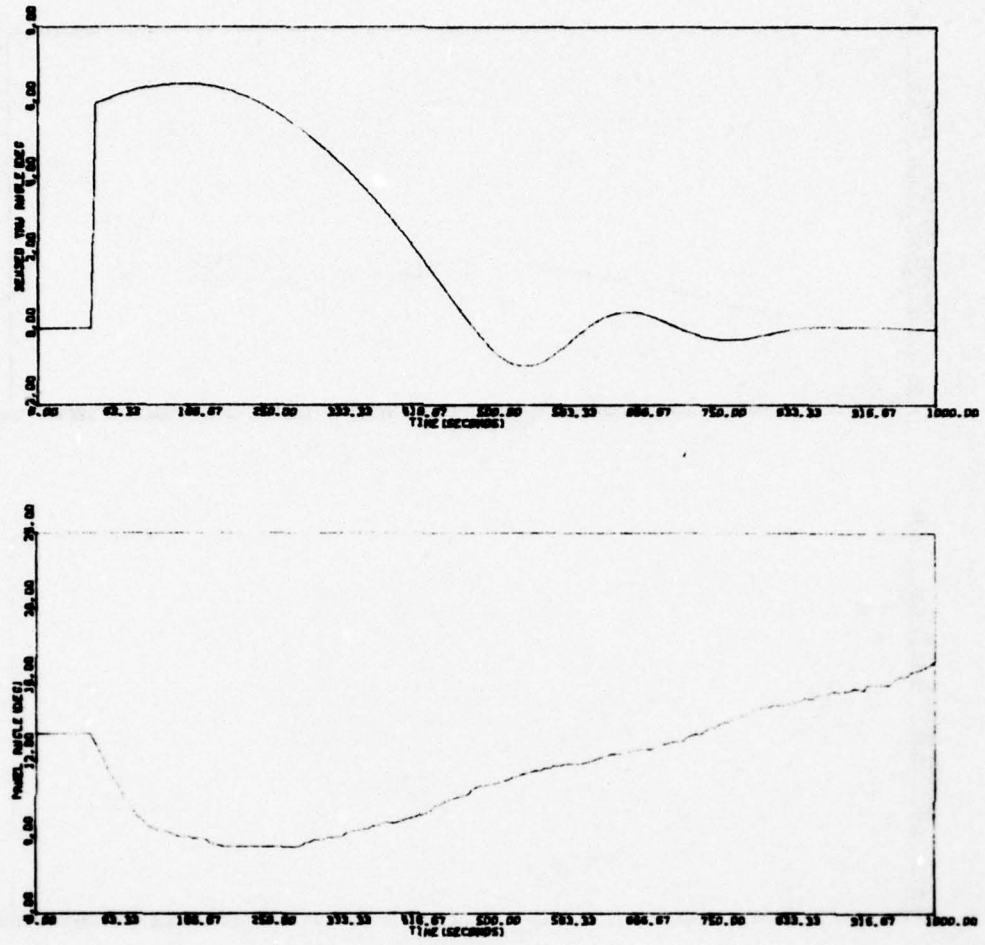

Figure 136. Run ECL03A (concluded)

The conclusions to be drawn from the eclipse runs are as follows:

- Some form of noon turn will be performed at emergence from eclipse depending on the yaw angle at emergence. As seen in Figure 134 which assumes no bias on the yaw sun sensor, the satellite emerged from eclipse with yaw angle equal to 180 deg and did a complete 180 deg turn. In Figure 121, the 1.0 deg bias on yaw sun sensor built up yaw rate; the resulting yaw angle at emergence from eclipse equaled 96 deg. In this case the satellite noon turn consisted of a 96 deg rotation.

- The output of the yaw sun sensor at emergence is a function of the yaw angle at emergence. At the 180 deg yaw angle condition with the panels at 14 deg, sensed yaw angle is almost zero. However, as you rotate 90 deg, sensed yaw angle becomes the angle between the satellite z axis and the sun line which at emergence from eclipse is approximately 14 deg (the 6.0 deg value shown in Table 26 results from the low sensor gain condition and the fact that the panel is offset from the xy plane 14 deg). Runs ECL01 and ECL02 represent the extremes in yaw sensor output at emergence with the 180 deg condition being the lowest and the 90 deg condition being the highest (though not sensing yaw).

- Run ECL03, Figure 136, is a repetition of run ECL02; run ECL03 was initiated just prior to emergence from eclipse using data that was generated in run ECL02. Also the solar array drive was active upon emergence and the array pitch sun sensor compensated for temperature affects similar to the yaw sun sensor. Although Figure 136 shows more activity than in the fixed panel run, there appears to be no problem in regaining fine sun tracking.

- Biases in the yaw sensor will eventually lead to limitation of wheel momentum in the yaw axis and equivalent 0.25 deg/sec yaw rate. The yaw angle at emergence will be a function of the magnitude of the bias but the yaw rate will not exceed 0.25 deg/sec. Investigation of the two extremes in yaw angle at emergence indicates no problems with satellite performance coming out of eclipse.

Momentum Dumping

When wheel momentum exceeds 0.25 ft-lb-sec in the pitch and roll axis, reaction jets are fired to force the reaction wheels' control system to unload the wheels. The procedure is as follows:

1. The magnitude of wheel momentum and the status of jet heater beds are checked each hour. If momentum exceeds 0.25 ft-lb-sec by axis and the heater beds are turned on, reaction jets are fired as specified in Table 27. Polarity of jet firing is determined at this check. If momentum exceeds 0.25 ft-lb-sec by axis and the heater beds are not on, the heater beds are turned on. If the heater beds are on and the momentum is less than 0.25 ft-lb-sec, the heater beds are turned off.

2. The duration of the firing time is selectable from four values from the ground as a function of tank pressure and resultant jet thrust. The desired momentum reduction per dump is 0.16 ft-lb-sec.

3. The momentum dumping frequency is expected to be one every five days. A rough check on momentum dumpings required as a function of solar torque was discussed in Section III.

Four simulation runs were made to check momentum dumping procedures. They are summarized in Table 28. Uncertainties are summarized in Table 29. Time histories of the runs are given in Figures 137 through 140.

TABLE 27. MOMENTUM DUMP JET FIRING TIMES

Pitch Momentum Dump Firing Times (sec)	Roll Momentum Dump Firing Times (sec)
0.1	0.8
0.3	2.4
0.5	4.0
0.7	5.6

TABLE 28. MOMENTUM DUMP SIMULATION RUNS

Run	Roll Jet On Time (sec)	Pitch Jet On Time (sec)	Wheel Momentum (ft-lb-sec)		Wheel Momentum (ft-lb-sec)		ϕ_E (deg)	θ_E (deg)	Uncertainties	Comments
			$H_{x_{1c}}$	$H_{y_{1c}}$	H_{x_F}	H_{y_F}				
MD01A	2.4	0.0	0.25	0.0	0.77	0.0	0.59	0.0028	No	
MD02A	0.0	0.3	0.0	0.25	0.0	0.122	0.0018	0.77	No	
MD03A	2.4	0.0	0.25	0.0	0.077	-0.028	0.59	0.21	Yes	
MD04A	2.4	0.0	0.0	-0.25°	-0.0596	0.0502†	0.45	0.122	Yes	Noon turn

°Transferred into

†After 180 deg rotation

TABLE 29. OFF-NOMINAL CONDITIONS FOR MOMENTUM DUMP SIMULATION

Earth Sensor Gain	High
Yaw Sensor Gain	Low
Wheel Misalignment	
--Cone	1 deg
--Cant	1 deg
I_{xy}	187.88 slug ft^2
I_{yy}	94.458 slug ft^2
I_{zz}	211.58 slug ft^2
I_{xy}	-0.7221 slug ft^2
I_{xz}	-0.0081 slug ft^2
I_{yz}	-0.0091 slug ft^2

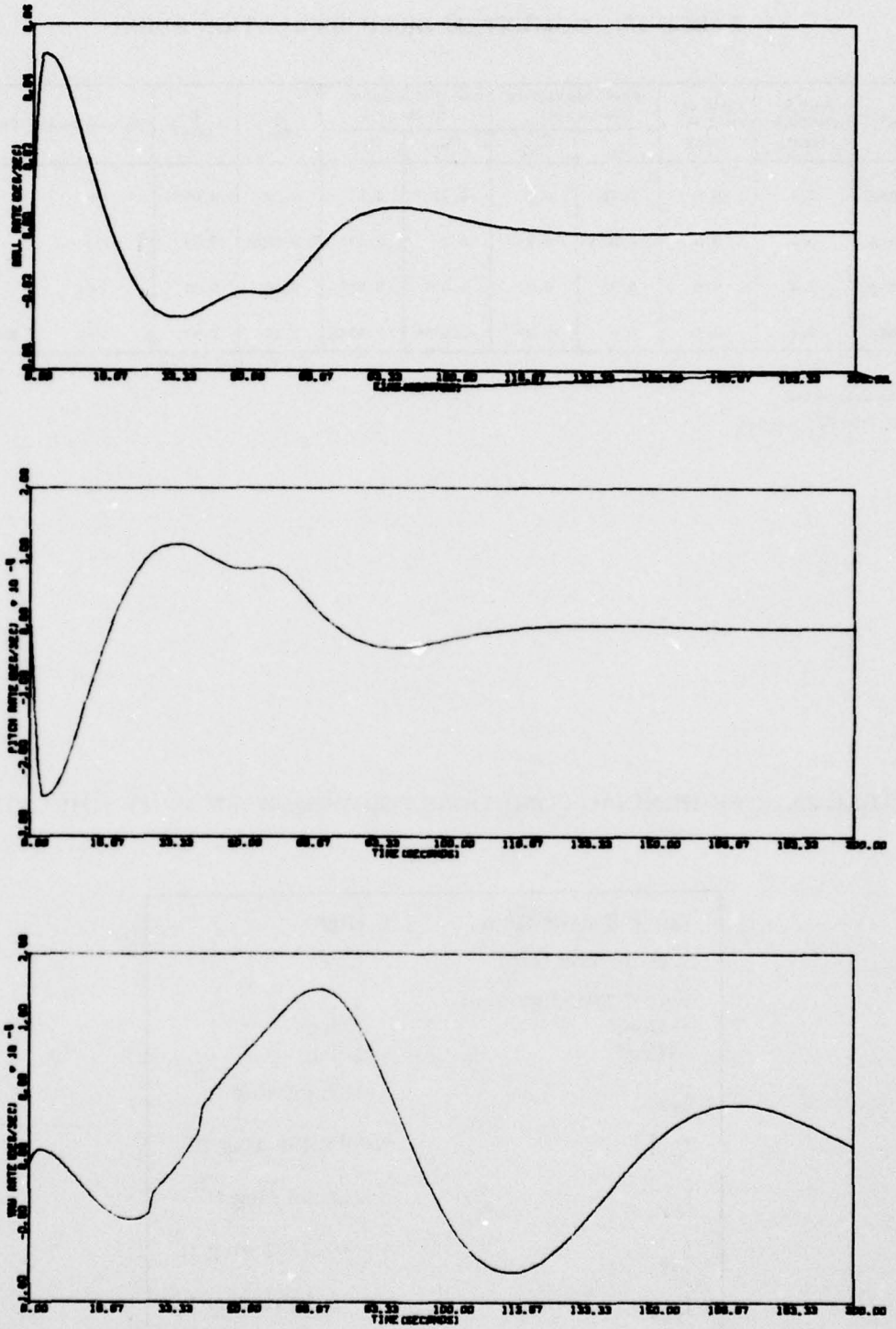

Figure 137. Run MD01A

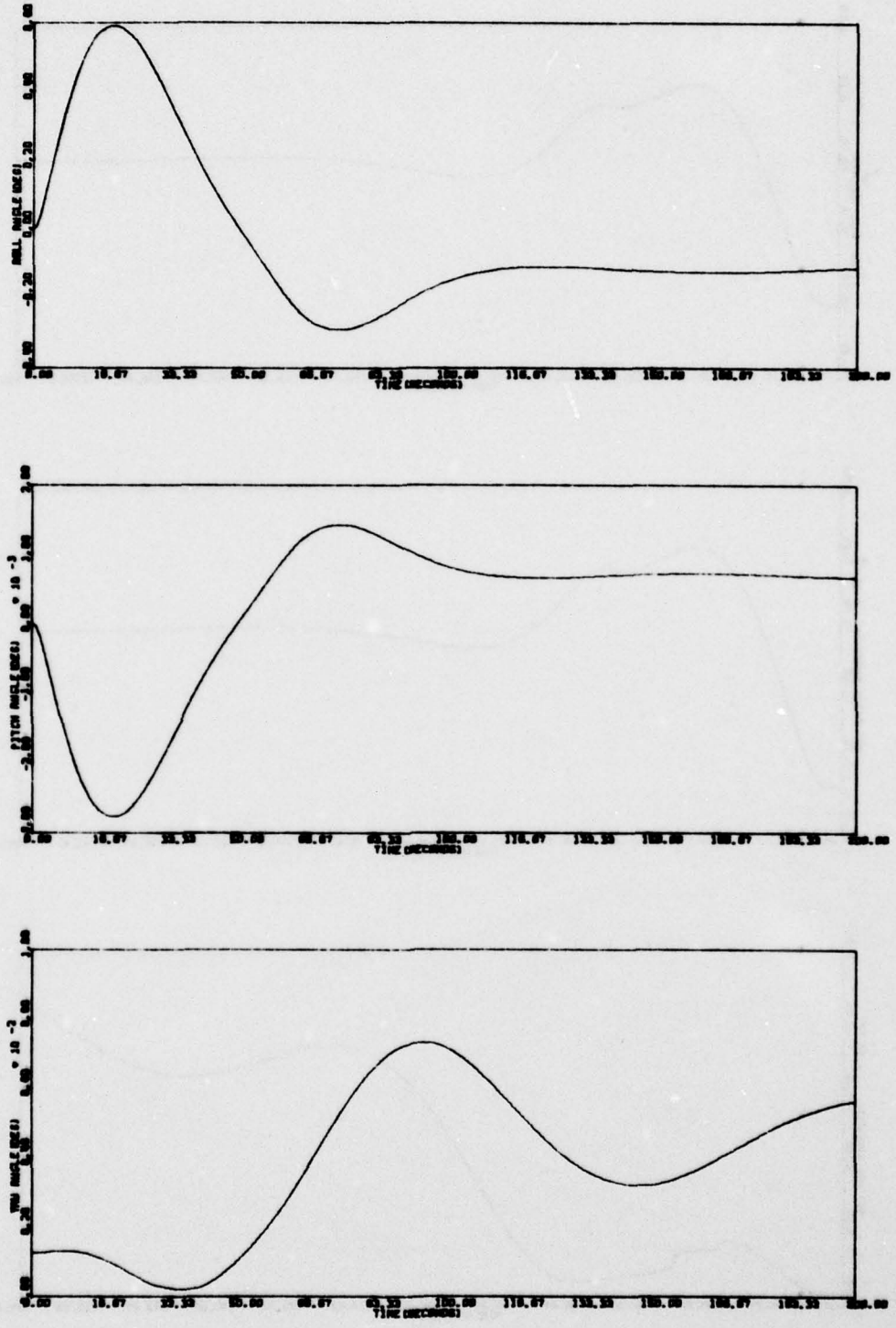

Figure 137. Run MD01A (continued)

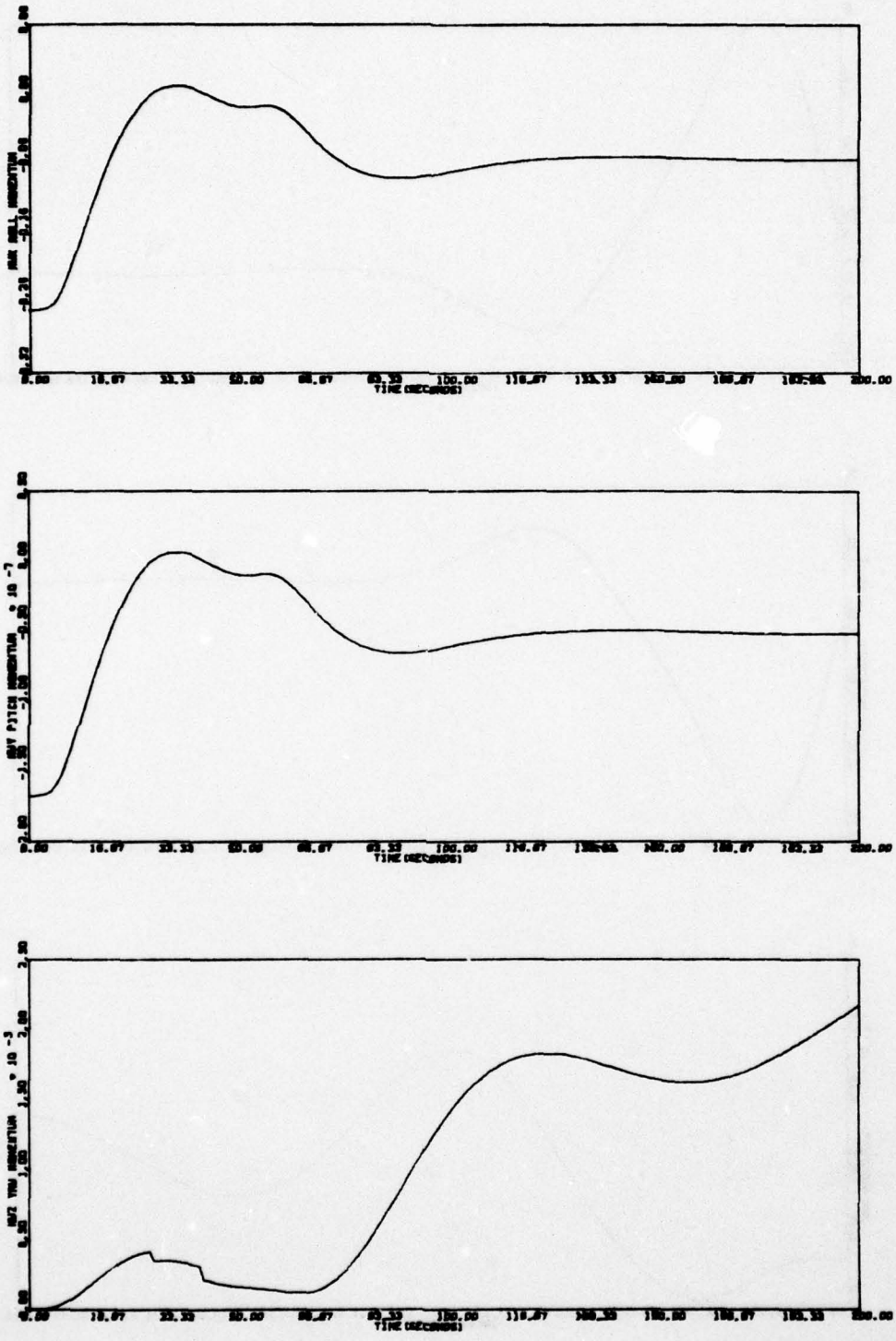

Figure 137. Run MD01A (concluded)

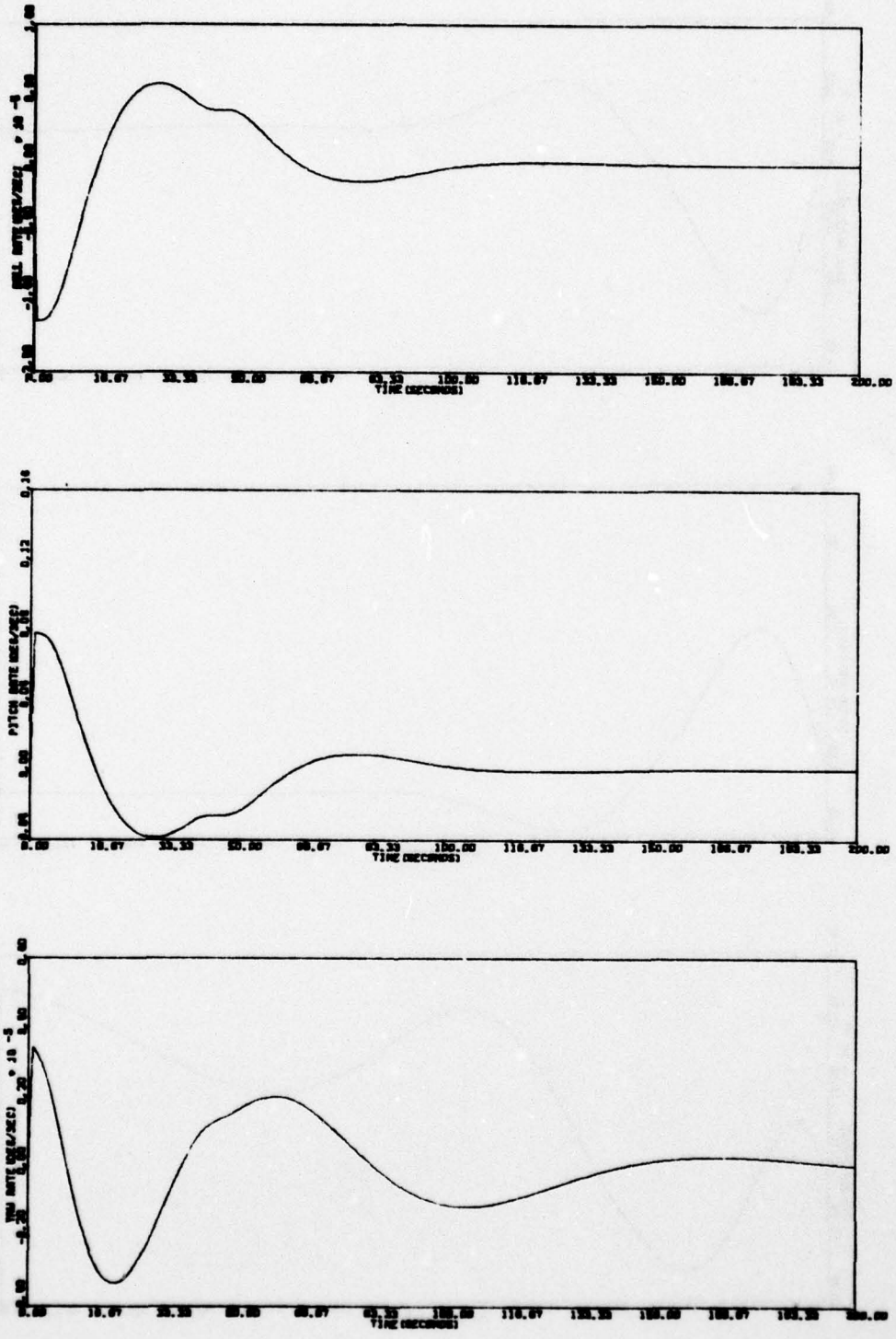

Figure 138. Run MD02A

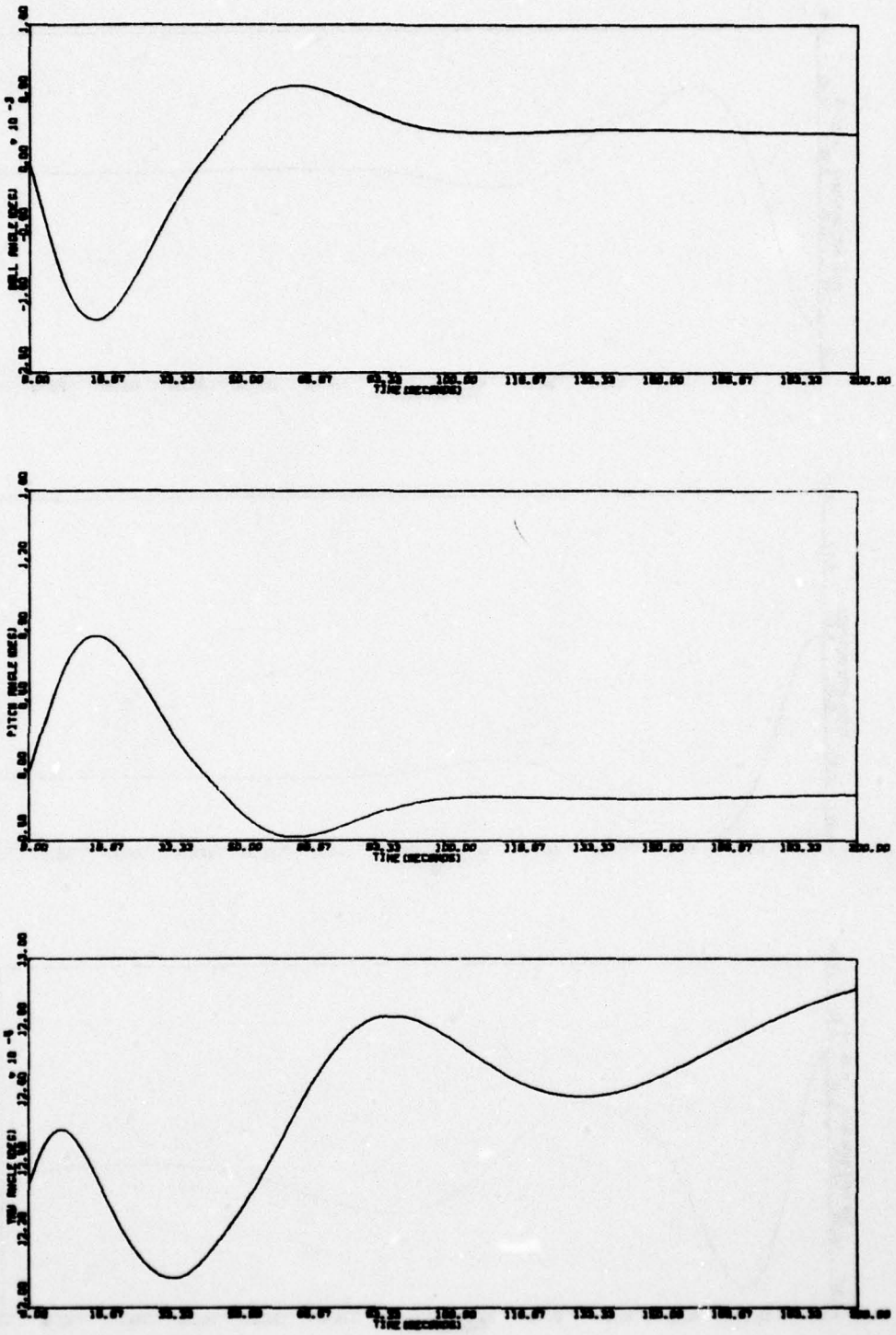

Figure 138. Run MD02A (continued)

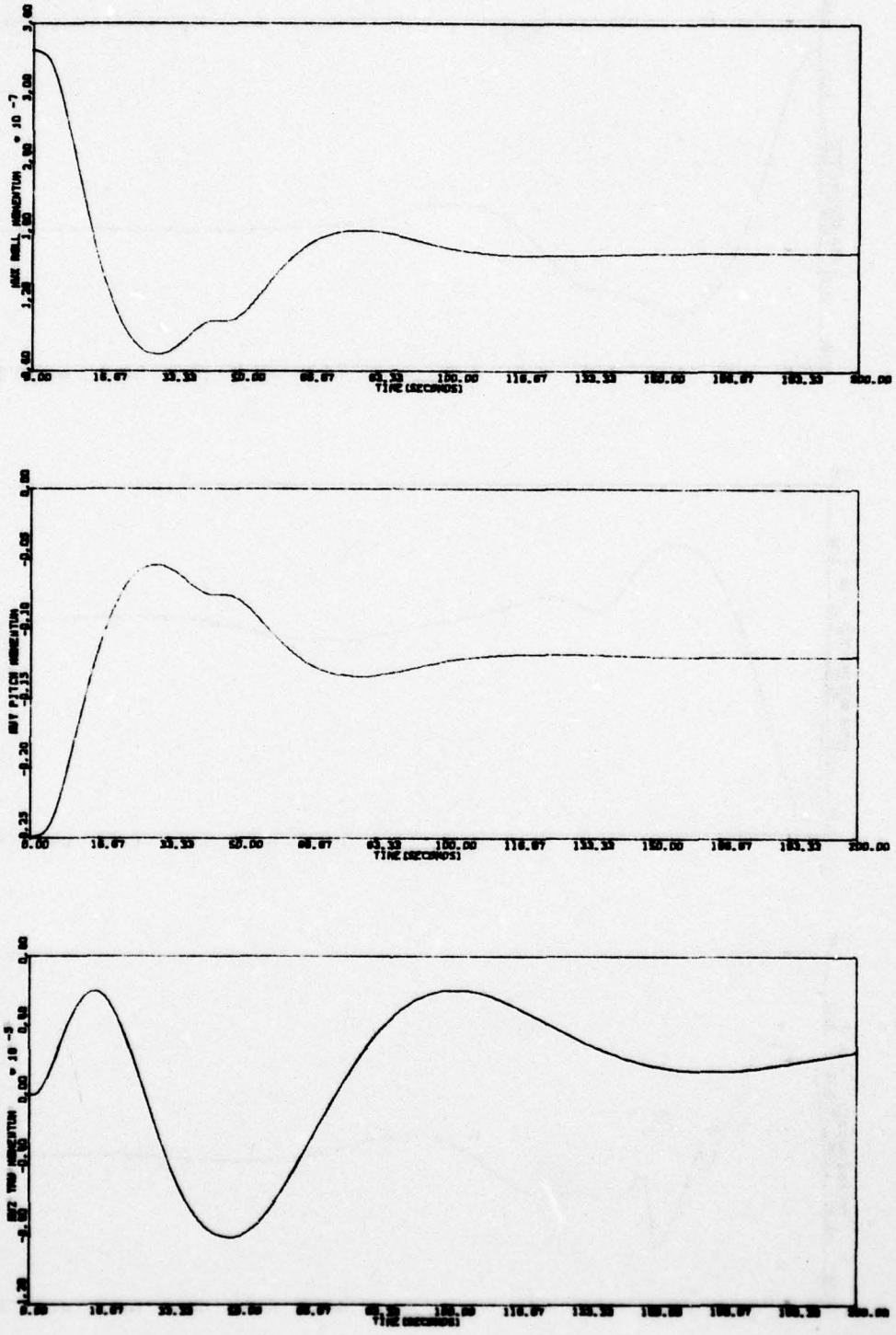

Figure 138. Run MD02A (concluded)

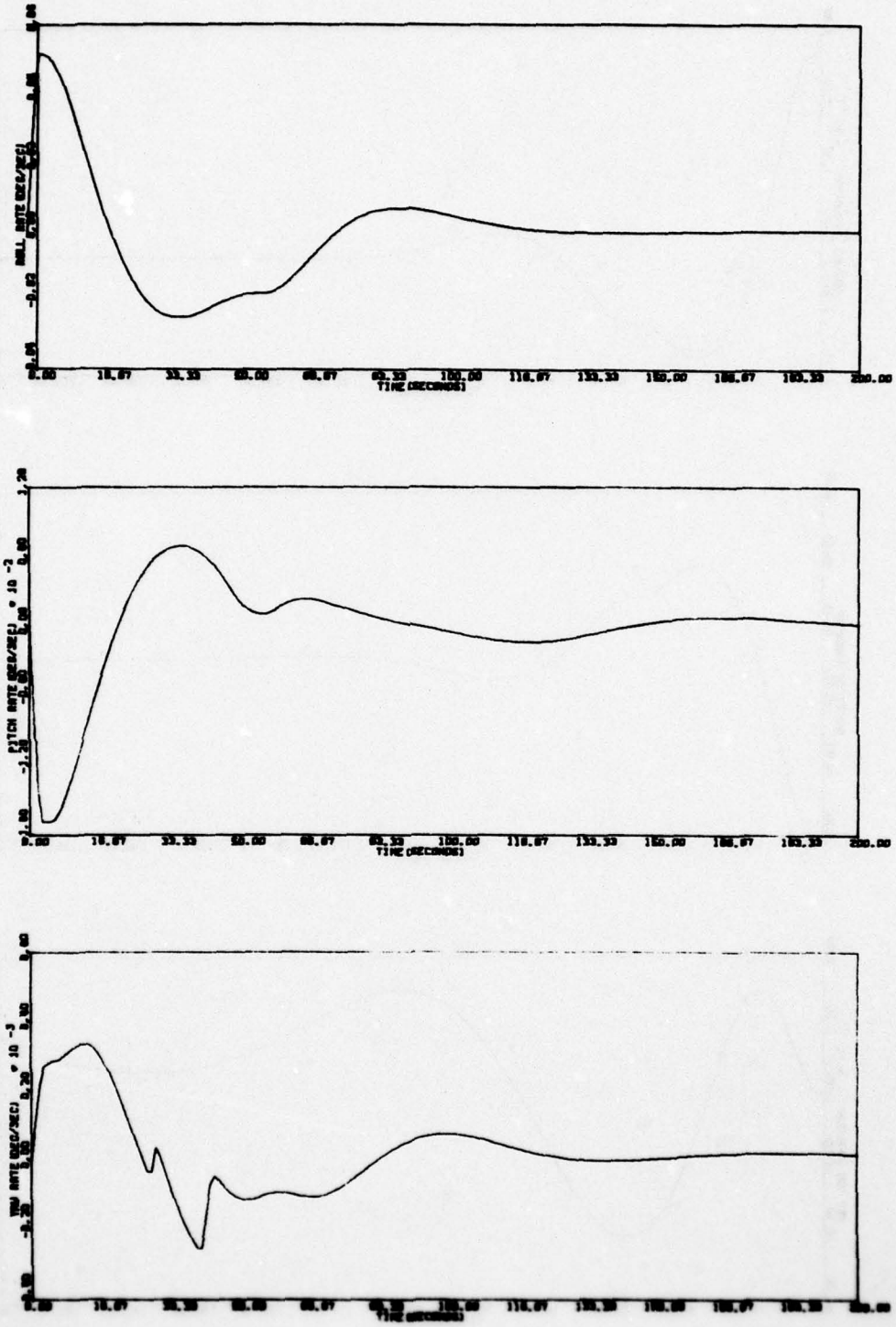

Figure 139. Run MD0CA

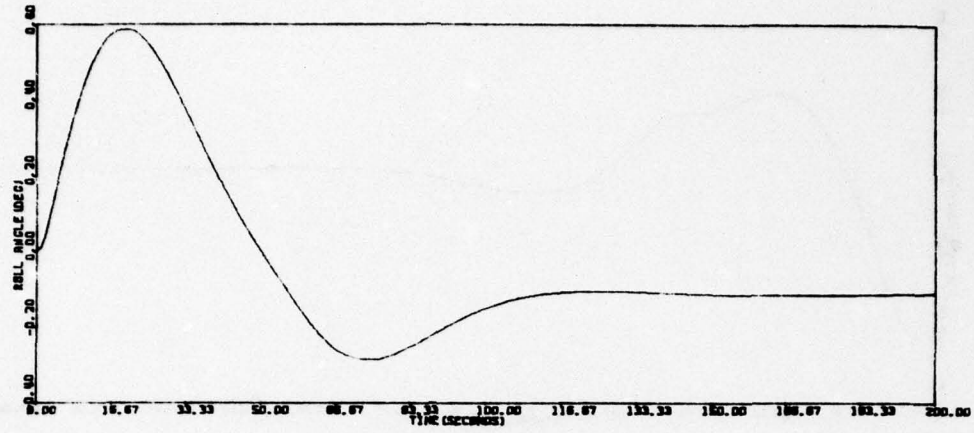

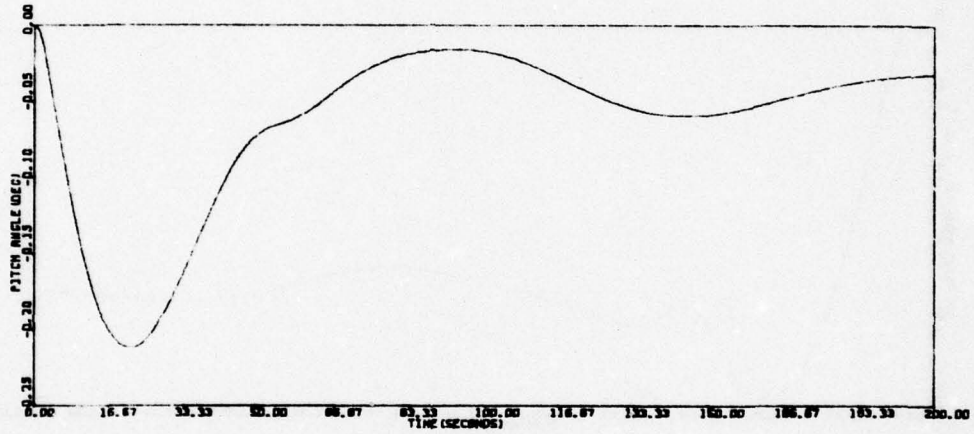

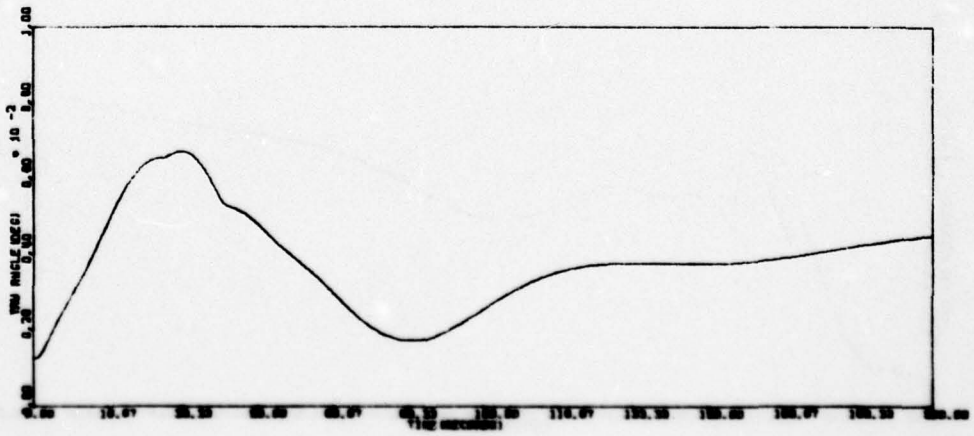

Figure 139. Run M103A (continued)

AD-A056 811 HONEYWELL INC MINNEAPOLIS MINN SYSTEMS AND RESEARCH --ETC F/G 17/7
INDEPENDENT STABILITY AND CONTROL ANALYSIS OF NAVIGATION DEVELO--ETC(U)
JAN 78 R E POPE, M D WARD, M F BARRETT F04701-75-C-0135
UNCLASSIFIED 78SRC10-VOL-1 SAMSO-TR-78-74-VOL-1 NL

4 OF 4
ADA
056811

END
DATE
FILMED
9-78
DDC

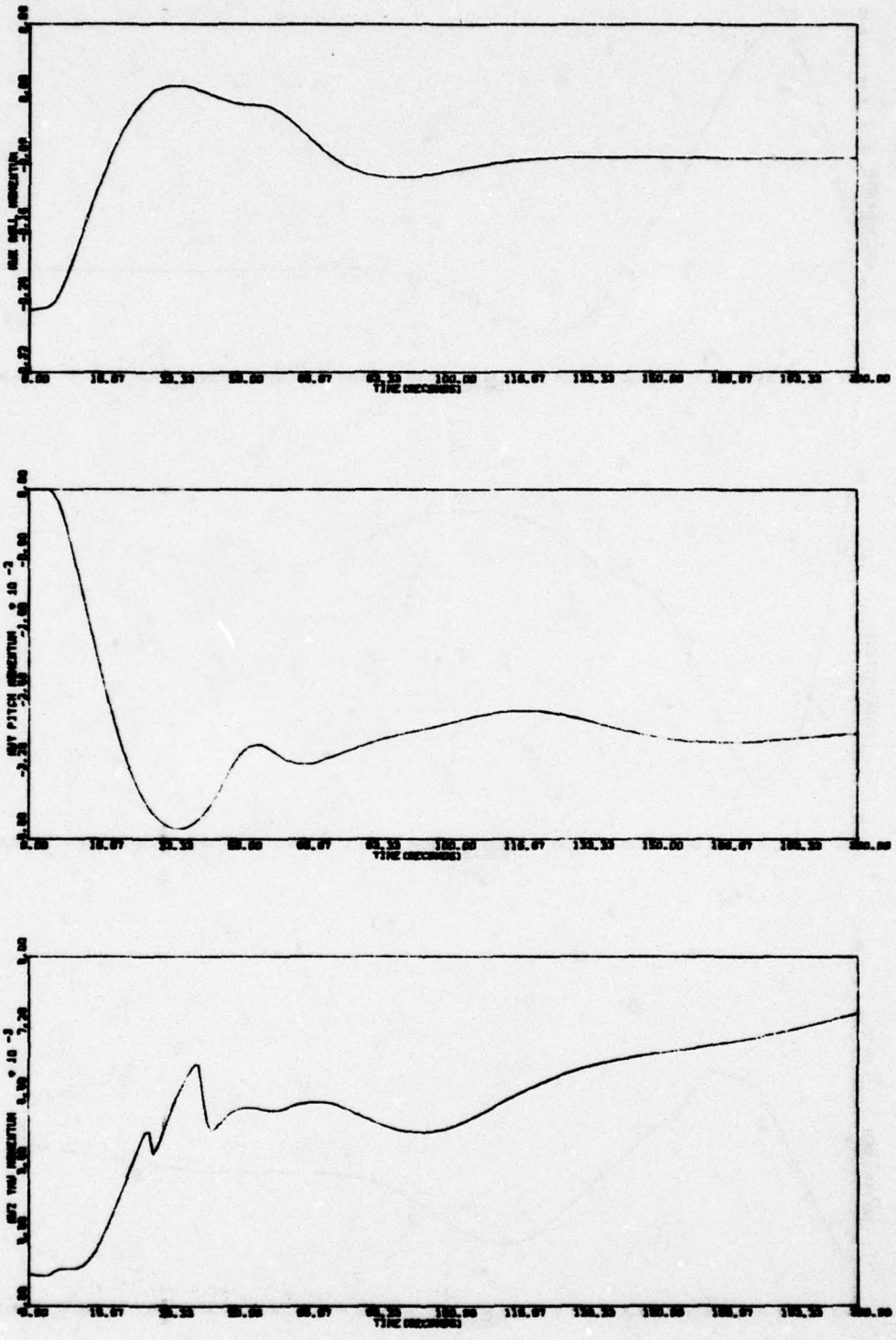

Figure 139. Run MD03A (concluded)

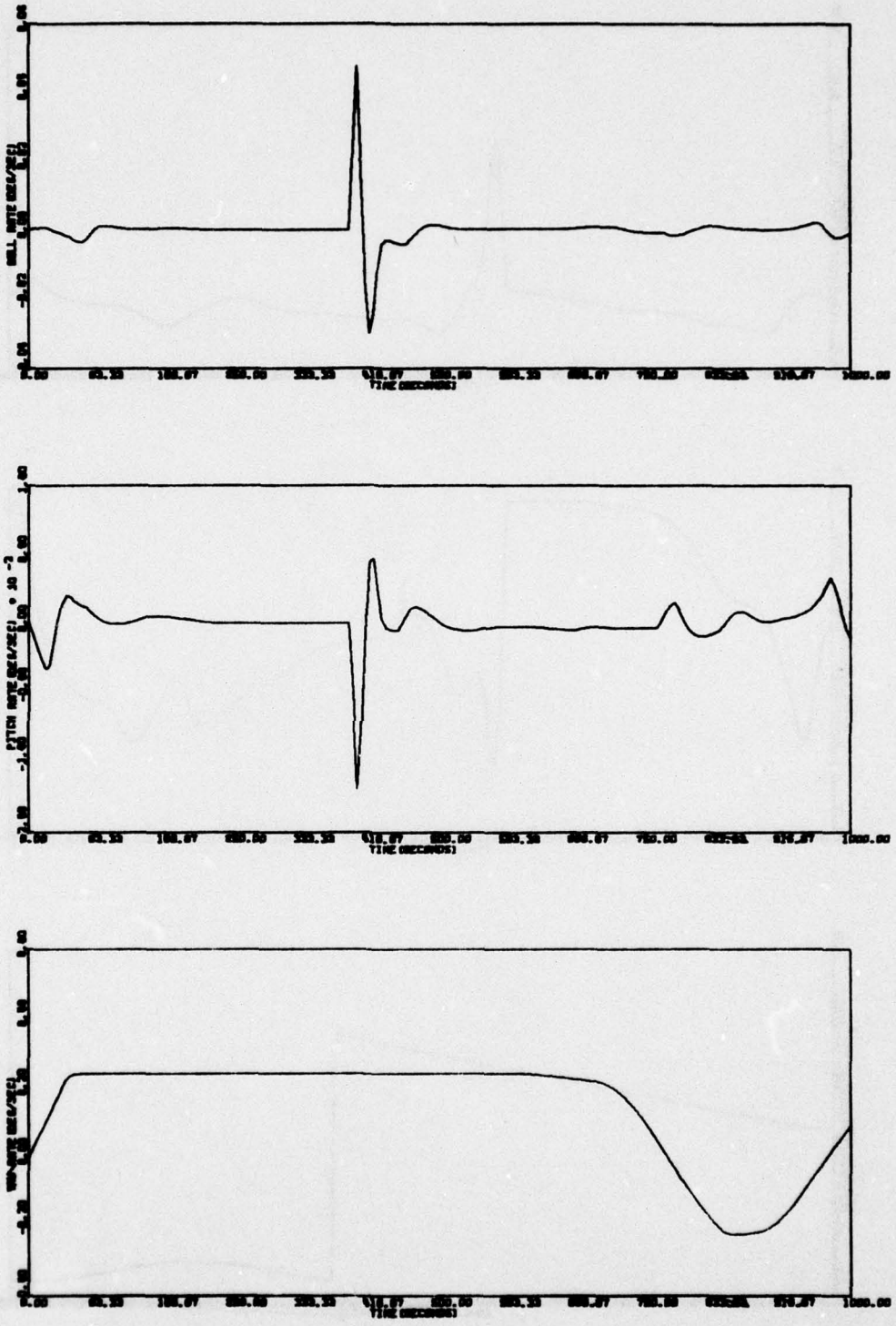

Figure 140. Run MD04A

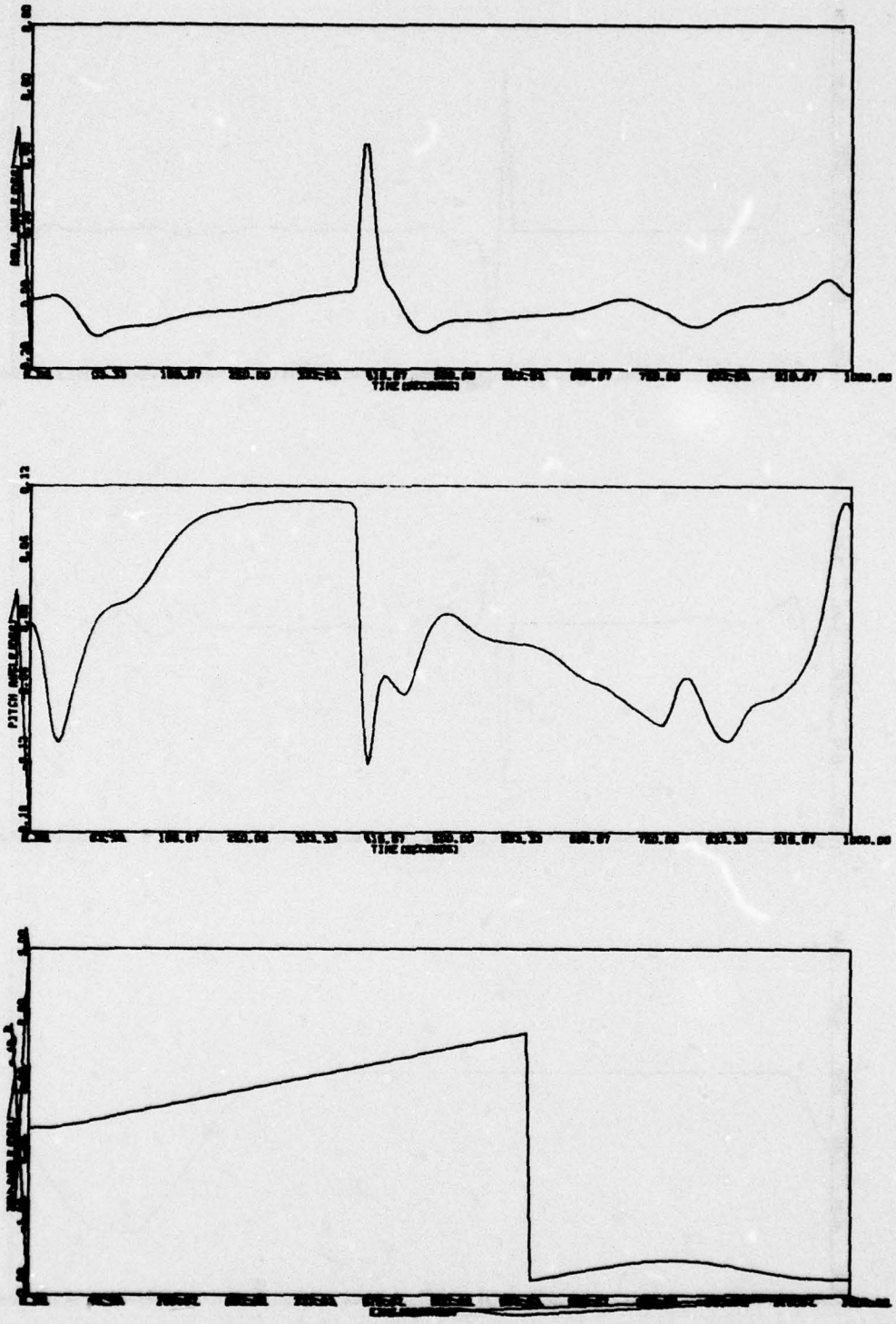

Figure 140. Run MD04A (continued)

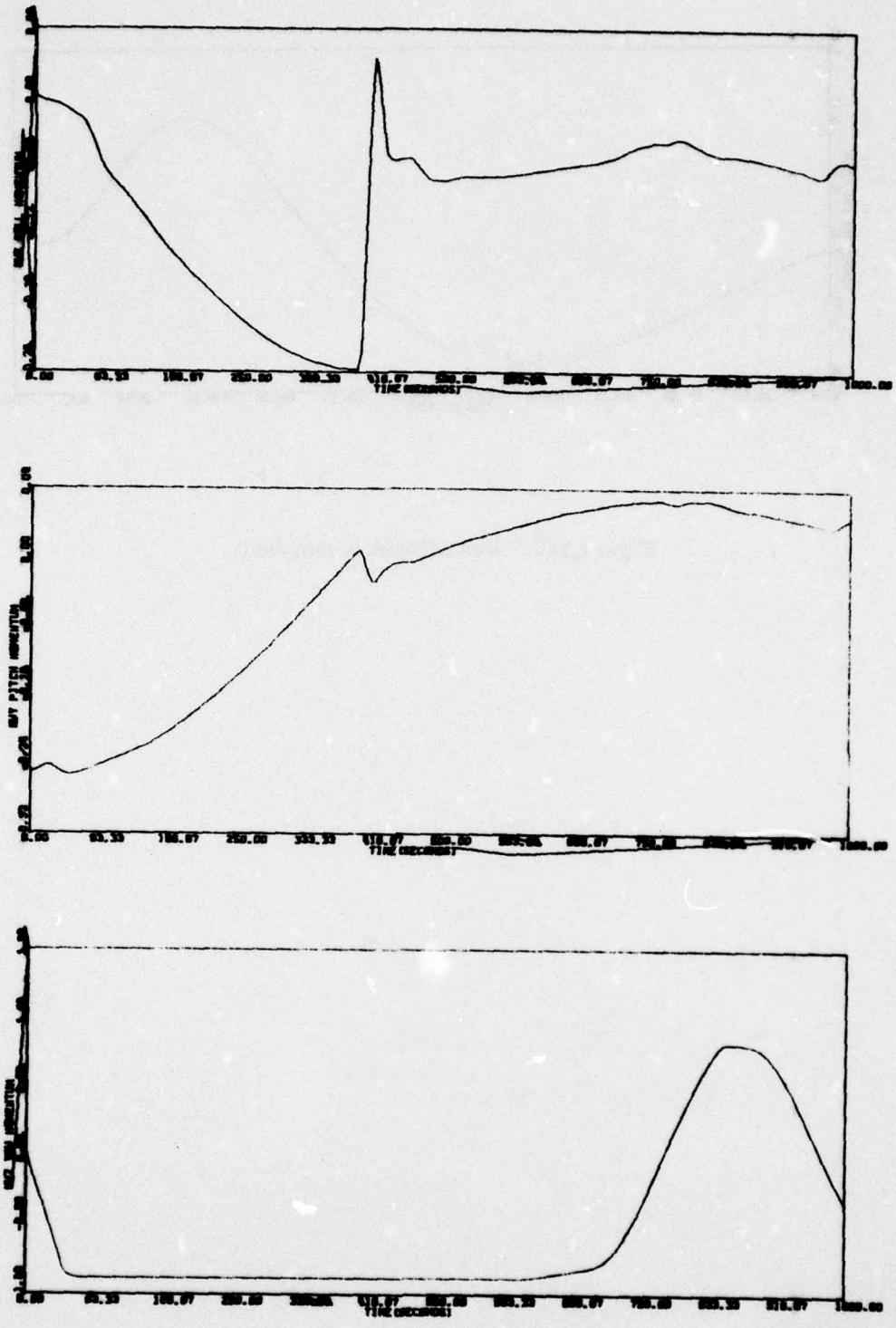

Figure 140. Run MD04A (continued)

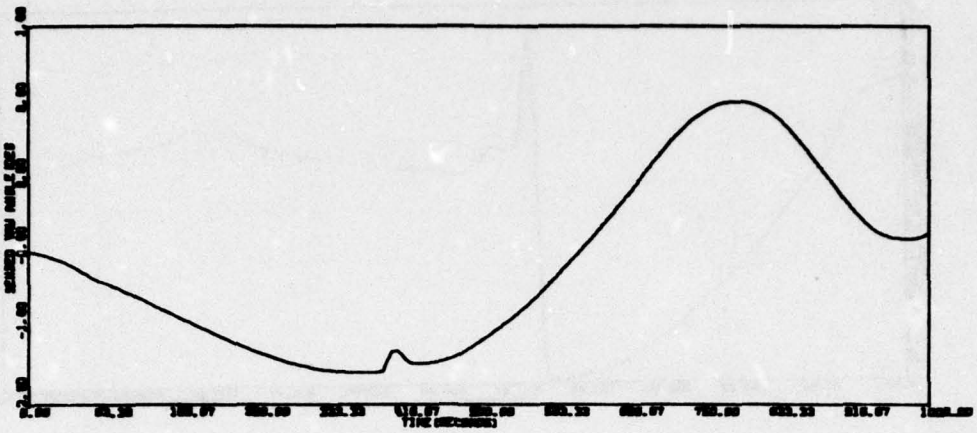

Figure 140. Run MD04A (concluded)

The following are results of the momentum dumping simulation runs:

- Momentum dumping procedures are adequate. Transient attitude errors are less than 1.0 deg during dumping, assuming worst case wheel alignment, thruster misalignments, thruster mismatches, and center of mass offsets.
- Momentum dumping during noon turn, as shown in Figure 140, presents no problem.

Failed Reaction Wheels

Performance of the wheel control system under both compensated and uncompensated wheel failure conditions was investigated. The severest control requirements exist at noon turn; hence, wheel failure performance was investigated at noon turn. Since both pitch and roll loops behave identically and since any wheel failure loss affects yaw, only wheel 2 failures were investigated. Table 30 summarizes the results of wheel 2 failures both uncompensated and compensated at the noon turn condition. Transient response histories are given in Figures 141 and 142.

TABLE 30. WHEEL FAILURE SIMULATION RUNS

Run	Failed Wheel	Peak Attitude Error (deg)		Peak Momentum (ft-lb-sec)		
		ϕ	θ	H_x	H_y	H_z
WF01A Uncompensated	2	0.31	5.28	-0.33	0.42	-1.18
WF01A Compensated	2	-0.27	0.36	-0.27	0.28	-0.89

Results of the failed wheel simulation runs indicate that even under uncompensated conditions a failed wheel condition is stable though sloppy. Compensating for this wheel failure returns performance to satisfactory levels.

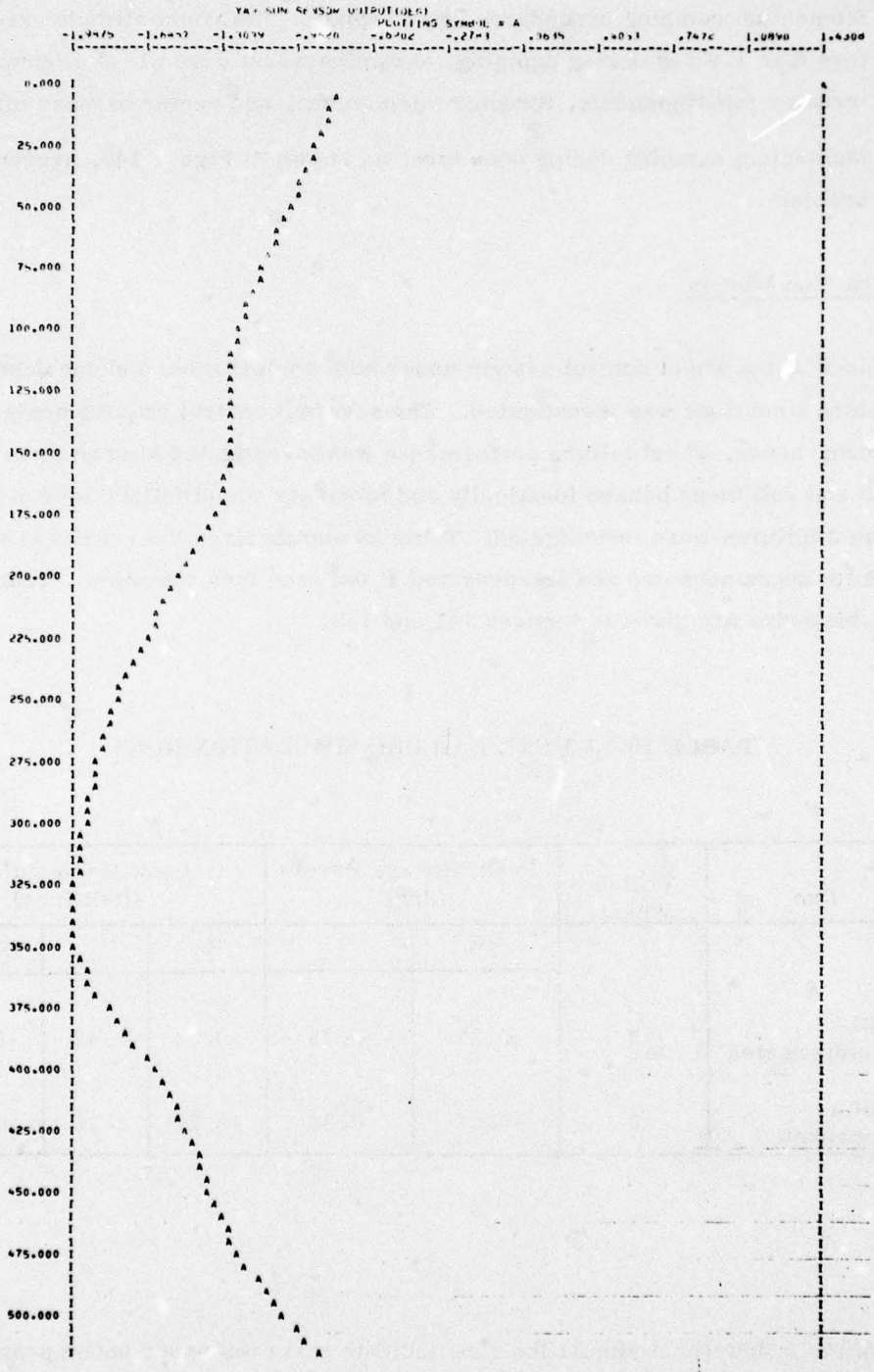

Figure 141a. Wheel 2 Failure, Uncompensated

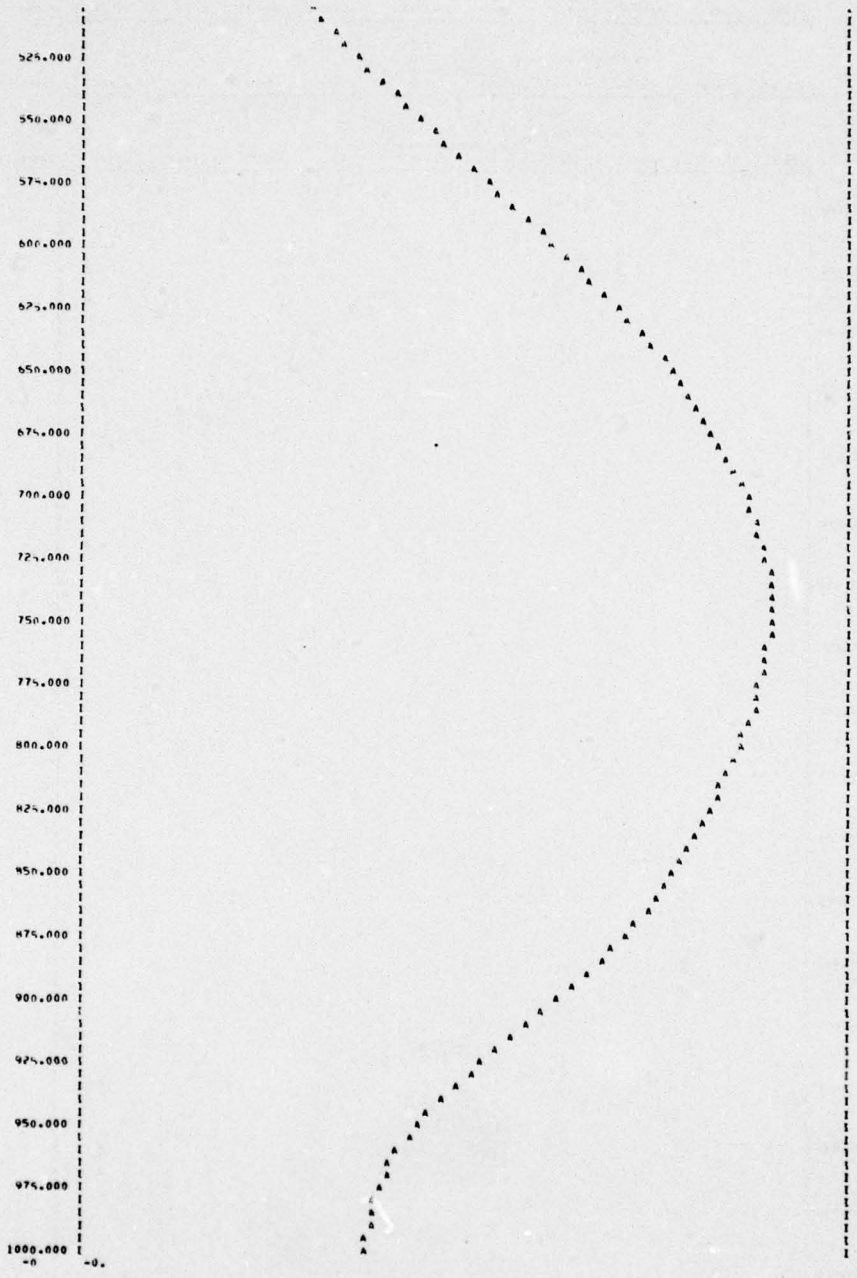

Figure 141a. Wheel 2 Failure, Uncompensated (concluded)

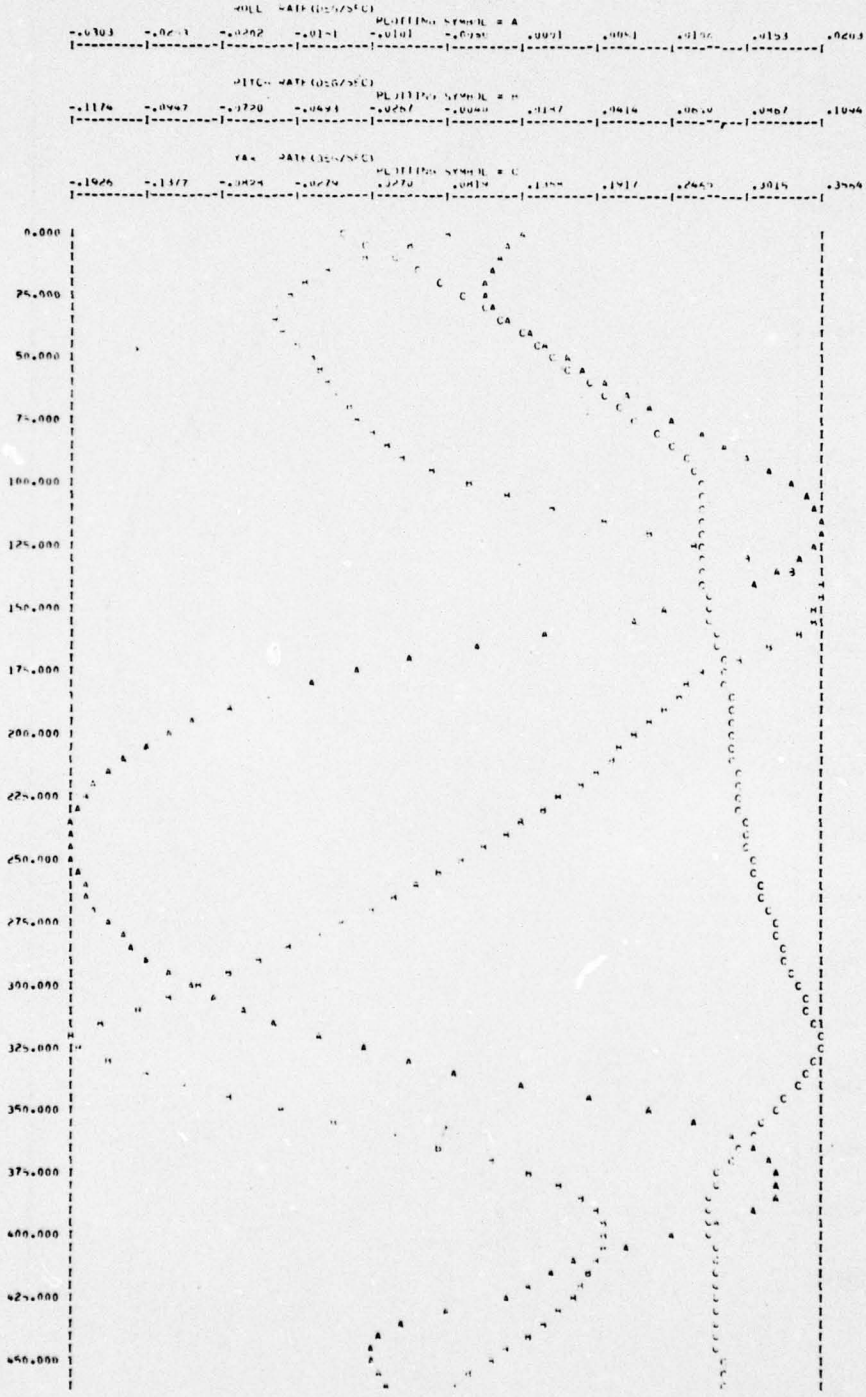

Figure 141b. Wheel 2 Failure, Uncompensated

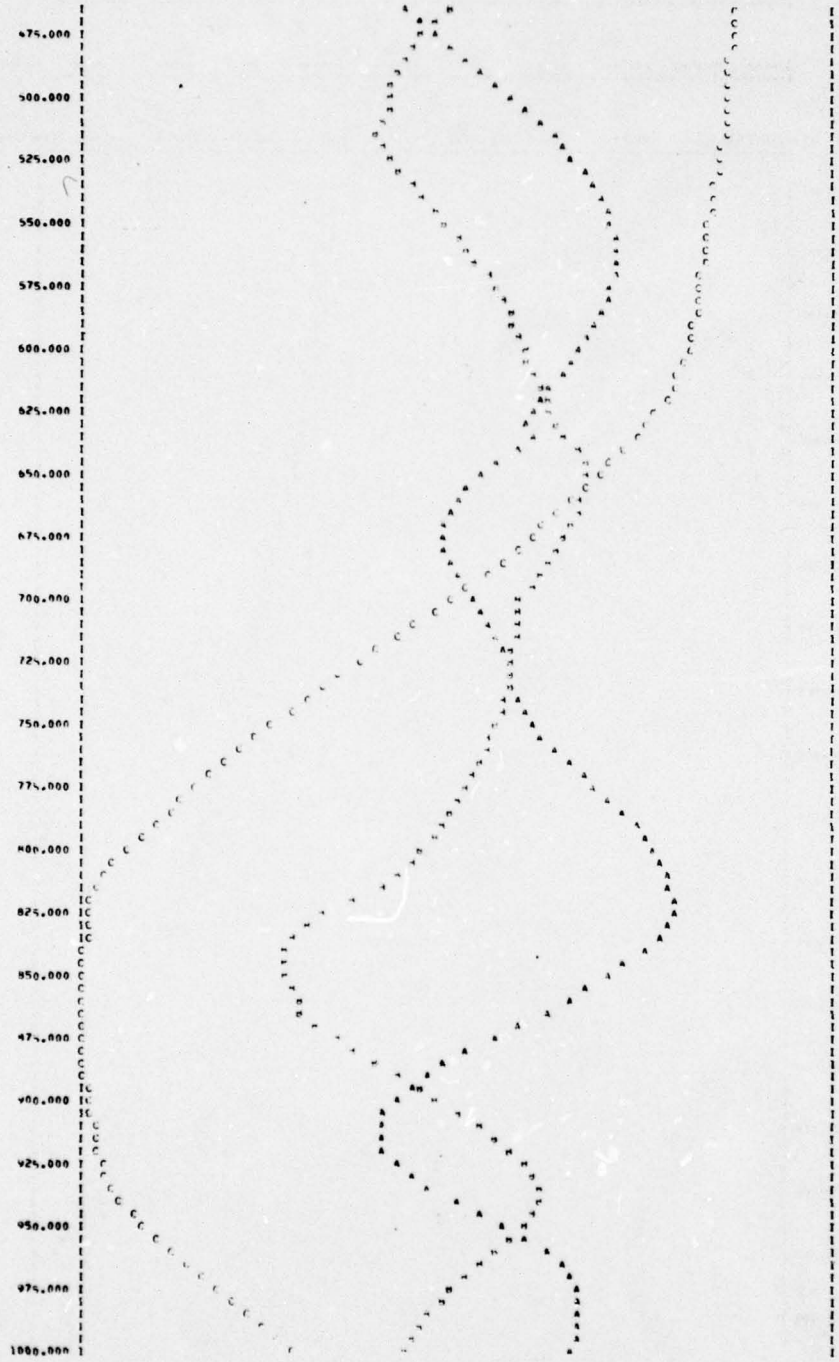

Figure 141b. Wheel 2 Failure, Uncompensated (concluded)

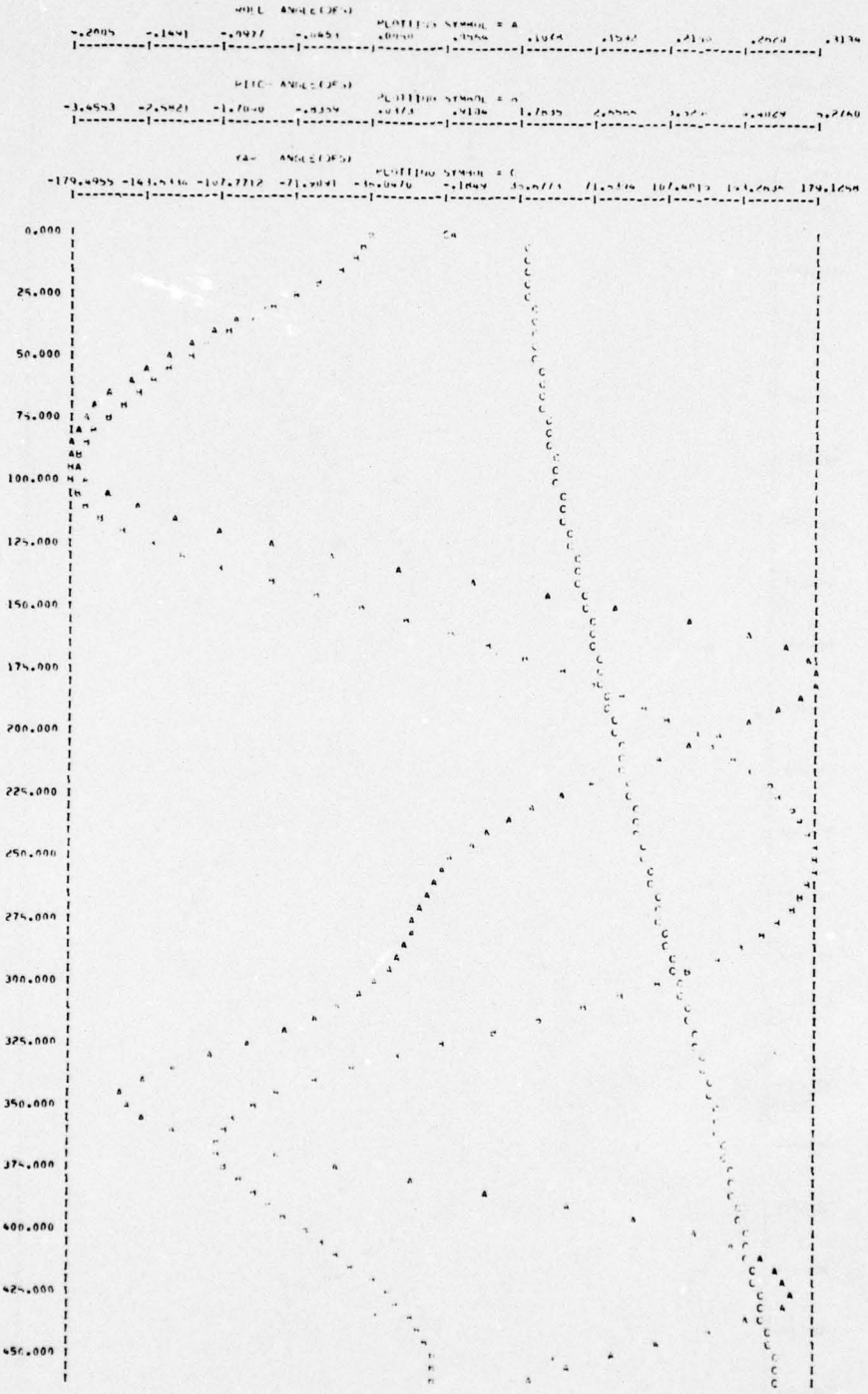

Figure 141c. Wheel 2 Failure, Uncompensated

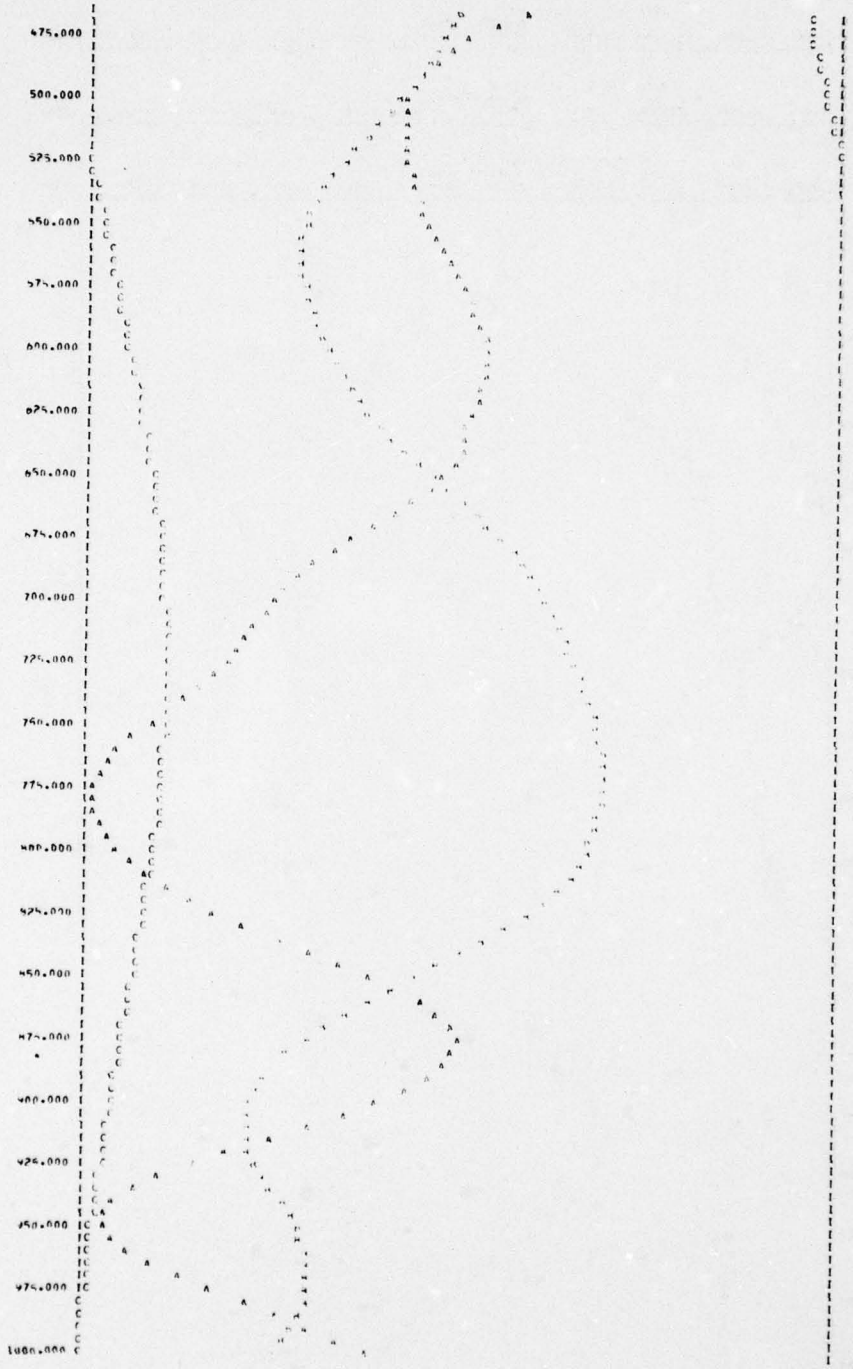

Figure 141c. Wheel 2 Failure, Uncompensated (concluded)

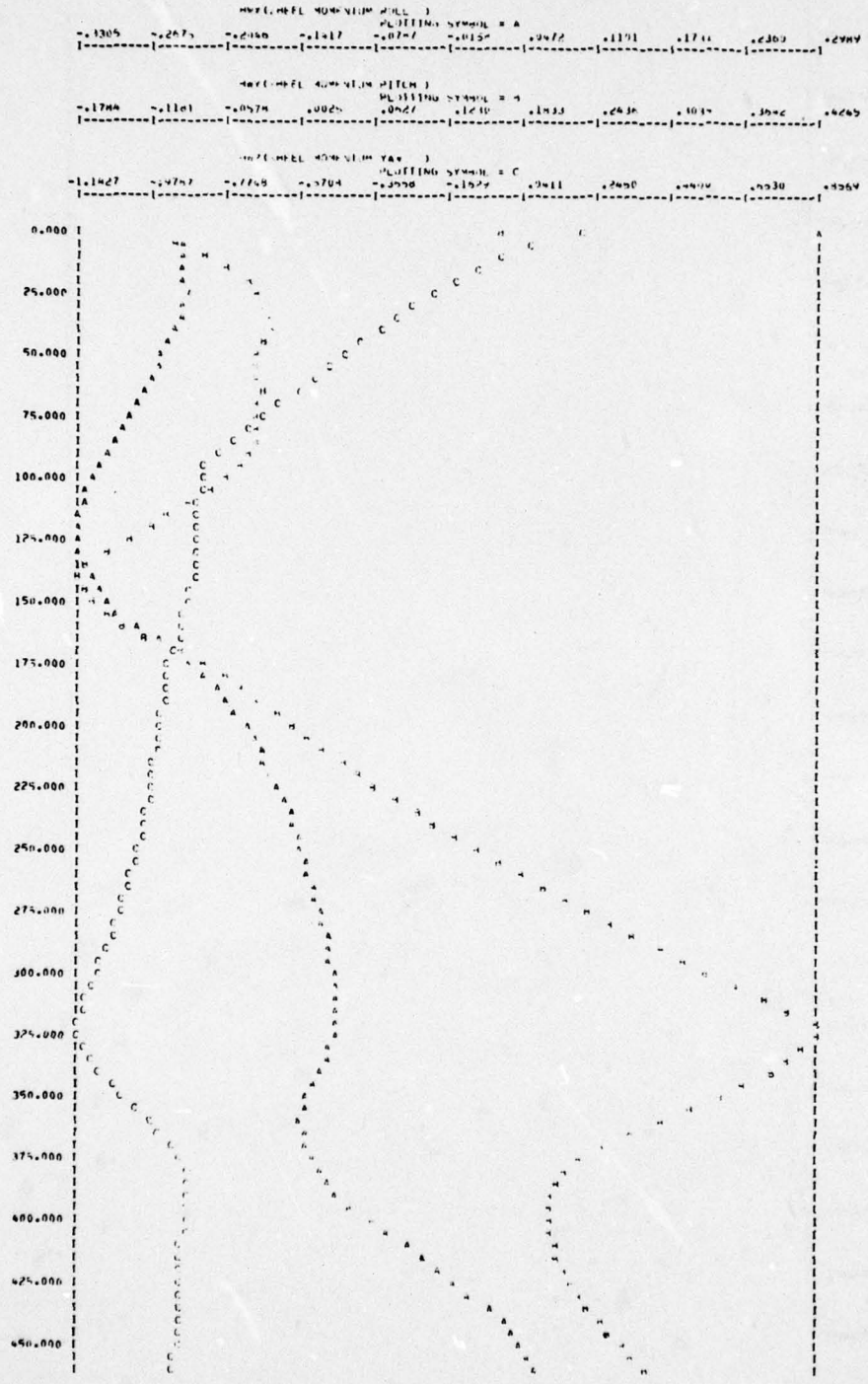

Figure 141d. Wheel 2 Failure, Uncompensated

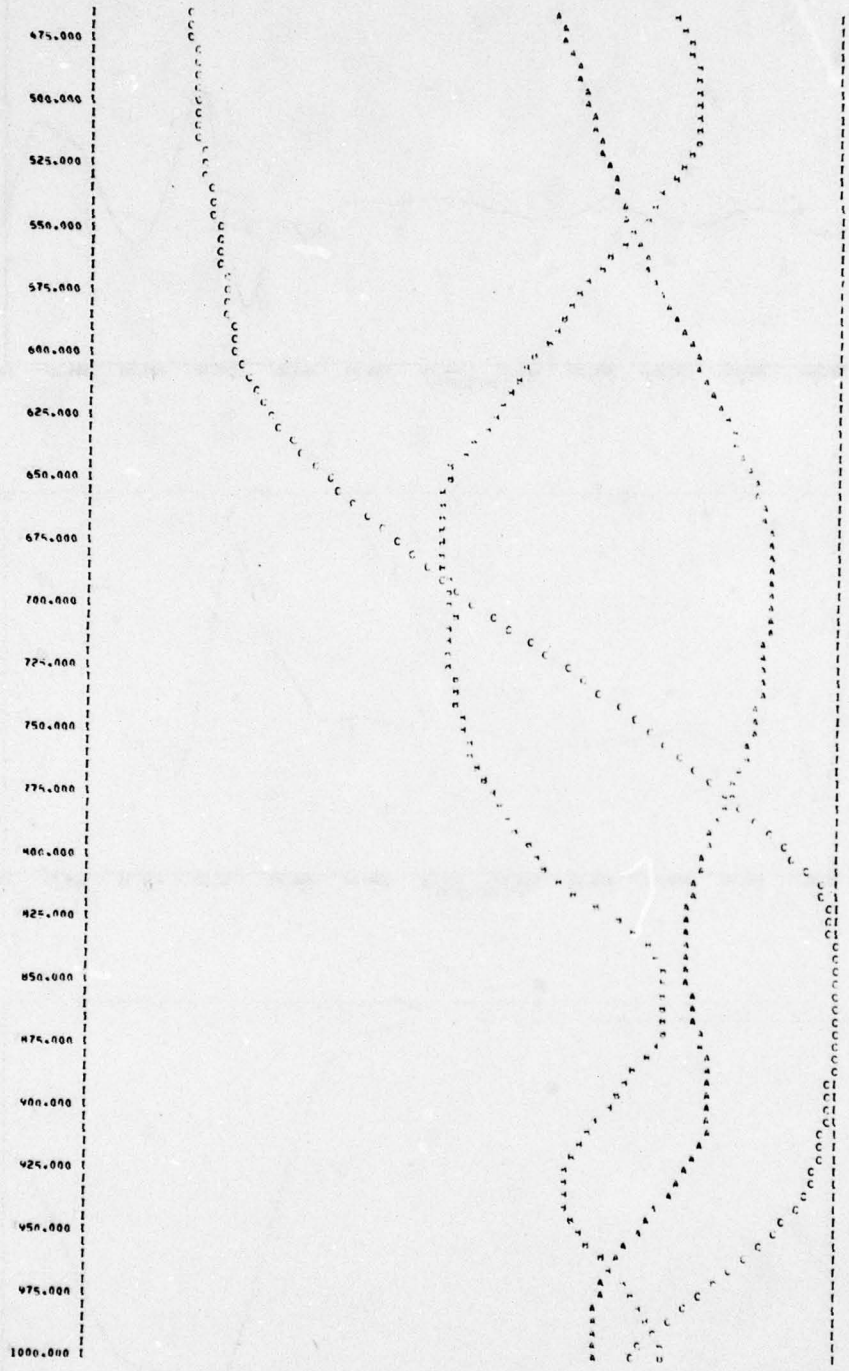

Figure 141d. Wheel 2 Failure, Uncompensated (concluded)

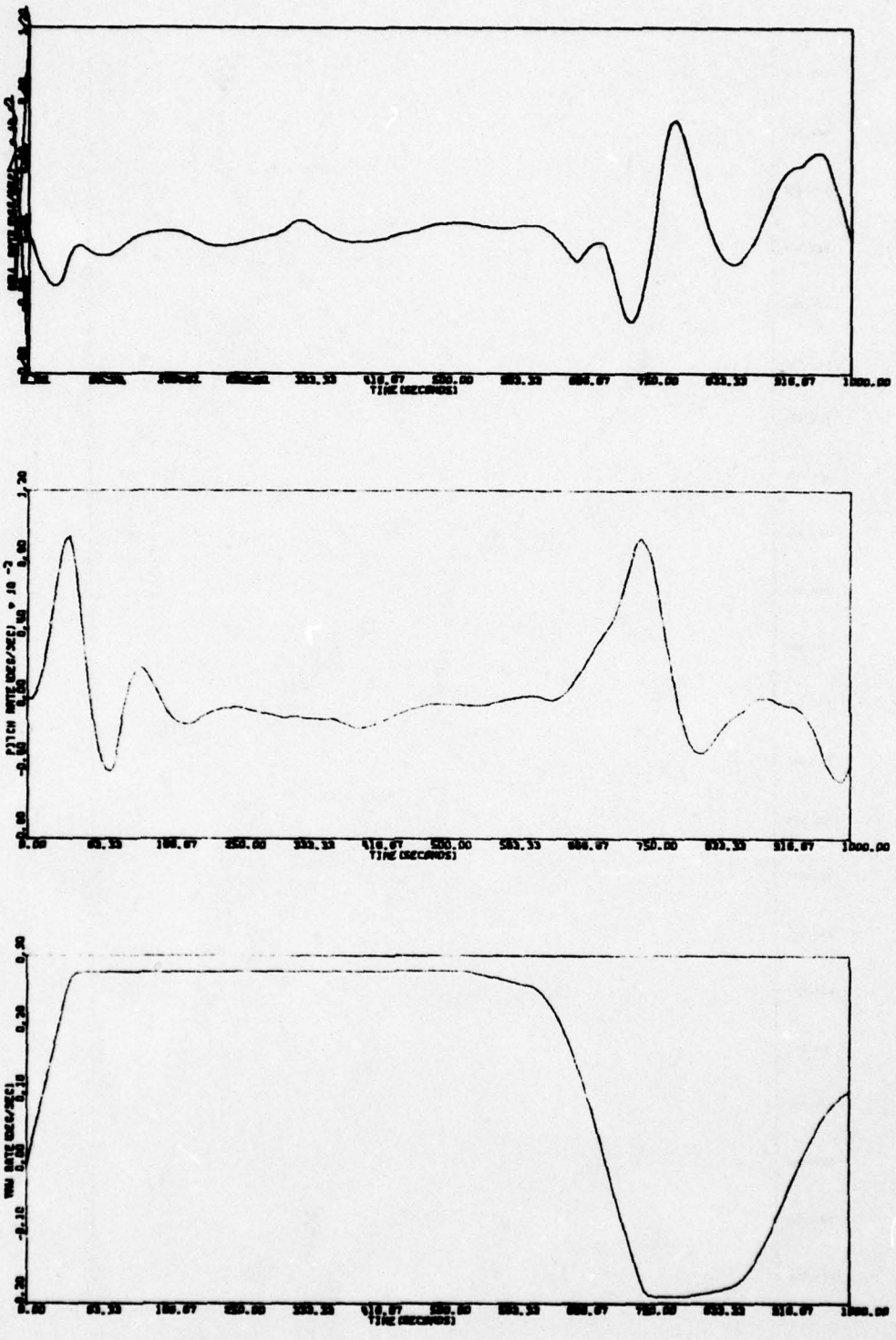

Figure 142. Wheel 2 Failure, Compensated

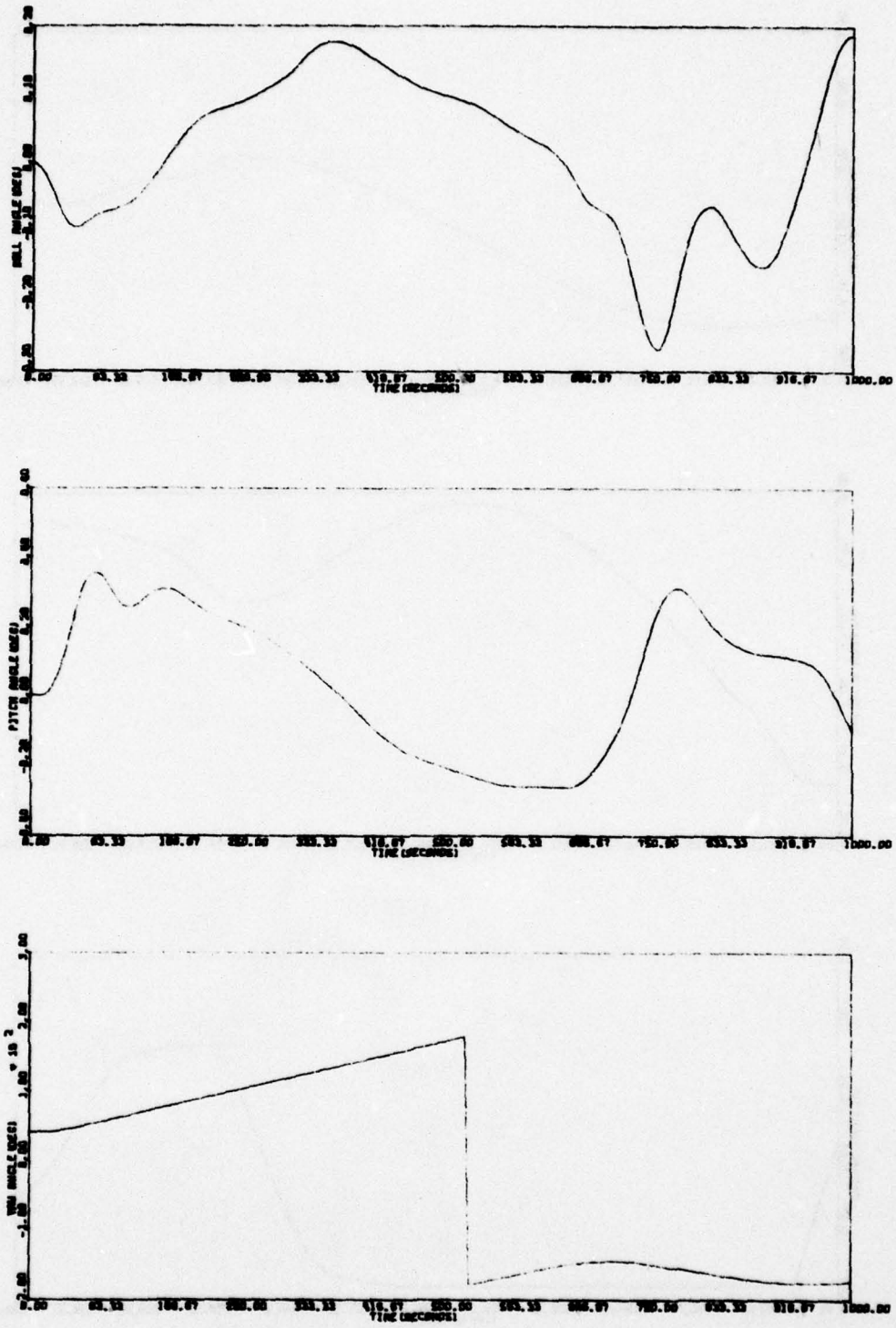

Figure 142. Wheel 2 Failure, Compensated (continued)

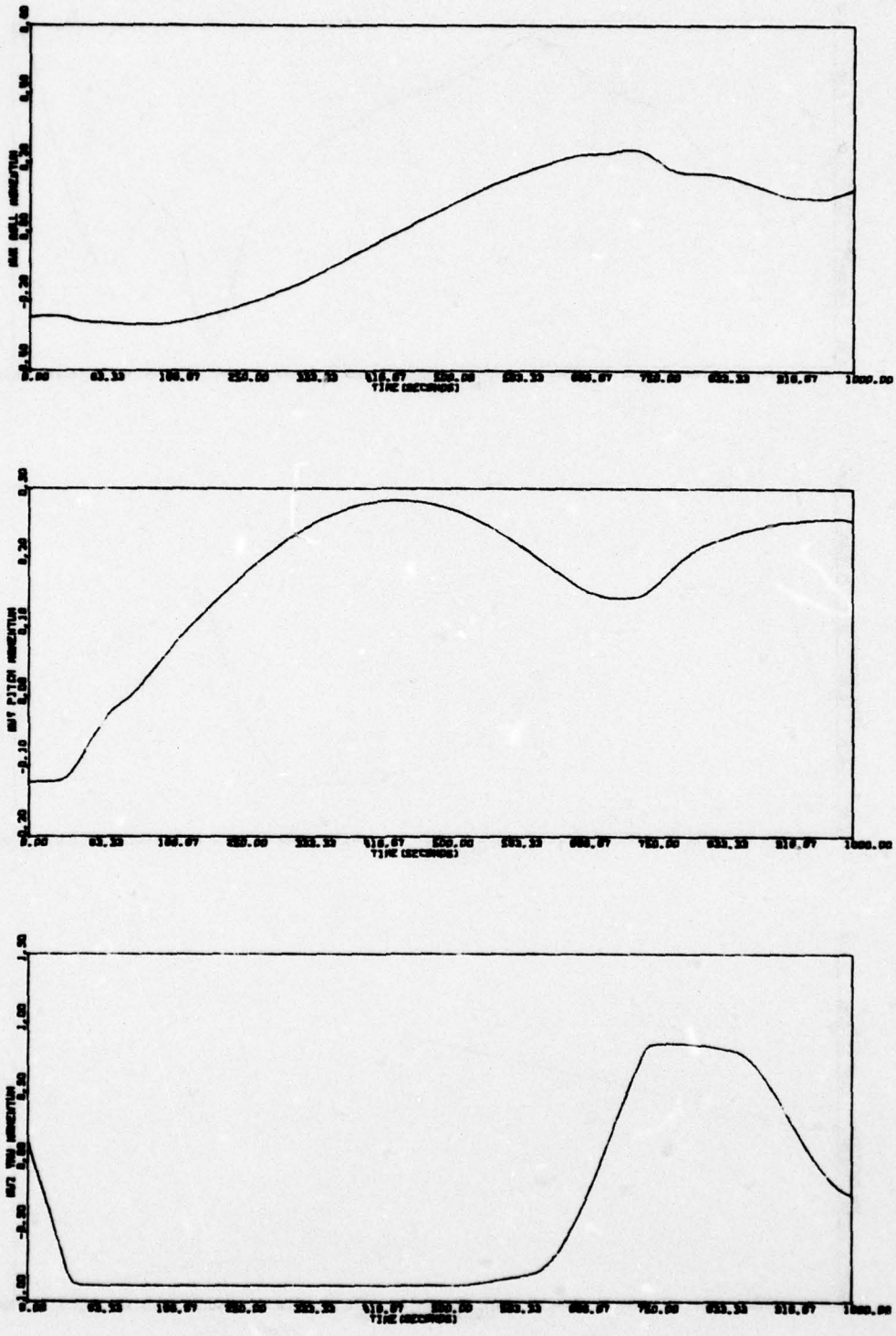

Figure 142. Wheel 2 Failure, Compensated (continued)

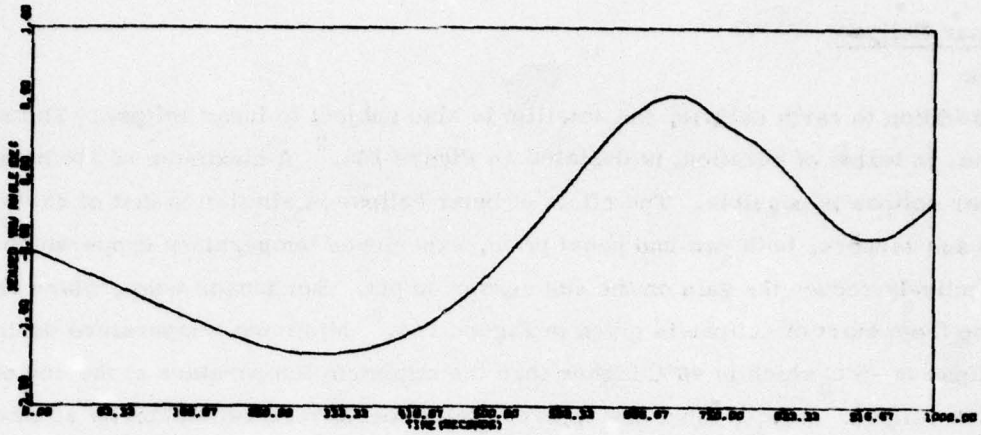

Figure 142. Wheel 2 Failure, Compensated (concluded)

Lunar Eclipse

In addition to earth eclipse, the satellite is also subject to lunar eclipse. The worst case, in terms of duration, is depicted in Figure 143.[2] A maximum of two hours' lunar eclipse is possible. The effect of lunar eclipse is similar to that of earth eclipse; the sun sensors, both yaw and panel pitch, experience temperature drops which effectively reduce the gain on the sun sensor output. Sun sensor temperature versus time from start of eclipse is given in Figure 144.[3] Minimum temperature during lunar eclipse is -5°C which is 40°C higher than the minimum temperature at the end of the earth eclipse. Hence, since the control system performed satisfactorily at emergence from earth eclipse, there is little reason to believe that it will perform any worse at the lunar eclipse condition under a wider gain variation.

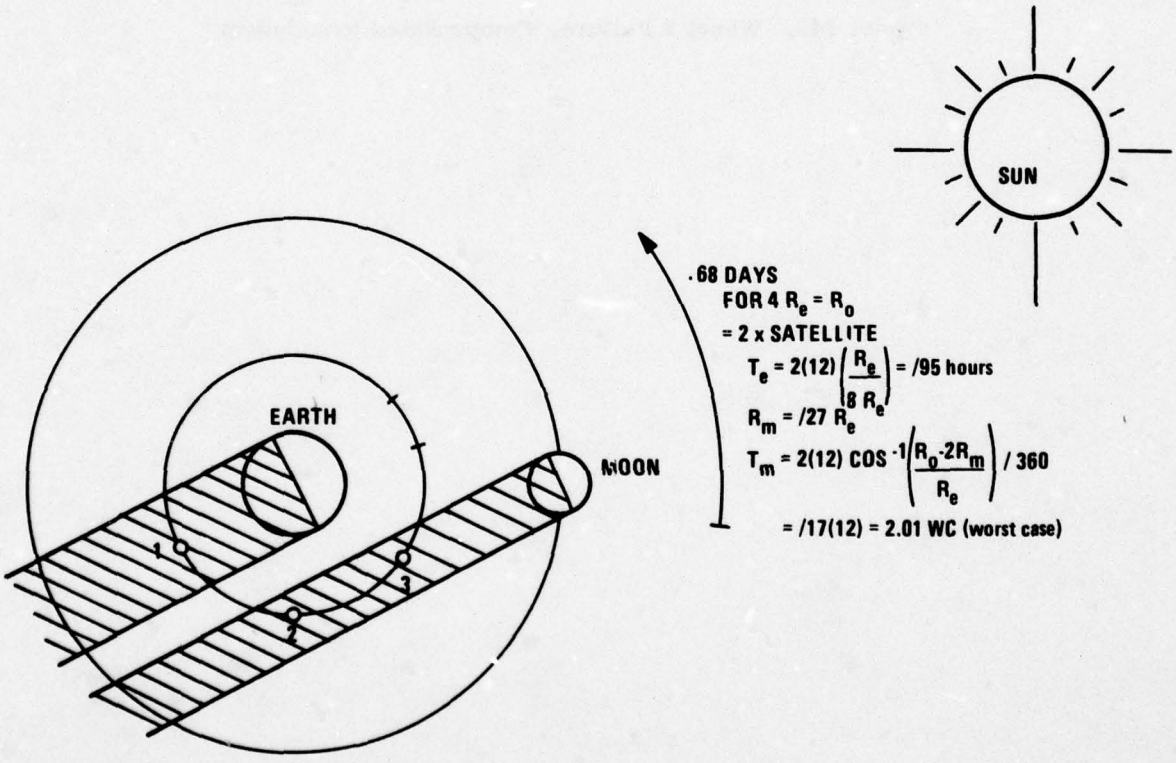

Figure 143. General Geometry for Eclipses

---

[2] S. Pierce, Aerospace Corporation, Los Angeles, CA, September 1976.

[3] Rockwell Lunar Eclipse Design Review, December 21, 1976.

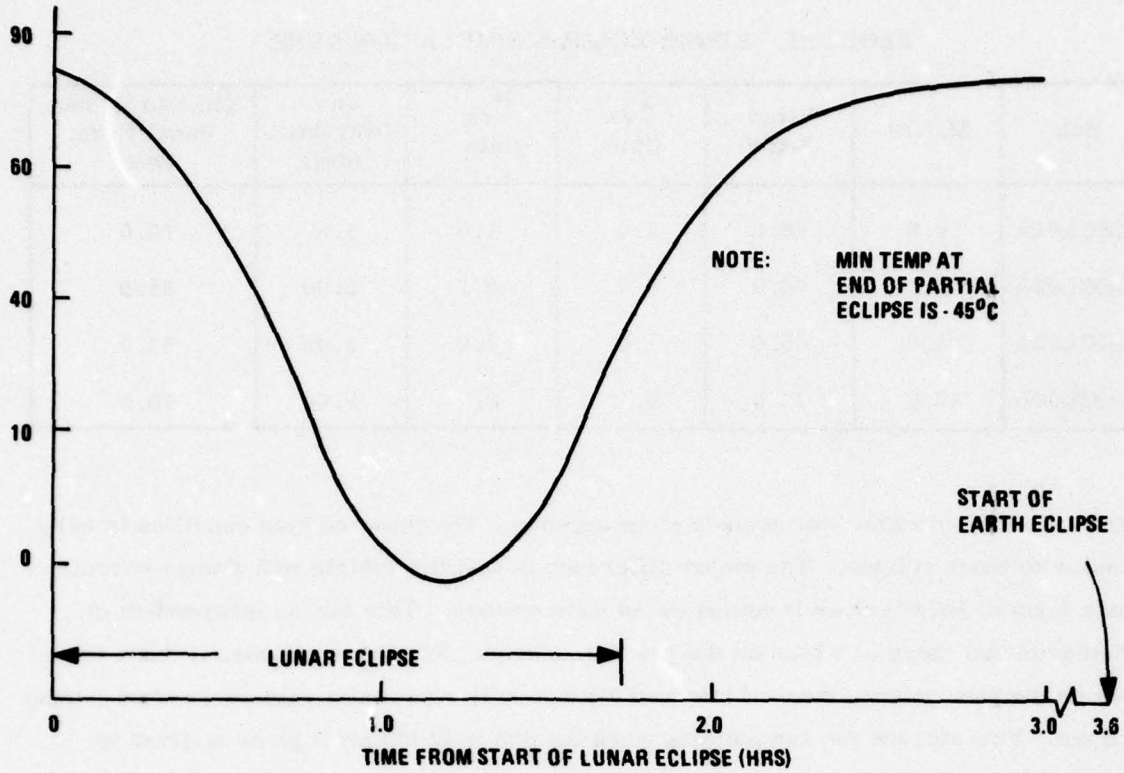

Figure 144. Sun Sensor Temperature during Lunar Eclipse

To demonstrate the fact, four simulation runs were made to investigate yaw sun tracking performance under reduced gain conditions. These are summarized in Table 31. Transient response histories for these runs are given in Figures 145 through 148. Included in the transient response histories are plots of the (1) difference between perfect yaw angle for sun tracking and actual yaw angle, and (2) difference between perfect panel angle for sun tracking and actual panel angle. Both yaw angle and panel angle were offset 10.0 deg from the perfect condition at the beginning of each run. The low gain condition of .7 represents a reduction factor of 0.6 percent/°C from the 25 deg nominal condition with additional 12 percent margin added. As can be seen from Figures 145 through 148 and Table 31, performance is only slightly degraded at the low gain condition.

The second consideration that must be investigated in lunar eclipse analysis is yaw attitude and panel attitude at the emergence from lunar eclipse.

TABLE 31. LUNAR ECLIPSE SIMULATION RUNS

Run	SL/OP	Panel Angle	Y_{ss} Gain	P_{ss} Gain	Yaw Overshoot (deg)	Time to Reduce Panel Error (sec)
LECL01A	0.0	90.0	1.0	1.0	1.8	50.0
LECL02A	0.0	90.0	0.7	0.7	2.00	65.0
LECL03A	45.0	45.0	1.0	1.0	2.46	65.0
LECL04A	45.0	45.0	0.7	0.7	2.49	70.0

First, we will consider yaw attitude at emergence. The lunar eclipse condition is very similar to earth eclipse. The major difference is that the vehicle will always execute some form of noon turn as it comes out of each eclipse. This fact is independent of whether or not there is a bias on the yaw sun sensor. For lunar eclipse, if there is no bias on the yaw sensor, then vehicle yaw attitude will essentially remain constant during eclipse. Yaw attitude for sun pointing when the sun is in the orbit plane is given in Figure 149 versus orbit origin. As can be seen, there is no required attitude change during the lunar eclipse period so constant attitude in that period is desirable. If there is a bias, it will probably result in yaw momentum saturation and the resultant 0.26 deg/sec rate. As seen in the earth eclipse condition, the satellite can recover from this. Since the yaw gain is higher at emergence from lunar eclipse than from earth eclipse, we see no problem in yaw attitude control following lunar eclipse.

The panels are a slightly different story. When the sun is in the orbit plane, the panels will track the sun at orbit rate. Hence, in a lunar eclipse lasting two hours the panels could have a 60 deg pointing error at emergence. Figure 150 shows the transient response of the system with a 60 deg panel offset. After an initial transient, tracking performance is satisfactory.

Jet Backup to Wheel Control

Using the jets to back up the wheel loop was investigated in simulation. A 3.0 deg error was inserted into each control axis in order to alleviate the jet control system. Transient response history of the run is given in Figure 151. Also shown in the figure is standard wheel response without jet backup. As can be seen, the basic result is a quickening of response accompanied by considerable overshoot. We do not see any difficulty with this approach nor do we see any need for it.

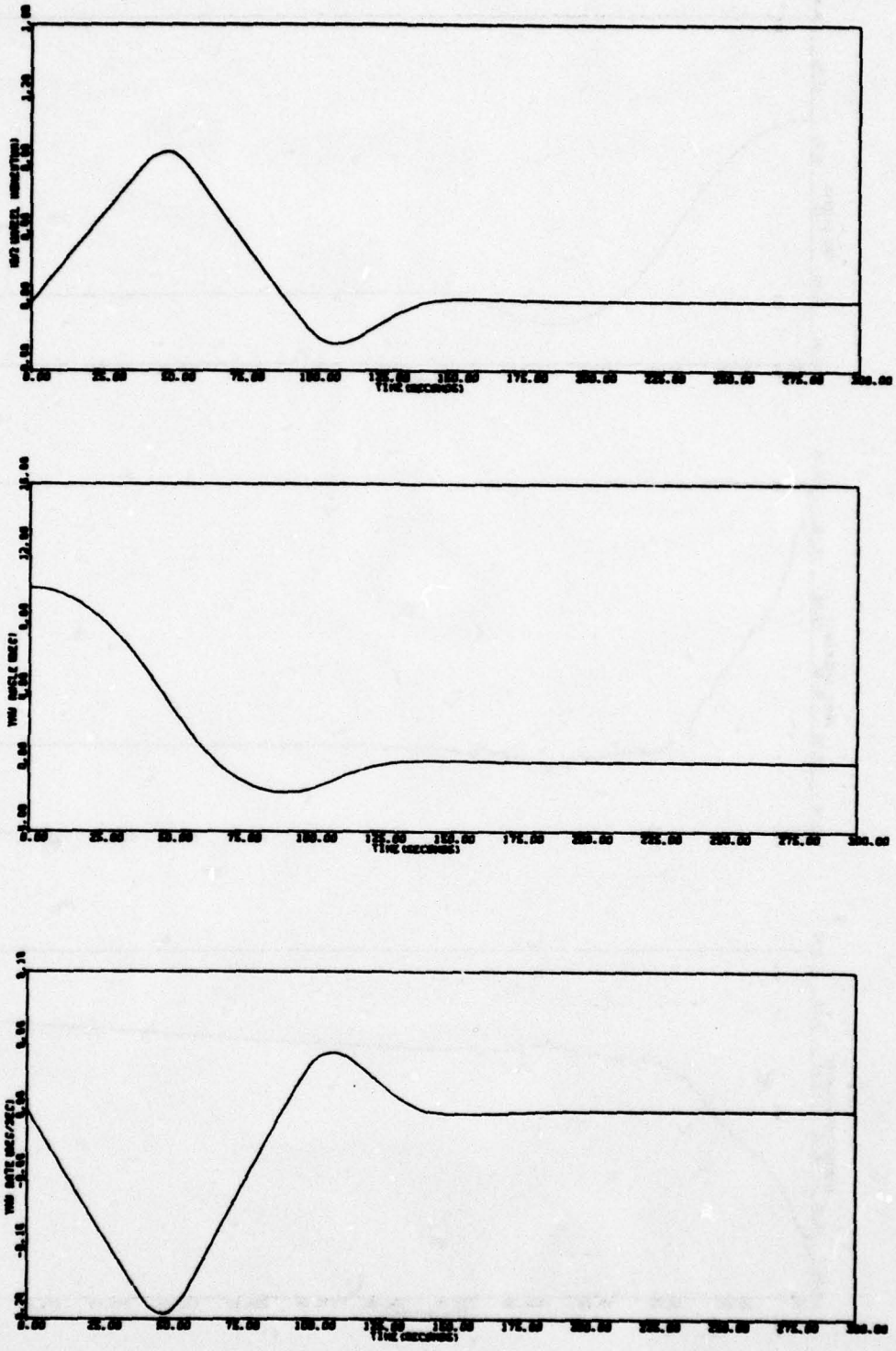

Figure 145. Run LECL01A

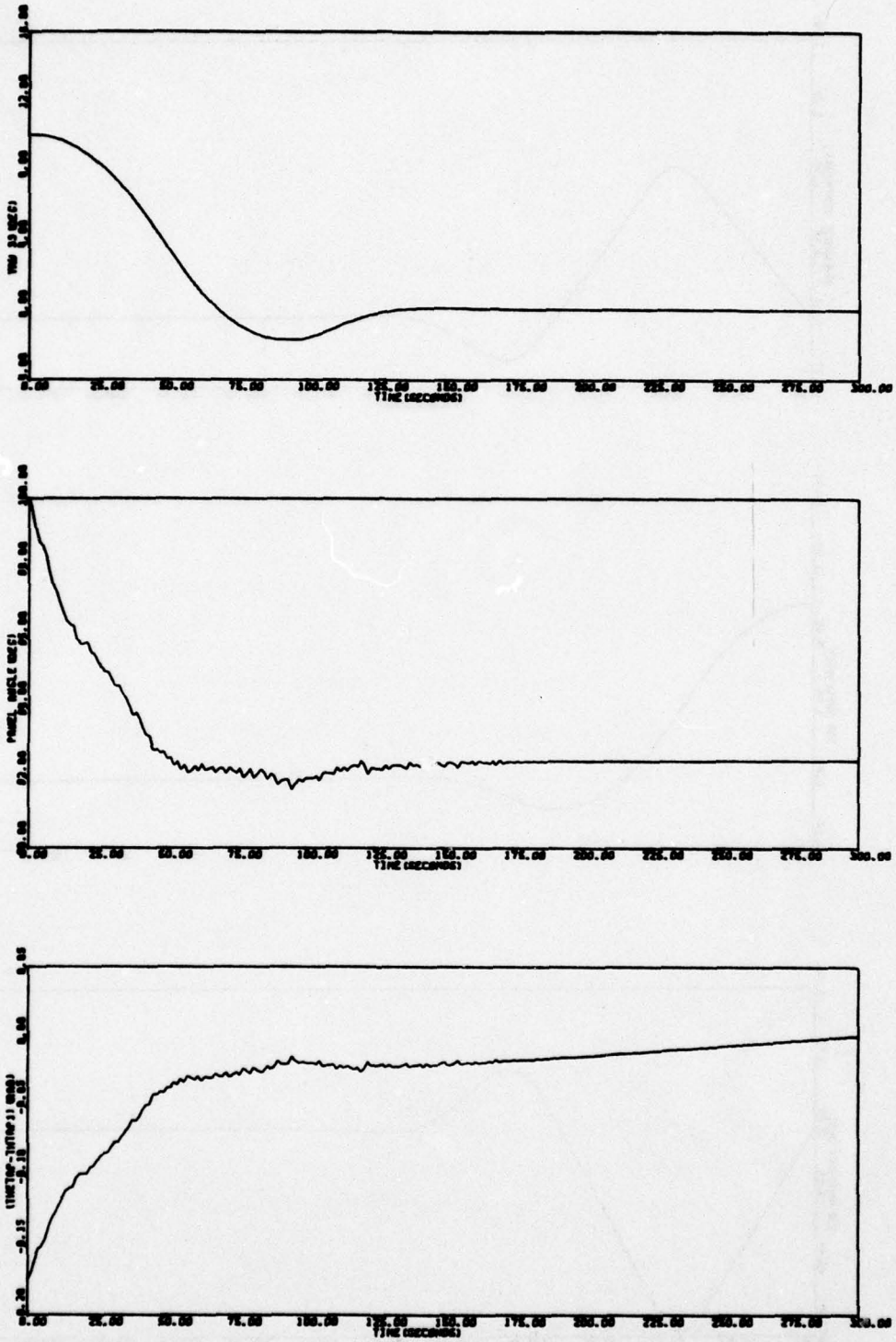

Figure 145. Run LECL01A (concluded)

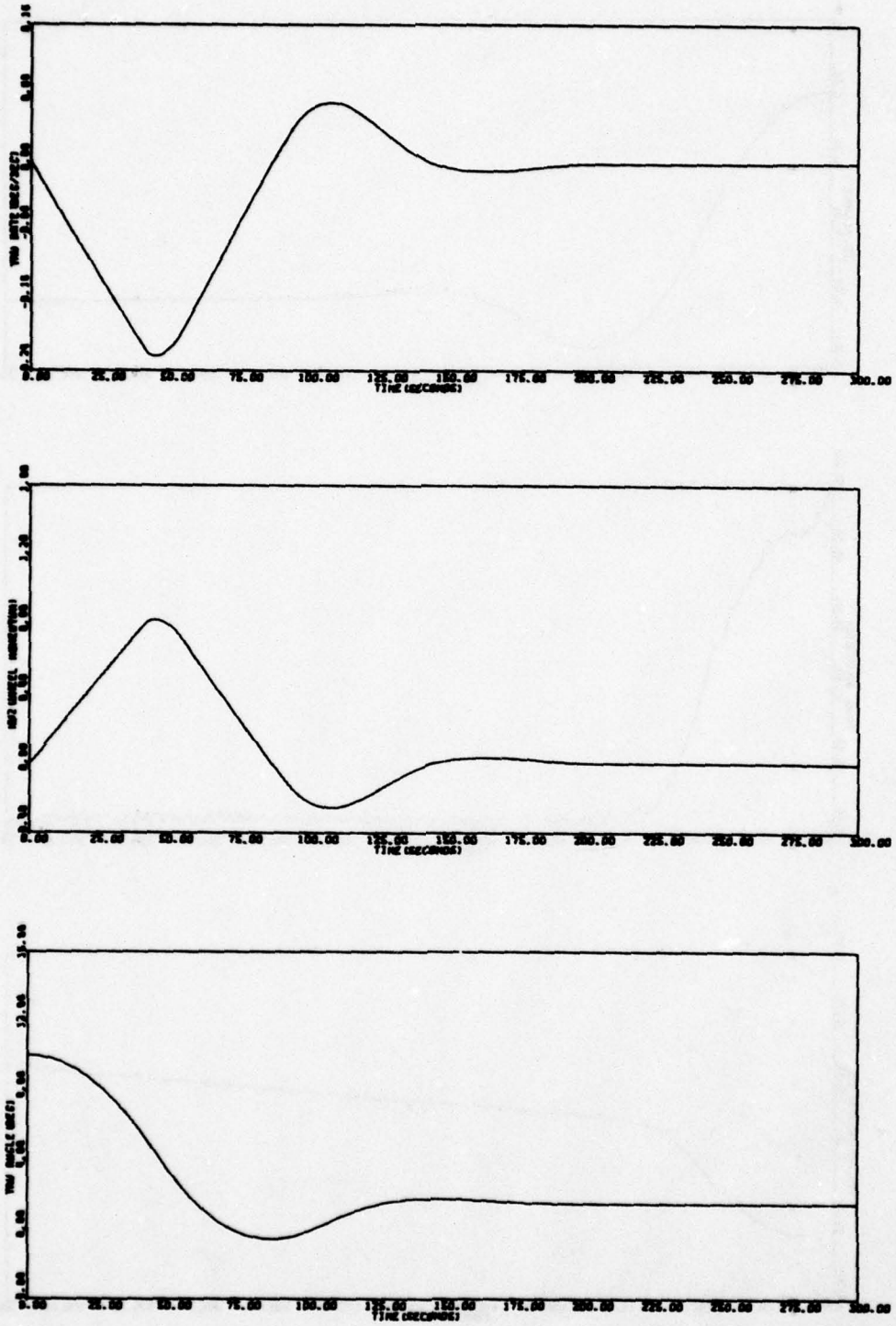

Figure 146. Run LECL02A

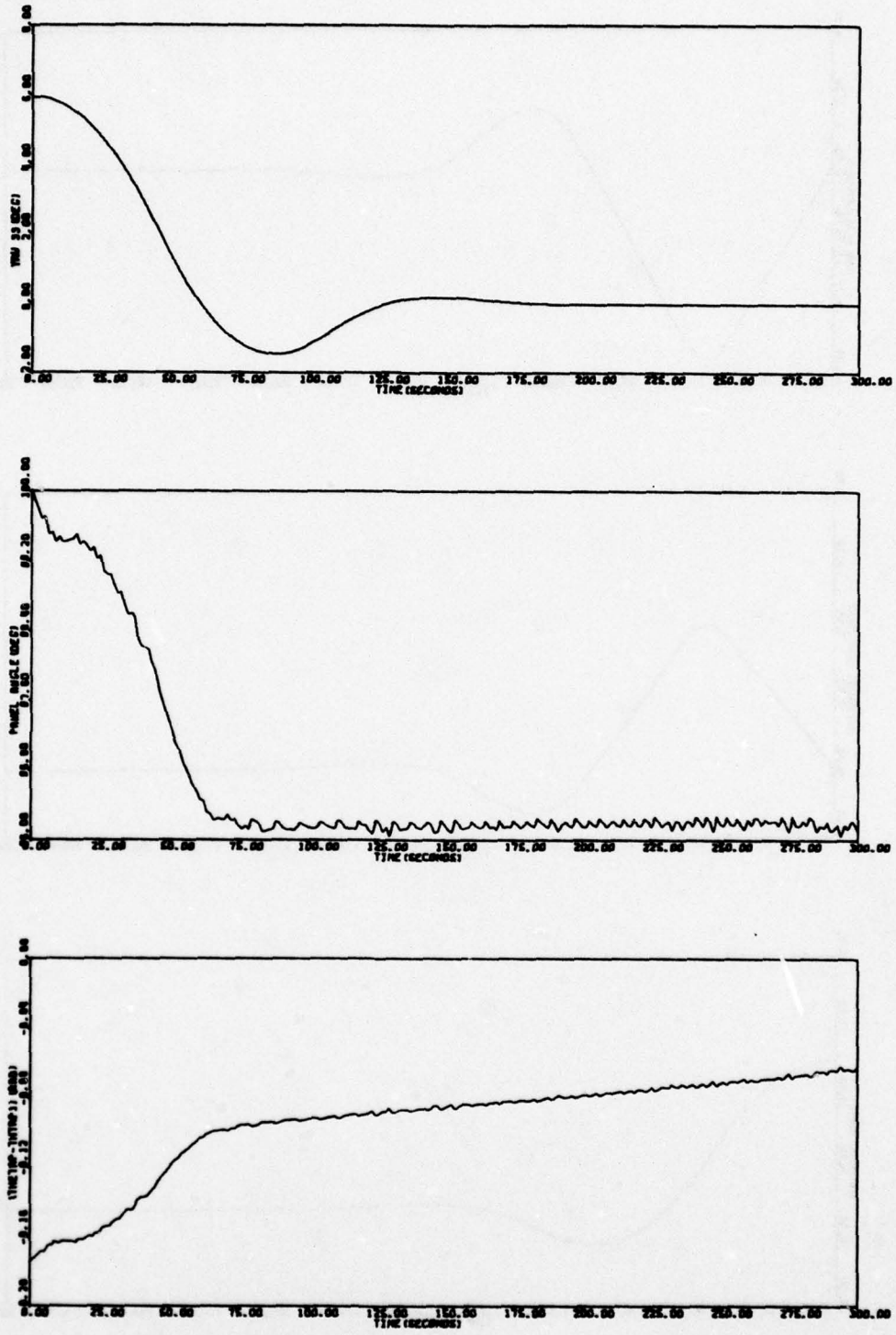

Figure 146. Run LECL02A (continued)

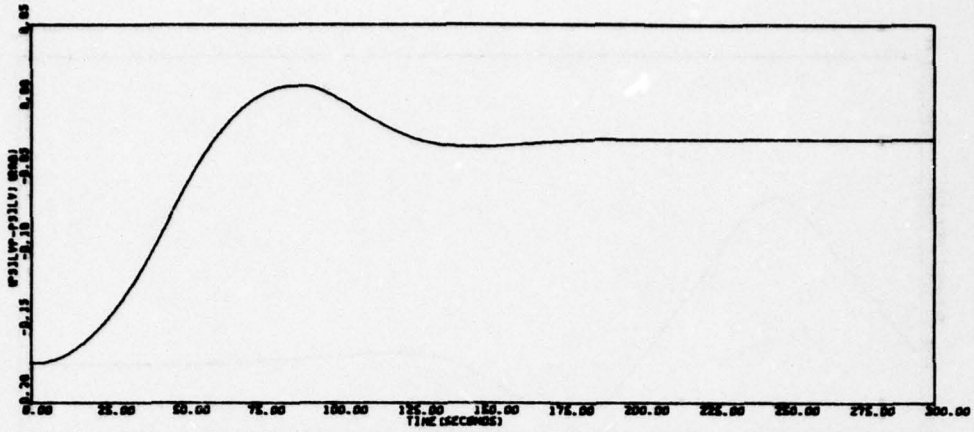

Figure 146. Run LECL02A (concluded)

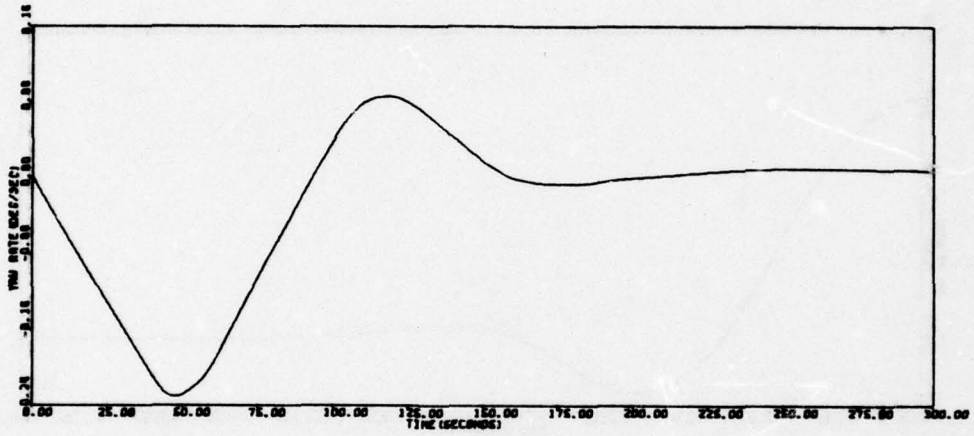

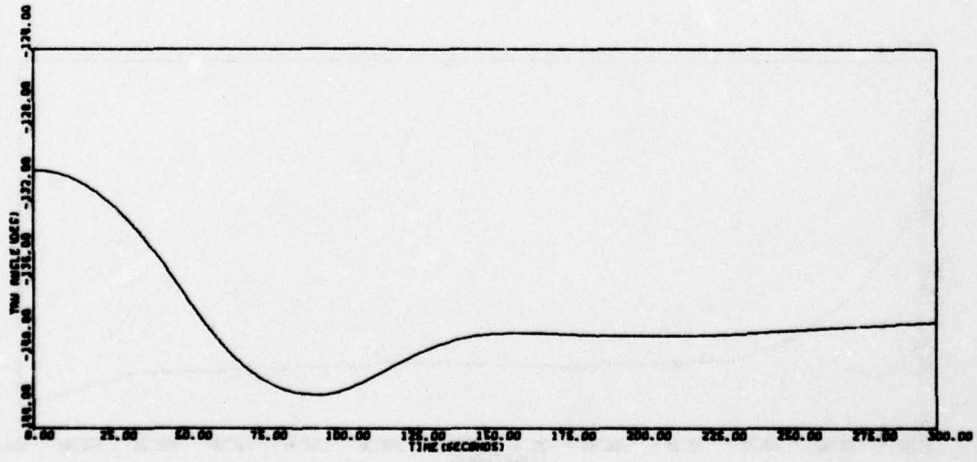

Figure 147. Run LECL03A

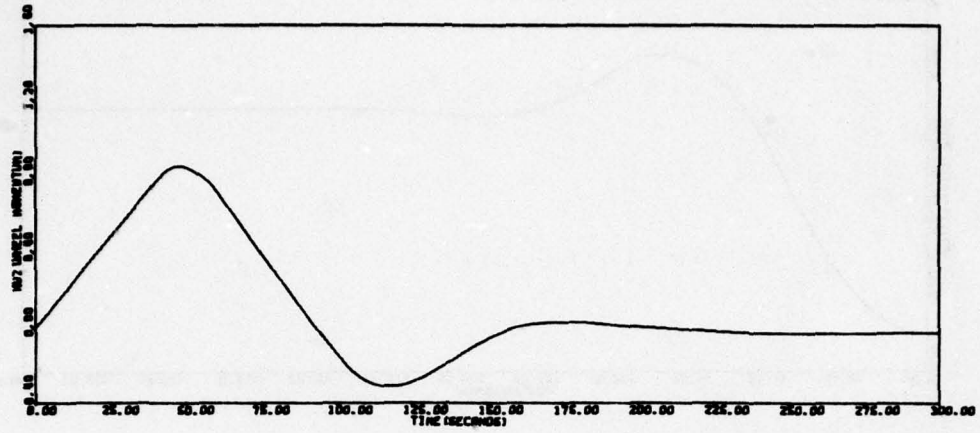

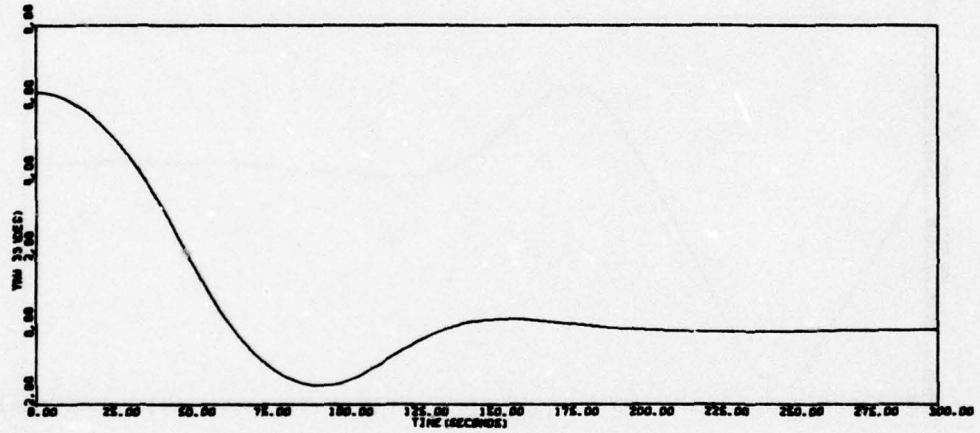

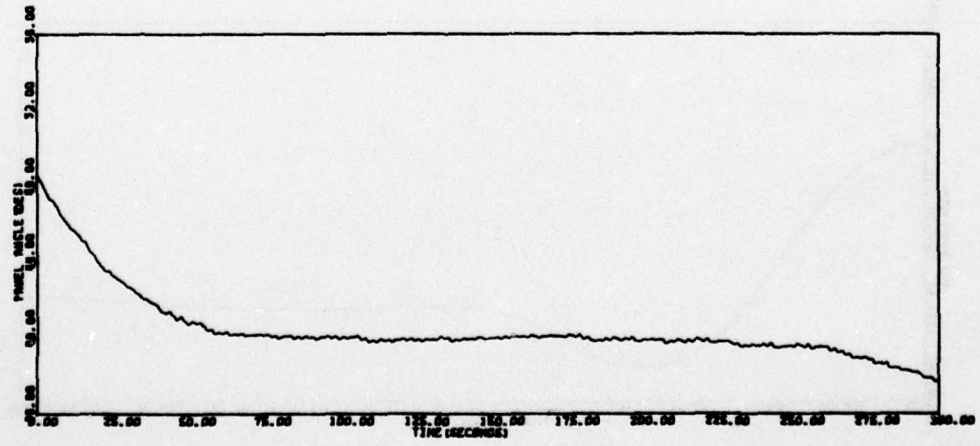

Figure 147. Run LECL03A (continued)

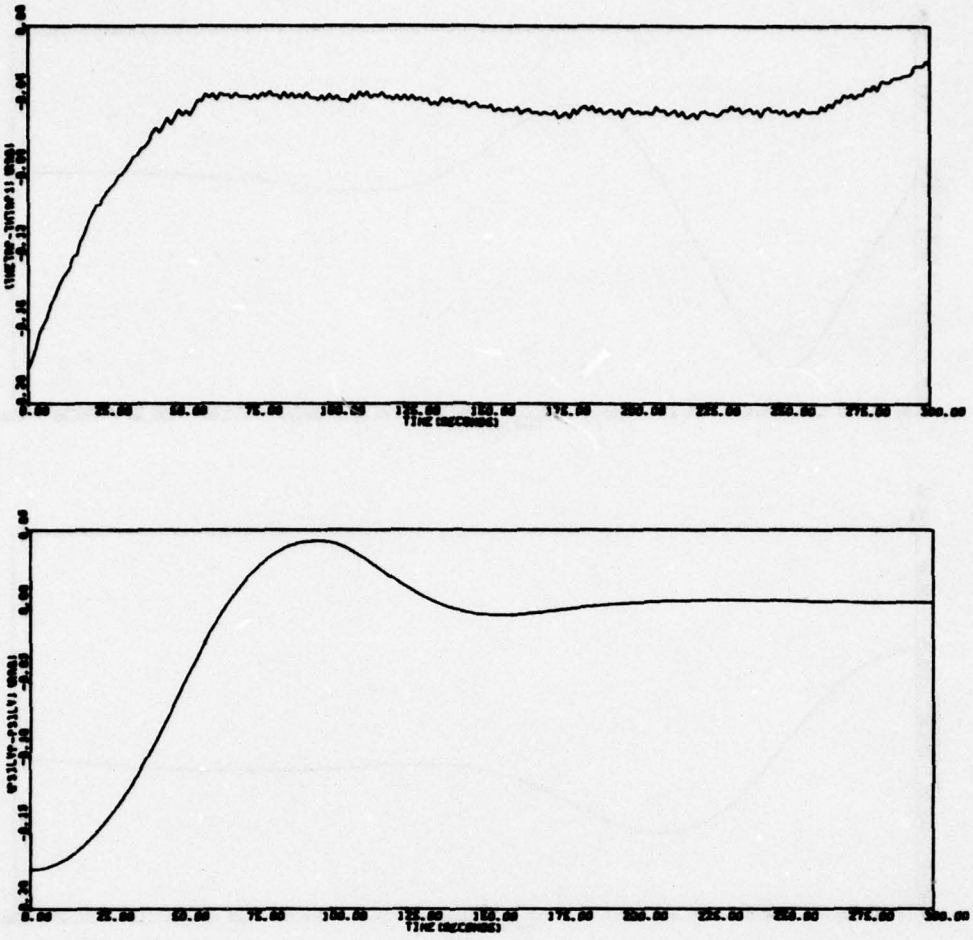

Figure 147. Run LECL03A (concluded)

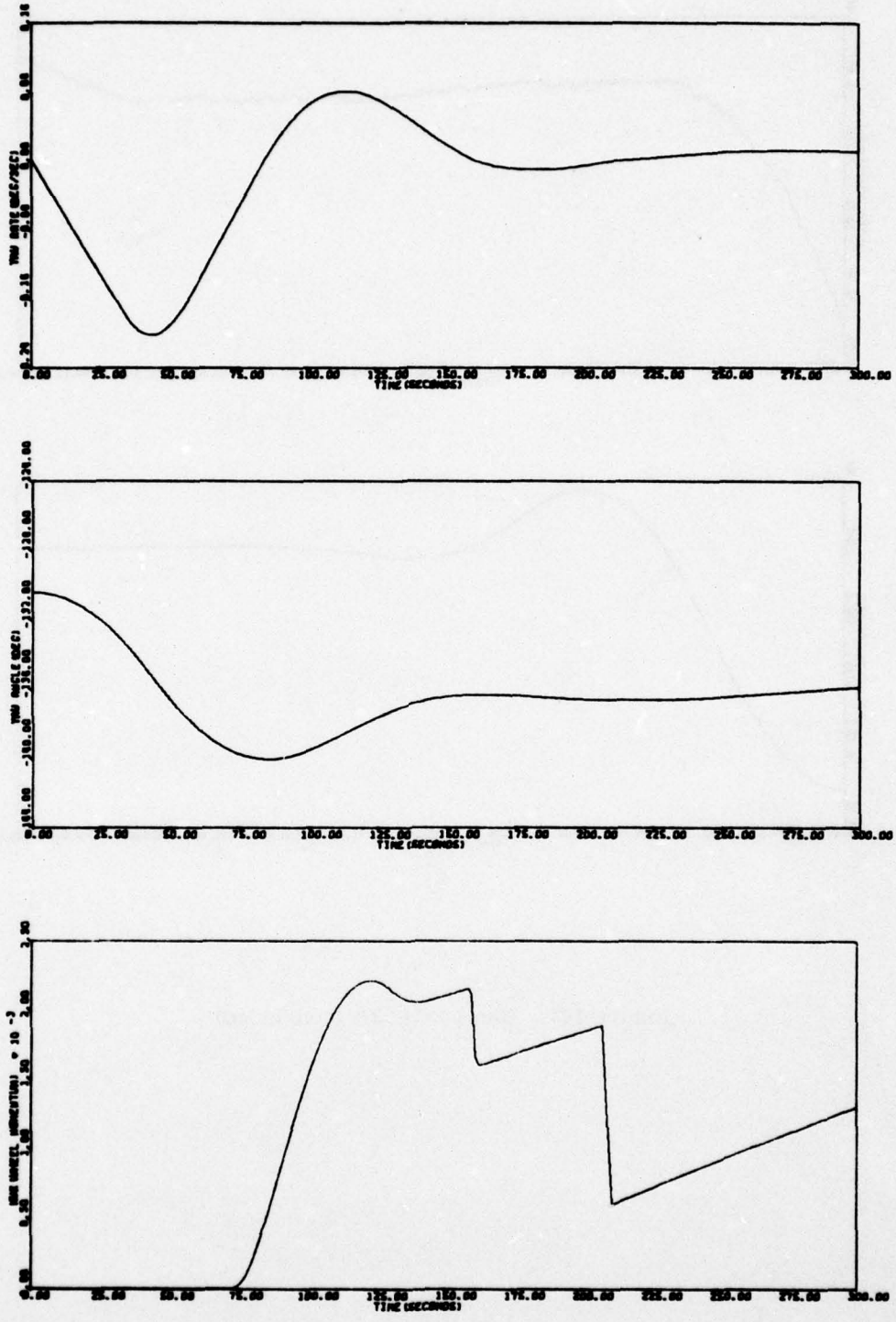

Figure 148. Run LECL04A

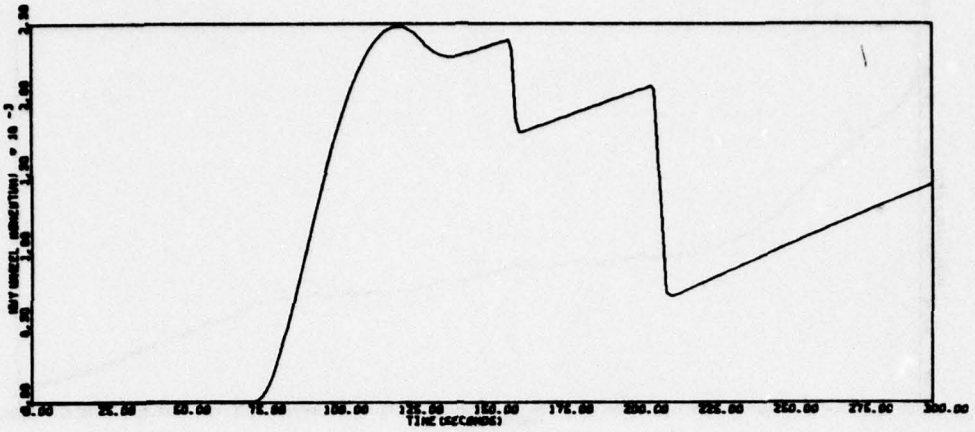

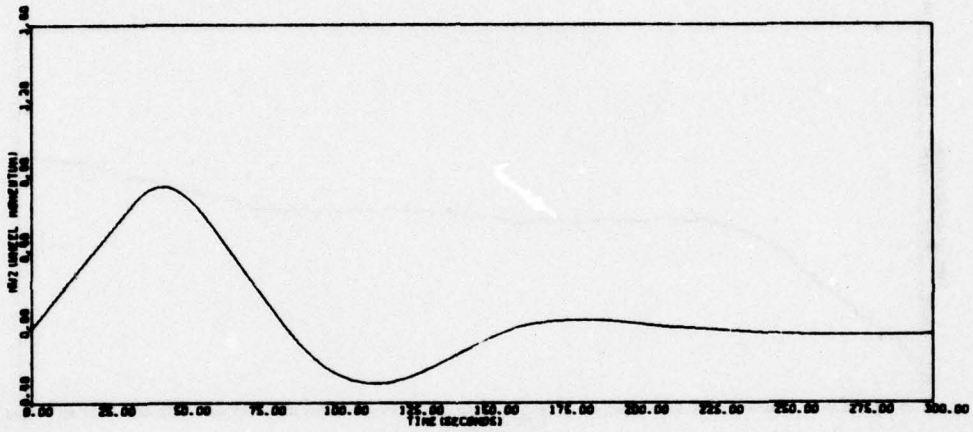

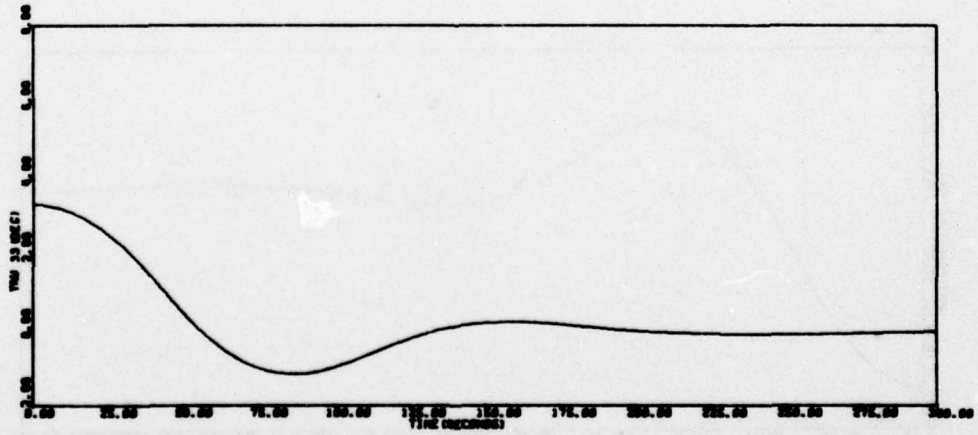

Figure 148. Run LECL04A (continued)

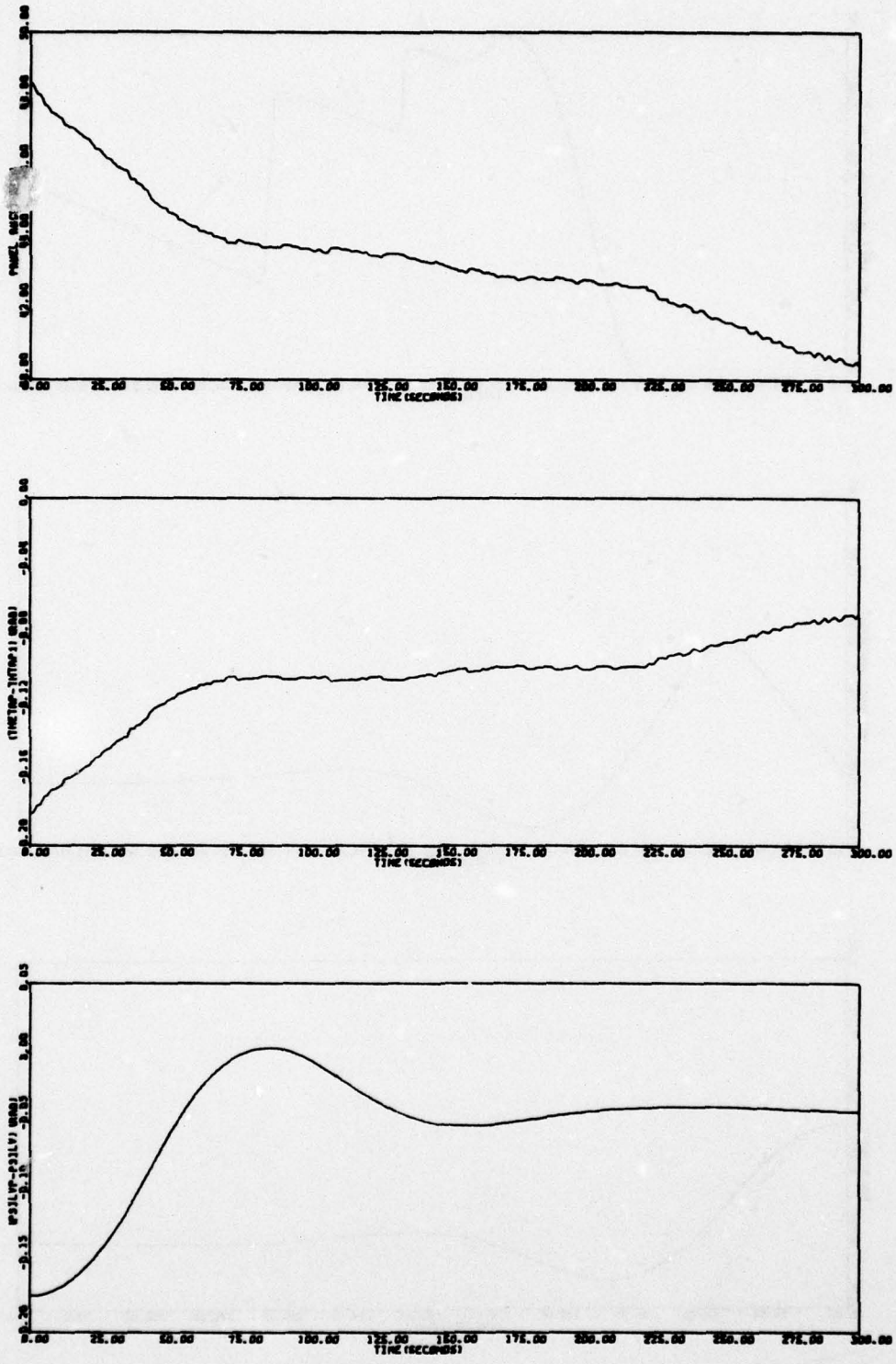

Figure 148. Run LECL04A (concluded)

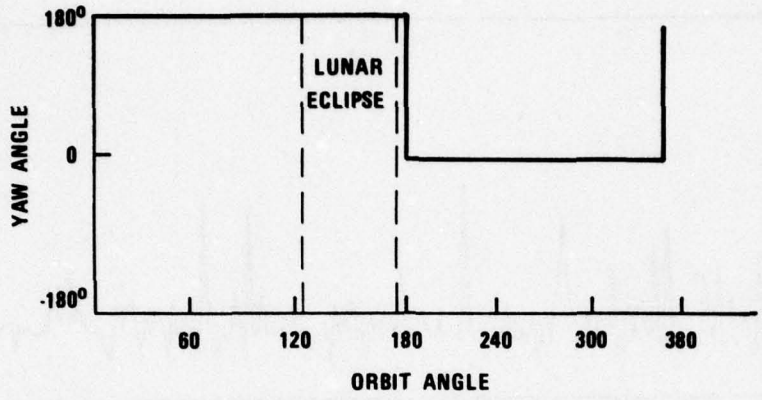

Figure 149. Yaw Attitude for Sun Pointing (Sun in Orbit Plane)

Solar Array Autotrack

Positioning of the solar arrays is performed independent of other spacecraft attitude control functions. Linkage between each solar array and the spacecraft is through the solar array drive motor. Arrays are held in position by a braking device which exerts a maximum braking torque of 65 in-oz. Without the braking device, interaction between the arrays and the vehicle would be limited to solar array drive pulse effects. Worst case interaction occurs if the arrays are rigidly attached to the space vehicle. This assumption was verified in the NTS-2 solar array flexibility analysis where both a locked and a free-wheeling solar array configuration was studied. For NDS analysis, a locked array configuration was assumed.

The effect of solar array flexibility on satellite attitude control and array sun tracking was investigated in the following steps:

- Solar array flexibility stability analysis
- Solar array drive/wheel array flexibility interaction
- Jet/array flexibility interaction
- Autotrack at low spin rates
- Solar array attitude control at high spin rates

The results of the investigation will now be presented.

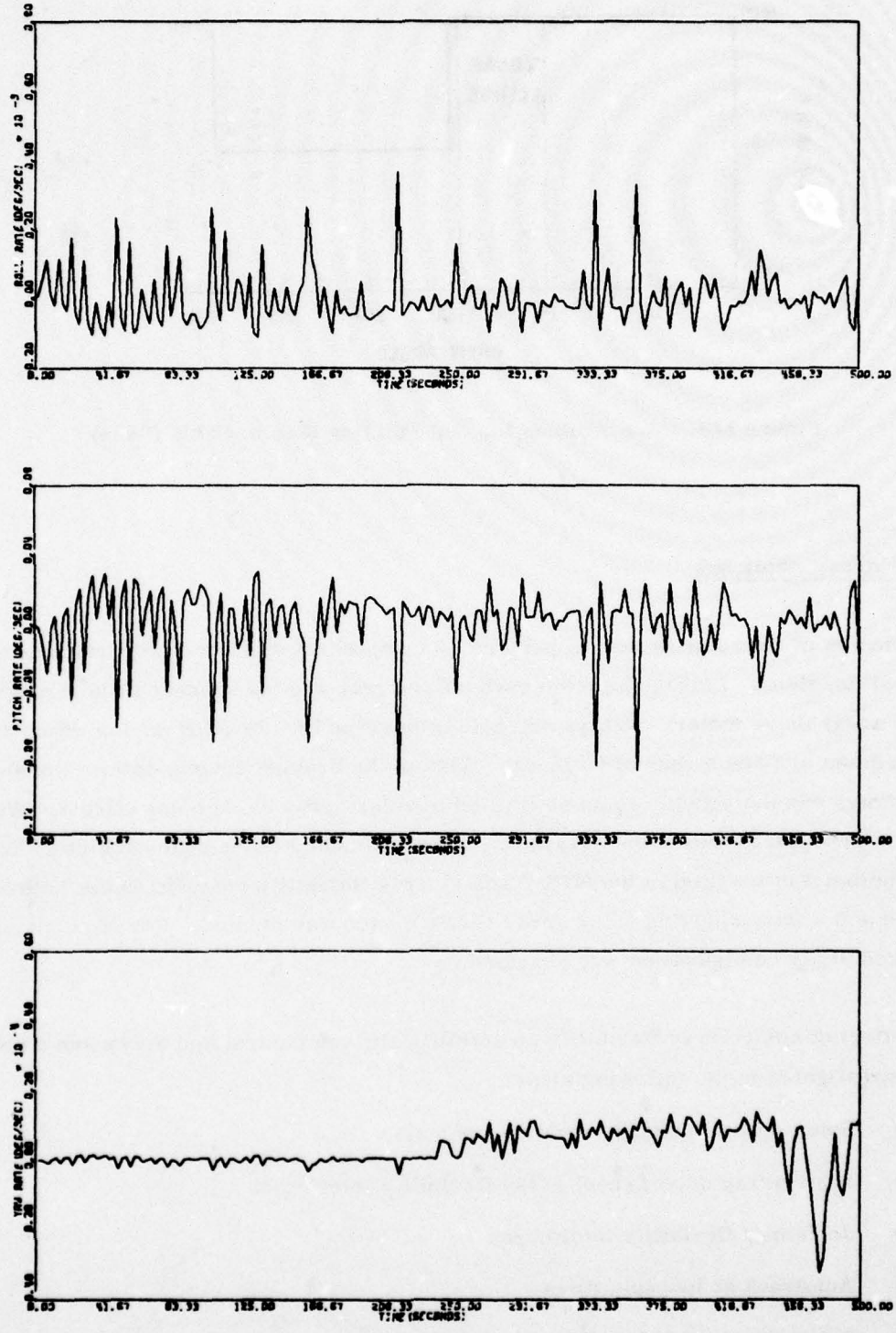

Figure 150. Post Lunar Eclipse Array Autotrack

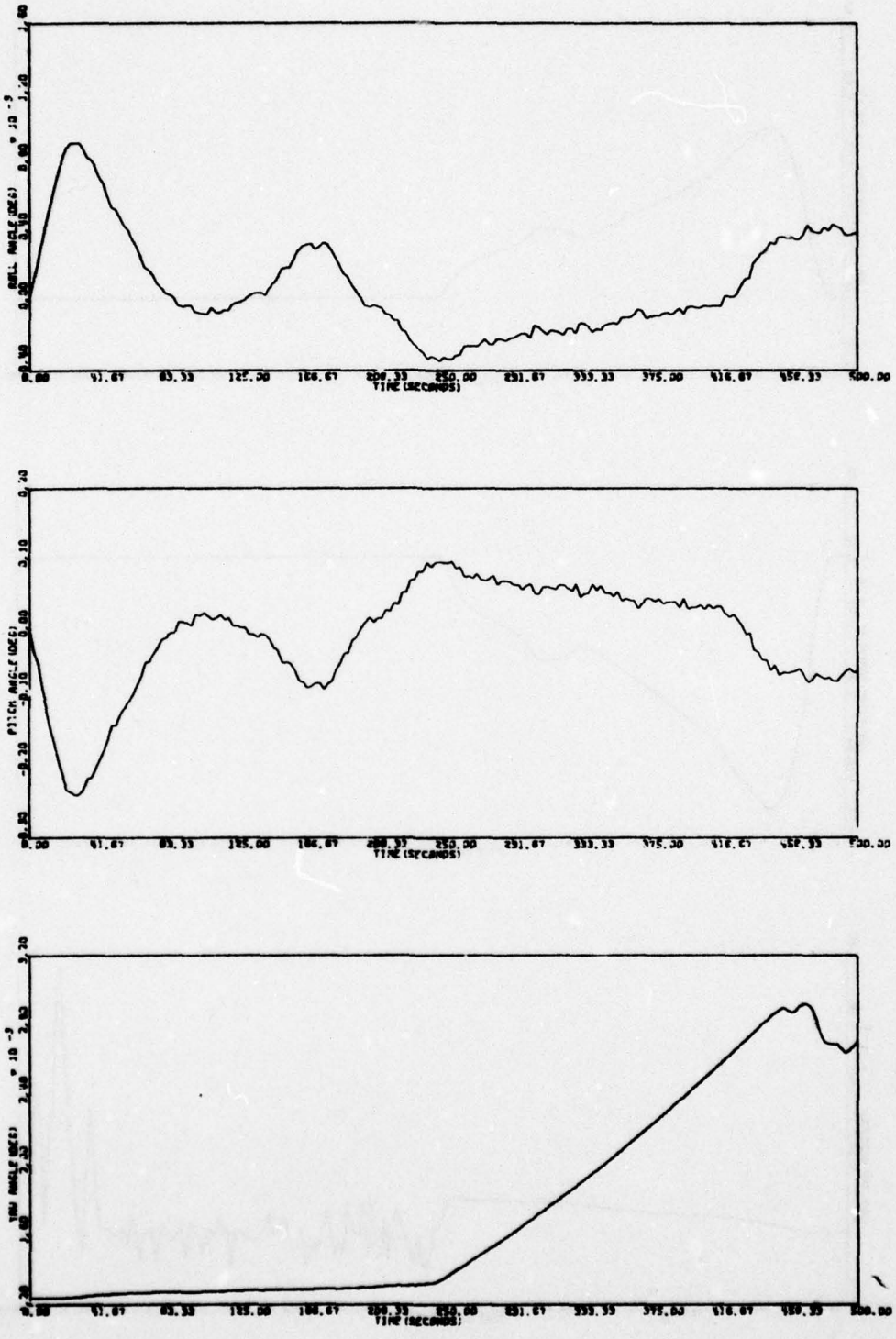

Figure 150. Post Lunar Eclipse Array Autotrack (continued)

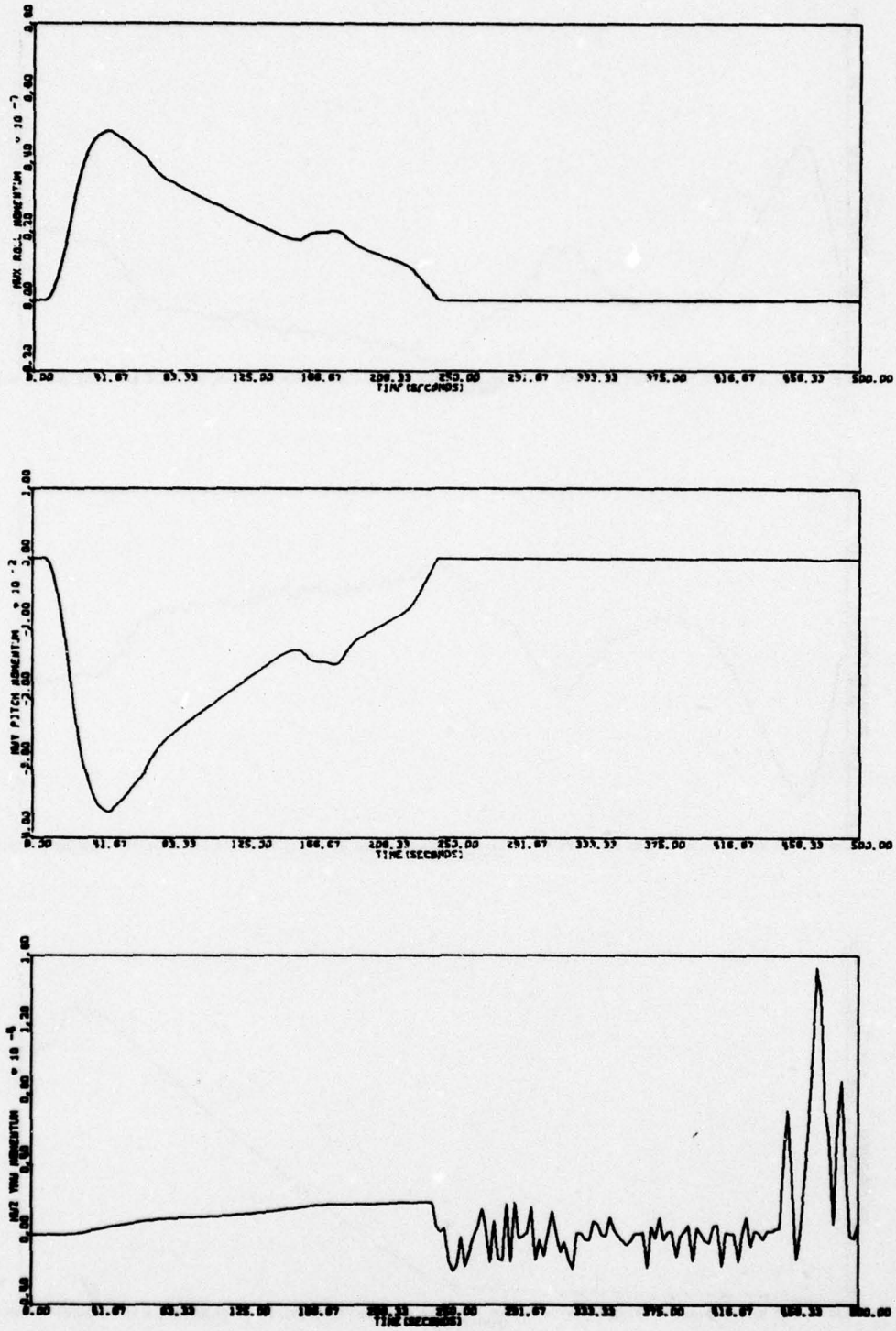

Figure 150. Post Lunar Eclipse Array Autotrack (continued)

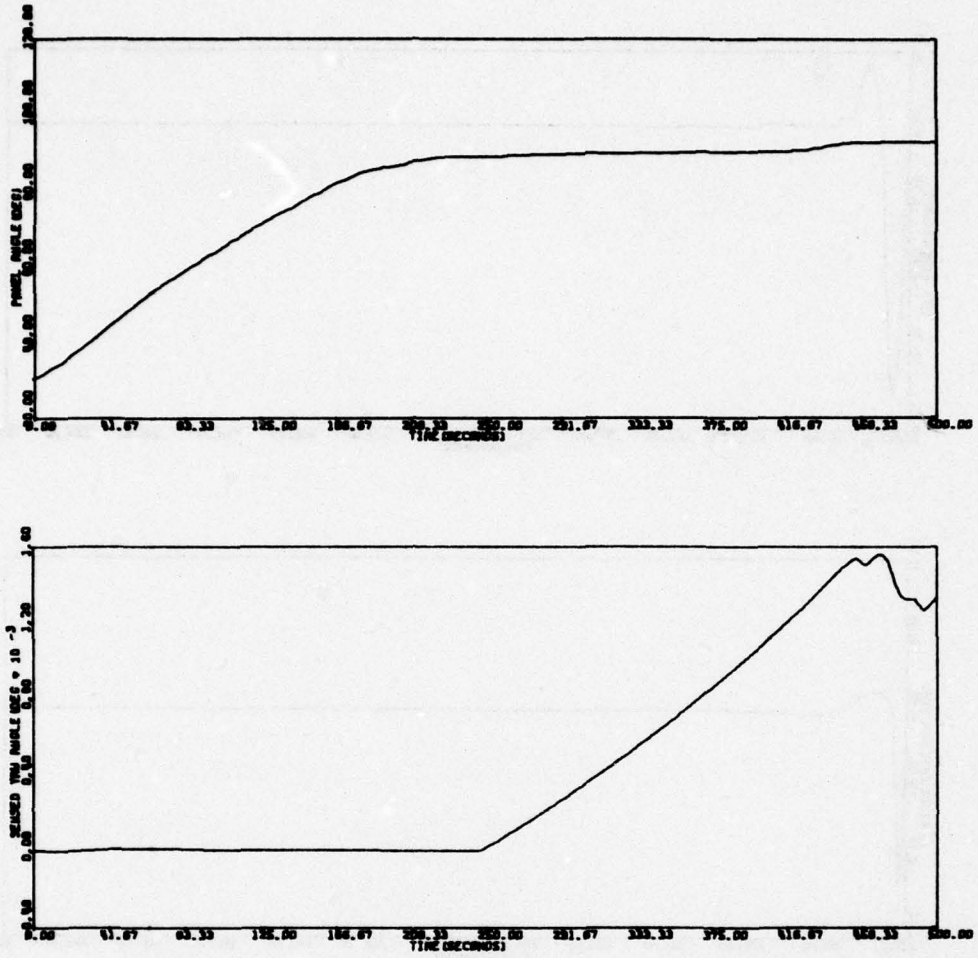

Figure 150. Post Lunar Eclipse Array Autotrack (concluded)

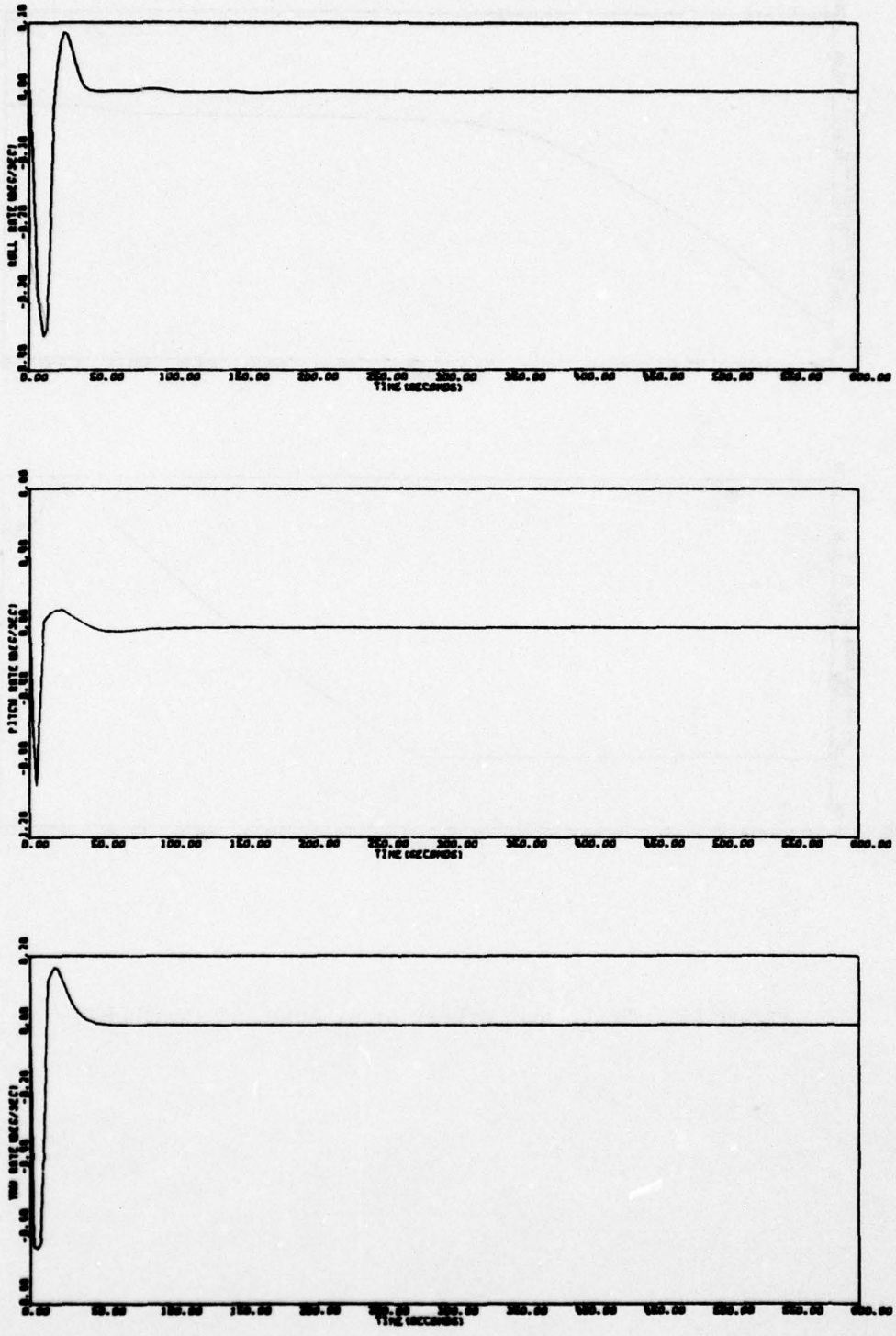

Figure 151. Jet Backup to Wheel Loop Transient Response

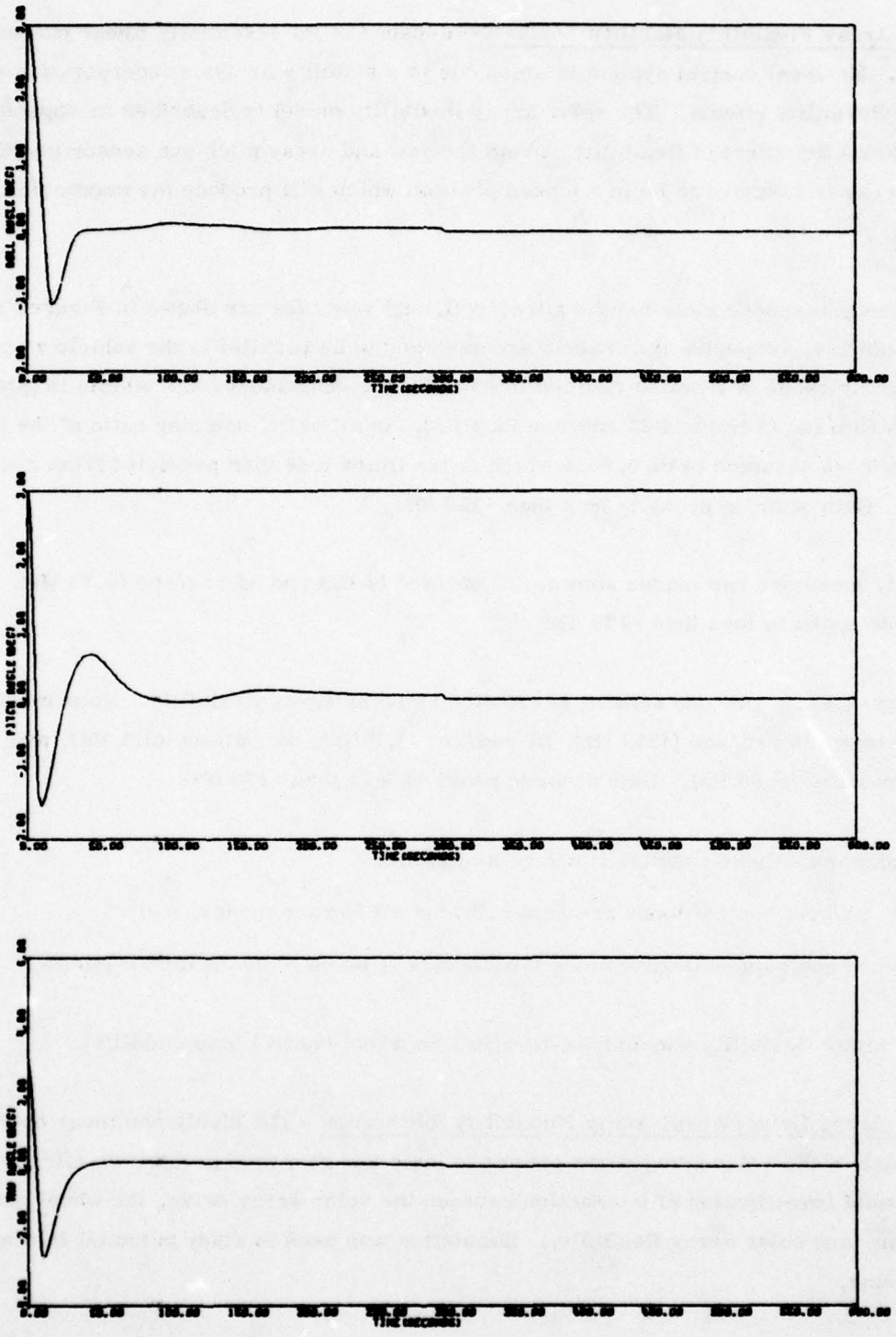

Figure 151. Jet Backup to Wheel Loop Transient Response (concluded)

Solar Array Flexibility Stability Analysis--Because of its essentially linear characteristics, the wheel control system is amenable to a stability analysis incorporating solar array flexibility effects. The solar array flexibility model is described in Appendix I. It includes the effect of flexibility at both the yaw and array pitch sun sensor positions. The array is assumed to be in a locked position which will produce the maximum interaction.

Frequency response plots for the pitch, roll, and yaw axes are shown in Figures 152, 153, and 154. respectively. Panels are assumed to be parallel to the vehicle zy plane. Frequency range is from 20 rad/sec to 60 rad/sec. Two modes are visible in pitch at ≈25 rad/sec (4 Hz) and 32 rad/sec (5.1 Hz). In all axes, damping ratio of the free modes were assumed to be 0.0035 which is ten times less than predicted from ground tests. Gain at mode peaks is less than -150 dB.

In roll, there are two modes shown: 25 rad/sec (4 Hz) and 36 rad/sec (5.75 Hz). Gain at mode peaks is less than -120 dB.

In the yaw axis, yaw sun sensing is affected by solar array flexibility. Four modes are shown: 26 rad/sec (4.14 Hz), 31 rad/sec (4.9 Hz), 32 rad/sec (5.1 Hz), and 35.5 rad/sec (5.65 Hz). Gain at mode peaks is less than -100 dB.

To summarize these results, it can be stated that

- Wheel control loops are gain stable at all flexure modes, and
- Peak gain at flexure mode frequencies is below -100 dB for all modes.

Solar array flexibility should have no effect on wheel control loop stability.

Solar Array Drive/Wheel Array Flexibility Interaction--The highly nonlinear characteristics of the solar array drive command logic and response prohibit an effective analytical investigation of interaction between the solar array drive, the wheel control system, and solar array flexibility. Simulation was used to study potential interaction problems.

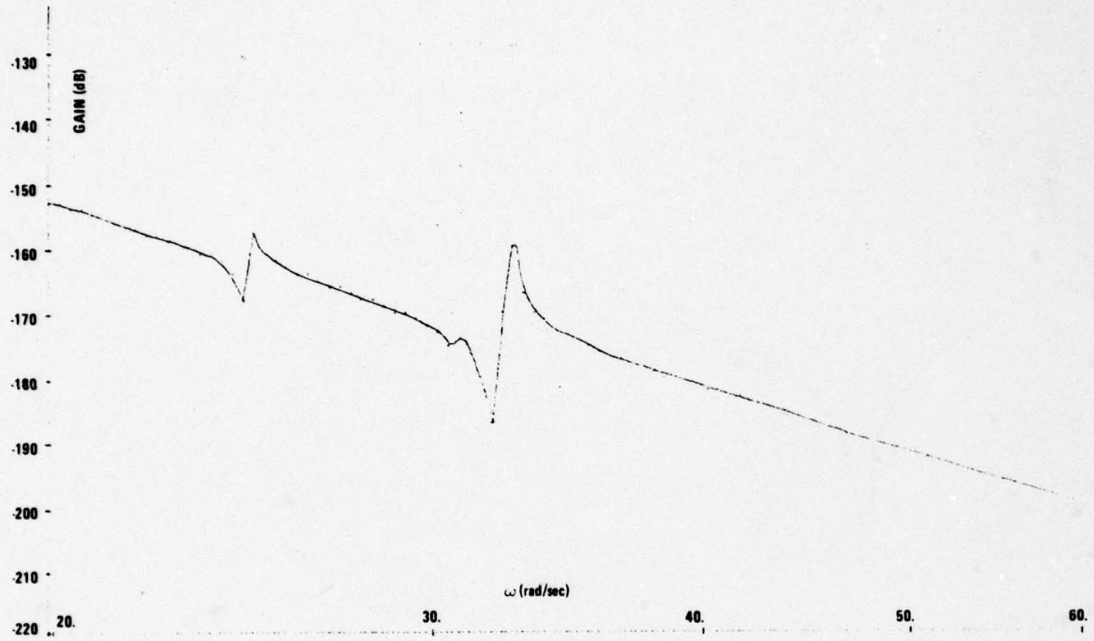

Figure 152. Pitch Wheel Control Loop Frequency Response (with Solar Panel Flexibility)

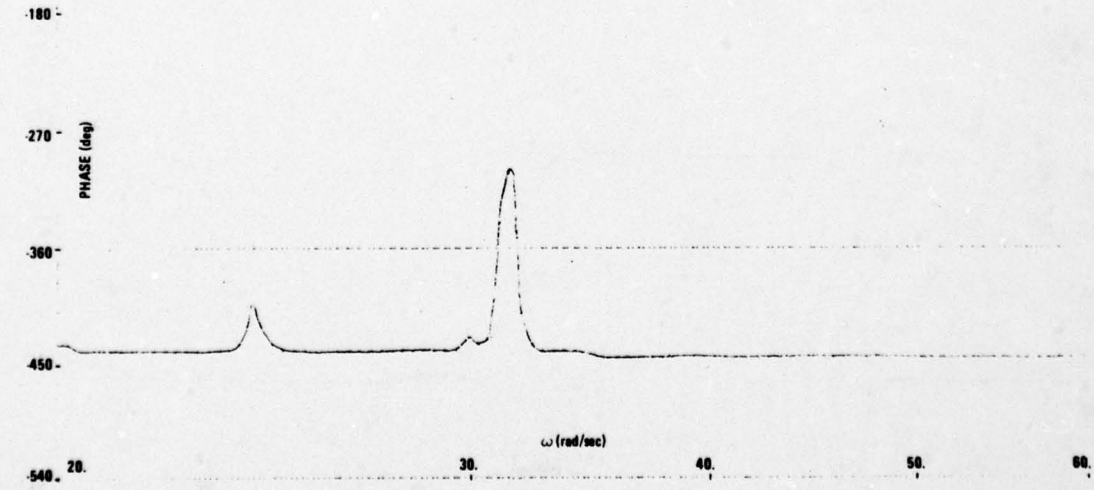

Figure 152. Pitch Wheel Control Loop Frequency Response (with Solar Panel Flexibility) (concluded)

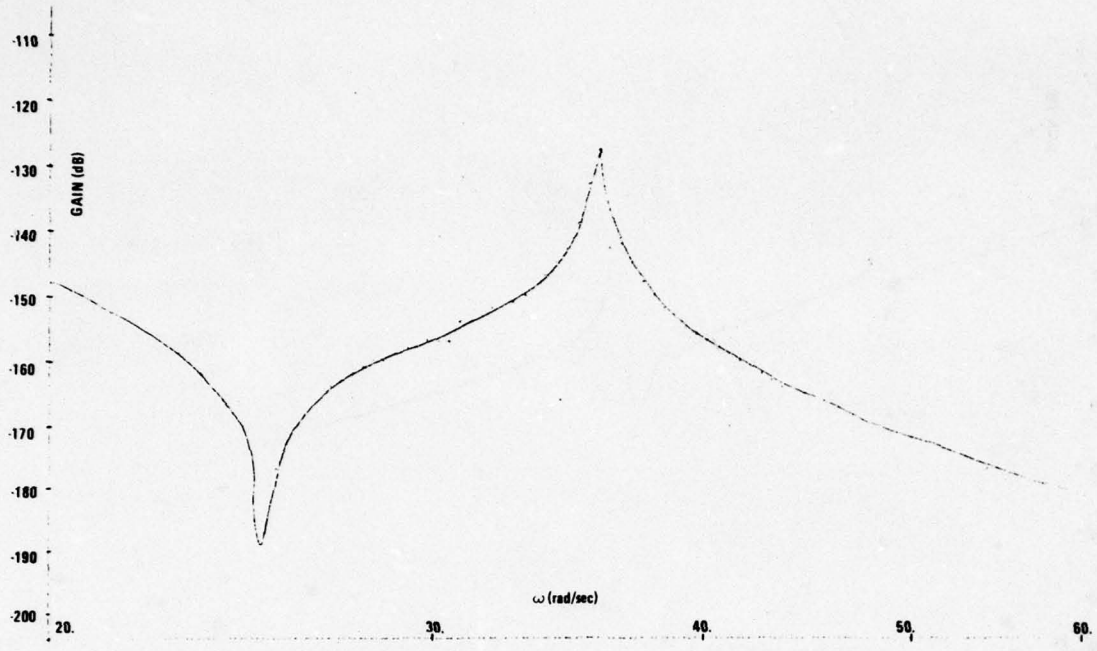

Figure 153. Roll Wheel Control Loop Frequency Response (with Solar Panel Flexibility)

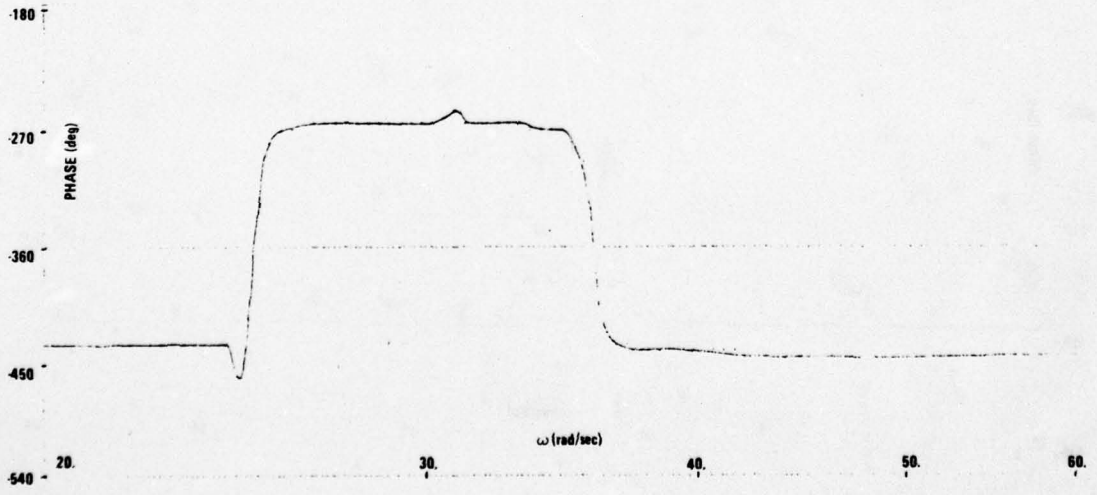

Figure 153. Roll Wheel Control Loop Frequency Response (with Solar Panel Flexibility) (concluded)

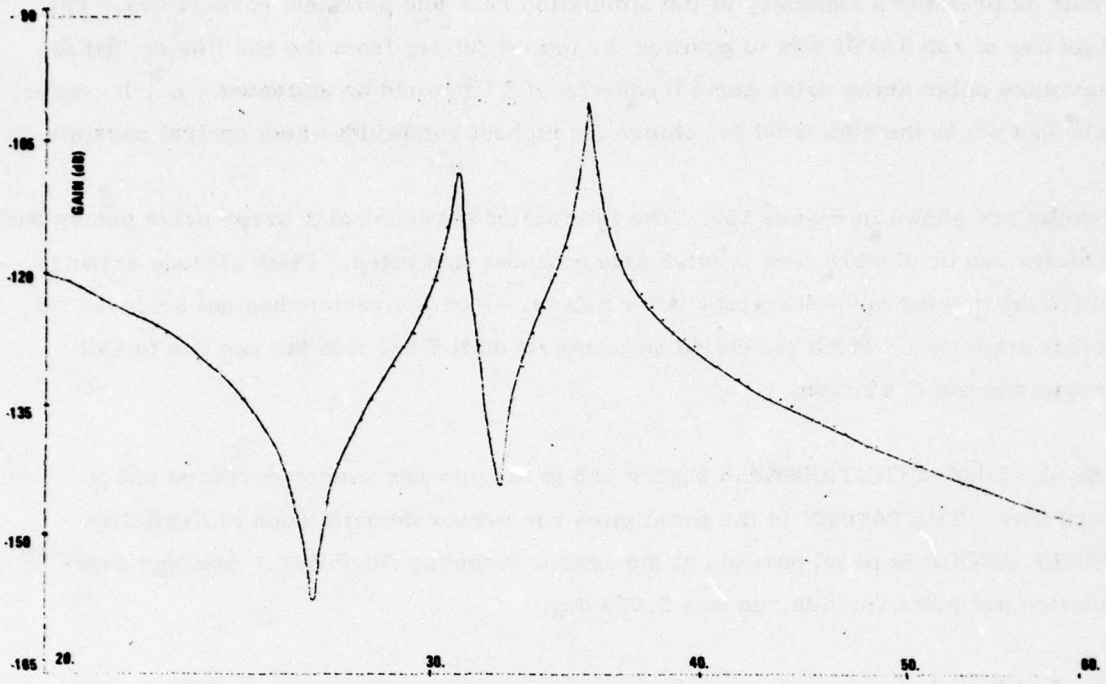

Figure 154. Yaw Wheel Control Loop Frequency Response (with Solar Panel Flexibility)

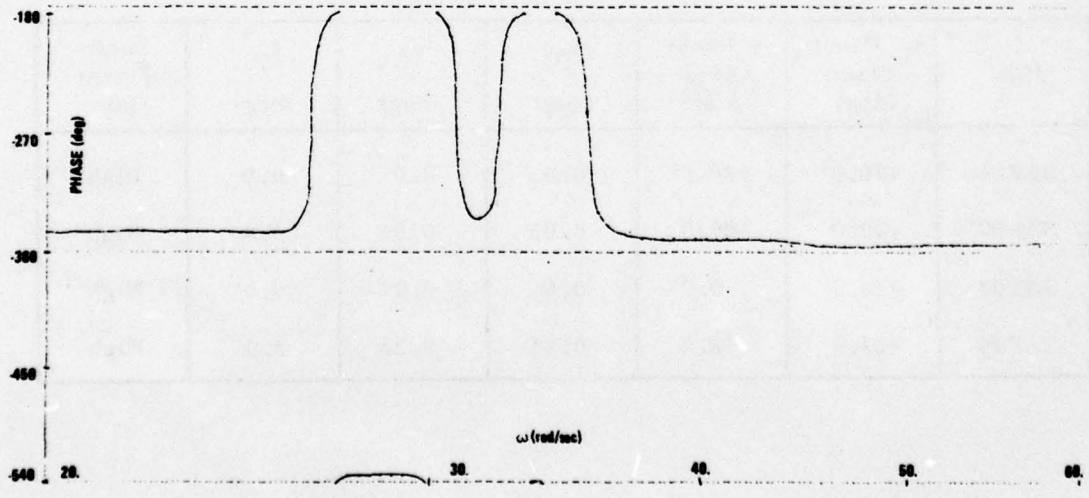

Figure 154. Yaw Wheel Control Loop Frequency Response (with Solar Panel Flexibility) (concluded)

Table 32 presents a summary of the simulation runs and pertinent parameters. The objective of run SAF01 was to position the arrays 20 deg from the sun line so that the maximum solar array drive pulse frequency of 2 Hz would be activated. Earth sensor gain was set to the high level to achieve the highest bandwidth wheel control possible.

Results are shown in Figure 155. The interaction between solar array drive pulses and vehicles can be clearly seen in pitch axis attitudes and rates. Pitch attitude error is due to orbit rate, not solar array drive pulses, since the vehicle has not achieved its steady state rate. Pitch wheels do not come on until 7 sec into the run due to CES errors and wheel stiction.

The plot labeled THETASUBZ in Figure 155 is the yaw sun sensor deviation due to flexibility. THETASUBY is the panel pitch sun sensor deviation due to flexibility. PANEL ANGLE is panel position at the sensor including flexibility. Average panel rotation per pulse for this run was 0.065 deg.

Run SAF02 includes the effect of wheel activity on the condition of run SAF01. No undesirable effects can be observed. Response is shown in Figure 156.

TABLE 32. SOLAR ARRAY DRIVE/WHEEL/ARRAY FLEXIBILITY INTERACTION RUNS

Run	+y Panel Offset (deg)	-y Panel Offset (deg)	ϕ_{IC} (deg)	θ_{IC} (deg)	ψ_{IC} (deg)	Earth Sensor Gain
SAF01	+20.0	+20.0	0.0	0.0	0.0	High
SAF02	+20.0	+20.0	0.25	0.25	3.0	High
SAF03	+12.0	0.0	0.0	0.0	0.0	High
SAF04	+12.0	+8.0	0.25	0.25	3.0	High

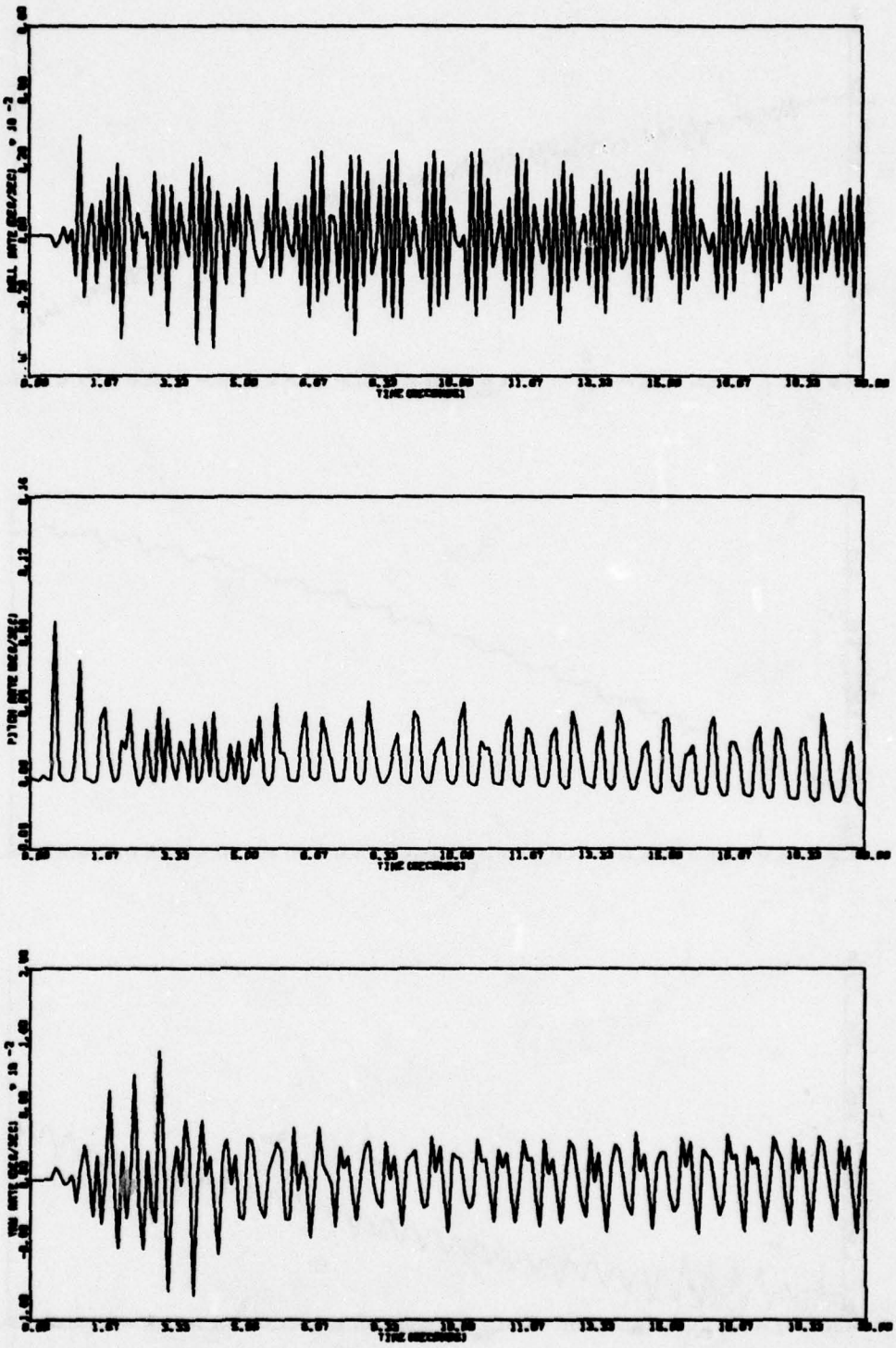

Figure 155. Run SAF01

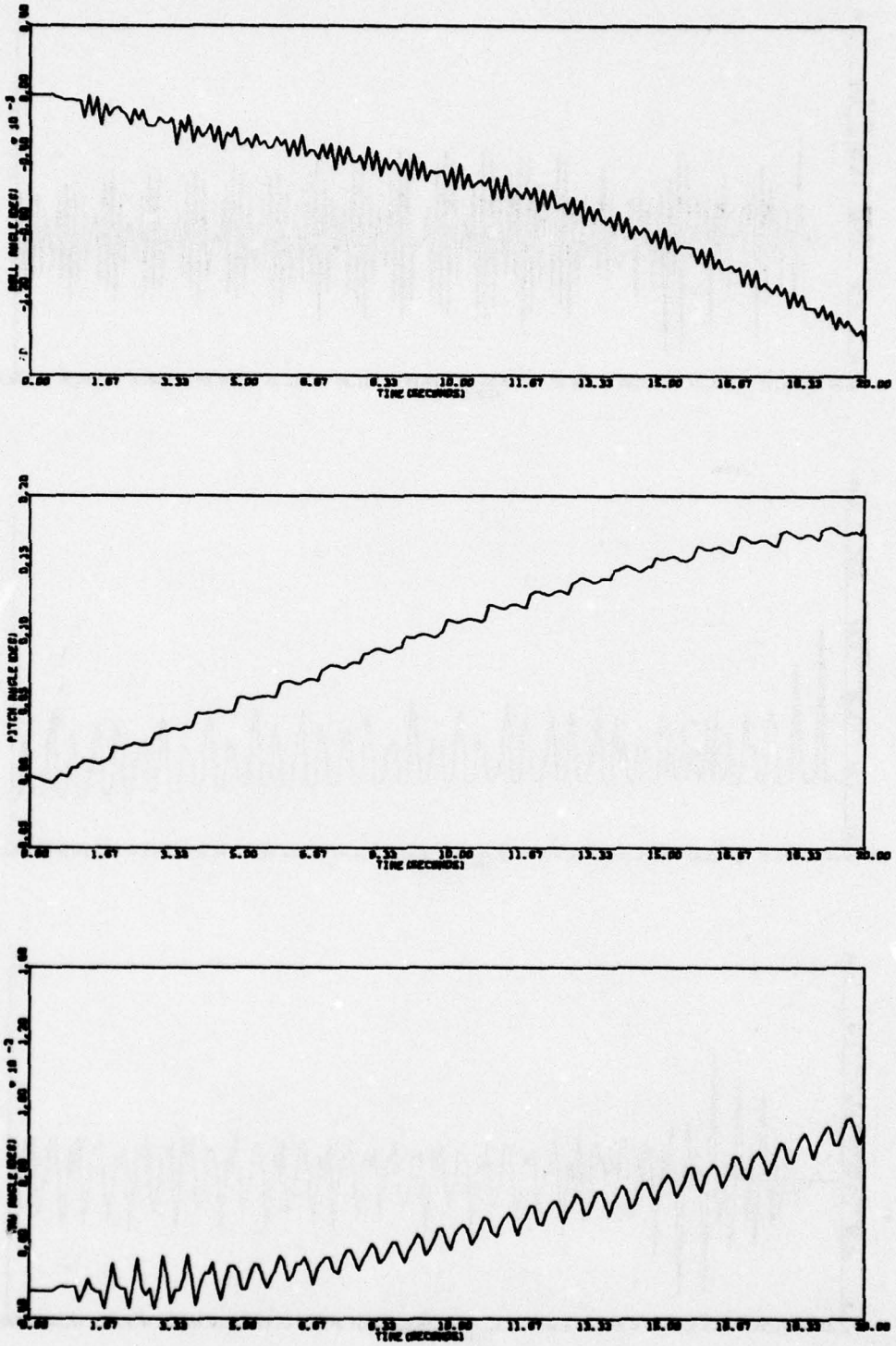

Figure 155. Run SAF01 (continued)

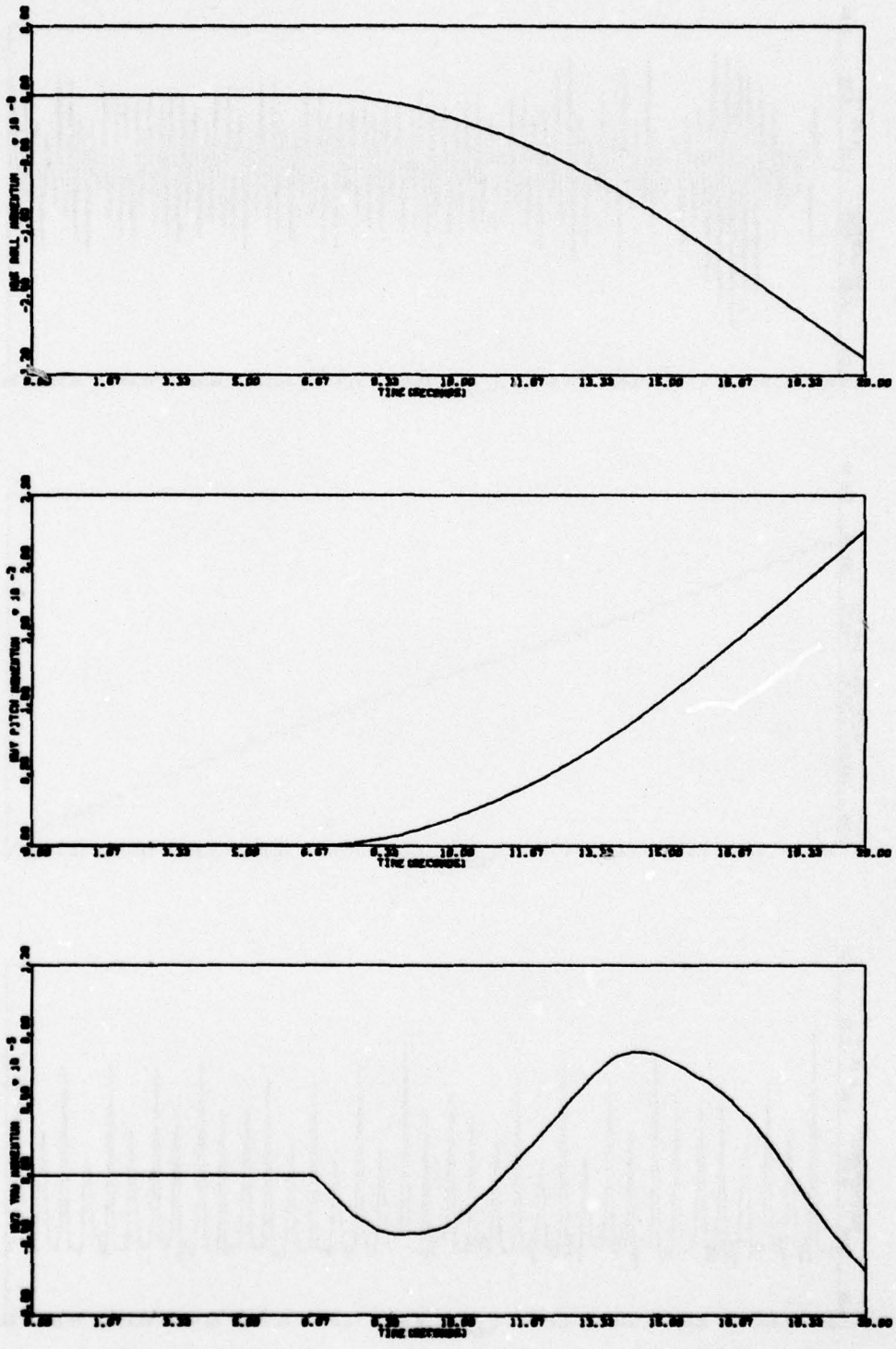

Figure 155. Run SAF01 (continued)

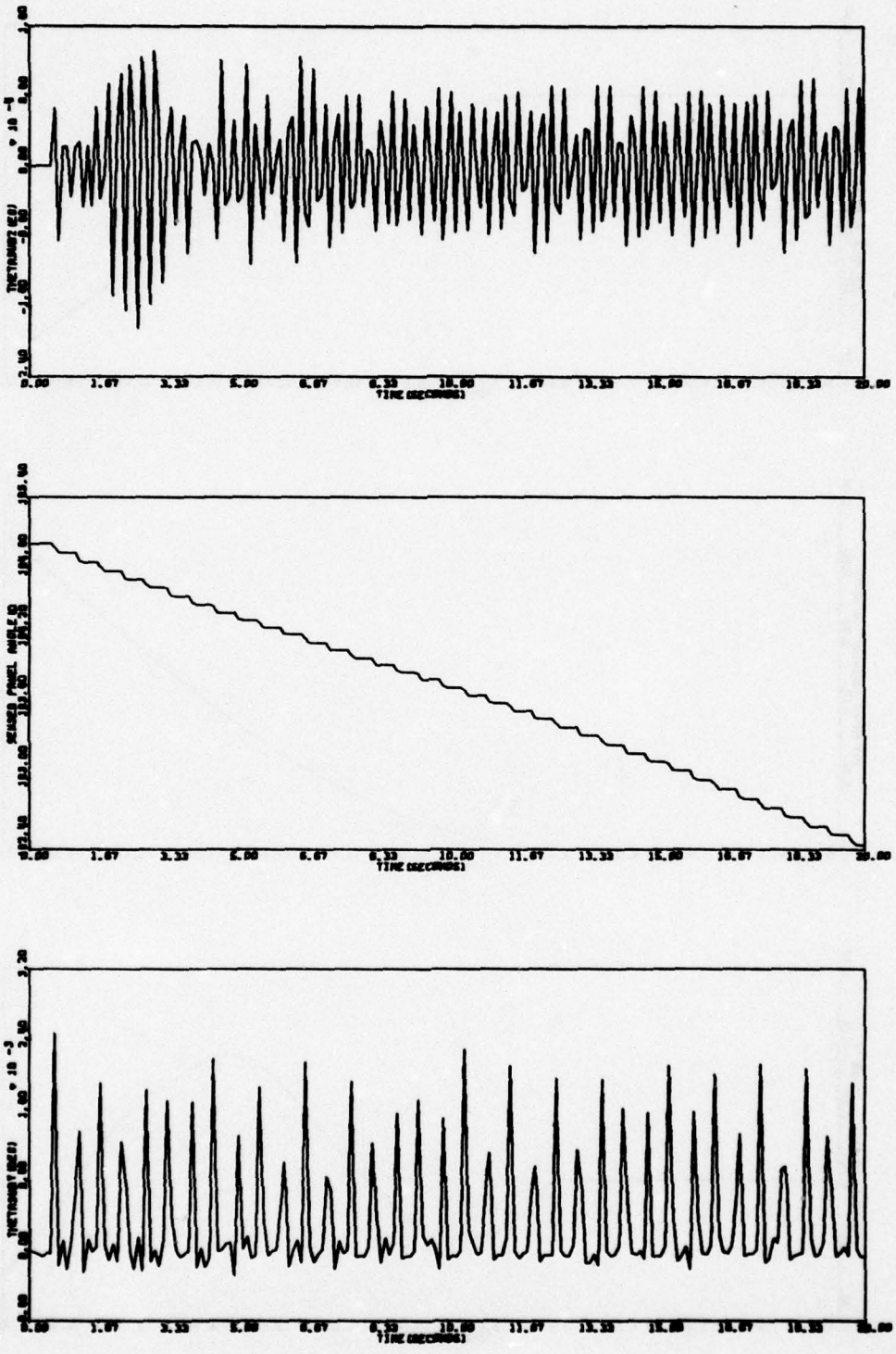

Figure 155. Run SAF01 (continued)

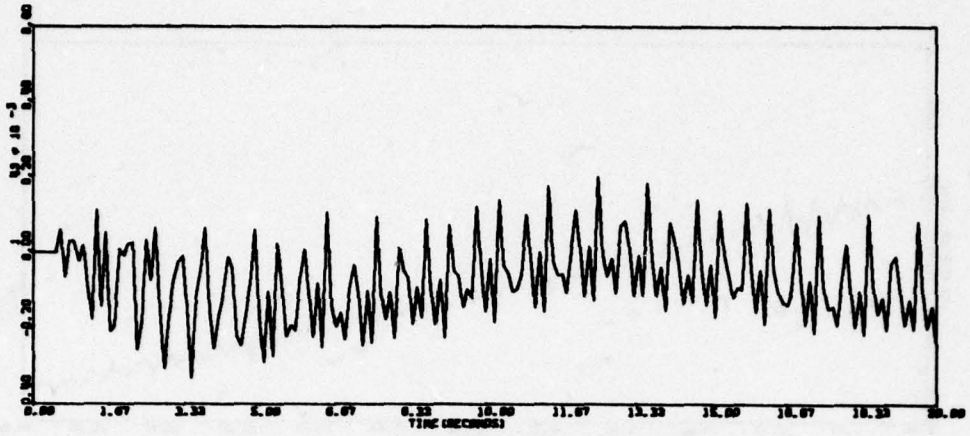

Figure 155. Run SAF01 (concluded)

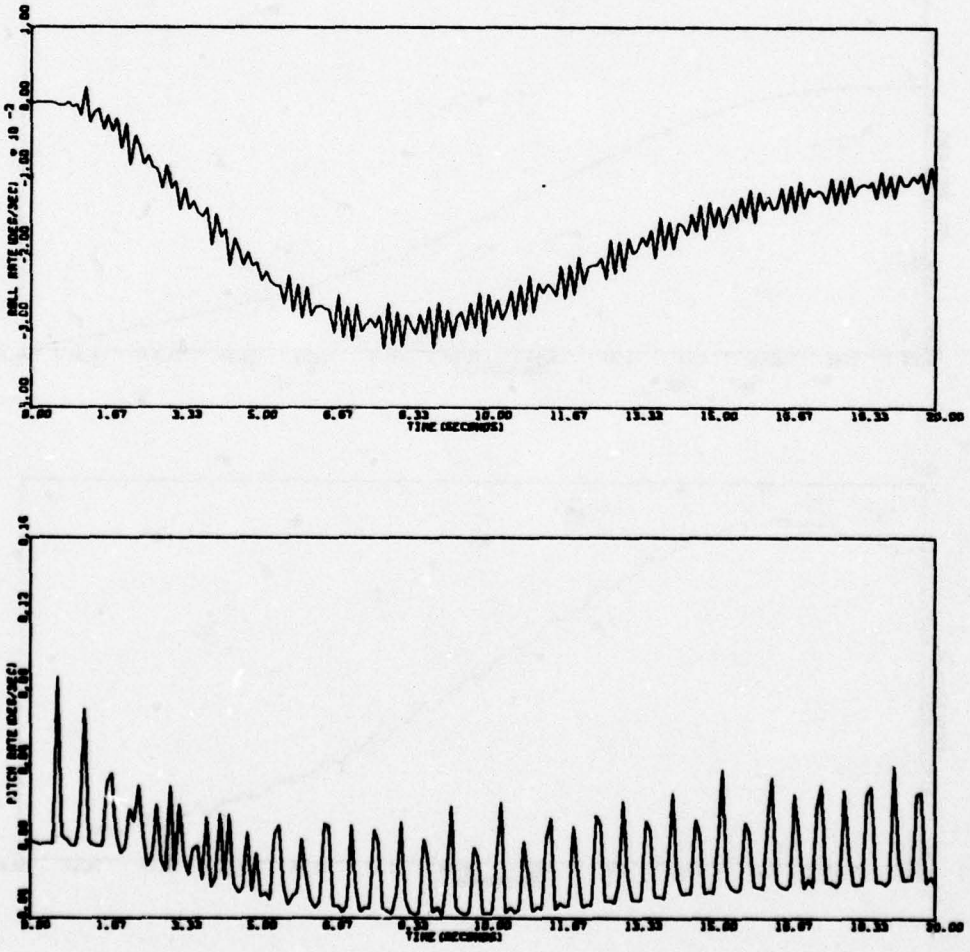

Figure 156. Run SAF02

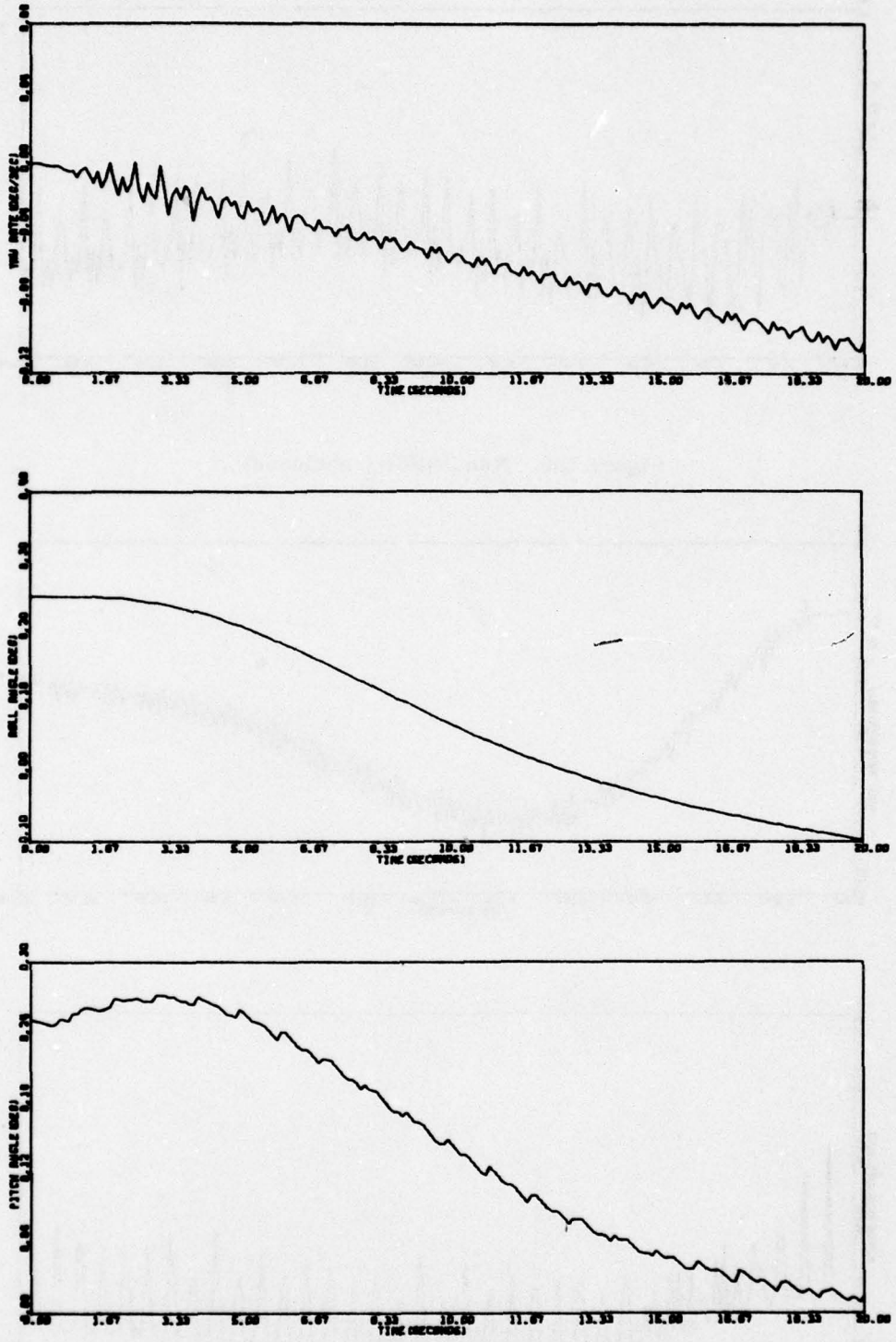

Figure 156. Run SAF02 (continued)

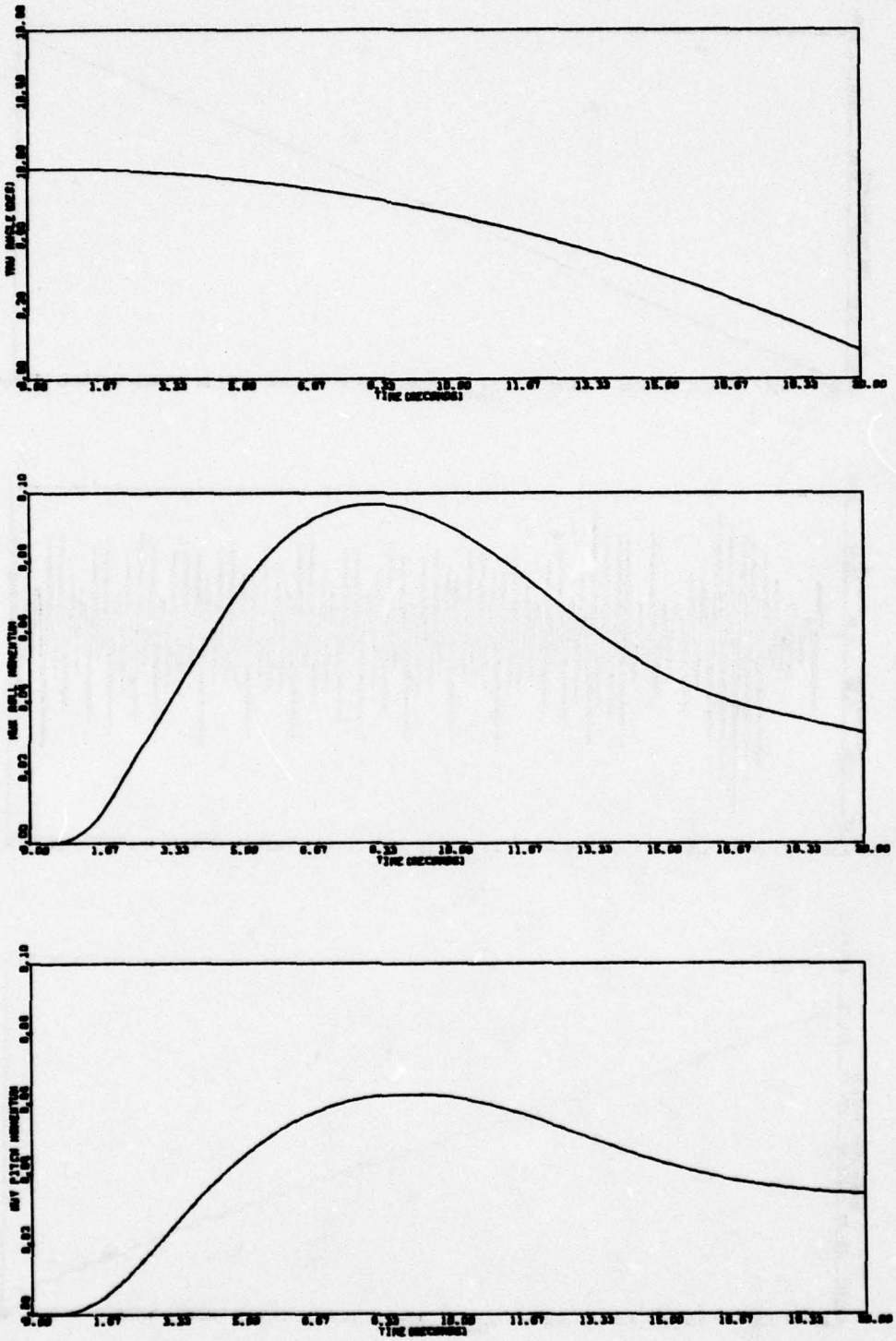

Figure 156. Run SAF02 (continued)

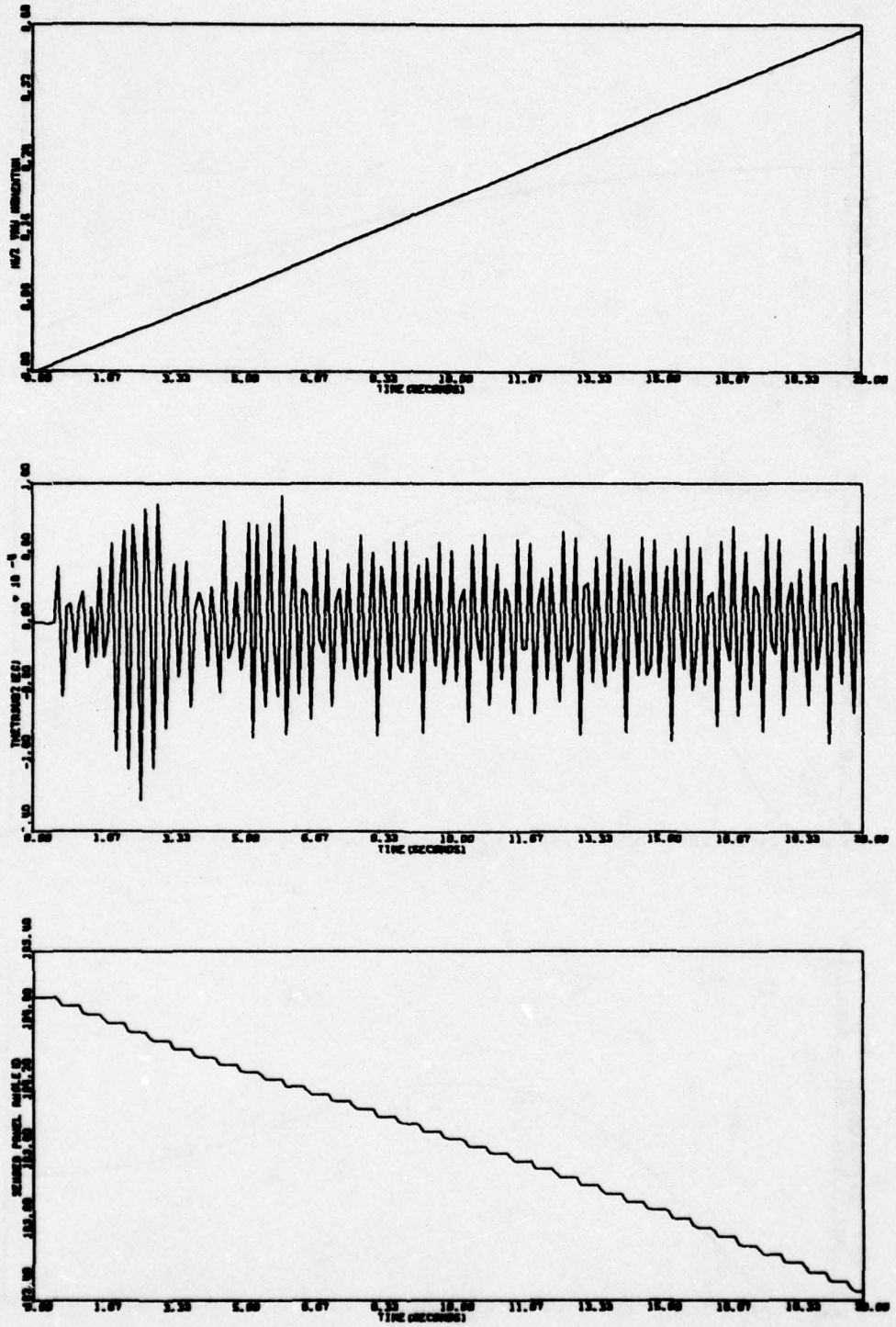

Figure 156. Run SAF02 (continued)

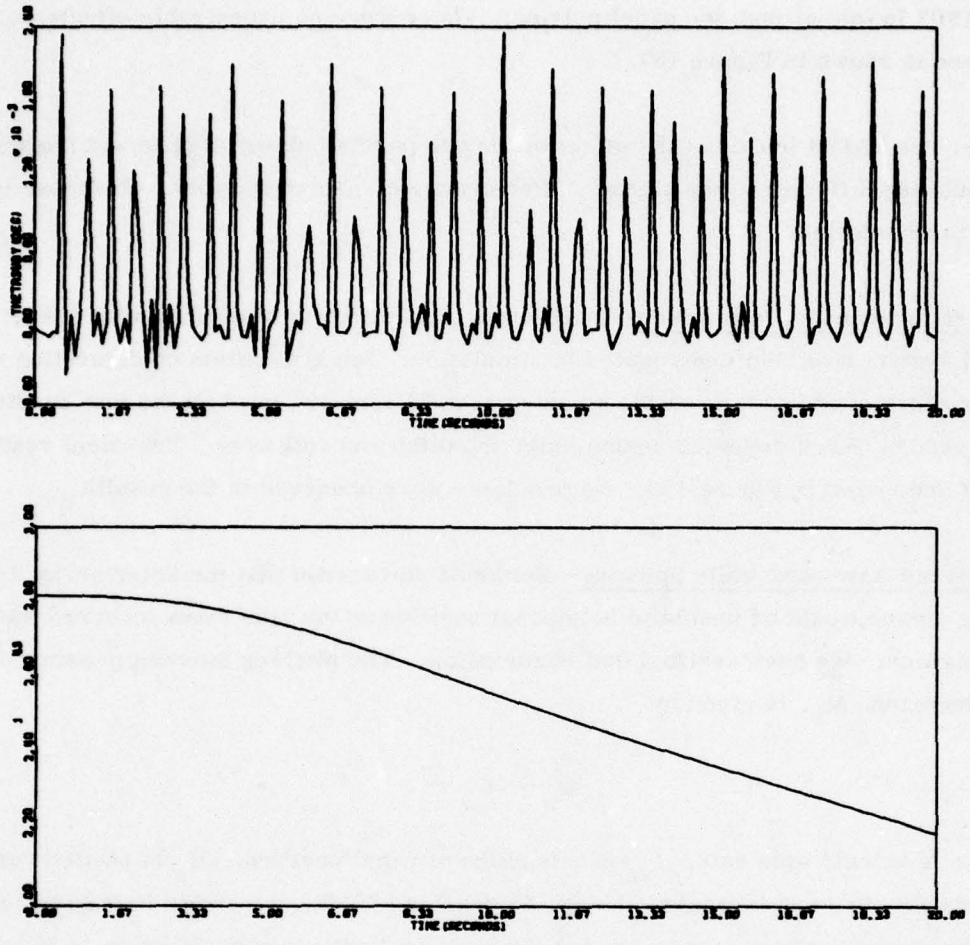

Figure 156. Run SAF02 (concluded)

Run SAF03 looked at just one panel pulsing. There were no undesirable effects. Response is shown in Figure 157.

Finally, run SAF04 looked at the effect of the two panels pulsing at different frequencies by simulating different error signals. Performance was satisfactory. Response is shown in Figure 158.

Jet/Array Flexibility Interaction--Interaction of solar array flexibility with the jet control system was also investigated in simulation. Sun acquisition configuration with one panel deployed and the vehicle spinning at 0.75 rpm was used as the test condition. Initial errors of 2.0 deg were assumed for the pitch and roll axes. Transient response results are shown in Figure 159. No problems were observed in the results.

Solar Array Autotrack while Spinning--Rockwell discovered that the solar array drive braking device would be unable to hold panel position at the spin rates incurred during reacquisition. We have verified that observation. The pitching moment generated while spinning, M_s, is given by

$$M_s \cong -I_{xz}\, r^2$$

where r is vehicle spin rate. I_{xz} is a function of panel position. M_s is plotted versus spin rate for three panel angles, 5 deg, 45 deg, and 90 deg, as shown in Figure 160. Also shown are the spin boundaries for the braking device torque (30 oz-in to 65 oz-in). The worst condition is at 45 deg (135 deg, 215 deg, etc.) where I_{xz} is largest. At that condition, the solar array drive would have difficulty holding position at spin rates greater than 2 rpm. Similar conclusions can be drawn from the other plots.

Two equilibrium points, at 0 and 180 deg, exist. If the array is initially in either of these two positions, it will try to stay in these positions if the vehicle is spun up.

Because of this difficulty, Rockwell has redefined the acquisition procedure. Contract constraints did not permit an analysis of the redefined procedure.

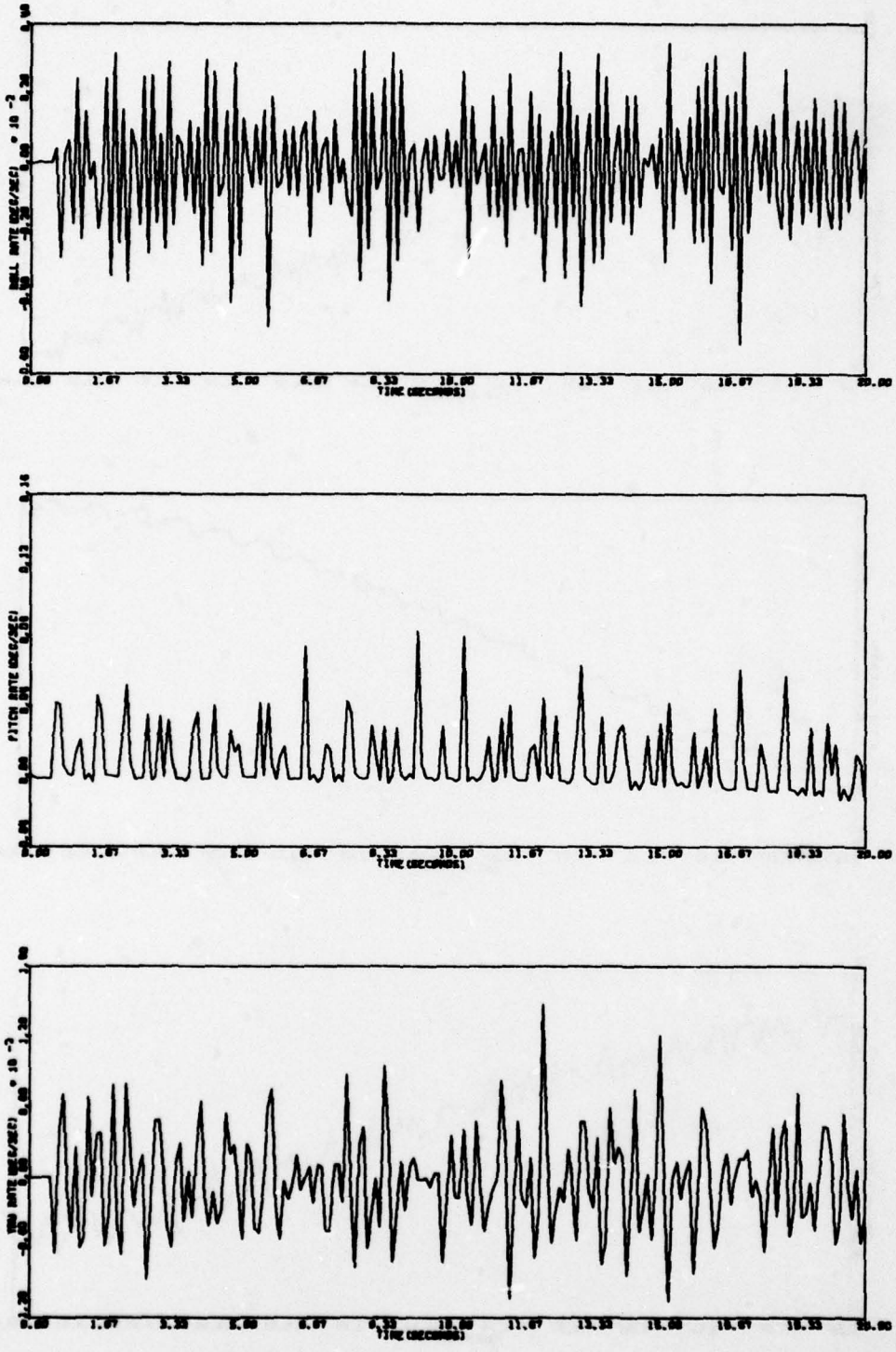

Figure 157. Run SAF03

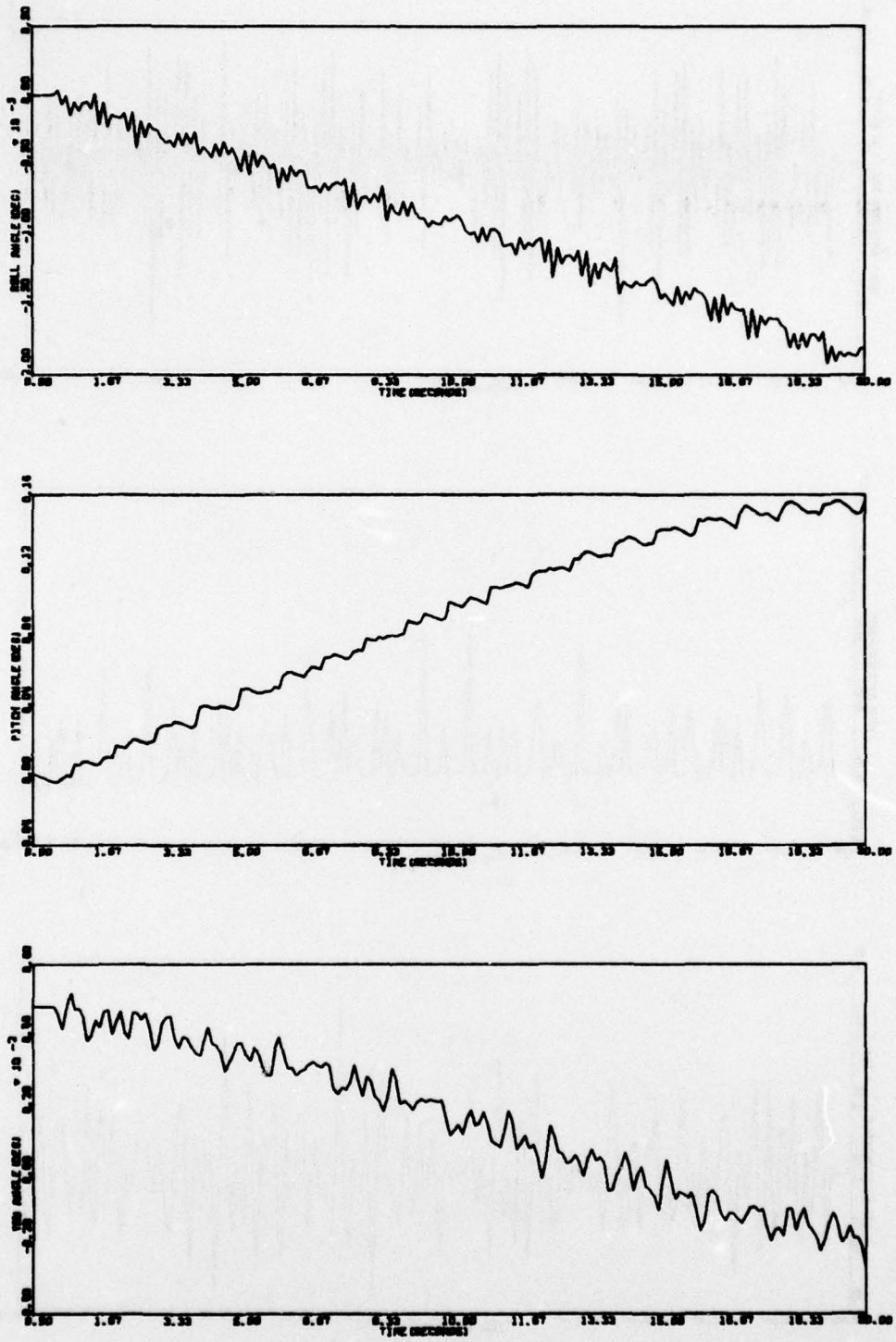

Figure 157. Run SAF03 (continued)

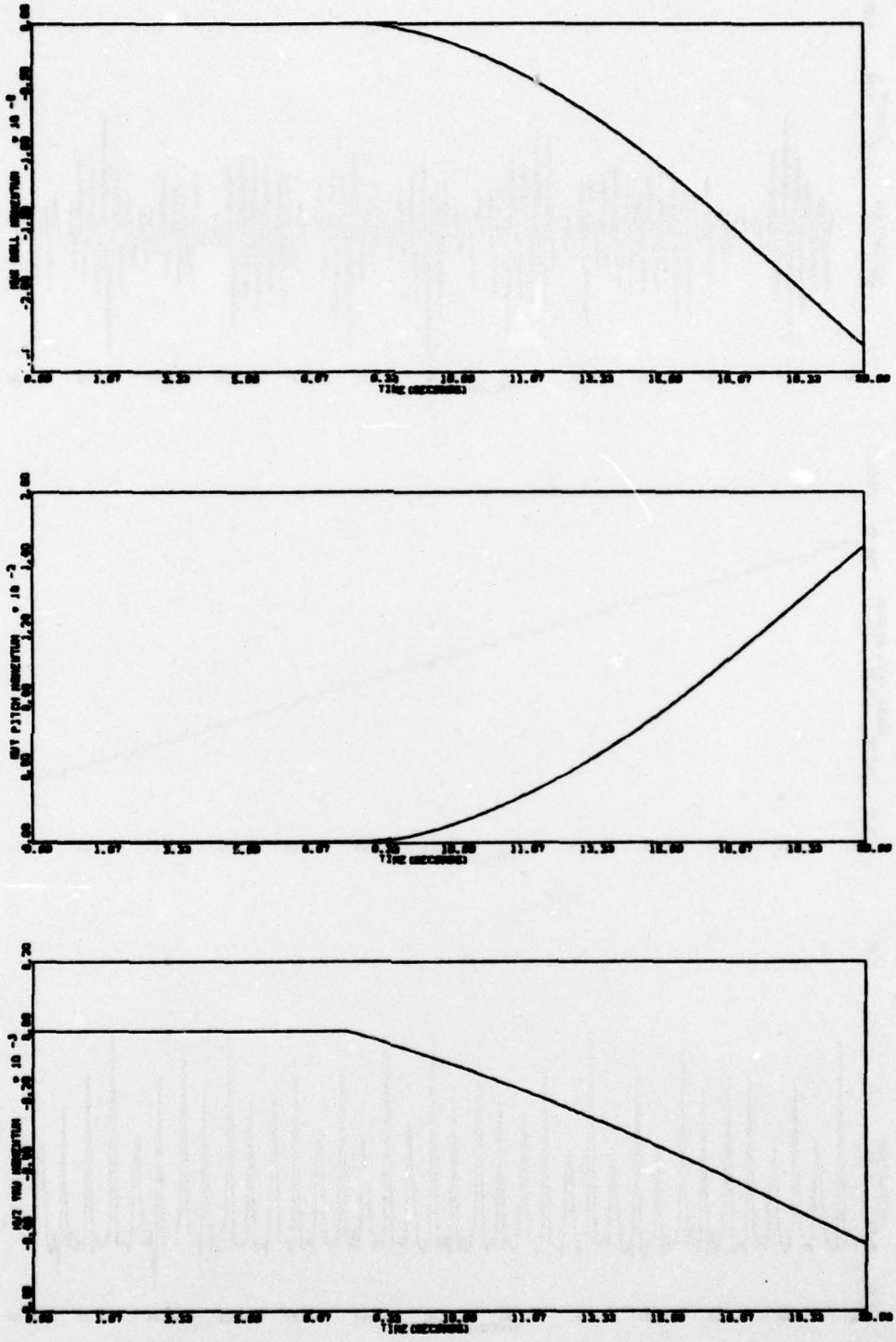

Figure 157. Run SAF03 (continued)

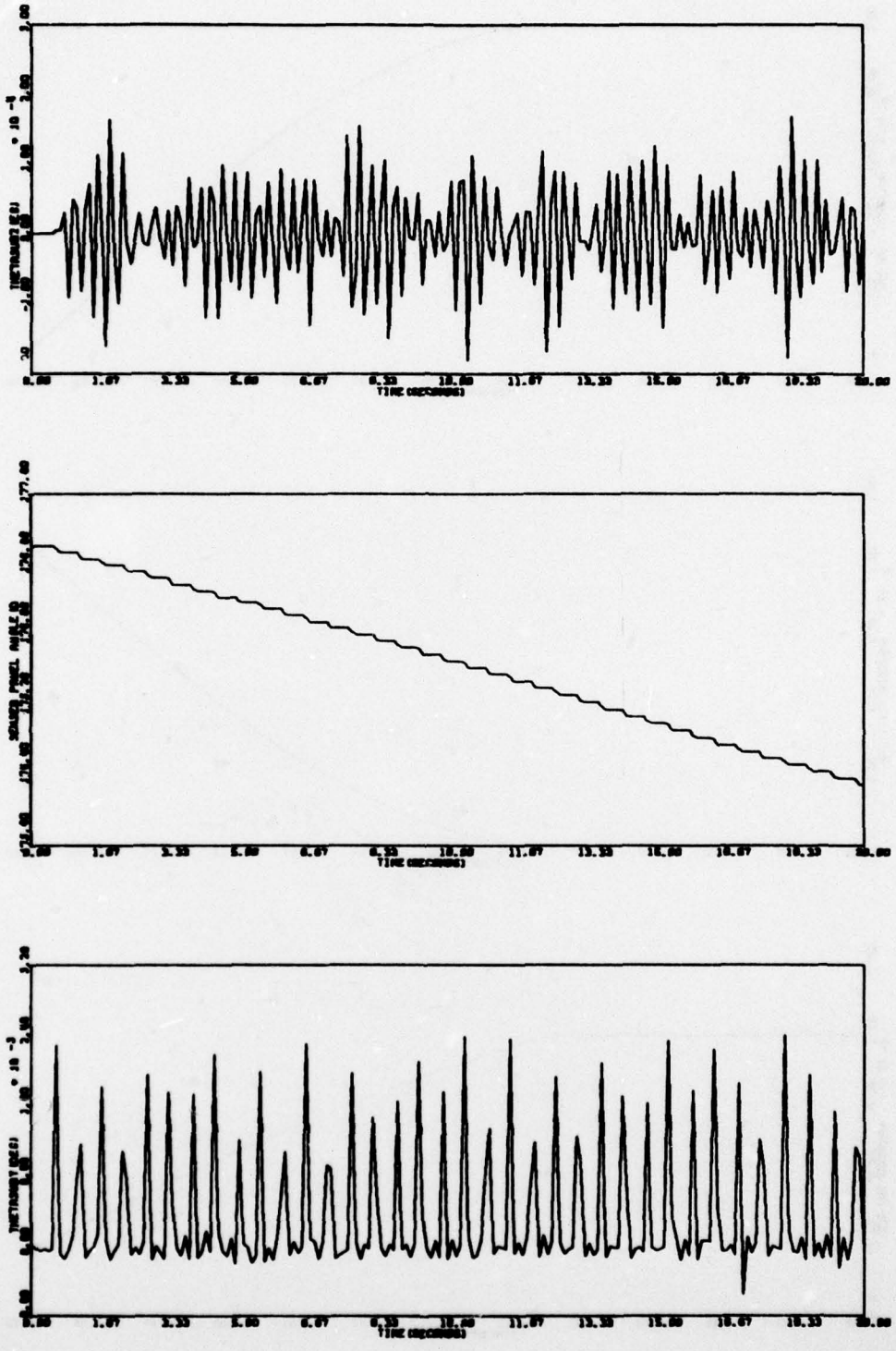

Figure 157. Run SAF03 (continued)

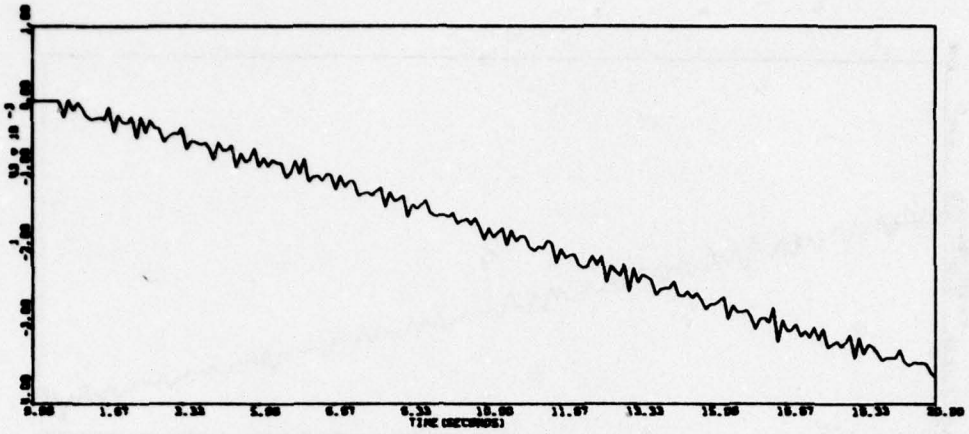

Figure 157. Run SAF03 (concluded)

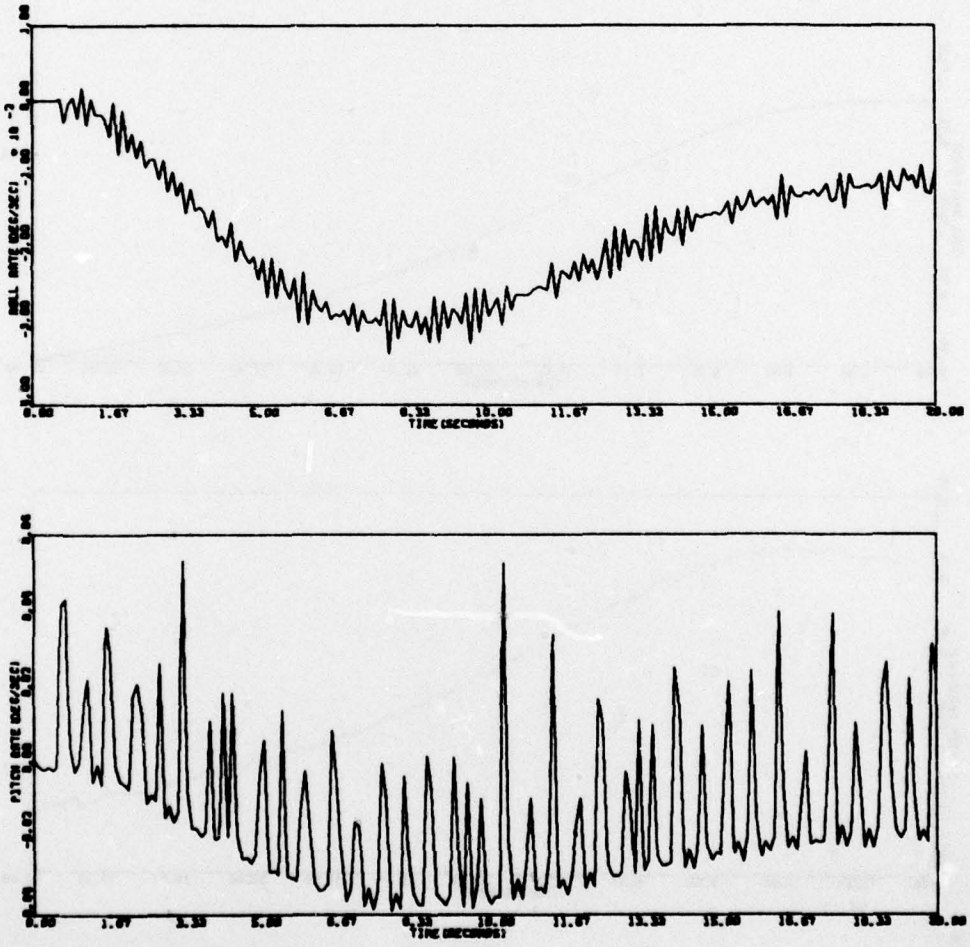

Figure 158. Run SAF04

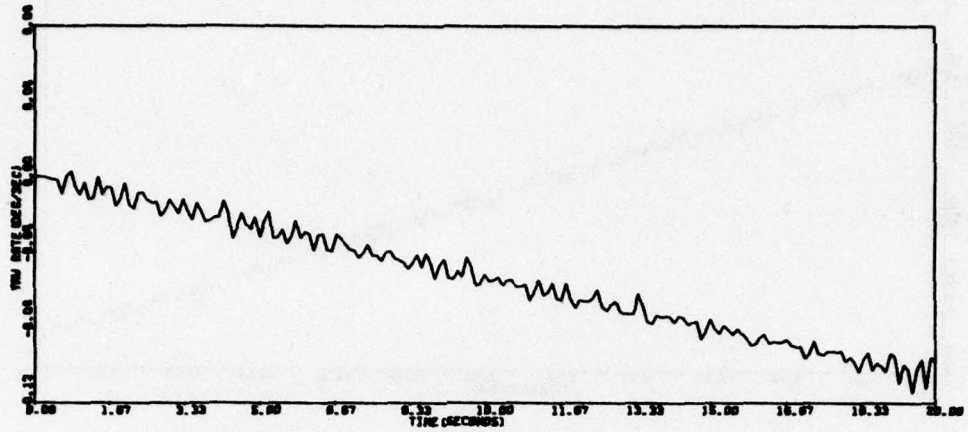

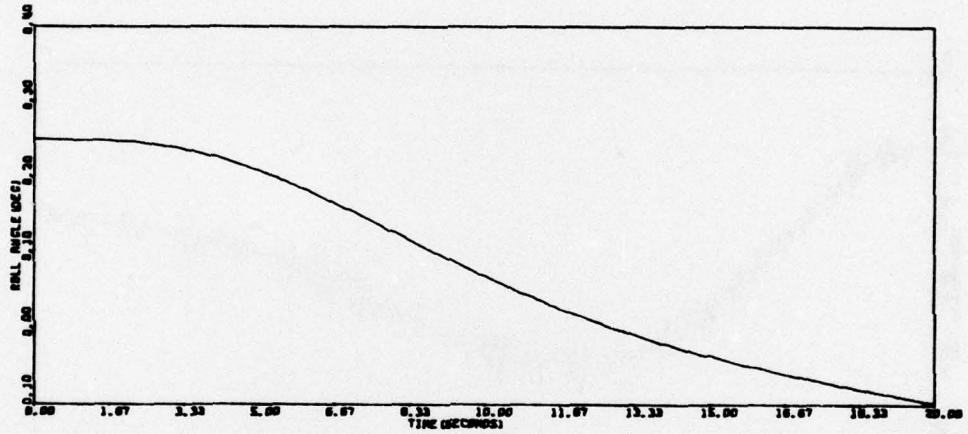

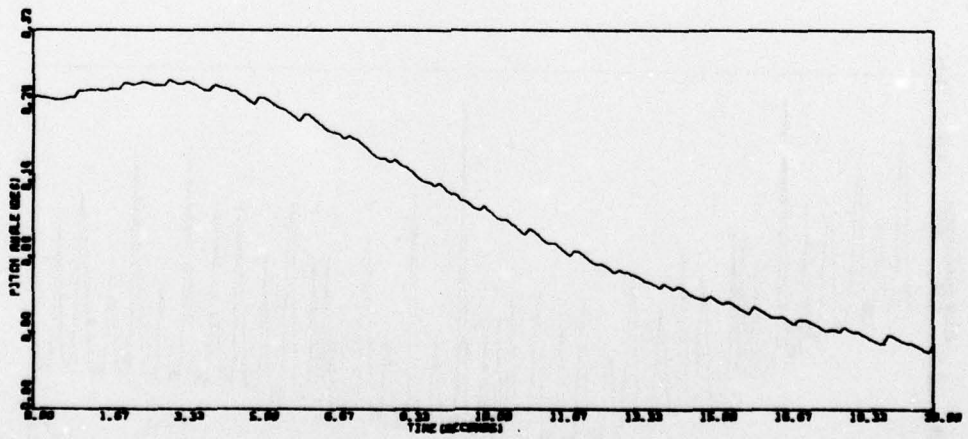

Figure 158. Run SAF04 (continued)

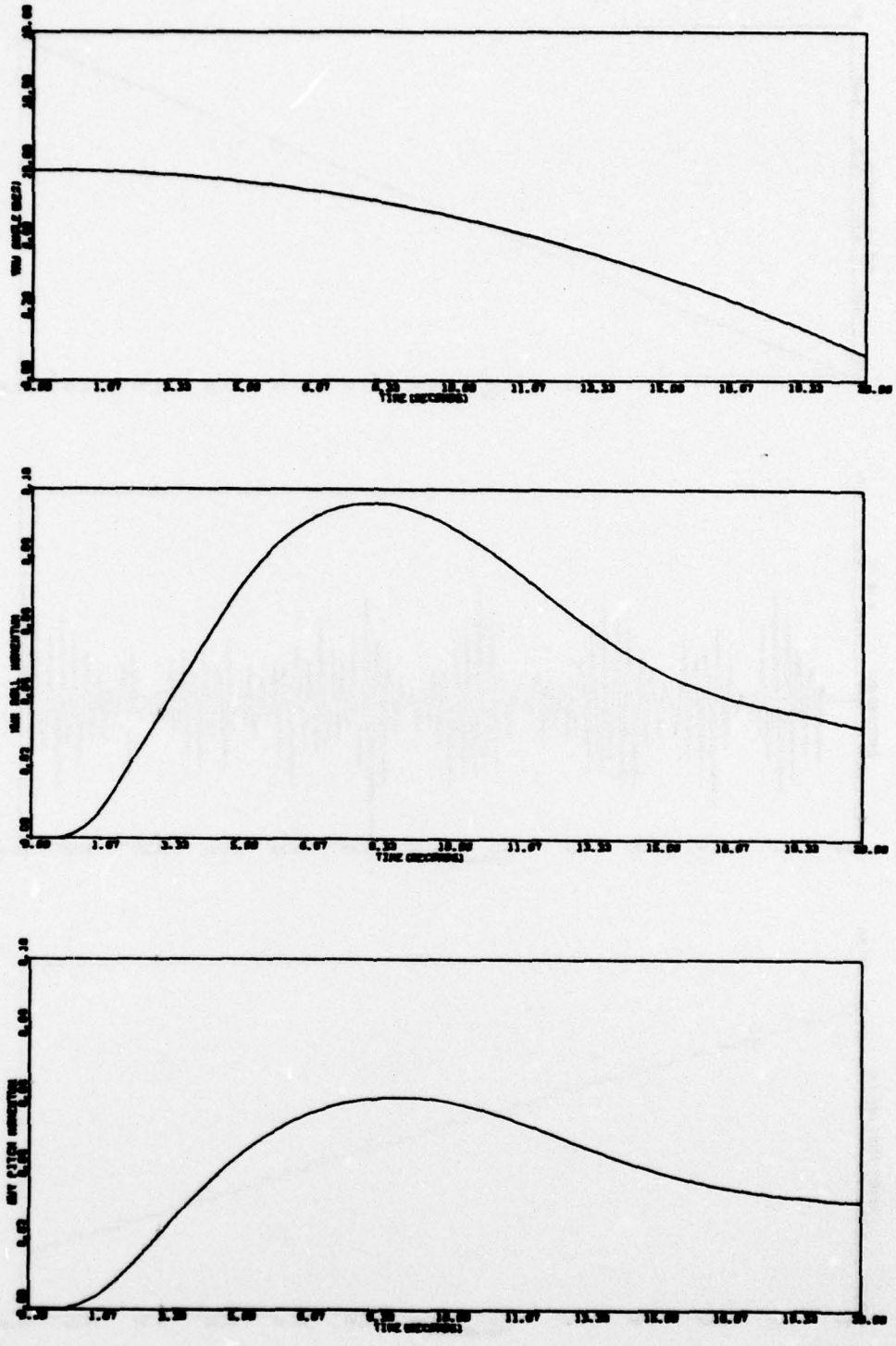

Figure 158. Run SAF04 (continued)

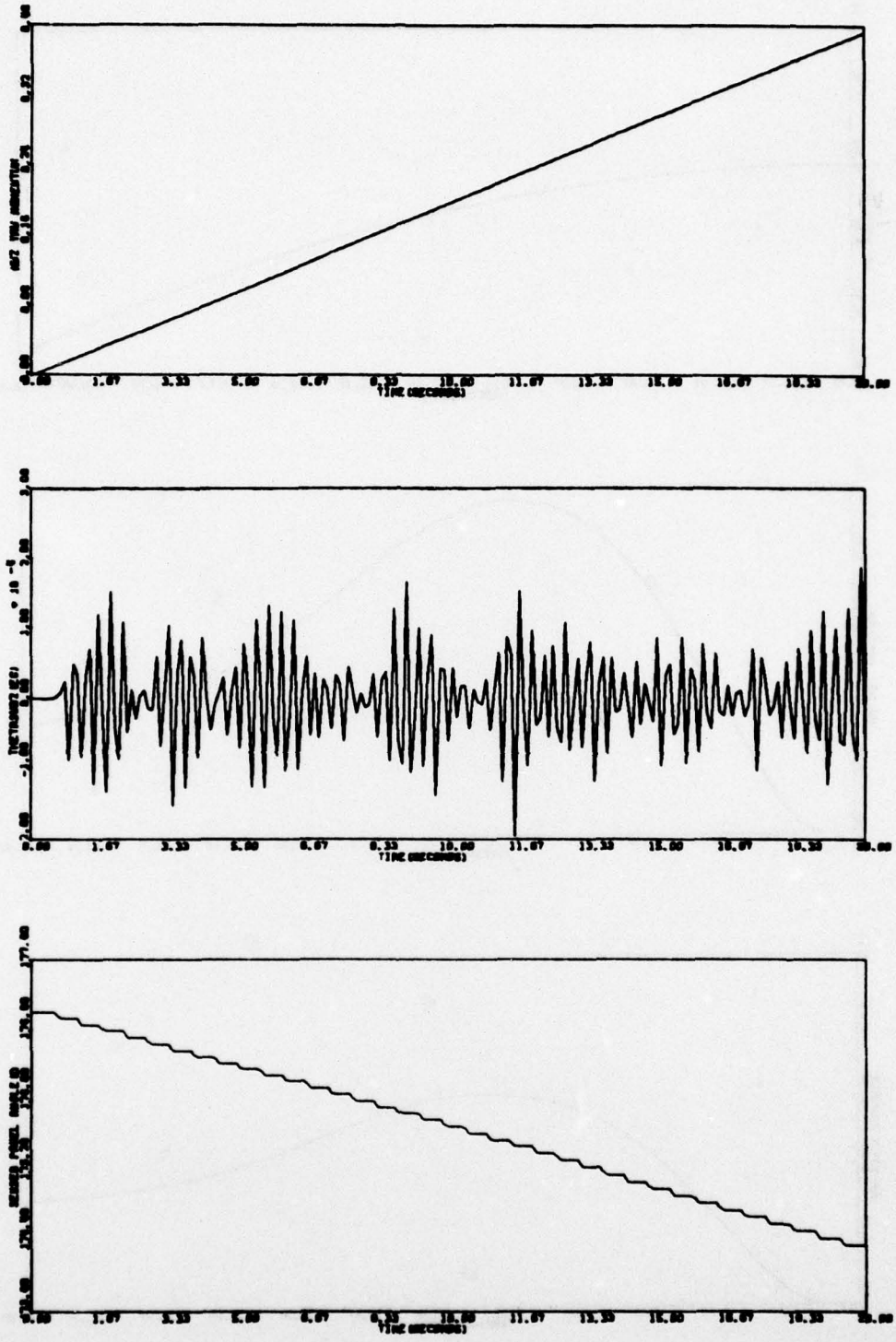

Figure 158. Run SAF04 (continued)

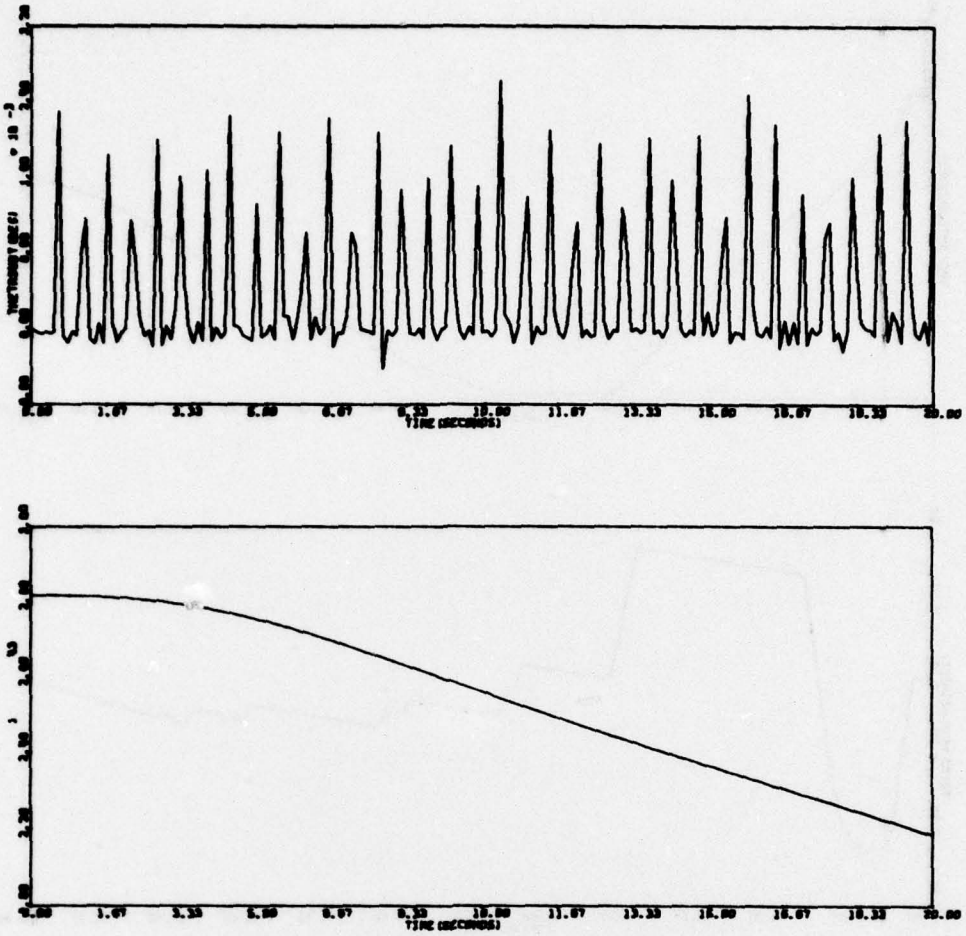

Figure 158. Run SAF04 (concluded)

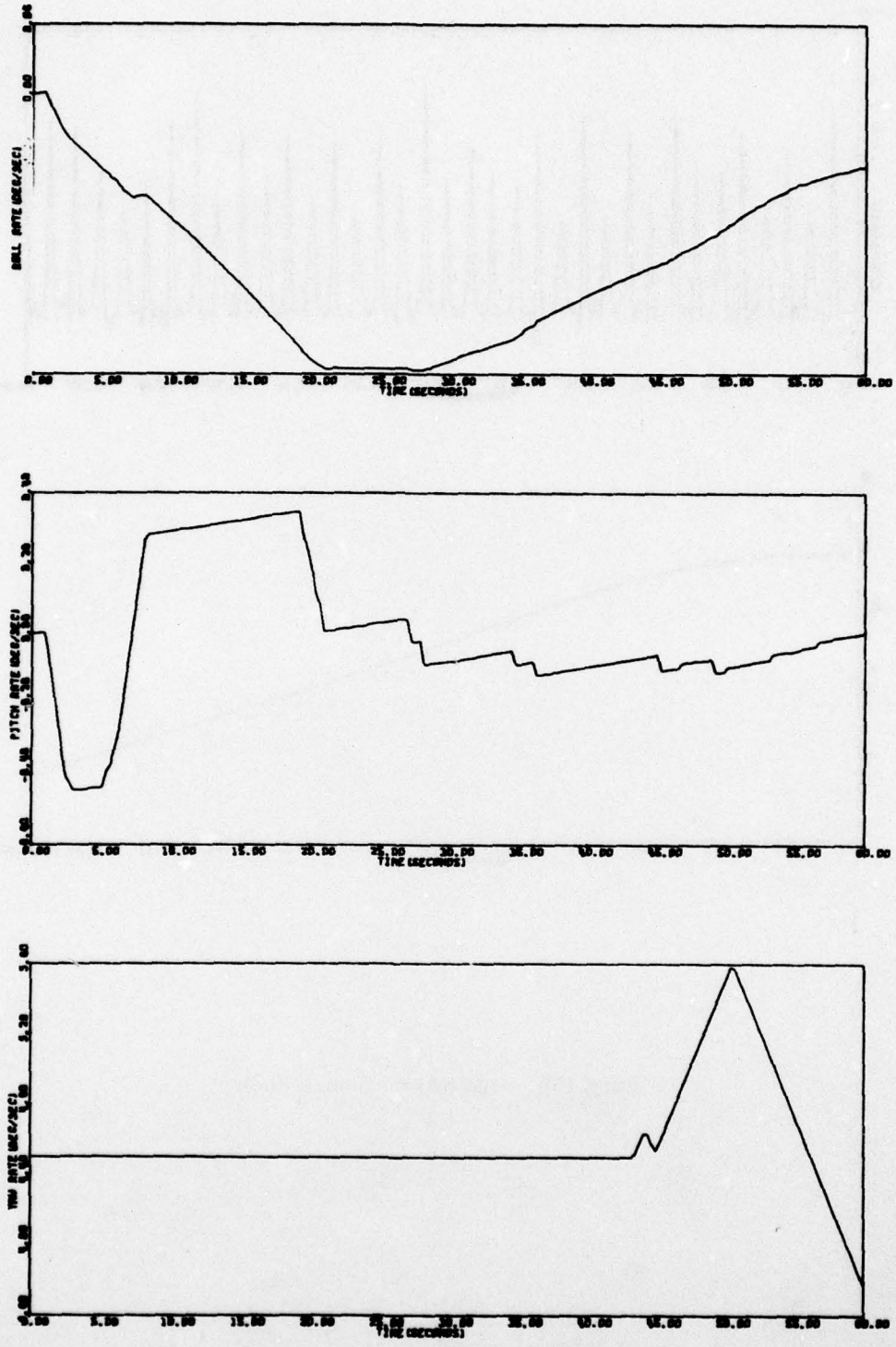

Figure 159. Sun Acquisition with Flexible Arrays

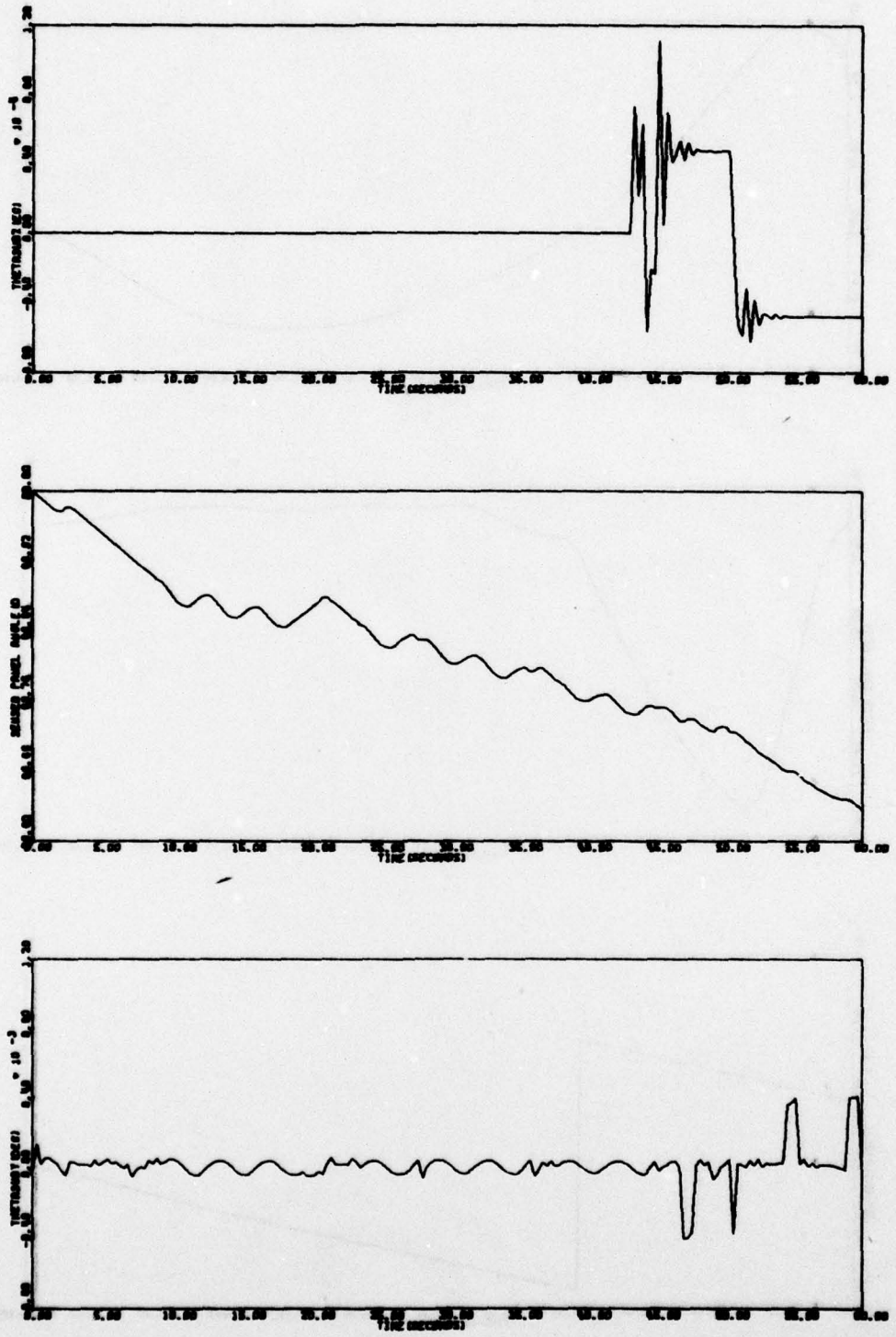

Figure 159. Sun Acquisition with Flexible Arrays (continued)

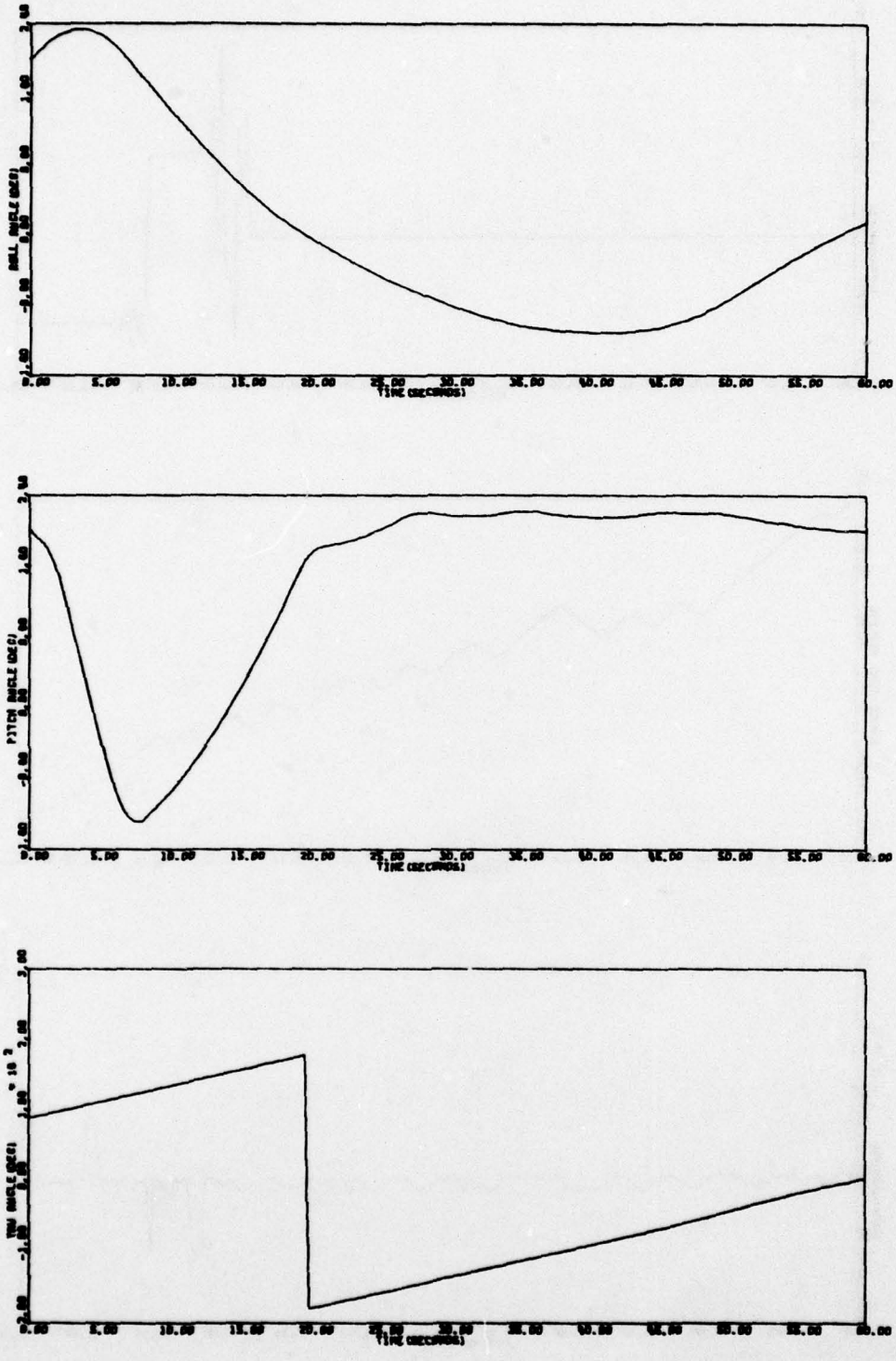

Figure 159. Sun Acquisition with Flexible Arrays (continued)

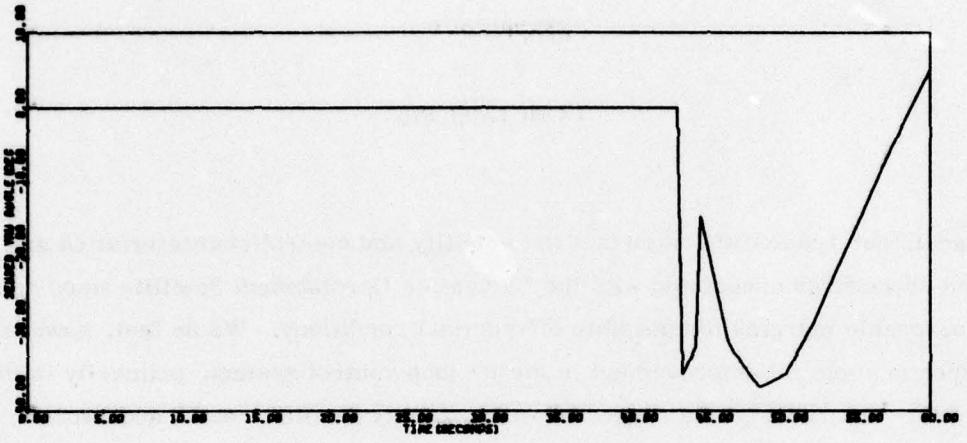

Figure 159. Sun Acquisition with Flexible Arrays (concluded)

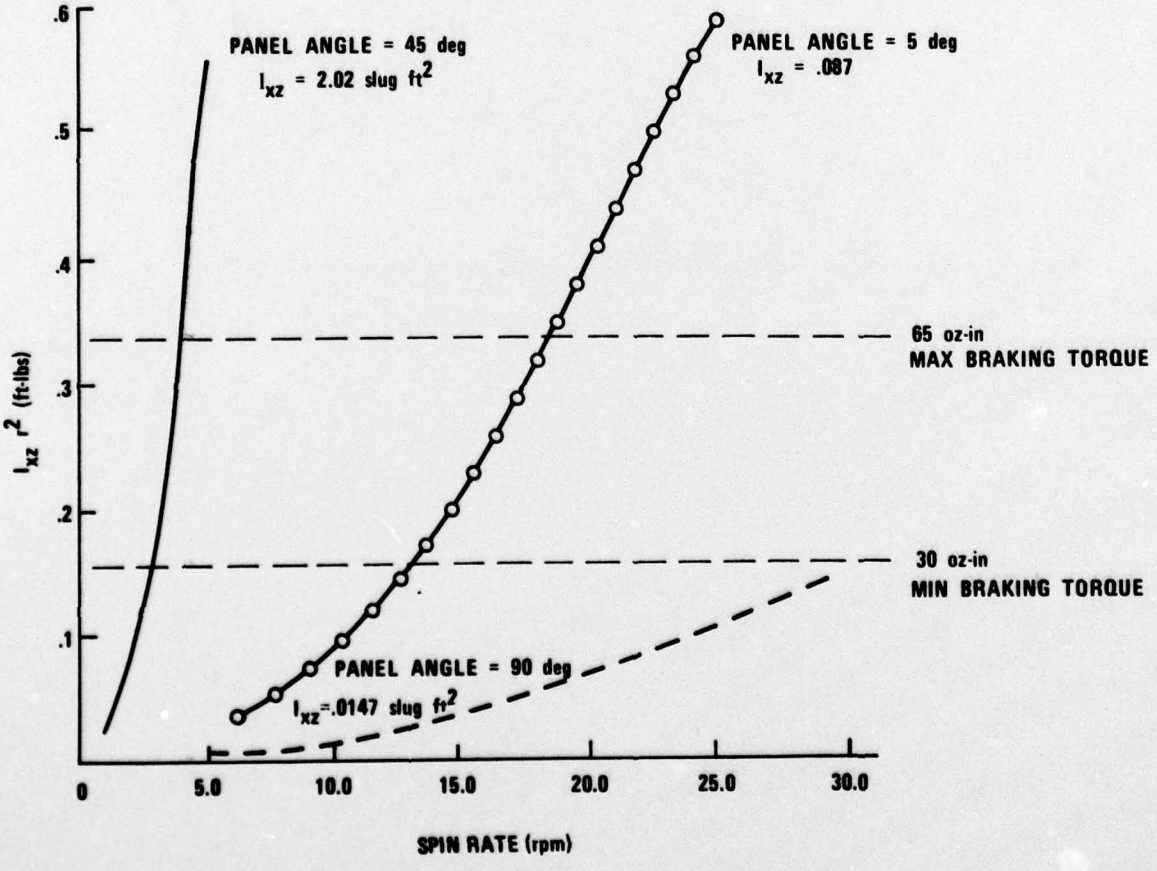

Figure 160. Body Pitching Moment versus Spin Rate

SECTION V

CONCLUSIONS

In general, our results indicated that the stability and control characteristics and mission procedures associated with the Navigation Development Satellite were adequate with reasonable margins for possible off-nominal conditions. We do feel, however, that there is room for improvement in the jet loop control system, primarily in the pitch axis. The redesign we suggested would greatly facilitate earth acquisition procedures.